The metallogenic system and the redox trap in the roll-front type uranium deposit of Zoovch Ovoo, Mongolia. Role of the C and S phases

Dimitrios Rallakis

Université de Lorraine, Collegium Sciences et Technologies
Ecole Doctorale SIRENA "Ressources, Procédés, Produits, Environnement"

Thèse

Présentée pour l'obtention du grade de
Docteur de l'Université de Lorraine
mention "Géosciences"

Par Dimitrios RALLAKIS

Le système métallogénique et le piège redox dans le gisement d'uranium de type roll-front de Zoovch-Ovoo, Mongolie. Rôle des porteurs du carbone et du soufre.

Soutenance publique le 5/07/2019

Membres du jury:

Rapporteurs:

Mrs. Isabel SUAREZ-RUIZ	Instituto Nacional del Carbón (INCAR), CSIC, Spain
M. Jean-Dominique MEUNIER	Directeur de Recherche, Cerege, France

Examinateurs:

Mrs. Anne-Sylvie ANDRE-MAYER	Professeur à l'Université de Lorraine
M. Benjamin BRIGAUD	Maître de Conférences à l'Université de Paris-Sud

Directeurs de thèse:

M. Michel CATHELINEAU	Directeur de Recherche CNRS, Université de Lorraine
M. Raymond MICHELS	Chargé de Recherche CNRS, Université de Lorraine

Invités:

M. Marc BROUAND	Ingénieur à ORANO Mining
M. Olivier PARIZE	Ingénieur à ORANO Mining

Faculté des Sciences et Techniques – Campus des Aiguillettes – Entrée 3B – 54506 Vandœuvre-lès-Nancy Cedex

Université de Lorraine, Collegium Sciences et Technologies
Ecole Doctorale SIRENA "Ressources, Procédés, Produits, Environnement"

Thèse

Présentée pour l'obtention du grade de
Docteur de l'Université de Lorraine
mention "Géosciences"

Par Dimitrios RALLAKIS

The metallogenic system and the redox trap in the roll-front type uranium deposit of Zoovch Ovoo, Mongolia
Role of the C and S phases.

Soutenance publique le 5/07/2019

Membres du jury:

Rapporteurs:

Mrs. Isabel SUAREZ-RUIZ	Instituto Nacional del Carbón (INCAR), CSIC, Spain
M. Jean-Dominique MEUNIER	Directeur de Recherche, Cerege, France

Examinateurs:

Mrs. Anne-Sylvie ANDRE-MAYER	Professeur à l'Université de Lorraine
M. Benjamin BRIGAUD	Maître de Conférences à l'Université de Paris-Sud

Directeurs de thèse:

M. Michel CATHELINEAU	Directeur de Recherche CNRS, Université de Lorraine
M. Raymond MICHELS	Chargé de Recherche CNRS, Université de Lorraine

Invités:

M. Marc BROUAND	Ingénieur à ORANO Mining
M. Olivier PARIZE	Ingénieur à ORANO Mining

Faculté des Sciences et Techniques – Campus des Aiguillettes – Entrée 3B – 54506 Vandœuvre-lès-Nancy Cedex

PREFACE

This thesis was financed by ORANO Mines though CREGU (Centre de Recherches sur la Géologie des Matières Premières Minérales et Energétiques).

The analytical experiments were carried out mainly in the Laboratory of GeoRessources (Université de Lorraine, Nancy, France) and partly in CRPG (Centre de Recherches Pétrographiques et Géochimiques, Vandœuvre-lès-Nancy) and in the Laboratory IJL (Institut Jean Lamour, Nancy).

The field mission in Mongolia was conducted between July-August 2017 with the vital contribution of COGEGOBI, the subsidiary company of ORANO in Mongolia.

ACKNOWLEDGEMENTS

There are not enough words to describe how grateful I am to have my PhD thesis elaborated under the supervision and direction of Dr. Michel Cathelineau and Dr. Raymond Michels. Their scientific expertise and their team spirit were the keys that led to the completion of the present thesis. I highly aknowledge with my sincere gratitude Mrs Nathalie Foucal, Mrs Laurence Moine and Mr. Patrick Lagrange from CREGU for their professionalism and unwavering support that played a catalytic and definitive role to the completion of this thesis.

Since 2015, I was privileged to study at the University of Lorraine and work at the laboratory of GeoRessources. I therefore extend my gratitude to the director of the doctoral school Dr. Jérôme Sterpenich and to the director of the laboratory Dr. Jacques Pironon. I was eager to cooperate with the labarotory's academic and technical personnel in all levels. In particular I thank Dr. Michel Cuney for offering to me his book on the uranium deposits of the world. Dr. Julien Mercadier for helping me to arrange the isotope sessions in CRPG and IJL but also for discussing the obtained results. Dr. Cedric Carpentier for helping with the cathodoluminescence analysis. Dr. Marie-Christine Boiron and Dr. Chantal Peiffert for their contribution to the REE in situ analysis. Dr. Odile Barres for the manipulation of the FT-IR analytical means and the interpretation of the obtained results. Mrs Catherine Lorgeoux and Mrs Delphine Catteloin for their determined support in the organic geochemistry analyses and the interpretation of the results but also for being very open and friendly since my first day in the lab. Dr. Andreï Lecomte and Dr. Olivier Rouer are acknowledged for the crystal chemistry analyses in SEM and EPMA. Mr. Alexandre Flammang and Mr. John Moine for the preparation of the thin sections and polished blocks. Mrs Karine Pistre for helping with the calibration of the microscopes and photometers. Mr. Cedric Demeurie for helping with the storage of the samples and for the training on radioactivity protection. A special thanks to Thomas Rigaudier

and Nordine Bouden from the laboratory of CRPG in Nancy for their contribution towards the bulk-rock and *in situ* analysis of the C, O stable isotopes. Likewise, I am grateful to Denis Mangin from the Institute of Jean Lamour of the School of Mines in Nancy for working together to obtain the S isotopes.

By the same token I would like to acknowledge all the experts from the ORANO Mining Group, Dr. Marc Brouand, Dr. Olivier Parize and Dr. Rémy Chemillac. Their direction and the very frequent scientific exchange determined the success of the thesis. I am indebted to ORANO for providing the funding and the necessary equipment that were required for the completion of the thesis. I am deeply indebted to the team of COGEGOBI, namely to the gentlemen Sebastien Hocquet, Julien Salabert, Vincent Blanchard and all the people from the Dulaan Uul camp for always being friendly, cooperative and supportive despite facing heavy daily schedules. I would like to underline that the logistics and the hospitality provided during our mission in Gobi Desert were outstanding.

I highly acknowledge the members of the jury, Dr. Isabel Suarez-Ruiz, Dr. Jean-Dominique Meunier, Dr. Anne-Sylvie André-Mayer and Dr. Benjamin Brigaud. I truly thank them for accepting the invitation to review my manuscript and participate in my defence.

I am also grateful to the members of my PhD follow-up committee, Dr. Vincent Lagneau and Dr. Mohammed Bussafir for their interest in my subject and for their effort in examining my annual reports.

I would also like to thank all the people that I met and became friends with, during my staying in Nancy. I am very glad to have met Dr. Coralie Biache and Dr. Marine Boulange for being very friendly and supportive, willing to discuss in scientific and personal level. Of course my lab mates, Dr. Nestor Camilo Leguizamon, Mr. Alexy Bahnan as well as Mrs Eleonora Carocci, Mrs Jessica Strydom and Dr. Guillaume Barré, for being honest friends and for helping me to proceed with my experiments and interpretations by exchanging ideas on our Phds.

I am beholden to my parents Athanasios and Vasiliki for enduring throughout my studies, especially during my time abroad and for assisting me unconditionally in every possible way. I am also grateful to my brother Stavros and his fiancée Eleni for willing to discuss my progress and for providing me with their valuable academic advices. I am very eager to have had Anna by my side towards the end of my PhD life. Her patience and profound belief in my success encouraged me and supplied me with the strength to do my best to complete my tasks and this manuscript. Thus, I thank everyone from the bottom of my heart.

Dimitrios Rallakis

5/7/2019

RESUME ETENDU

L'objectif de la thèse consistait à identifier et caractériser les processus qui gouvernent les relations carbone-uranium-soufre dans le gisement uranifère de type roll-front de Zoovch Ovoo (Mongolie). Les réservoirs silicoclastiques de la formation cénomanienne Sainshand contenant le dépôt métallifère ont été déposés dans un environnement fluvio-lacustre caractérisé par des sédiments silto-argileux à sableux (arénitiques à sub-arkoses) non consolidés. Occasionnellement certains bancs sableux décimétriques sont cimentés par de la dolomite.

Les ciments dolomitiques.

Quatre fabriques dolomitiques sont reconnues dans ces ciments et classées selon la géométrie des cristaux et leur géochimie. Elles ont été identifiées comme microcristalline, automorphe, subautomorphe et xénomorphe (Figure A1). La dolomite microcristalline présente de la taille du micron et atteignent occasionnellement 10µm. Ces cristaux plus grands ne sont pas nécessairement visibles en microscopie optique sous lumière naturelle ou polarisée mais sont révélés par cathodoluminescence. Leur distribution est unimodale, ils sont zonés avec des limites nettes. Ces caractéristiques permettent de les identifier dans la masse plus finement microcristalline, qui est terne, rougeâtre et sans structure. Cette dolomite microcristalline est trouvée 1) en ciment des espaces entre des grains non jointifs (grains «flottants») ou 2) sous forme d'agrégats arrondis épars (ayant une taille jusqu'à 0.5mm). Dans ce dernier cas, les relations texturales avec la dolomite polymodale adjacente suggère un phénomène de remplacement graduel. Souvent les agrégats sont associés à de la sidérite.

Le ciment à fabrique automorphe peut apparaître en remplacement du ciment microcristallin mais il apparaît aussi dans l'espace intergranulaire. Il est constitué de rhomboèdres équants bien exprimés avec des faces cristallines nettes et un nucléus sombre en sidérite. La plupart du temps les cristaux sont unimodaux avec une taille maximale de 50µm et des coeurs sidéritiques de 25µm. Les cristaux automorphes peuvent presenter des surcroissances et forment alors une texture poecilitique par ajout de ciment syntaxial. Les cristaux poecilitiques peuvent atteindre 100µm, montrent un parfait emboîtement et induisent une forte diminution de la porosité intergranulaire. Le ciment à fabrique subautomorphe ressemble au type précédent mais se distingue par des bordures cristallines plus irrégulières. En lumière polarisée, ce ciment apparaît non différencié et massif avec une biréfringence d'ordre supérieur et en cathodoluminescence de couleur plus rouge-orangé que les ciments précurseurs. Les cristaux ont une distribution polymodale mais sont bien connectés laissant

très peu de porosité. Les cristaux rhomboédriques pouvent atteindre 50µm et présentent des zonations. Localement, des recristallisations sont reconnaissables par des cristaux jaunâtres plus clairs au sein de la fabrique subautomorphe. Le ciment à fabrique subautomorphe n'est observé que dans les échantillons ayant été affectés par les eaux de roll-front. Le ciment à fabrique idiomorphique consiste en des cristaux aux faces irrégulières, non zonés densément organisés. Sous lumière polarisée le ciment a une allure très massive. Ces cristaux de dolomite apparaissent très différents de ceux des autres types de ciments, avec notamment un pseudo-clivage analogue à celui de la calcite. Sous cathodoluminescence, la fabrique idiomorphique est de couleur orange brillante avec des cristaux non zonés et sans évidence de recristallisation d'un ciment antérieur. Les grès qui contiennent le ciment dolomitique idiomorphique sont caractérisés par une porosité intragranulaire plus élevée que les autres. La pétrographie par microscopie électronique montre clairement que la dolomite idiomorphique est postérieure à toutes les autres phases interstitielles (les autres ciments dolomitiques, les sulfures, le quartz authigénétique). Elle est par conséquent très probablement la dernière expression de la succession diagénétique. Elle est présente à l'intérieur et en-dehors des zones de roll-front.

Malgré ces distinctions pétrographiques, les ciments dolomitiques présentent des compositions isotopiques en O et C plutôt homogènes avec des valeurs moyennes de $\delta^{18}O$=-10±1‰ (PDB) and $\delta^{13}C$=-7±1‰ (PDB). Les valeurs de $\delta^{18}O$ sont interprétées comme héritées d'eaux météoritiques typiques de composition isotopique proche des eaux actuelles. Les valeurs de $\delta^{13}C$ suggèrent un carbone probablement hérité de l'érosion de roches du socle. Une décroissance des teneurs en Mn et terres rares dans la séquence diagénétique des ciments dolomitiques est observée. Par exemple, les teneurs en terres rares décroissent d'un facteur 30 de la variété microcristalline à automorphe, subautomorphe puis idiomorphique, accompagné d'une augmentation des terres rares lourdes. Ceci suggère que ces variétés de ciments sont génétiquement liées par des épisodes de recristallisation successifs.

En prenant en compte l'ensemble des données, une succession paragénétique pour les ciments dolomitique est proposée, qui reflète une évolution dans les interactions fluides-roches (incluant les activités de roll-front). Le premier ciment dolomitique (microcristallin) est formé sous contrôle de l'environnement de dépôt tandis que les trois générations suivantes reflètent la diagénèse d'enfouissement. La troisième génération (fabrique subautomorphe) est exclusivement liée aux activités de roll-front et la quatrième génération (fabrique idiomorphique) est postérieure à toutes les autres phases interstitielles. Dans l'ensemble de sédiments très majoritairement non consolidés de la formation Sainshand, les ciments dolomitiques forment ainsi le seul indicateur d'une évolution diagénétique dans l'histoire d'enfouissement de la formation Sainshand (Figure A2).

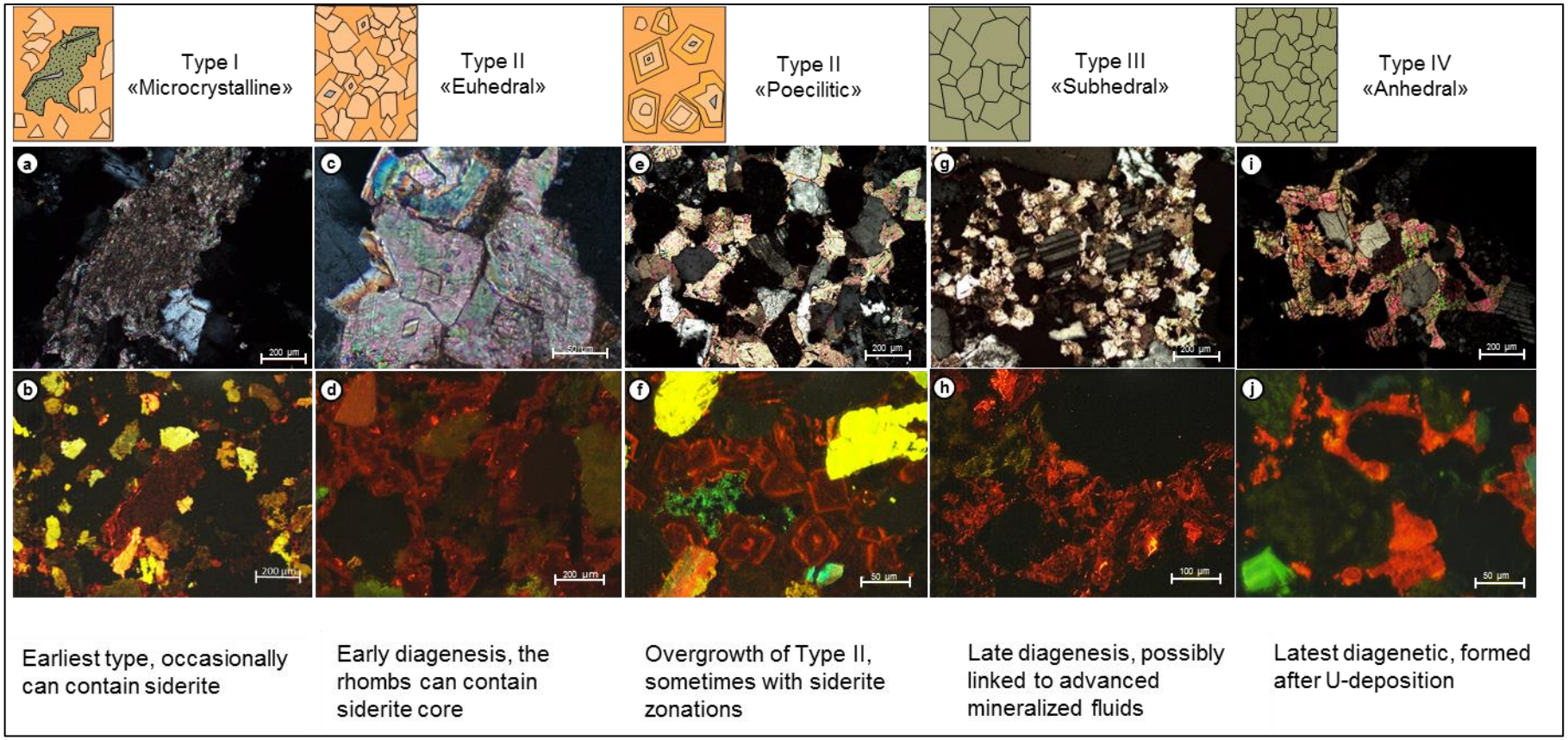

Figure A1: Photographies de microscopie optique polarisée/analysée (en haut) et de cathodoluminescence (en bas); (a, b) La fabrique microcristalline apparaît comme un ciment uniforme ou en paquets et peut localement contenir de la siderite; (c, d) Les cristaux rhomboédriques de la fabrique automorphe peuvent évoluer vers de grands cristaux poecilitiques par surcroissance syntaxiale et présentent souvent des coeurs/zonations de sidérite ; (e, f); (g, h) La fabrique subautomorphe se développe au dépend des autres fabriques; (i, j) La fabrique idiomorphique se présente sous forma d'un ciment uniforme dans lequel les cristaux ne peuvent être distingués.

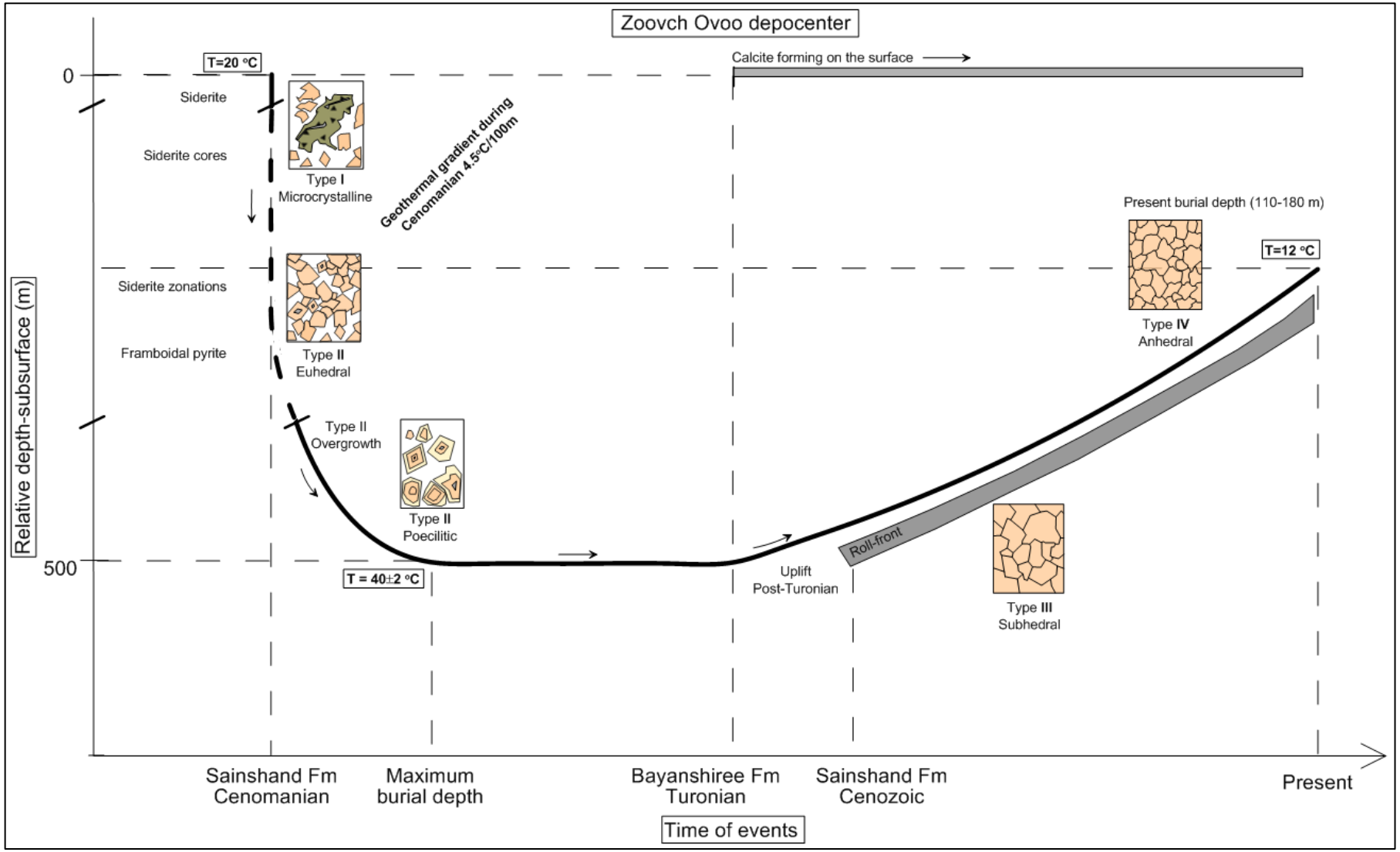

Figure A2: Modèle proposé pour l'évolution des ciments dolomitiques de la formation Sainshand de Zooch Ovoo. La température de surface et le gradient géothermique sont de Prost (2004). Les flèches noires indiquent le régime d'enfouissement.

Pétrographie et cristallochimie des pyrites.

L'étude cristallochimique des pyrites permet d'identifier huit formes différents, caractérisés par la morphologie des cristaux, leurs contenances en éléments traces et leurs relations paragénétiques aux autres minéraux (autres sulfures, minéraux d'uranium, dolomite). Les types de pyrites associées aux minéraux d'uranium présentent des caractéristiques particulières dans leurs contenus en éléments traces. L'ensemble des données obtenues a conduit à identifier au moins 4 générations de pyrites, ainsi que le polymorphe marcassite (Figure A3). Elles se présentent sous forme framboïdale, en surcroissance concentriques et automorphes (antérieures et contemporaines de la minéralisation).

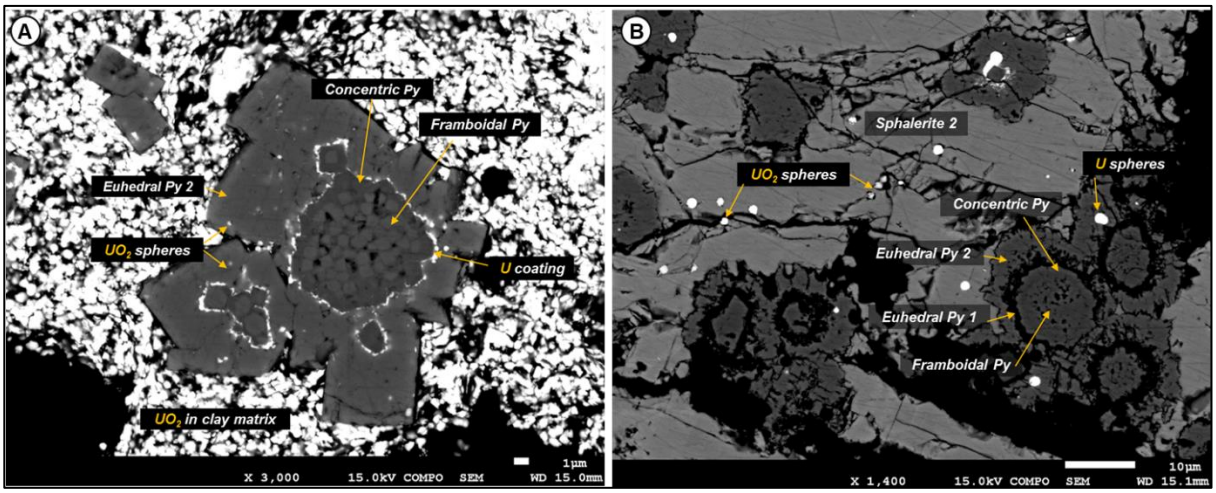

Figure A3: Les quatres générations de pyrites; (A,B) sphères de UO_2 dans les cristaux automorphes.

Parmi les caractéristiques géochimiques, de remarquables variations dans les valeurs de $\delta^{34}S$ sont observées. En effet, les valeurs isotopiques s'étendent de -50 à +50 ‰. Les framboïdes isolés présentent plutôt des valeurs positives centrées sur 10±5 ‰, tandis qu'elles sont plutôt négatives (-18±5 ‰) pour la pyrite automorphe. En l'absence de minéraux contenant du soufre dans les sédiments détritiques, cet élément pourrait provenir de la dissolution des sulfates (gypse ou célestite) formés par évaporation des eaux de surface et transférés par les eaux météoriques dans le fluide minéralisateur des roll-fronts. Selon la littérature, la valeur initiale de $\delta^{34}S$ de sulfates dérivant de l'évaporation en milieu continental s'échelonne entre +20 et +35 ‰. Les valeurs isotopiques très négatives du soufre réduit est cohérente avec l'action des microorganismes sulfato-réducteurs. L'étalement des données jusqu'aux valeurs très positives pourraient s'expliquer par du fractionnement isotopique dans un système fermé. Ceci suggère que les roll-fronts à Zoovch Ovoo fonctionneraient en système semi-ouverts dans lesquels de nouvelles charges de sulfate seraient introduites puis évolueraient isotopiquement vers des compositions enrichies en isotopes lourds pendant les périodes sans apport hydrique supplémentaire. Ceci expliquerait pourquoi les types pétrographiques de pyrite ne peuvent pas

être systématiquement discriminés sur la base de leurs valeurs en $\delta^{34}S$ puisque la composition isotopique du soufre n'était pas homogène le long des roll-fronts à travers le temps.

Relations entre matière organique et uranium.

Les particules de matière organique, la pyrite et l'uranium sont très intimement liés. La matière organique présente dans les faciès silto-argileux, les silts et les structures sédimentaires des sables (par exemples dans les intraclastes de base de banc ou dans les litages obliques) est en majorité représentée sous forme d'éléments détritiques mal préservés provenant de plantes supérieures et de très faible maturité thermique (Ro<0.4%). Les fortes valeurs de Tmax cependant notées sont liées à la forte altération de la matière organique (confirmée par PyGCMS ety la microspectroscopie infra-rouge), attribuée à l'oxydation et la radiolyse. Le gaz désorbé des échantillons contient 92% de CO_2 et 2.5% de CH_4 dont les compositions isotopiques suggèrent une origine bactérienne. Les alcènes présents en traces trouvent leur origine dans la radiolyse de la matière organique.

Les particules de matière organique contiennent jusqu'à 50% en masse d'uranium sans expression minérale. Le remplacement épigénétique des particules de matière organique par UO_2 (avec préservation partielle des structures macérales) est très souvent observé (Figure A4).

Le minerai d'uranium se trouve sous la forme d'uraninite (UO_2) et moins souvent comme phospho-coffinite $(U,P)SiO_4$. Le calcium est souvent présent dans ces minéraux et peut atteindre 5% en masse. L'uranium se trouve ainsi (i) dans la matière organique (kérogène de type III sous forme d'éléments détritiques) exprimé ou non sous forme minérale (ii) en inclusions à l'intérieur de la pyrite automorphe et la sphalérite (iii) en épigénèse des ciments de pyrite et de sphalérite (iv) en ciment dans les matrices argileuses (v) en ciment entre les cristaux automorphes du ciment dolomitique (vi) associé au ciment quartzeux (vii) en remplacement des oxydes de fer-titane (vii) à l'intérieur de la porosité de silicates détritiques.

Les observations pétrographiques associées aux données géochimiques permettent de distinguer au moins quatre épisodes majeurs de dépôt d'uranium liés à l'activité des roll-fronts. Le premier épisode de dépôt a lieu directement après la cristallisation de la première génération de pyrite automorphe et se traduit sous forme de fine surcroissance. Mis à part la possibilité d'un piégeage synsédimentaire (stade de préconcentration qui n'a pas pu être formellement démontrée), la fixation de l'uranium sur la matière organique (adsorption/complexation) serait contemporaine de ce premier épisode. Le second épisode de formation de pechblende est contemporain de la précipitation de la seconde génération de pyrite automorphe et de la sphalérite dans lesquelles elle se trouve sous formes de micro-sphérules. Le troisième épisode de dépôt est caractérisé par une pechblende massive formant

un ciment entre les grains détritiques. Enfin, le quatrième épisode dépose un minéral d'uranium dont la composition est de type phospho-coffinite. Il a aussi été observé que la pechblende peut subir une coffinitisation limitée en phase tardive de diagénèse. Les échantillons qui contiennent la phospho-coffinite présentent également un ciment de quartz d'extension locale à l'échelle du microscope. Sous cathodoluminescence, le quartz détritique peut présenter des franges d'altération radiolytique en absence de minerai d'uranium. Ceci indique des épisodes antérieurs de dépôt et de dissolution liés aux activités de roll-front.

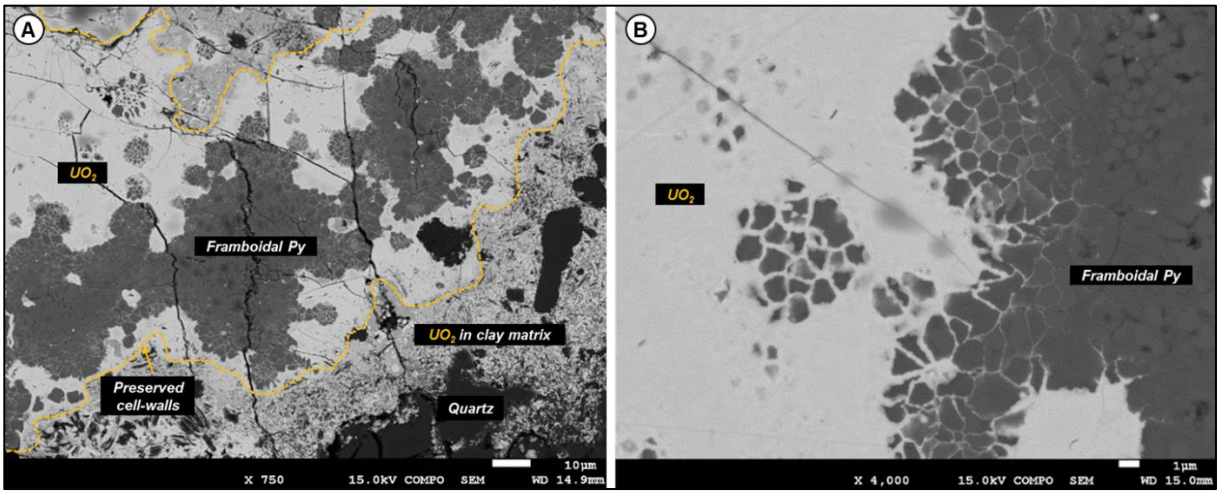

Figure A4: Le remplacement épigénétique des particules de matière organique par UO_2 qui ont été remplacés par pyrite antérieurement.

Mécanismes de précipitation de l'uranium.

Malgré une association systématique de l'uranium avec la matière organique, le carbone organique ne peut pas être considéré comme un réducteur direct de $U^{(VI)}$ à cause d'une trop faible température d'enfouissement (max 50°C) et donc d'une diagenèse très limitée.

La présence de la pyrite posait la question de l'origine du soufre réduit dans des sédiments silico-clastiques. Cependant, le sulfate est présent dans les eaux de roll-front et est la seule source de soufre. La pétrographie et la cristallochimie de la pyrite révélait que le soufre réduit était attribué à l'activité de microorganismes sulfato-réducteurs. Le seul substrat carboné disponible dans ces sédiments est la matière organique fossile à laquelle la pyrite est intimement associée. Ainsi, la matière organique détritique est-elle considérée comme substrat nutritif entretenant et focalisant l'activité bactérienne dans des structures sédimentaires spécifiques.

Cependant, il est démontré dans la littérature que des bactéries utilisant des métaux multivalents (comme le $Fe^{(III)}$) comme source d'électron pour maintenir leur métabolisme préfèrent l'uranium lorsqu'il est présent dans le milieu de culture. Les bactéries réduiraient ainsi l'$U^{(VI)}$ afin de former l'uraninite ou la coffinite, tel qu'observé à Zooch Ovoo. La littérature indique aussi que la biomasse bactérienne peut piéger l'uranium sous une forme non cristalline

d'$U^{(VI)}$, ce qui expliquerait les très fortes concentrations d'uranium dans les particules de matière organique.

Ainsi, les communautés bactériennes utilisant la matière organique fossile comme source de carbone catalyserait la réduction du soufre et de l'uranium, ce qui conduit à deux conséquences majeures : 1) la fixation de l'uranium et/ou la précipitation de UO_2 à la surface des particules organiques et 2) la formation de la pyrite qui agit comme un autre réducteur majeur de $U^{(VI)}$. En plus de la distribution de la matière organique détritique dans le système sédimentaire, la localisation des dépôts d'uranium sera aussi pilotée par le réseau de perméabilité du réservoir qui contrôle les apports de S, U et des micro-organismes.

Le piège biogéochimique de Zoovch Ovoo.

En considérant toutes les discussions précédentes, un modèle métallogénique pour le dépôt de l'uranium et des phases associées peut être proposé (Figure A5).

Dans ce modèle il n'y a pas de pré-concentration significative en uranium. Trois zones sont considérées, respectivement oxydée, réduite et leur interface, là où l'uranium est déposé. L'$U^{(VI)}$, le sulfate et les bactéries sont transportés en solution par les eaux oxydantes météoriques qui percolent à travers le réservoir sableux. Les minéraux uranifères et la pyrite déposés antérieurement sont oxydés, ainsi U et S sont remobilisés. Dans la partie réduite du roll-front, $U^{(VI)}$ est piégé au contact des particules de matière organique, par l'association matière organique-biomasse bactérienne, les sulfures (principalement la pyrite), les oxides Fe-Ti, les argiles contenant du fer réduit et adsorbant du soufre natif. Les épisodes successifs d'oxydation et de réduction induits par les mouvements du roll-front à travers le temps permettent d'augmenter la quantité d'uranium à l'interface des zones oxydantes et réduite.

Les agents réducteurs de l'uranium sont de deux types, abiotique et biotique. Le premier type concerne la réduction de l'uranium par la pyrite (c'est-à-dire principalement le soufre réduit, mais aussi le $Fe^{(II)}$ à la surface du solide), les oxydes Fe-Ti (magnétite et ilménite). Le second type concerne la réduction liée à l'activité de consortia de bactéries (par exemple, réductrice du $Fe^{(III)}$, sulfato-réductrices, méthanogènes) responsables du piégeage de l'uranium dans la matière organique, de la formation de UO_2 et de la coffinite par réduction de $U^{(VI)}$.

En conséquence la matière organique joue un rôle primordial dans la formation du gisement de Zooch Ovoo en jouant le rôle de substrat nutritif pour les bactéries qui contrôlent de façon directe et indirecte la réduction de l'uranium dans le roll-front.

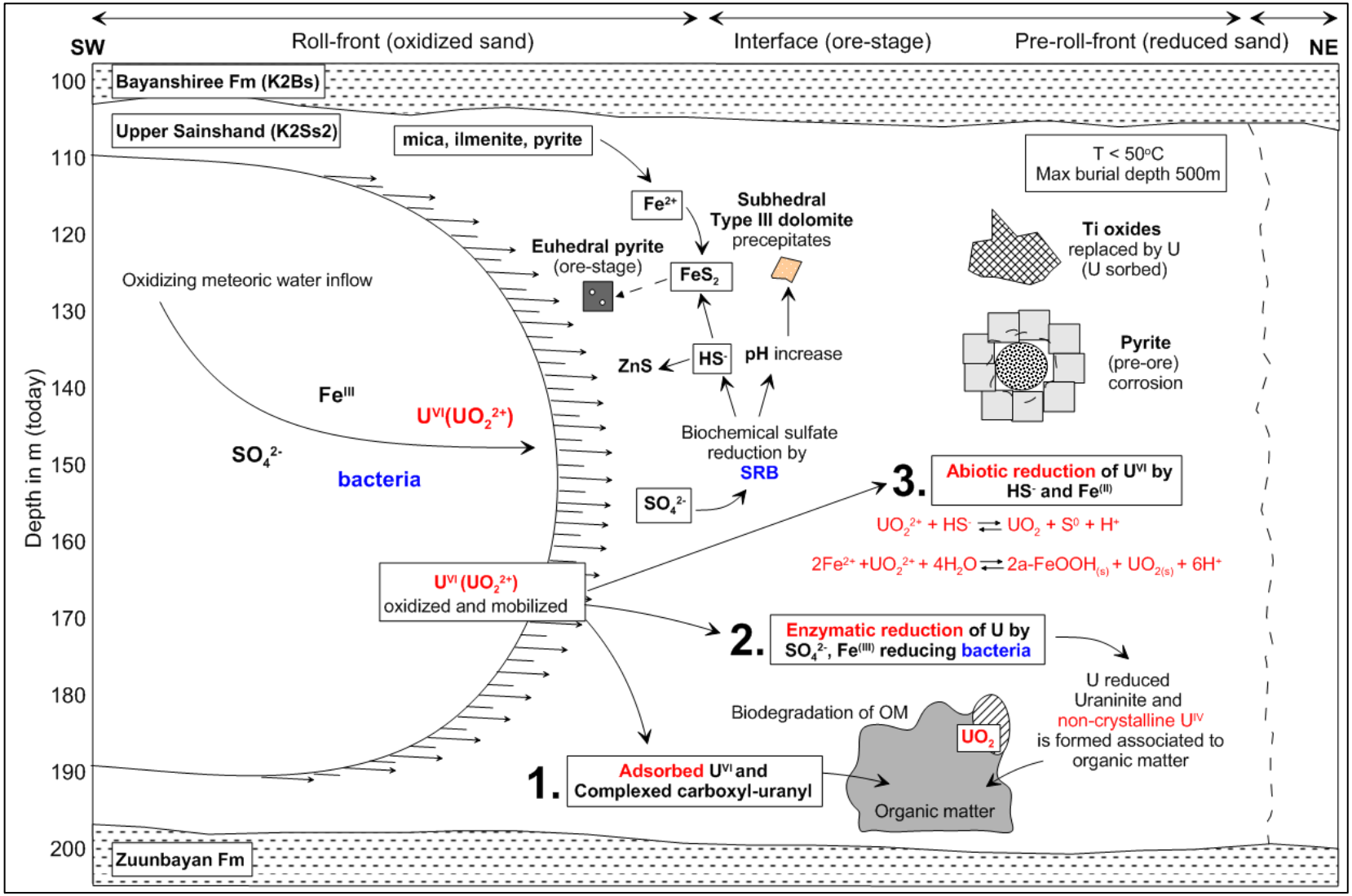

Figure A5: Proposition de modèle métallogénique pour le dépôt de l'uranium et les phases diagénétiques associées à Zooch Ovoo. L'épaisseur maximale du réservoir est de 100m.

Ainsi, il apparaît que les bactéries sont essentielles au contrôle des conditions des réactions d'oxydo-réduction dans les roll-fronts de Zooch-Ovoo.Elles sont impliquées dans :

i. La réduction directe de $U^{(VI)}$ en $U^{(IV)}$ par des bactéries qui utilisent $U^{(VI)}$ comme source d'électrons plutôt que le Fe(III) par exemple. Ce mécanisme permet la formation de l'uraninite ou de film biologiques enrichis en U (pas de forme minérale exprimée).
ii. La réduction du sulfate en des espèces réduites du soufre tel que S_0, des sulfures de fer amorphe soufre réduit (mackinawite), marcassite, spahlérite, pyrite. La pyrite est essentielle dans le mécanisme rédox de piégeage de l'uranium.
iii. L'analyse des gaz désorbés des échantillons de Zooch Ovoo révèlent la présence de CO_2 et de CH_4 provenant d'une activité bactérienne actuelle. Le CO_2 (98% de la composition du gaz) est lié aux activités bactériennes aérobies dans la partie oxydée des rolls-fronts. Le méthane provient d'une communauté méthanogène située dans la partie réduite.

Conclusion.

Dans le gisement d'uranium de Zooch Ovoo, la matière organique fossile provenant de plantes supérieures apparaît comme un substrat nutritif pour les activités bactériennes responsables de la réduction du soufre et de l'uranium. Le contrôle de premier ordre de la distribution de la matière organique dans le dispositif sédimentaire était l'environnement de dépôt qui concentrait le kérogène dans les structures des bancs sableux. Ces derniers font aussi partie du réseau perméable permettant la circulation des eaux et ainsi l'apport de S, U et des microorganismes. Ceci explique pourquoi l'uranium est systématiquement associé aux particules de matière organique et à la pyrite, présentes spécifiquement dans les faciès sableux. Les aquifères peu profonds ont été le siège d'une activité bactérienne quasiment continue qui est responsable des nombreuses caractéristiques et processus contrôlant la précipitation de l'U et de sulfures. Les principaux événements de dépôt de l'uranium ont lieu depuis le début de la phase d'exhumation lorsque les eaux météoriques commencèrent à percoler dans la formation Sainshand, entretenant l'activité de roll-front. Ces derniers déplacent et combinent les ingrédients du piège biogéochimique permettant un enrichissement en uranium à travers le temps. Les mécanismes de piégeage impliquent la complexation (complexes uranyl-carbonyl par exemple), l'adsorption (sur les particules détritiques organiques, les biofilms et les argiles), la réduction par les bactéries (uraninite et en formes mal cristallisées d'U des biofilms) et la réduction par la pyrite.

Table of contents

Figures

Tables

Table 1: Abbreviations used in the text for mineral names and analytical techniques.

Mineral Name	Symbol	Mineral Name	Symbol
Quartz	*Qz*	Ilmenite	*Ilm*
Feldspar	*Fsp*	Anatase	*Ant*
Muscovite	*Ms*	Barite	*Brt*
Plagioclase	*Pl*	Sphalerite	*Sp*
Microcline	*Mc*	Zirconium	*Zrn*
Albite	*Ab*	Magnetite	*Mag*
K-feldspar	*Kfs*	Tourmaline	*Tur*
Carbonate minerals	*Cb*	Pyroxene	*Px*
Chlorite Group	*Chl*	Hematite	*Hem*
Biotite	*Bt*	Marcasite	*Mrc*
Amphibole	*Amp*	Rutile	*Rt*
Sericite	*Ser*	Xenotime	*Xtm*
Hornblende	*Hbl*	Apatite	*Ap*
Pyrite	*Py*	Monazite	*Mnz*
Clay minerals	*Clays*	Lithic elements	*Lith*
Mica Group	*Micas*	Organic matter	*O.M*

Abbreviation	Definition
LPA	Polarized Light (*Lumière polarisée analysée*)
LPNA	Plain light petrography (*Lumière polarisée non-analysée*)
RL	Reflected Light (*Lumière réfléchie*)
BSE	Back-scattered electrones
CL	Cathodoluminescence
EMPA	Electron Micro-Probe Analysis
SEM-EDS	Scanning Electron Microscopy-Energy Dispersive Spectroscopy
LA-ICP-MS	Laser Ablation-Inductively Coupled-Mass Spectroscopy
D.L	Detection Limit
b.d.l	Below Detection Limit
REE	Rare Earth Elements
at%	Atomic percent
wt%	Weight percent
TIC	Total Inorganic Carbon
FT-IR	Fourier transform infrared spectroscopy
XRF	X-ray Fluorescence
PyGCMS	Pyrolysis Gas Chromatography Mass Spectrometry
TMAH	Tetramethylammonium hydroxide
DCM	Dichloromethane
EXAFS	Extended X-ray absorption fine structure

CHAPTER I

Introduction, state of the art, objectives of the thesis

1.1 INTRODUCTION

Uranium deposits are internationally classified between 12 or 15 types with the first 12 being more typical (Table 2). This study focuses on the roll-front sandstone type deposits. The roll-front deposits are epigenetic and occur in feldspar rich, medium to coarse-grained, sandstones (arkoses), deposited in terrestrial (fluvial) and marginal marine settings (Sanford, 1994). There are over seven common minerals that contain uranium in high quantity and can contribute to uranium ore (Table 3).

No	Type of Deposit
1	Sandstone type
2	Related to Proterozoic unconformities
3	Related to breccia complexes
4	Volcanic type
5	Intrusive type
6	Metasomatic type
7	Vein type
8	Related to quartz-conglomerates
9	Superficial type
10	Metamorphic type
11	Breccia-pipe infill type
12	Associated with phosphate
13	Related with lignite and coal
14	Related with black shales
15	Other types

Table 2 (left): Different types of Uranium deposits sorted according to the 2007 production rates (Lagny et al., 2010).

Table 3 (down): The most common uranium minerals (Cuney and Kyser, 2009).

Mineral	Chemistry	Typical Depositional Environment
Uraninite	Uranium Oxide **UO_{2+x}**	Magmatic, hydrothermal or sedimentary-hosted deposits
Pitchblende	Uranium oxide **UO_{2+x}** (botryoidal variety of uraninite)	Hydrothermal or sedimentary-hosted deposits
Coffinite	Uranium silicate **$USiO_4$**	
Brannerite	Uranium titanate **$(U,Ca,Ce)(Ti,Fe)_2O_6$**	
Carnotite	Uranyl vanadate **$K_2(UO_2)_2(VO_4)_2 \cdot 2H_2O$**	Sandstone-hosted deposits, calcrêtes
Tyuyamunite	Uranyl vanadate **$Ca_2(UO_2)_2(VO_4)_2 \cdot 8H_2O$**	Sandstone-hosted deposits
Uranophane	Uranyl silicate **$Ca(UO_2)_2(SiO_3OH)_2 \cdot 5H_2O$**	Sandstone-hosted deposits Alteration of Uranium Oxide

Fifteen countries own the 95% of the proven global uranium reserves. In this context the share of Mongolia is 2% up to 2018 (Figure 1). Currently the exploration is focused in sandstone deposits ameneable to in-situ leaching (ISL) located in southern Mongolia. The sandstone deposits are divided in five main sub-types, namely: basal channel, tabular, roll-front, tectonic/lithologic and mafic dyke/sill deposits (IAEA, 2018). The present study is about the roll-front type deposit of Zoovch Ovoo located in the Zuunbayaan sub-basin located in East Gobi Basin, in SE Mongolia.

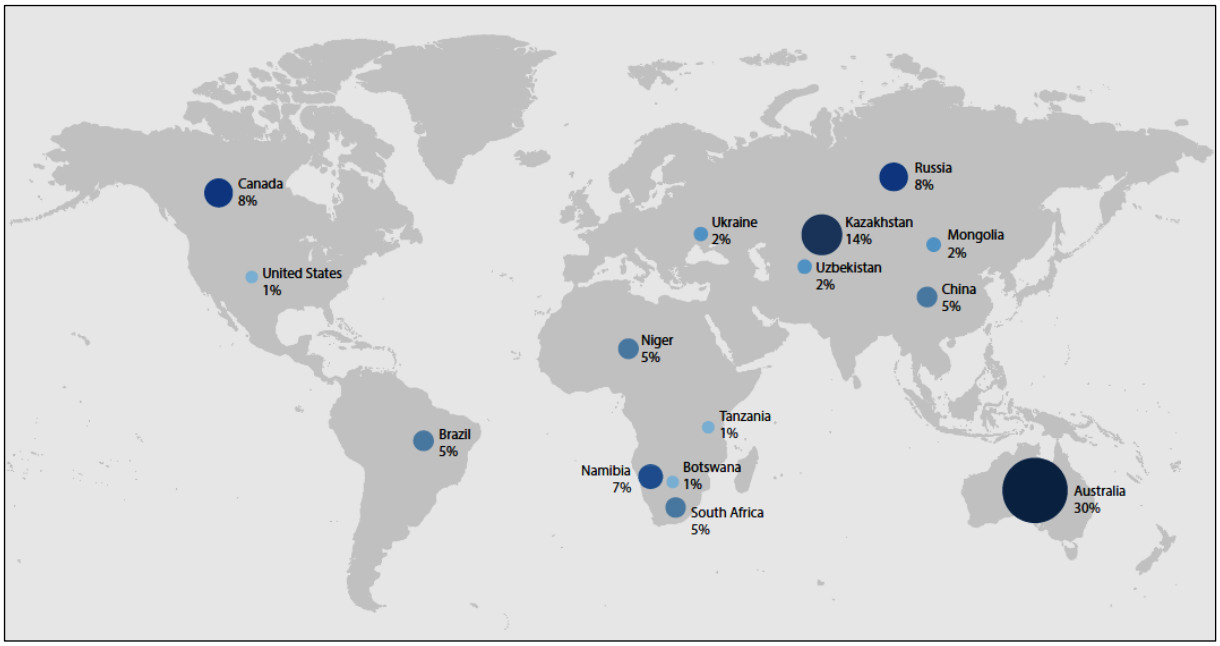

Figure 1: The worldwide distribution of the global uranium resources in countries that are currently producing U-ore or have high potential in exploiting in the near future. The 15 countries illustrated possess the 95% of the global uranium reserves. The rest 5% is spread among 22 countries. Mongolia is currently owing the 2% of the world's uranium proven reserves (IAEA, 2018).

1.2 ROLL-FRONT TYPE DEPOSITS

1.2.1 Definition of a roll-front

The roll-front deposits have crescent geometry (C-shape) and occur more commonly in sandstone beds that are confined in between semi-permeable formations. Uranium is being carried in solution by mineralizing fluids as $U^{(VI)}$ that advance through the permeable sandstones following the geometry of the hydrologic gradient. When the carrier fluid encounters reducing agents (e.g. organic matter, pyrite), uranium is reduced to $U^{(IV)}$ and occupies the intergranular porosity of the sandstone bodies, as cement. The roll-fronts are inclined, usually with a dip around 3^{o}. They have diffusive boundaries with the downward reduced sandstone and sharp edges with the onward oxidized sandstone (Figure 2). Hence, the interface between the oxidizing and reducing zones is a dynamic system where the redox status is controlled by the movement of the mineralizing fluid. The zones of mineralization are elongated, almost parallel to the strike and perpendicular to the direction of the groundwater flow (Dahlkamp, 1993). The roll-front type deposits can contain up to several thousands of tons of U with grades ranging between 0.05-0.25%. Currently the most important discoveries being located Kazakhstan, United States and Uzbekistan (IAEA, 2018).

1.2.2 Introduction to the roll-front systems

The most typical examples to study roll-front deposits are found in Wyoming, where four districts host U-mineralization, the Wind River, the Shirley, the Powder and the Great Divide

basins. The concentration of uranium in these basins ranges around 0.05-0.25 wt% and the age of the host rocks is Cenozoic. The lithology of the host rock is mainly described as friable fine to coarse-grained or pebbly, arkosic sandstone with considerable amounts of pyrite and carbonate minerals. The carrier bed has greenish to grey color in the reduced state. The extension of the roll-fronts varies from tens of km up to 100 km from one basin to another. The oxidation of the sandstone bodies with the progressive development of the roll-front leads to the formation of uranium mineralization on one hand and higher Se, $CaCO_3$, organic carbon and sulfate contents on the other (Figure 2). Iron minerals e.g. pyrite and magnetite are also partially or completely replaced in favor of U-mineralization. The principal uranium ores in the Wyoming districts are uraninite and coffinite (Table 3). They occur as coatings on the sand grains but also as pore fillings and as organic matter associations. Hence, the unconsolidated coarse-grained water saturated arkose reservoirs host disseminated uraninite ore. Authigenic (non-detrital) minerals are limited to massive uraninite, pyrite-marcasite and occasionally barite. The most probable sources for uranium in Wyoming are the Archean-Lower Proterozoic granitic rocks which surround the sedimentary basins and compose the basement, as well as the Eocene volcanic tuff horizon that overlies the host-sandstones (Dahlkamp, 1993; Cuney and Kyser, 2009).

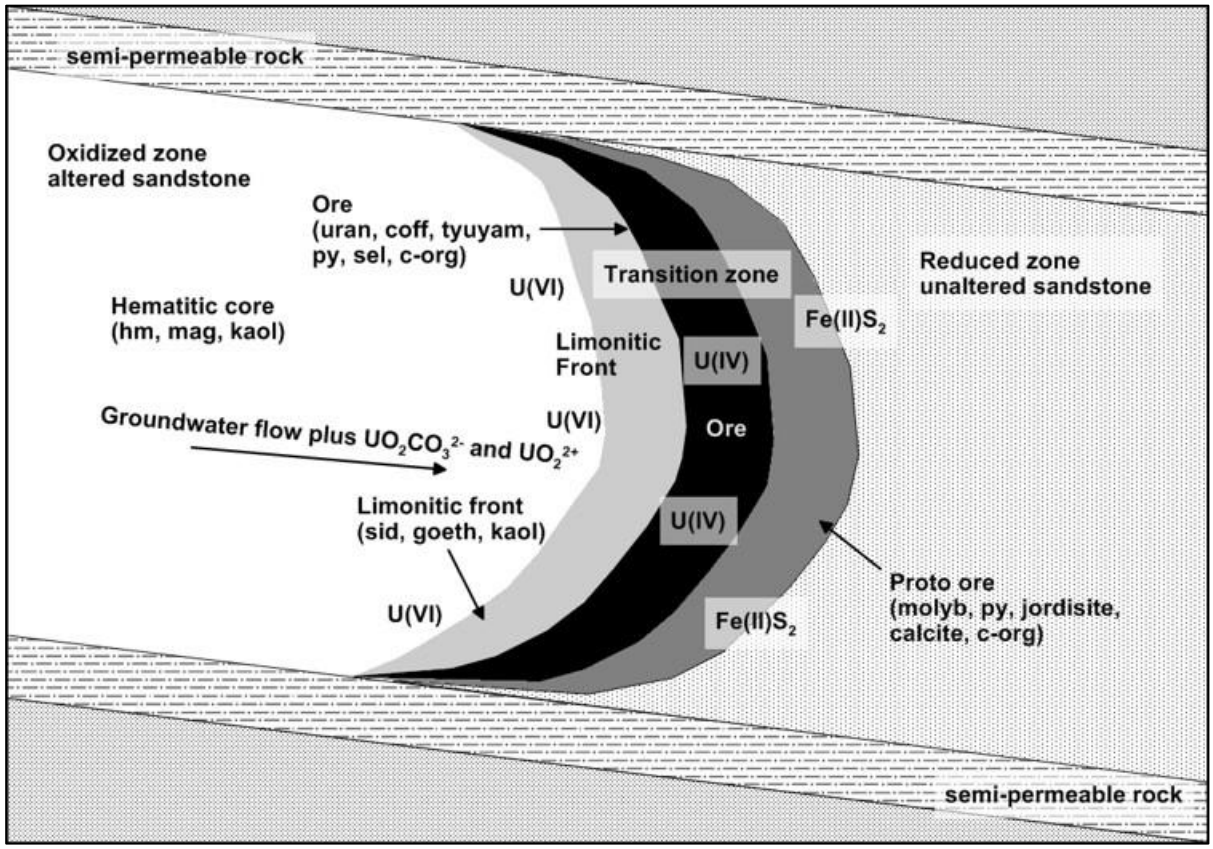

Figure 2: Conceptual model of a roll-front U-deposit with the zones of alteration and associated minerals, namely: hm/hematite; mag/magnesite, kaol/kaolinite; sid/siderite; goeth/goethite; uran/uraninite; coff/coffinite; tyuyam/tyuyamite; py/pyrite; sel/selenite; molyb/molybdenite; c-org/organic carbon (Cuney and Kyser, 2009).

1.2.3 Main features of roll-front deposits

Roll-type uranium deposits illustrate the importance of oxydo-reduction processes in sedimentary deposits. The formation of these deposits is the result of the oxidation of sedimentary reservoirs by waters equilibrated with the atmosphere, generally following tectonic movements affecting a geological formation originally buried and confined in a confined environment. The arrival of meteoric waters will therefore oxidize and dissolve a number of elements. A redox front is formed in contact with neutral to alkaline oxygen infiltration water and reductive rock and moves through the receiving formation (Granger and Warren, 1969; Harshman, 1972; Rackley, 1972). As a result, the geochemical characteristics of the host rock are modified. Field observations reveal an epigenetic zone of the surrounding rock in which an oxidized zone is roughly distinguished according to the direction of water flow, a mineralized zone at the interface and a reduced zone with roll-type mineralization (Figure 3).

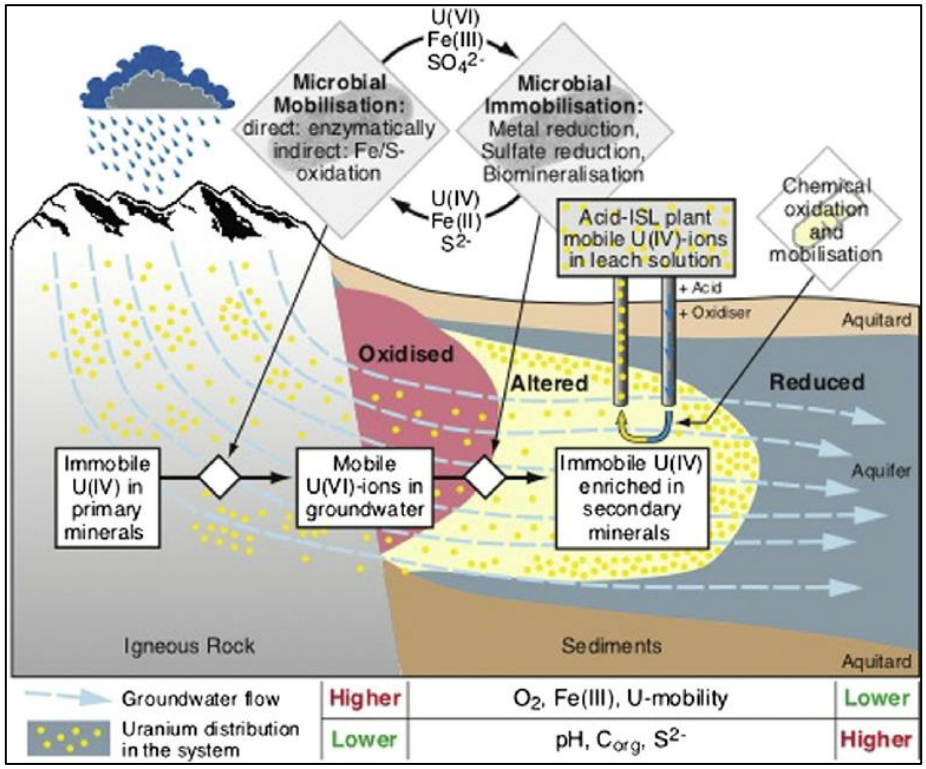

Figure 3: Model of roll-front U deposit proposed by Zammit et al. (2014).

The infiltration water will gradually enrich itself with various elements (i.e. uranium, vanadium, copper, iron, selenium) by altering the minerals disseminated in the formation. Due to the diversity of their oxidation state, these elements will be involved in redox reactions. However, only the most abundant ones will significantly modify the physical-chemical characteristics of the carrier fluid in the geological medium according to the overall redox state. The elements to be considered are: (i) dissolved oxygen in sub-surface solutions, (ii) iron in ferrous and ferric form, and (iii) sulfur species (sulfides, sulfates, polysulfides). The presence of organic matter

and bacteria (sulfate oxidizing or reduction agents, iron oxidizing etc.) will also alter the redox state of the mineralization carrier solution. The reactions between these species that determine the redox state of the solutions in the sedimentary rocks.

These features are in part still the ones of the present-day conditions, e.g. those that occur during the *in situ* leaching (ISL) recovery.

1.2.4 Physical-chemistry of the roll-front

Initially oxidizing percolating solutions gradually lose their oxidizing character in contact with reduced formation. These processes involve chemical and/or biochemical reactions and are responsible for pH variations. The initially slightly alkaline solutions (pH=7 to 8.5) entering the reduced formation will have their pH decreased as a result of the sulfide oxidation reactions (H_2SO_4 release).

Thus, the transition zone between oxidizing and reducing conditions constitutes a geochemical barrier to the transfer of uranium and many other elements, whose operation is largely based on redox (Eh) and acid-base (pH) phenomena. The study of this zone allows to understand the physico-chemical conditions necessary, for example for the precipitation of uranium in a geological environment. This seemingly simple scheme is actually more complex because it depends on different parameters such as temperature, pressure, partial CO_2 pressures, O_2 and H_2S. The presence of organic or inorganic ions or ionic complexes and the presence of bacteria, which can significantly alter the geochemical characteristics of the deposit.

To explain the high uranium content of some rolls, particularly those of the Colorado plateau, it was suggested that oxidizing and acidic solutions circulated through the host formation. These solutions induced the dissolution of the old roll, transporting and accumulating the uranium and associated minerals a little further downstream in the reductive zone. These rolls are identical in every respect to the paleo-rolls in the concentric distribution of the various minerals which suggests similar physico-chemical conditions.

A roll-type deposit is characterized by three zones: a reduced zone, an alteration front corresponding to the deposit and an altered zone (Figure 4). The deposition environment and oxy-reduction conditions can vary significantly from one roll to another depending on the ponds considered. Roll-like uranium deposits in the Wyoming basins (Wind River, Powder River, Shirley, Great Divide) are primarily located in the Lower Eocene formations of the Wind River (Gas Hills, Wind River), Wasatch (Powder River) and the Lower Cretaceous Lakota (Black Hills) Formation. These formations are composed of river sediments removed from the surrounding mountains and deposited in the basin. They are composed of arkosic and siliceous sandstones, conglomerates, with intercalations of silstones and shales (e.g. Gas Hills, Shirley

and Black Hills). The abrupt change in physical-chemical conditions explains the geochemical features and composition of the epigenetic zones.

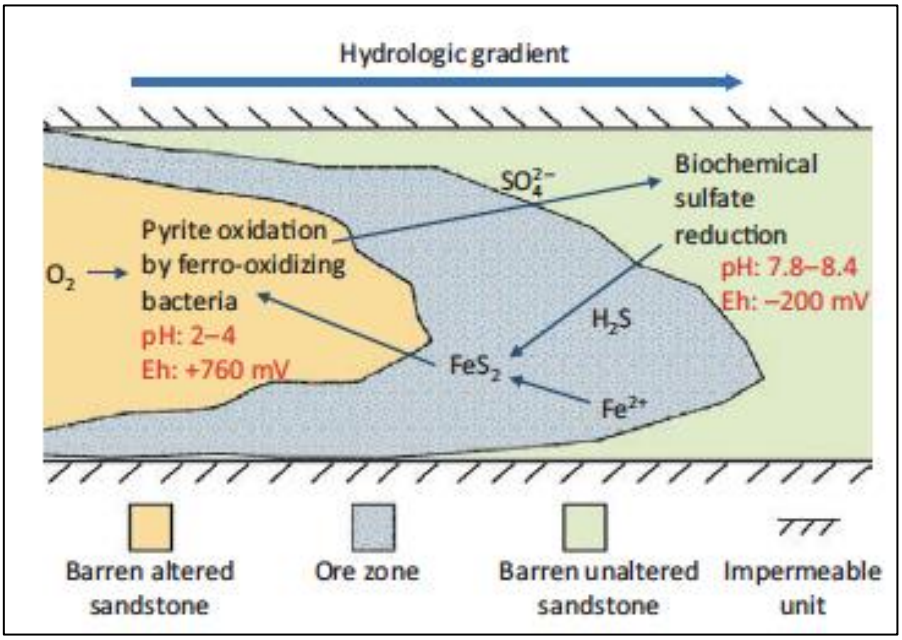

Figure 4: Model proposed recently by Hough et al. (2019) from Rackley (1972). The redox interface is established between ferro-oxidizing bacteria in the barren, altered sandstone and sulfur reducing bacteria (SRB) in the barren, unaltered sandstone. Ferro-oxidizing bacteria oxidize pyrite and produce sulfate that is flushed across the roll with groundwater. SRB reduce sulfate and generate H_2S, which drives reprecipitation of ore zone pyrite. An Eh gradient is established across the ore zone from +760 to –200 mV, and a pH gradient gradually from pH 2 to 4 to pH 8 (Jones and Starkey, 1962; Kuznetsov et al., 1963; Rackley, 1972).

In the first stages of infiltration into the encasing formation the waters lose their oxidizing character by fixing oxygen by oxidation of the supporting phases, such as S, Fe, Se and Ba, by the consumption of oxygen during biochemical reactions.

Similarly, the destruction of pyrite by oxidation will lead to a decrease in Eh and pH and the formation of sulfur-oxidized species such as sulfates. The redistribution of iron species and the conversion of ferrous iron into ferric iron in goethite and/or limonite, and the destruction of organic matter in the altered area confirm the oxidizing character of the percolating solution. It has been suggested that the potential for oxydo-reduction of groundwater varies from +300mV to -300mV during its flow from the oxidized zone to the reduced zone (Jones and Starkey, 1962; Kuznetsov et al., 1963; Rackley, 1972).

1.2.5 Formation of the roll enriched in U

The observed zoning in a roll-front is in good agreement with the evolution of the Eh-pH features of the percolating water. The formation of the deposit requires a significant decrease in Eh. In fact, when the aqueous medium is highly oxidizing, it affects ferrous compounds, degrades woody organic matter and kerogens and solubilizes traces of metals that are more soluble in their superior valence form. There are then mainly reactions of dissolution, and no

secondary mineral precipitation of trace metals near the front. This phenomenon is essentially dispersive. When the oxidizing flux is less than the capacity to reduce the volume of accessible rock, the oxidation processes become incomplete and leads to ions and complexes of intermediate oxidation levels (Boulègue, 1981). It is this phenomenon that becomes the engine of the uranium concentrator processes and related elements (Se, Mo, V and others).

In the reduced zone, the pH of the solution increases while the conditions remain overall reductive. The biochemical model involves anaerobic bacteria such as sulfate-reducing bacteria that turn sulfates into sulfides in the presence of organic matter, creating an environment of pH 7.8 to 8.4 and Eh -200mV. The sulfides react with the iron and the available sulfur in solution giving rise to the formation of secondary pyrite in the surrounding rock which can act as a reducer for uranium precipitation (ore-stage pyrite).

In general, two hypotheses have been put forward to explain the formation and preservation of uranium deposits of roll types: (i) the first, based on experimental considerations, proposes an inorganic oxidation of pyrite by the mineralizing solution to give metastable sulfur species capable of reducing uranium (Granger and Warren, 1969), (ii) the second suggests that migration of fluids rich in organic ligands and hydrogen sulfide, through the faults under the effect of compaction, allowed to install locally an environment favorable to the reduction of sulfates, then to the preservation of uranium mineralizations (Reynolds et al., 1982).

1.2.6 Organic matter and microbial activity

In some deposits, organic matter, generally abundant, is assumed to have controlled the distribution of uranium mineralization either directly through complexation, adsorption and reduction processes or indirectly by providing the energy needed for the bacterial reduction of uranium (Rackley, 1972; Huang, 1978). Organic matter can directly contribute to the reduction of the oxidizing character of the mineralizing solution but also constitutes in addition a nutrient for bacteria.

Conversely, in the absence of organic matter the decrease in oxidative properties of water is due to chemical reactions involving silicates containing ferrous iron (biotite, chlorites, amphiboles and pyroxenes), sulfides (mainly of iron) and ferrous carbonates (siderite). During these reactions, the pH tends (i) to be lowered by the sulfide oxidation reactions and (ii) to move towards higher values due to the dissolution of the carbonates present in the sandstone or the hydrolysis of the silicates. Water can eventually become progressively alkaline and reductive.

Following Spirakis (1996), in sandstone rich in O.M (containing plant debris), the O.M reduces uranium directly either by acting as a catalyst or by reacting with biogenic hydrogen sulfide (H_2S). In relatively poor sandstones in O.M, the reduction is caused either by reaction with

biogenic or non-biogenic H_2S (product of the interaction of oxidizing meteoric waters with pyrite) or by reaction with reduced liquid gases (H_2S and/or hydrocarbons) along favourable structures.

The speed of biochemical reactions depends on whether organic matter is present and on its potential to be degraded. In the presence of organic matter, bacteria quickly consume all oxygen by producing CO_2 and H_2S. Some bacteria are capable of releasing hydrogen, bringing the redox potential to values close to the lower limit of water stability. Biochemical reactions also induce a decrease in pH. Anaerobic bacteria developing on pyrite such as *Thiobacillus ferrooxidans* increase the acidity of the medium to a pH close to 1.8. Under these conditions, many ions, such as sulfur species, can persist for a long time in the metastable state. The biological control of uranium mineralization can alter the abundance, distribution and texture of pyrite and marcasite (Reynolds et al., 1982).

In the Wuyiyi deposit (China), Min et al. (2001) showed that microbial degradation of organic matter has been successful in maintaining a reducing local environment due to CH_4 production, H_2S or H_2SO_3, favourable to the reduction of hexavalent uranium (+VI) and the mineralization of tetravalent uranium (+IV). The study of the Chinese roll-front systems showed that U may be reduced in roll-front systems by bacteria and fungi, confirming the laboratory experiments of Lovley et al. (1991). During the mineralization stage it is possible to enzymatically reduce U into uraninite/coffinite by dissimilatory bacteria, which could use $U^{(VI)}$ as the sole electron acceptor instead of other multivalent metals such as $Fe^{(III)}$. Amorphous UO_2 may also be the result of such processes. Indeed, besides complexation and adsorption, a third mechanism was recently proposed by Bhattacharyya et al. (2017): the formation of $U^{(IV)}$ biofilms which evolve into biogenic non-crystalline $U^{(IV)}$ compounds. Using EXAFS spectroscopy data, these authors revealed the role of microorganisms in the reduction of $U^{(VI)}$ and the formation of disseminated $U^{(IV)}$ in organic matter which acts as nutrient and a trap.

1.3 THE CENTRAL ASIA U-PROVINCE

The Central-Asia Uraniferous Province extends from Kazakhstan to the West towards the Transbaikal region to the East. Consequently major roll-front deposits exist in Kazakhstan (Chu-sarysu), China (Bayinwula) and Mongolia (Dulaan Uul and Zoovch Ovoo). Mineralization in Chu-sarysu occurs in Paleocene continental arkosic sands deposited in fluvial settings, sourced from surrounding volcanic rocks (Munara, 2012). The whole sequence has been covered by vitrinitic organic matter and was subjected to shallow burial. The main facies associated to U-mineralization is pyrite of biogenic and hydrothermal origin (Lach et al., 2015). The Bayinwula deposit in the Erlian Basin (NE China) is hosted in Early Cretaceous medium

to coarse-grained sandstones and occurs in the form of coffinite associated to organic matter and pyrite (Bonnetti et al., 2015; 2017).

1.3.1 The roll-front type deposits of Kazakhstan

Most data on Kazakhstan deposits are found in Aubakirov (1998), Petrov (1998), Munara (2012), and some geochemical aspects especially of the present day features of the systems can be found in the Vergnaud and Langanay (on-going PhD theses in Mines ParisTech).

The Chu-Sarysu Basin which is more mineralized than the Syrdarya Basin consists of sediments deposited from late Cretaceous to Paleogene. Large deposits include Inkai, Muyunkum, Karamurun and Zarechnoe (Figure 5).

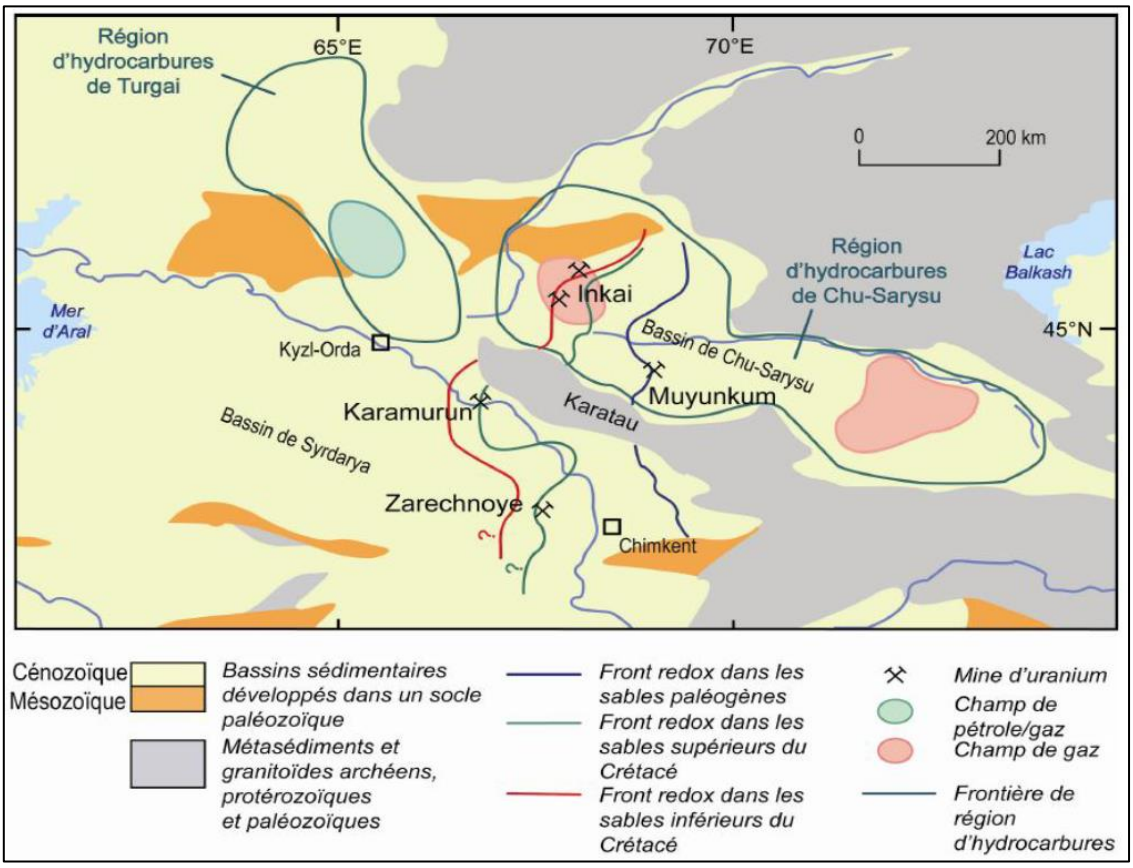

Figure 5: Location of the uranium deposits and hydrocarbon occurrences of the Chu-Sarysu basin (Munara, 2012; modified after Jaireth et al., 2008).

At the Muyunkum deposit, the mineralizations are found in the paleogenic formations, between 500 and 700 m deep in the southwest part at the foot of the Karatau, 300 and 500 m deep in the central part of the Suzak depression, 200 and 400 m in the northeast part (Tortkuduk). There are three mineralized horizons for the Muyunkum deposit: the Uvanas-Kanjugan (Paleocene), the Uyuk (Lower Eocene) and the Ikansk (Middle Eocene). The most important level of its uranium reserves is the Uyuk horizon. According to Pb-Pb isotope analyses (Mihailov and Petrov 1998), mineralization occurred in two main stages, from the end of Oligocene to the middle of Miocene and from the end of Pliocene to Quaternary.

The mineralizations are localized at the level of oxy-reduction fronts materialised by a contact between oxidized yellow sands and reduced grey sands, a context similar to those described for roll-front-type deposits.

According to Petrov, 1998 (data in Munara, 2012), the mineralizations are attributed to Late Pliocene and Quaternary coincide with phases of intensification of tectonic activity associated with the orogenesis of Tian-Shan (associated with the uplift of the Karatau Mountains), along a network of pre-existing regional faults, which controls the current hydrodynamic regime. Groundwater circulations associated with the elevation of the Karatau Mountains would have only led to secondary changes and the remobilization of the mineralization formed between late Oligocene and medium Miocene (Figure 6).

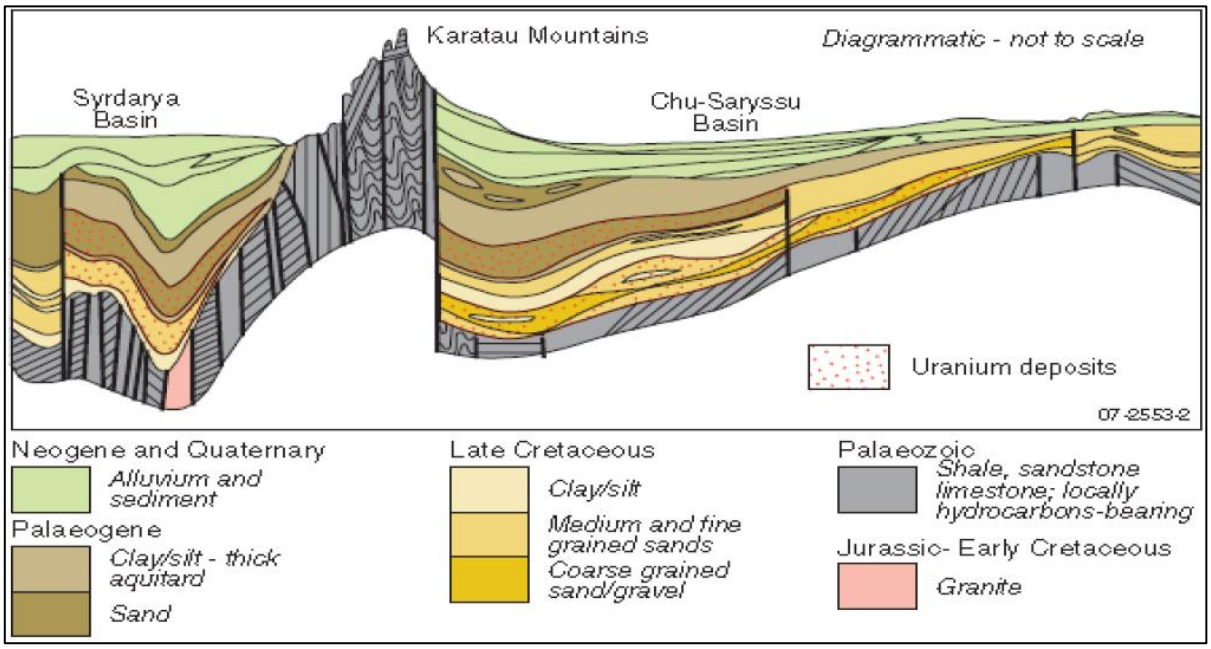

Figure 6: Geologic cross-section of the Chu-Sarysu and Syrdaya basins (Yazhikov, 1996).

Although the proportion of O.M in mineralized grey sandstone is very low (generally 0.03-0.05% C), Petrov (1998) suggests that this proportion is sufficient with a minor contribution of iron sulfides to produce large deposits of uranium in sandstone. The same author attributes the lack of a direct correlation between uranium and the concentration of organic migrates (MOs) from coalification, which has led to the degradation of active reducing organic compounds such as wax bitumen and humic acids.

It must be noted that a totally different model is proposed by Jaireth et al. (2008) who suggests that the redox conditions have been favored by the upwards migration of gases from the oil field located below the Cretaceous sediments (Figure 7). Thus, the other important parameter could be the gases expelled by the Permian reservoirs (including H_2S). A rapid and localized reduction could be able to form large deposits and the activation of faults at the end of

Oligocene and Middle Miocene could have facilitated the recovery of the necessary gases, especially at the edge of hydrocarbon reservoirs.

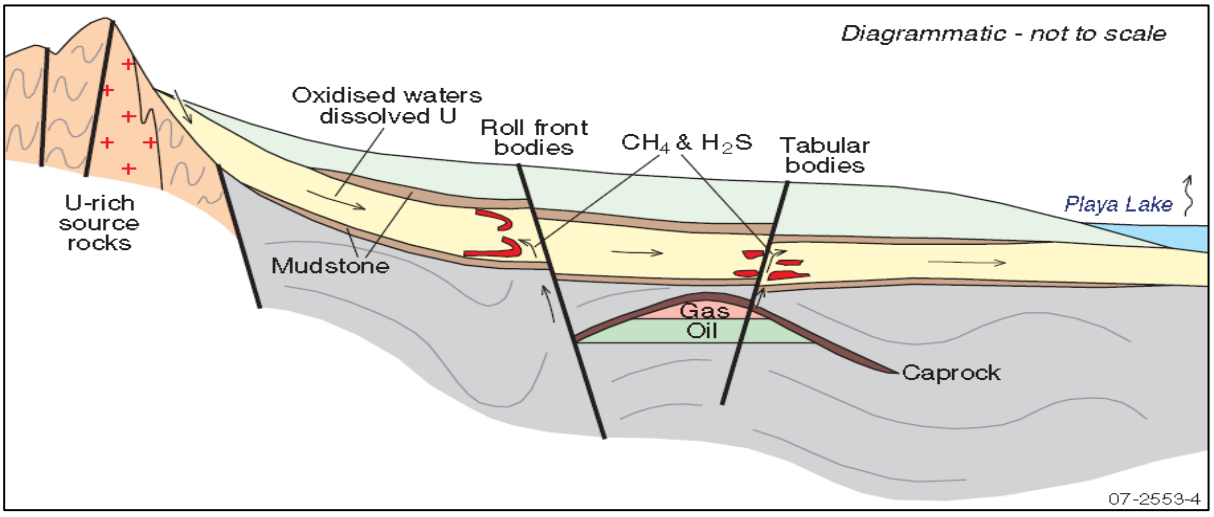

Figure 7: The model proposed by Jaireth et al. (2008) for the Kazakhstan roll-front U-deposits with changes in fluid flows, and upward migration of gases along faults (arrows indicate paleofluid and present day flows).

1.3.2 The roll-front type deposits of China

As in Kazakhstan, uranium deposits in sandstones closely associated with hydrocarbon ponds have been identified in the Ordos and Songlio basins in China (Huang Xian-Fang et al., 2005; Figure 8). These uranium mineralizations in formations poor in organic matter have been attributed by several researchers to the input of H_2S, along faults from deep hydrocarbon reservoirs (Reynolds and Goldhaber, 1978).

Some of these deposits were intensively studied in the last decade, and several results point out the contribution of biological activity within the sedimentary reservoirs to explain the U reduction. The role of hydrothermal fluid in the systems is ambiguous and rarely proven, at the rare exception of deposits where fluid nclusions attest to the circulation of hot brines sometimes with hydrocarbons or gases (Figure 9).

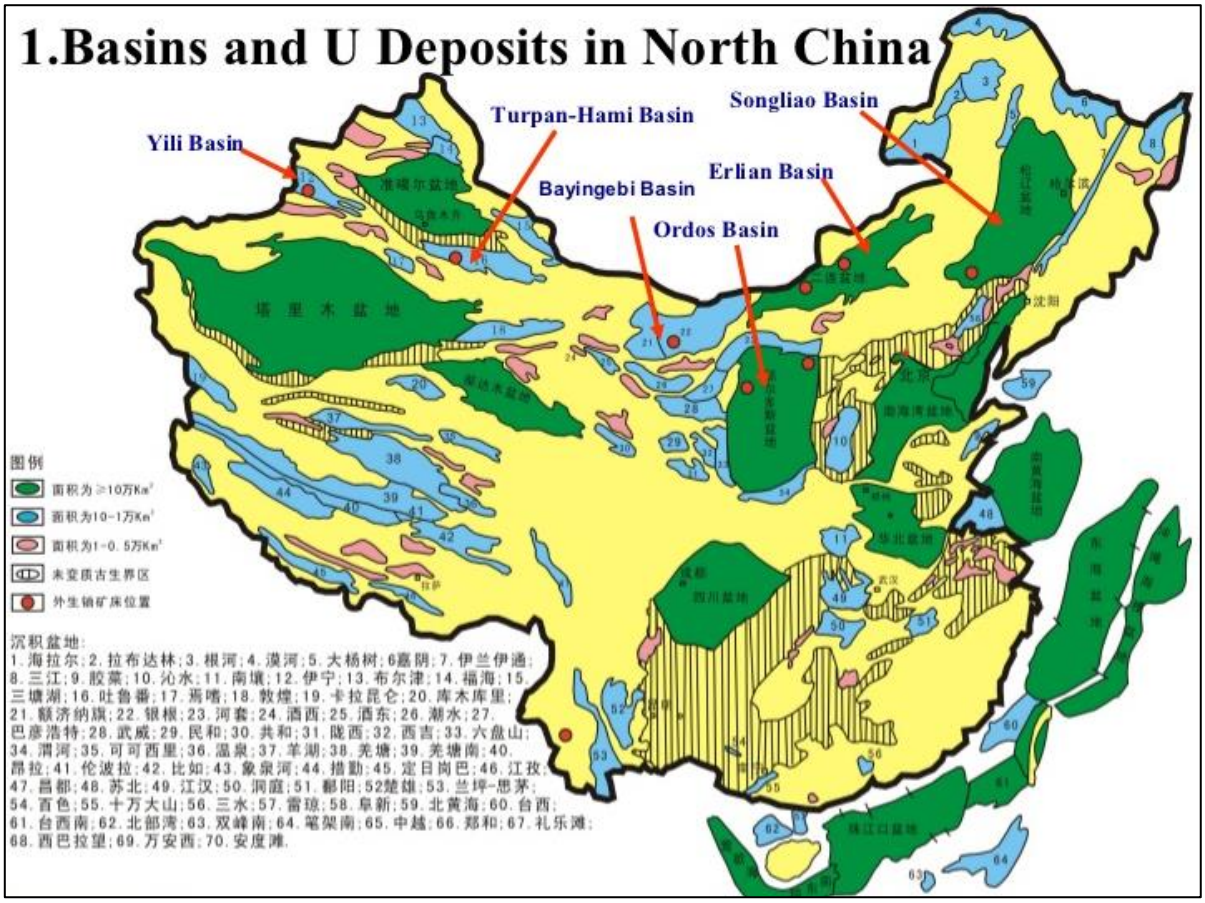

Figure 8: The main U deposits in north China (Zhu et al., 2012)

Uranium Mineralization Characteristics in Different Basins

Basin Features		Yili	Tuha	Ordos	Bayingebi	Erlian		Kailu
						Bayanwula	Nuheting	
Geologic setting		T-downfault(Pz) Depression(Mz) Compression(Cz)	T-DF(Pz) Dep. (Mz) Comp. (Cz)	Craton Dep.(-J_2) Foreland(J_3-K_2) Rim graben(Cz)	Strike slip-pull apart(Mz) S. slip Comp. (Cz)	Rift (J_1-J_3) Rift (K_1) Uplift (K_2-Cz)		Downfault (K_1) Depression(K_2) Reversal fold(Cz)
Ore bearing formation	Epoch	J_1-J_2	J_2	J_2	K_1	K_1	K_2	K_2
	Faceis	Fan delta	Braided delta	Braided channel	Braided delta	Braided channel	Semi-deep lacus	Braided channel
Reductant		Carbonaceous fragments	C-fragments	C-fragments +Hydrocarbon	C- fragments	C-fragments +Hydrocarbon	C-fragments +Hydrocarbon	C-fragments +Hydrocarbon
U-mineralization age		12±4 5±1 2±0	48±2 28±4	120±11 80±5 0±2	115±1.5 111.6±8.1 109±1.5	63±11	85±5.9 41±5 10±0.1	53±3 7±0
Ore body shape		roll-front	roll-front	roll/tabular	tabular	Roll/tabular	tabular	roll/ tabular
Epigenetic reform		?	?	Hydrothermal fluid	Hydrothermal fluid	Hydrothermal fluid	Hydrothermal fluid	Hydrothermal fluid

Figure 9: Uranium mineralization characteristics in different basins in north China (Zhu et al., 2012).

Erlian basin

In the case of the Nuheting deposit (Erlian basin) where hydrocarbons and associated gases were invoked as potential reductants by some authors (Niu et al., 1995; Zhang and Ding, 1996 cited in Bonnetti, 2013; Bonnnetti et al., 2015) it was finally concluded that the data obtained do not support that migrated hydrocarbons were involved as a reducing agent for uranium mineralization. Thus, Bonnetti et al., 2015 indicated that the Nuheting deposit underwent three main stages of mineralization: (i) a synsedimentary/early diagenetic uranium concentration and mineralization, (ii) a late diagenetic *in situ* uranium remobilization and deposition on pyrite and (iii) an epigenetic cementation. Rock-Eval pyrolysis (Figure 10) indicated that the organic matter contained in the host-rocks of the Nuheting deposit is of type IV, inherited from land plants and does not contain free hydrocarbons (very low S1).

It can be noted that this deposit is one of the rare deposit where the organic matter was studied thoroughly.

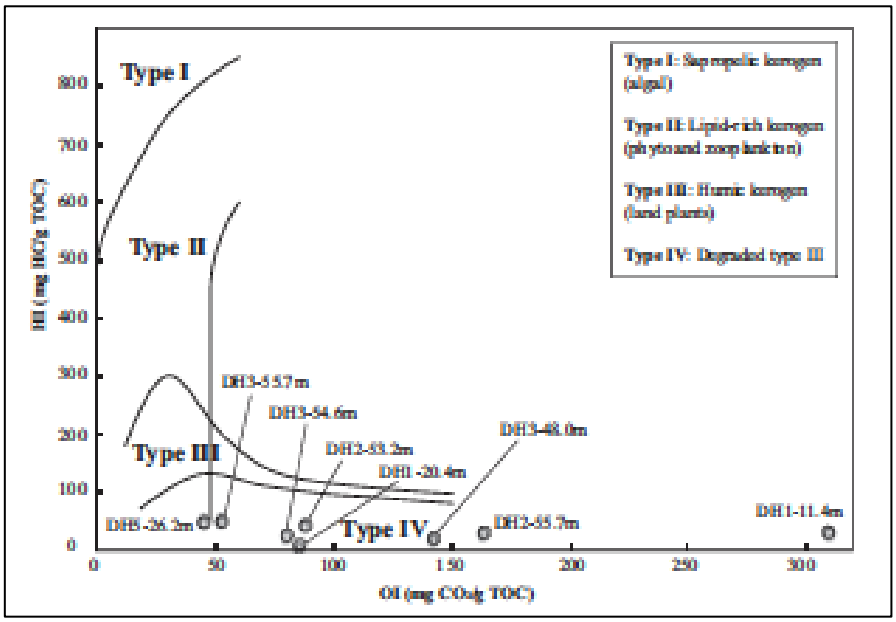

Figure 10: Organic matter of type IV from Nuheting characterized by a very low hydrogen index (HI) and a relatively high to very high oxygen index (OI). The Tmax values lower than 435 °C correspond to thermally immature organic matter following Espitalie et al. (1985).

Ordos basin

Following Yue et al. (2016) in the Ordos basin, the sandstone-type uranium deposit are hosted within large-scale skeletal sandbodies in the Middle Jurassic Lower Zhiluo Formation. Sediments deposited in braided river and delta systems (Zhao and Ou, 2006; Zhang et al., 2010).

The Diantou uranium deposit is considered as generated by an oxidation-reduction zone in a shallow buried reservoir during a late period of burial diagenesis equivalent to epigenesis (Chen et al., 2006a,b; Li and Xu, 2006; Liu et al., 2007; Xing et al., 2008).

The Dongsheng uranium deposit experienced multistage uranium mineralization, and the processes can be divided into four main stages: i) a preliminary enrichment during diagenesis, b) an oxidation during Late Jurassic to Paleocene, iii) oil and gas reduction yielding to ore preservation in the Early Cretaceous, and iv finally late oxidation from Miocene to present (Xiang et al., 2005, 2006; Han et al, 2008; Yang et al., 2009; Xue et al., 2011).

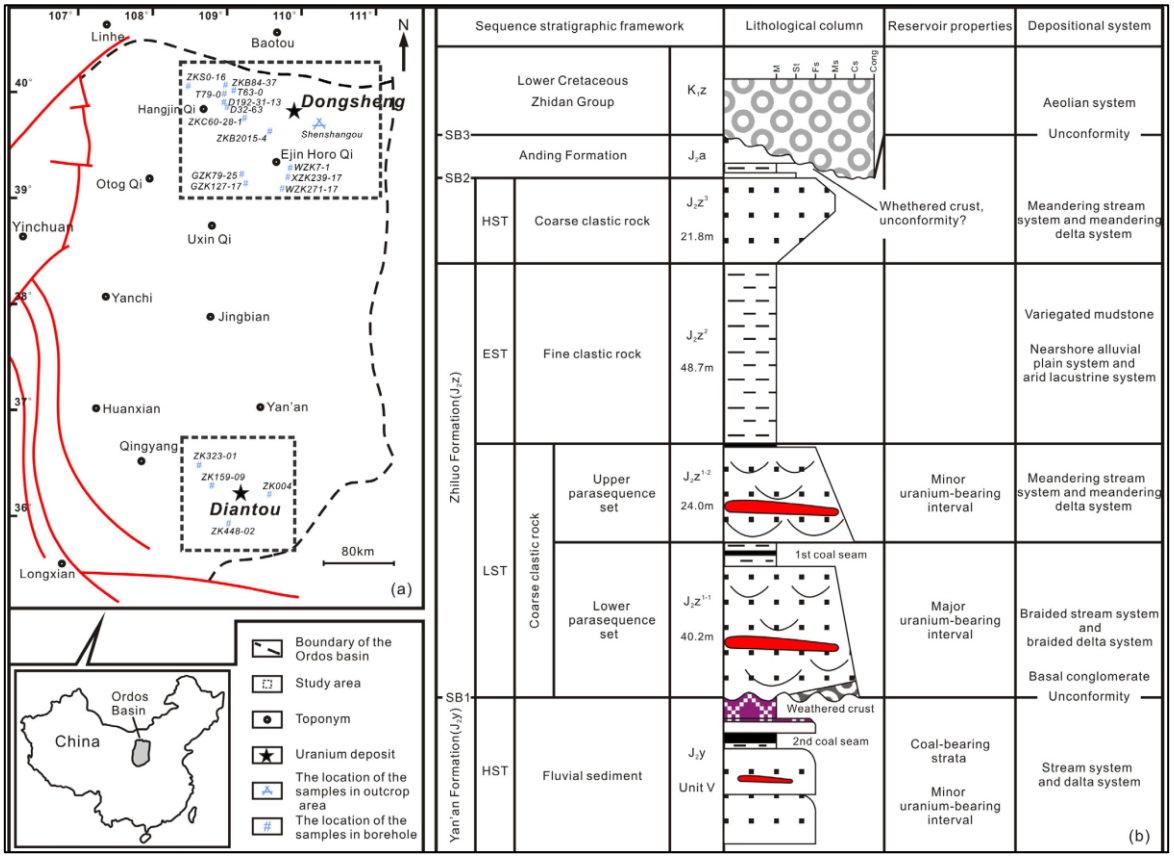

Figure 11: Location of the U-deposits in the Ordos Basin and spatial relationship between the Jurassic sequence stratigraphic framework. Yue et al. (2019) on the basis of data from Ritts et al. (2004) and Jiao et al. (2016).

Allochtonous hot fluid input

Following the model by Jaireth et al. (2008), Yue et al. (2019) on the basis of former data proposed that several sources of sulfur may be involved in the processes, such as a biogenic origin associated with BSR process but also a hydrothermal source in an open system.

Cao et al. (2016) considered that hydrocarbon migration has an important role in uranium reduction and precipitation and proposed a genetic model including: an early coupled bacterial uranium mineralization, and hydrocarbon oxidation followed by a later recrystallization of ore phases in association with low-temperature hydrothermal solutions under hydrocarbon-induced reducing conditions (Figure 12).

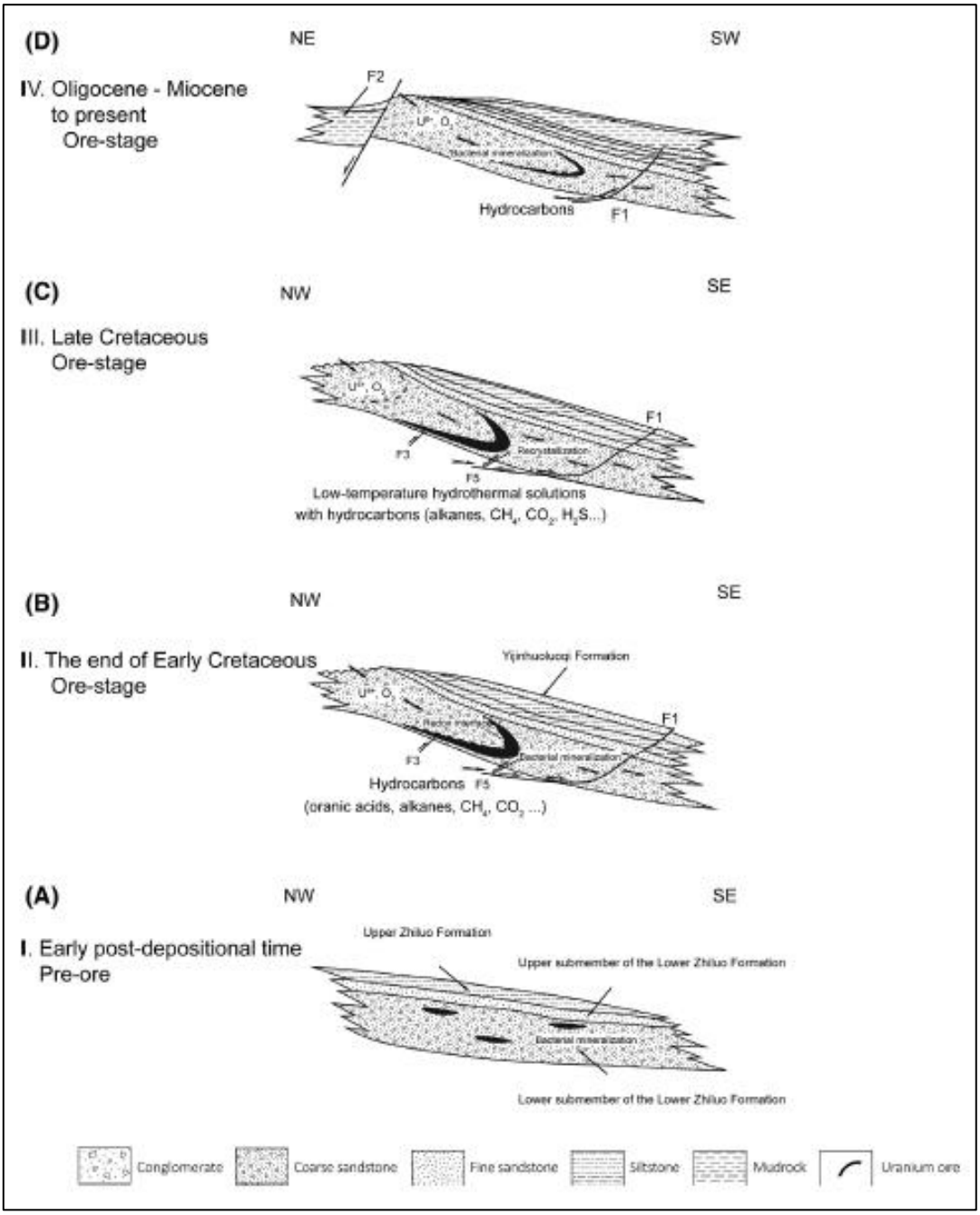

Figure 12: Model developed for the Dongsheng roll front deposit by Cao et al. (2016).

The same model is proposed by Cai et al (2007). They considered that SRB was likely to reduce sulfates to sulfides simultaneously with petroleum oxidization, and caused direct or indirect reduction of U(VI) to U(IV). The petroleum oxidation was proposed because bio-degraded oils were identified in fluid inclusions.

A recent article by Akhtar et al., (2017) proposes a very surprising interpretation of O, H isotopic data for Ordos U deposits, including meteoric waters mixed with magmatic waters (more probably waters deeply equilibrated with sediments), although the main processes such as

pyrite and U deposition are considered as resulting from sulfur bacterial sulfate reduction (BSR) within a rather classical oxidation-reduction model.

In both contributions, data of fluid inclusions (quartz overgrowth and sparite cements) tend to indicate the venue of rather saline (10-17 eq wt % NaCl, some inclusions with NaCl crystals), hot (100-150°C) fluids with traces of CH_4 and hydrocarbons coming from rather deeply buried sediments (Paleozoic to Triassic series).

Bacterial induced processes

Jiao et al. (2018) and Zhang et al. (2018) insist on the fact that carbonaceous debris in the form of retention sediments occurs in the uranium reservoir sandbodies, enhancing the reducing power of sandstone to a great extent. Yue et al. (2019) indicate that the carbonaceous debris can supply the energy for the bacterial sulfate reduction process, and the biotite can provide the source of iron for pyrite precipitation. The ferrous iron can be adsorbed on the surface of the clay minerals (Figure 13)

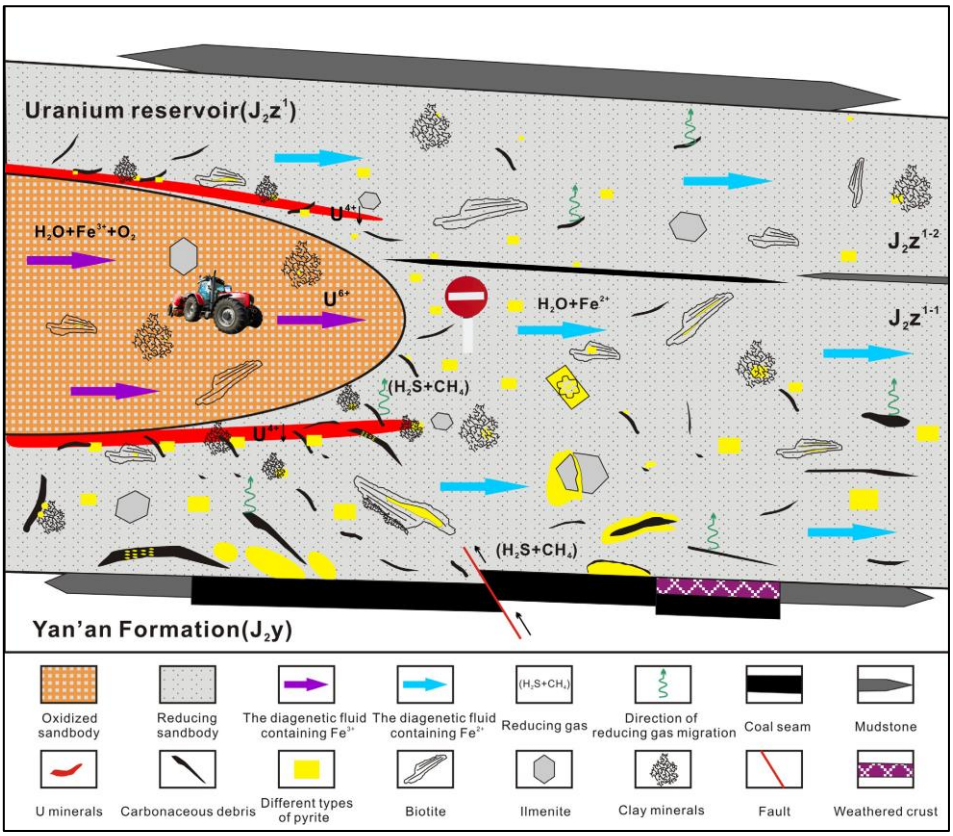

Figure 13: Model proposed by Yue et al. (2019) for the Ordos U deposits and the formation of pyrite.

There is therefore a clear heterogeneity in the scientific literature available on the Ordos basin about the genetic models. The main difference with other basins is the clear upward penetration of hot diagentic fluids, a process which is not identified in Kazakhstan, Mongolia, or other Chinese basins.

The Bayinwula roll front-type uranium deposit

This deposit is also hosted in sandstones of the Early Cretaceous, particularly in Saihan Formation (Bonnetti et al., 2015). Petrographic observations and Rock-Eval data indicate that organic matter occurring in the host sandstone is mainly inherited from land plants and corresponds to type III or type IV kerogens. Organic matter fragments disseminated in sandstones may also contain significant pre-ore uranium concentration (Figure 14). Framboidal and collomorph ore-stage iron disulfides have moderate to high concentrations of As, Ni, and Co and have a light sulfur isotope signature characterized by $\delta^{34}S$ values from -30.5 to -7.5‰, suggesting that sulfur originated from bacterial sulfate reduction.

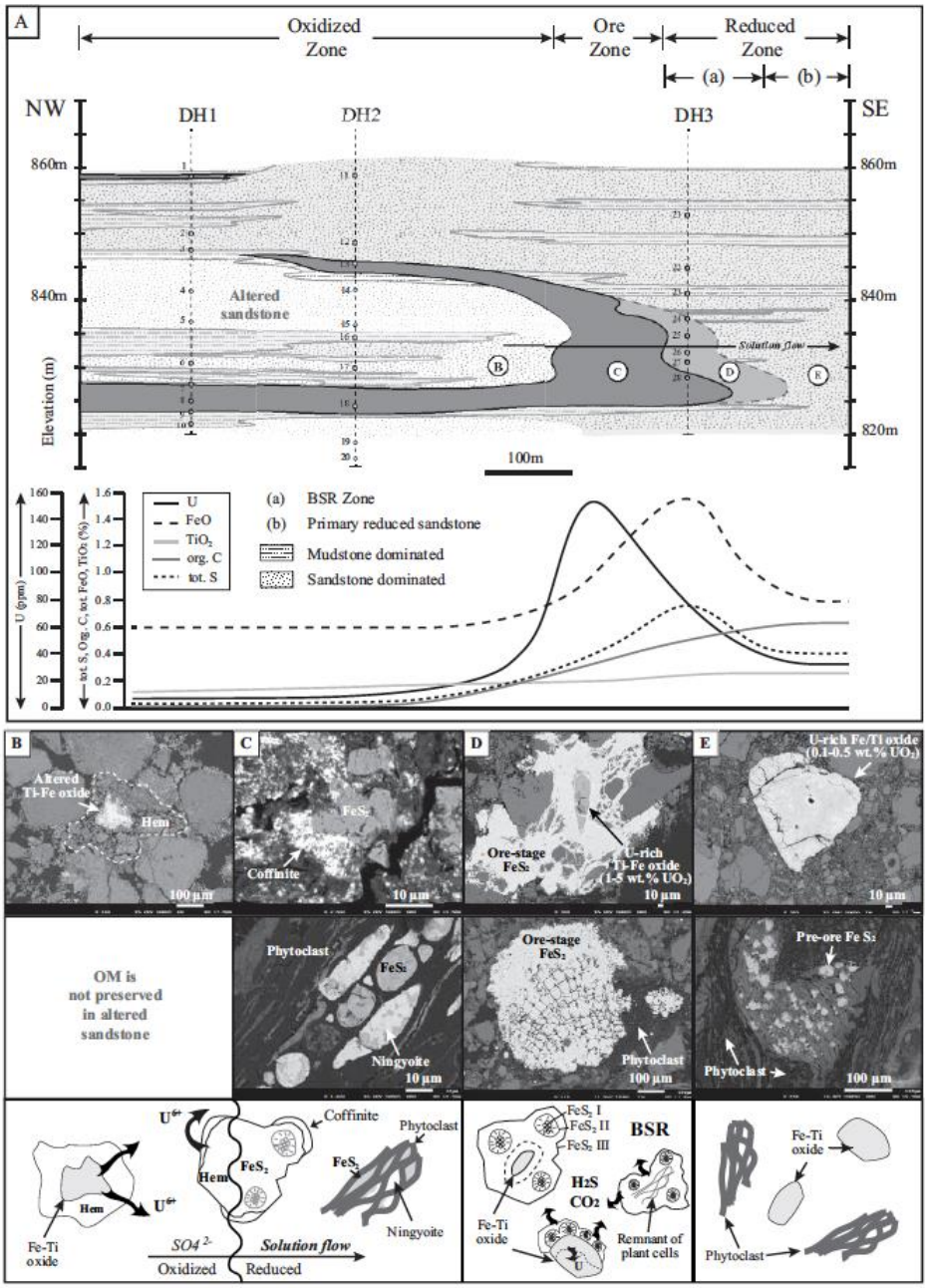

Figure 14: The metallogenic model proposed by Bonnetti et al. (2015) for the Bayinwula roll front-type uranium deposit.

Bonnetti et al. (2015) suggest that bacteria enhanced:

(1) The liberation of U from Fe-Ti oxides and organic matter, although the pristine concentration in U has not yet been fully understood.

(2) The generation of ore-stage iron disulfides.

(3) The production of a secondary H_2S-rich reducing barrier involved in the reduction of U(VI) and the precipitation of U(IV). Uranyl and sulfate ions were transported through the host sandstone by low-temperature oxygenated groundwater and U(IV) was precipitated at the redox front as P-rich coffinite and ningyoite, dominantly as replacement of ore-stage iron disulfides which have partly to totally replaced organic matter and Fe-Ti oxides.

1.3.3 Other roll front deposits in northern China: the Xinjiang province

Sandstone-hosted roll-front type U deposits (Wuyer, Wuyisan and Wuyiyi) are located near the Kazakhstan border in the Yili Basin (Yili), and are considered to be an extension of the large U province covering Kazakhstan and Uzbekistan (Min et al. 2005; Figure 15).

Figure 15: The Xinjinag province in north-western China (map from Pirajno et al., 2011).

The role of microorganisms was once more put forward by Min et al. (2005) in the case of the deposits located in Xinjiang province (Wuyiyi, Wuyier, and Wuyisan U deposits) which is located south of Mongolia. There, uraninite and coffinite (± sphalerite, marcasite), are considered to be biogenically precipitated and pseudomorphically replace fungi and bacteria. Min et al. (2005) also considered that U(VI), which was the sole electron acceptor, was likely to have been enzymically reduced, and that post-mortem accumulation of uranium may have also occurred through physico-chemical interaction between uranium and negatively-charged cellular sites and inorganic adsorption or precipitation reactions.

Authors develop however their theory on a limited number of arguments, mostly SEM images of U phases close to fungi or organic matter and framboidal pyrite.

1.3.4 The roll-front type deposits of East Gobi Basin in Mongolia

Mongolia can be separated into four metallogenic provinces that host U mineralization (Dahlkamp, 2009). These regional features are namely, the Gobi-Tamtsag, the Khentei-Daur and the North Mongolian Province, which contain mainly uranium ore and the Mongol-Priargun that is a more general metallogenic province. This study focuses in the Gobi-Tamtsag metallogenic province, where the host-rock formation for U-mineralization is the Upper Cretaceous Sainshand Formation, composed of medium to coarse grained sand. This siliciclastic reservoir is part of the sedimentary infill of the East Gobi Basin, which is separated in two sub-basins namely, the Unegt and Zuunbayan that in turn contain two uranium deposits, the Dulaan Uul and the Zoovch Ovoo, respectively. Both deposits are epigenetic and are controlled by stacked oxidation-reduction fronts. The resources in Dulaan Uul are estimated at 6.500 t with 150 ppm U and in Zoovch Ovoo at 54.500 t with 223 ppm U (Le Goux et al., 2015).

1.3.5 Geological setting

The East Gobi Basin extends for 700 km in E-W trend and 300 km in the N-S (Meyerhoff and Meyer, 1987; Prost, 2004). It is a northeast-southwest trending continental basin of multiphase deformation formatted by Mesozoic extension events (Johnson and Ritts, 2012). The East Gobi Basin covers a cumulative area of 1.5 million km^2 (Johnson, 2004) and includes the following four morpho-tectonic elements: the Unegt sub-basin, the Zuunbayan sub-basin, the Khovsgol sub-basin and the Sainshand sub-basin. The studied dataset originates from the Zuunbayan sub-basin, which has NE orientation and is 20 km wide and 100 km long. Although its geometry is not well defined, seismic surveys reveal the presence of two depocentres, one perimetrically and another about 50 km southwest of the Tsagaan Els oil field, respectively. The Mesozoic-Cenozoic sedimentary sequence is estimated to approach 4000 m in thickness. The granitic outcrops in the NE and S parts of the basin, suggest the presence of quartz arenite sandstone sources (Prost, 2004; Figure 16).

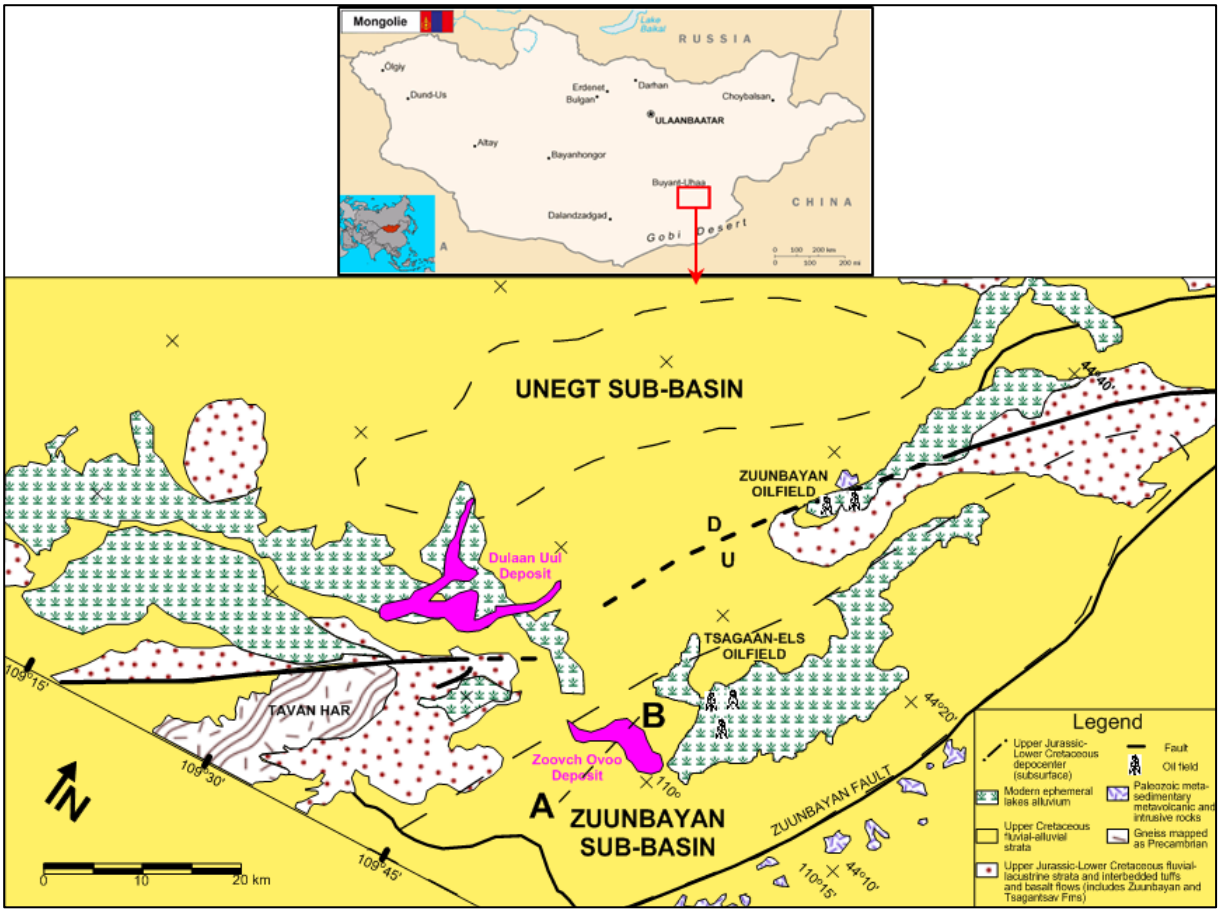

Figure 16: Simplified geological map of the Zoovch Ovoo and Dulaan Uul U roll-front deposits at Zuunbayan and Unegt sub-basins, respectively (based on Graham et al., 2001).

1.3.6 Tectonic history

The East Gobi Basin is a multiphase deformation area (plate interior poly-phase basin) that according to recent studies was subjected to discrete cycles of deformation and subsidence.

Hence, based on petroleum-exploration seismic profiles (Prost, 2004; Johnson and Ritts, 2012; Heumann et al., 2014), four phases formatted the East Gobi Basin (Figure 17) from Late Paleozoic to Cenozoic as summarized below:

- The Late Permian post-collisional basin due to the closure of the Paleo-Asian Ocean. As a result the basement consists of turbiditic sequences of Permian age that are unconformably overlain by non-marine Permo-Triassic sediments (**Phase 1**).
- The Early Mesozoic transpressional foreland created by a major sinistral shear zone lasting until Late Triassic and “thrusting” Precambrian and early Paleozoic carbonate klippe (**Phase 2**).
- The Late Mesozoic rift basin lasting from Late Jurassic to Late Cretaceous, which is marked by the development of high angle normal faults (**Phase 3**).

- The Late Cretaceous post-rift succession and the development of a strike slip basin, marked by the regional unconformity and basin inversion. Although the sediments overlying the Late Cretaceous are characterized as a post-rift thermal sag phase, there were probably left lateral strike-slip faults developing during Early Cenozoic (**Phase 4**).

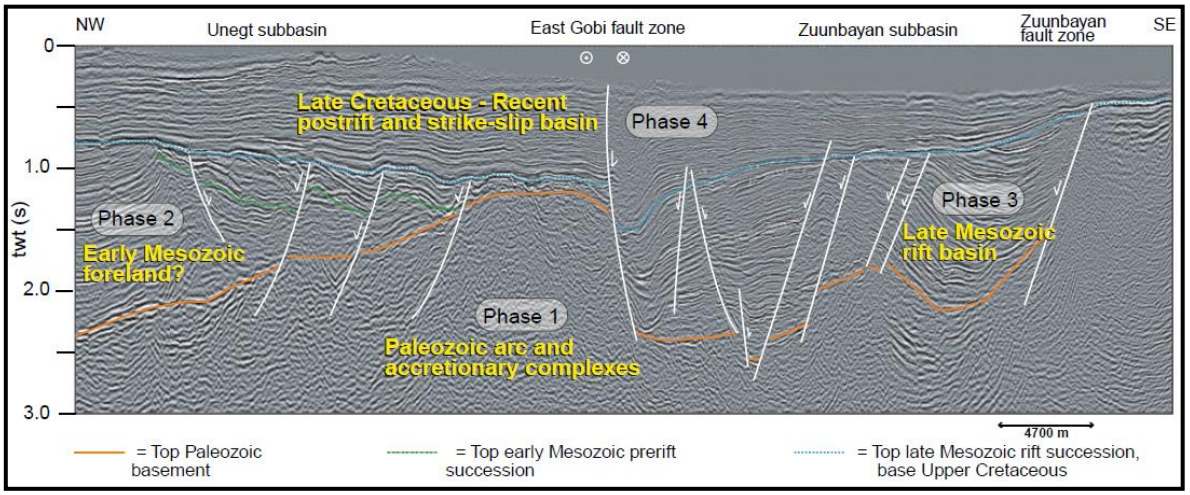

Figure 17: Seismic profile across the East Gobi Basin featuring the four tectonic events that affected the development of the basin. The seismic profile is used to illustrate the Late Cretaceous sedimentary infill in Zuunbayan sub-basin. Note that the depth is measured in two-way-travel-time (Johnson and Ritts, 2012).

Finally, the Mesozoic sequence is covered by Tertiary-Quaternary fine to coarse low thickness alluvial sedimentation, forming anticlines of up to 5 km in length and 1-2 km in width. Uplift episodes during the Early Cenozoic are also likely as older units outcrop locally the Tertiary-Quaternary deposits (Prost, 2004), probable due to the primary extension of the Altyn Tagh fault in China during Oligocene-Miocene that reactivated the East Gobi Fault Zone resulting into continental extrusion (Johnson and Ritts 2012).

1.3.7 Lithostratigraphy

The lithostratigraphy of the East Gobi basin is presented in Figure 4. The base of the stratigraphy (Devonian-Permian) consists of widely spread metamorphosed Paleozoic arc-related volcanics and marine siliciclastics, setting up the Tavan Tolgoy Formation (Traynor & Sladen, 1995; Lamb and Badarch, 1997; Graham et al., 2001; Prost, 2004). The Paleozoic basement is overlain unconformably by a 1000-4000 m thick sedimentary succession. The cumulative sedimentary record ranges from Jurassic to Tertiary and is composed of continental sediments (Meyerhoff and Meyer, 1987; Prost, 2004). Generally, the whole Triassic-Early Jurassic sequence is missing from the record due to repeated episodes of block faulting and multiphase deformation (Itterbeeck et al., 2005; Johnson, 2004); hence a hiatus of variable thickness exists between Permian and Middle Jurassic. The Khamar Khovoor Formation was deposited during Middle-Upper Jurassic times and is 750 m thick. The depositional setting at that time was paralic to marginal marine, setting up a combination of fluvial, lacustrine, deltaic

and swamp-organic sedimentation. The fluvial character is expressed by braided rivers depositing sandstones with channel shape geometry and the paralic by dominant shale deposits. The Khamar Khovoor Formation forms a hiatus with the overlying Upper Jurassic (Tithonian-Kimeridgian) Sharlyn Formation that consists of 200 m of well-defined braided fluvial sandstones, conglomerates and to a lesser extent finer deposits, like lacustrine shales (Graham et al., 2001; Prost, 2004), before gradually passing to a 300-700 m thick sequence consisting mainly of shales interbedded with coarser fractions (dark-colored sandstones, conglomerates, siltstones) and volcanics (red-colored tuffs, basalts) forming gradually the Tsagaan Tsav Formation of Early Cretaceous (Valanginian) age.

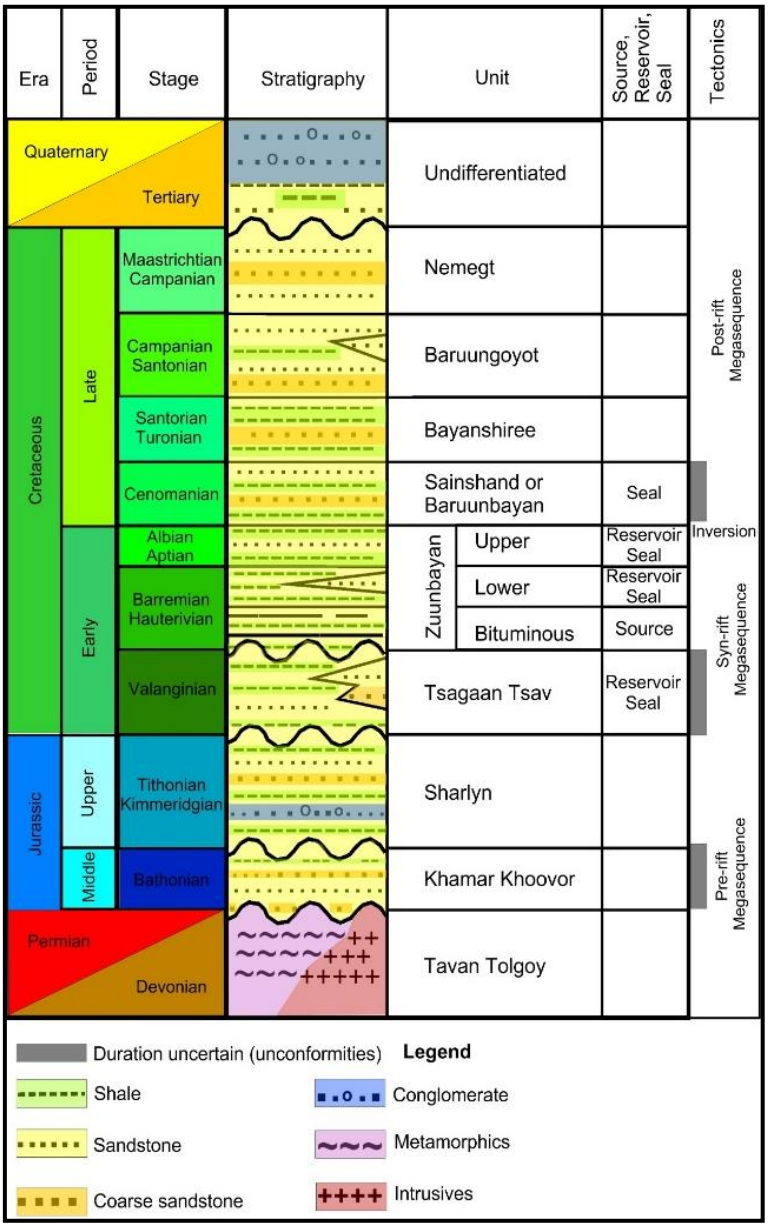

Figure 18: Lithostratigraphical column of the East Gobi Basin including potential unconformities and tectonic episodes. Modified from Prost (2004).

The Tsagaan Tsav Formation is composed of a fining upwards sequence of alluvial fan and braided stream deposits, which is topped by fine material deposited during flooding events

(overbank deposits) and lacustrine facies (Graham et al., 2001; Johnson, 2004; Prost, 2004). The coarser sandstone part of the Tsagaan Tsav Formation is the reservoir unit for the Tsagaan Els and the Zuunbayan oil fields. The Zuunbayan Formation has Hauterivian to Albian age and is composed of 970 m of non-marine poorly compacted sandstone, interbedded with shales and volcanic tuff. Together with the underlying Tsagaan Tsav Formation they are 1500 m thick. Furthermore, the Zuunbayan Formation can be divided in three different units. The basal unit is organic rich and contains bituminous shales with petroleum source potential. The mid and upper units contain coals and sandstones with channel geometry along with basaltic flows (Prost, 2004). There is a clear unconformity between Late and Early Cretaceous that separates the Zuunbayan Formation by the Late Cretaceous (Cenomanian) Sainshand Formation. This unit is composed of red sandstones, claystones and conglomerates, reflecting high energy fluvial deposits.

The Sainshand Formation hosts both uranium deposits in East Gobi Desert, namely the Dulaan Uul and Zoovch Ovoo (Parize, 2013; Le Goux et al., 2015). The Sainshand Formation has Cenomanian age and its thickness varies between 100-350 m. It can be separated into respective sub-units that reflect different cycles of lacustrine and alluvial sedimentation setting up a combination of conglomerate, sand, silt and clay sedimentation (Dahlkamp, 2009; Figure 19). The Sainshand Formation is overlayed by the Late Cretaceous (Santonian-Turonian) Bayanshiree Formation, consisting mainly of reddish to grayish shales with minor input of sandstones with channel-shape geometry (Graham et al., 2001; Johnson, 2004).

The thickness of the next two Late Cretaceous lacustrine coarse clastic units, namely the Santonian-Campanian Baruungoyot Formation and the Campanian-Maastrichtian Nemegt Formation is variable. The Upper Cretaceous post-rift sequence was certainly deposited during a sag-basin story (sediment starvation). It has also recorded the tectonic events (strike slip tectonic) during Cenozoic: the deposits related to this sequence could be strongly dipped along the faulted boundaries of these sub-basins whereas they are cropped generally flat and sub-horizontal in the syncline heart. Locally it is also possible to include Tertiary and Quaternary strata due to the re-activation of the EGFZ (Heumann et al. 2008; Johnson and Ritts, 2012), though they are generally undifferentiated with granular sizes ranging from very fine to coarse that top-up unconformably the Late Cretaceous strata (Prost, 2004).

As already stressed the Dulaan Uul (Unegt sub-basin) and the Zoovch Ovoo (Zuunbayan sub-basin) uranium deposits are contained inside the Upper Cretaceous strata which stands for the late infilling of the East Gobi Basin. In more detail the uranium deposits are hosted inside the upper part of the post-rift Sainshand Formation (codenamed K2Ss2 in the COGEGOBI data), which is a coarse to medium-grained siliciclastic reservoir (Figure 19).

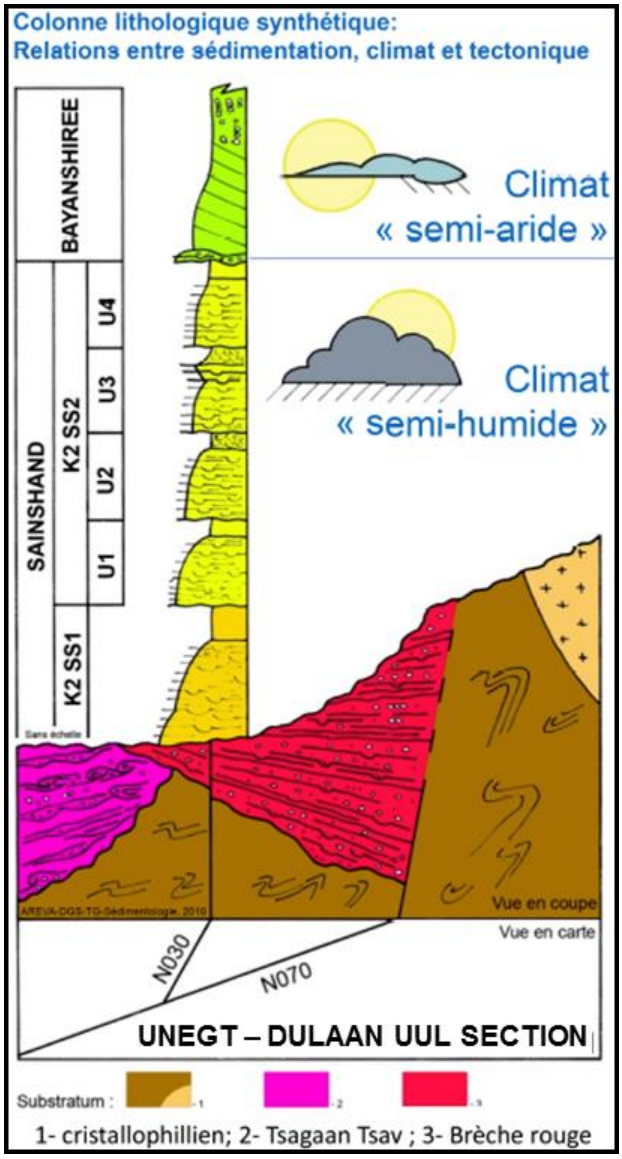

Figure 19: Upper Cretaceous infilling of Unegt sub-basin and inferred relationships with climate evolution. Within the basement, red deposits correspond to “reddish breccias” and pink deposits to Tsagan Tsav volcano-clastic deposits (in Parize, 2013).

1.3.8 Uranium mineralization and associated phases in Zoovch Ovoo

The Upper Cretaceous uraniferous sequence displays about 600 m thick clastic deposits with mixed depositional signature, ranging from alluvial fans and braided plains, mainly within the Unegt sub-basin, to flood-dominated deltas and lacustrine systems, within the Zuunbayan sub-basin (Parize, 2013; Le Goux et al., 2015).

As in many cases of roll fronts in unconsolidated sands i.e. in Kazakhstan (Munara, 2012) and China (Bonnetti et al., 2015a, 2015b, 2016), most of the processes concerning the U mineralization are concentrated on a very small portion of mineral phases (sulfides ± Ti minerals ± organic matter + U phases) dispersed within the quartz-feldspar grains and finally in the intergranular porosity of dolomite cement.

In the studied dataset the **U** phases encountered are listed below:

- Either pyrite clusters cementing the detrital grains, and becoming the nucleus for the U phase precipitation, when the sample is mineralized.
- Organic matter which may evolve from barren clasts towards complex clusters that become the first nucleus of pyrite formation (different types of habitus from early framboids to euhedral pyrite) and in some cases a location for the precipitation of U phases or becoming in turn a U bearing phase without any recognizable U-bearing micro-phases.
- Fe-Ti oxides that are gradually fully replaced by U while preserving their crystal structure unchanged i.e. cleavage, morphology of crystals.
- Feldspars, with a porosity filled by U oxides ± organic matter.

In most cases, the three constituents are associated spatially.

1.4 OBJECTIVES OF THE THESIS

The aim of the thesis is to address the metallogenic characteristics, i.e. the mineralogy and geochemistry, of the carbon-uranium-sulfide system in the formations which host the roll-front type uranium deposit of Zoovch Ovoo, located in the East Gobi Basin and in particular in the sub-basin of Zuunbayan, in southeastern Mongolia.

In detail the primary objectives of the thesis are:

1. To characterize the textural/genetic relationships between U-ore formation, diagenetic cements, organic matter (OM) and sulfides in continental sandstones affected by redox processes taking into account the depositional context.
2. To characterize the U-ores and gangue minerals (mineralogy, crystal-chemistry, trace elements), as well as the petrography and geochemistry of organic matter (kerogen, molecular geochemistry). The petrographic and geochemical relations of uranium to organic matter are among the major concerns.
3. To characterize the sources of C, S (isotope geochemistry).
4. To develop a genetic model for the formation of the U-ores with evaluation of the relative role of the organics, carbonates and sulfides in the redox trap for uranium.
5. Finally, to compare the genetic model with similar studies done in basins adjacent to the Central Asia Uraniferous Province (e.g. Kazakhstan and China) to understand the mechanisms contributing to the formation of the uranium deposits.

1.5 SCIENTIFIC APPROACH - METHODOLOGY

The current study was elaborated on samples recovered during the exploration campaigns of COGEGOBI between 2011-2017 in Zoovch Ovoo and on some calcite samples provided by J. M. Schmitt (ORANO Mining), originating from the areas of East Hongor Tolgoy & Bayangshiree Plateau, also discussed in the thesis of P. Grizard.

The samples' set is composed of 262 samples in total. In more detail:

a) 103 samples are coming from the 9659 study (2014 sampling) recovered from depths ranging between 120-220 m, from 36 different wells, targeting the Upper Cretaceous uranium bearing Sainshand Formation. The samples were selected in a discontinuous order from the Zoovch Ovoo deposit's drill cores, along profiles perpendicular or in the axis of the main direction of flows in the vicinity of redox front U mineralization. The sampling was focused in particular in those parts that had high carbonate, organic matter and uranium contents in order to build-up a diversified database. In more detail, 42 samples originate from Profile SW-NE_01300, 48 from the SW-NE_03600 and 13 samples from the punctual drillings that spread randomly throughout the deposit (Table 14).

b) 89 samples are coming from the 9606 study (2011 sampling) from 6 different wells and from depths ranging between 110-200 m (Table 15).

c) 6 samples are coming from the outcrops of the Bayangshiree Plateau and East Hongor Tolgoy in the vicinity of the Zoovch Ovoo roll-front, in Zuunbayan sub-basin. These samples are either calcites or calcite cemented sandstones and are used in contrast to the dolomite cemented sandstones of Zoovch Ovoo (Table 16).

d) 64 samples are coming from the 9704 study (2017 sampling) which is divided in three parts. Samples located outside the mineralization zone, towards the reduced area that has not been breached by the oxidizing waters. Samples from the interior of the mineralization zone, enriched in uranium, organic matter and carbonates. Finally, fresh samples recovered from drill-cores during the 2017 exploration campaign that were used for molecular geochemistry studies (Table 17, Table 18).

1.5.1 Analytical techniques

The typology of each carbonate-pyrite-uranium-organic matter facies is supported by petrographical (often cathodoluminescence) and SEM-EDS observations. With respect to the crystal-chemistry of the carbonates, the EMPA is used to obtain information on the major elements and the LA-ICP-MS on the REEs and trace elements. Ultimately, the study yields to a general paragenetic sequence for the diagenetic facies recognized. A detailed approach of the techniques used is given below.

Petrography and crystal-chemistry

Polished thin sections (~30 µm thick) were prepared and were studied using optical microscopy (in transmitted and reflected light modes). The petrography was used to characterize with precision the morphology, the nature and the composition of the different types of mineralization encountered along the redox front. The two methodologies used for the classification of the samples are based on Dott (1964) for petrography and Wentworth (1922) for granulometry (although point-counting was not performed in any sample).

To complete the petrographic study a CATHODYNE OPEA optical microscope was used to conduct the cathodoluminescence study. The analysis was performed under vacuum and the acceleration voltage and beam current intensity were continuously regulated. A PHILIPS XL30 Scanning Electron Microscope (SEM), equipped with an energy dispersive spectrometer using a Si-(Li) semi-conductor detector, coupled with a HITACHI S-4800 scanning electron microscope (SEM) at SCMEM-Nancy, in order to establish the mineral paragenesis.

The Electron Microprobe Analysis (EPMA) of carbonates was performed using a CAMECA SX100 at SCMEM-Nancy. The calibration was made using natural and synthetic oxides or alloys (orthoclase, albite, $MnTiO_3$, wollastonite, hematite and olivine). The analytical conditions were: 10 nA current, accelerating voltage of 15 kV, 10 s counting time for (K, Na, Ca), 20 s for (Al, Fe, Mn), 40 s for (Mg). The accelerating voltage was raised from 15 kV to 25 kV to amplify the detection limit in particular when investigating the uranium-dolomite relationships and to construct the chemical maps.

Organic petrography sample preparation

The samples were initially screened for their organic matter content, contained inside the poorly consolidated sands or carbonate cemented sandstones. Up to date only the organic matter found inside the poorly consolidated sands, or carbonate cemented sandstones or claystones.

The organic matter contained inside the loose sands could be recovered by two ways, either by mechanical separation (careful extraction of the organic rich layers) or by flotation (density separation), which implies the use of a chemical solution of a given density, i.e. $ZnCl_2$ with ρ=1.6 gr/cm^3 (ρ is density) that would enable the organic matter to float and the inorganic part to immerse, allowing skimming to be performed. This method was avoided because the organic matter would be contaminated with Zn rendering it ineligible for any chemical studies. Hence, the organic matter was mechanically recovered from the sand bodies, aiming each time to recover the least inorganic part possible. The recovered material (a mixture of organic and mineral matter) was then hand-crushed using agate mortar. The use of a crushing machine in organic matter studies holds the risk of producing very fine grained particles that would be

too small and could not therefore be studied by means of optical microscopy, especially when only minute quantities of samples are available.

The detailed methodology followed for the preparation of the polished blocks as well as for the polishing is described below step-by-step.

1) Weight approximately 18 gr of each sample and hand-crush them to finer pieces using agate mortar.

2) Sieve the crushed samples and assort 3 fractions (different grain sizes). The first fraction being larger than 1 mm, the second in between 1 mm and 45 μm and the third smaller than 45 μm, by using the respective sieves. The first size is kept as a reference for future analysis, the second is being used to produce the polished blocks and the third which is in powder form can be used for the FT-IR analysis.

3) Place the < 1 mm sample fraction inside cylindrical silicon matrices and then pour in a few drops of epoxy resin until the grains are just covered.

4) Intermix the resin with the grains until they become wet (saturated). Inadequate mixing will result in the formation of air globules (air-trapping) during the solidification process.

5) Let the mixture to rest in order for the grains to immerse at the bottom of the matrix for approximately 30 minutes before pouring the rest of the resin in the matrix. This is a very important step because if the resin is being poured all at once, the inorganic part that is of higher density will submerge faster, leaving the organic matter concentrated at the bottom of the polished block.

7) After 2 hours the resin is almost solid. At that moment the label with the sample name can be placed at the backside of the block. If this step is done earlier the label will be deeply submerged in the resin, rendering it unreadable.

8) Let the polished blocks to cool down for at least 24 hours, if possible in a moisture free environment preferably in an oven of 40^{o}C or inside a glass vial with silica gel.

9) Unmount the blocks from the matrices and prepare for polishing. The method used for polishing is a modified version of the technique described in Pontolillo and Stanton (1994) and was elaborated as follows:

10) Grind the block using the automatic polishing machine starting with coarser grit papers and passing progressively to finer (180 – 800 – 1200 μm). Rinse the blocks with distilled water if necessary when switching grit papers. The grinding must be performed on dry grit papers (no water or other lubricant) and the blocks should be rotated when polishing to avoid directional polish.

11) Clean the blocks ultrasonically for 3-4 minutes and rinse again with distilled water.

12) Rough polish on a 15 μm aluminum oxide paste for 5-10 minutes. Rinse with distilled water

13) Rough polish on 0.03 amorphous colloidal polishing compound. Rinse with distilled water.

14) The polished blocks are ready for oil-immersion studies.

Vitrinite reflectance

The random vitrinite reflectance (R_r%) measurements were applied on polished blocks Ø±1, mounted on epoxy resin according to ISO 7404-2 (2009). A Zeiss (Axio Imager D1M) microscope equipped with oil-immersion objectives in total 50x magnification was used. The vitrinite reflectance was conducted following ISO 7404-5 (2009). Theoretically, a hundred measurements should be taken on vitrinite on a single sample, but a satisfactory mean average can also be achieved with less measurements (i.e. 30) depending on the organic matter content of the studied sample (Rallakis et al., 2013). In this case the reflectance measurements were made on vitrinite using spinel (%R=0.420) as a standard and a photomultiplier tube (PMS) coupled to SpectraVision A.S&Co software.

Trace elements in carbonates, pyrite and uranium minerals and rare earth elements (REE) in carbonates and uranium minerals

The Laser Ablation-Inductively Coupled Mass Spectrometry (LA-ICPMS) was used to study the Rare Earth Elements (REEs) dolomite, calcite and uraninite. The analyses were carried out at the Laboratory of GeoRessources-Nancy. Laser sampling was performed with a 193 nm GeoLas Pro ArF Excimer laser (Microlas®, Göttingen, Germany) equipped with beam homogenization optics. Ablation was performed by focusing the beam at the sample surface with a constant fluency of 10 J/cm^2 and constant repetition rate of 5 Hz. Helium was used as a carrier gas to transport the laser generated aerosols from the ablation cell to the ICP-MS. Ablated material was analyzed by an Agilent 7500c Quadrupole ICP-MS (Agilent®, Santa Clara, California) equipped with an Octopole Reaction System with enhanced sensitivity optional lenses (Cs type, Agilent). The certified glass standards NIST610, NIST612 and NIST614 SRM were used as reference materials (concentrations from Pearce et al., 1997) for the calibration of the LA-ICP-MS. The protocol for routine analysis of REE in carbonate was checked using GSR6 reference carbonate standard (Xie et al., 1989). Absolute concentrations and limit of detection were obtained from the equations developed by Longerich et al. (1996).

For dolomite and calcite the suite of elements analyzed by LA-ICP-MS was La, Ce, Pr, Nd, Sm, Eu, Gd, Tb, Dy, Ho, Er, Tm, Yb, and Lu, in addition to Na, Mg, Ca, Ti, Mn, Fe, Cu, Zn, Rb, Sr, Y, Ba, Th and U. Detection limit range from a few ppm for Ce to down to 0.5 ppm for heavy

rare earth elements. The REE spectra were normalized both to PAAS (McLennan, 1989) and versus chondrite (Masuda et al., 1973; Anders and Grevesse, 1989).

With respect to pyrite the suite of elements analyzed was V, Co, Ni, Cu, Zn, As, Se, Mo, Ag, Cd, Sb, Pb) and with respect to uranium minerals the suite of elements analyzed was Na, Mg, Si, P, Ca, Ti, Mn, Fe, Ni, Cu, Zn, Rb, Sr, Y, Ba and Pb.

C, O Isotopic analysis (bulk and *in situ*)

For the C, O stable isotopes 32 whole rock samples have been selected. In more detail the dataset consisted of 26 dolomite cemented plus 6 calcite cemented sandstones. The latter originate from outcrops at the regional area of Zoovch Ovoo and were used for comparison. All isotopic measurements were performed at CRPG laboratory (Vandoeuvre-lès-Nancy, France) using continuous acidification under He flow and calculated the bulk carbonate composition following the method described in Scheffer et al. (2016). The isotopic measurements were systematically doubled in order to check homogeneity of analyses. Isotopic compositions are quoted in the standard delta notation in ‰ relative to V-PDB and for oxygen. Carbon and oxygen isotopic compositions of calcites and dolomites were determined by using an auto sampler Gasbench coupled to a Thermo Scientific MAT253 isotope ratio mass spectrometer (IRMS). 250–300 µg of each carbonate sample was collected using a Dremel tool (1 mm diameter sampling hole). The obtained powder was then reacted with 2 mL of supersaturated orthophosphoric acid at 70 °C for at least 5 h in a He atmosphere. 10 measurement cycles of the produced CO_2 isotopic composition were performed with a Thermo Scientific MAT 253 continuous flow isotope ratio mass spectrometer. All sample measurements were adjusted to the internal reference calibrated on the international standards IAEA CO-1, IAEA CO-8 and NBS 19.

For *in situ* C, O isotopic analysis the instrument used was a Cameca IMS 1270 ion probe at CRPG (Nancy), using an in house dolomite standard (G119). When analyzing mixed dolomite-siderite phases, the same dolomite standard was considered. The thin sections were gold coated before mounting. During the analysis, the dolomite cements were sputtered with a Cs^+ beam source of 2-3 nA intensity inside a vacuum chamber, with 10 kV acceleration voltage. Each spot analysis was performed under 40 cycles of 5 seconds each. The results were first reported as per mil deviations from the international standard SMOW (Standard Mean Ocean Water) with respect to $\delta^{18}O$ and in V-PDB for $\delta^{13}C$.

For consistency and to compare with the bulk rock values, the oxygen values were converted to PDB based on the following formula: $\{\delta^{18}O_{V\text{-}SMOW}=1.03086*\delta^{18}O_{V\text{-}PDB}+30.86\}$ after Friedman and O'Neil (1977); Kendall and Caldwell (1998); Hoefs (2009); Zhao and Zheng (2013).

Sulfur isotopic analysis (*in situ*)

To determine the origin of the sulfur we have dedicated a week of ion probe sessions on the isotopic chemistry of pyrite, in collaboration with CRPG Nancy and the Jean Lamour Institute. The session was focused on the measurement of the $\delta^{34}S$ of the different pyrite occurrences. The results were normalized using an in-house pyrite standard (Spain) and then treated using the formula described in Kitayama et al. (2012).

Organic Matter-Uranium relationships

The organic matter-uranium relationships were studied by means of conventional petrography, of organic petrography (oil-immersion) and of electron microscopy (SEM-EDS and EMPA). The objective was to make the link between the organic matter types with the uranium phases. Wherever the sedimentological logs and core photographs were available the relationships with the associated sedimentological facies were discussed.

The methodology followed for the sampling was based on Brouand (2015). A modified version was used in order to sample the organic matter. The aim was firstly to avoid long term contact with plastic surfaces that would affect the chemical properties of the organic matter and secondly with the atmospheric air that would as well oxidize the organic matter. Therefore, these samples were preserved inside aluminum bags under vacuum (Figure 194).

The step-by-step methodology for the sampling of the organic matter presented in the Appendix (Figure 194) and is as follows: 1) Thermal welding device. 2) Preparation of bags from aluminum heat-sealable coil. 3, Sorting and 4) placement of the O.M-rich sample in the aluminum bag. 5) Thermo-sealing of the aluminum bag. 6) Mini-vacuum pump. 7) Sealing-off and vacuum establishment. 8) Samples stored under vacuum - O.M is preserved.

67 samples were collected in total during the 2017 exploration campaign. In particular 47 of the samples come from the older drill-cores (Appendix Table 17) and 18 from the new wells. (Appendix Table 18). Some cores, namely the ZOOV_1155, 1156, 1157 were also logged in terms of lithology and in certain cases sedimentology. The objective was identify the sedimentological context as well as the redox status of the adjacent formations.

Rock-Eval

The core intervals that were relatively enriched in organic carbon were selected for that study. Such intervals, contained coal as thin laminas mixed with clays, or coal dispersed inside carbonate cemented sands or loose sands. In this framework 16 samples representing organic matter mechanical concentrates in powder form were sent to ISTO-Orleans to perform Rock-Eval pyrolysis.

Organic molecules characterization

Lipid organic matter was extracted using dichloromethane (DCM) with an automatic extractor (Dionex ASE 350) at 100°C and 10^6 Pa. In order to avoid spectrometer damage due to the presence of elemental S, it was removed by the addition of metallic Cu. The insoluble fraction (residual matter) was analyzed using Py-GCMS with tetramethylammonium hydroxide (TMAH). This method is suitable for investigating the molecular organic matter and in particular the tracers utilized to separate terrestrial vs aquatic input (Frazier et al., 2003; Jeanneau et al., 2014). The solvent-extracted SPM was mixed with solid TMAH in excess (1:5 wt%; Hatcher and Clifford, 1994). An aliquot (10-15 mg) was placed into a quartz tube and Py-GCMS analysis carried out using a split/splitness injector. On-line flash pyrolysis at 620°C was performed with a CDS 2000 Pyroprobe for 15 seconds. Pyrolysis products were separated on a DB 5-MS 60 m_0.25 mm_0.1 mm column. Samples were injected in splitness mode at 300°C. The oven was cooled to 0°C (held 10.5 min) by injecting liquid CO_2 and was programmed to 40°C (held 10 min) at 45°C/min, then to 315°C (held 10.5 min) at 5°C/min. Pyrolysis products were identified from GC retention times and mass spectra from comparison with the Wiley and NIST spectral libraries. MassHunter Software was used to treat the signals and to obtain clean spectra, after deconvolution and to compare with the libraries. Assignments were also carried out from comparison with published mass spectra of pyrolysis products. Assignments were also carried out from comparison with published mass spectra of pyrolysis products (Challinor, 1995; Mason et al., 2012). The peak area of the selected m/z value for each compound was integrated and corrected via a correction factor. The proportion of each compound class was calculated by dividing the sum of the areas of the compounds in the class by the sum of the peak areas of all analyzed compounds multiplied by 100. Eight lignin phenols were selected to describe the lignin composition, and six permethylated deoxy aldonic acids (glucose, mannose, galactose, xylose, rhamnose and fucose) to describe oses. The distribution of the FAs in the refractory fraction (Ref-FAs) was also used (n-C6 to n-C26). The extracts were also analyzed with GC–MS for Lip-FAs, PAHs and sterols. Only the PAHs were quantified using internal standards and were analyzed separately. Four perdeuterated PAHs were added to each extract (naphthalene D8, acenaphthene D10, chrysene D12, perylene D12). In addition, four oxygenated-PAHs (O-PAHs) and nitrogenous-PAHs (N-PACs) were added (quinolone D7, anthraquinone D8, dibenzofuran D, 9H and fluorenone D8). PAHs are expressed in mg/g dry SPM. PAH quantification was performed using a Shimadsu-2010 plus-QP2010 Ultra. This apparatus was equipped with a DB 5–MS column (60 m _ 0.25 mm _ 0.1 mm) and was operated in selected ion monitoring (SIM) mode. Samples were injected in split mode (split ratio 1:5) at 300°C. The GC oven temperature was programmed from 70°C (held 2 min) to 130°C at 15°C/min, then from 130°C to 315°C (held 2 min) at 4°C/min. Sterols and Lip-FAs

were analyzed qualitatively after derivatization using N,O-bis(trimethylsilyl)trifluoroacetamide (BSTFA)/trimethylchlorosilane (TMCS). Sterols and Lip-FAs were characterized using an Agilent GC7820/MS75. This apparatus was equipped with a DB 5–MS column (60 m_0.25 mm_0.25 mm) and operated in selected ion monitoring (SIM) scan mode, following several characteristic ions for maturation characterization with SIM mode. In scan mode the scan was set between 50 to 550 m/z. Samples were injected in split mode (split ratio 1:5) at 300°C. The GC oven temperature was programmed from 70°C (held 2 min) to 130°C at 15°C/min, then from 130 to 315°C (held 2 min) at 4°C/min. We aimed to follow several characteristic ions for maturation characterization with SIM mode.

Gas analysis

Rock of various facies were collected from the freshly drilled cores during the drilling campaign of July 2017 in Zoovch Ovoo. Core sections were loaded into air tight aluminum lined sampling bags. Air was removed by primary vacuum pump and the bags sealed. After several weeks of storage at ambient conditions, the bags inflated. The gas in the bags was collected using a gas transfer line equipped with needles connecting the sampling bags to vacuumed glass containers (vacutainer). Gases were sampled by allowing pressure equilibrium between sampling bag and vacutainer. In total 37 samples were collected for gas analysis with only three of them presenting very important inflation.

GCIRMS analysis of gases

Gases were analyzed at the organic geochemistry laboratory at the University of Oklahoma (USA). Aliquots of gas were sampled by syringe through the vacutainer septum and injected in split mode into a GCIRMS equipped with a PoraPLOT Q (length: 27.5m; diameter: 0.32mm; film thickness: 0.10µm). Chromatography program was 40°C held for 10 min, following a heating rate of 15°C/min to 220°C and isotherm held for 13 min. The oxidation furnace was run at 960°C and the HTC reactor at 1440°C.

Fourier Transform Infrared Spectroscopy (FT-IR)

The FT-IR analyses were performed to determine the presence of oxygenated functions of the organic matter (peat to lignite maturity in terms of coalification) that are important for uranium adsorption, forming organo-uranyl complexes. The infrared spectra are recorded in transmission mode using a BRUKER Equinox IFS 55 Fourier transform infrared spectrometer equipped with a DTGS detector (deuterated triglyceride sulfate) at a spectral resolution of 2 cm^{-1}. Pellets are made by mixing 2 mg of sample with 200 mg of potassium bromide (KBr) stored in an oven at 80°C. The mixture is thoroughly crushed in an agate mortar and then placed in a 13 mm pellet die. The pressure applied in the pellet press is 10 T/cm^2. The reference is a KBr pellet.

X-ray Diffraction (XRD)

The mineralogical analyses were performed on bulk rock powder of carbonate cemented sandstones and on oriented clay extracts using a Bruker D2 Phaser equipped with a LynxEye XE-T detector. The interpretation software package used for the evaluation of the diffractograms was Diffrac.Suite along with EVA.

Micro X-Ray Fluorescence

Micro-XRF mapping was effected using the Bruker-Nano M4 Tornado instrument. This system has a Rh X-ray tube with a Be side window and polycapillary optics giving an x-ray beam with a diameter of 25-30 µm on the sample. The X-ray tube was operated at 50 kV and 200 µA. X-rays were detected by a 30 mm^2 xflash® SDD with an energy resolution of <135 eV at 250,000 cps. All analyses were carried out at 2 kPa vacuum. Main elements such as Ca, Mg, Mn, Fe, Ti, Al, K, Na and Si were mapped and composite images were generated.

CHAPTER II

General petrography and sedimentology

2.1 INTRODUCTION

A descriptive petrographic sheet was created for each thin section studied (example of which is available in the appendix, Figure 30 and Table 18) to record the results and allow traceability. These sheets were used to record the characteristics observed with photographic illustrations and to enhance further means of investigation (cathodoluminescence, SEM-EDS, and further geochemistry analyses) as the study progressed. This chapter is an introduction to the sample database and as such it discusses the sedimentological features of the cores and the most important petrographic observations on a basis of 165 thin sections referenced in the appendix section.

2.2 PETROGRAPHY AND SEDIMENTOLOGY OF THE SAMPLES

The Sainshand Formation in the Zoovch Ovoo depocenter is mostly composed of uncemented sediments, such as clays, silts and sands, most of the times grain supported as well as of few consolidated facies represented by dolomite cemented and by matrix (clay) supported sandstones (Figure 20 and Figure 195). On average, dolomite cement accounts for 30% of the sandstone by volume (calculated on bulk rock analysis).

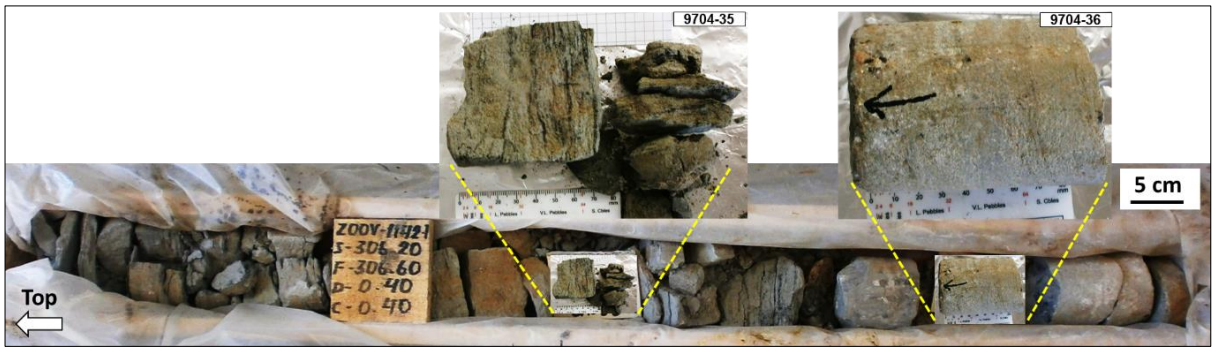

Figure 20: Example of a core sequence in Zoovch Ovoo (well ZOOV_1142, depth 306.20 m). From left to right: reduced matrix supported sandstone, oxidized matrix supported sandstone, reduced matrix supported sandstone with O.M, and reduced carbonate cemented sandstone.

The sediments of the Tsagaan Els depression at the Zuunbayan sub-basin indicate a fluvio-lacustrine depositional environment. They correspond to the Cenomanian Sainshand Formation and in particular to its upper part, codenamed “K2Bs2”. According to their position to the roll-front the sediments can be oxidized, oxidized/reduced or reduced, indicating post roll-front, on-going roll-front and pre roll-front activity (Figure 21 and Figure 22). Hence, the roll-front sediments can be grouped in two distinct units. According to the sedimentological study (Parize et al., 2013), the first lithological unit is composed of finely laminated to stratified homolithic to heterolithic silty to sandy-clay. These fine sediments correspond to varves and compose the background (annual) sedimentation. The second unit is very coarse, sandy to (micro)conglomeretic, most of the time homolithic, with granules of intraclasts originating from

the fine unit. The coarse sediments correspond to sudden flow episodes. As such they are indicating, for most of their part, flood episodes.

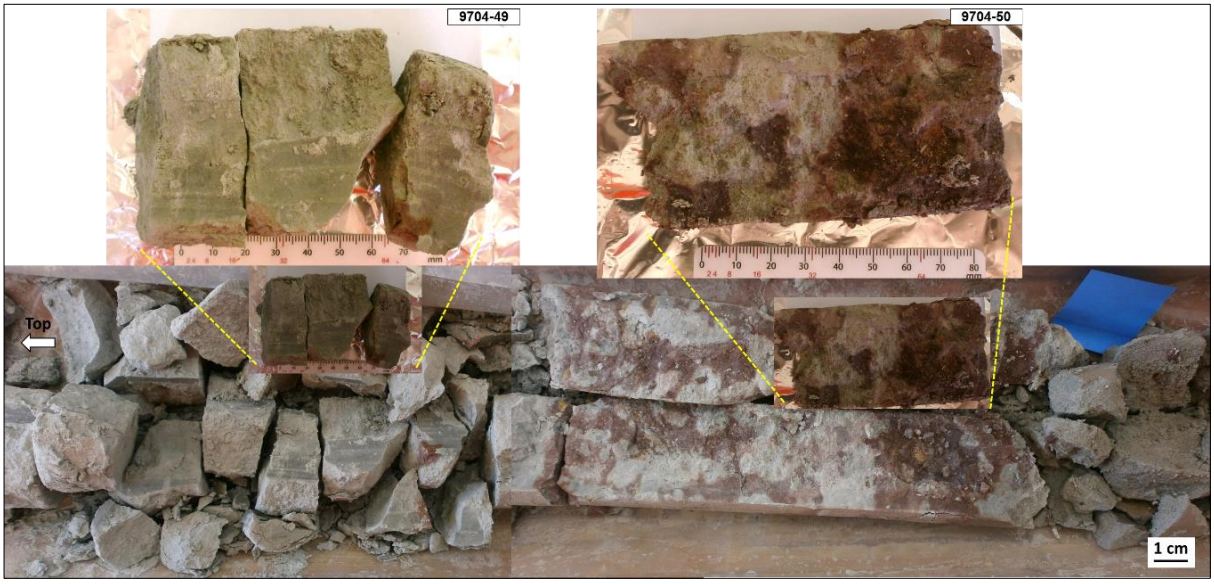

Figure 21: Example of a usual core sequence in Zoovch Ovoo (well ZOOV_1154, depth 164.10 m). Reduced (left) and oxidized (right) consolidated facies ranging from silty claystone to very fine sand.

Figure 22: Example of a usual core sequence in Zoovch Ovoo (well ZOOV_0738, depth 139.10 m). Reduced compacted black (organic rich) claystone and oxidized carbonate cemented sandstone.

Previous detailed petrographic studies from Gaudare (2014), Brouand (2015) and sedimentological studies from Parize (2015) show that the lithofacies encountered in the Zoovch Ovoo depocenter have a very broad granulometric range from silty clays to gravels when considering the unconsolidated facies and from silty claystones to microconglomerates. Furthermore, on the basis of 93 samples analyzed by point-counting, the major lithofacies encountered in Zoovch Ovoo were by 34.5% silts to poorly consolidated sands with clay matrix

and by 22.6% medium to coarse sands with no silty or clay material. Hence the current results, can verify the previous work.

The petrographic observations show that the lithologies encountered in Sainshand Formation at Zoovch Ovoo are sub-arkoses, arenites and silty claystones. The consolidated phases are only some dm thick in the core succession and concern dolomite and pyrite cemented sandstones, with the cements accounting for 30% of the sandstone volume on average.

In more detail, the sandstones are mostly composed of quartz (40 to 80%), feldspars as K-feldspars (microcline, orthoclase, some % to 25%) and plagioclases (5 to 20%), minor phases (apatite, ilmenite) and a few accessories from magmatic origin (monazite, zircon, xenotime, rutile, and anatase). The clay/phyllosilicate fraction (biotite, chlorite, muscovite in the coarse grained fraction) is not abundant and not systematically present. The predominant clay fraction is smectite, on the basis of X-Ray diffraction analysis. Organic matter as detrital coal particles is very frequent in all the above described lithologies. It can be found as dispersed particles inside the sands, silt and clay or concentrated within laminae.

2.3 URANIUM LOCATION IN THE SAINSHAND FORMATION

The Sainshand Formation is a Cenomanian siliciclastic reservoir located in the Zuunbayan sub-basin in East Gobi Basin (SE Mongolia), hosting disseminated uranium ores in the Zuunbayan sub-basin (Cardon et al., 2015; Le Goux et al., 2015). The thickness of the Sainshand Formation varies between 100-350 m and its depositional signature is mixed, ranging between flood-dominated deltas and lacustrine systems that can be separated into two to three sub-units, which reflect different cycles of lacustrine and alluvial sedimentation (Dahlkamp, 2009; Parize, 2015; Le Goux et al., 2015). The uranium distribution assimilates that of a typical roll-front system and thus follows a crescent down-dip geometry.

In this sedimentological framework, uranium mineralization is confined in between the coarse and fine unit as explained earlier. A typical drill-core sequence recovered from the U-mineralized zone is presented in Figure 23. In particular the sand dunes of the lacustrine system serve as uranium reservoirs. There is absence of coal layers inside the reservoir zone and the organic matter contained in the Zoovch Ovoo sands occurs as detrital particles deposited in accordance with the sedimentary bedding structures. The coarse, angular and poorly sorted organic particles are linked to distant transport (reworked), within high energy depositional conditions associated to coarse to medium sized lithologies (coarse to fine grained sands). Organic matter particles encountered in fine clay (organic rich) layers are better preserved and linked to calm depositional conditions under less oxygenated conditions. Finally, the well preserved phytoclasts, such as root remains associated to fine grained organic rich

lithofacies could be indicative of higher plants which grew within the depositional environment setting (no significant transport).

Photo-micrographs

Figure 23*:* Example of a typical drill core sequence (A-C) containing uranium associated to organic matter (D) and silicates/pyrite (E). In more detail:

Sample 9704-8 (well Zoov_0738_1, 123.20 m depth, coarse sand with O.M fragments and yellow product)

A) Drill-core recovered from 123.20 m depth targeting the U-reservoir, Sainshand Formation. Abbreviations: GR (granules); CVC (coarse to very coarse sand), VC (very coarse sand), C (coarse sand) and MC (medium coarse sand). Radioactivity measurements in blue expressed in c/s (counts per second);

B) Two upward-fining sequences are distinguished, starting with granules and ending with medium coarse sand in both cases. The sequences are separated by an erosional surface that contains silty clay and organic matter in dispersed and laminated form;

C) A zoomed image of (B) highlighting the areas of organic matter and of higher uranium concentration. The intense bright yellow color at the base of the first upward fining sequence shows that uranium concentration is highest towards the top of the section at the contact with the erosional surface;

D) Organic matter particle containing between 7-13 wt% uranium, without mineral expression. Image under BSE.

E) Silicate grains coated by phospho-coffinite intermixed with clays. Image under BSE.

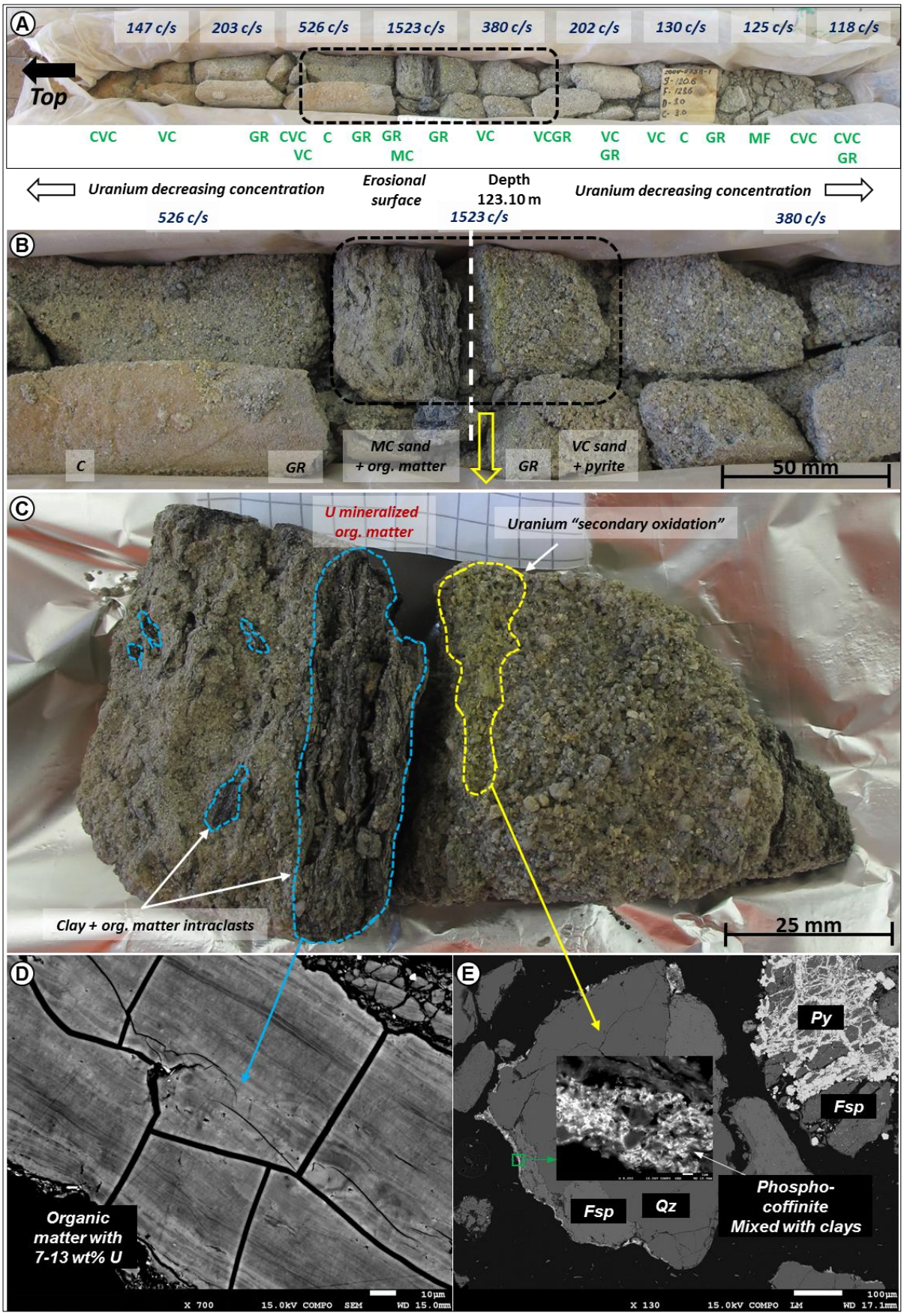

Figure 23: Typical drill core sequence (A-C) containing uranium associated to organic matter (D) and silicates/pyrite (E).

2.4 PETROGRAPHIC FACIES

The methodology followed during the sampling of the cores was focused on horizons with specific textural characteristics i.e. carbonate, organic matter and uranium content in order to complete the thesis objectives; Nevertheless and despite the study not be exhausting, the number of thin sections studied (x161), coming from different depths, from diversed distances from the roll-front, with variable lithologies and redox status cover a wide range of the lithofacies of the Zoovch Ovoo sediments. The two methodologies used for the classification of the samples were based on Wentworth (1922) for granulometry (Table 4) and on Dott (1964) and Pettijohn (1987) for the petrography of the sands (Figure 24).

Table 4: Classification of sediments and consolidated rocks based on granulometry.

Particle diameter (mm)	Sediments	Consolidated rocks	Class
10	Gravels and blocks	Conglomerate	rudite
2	Gravel	Microconglomerate	2 mm
1	Very coarse sand	Very coarse sandstone	1 mm
0,5	Coarse sand	Coarse sandstone	500 µm
0,25	Medium sand	Medium sandstone	arenite
0,125	Fine sand	Fine sandstone	250 µm 125 µm
63(µm) 0,063	Very fine sand	Very fine sandstone	63 µm
2 (µm) 0,002	Silts	Siltstone	lutite
	Clays	Claystone	

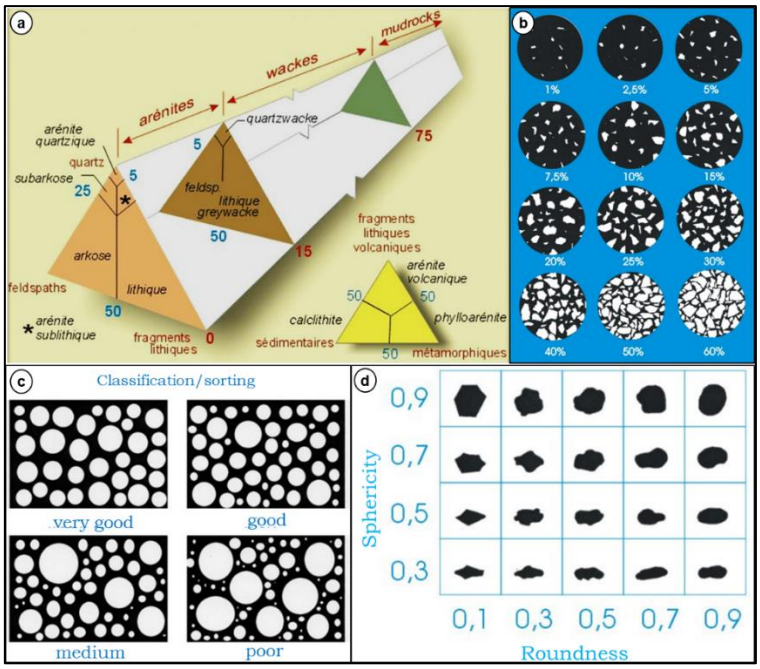

Figure 24: (a) Petrographic classification of detrital rocks (Dott, 1964 and Pettijohn et al. 1987); (b) map of relative visual abundance of grains; (c) classification of grains; (d) sphericity of the grains.

2.4.1 Detrital grains

The major detrital elements are presented in this section according to the criteria of nature, size, shape, texture and degree of alteration. Overall, the detrital elements are mainly grains of quartz and feldspars and also frequently lithic elements. They range from angular to sub-round with a maximum grain size of about 1mm. The presence of the lithic elements is variable, i.e. the series of samples AA (Profile SW-NE_01300) containing less than those of the series BB (SW-NE_03600) and CC (peripheral drilling). There are three types of detrital micas: biotite (often chloritized), muscovite, and chlorite. Feldspars often have sericite alterations to varying degrees. A summary of the detrital grains is presented in Figure 25. Each mineral phase is described below.

Quartz (SiO_2)

The quartz grains are mostly sub-angular and are contained in silty to coarse grained sand. Sometimes they contain inclusions. They are often monocrystalline, but may appear polycrystalline (and then be considered as lithoclasts see "lithic elements" below). In the latter case they can be deformed ("undulose" extinction), or present granophyric and myrmekite textures.

Feldspar

Feldspars recognized concern both plagioclases and alkali-feldspars. The plagioclase grains are sub-rounded to euhedral. Their granulometry varies from silt to medium sand. They are colorless in LPNA, but may appear slightly yellowish-brownish, in association with alterations, often in sericite which leads to paragenesis of muscovite. The polysynthetic twinning of albite is often well marked. Locally, large feldspars (>1mm) appear to contain a former liquid phase inside their fracture porosity, which under LPNA has brownish color. The alkali-feldspar grains are more often sub-angular and their granulometry ranges from silt to medium sand. They are colorless in LPNA, but can sometimes appear yellowish-brownish because of alterations. Often distinctly mated. The typical perthite and micro-perthite textures are often observed. Finally the granophyric or myrmekite textures are also very often encountered. In grains with a granophyric texture, the alkali feldspar is often brownish in LPNA due to weathering while quartz is translucent. In LPA the individual grains are typically automorphic.

Micas

Micas (biotite, muscovite) and less often chlorites are generally well preserved, sometimes curved or elongated without preferential orientation within the grains. Their length is usually longer than 0.2 mm. Muscovite is colorless in LPNA and has clear cleavages. Biotite and chlorite have brown and green pleochroism respectively. In LPA muscovite presents bright

colors of third order. Biotite and chlorite have a strong birefringence and their natural colors mask the colors of polarization.

Carbonates (detrital)

Detrital carbonate grains were also identified, with dolomite stoichiometry. These are microcrystalline dolomite spherical patches void of other detrital grains. The size of grains can be larger than 0.5mm. Very often the grains are associated to siderite. Petrography suggests that detrital dolomite is the earliest dolomite type. It was recognized in samples of the oxidized but also of the reduced parts of the roll-front.

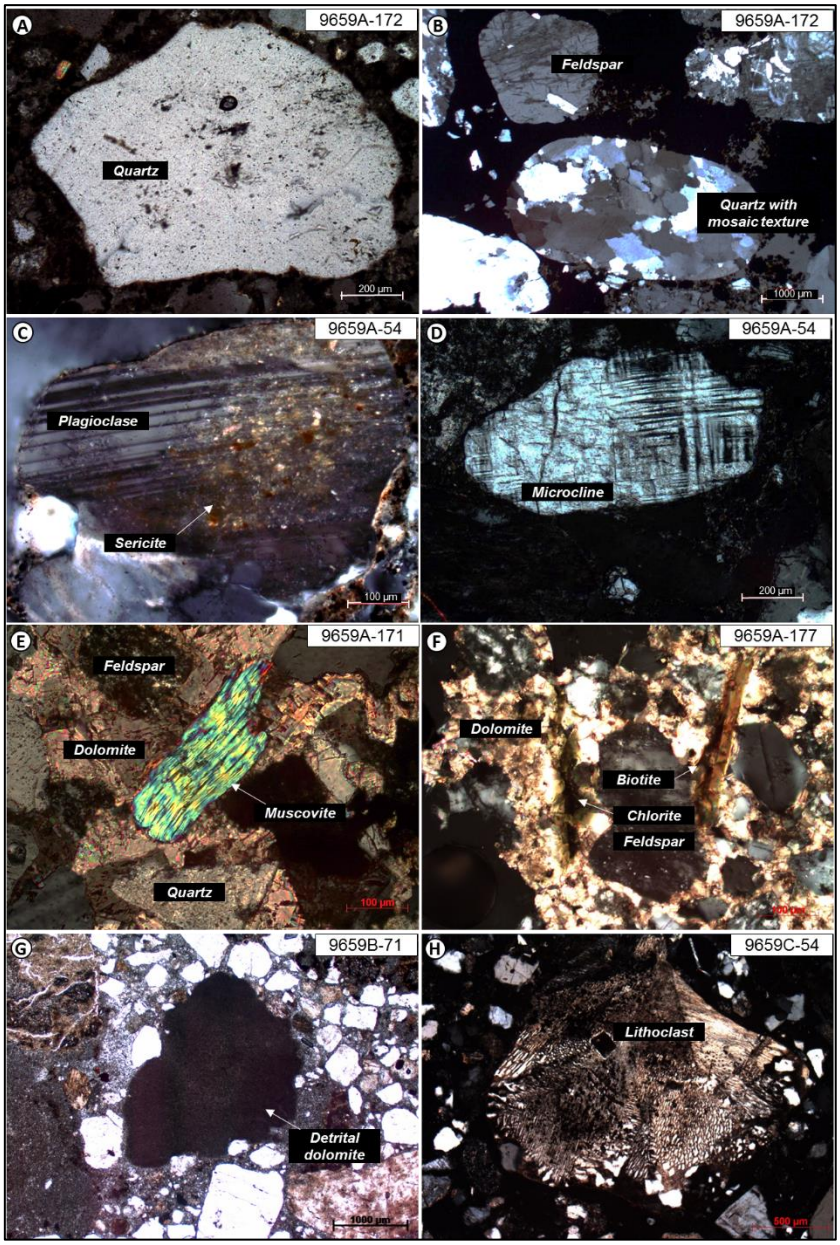

Figure 25: Summary of the main siliciclastic and carbonate elements presented in the Zoovch Ovoo sands. (A, B) Monocrystalline and polycrystalline quartz. (C, D) Plagioclase and microcline with polysynthetic and cross-hatched twinning respectively. The plagioclase also shows sericite alteration. (E, F) Mica input, muscovite, chlorite, biotite. (G) Detrital dolomite grain, (H) Lithic element showing granophyric texture. All pictures under LPA; (G) under LPNA.

Fe-Ti oxides and apatite

Detrital apatite and metallic minerals are also very common among the detrital grains, mainly as Fe-Ti oxides i.e. ilmenite, anatase and rutile. Ilmenite is an oxide of titanium and iron present in almost all thin sections. It is very often associated to pyrite. Ilmenite is opaque in LPNA and has grey reflectance in LR. The two polymorphs of TiO_2 are also very often observed in the samples. The anatase is brown to whitish in LR. Rutile is differentiated from anatase by its acicular form. It sometimes highlights relics of ilmenite crystals.

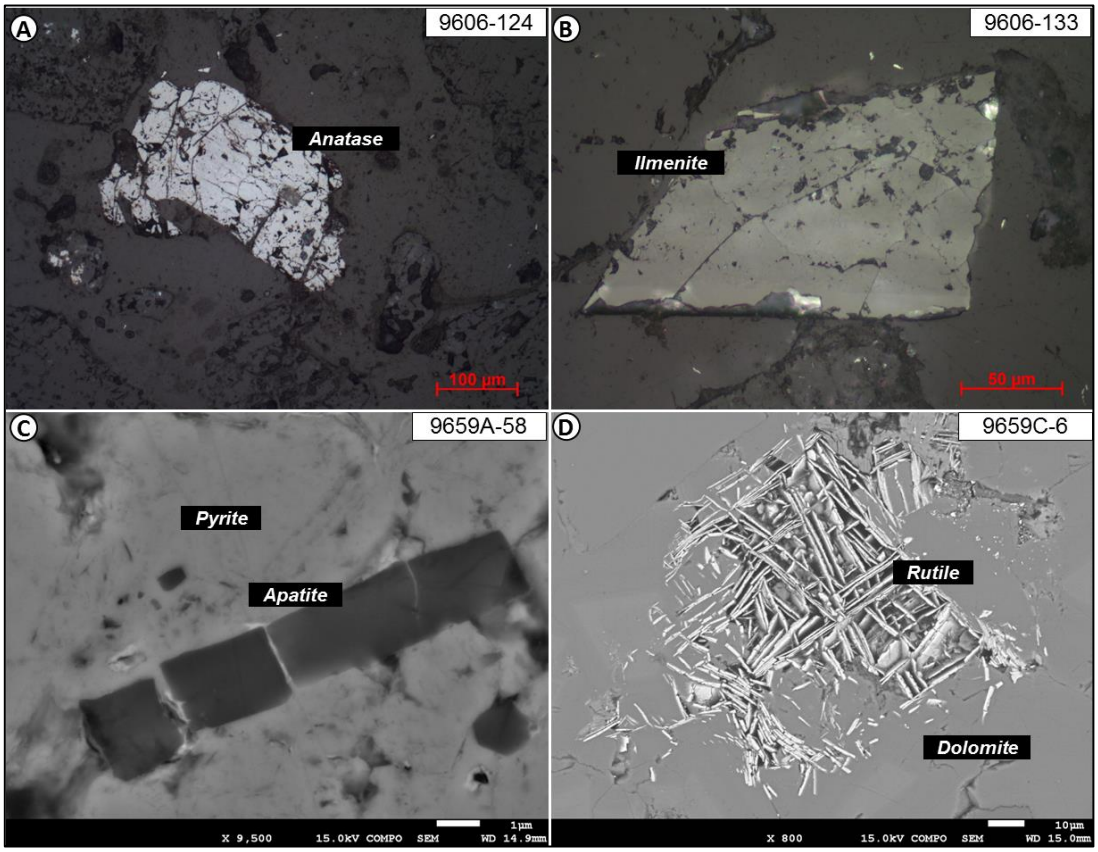

Figure 26: The most common oxides contained in the Zoovch Ovoo sands. A) anatase in RL; B) ilmenite in RL; C) apatite in SEM and D) rutile in SEM.

Lithic clasts

The lithic elements are common but not necessarily present in all samples. They often have a larger dimension than other detrital elements, sometimes over 1mm. Lithic quartz elements can have mosaic or microgranular texture. Some lithoclasts contain quartz-feldspar, quartz-micas and feldspar-micas.

The latter lithic elements preserve certain textures of the detrital sources. The textures recognized in the Zoovch Ovoo sands include doleritic and granophyric indicating igneous sources along with mylonite and myrmekite indicating tectonic deformation episodes (Figure 27).

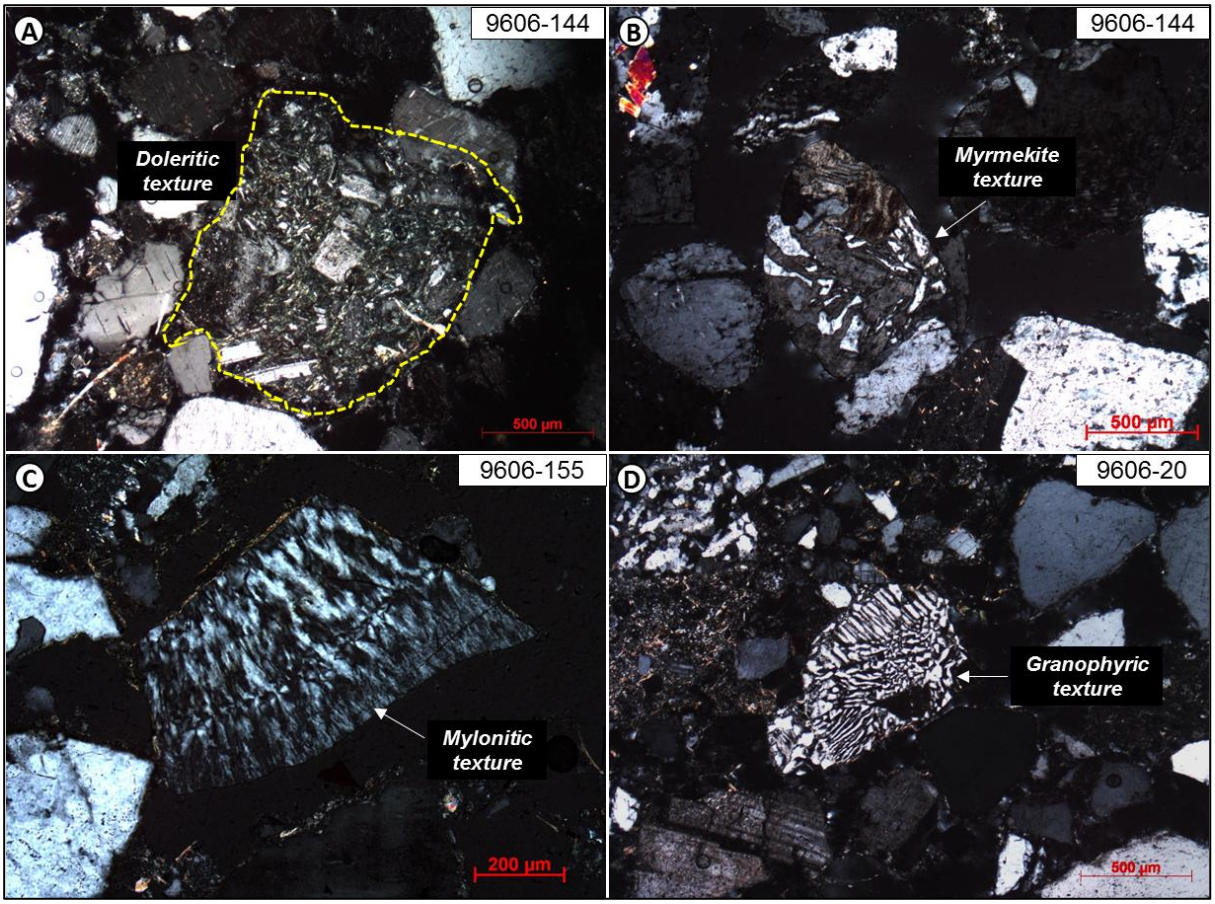

Figure 27: Lithic elements of the Zoovch Ovoo sands with (A) doleritic, (B) myrmekite, (C) mylonitic and (D) granophyric textures, inherited from igneous sources.

Accessory minerals

The identified accessory minerals are zircon, tourmaline, xenotime, monazite, pyroxene and glauconite. The zircon is recognizable by the strong relief the absence of color in LPNA and the higher birefringence colors under LPA. Very often it is zoned and can develop a halo of pleochroism in relation to its U-Th content. The tourmaline is pleochroic with dark to dark green color in LPNA and was encountered very rarely in the studied samples. The yttrium phosphate, xenotime can be confused with zircon although xenotime grains, however, do not have the same shape as zircon despite belonging to the same crystallographic class and they do not have zoning. Monazite is a thorium phosphate that has a very strong refraction with third order colors in LPA but is not zoned like zircon.

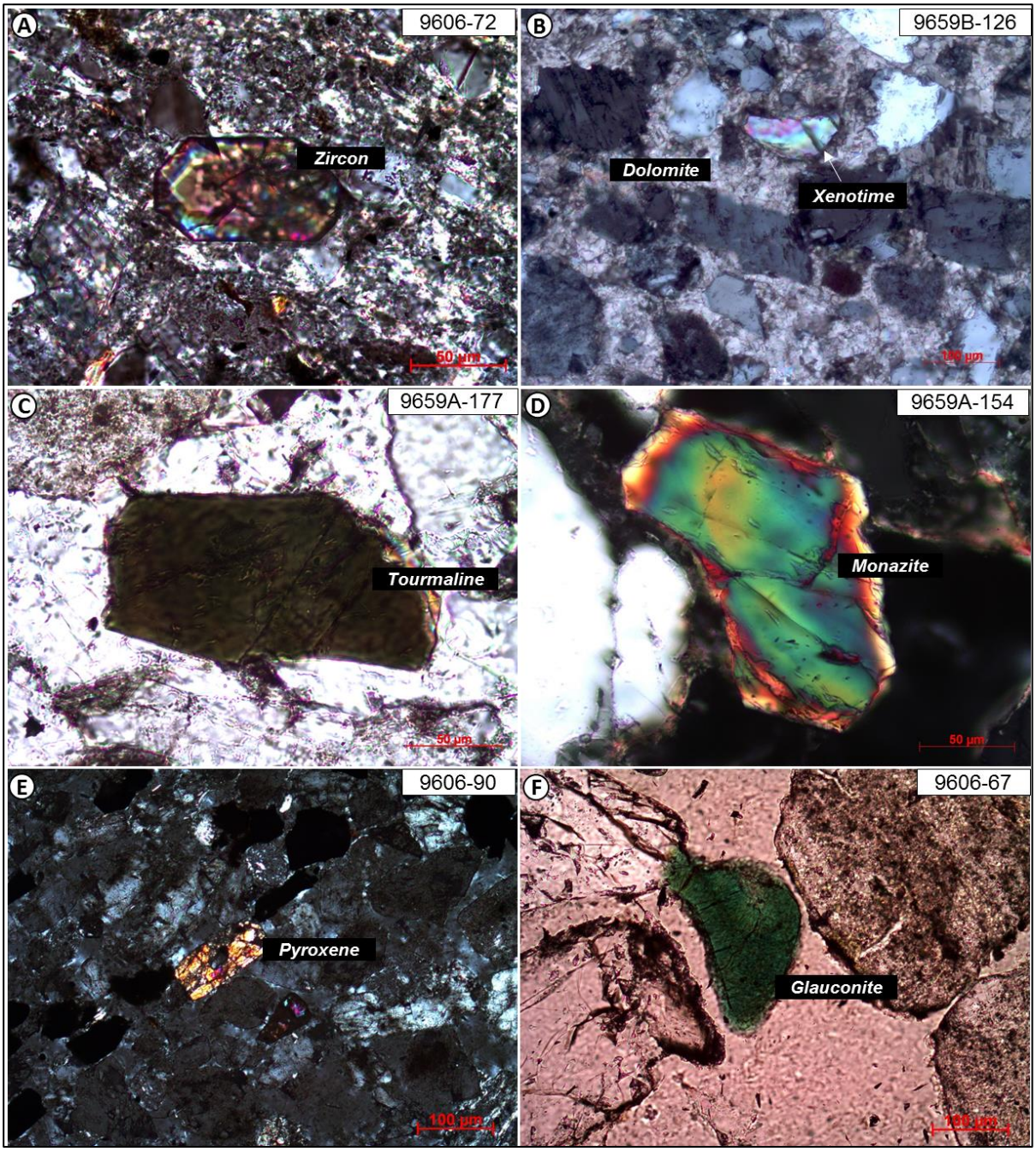

Figure 28: Accessory minerals contained in the Zoovch Ovoo sands. A) zircon in LPA; B) Xenotime in LPA; C) Tourmaline in LPNA; D) Monazite in LPA; E) Pyroxene in LPA and F) Glauconite in LPNA.

2.4.2 Matrices and cements

Matrices

The most common binding phase encountered is the clay matrix. The color of the matrix is often yellowish-brown in LPNA. In some cases, the clay matrix contains altered micas. Rarely, disseminated dolomite rhombs can be found inside the clay matrix in very small quantities. In mineralized sands (U-rich) the clay matrix contains uranium minerals as cement.

In certain cases dolomite can also be characterized as matrix. Specifically, it occupies the intergranular porosity cementing the sandstone, while the sand grains are not in contact with each other (floating grains). This particular dolomite cement is microcrystalline but it differs from the microcrystalline detrital dolomite grains.

Cements

Dolomite, sulfides (mainly pyrite) and uranium minerals are the major cements identified in the Zoovch Ovoo sandstones. The shape of the crystals of the dolomite cement varies from euhedral to subhedral and final anhedral. The euhedral crystals (rhombs) can have siderite cores and zonations. With respect to sulfides, euhedral pyrite appears as cement binding sand grains, sometimes containing relics of framboidal pyrite. Another less common sulfide acting as cement is sphalerite. Finally, uranium minerals were also identified, cementing sand grains and are always associated to reducing agents, mainly organic matter and pyrite.

2.4.3 Authigenic minerals

A series of many different authigenic minerals were recognized, formed during different stages of the reservoir's burial history. The authigenic minerals are discussed independently in the sulfides and dolomite chapters.

Pyrite

Pyrite is the most common authigenic mineral and was recognized in three forms, as framboids, as concentric overgrowth formed around framboids and as euhedral or cubic.

Marcasite

The polymorph of FeS_2 marcasite was also recognized, forming around euhedral pyrite.

Other sulfides

Sphalerite is by far the most common sulphide after pyrite and was encountered quite often in mineralized samples. Other sulfides include galena (PbS), greenockite (CdS) and acanthite (Ag_2S). These associated minerals are found rarely and they are most of the times contained in uranium rich samples.

Sulfates and Selenides

Barite ($BaSO_4$), gypsum ($CaSO_4x2H_2O$) and the selenides namely, clausthalite (PbSe) and Stilleite (ZnSe) were recognized in minute quantities. Native selenium is often found associated to organic matter, particularly being contained inside O.M cell-walls.

Fe oxides/hydroxides

In the leached area at the rear of the roll-front Fe-hydroxides and oxides, namely limonite ($FeO(OH)\cdot nH_2O$), goethite ($FeO(OH)$) and hematite (Fe_2O_3), are present. In fact entire layers of reduced claystone can become partially red due to the presence of these authigenic iron facies, depending their position in the roll-front (Figure 21).

2.5 CLAY MINERALOGY

Some tests on the clay mineralogy were conducted by means of X-Ray Diffraction as to set comparison with Reinholdt et al., (2016) (ORANO-Univ. Poitier internal report). The analysis was repeated twice, one before (air-dried) and one after ethylene-glycol treatment, since swelling clays were identified (Figure 29). It was concluded that the predominant clay fraction is smectite (recognized by the typical swelling at 14-17 Å followed by kaolinite, which is in accordance to Reinholdt et al., (2016). In total 6 clay samples were analyzed, revealing the same pattern.

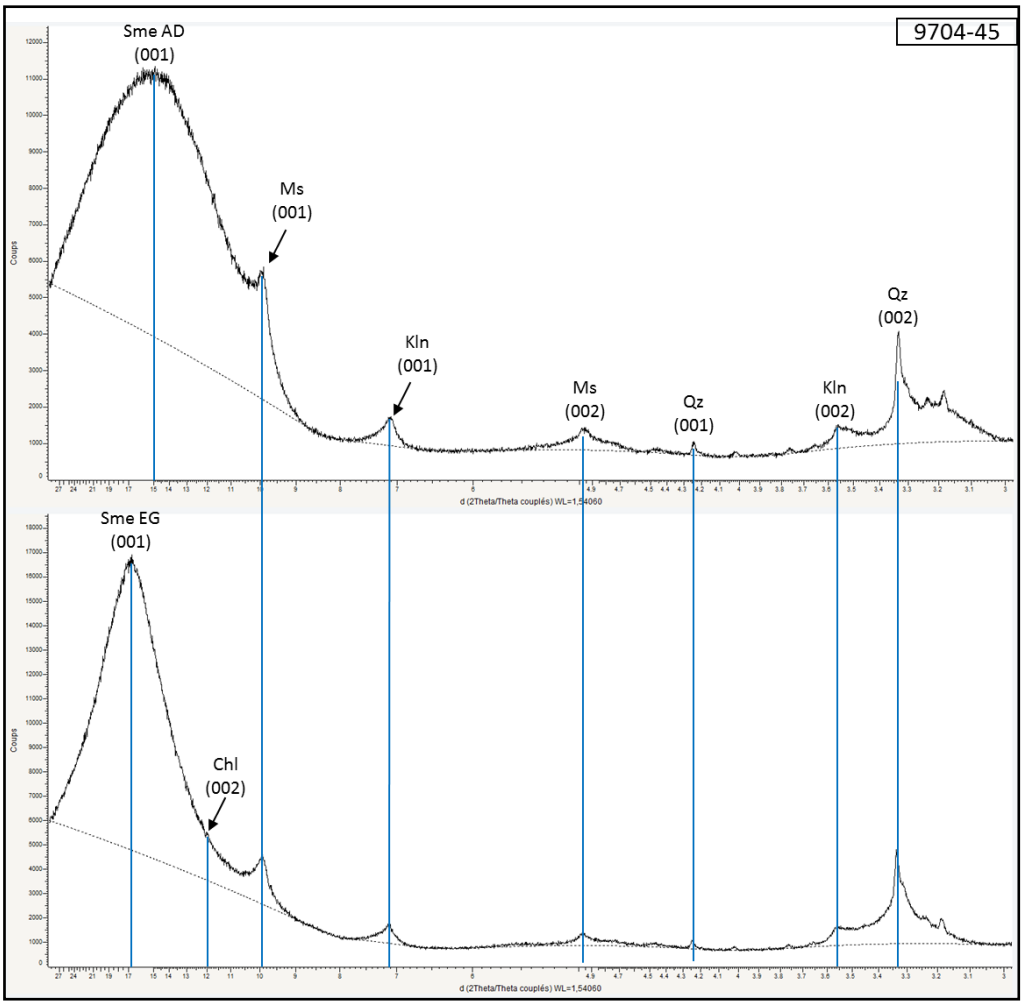

Figure 29: Diffractogram of oriented section under air-dried (AD) conditions and after ethylene-glycol (EG) treatment, for the sample 9704-45 (black silty-clay from the mineralized zone).

2.6 GEOCHEMICAL CHARACTERISTICS OF THE SEDIMENTS

This chapter is based on data from bulk rock geochemistry obtained by ICP-MS techniques and they consider a series of samples, from barren to heavy U-mineralized. The objective was to understand how these two elements are associated and then to use these data to describe the mineral and organic facies that are linked to these elements. Two simple binary plots are presented, first for uranium versus sulfur and then for uranium versus organic carbon.

2.6.1 Geochemical characterization of the barren and mineralized facies

According to petrography, the detrital organic matter present in the samples is often associated to U. Hence, based on the whole rock U-C_{org} diagram (Figure 30A) four trends may be distinguished:

- An increase of organic C at very low U content, indicating no relationship. In these cases, organic matter is barren of U.
- An increase in U content from a few ppm to more than 5.500 ppm at low C_{org} value which indicates the presence of U phases (U oxides or silicates) in samples containing low concentrations of organic matter.
- A correlation between organic matter content and the U content, which suggests the presence of U rich OM. In this case, organic matter would be associated with up to 20 wt% of U, corresponding to the end-member of the trend (for instance 80 wt% C_{org} would contain 20 wt% U).
- Some data points are intermediate between the two last trends and may correspond to the occurrence of UO_2 independently of the presence of organic matter.

Likewise, according to petrography the only mineral facies that contain sulfur in the studied samples are exclusively the sulfides, in particular pyrite. Generally there is absence of evaporites and other sulfates and the few occurrences are limited to secondary products of pyrite alteration. Having this constraint in mind three trends may be identified on the U-S binary plot (Figure 30B).

- The first trend shows no association of U to S. Uranium increases from a few ppm to 5500 ppm while S makes less than 0.5 wt% of the bulk rock.
- In the second trend, S increases from a few percent to 3.6% while the U content remains less than 500 ppm indicating that S is independent of U.
- In the third trend the concentration of uranium tends to increase when sulfides are available. In this frame, U increases proportionally with S concentration. This supposed relationship needs further investigation to be confirmed and explained.

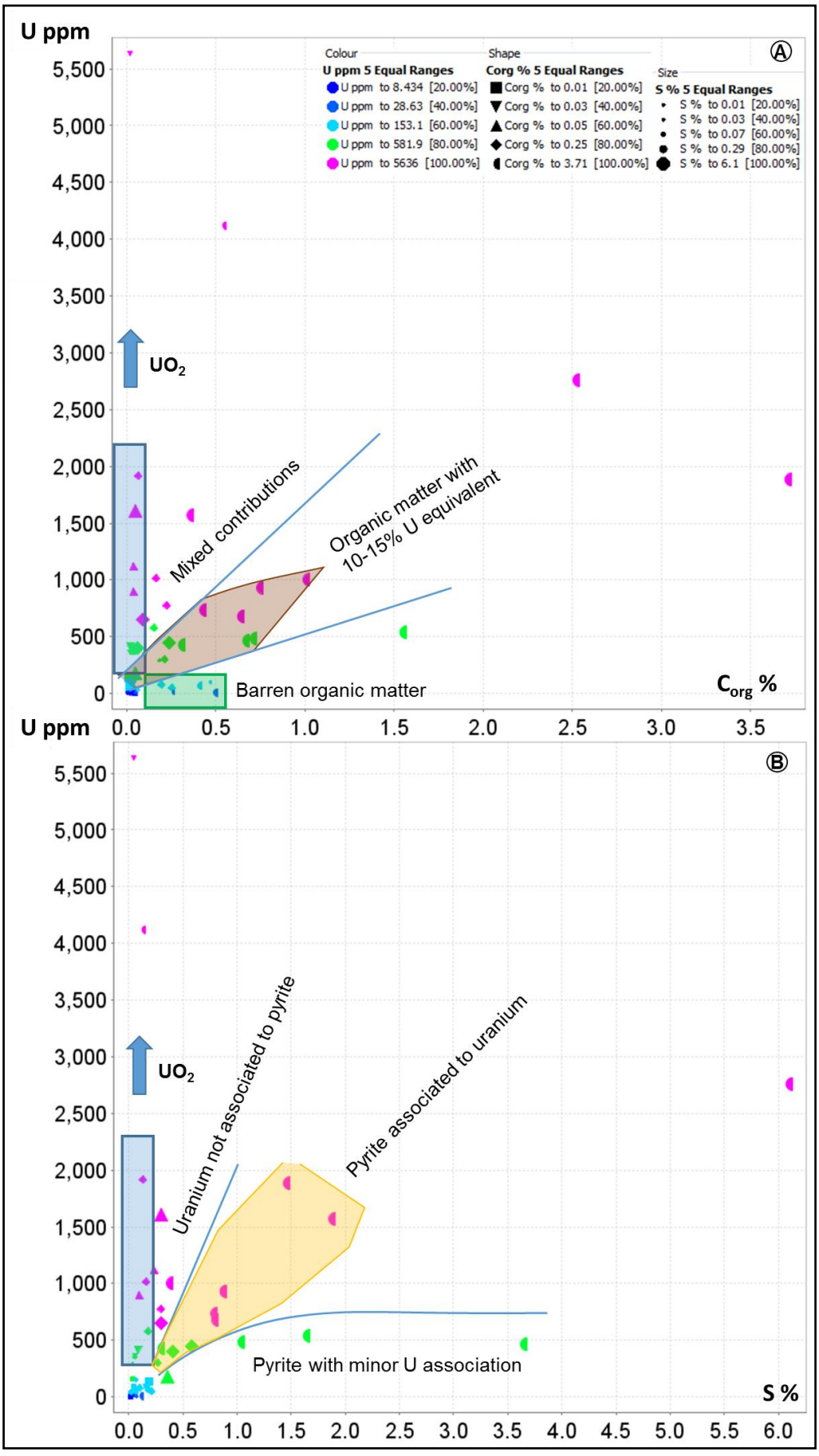

Figure 30: Uranium vs organic carbon (A) and uranium vs sulfur (B) indicating potential associated geochemical trends. Data from ICP-MS on whole rock.

2.7 CONCLUSION

The sedimentary sequence in the Zoovch Ovoo deposit can be separated in two distinct lithological units. The first unit refers to the background annual sedimentation, consisting of silty to sandy clay, forming varves. The second unit refers to very coarse sandy to microconglomeratic lithologies often containing intraclasts of the first unit, corresponding to sudden flow episodes. Uranium mineralization is confined between these two units as a function of permeability. Based on petrography the reservoir of Sainshand Formation (K2Bs2 unit) in Zoovch Ovoo is composed of sub-arkose, arenite and silty claystone lithologies. The sands contain lithoclasts of igneous sources that underwent tectonic deformation. Detrital organic matter is often contained as intraclast inside the coarse reservoir unit. As a result the uranium geochemical anomalies are systematically associated to organic rich layers or intraclast accumulations. Hence, the sediments accompanying the anomalies are usually very coarse to coarse. This feature suggests that the uranium bearing fluid is initially controlled by permeability, migrating along the coarser part of the sand layers (and along layer boundaries/ erosional surfaces). Detrital organic matter particle accumulations in the vicinity of these highly permeable layers will then act as reducing agents to $U^{(VI)}$ by the processes explained above. Since grain size of the sediments and organic matter distribution are directly inherited from the sediments' depositional system, it could be suggested that the migration of the U bearing fluids as well as the U trapping by the organic matter are under sedimentological control at core scale.

CHAPTER III

Dolomite cement study

3.1 INTRODUCTION TO THE CARBONATE STUDY

The present chapter is dedicated to the mineralogy and geochemistry of the different carbonate cemented facies contained inside the fluvio-lacustrine deposits of the Upper Cretaceous Sainshand Formation (K2Ss2 unit) in the goal to understand their origin and conditions of formation. The studied samples are placed on the Profiles SW-NE_01300 and SW-NE_03600 (Figure 31 and Figure 32) to better illustrate the distribution and evolution of the different carbonate cemented facies. The typology of each carbonate facies is supported by petrographical, cathodoluminescence and SEM-EDS observations. Examples from the bibliography are also used to compare the findings. With respect to the crystal-chemistry of the carbonate cements, the EPMA is used to obtain information on the major elements and the LA-ICP-MS on the REE's. Ultimately, the study yields to a first series of hypotheses about the conditions of carbonate cement formation and their interpretation.

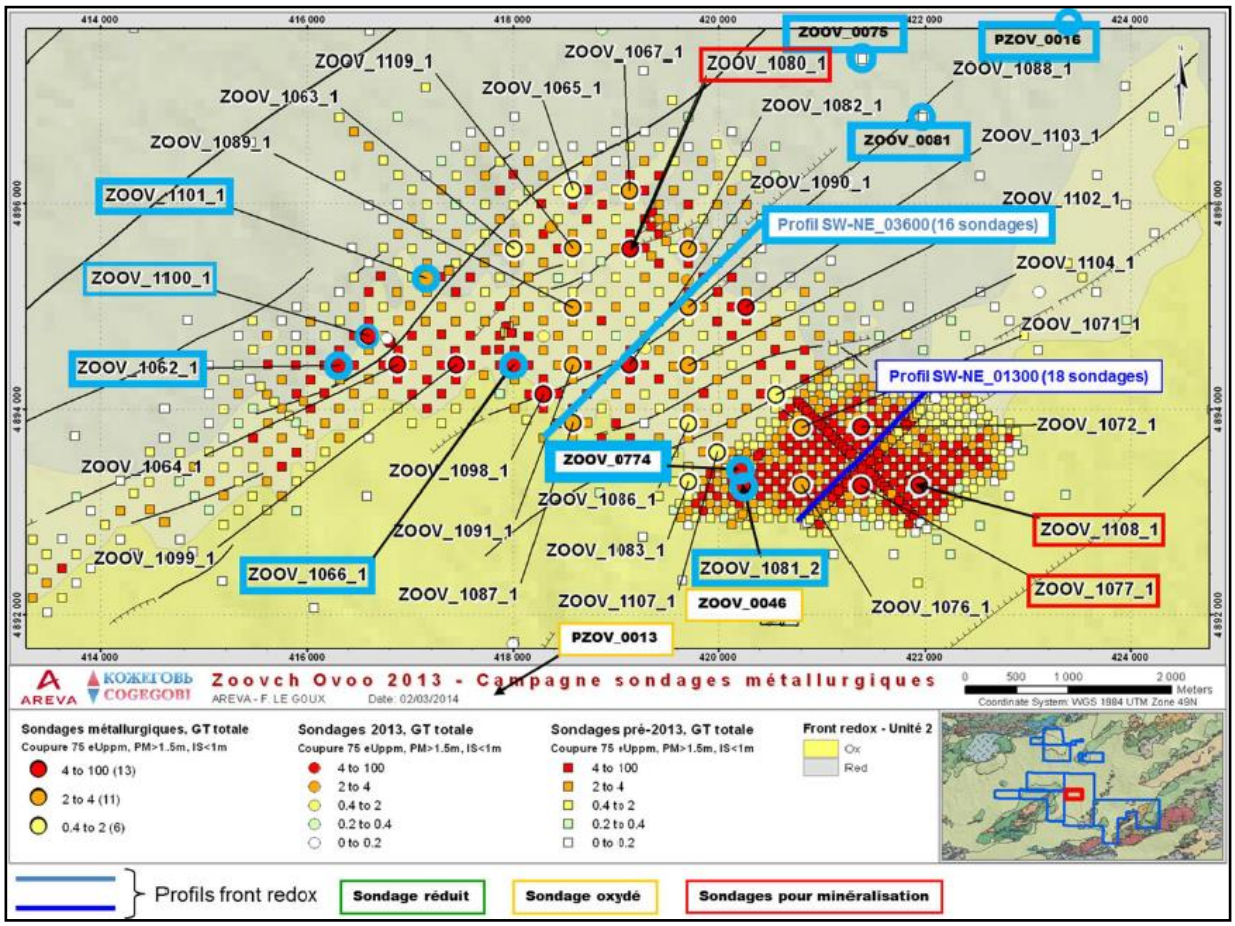

Figure 31: Schematic overview of the Zoovch Ovoo roll-front type deposit in Zuunbayan sub-basin. Highlighted in blue color the localities containing carbonate cemented sandstones outside Profile SW-NE_013000 and Profile SW-NE_03600 (in BROUAND, 2015-COGEGOBI)

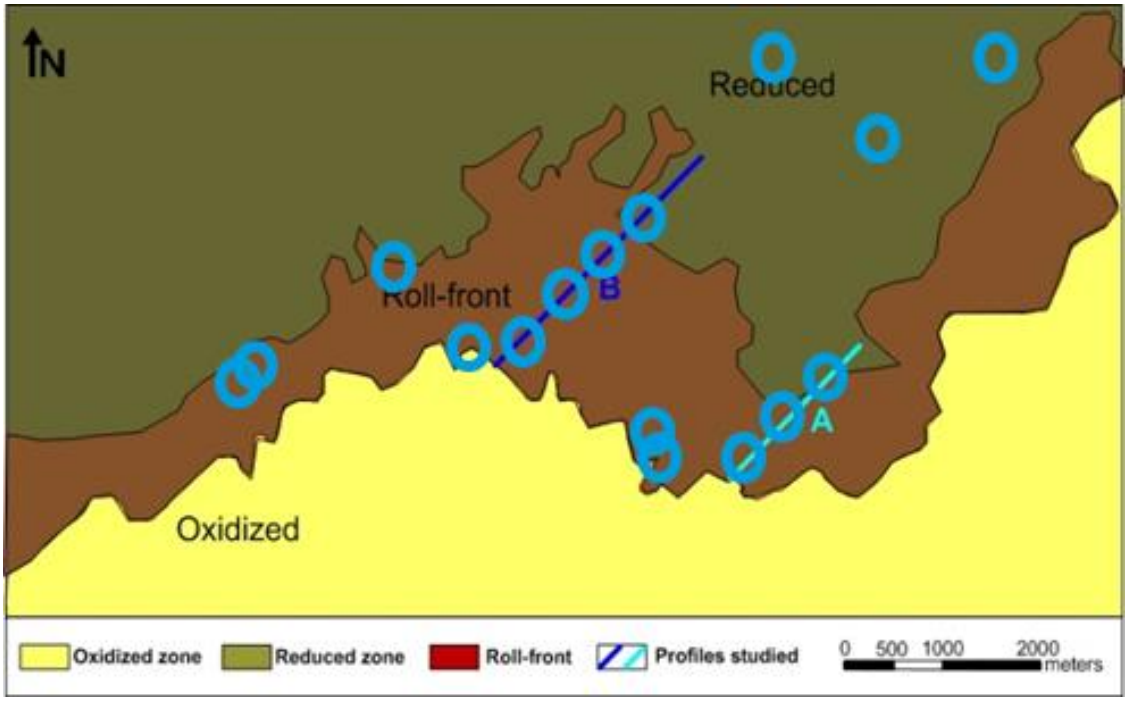

Figure 32: Graphical representation of the Zoovch Ovoo roll-front in planar-view (simplified Figure 31). Location of the two studied A and B in teal (SW-NE 01300) and blue (SW-NE-03600), respectively.

3.2 CARBONATES CEMENTS: TYPES AND TEXTURES – CRYSTAL CHEMISTRY

3.2.1 Spatial distribution

The carbonate cement facies distribution alongside the roll-front Profiles SW-NE_01300 (prefix AA-) and SW-NE_03600 (prefix BB-) is not uniform inside the roll-fronts on the two studied profiles (Figure 33 and Figure 34) and the punctual drills illustrated in Figure 31 and Figure 32. Hence, a simple geometric (lateral/vertical) or time evolution is not easy to address. However and despite the sampling being not exhaustive, it is evident that Profile SW-NE_03600 (prefix BB-) is richer than Profile SW-NE_01300 (prefix AA-) in terms of occurrences of carbonate cemented sandstones. Furthermore, the carbonate cemented sandstones are “bounding” the mineralization zone except for three samples that are located inside the zone, namely: AA-36, BB-37 and BB-133. They occur above (e.g. Profiles SW-NE_01300 and SW-NE_03600) or below (e.g. Profile SW-NE_03600) the mineralization zone.

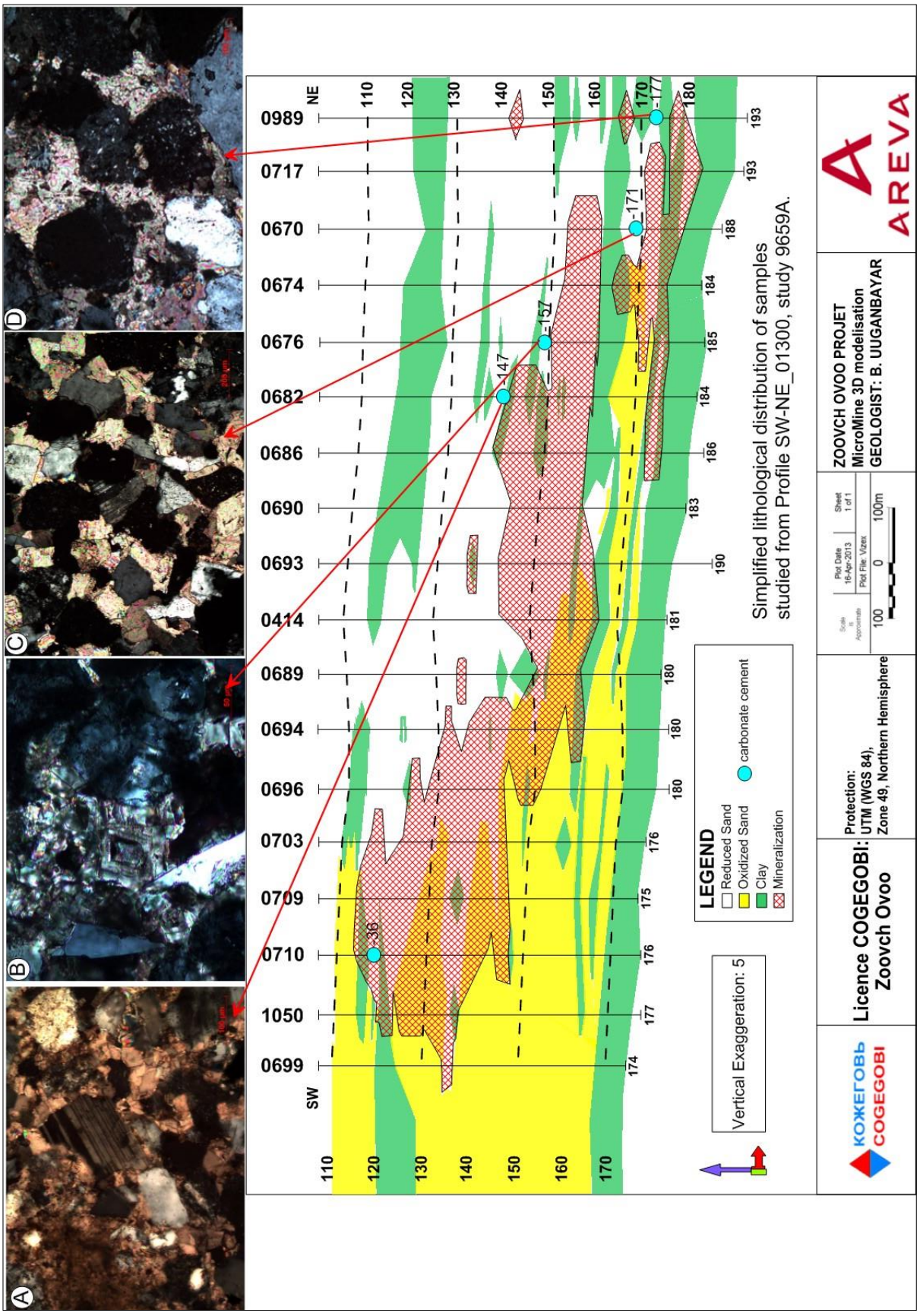

Figure 33: The distribution of the different carbonate cements along **Profile SW-NE_01300** marked with blue color in **Figure 31** (sample prefix AA-).

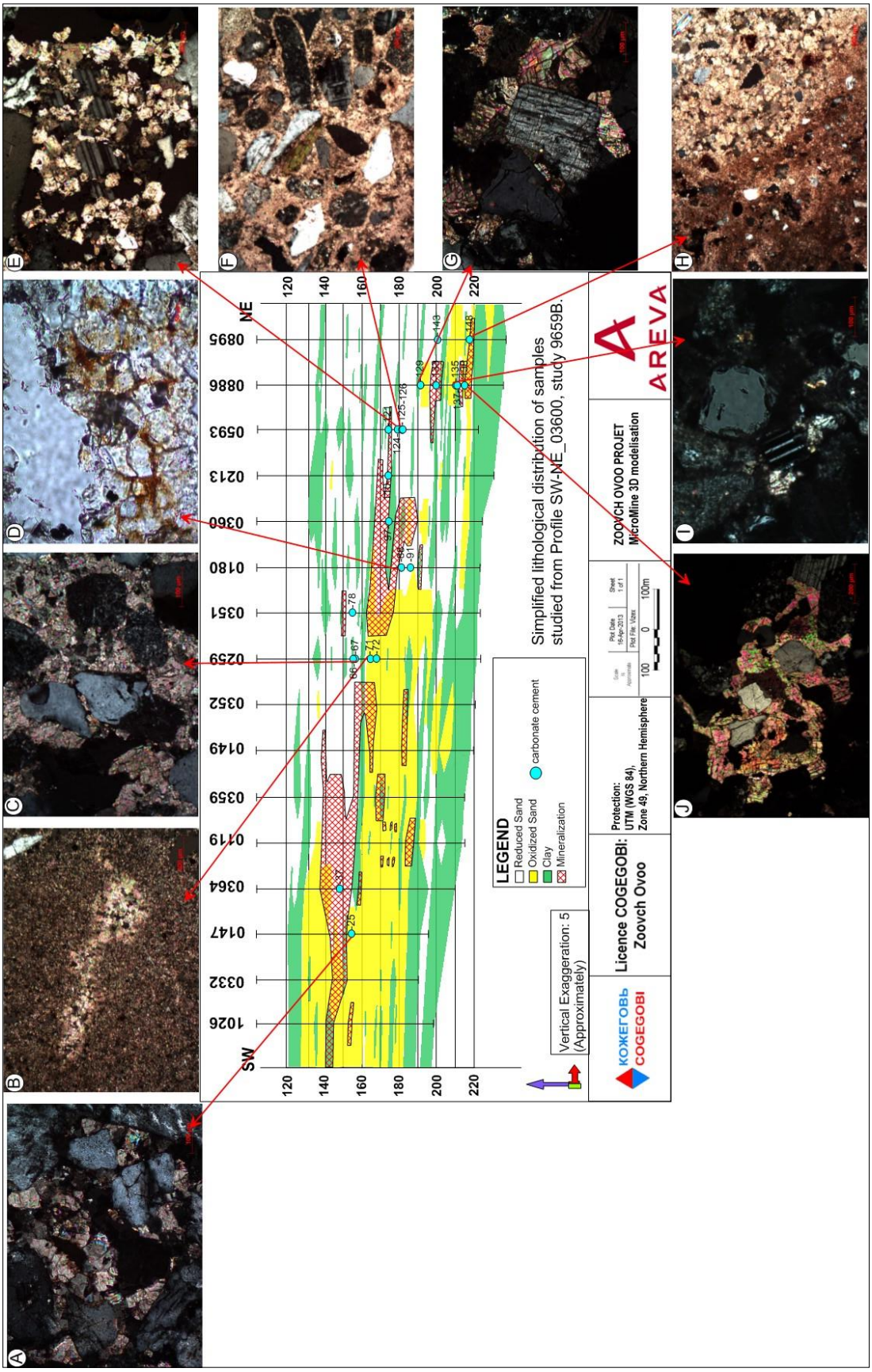

Figure 34: The distribution of the different carbonate cements along **Profile SW-NE_03600** marked with teal color in **Figure 31** (sample prefix BB-)

3.2.2 Typology

Dolomite is the dominant carbonate mineral inside the Zoovch Ovoo roll-front and the presence of pure calcite has not been confirmed. The carbonate classification scheme adopted in this study was primarily based on the optical properties of the carbonate minerals. Initially the carbonate fabrics were divided in two groups regarding the crystal boundaries; hence they were separated in those with planar geometry (idiotopic) and those with non-planar (xenotopic). Then they were grouped according to their crystal size distributions which could be unimodal or polymodal. Finally, the carbonates were classified among their degree of preservation that indicates the resemblance of precursor allochem fabric; hence two varieties were recognized: (i) the mimic (fabric preserving) and (ii) the non-mimic (fabric destroying). A schematic overview of the four main dolomite fabrics identified inside the Zoovch Ovoo sands is presented below (Figure 35).

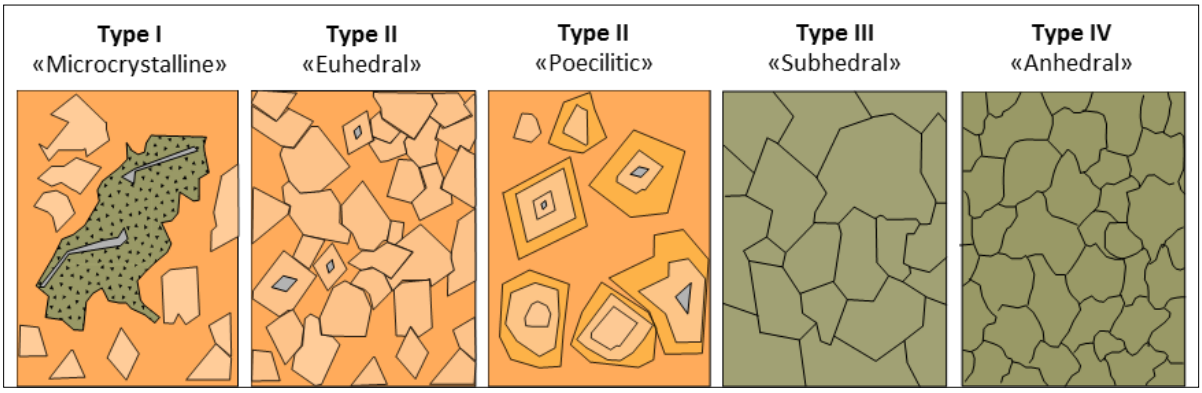

Figure 35: Classification of the dolomite fabrics identified in the Zoovch Ovoo sands (based on Scholle and Ulmer-Scholle, 2003).

The main types of dolomite textures identified during the study of the Zoovch Ovoo sands could be summarized and classified into four categories according to the nature of their crystal boundaries. For simplicity reasons each type was referred by a number as was presented in Figure 35 and is discussed below:

Type I: Microcrystalline

Finely crystalline dolomite fabric consisting of very fine grained dolomite crystals. Therefore the fabric cannot be termed as cryptocrystalline. This dolomite fabric is found in dispersed patches; most typically in samples (9659) A-147, A-157, B-71 and C-6 (Table 14). Small individual crystals are not visible by ordinary microscopy, but when studied under cathodoluminescence they are discrete and have dull red color. They are unimodal and appear to have early zoning (Figure 36). It might be concluded that these small crystals are gradually evolving into the next fabric, which is termed euhedral. Locally the microcrystalline dolomite can be associated to a siderite phase (Figure 36f).

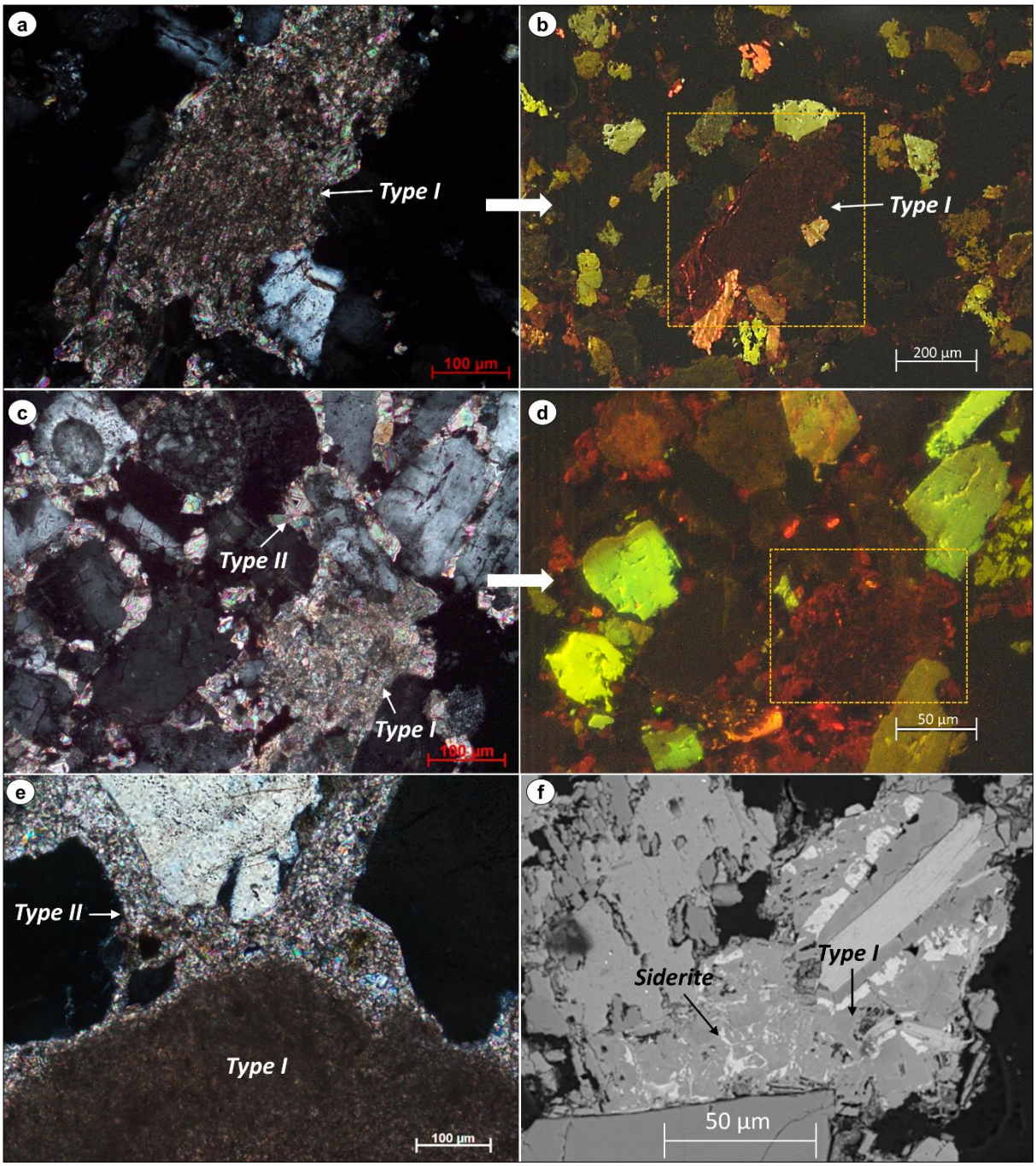

Figure 36: Samples 9659AA-147, 9659B-71: Optical photomicrographs under cross-polarized light (a, c) and their corresponding cathodoluminescence (c) image (magnified x10) and BSE images (d). Although conventional petrography suggests the single presence of microcrystalline dolomite carbonates, the BSE images prove that there is a siderite phase associated.

On the other hand in Figure 37 the microcrystalline cement covers the bulk intergranular porosity. In more detail there are two phases of dolomite, the microcrystalline and the later replacement phase. The replacement phase is polymodal and has early zoning. It is possible that late crystallization presented in Figure 37a occurred on a ghost-grain (or burrow) that has been removed or dissolved since it has been observed that the microcrystalline cement has the potential of penetrating fractures and secondary porosity of the associated grains.

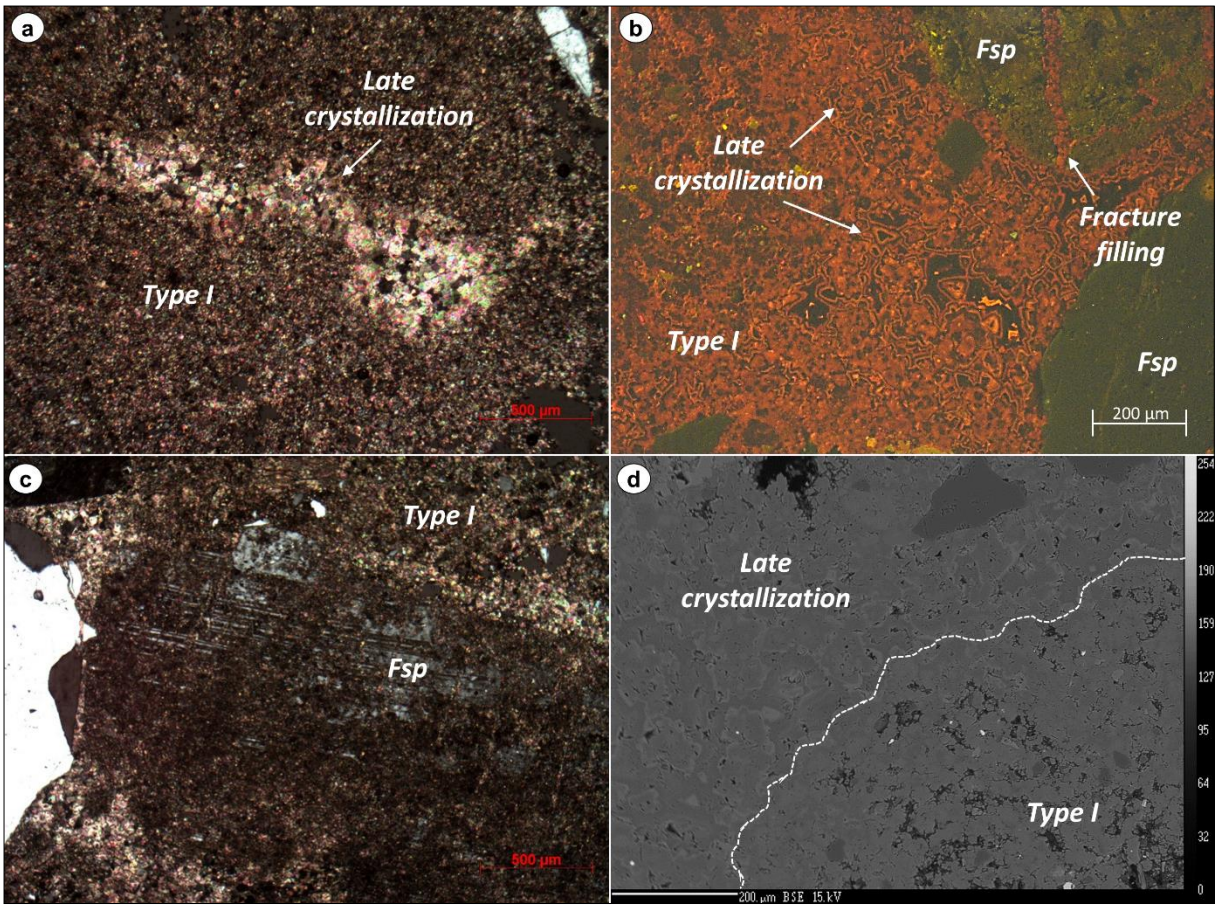

Figure 37: Optical photomicrographs under cross-polarized light (A, C), cathodoluminescence spectra (B) and SEM-image (D) for sample BB-71. Although conventional petrography suggests the presence of microcrystalline carbonates, with cathodoluminescence it is obvious that the assemblage consists of rhombohedral crystals of up to 20 µm in diameter.

Type II: Planar-e (Euhedral)

The planar-e fabric is the evolution of the microcrystalline. It consists of well-expressed euhedral rhombohedral crystal boundaries with dark nuclei (inclusional zoning) and several zonations (Figure 38). Most of the times they are unimodal and they can overgrow to form poecilitic texture by adding syntaxial cement. The poecilitic crystal size can reach up to 100µm.

Although both varieties are euhedral they are very different under cross-polarized light. The early type has darker color and is expressed by well-developed sharp crystal faces. It is as well characterized by inclusional zoning. The poecilitic texture is brighter (probably due the presence of Fe+Mn) and very blocky/massive under cross-polarized light. There is a clear distinction between the different dolomite overgrowths, down to a few µm, possibly reflecting slow process of crystallization with oscillatory changes in water chemistry which explains the light changes in mean “Z” on BSE images. Many times the dolomite rhombs or the overgrowths contain siderite cores and siderite zonations.

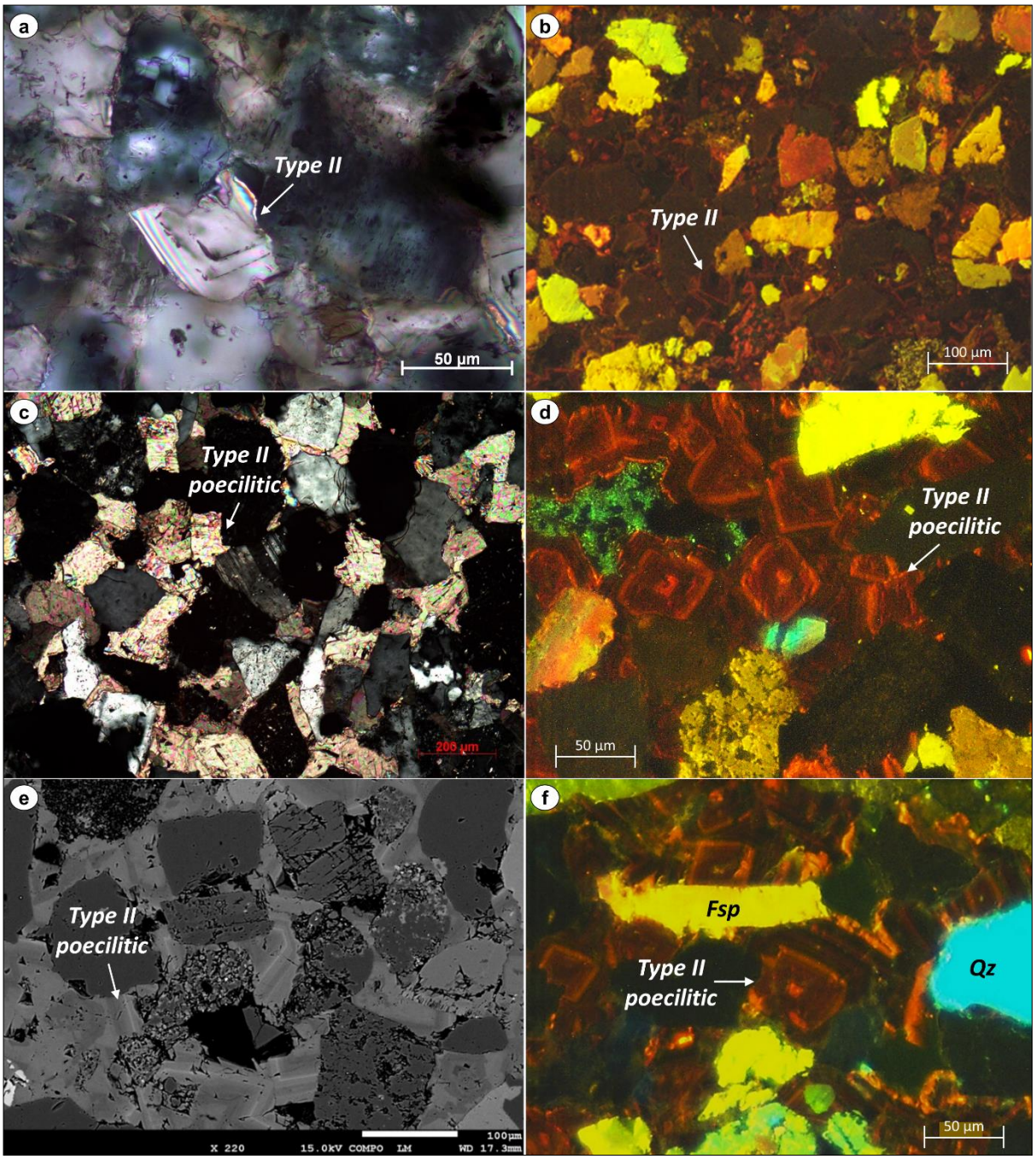

Figure 38: Optical photomicrographs under cross-polarized light (A, C) and CL images (B, D) for samples AA-157 and AA-171, representing the planar-e (euhedral) fabric. SEM-image (A) and CL image (B) for samples AA-177 and AA-171, showing euhedral-poecilitic texture.

Type III: Planar-s (Subhedral)

The planar-s fabric resembles the previous type with the difference that its crystal boundaries are more compromised (Figure 39). It is undifferentiated, massive and very bright under polarized light and has strong red-orange luminescence. The crystal distribution is polymodal but still well connected, hardly leaving any porosity. The rhombohedral structures are becoming less discrete. There is evidence for recrystallization highlighted by the bright yellow spots inside the subhedral fabric.

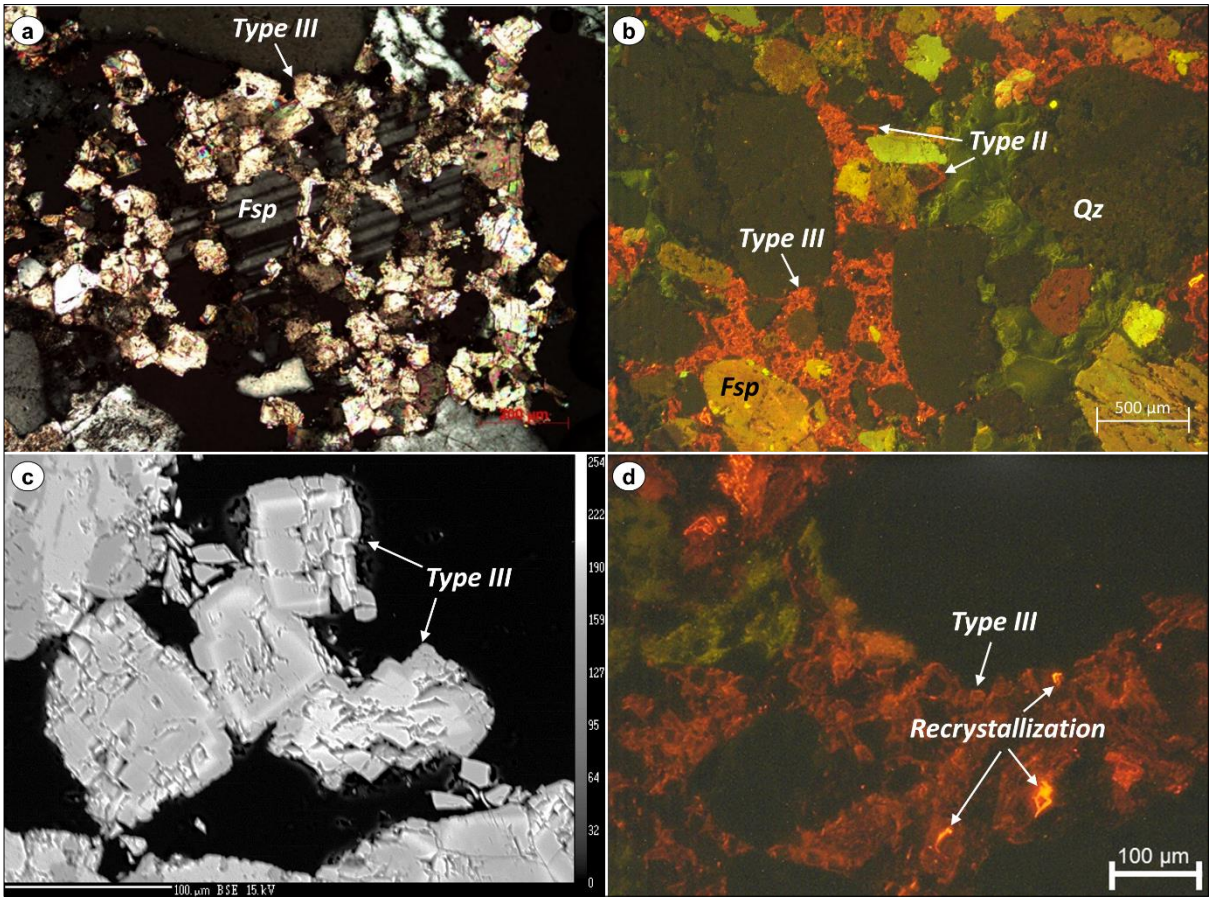

Figure 39: Optical photomicrographs under cross-polarized light (A) and CL images (B, C, D) for sample BB-91, indicating the subhedral dolomite fabric.

Type IV: Non-planar (Anhedral)

The anhedral fabric consists of densely packed crystals with irregular crystal boundaries. In cross-polarized light the dolomite crystals are very different from the other types. It is characterized by a sort of pseudo-cleavage. It is very massive, but there are evidences of porosity increase, probably due to dense packing. Under cathodoluminescence, the anhedral fabric has bright orange color. It is undeveloped and has irregular crystal boundaries. It shows no sign of zoning or earlier fabric (Figure 40). On the SEM images, it is clear that the anhedral dolomite post-dates both the framboidal and euhedral cubic pyrite. It is very possible that this type is the latest diagenetic.

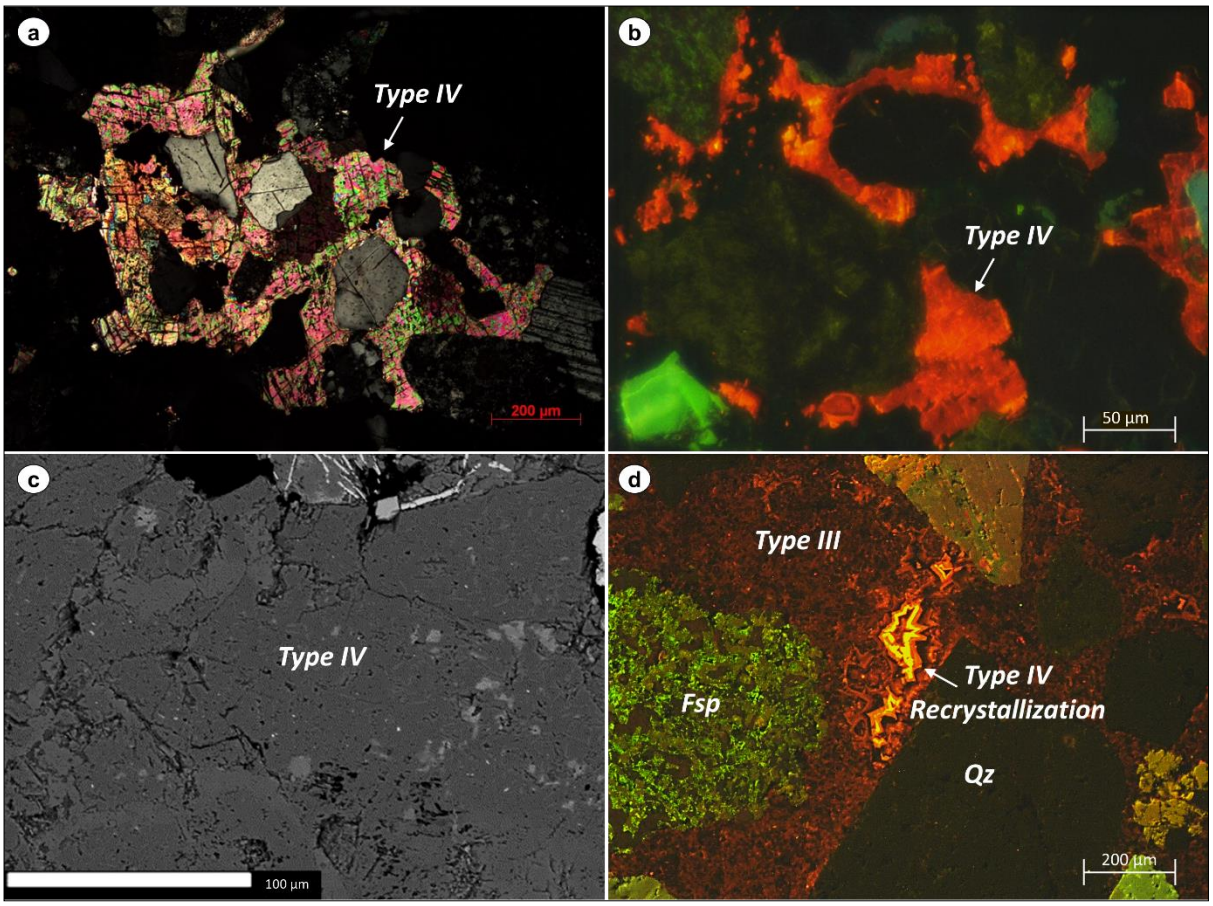

Figure 40: Optical photomicrographs under cross-polarized light (A) and the corresponding CL image (B), SEM-images (C) and (D), showing the anhedral fabric for sample BB-138. It is evident that the anhedral fabric postdates the framboidal and euhedral-cubic pyrite (C, D).

By placing the dolomite fabric types on the Profiles it becomes clear that the predominant type for Profile SW-NE_01300 (Figure 41) is the microcrystalline Type (I) fabric, whereas for the Profile SW-NE_03600 (Figure 42) is the anhedral Type (IV) fabric. This trend may imply a NW evolution of crystallization, moving from the outer towards the central part of the roll-front. However, Profile SW-NE_03600 contains many intermediate dolomite facies that require further study to be assuredly categorized.

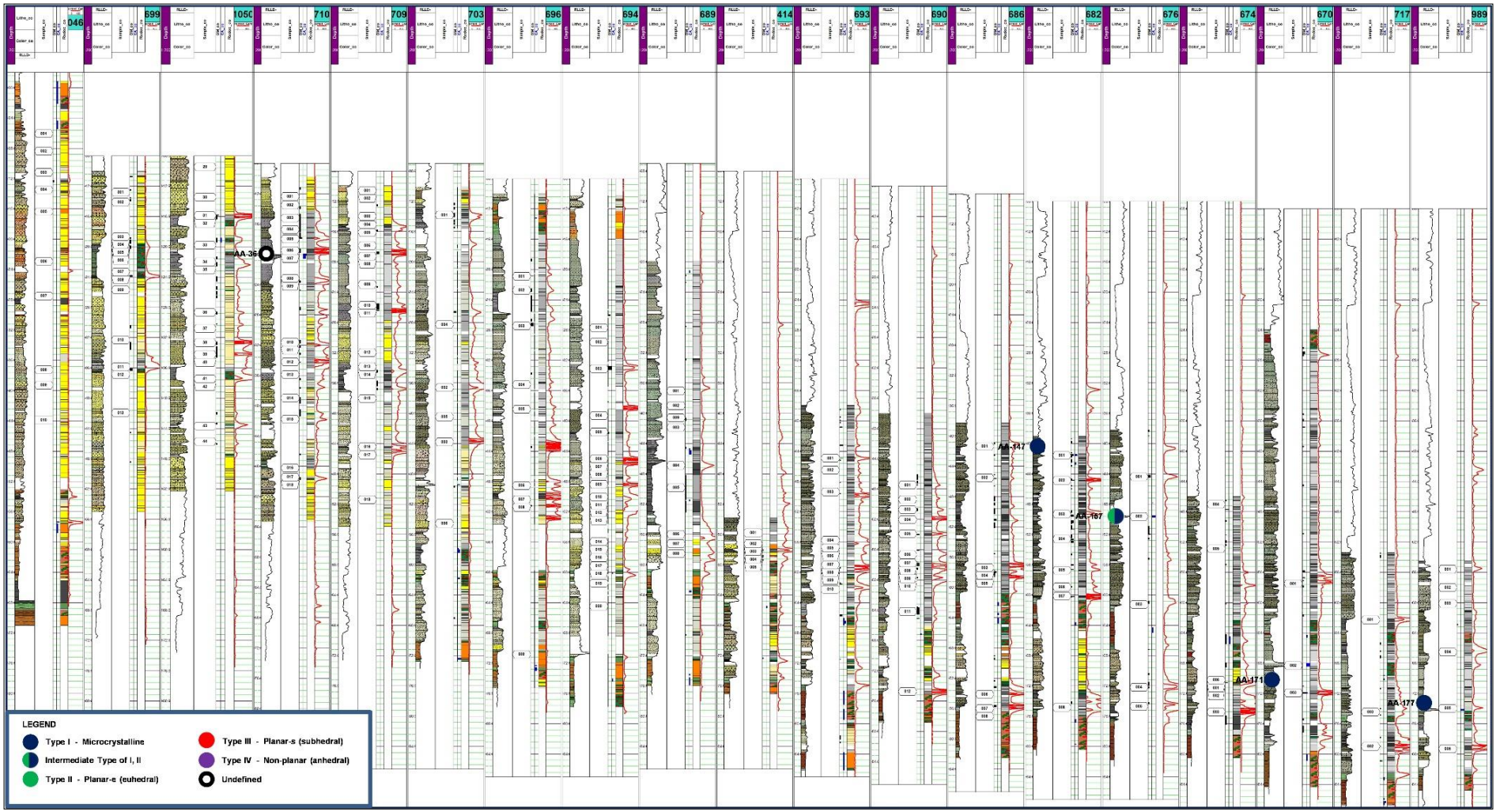

Figure 41: The distribution of the different carbonate cements along Profile SW-NE_01300 marked with blue color in Figure 32 (sample prefix AA-).

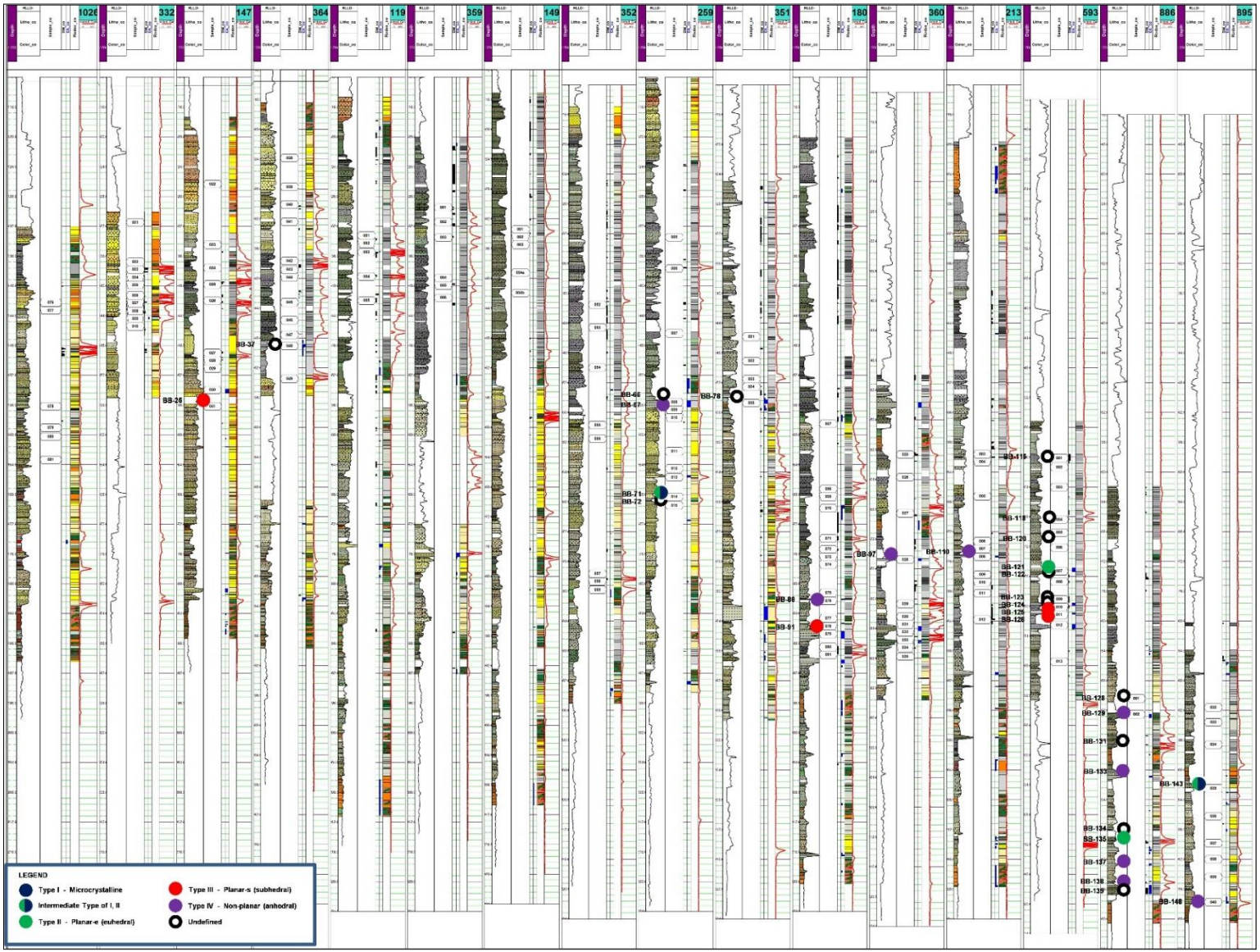

Figure 42: The distribution of the different carbonate cements along Profile SW-NE_03600 marked with teal color in Figure 32 (sample prefix BB-).

3.2.3 Calcite outcrops

Results revealed that dolomite and limited siderite are the exclusive cements present in the aquifers, while calcite is entirely lacking despite being present on surface outcrops. Hence, a few calcite samples were recovered from outcrops of the Bayanshiree Formation (Turonian), at the vicinity of the East Hongor Tolgoy and Bayanshiree Plateau (Figure 45). The calcite samples occur as cement in sandstones or as concretions, the latter case referring to pure calcite (absence of sand grains).

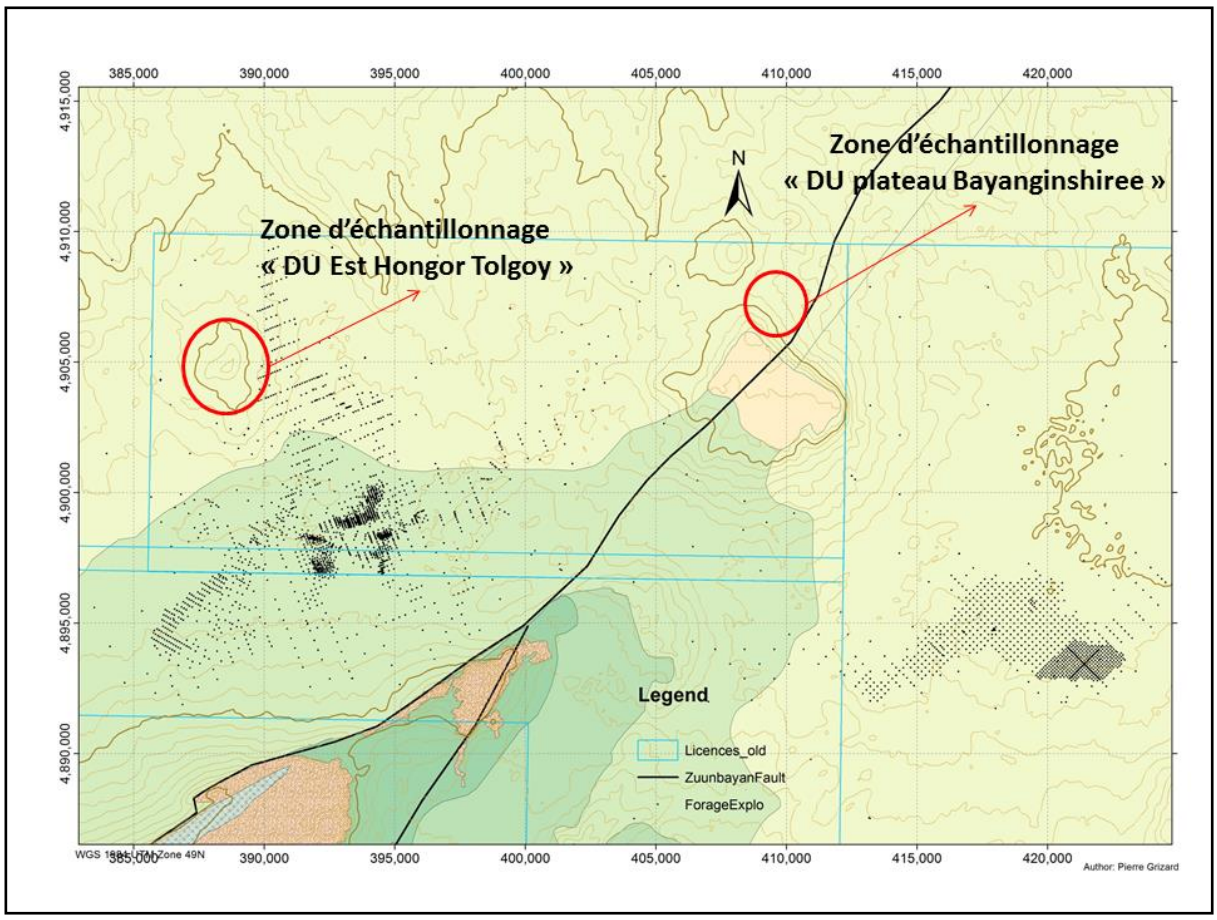

Figure 43: Schematic overview of the East Gobi Basin used to illustrate the spatial distribution of the 2015 sampling (K2Bs study), performed by J.M SCHMITT. The Zoovch Ovoo deposit is depicted on the right side and the Dulaan Uul on the left side (from Grizard, 2017a).

Generally, two different calcite varieties were identified (Figure 44). The first is sparite cement that can contain sand grains. Sparite crystals have birefringence colors of higher order. The second referred as micrite (crystals smaller than 4 µm) has birefringence colors of lower order. It is found as cement binding sand grains or as calcite concretions void of detrital elements. These micrite samples contain a secondary calcite variety with sparite crystals, as veinlets. Furthermore, iron hydroxides were found associated to calcite crystals that show a certain zonation under cathodoluminescence.

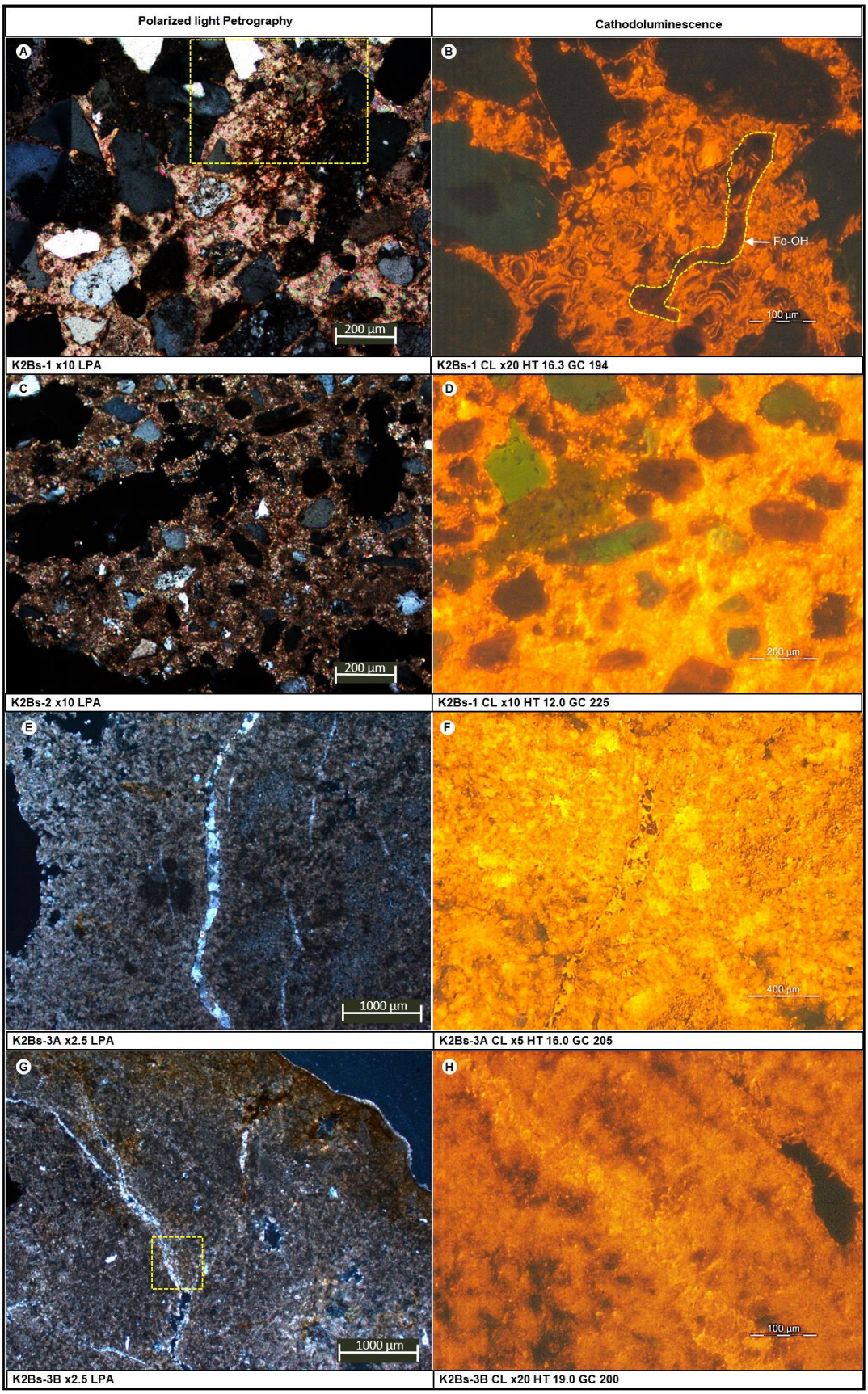

Figure 44: Petrographical review of the calcite samples (left) with the corresponding cathodoluminescence images (right). The samples are presented in an order of increase in calcite abundance. (A-D) sparite with Fe-OH that show zonation; (E-H) micritic calcite with secondary sparite veinlets.

3.2.4 Crystal chemistry

The crystal chemistry of 22 carbonate cemented sandstone samples, located in the vicinity of the Zoovch Ovoo roll-front, was analyzed by means of EPMA to calculate the major and minor element concentrations; with major element being used also as internal standard for LA-ICPMS in order to calculate the REE content. In more detail, 12 of them come from the 9659 study (Table 14), 6 from the 9606 (Table 15) and the last 3 from the K2Bs (Table 16). The first two studies represent samples recovered between 120-200 m depth inside the roll-front area, whereas the third study stands for carbonate outcrops originating around Zoovch Ovoo.

Major and trace elements

SEM-EDS analyses (spot and profile measurements) were performed on individual dolomite crystals to identify potential chemical variations. The most appropriate fabrics for this type of analysis were the poecilitic textures, where the zonations are very discrete. The first non-systematic calculations showed that there are variations for both Fe and Mn contents within the different zonations although not linear (Figure 45).

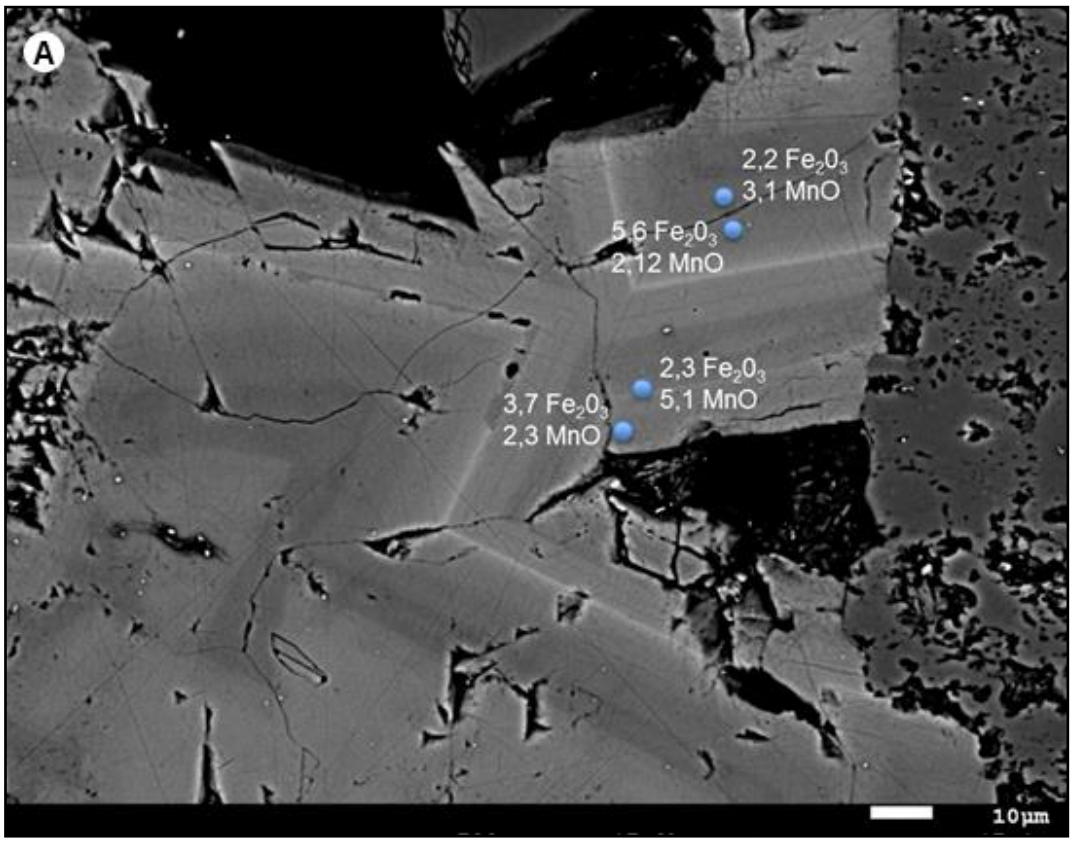

Figure 45: Non-systematic SEM-EDS analysis on euhedral dolomite, focusing on zonations (AA-177).

By performing systematic analysis from the interior of the crystal towards the exterior it was observed that the Ca and Mg contents are more or less constant, fluctuating between 27±1 and 18±1 at%, respectively. On the other Fe content is gradually increasing, from 1.12 at% and reaching 1.57 at% in Profile A, from 1.58 to 3.5 wt% in Profile B (Figure 46).

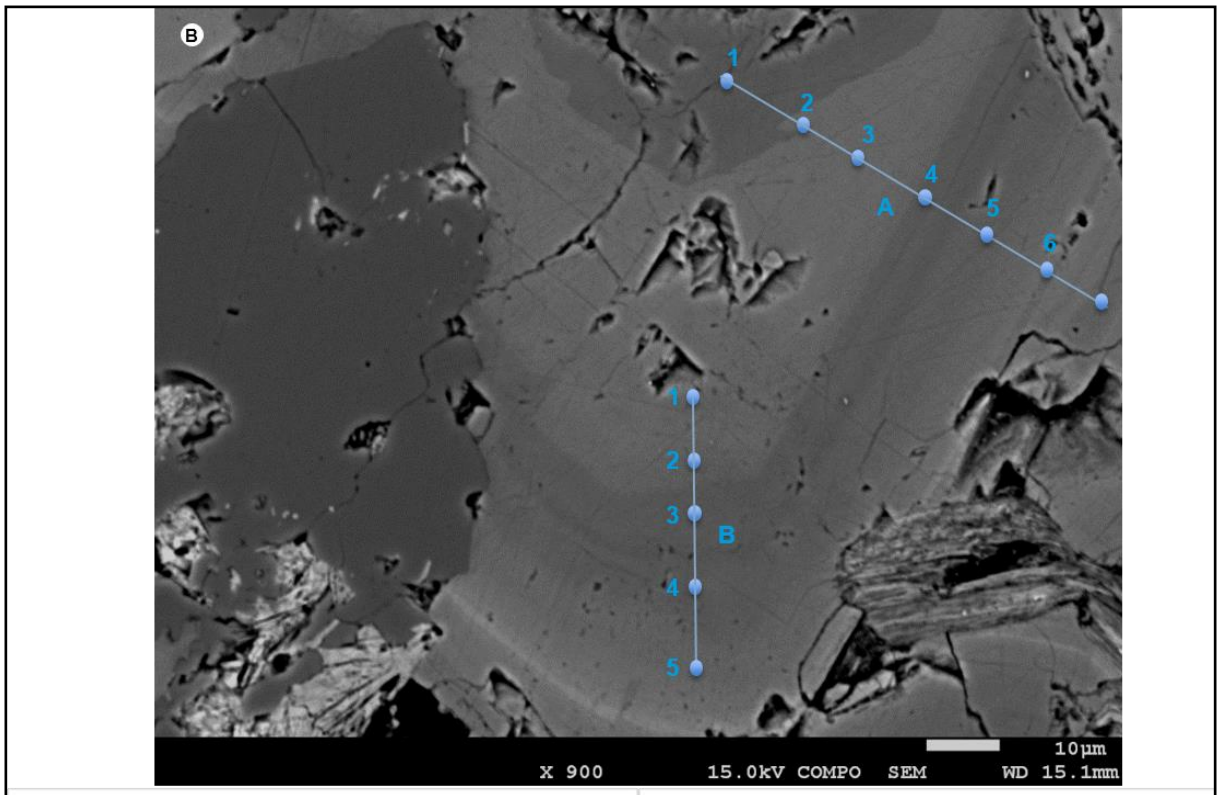

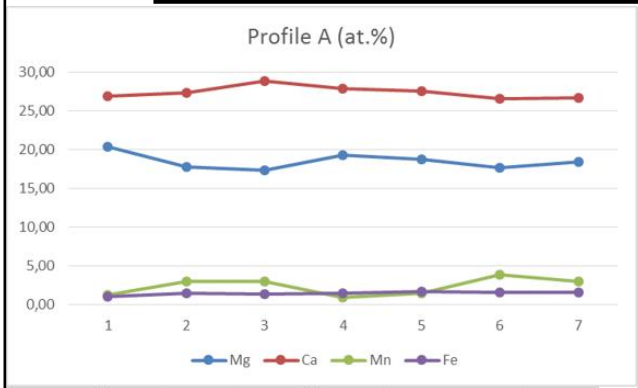

A (at.%)	1	2	3	4	5	6	7
Mg	20,37	17,8	17,35	19,26	18,77	17,62	18,36
Ca	26,90	27,29	28,8	27,84	27,53	26,51	26,66
Mn	1,33	3,05	3,06	1,01	1,51	3,85	3,01
Fe	1,12	1,49	1,44	1,51	1,75	1,62	1,57

B (at.%)	1	2	3	4	5
Mg	18,08	18,16	19,73	18,83	17,83
Ca	26,42	27,13	26,85	26,99	25,91
Mn	2,52	2,49	1,58	1,63	1,77
Fe	1,58	1,77	1,48	2,04	3,59

Figure 46: SEM-EDS analysis performed on a poecilitic dolomite of sample AA-177 (above) and the results for the chemical analyses of major elements Mg, Ca, Mn and Fe performed along the Profiles A and B.

The same relationship is observed in Figure 47 (reverse linear measurement). Calcium and Mg content remain stable at 27±1 and 18±1 at%. The Fe content in Profile C (Figure 47) is increasing towards the center from 1.8 at% at the rim to 2.7 at% at the centre. The Mn content does not follow any linear relationship, but it seems that it is increasing whenever there is a decrease of Mg. This Mn-Mg trend is observed in all three profiles with the most typical example displayed in Profile C, point 7. Eventually, it might be stressed that the brightest zonations have higher Mn content.

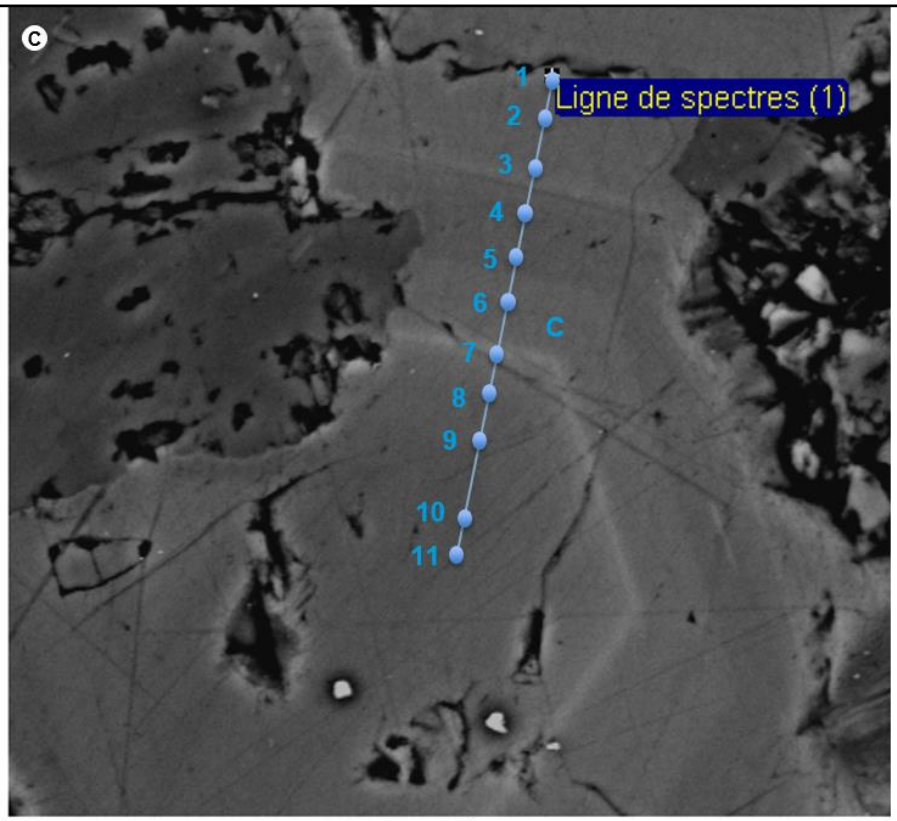

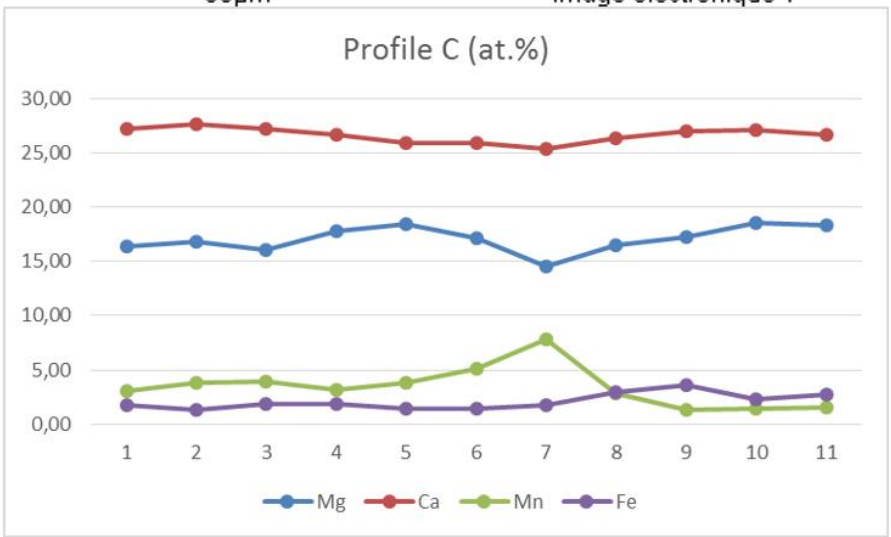

C (at.%)	1	2	3	4	5	6	7	8	9	10	11
Mg	16,43	16,77	16,07	17,85	18,48	17,12	14,59	16,53	17,25	18,52	18,36
Ca	27,21	27,69	27,28	26,65	25,92	25,97	25,40	26,36	27,00	27,17	26,70
Mn	3,04	3,85	3,88	3,15	3,77	5,13	7,81	2,84	1,28	1,46	1,57
Fe	1,80	1,35	1,82	1,88	1,47	1,43	1,76	2,92	3,57	2,28	2,70

Figure 47: SEM-EDS analysis performed on a poecilitic dolomite of sample AA-177 (above) and the results for the chemical analyses of major elements Mg, Ca, Mn and Fe performed along Profile C.

Based on EPMA measurements performed on all different dolomite fabrics and some calcite, three ternary plots were constructed to illustrate the mineralogy of all the occurrences and to identify potential deviations in major and minor elements (Figure 48; Table 20). Each plot aims to present the combined significance of Fe+Mn and of Fe and Mn separately. The first is a Ca/Mg/Fe+Mn plot, the second a Ca/Mg/Fe and the third a Ca/Mg/Mn. The majority of the carbonate samples studied are plotted close to dolomite stoichiometry $(Ca_{0.5}Mg_{0.5})CO_3$±10%, without any particular trend being visible. With respect to the Fe+Mn concentration it varies from zero to up to 22%, but it usually fluctuates at around 10%.

Exceptions occur for the microcrystalline (Type I) and euhedral (Type II) fabrics. The microcrystalline fabric can contain 10% more Ca. According to Morrow (1982) early diagenetic dolomites have higher Ca content and medium to coarsely crystalline dolomites are more stoichiometric. The siderite phase that is found sometimes at the core of euhedral dolomite rhombs has Fe+Mn=75-85%, Ca≈10% and Mg≈5%. Furthermore, the typical rhombohedral dolomite (euhedral crystals), can sometimes contain siderite chemical zonations inside the dolomite rhombs, as was shown before, with Fe+Mn≈50%, Ca≈30 and Mg≈20%.

The sample AA-147 containing the microcrystalline dolomite fabric (Type I) is richer in Ca reaching up to 60 at%. On the other hand, the sample BB-71 that is dominated by microcrystalline dolomite, is not as rich in Ca. The sample AA-157 that contains the euhedral fabric (Type II) and is thought to be the diagenetic product of AA-147, is plotted very closely with its precursor and shows an enrichment in Ca as well. Sample AA-171 which contains the euhedral poecilitic texture is more close to the dolomite 50-50 Ca/Mg stoichiometry. The rest of samples are plotted very tightly at the same position, inside the typical dolomite stoichiometry.

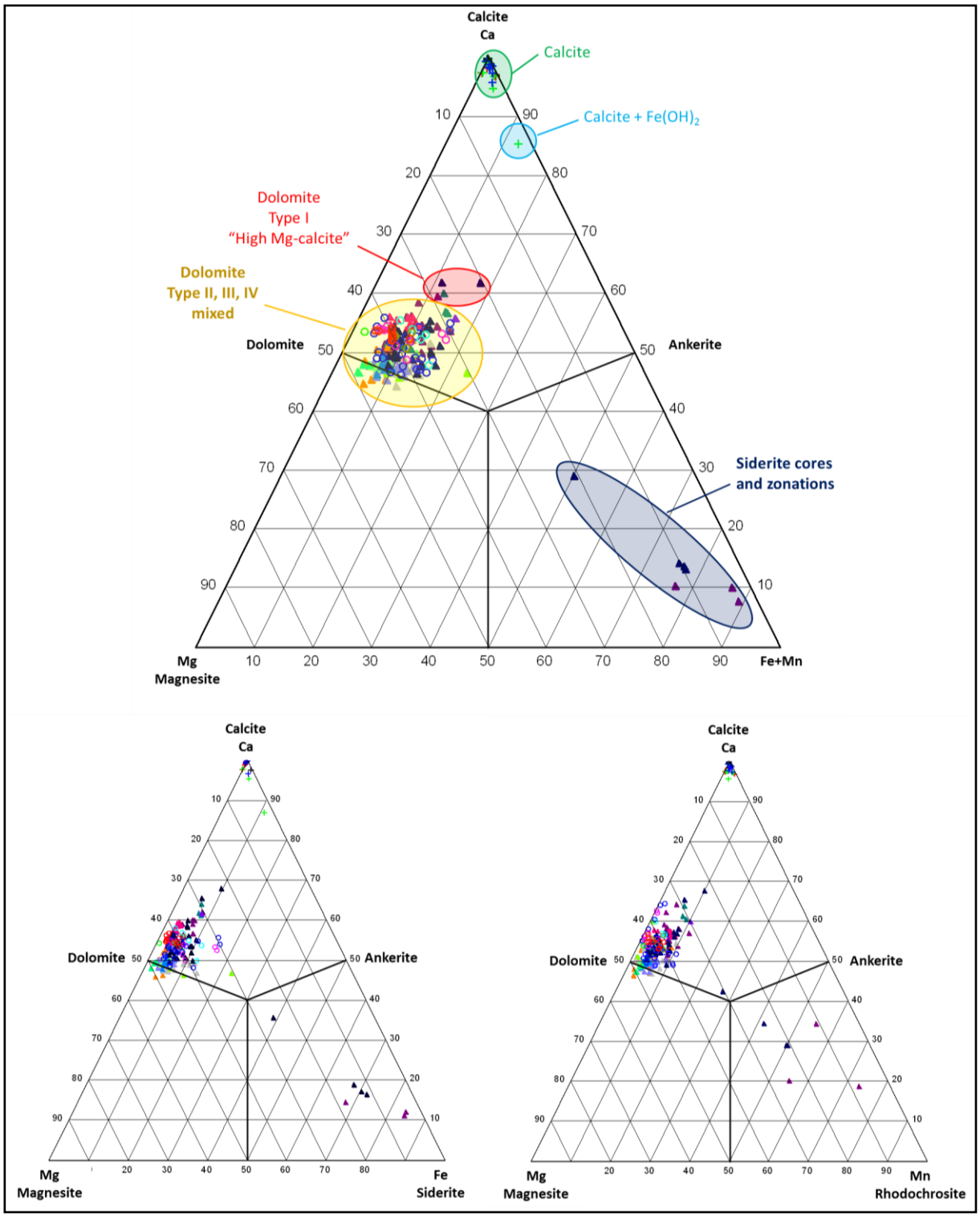

Figure 48: Ternary diagrams for 22 carbonate cemented sandstone samples. All analyses performed by means of EMPA. The samples from the "9659" and "9606" studies are in the vicinity of the Zoovch Ovoo roll-front, whereas the calcite samples "K2Bs" originate from the Bayangshiree Plateau and East Hongor Tolgoy and are used for comparison. It appears that the earliest dolomite (type I) is about 10 wt% Ca enriched compared to the average dolomite composition.

Another plot was constructed (Sr/Mn) to illustrate the depletion in trace elements as dolomitization progressed and also to compare with the calcite samples (Figure 49). This particular plot was selected because Sr is being depleted disproportionally to Mn which is more sensitive to water chemistry changes (Morrow, 1982). It was observed that the Sr is always lower than 600 ppm for the dolomite and below 1000 ppm for the calcite.

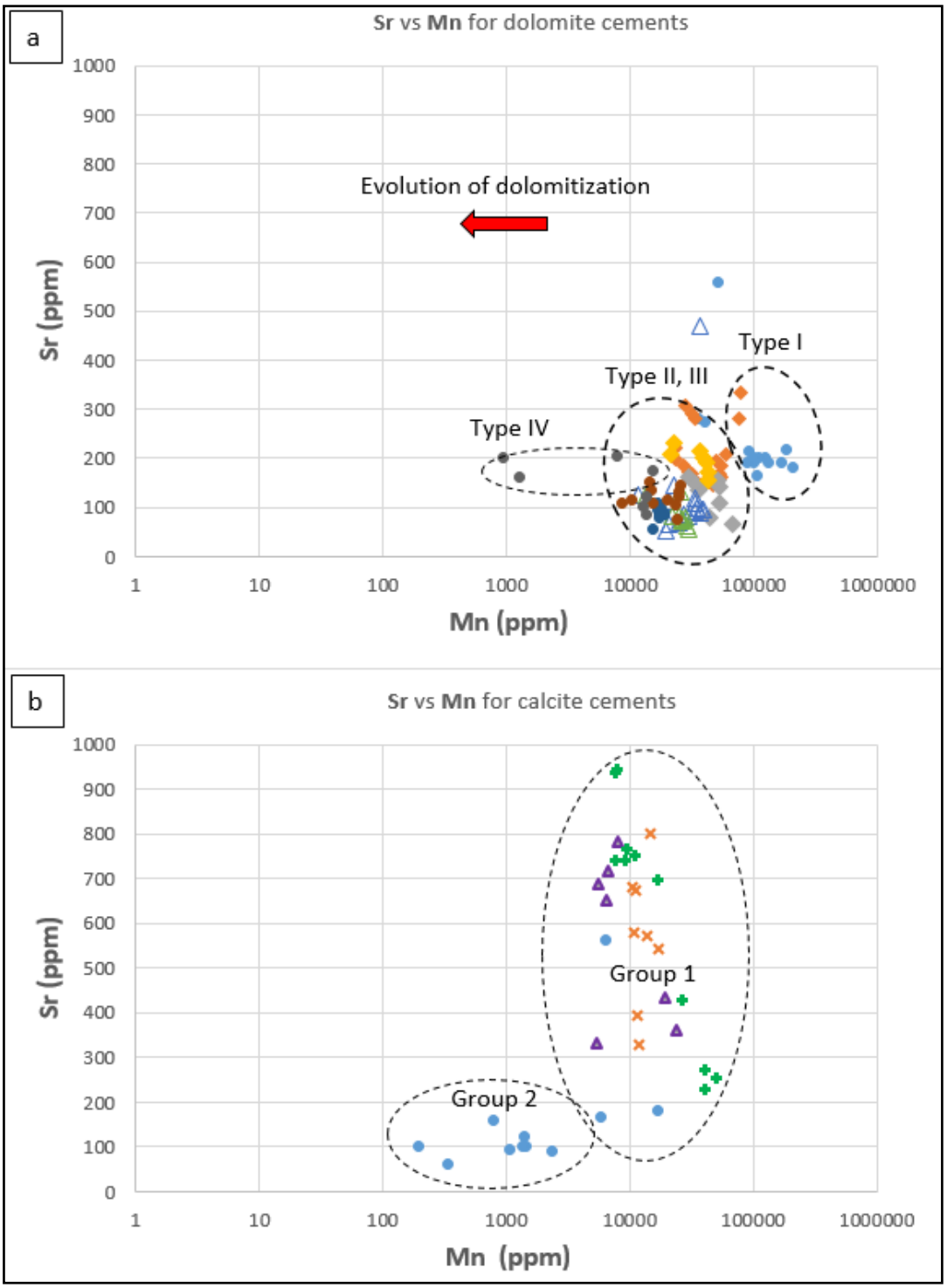

Figure 49: Scatter diagram of Sr vs Mn for the dolomite (a) and calcite (b) cements. Three groups for dolomite and two for calcite were recognized. Note that the x axis for Mn is expressed exponentially. Data from LA-ICP-MS.

In more detail, there are at least 3 trends visible where the microcrystalline type I dolomite, (Group 1) can be distinguished from the euhedral type II and subhedral type III (Group 2) and the anhedral type IV (Stage 3), by gradually decreasing their Mn content, each time by approximately an order of magnitude and with slight differences in Sr. In more detail the dolomite cements reach up to 200.000 ppm in rare cases, usually fluctuating around 150.000 ppm for the microcrystalline dolomite (Type I), around 10.000 to 100.000 ppm for (Type II and III) whereas a depletion is evident only for the latest dolomite phase (Type IV) reaching 1000 ppm.

With respect to the calcite samples from the K2Bs study there are at least two trends visible, one with Mn content fluctuating around 8.000-15.000 ppm (Group 1), locally reaching a maximum of 80.000 ppm and another more depleted in Mn (Group 2). The Sr content has wider distribution for the calcite cement even when looking at the distribution of one sample. Thus it is difficult to reach to conclusions, as there are certainly different generations of calcite cements in the same sample. In general, the calcite samples can be richer in Sr than the dolomite samples but poorer in Mn.

Rare earth elements plus yttrium (Y) and other related elements

Dolomite cements (in depth)

The dolomite cements were analyzed in terms of REE and other related elements by means of LA-ICP-MS. The suite contained namely, La, Ce, Pr, Nd, Sm, Eu, Gd, Tb, Dy, Ho, Er, Tm, Yb, and Lu, in addition to Ca, Y, U and Th (Table 21, Table 22, Table 23). The REE were normalized versus chondrite (Masuda et al., 1973). For simplicity most of the detailed analytical material was moved in the APPENDIX I (Figures) and only the summary of the REE is presented in this chapter.

In general, by observing the bulk composition (sum of REE; Table 21), it is noted that the carbonates from Profile SW-NE_03600 (prefix BB) are poorer than the carbonates coming from the Profile SW-NE_01300 (prefix AA).

Many samples contain more than one type of dolomite fabric and significant variations were observed between them; hence since the sum of the REE is not indicative, each texture was studied alone. The results for the four different fabrics, represented by AA-147, AA-171 for Type (I), AA-157, AA-171 for Type (II), BB-91 for Type (III) and BB-88 for Type (IV) are presented in Table 15. To better illustrate the results, the REE spectra of each spectra is accompanied by the representative microphotograph where the ablation was performed along with the corresponding REE calculation after chondrite normalization (Figure 196 to Figure 202).

- The spectra for the microcrystalline fabric (Type I) is fractionated and has the highest concentration of REE (Figure 196). The REE profile is enriched in LREE (measured on samples 9659 AA-147 and AA-171). The values range between 120 to 1800 times the chondrite. Although, there is an important range between the values it is obvious that the microcrystalline texture is the most enriched in terms of REE content. The microcrystalline fabric is found in patches in sample AA-147, while in sample AA-171 it is limited between poecilitic planar-e crystals.
- The euhedral fabric (Type II), or planar-e, is less fractionated (Figure 197) and the REE content fluctuates between 150 to 250 times the chondrite (measured on samples 9659 AA-171 and AA-157). Figure 198 shows the depletion in HREE occurring on poecilitic planar-e dolomite crystals. It is concluded that the REE content in poecilitic crystals is not uniform, which is also the case for the major elements (Figure 45, Figure 46 and Figure 47).
- The subhedral fabric (Type III), or planar-s, is less fractionated (Figure 199) and the REE content fluctuates around 70 times the chondrite (measured on sample 9659 BB-91). The depletion of REE is visible in the subhedral (planar-s) dolomite, although it is not linear as the HREE depletion is more resilient than the LREE.
- In the anhedral, (Type IV), or non-planar, the REE content is very poor, fluctuating between 30 to 80 times the chondrite (Figure 200) and the crystals are HREE enriched (measured on sample BB-88). Finally, a subtype of the anhedral fabric associated to $Fe(OH)_2$ is presented in Figure 201. The presence of $Fe(OH)_2$ "contaminates" the dolomite spectrum that appears enriched in HREE. The anhedral fabric can be contained as a single dolomite cement phase i.e. BB-138 or can be found locally (BB-88) inside the microcrystalline dolomite (Figure 202). The anhedral fabric is generally characterized by a depletion of REEs and strong fractionation. Some crystals are totally depleted with concentrations lower than 10 times the chondrite for La.

To sum up the microcrystalline dolomite cements (e.g. AA-147, AA-171; Figure 196) as well as the euhedral and poecilitic (e.g. AA-157, AA-177 and BB-135; Figure 197 and Figure 198) have remarkably higher concentrations in REEs. On the contrary the subhedral (BB-91; Figure 199) and anhedral fabrics (BB-129; Figure 200 and Figure 201) show significantly lower concentrations. Of course there are always intermediate phases, where the dolomite cement consists of two or more fabrics (BB-67, BB-71 and BB-88). The detailed values of the REEs are presented in Table 22.

With respect to the Ca content in the studied samples the concentration ranged between 19.0-24.0 wt%, the Y at $4x10^{-3}$-10^{-2} wt%, the Th at $3x10^{-2}$-10^{-1} wt% and the U fluctuates between just over the detection limit to $6x10^{-3}$ wt% but reaches a maximum of $3x10^{-2}$ wt% at sample BB-

71 (data from EPMA). It was observed in several cases that in some cases the dolomite cements, i.e. the microcrystalline type I and the recrystallized phase (Figure 202) in sample BB-71, can contain higher U-Th content.

Calcite cements (outcrops)

The spot LA-ICP-MS technique was also used to quantify the composition of the REE (La, Ce, Pr, Nd, Sm, Eu, Gd, Tb, Dy, Ho, Er, Tm, Yb, and Lu) and also certain trace elements (Na, Mg, Ca, Ti, Mn, Fe, Cu, Zn, Rb, Sr, Y, Ba, Th, U) of three of the calcite cemented samples K2Bs-1, 2, 3a and 3b (Table 16). The aim was to compare between the REE spectra (normalized again versus the chondrite standard) of the dolomite cemented sandstones and calcite cements and to see if they are genetically related, though hosted in different geological formations.

Detailed information on the petrographic features of the calcite crystals that were analyzed, as well as the respective spectra are also available in the APPENDIX I (Figures) from Figure 203 to Figure 210). The obtained results are discussed below.

In sample K2Bs-1, at least two different calcite varieties were identified, one with colours of higher birefringence and another with lower (Figure 203). The REEs and the trace elements of the calcite cements in Figure 204 were measured in seven different spots. However, despite being characterized by different optical properties, the same variations do not seem to apply to their chemistry, which appears to be mixed. Two trends may be seen in terms of REE content. It was observed that the calcite cements can be grouped in at least two categories, relative to their Ce content associated to the Fe and Mn, all of which appear depleted. In the LA spot 5c (Figure 204), there is both a Ce negative anomaly and a slightly positive Eu anomaly. One with a relative Ce depletion and another where Ce follows the general REE distribution. This could be indicative of variations in the redox setting and as a result of different calcite generations. The Ce is immobile in oxidative settings, resulting in Ce depleted fluids from which the calcite cements were precipitated. In more detail, the depletion of Ce is linked to the different mobility of Ce^{4+} and Ce^{3+}, which in turn are linked to negative and positive Ce anomalies in aqueous solutions, respectively, due to variations in the pH and Eh during continental chemical weathering (Alfimova et al., 2011). Therefore, in the case of the studied calcite samples it could be suggested that the depletion indicates that Ce was left in the same mineral phase (cerite?) or in the aqueous solution due to oxidative settings. With regards to the major and trace elements, the carbonate cements in K2Bs-1 (Figure 204) consist of Ca at 24-33 wt%, Mg up to 0.5%, Fe locally (i.e. 1a) up to 43 wt% which indicates an ankerite phase. That same phase shows also a depletion in Tb and is relative enriched compared to the other calcite cements of the same sample to Na, Mg, Mn, Cu, Sr and U. The rest of the elements analysed are contained close to the detection limit <0.1 wt%. According to Blamey et al. (2014)

the prominent Ce negative anomaly suggests oxidizing conditions that scavenged Ce in advance of calcite precipitation. Another explanation that is possibly more valid is that Ce was removed from the calcite after deposition due to dissolution and recrystallization that also resulted to the depletion of the primary calcite in Fe, Mn and the formation of Fe-hydroxides. Indeed it was found that Fe-hydroxides precipitate close to the Ce depleted calcite (spots 5a, 8a for Fe-hydroxides and spots 5c and 7a for Ce depleted calcite in Figure 204). Another factor is that when Ce is depleted, Mn and Fe are depleted as well. Therefore very probably the prominent Ce depletion occurred after calcite precipitation. The absence of Mn from the carbonates is typical of precipitation from very low salinity waters (Morrow, 1982); hence of meteoric water, a hypothesis that would also explain the oxidizing conditions which are needed for Ce scavenging, in case the calcite was re-precipitated. These late surface oxidizing conditions show that the calcite is not in equilibrium with atmospheric conditions in contrast to the near-surface aquifer (calcite equilibrated) and the deeper aquifer (dolomite equilibrated).

The results from the K2Bs-2 sample are presented in Figure 205 and Figure 206. The REE profile is different than in K2Bs-1. Here it appears to be only one generation of calcite as the REE signatures are very similar. In the calcite cement of the K2BS-2 sample there are also slight positive Gd anomalies. Figure 207 shows the results from sample K2Bs-3A. The profile is more asymptotic than of the other samples and shows locally more negative Eu anomalies. Micrite was identified in this sample, measured at the LA spot 2a, having a Ca content 10 wt% higher than the adjacent carbonates that fluctuate at 73-78 wt%. Late infillings of coarse grained calcite (sparite) are also present. The infillings yield the same REE distribution as the adjacent carbonates, which implies that they originated from the same source. On the other hand they appear depleted in Na and Fe relative to the adjacent carbonates. The infilling calcite in Figure 208 (spot 2a) yields a different REE pattern and is depleted in a series of elements, such as Na, Mg and Ti at the same time that is enriched in Mn. The positive Ce anomaly is indicative of reducing conditions Blamey et al. (2014). On the other hand in Figure 209 and Figure 210 it is evident that the late infilling calcite (spot 5a) is not marked by any Ce anomaly, but it is marked by higher Mn content (>4 wt%), relative to the adjacent calcite.

Comparison between dolomite and calcite in terms of REE

A synthetic plot of the REE spectra of the four dolomite fabrics compared to the four calcite cements is presented in Figure 50. In general the calcite cements are more abundant in REE and more accurately in LREE (La, Ce, Pr, Nd, Sm, Eu, Gd), resembling to a certain extent the early diagenetic dolomite. Therefore it could be stressed that the microcrystalline calcite (micrite) which dominates the calcite samples studied shows a similarity to the microcrystalline (Type I) dolomite. The spectra of the calcite cements appears more heterogenous as they can

show depletion and enrichment in several elements. For example some are enriched in Er and Gd, while others show depletion in Ce, Tb, Sm and Eu.

On the other hand the spectra of the dolomite cements are more homogenous and the preferential depletion of certain elements becomes evident only for the anhedral (Type IV) dolomite.

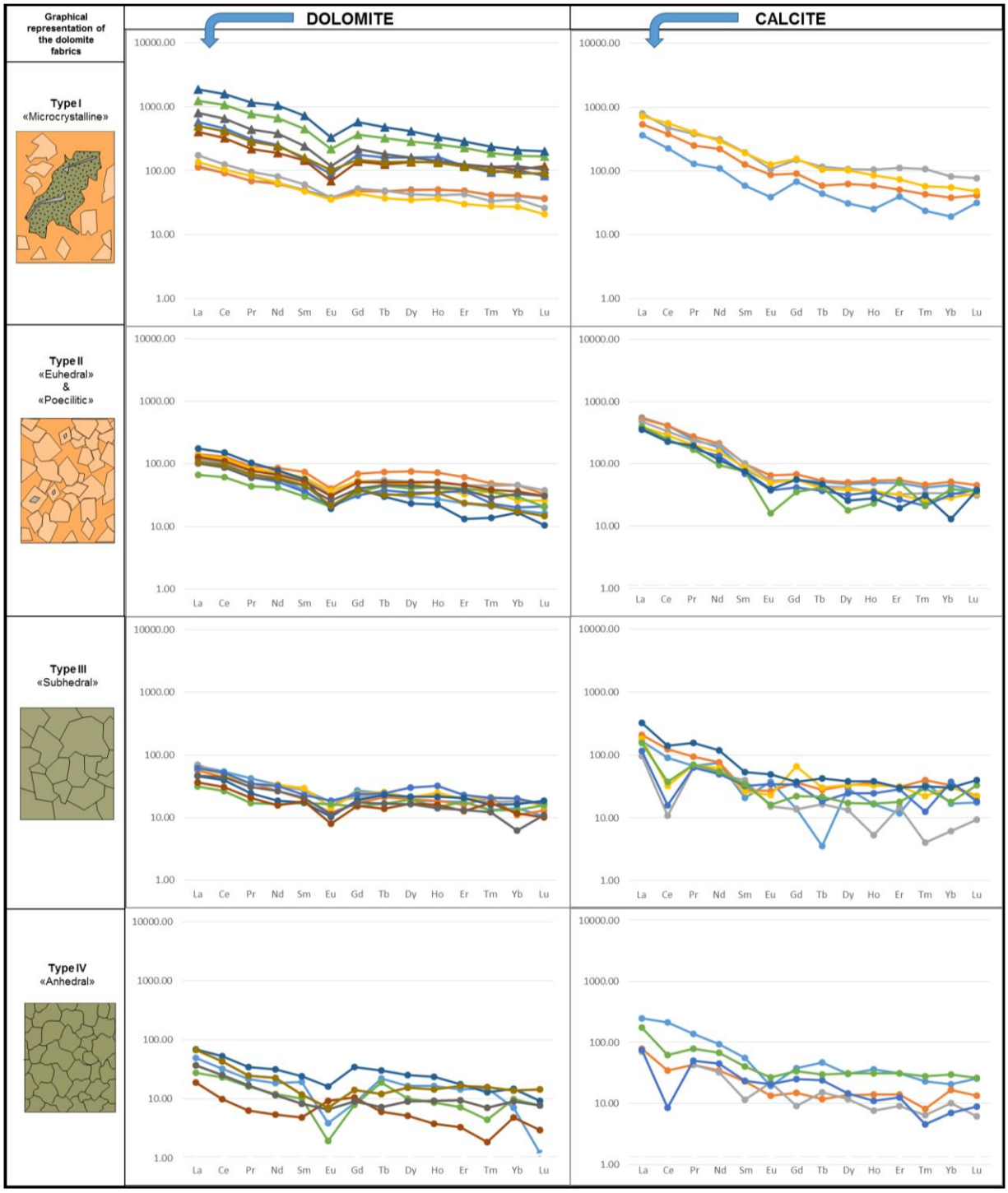

Figure 50: Comparison between the REE spectra for the dolomite fabrics (left) and several random calcite cements from the K2Bs study (right). The calcite cements are more abundant in REEs, particularly in LREEs resembling to a certain extent the early diagenetic dolomite. The spectra of the calcite cements are more heterogenous, showing depletion in Ce, Tb, Sm and Eu and enrichment in Er

and Gd. The spectra of the dolomite cements are more homogenous and the preferential depletion of certain elements becomes evident only for the anhedral dolomite.

For a better overview of the REE distribution on the four dolomite fabrics and the different calcite occurrences and ultimately to correlate their spectra, a synthetic plot has been made for both carbonate minerals (Figure 51). The REE spectra of each dolomite occurrence is normalized to the richest dolomite fabric, in this case the microcrystalline and for each calcite occurrence the spectra is normalized also to the richest which in this case is the micrite.

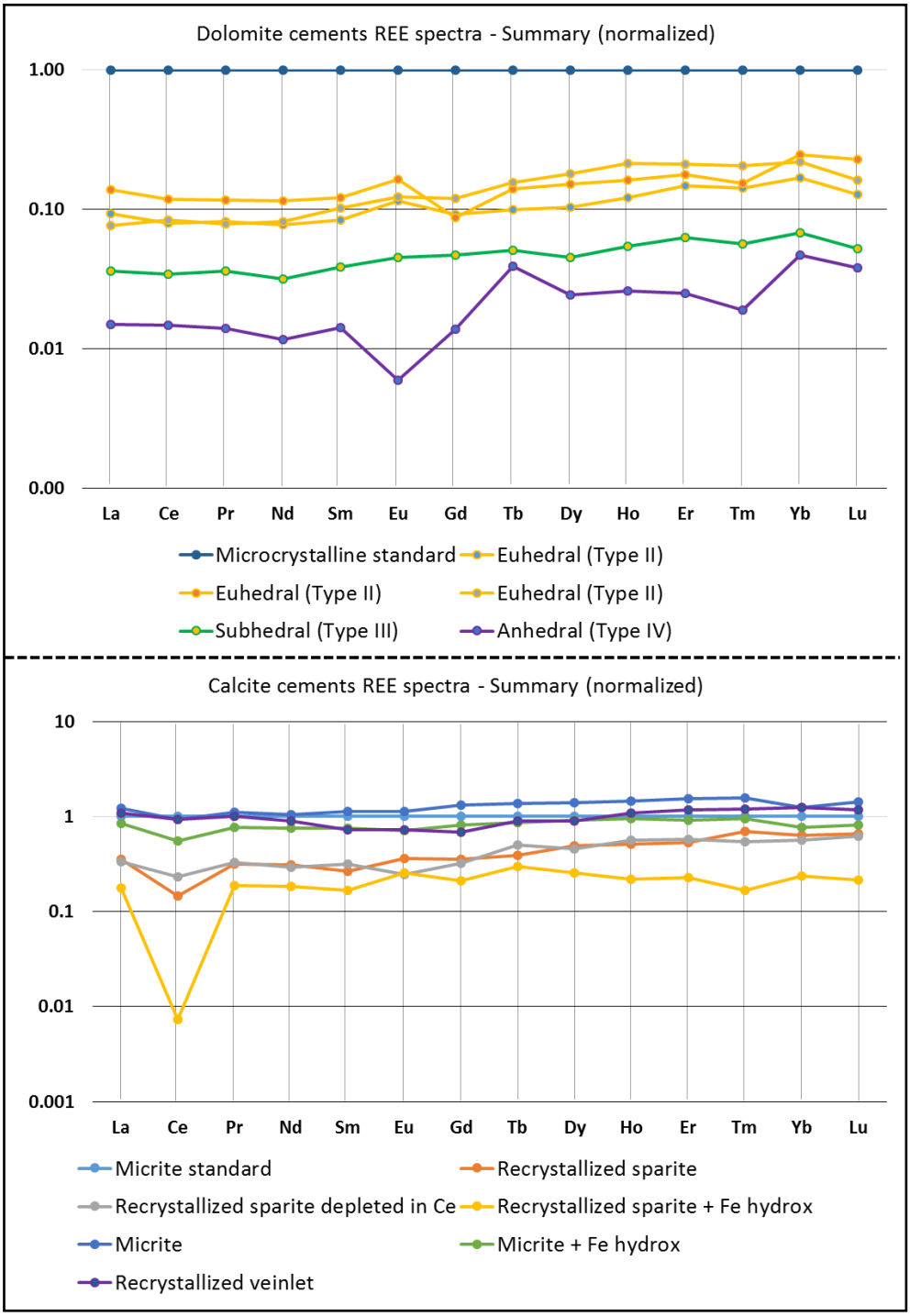

Figure 51: The REE spectra for each dolomite and calcite occurrence normalized to the most abundant dolomite and calcite in REE respectively.

It becomes clear that for the dolomite, the REEs are gradually depleted with the evolution of dolomitization, moving from type I which is very rich to type IV which is totally depleted. The overall spectra is also slightly modified as a function of dolomite type i.e. gradual HREE enrichment. Europium shows occasionally positive and negative anomaly, responding to redox fluctuations.

With regards to calcite, it is observed that all micrite occurrences, from all three samples have the same spectra and that the recrystallized phases show a general depletion and HREE enrichment. Special focus this time is given to Ce which can be totally depleted in contrast to the other LREE.

Yb/Ca vs Yb/La variation diagram

A plot between the Yb/La and Yb/Ca ratios was also constructed (Figure 52). All plotted samples (calcite and dolomite) plot at the same area, with 0.1-1 for Yb/La and 10^{-4}-0.1 for Yb/Ca. The samples are plotted close to the hydrothermal veins area. The decrease that is observed in regards to the ratio Yb/Ca, vertical trend may reflect fluid rock interactions i.e. loss of REE's due to dilution or contact with clays.

The horizontal trend for Yb/La may indicate remobilization processes and the diagonal trends are indicative of primary crystallisation fractionation (Möller, 1983; Dawson et al., 2013). The carbonate remobilization (horizontal trends) lead to LREE depletion relative to the original carbonate since HREE form more effective complexes with carbonates and bicarbonate anions (Bau and Möller, 1992).

According to Dawson et al. (2013) the fact that the samples are plotted close to the "hydrothermal veins field" does not mean that the mineralizing fluids had high temperature during carbonate precipitation. It could mean that the original process of fluid REE enrichment was related to active hydrothermal processes, or that acidic breakdown of material originally associated with high temperature processes, had high REE content (e.g. relatively fresh volcanic debris acid leached by migrating fluids), a concept that is applicable for the case of Zoovch Ovoo. Hence, the fluid that caused acidic breakdown of REE-rich minerals in the source must have been acidic i.e. a combination of sulfurous and carbonic acid (igneous process-derived fluid). Another explanation could be that a formerly high temperature fluid with high REE content migrated into the system and was mixed with a lower temperature fluid i.e. the meteoric fluids of Zoovch Ovoo (REE-poor), resulting in low temperature precipitation of minerals with high REE contents, for instance the microcrystalline (type I) dolomite

The calcite is encountered often on the surface of the regional area of Zoovch Ovoo on the top of fault zones, meaning that deep basinal fluids could be intermixed with meteoric waters, on the contrary to dolomite which is crystallized at depth. However, calcite appears to have similar

values to dolomite for both ratios and there is only a minor shift that could be due to LREE enrichment and HREE depletion.

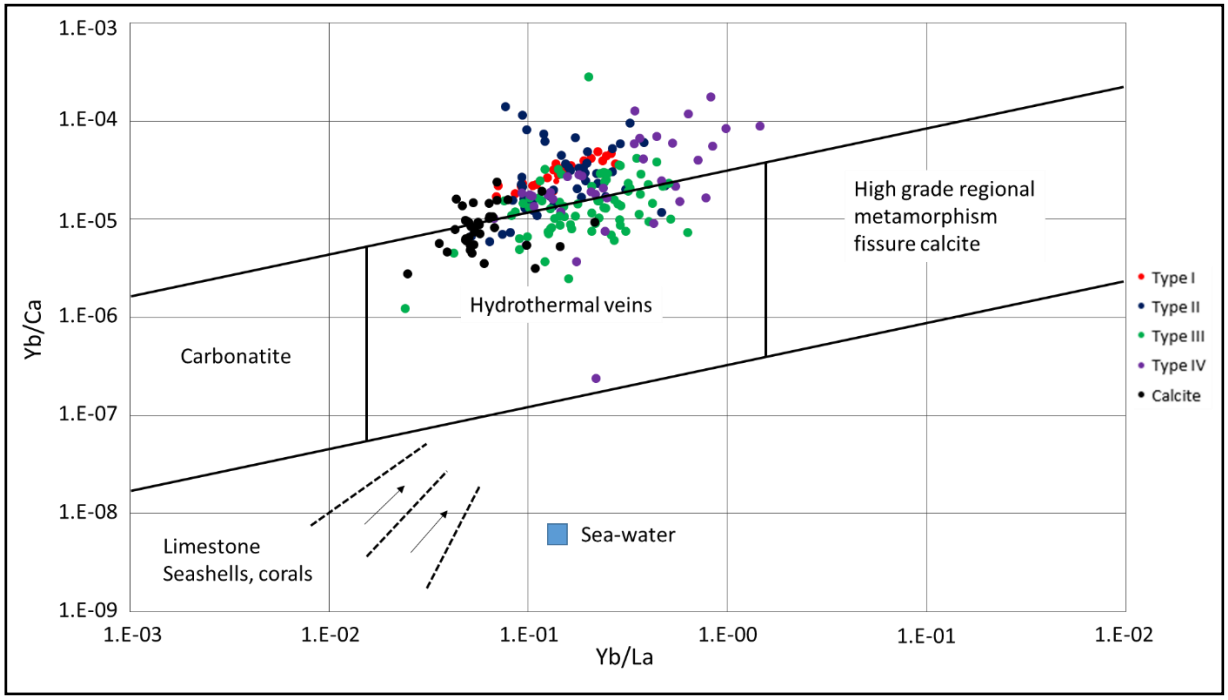

Figure 52: Variation diagram based on Dawson et al. (2013) first proposed by Möller (1983) for dolomite in the middle (Type I, II, III and IV) and calcite on the left part. Field positions plotted are based upon numerous analyses of samples from across the world. Samples that plot below the carbonatite-hydrothermal-metamorphic series are classed as "sedimentary process related", with the rough positions of marine carbonate types between the dashed lines, and sea water composition plotted for reference.

C, O stable isotopes of carbonates (dolomite and calcite)

The stable isotope compositions of the dolomite and calcite in the sandstone samples are provided in Table 24. The dolomite samples (on a basis of 26 samples) yield $\delta^{18}Ov\text{-}_{PDB}$ and $\delta^{13}C\ v\text{-}_{PDB}$ values ranging from -9.48 to -11.34 ‰ (mean -10.41‰) and from -5.59 to -7.71 ‰ (mean -6.65‰), respectively. The values for both the stable isotopes show little variation. With regards to the calcite samples (10 samples) the $\delta^{18}Ov\text{-}_{PDB}$ and $\delta^{13}Cv\text{-}_{PDB}$ values range from -10.92 to -13.78 ‰ (mean -12.35‰) and from -5.74 to -8.64 ‰ (mean -7.19‰), respectively. The $\delta^{18}O$ and $\delta^{13}C$ values have slightly larger variation for the calcite compared to the dolomite samples.

The $\delta^{18}O_{V\text{-}SMOW}$ was calculated using the conversion equation (Friedman and O'Neil, 1977; Kendall and McDonell, 1998; Hoefs, 2009; Zhao and Zheng, 2013), as provided below:

$$\delta^{18}O_{V\text{-}SMOW} = 1.03086\ \delta^{18}O_{V\text{-}PDB} + 30.86$$

The results are presented in Table 24. The conversion is necessary because in many carbonate studies the $\delta^{18}O$ values are expressed in SMOW, therefore having them at hand allows fast comparison.

The results in Table 25 are taken from Sanchez (2010, 2011) and are used for comparison. There are three different groups of samples codenamed, Bayanshiree, Sainshand and Du, all coming from the regional area of the Zuunbayan and Unegt sub-basins. Unfortunately, a detailed mineralogical description of these samples (calcite or dolomite) is not provided. The samples from Bayanshiree yield $\delta^{18}O_{V\text{-}PDB}$ and $\delta^{13}C_{V\text{-}PDB}$ values ranging from -9.33 to -11.34 ‰ (mean -10.34‰) and from -4.95 to -6.64 ‰ (mean -5.80‰), respectively, which is actually very close to the dolomite from Zoovch Ovoo. The samples from Sainshand range for $\delta^{18}O_{V\text{-}PDB}$ from -5.15 to -11.94 ‰ (mean -8.55‰) and for $\delta^{13}C_{V\text{-}PDB}$ from -0.19 to -6.46 ‰ (mean -3.33‰), which values are different than the other samples. The Du samples have $\delta^{18}O_{V\text{-}PDB}$ and $\delta^{13}C_{V\text{-}PDB}$ ranging from -7.78 to -14.73 ‰ (mean -11.26‰) and from -5.23 to -8.34 ‰ (mean -6.79‰), respectively, which are similar to the calcite of East Hongor Tolgoy and Bayangshiree Plateau.

The results from Table 24 and Table 25 are illustrated in Figure 53. In regards to the geological setting it is evident that the carbonates have non-marine origin as their $\delta^{13}C$ is lighter than -2‰, with two exceptions. Additionally, there are two major trends. One trend for the calcite with $\delta^{18}O_{V\text{-}PDB}$ values from -15.0 to -11.5 ‰ and $\delta^{13}C_{V\text{-}PDB}$ from -4.5 to -9.0 ‰ and another for the dolomite with $\delta^{18}O_{V\text{-}PDB}$ values from -11.5 to -9.0 ‰ and $\delta^{13}C_{V\text{-}PDB}$ -4.5 to -8.5 ‰, respectively. These two trends resulted from the analysis of the dolomite samples from the 9659 study and the calcite from the K2Bs study. For comparison, the data from Sanchez (2010, 2011) were also plotted. It is obvious that from the codenamed "Du" certain carbonates are plotted at the calcite realm and others fall close to the dolomite realm. The carbonates codenamed

“Bayanshiree” are plotted exclusively in the dolomite realm. On the contrary the samples codenamed “Sainshand” yield very diversified values. There is one sample close to the calcite realm, two fall in the dolomite realm, two fall in the lacustrine area and have $\delta^{18}O_{V\text{-}PDB}$ values from -6.0 to -5.0 ‰ and $\delta^{13}C_{V\text{-}PDB}$ from -2.5 to -3.0 ‰ and the last two are depleted in $\delta^{13}C$ and have $\delta^{18}O_{V\text{-}PDB}$ values close to -5.5 to -6.0 ‰.

It must be stressed that the stable isotope analyses were performed on whole rocks. Since there are often more than two different dolomite fabrics in a single sample, the consequence is that the isotopic signature measured is an average of the individual isotopic compositions of the carbonate phases. This caution being taken in account, the isotopic compositions of the carbonates may be discussed.

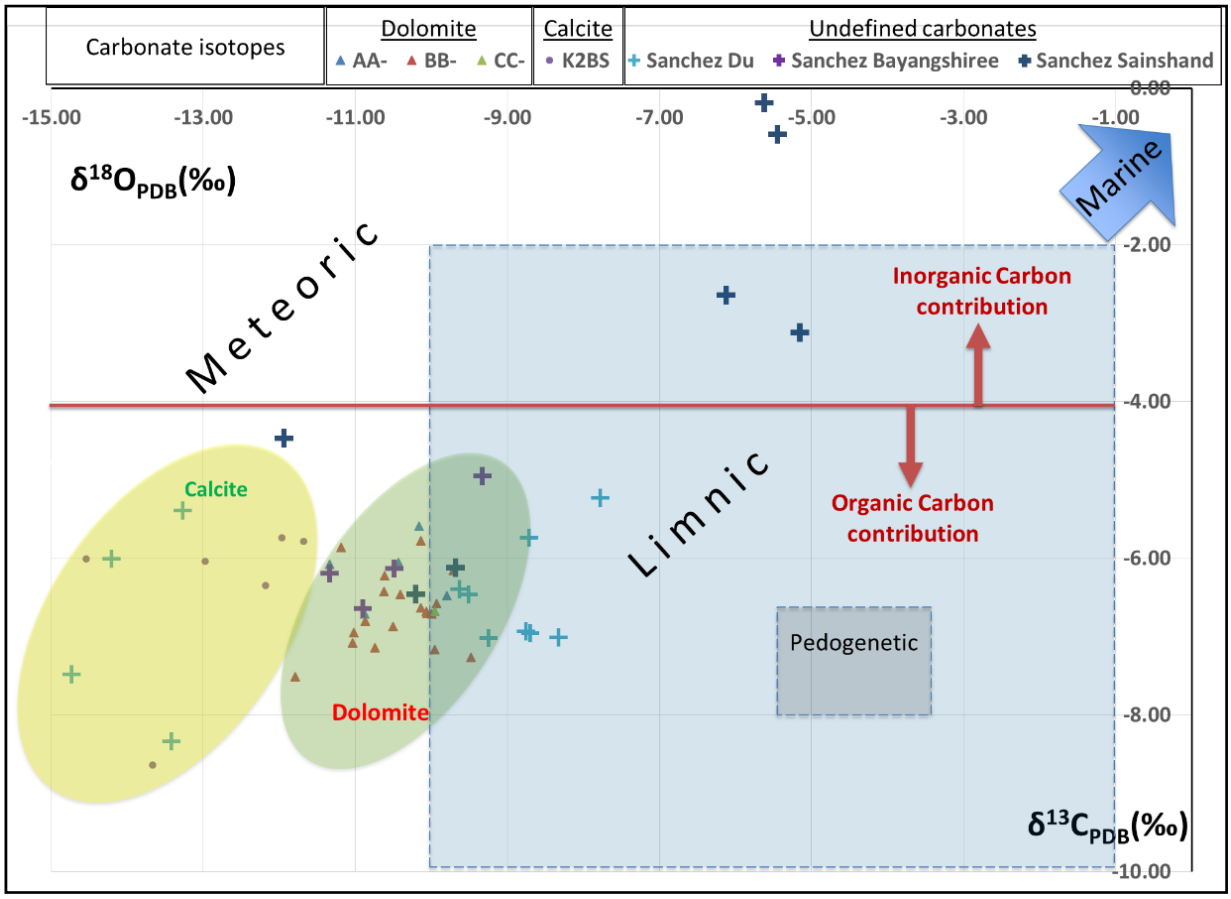

Figure 53: The isotopic composition of the dolomite cements from the 9659 study. For comparison, the calcite cements from the K2Bs study and the carbonates discussed in Sanchez (2010, 2011). It is noted that there is a clear distinction between the calcite and the dolomite cements, with the latter having a more heavy $\delta^{18}O$ isotopic signature. The diagram was constructed based on Hofer et al. (2013). According to Köster and Gilg (2015) purely organic carbon derived non-marine dolomite has $\delta^{13}C$ lighter than -8‰ and calcite has $\delta^{13}C$ lighter than -11‰ which were not confirmed in the studied dataset. On the other hand there is certainly an organic carbon contribution to the formation of the carbonates when the $\delta^{13}C$ values become lighter than -4‰

Interpretation of the carbon isotopic values

In general the carbon contained in the carbonates is enriched in ^{13}C, while the organic carbon is depleted in ^{13}C. Several aspects of the possible source for carbon may then be considered:

- The values of $\delta^{13}C$ ranging from -4 to 4 ‰ indicate inorganic carbon (Wang et al., 2016). Therefore it could be suggested that the carbonates with $\delta^{13}C < -4$‰ indicate a moderate organic carbon influence. In more detail, according to Suess and Whiticar (1989), values of $\delta^{13}C$ between -35.0 to -4.0 ‰ indicate organic carbon contribution, originating from the CO_2 that could be produced from the decarboxylation of organic matter i.e. bacterial fermentation (aerobic or anaerobic). In the case of Zoovch Ovoo the system is early diagenetic, hence there is *a priori* no possibility of thermal decarboxylation. In other studies, the $\delta^{13}C$ of CO_2 from organic matter decarboxylation ranges from -33 to -18 ‰ (Mack et al., 1991; Pearson and Nelson, 2005, Sensula et al., 2006; Wang et al., 2016).
- The $\delta^{13}C$ originating from the CO_2 in the atmosphere fluctuates at -7‰. However, due to the carbon isotope fractionation during the precipitation of the cements, the $\delta^{13}C$ of carbonates could be heavier by a maximum of 10‰ compared to the original $\delta^{13}C$ from which they were sourced.
- Dissolution and recrystallization at constant temperature does not affect the $\delta^{13}C$ value, considering that there is no other carbonate pool contributing to the system (Sensula et al., 2006; Wang et al., 2016).

This set of considerations may imply that the different dolomite generations have identical $\delta^{13}C$ values because there is no new carbon entering the system. Yet, their carbon isotopic values may be buffered by the mixture of two possible carbon sources:

- The theoretical pure organic source derived carbon that would induce a fractionation to carbonates with $\delta^{13}C$ fluctuating at -23 to -8 ‰.
- The theoretical pure inorganic sources which would be the atmospheric CO_2 from which fractionation may lead to $\delta^{13}C$ carbonates values at the range of 3 ‰ (Wang et al. (2016) and references therein).

It could be concluded that both the dolomite from Zoovch Ovoo and calcite from the East Hongor Tolgoy and Bayangshiree Plateau have the same mixed carbon source.

One more important observation was that there were other outcropping carbonates described in Sanchez (2010; 2011), which yield very different stable isotopic values i.e. for $\delta^{18}O$ from -5.15 to -6.12 ‰ and for $\delta^{13}C$ from -0.19 to -3.12. Liu et al. (2006) proposed that the $\delta^{18}O$ and $\delta^{13}C$ gradually become lighter because of water input and carbon biodegradation, which case could be applicable for the present study.

Interpretation of the oxygen isotopic values

Figure 54 from Köster and Gilg (2015) was used to calculate the oxygen isotope fractionation for dolomite-water and calcite water. By plotting the $\delta^{18}O_{V\text{-}PDB}$ values for the dolomite of Zoovch Ovoo (9659 study), which have an average value of -10‰ on the y axis and by assuming a near-surface temperature (<200 m depth and insignificant geothermal gradient change) of T°C =20-30 for dolomite precipitation on the x axis, it was possible to create an envelope for the $\delta^{18}O_{V\text{-}SMOW}$ of the associated dolomite water. These values were estimated at the range of -11±1‰ (Figure 54).

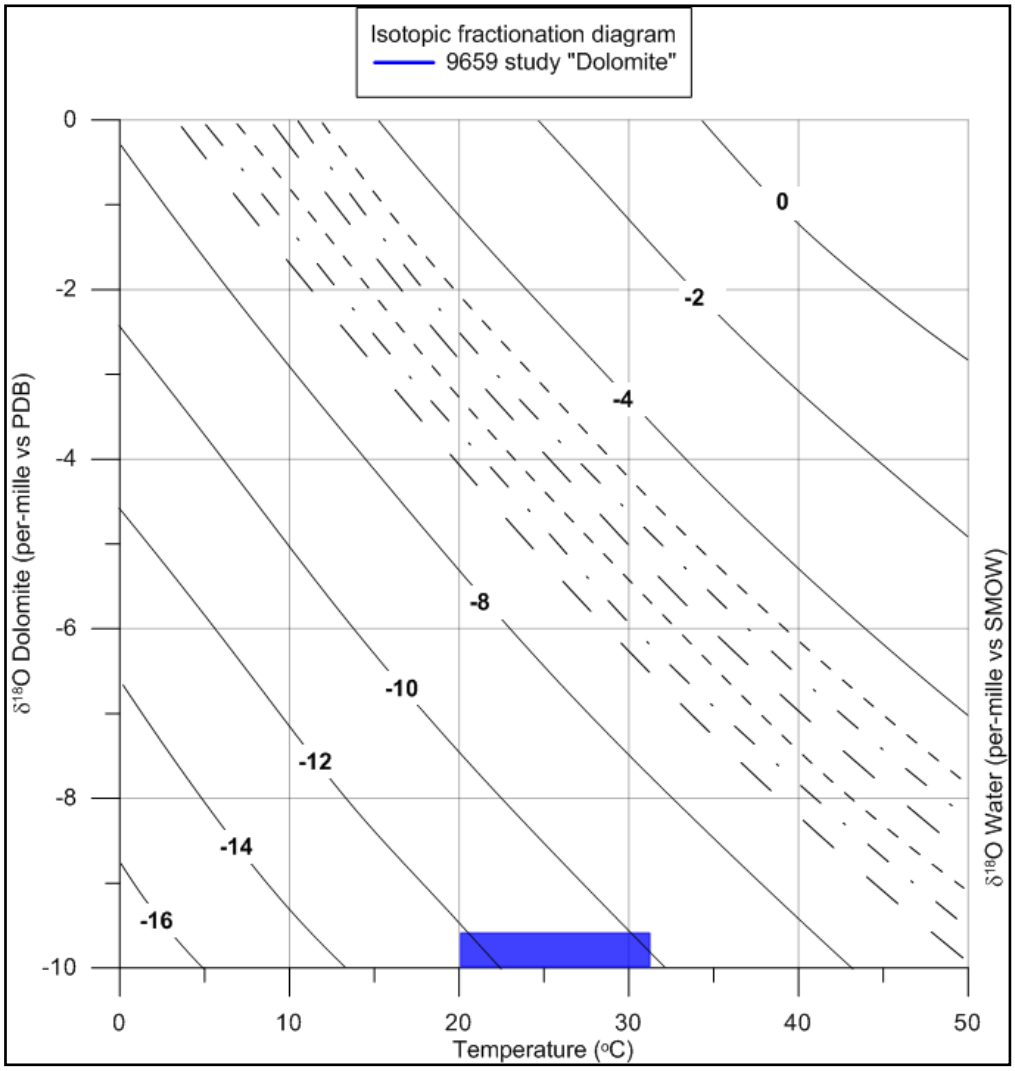

Figure 54: Diagrams of oxygen isotope fractionation for dolomite-water. Curves represent water $\delta^{18}O_{V\text{-}SMOW}$ values. Dotted, dotted-dashed and dashed lines represent oxygen isotope data of palustrine, ground and pedogenic waters as discussed in Köster and Gilg, 2015. Blue envelope: upper and lower temperature limits chosen for calculation.

Another diagram, discussed in Barbier et al. (2016), was used to estimate the calcite-water $\delta^{18}O_{V\text{-}SMOW}$ values (Figure 55). Again by considering a theoretical temperature of T°C =20-30 for calcite precipitation (near surface temperature), the $\delta^{18}O_{V\text{-}SMOW}$ of the calcite water (fluids in equilibrium with the calcite cements) was estimated at the range of -10.5±2.5 ‰.

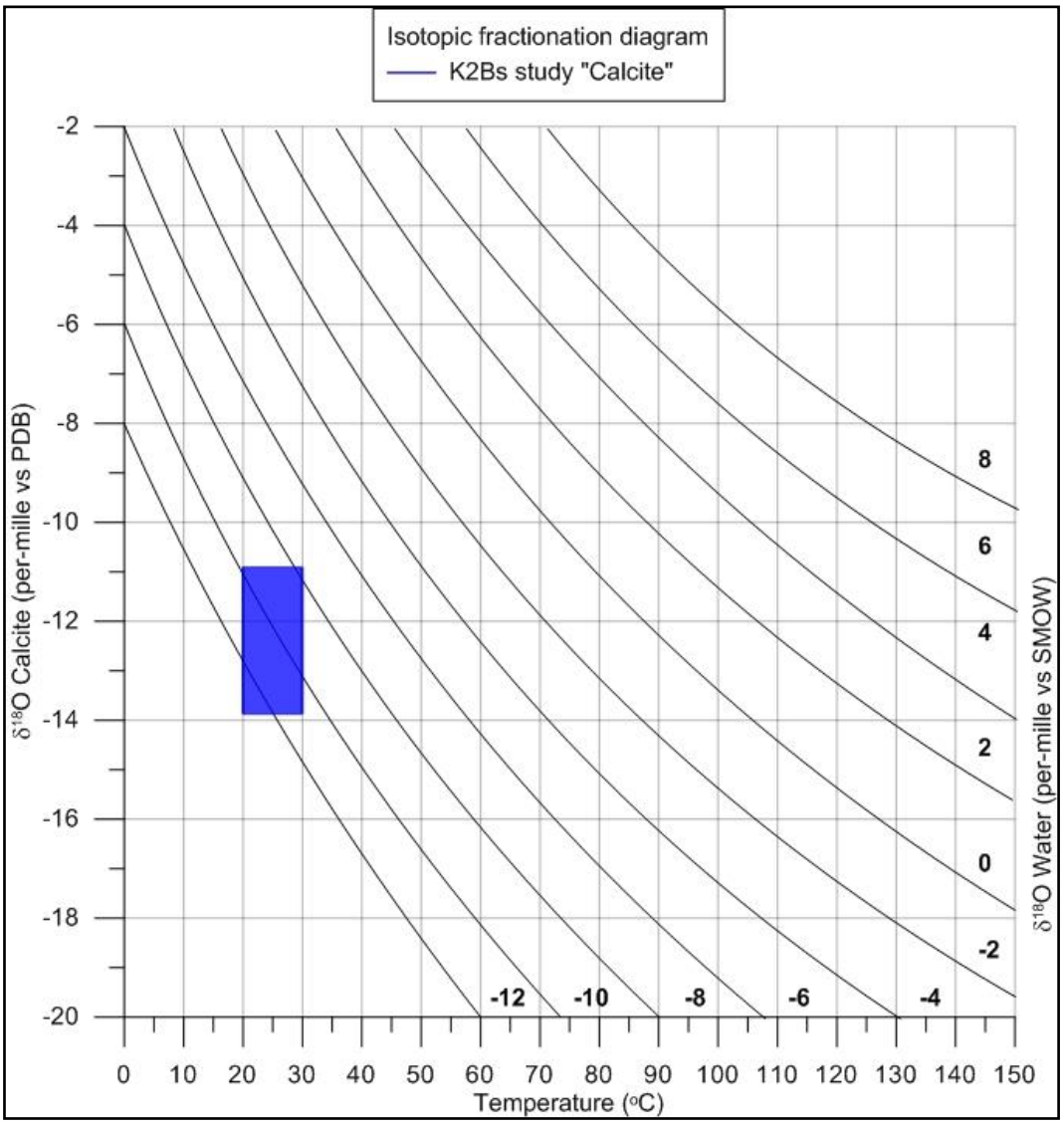

Figure 55: Isotopic fractionation diagram used to estimate the isotopic composition in $\delta^{18}O_{V\text{-}SMOW}$ of fluids in equilibrium with the calcite cements on the basis of 20-30°C, modified from Barbier et al. (2016) and references therein.

The carbonates from Sanchez (2010, 2011) were not plotted in neither diagram since very little is known on their mineralogical nature (calcite or dolomite). In any case their isotopic range for both the $\delta^{18}O$ for $\delta^{13}C$ is very wide, indicating that both dolomite and calcite were analyzed.

What is important though is to keep in mind that the waters from which both dolomite and calcite were precipitated (Figure 54 and Figure 55) are estimated to have overlapping $\delta^{18}O_{V\text{-}SMOW}$ values within the range of -11±1‰. The small contrast is due to the different thermodynamics of the calcite and dolomite formation (fractionation mechanics), since the calcite and dolomite waters show similar $\delta^{18}O_{V\text{-}SMOW}$ values, always on the basis of the theoretical temperature of T°C =20-30.

3.3 EVALUATION OF THE DOLOMITE MODEL

To further evaluate the model on dolomite formation, it was necessary to repeat the analyses on selected samples. Hence, more carbonate cemented sandstone samples were recovered, originating from the **reduced area** of the roll-front (N) which did not experience any roll-front influence and from the **leached area** (S) where uranium was already deposited and remobilized with imminent oxidizing water-charges.

By contrasting these two different groups of carbonate cemented samples it was possible to understand more about the diagenetic history of dolomite as well as of the effect of the roll-front waters on its evolution.

3.3.1 Dolomite cemented sandstones from the reduced area (pre-roll-front)

Dolomite cemented sandstones originating exclusively from the reduced area of the roll-front were studied in more detail to verify the previous obtained results. The aim was to understand

All the studied carbonate cements were recognized to be dolomite of different generations, based on petrographic observations and contrasted with previous studies. In particular there were identified dolomite type I, II and IV or microcrystalline, euhedral and anhedral, respectively. There was also a single case where Type II euhedral dolomite was identified to be associated to a liquid organic matter phase. The samples selected from this study are originating from three wells, located inside the reduced zone: Z0081_1, Z0738_1 and Z1154_1.

Photo-micrographs

Figure 56: Overview of the dolomite fabrics from samples collected in the **reduced part** of the Zoovch Ovoo deposit.

Samples 9704 - 3, 4, 10, 320 & 322. All photographs under LPA.

A, B, D: Anhedral (type IV) dolomite with the typical undoulous extinction, undefined crystal boundaries and associated porosity.

C: Euhedral (type II) dolomite with the typical blocky rhombohedral crystals, locally with siderite cores. All the porosity is filled by dolomite in contrast to the anhedral (Type II) dolomite. The additional syntaxial cement resulted in the formation of poecilitic overgrowth that filled the remaining porosity.

E: A patch of the microcrystalline (type I) dolomite, sometimes associated to a siderite phase.

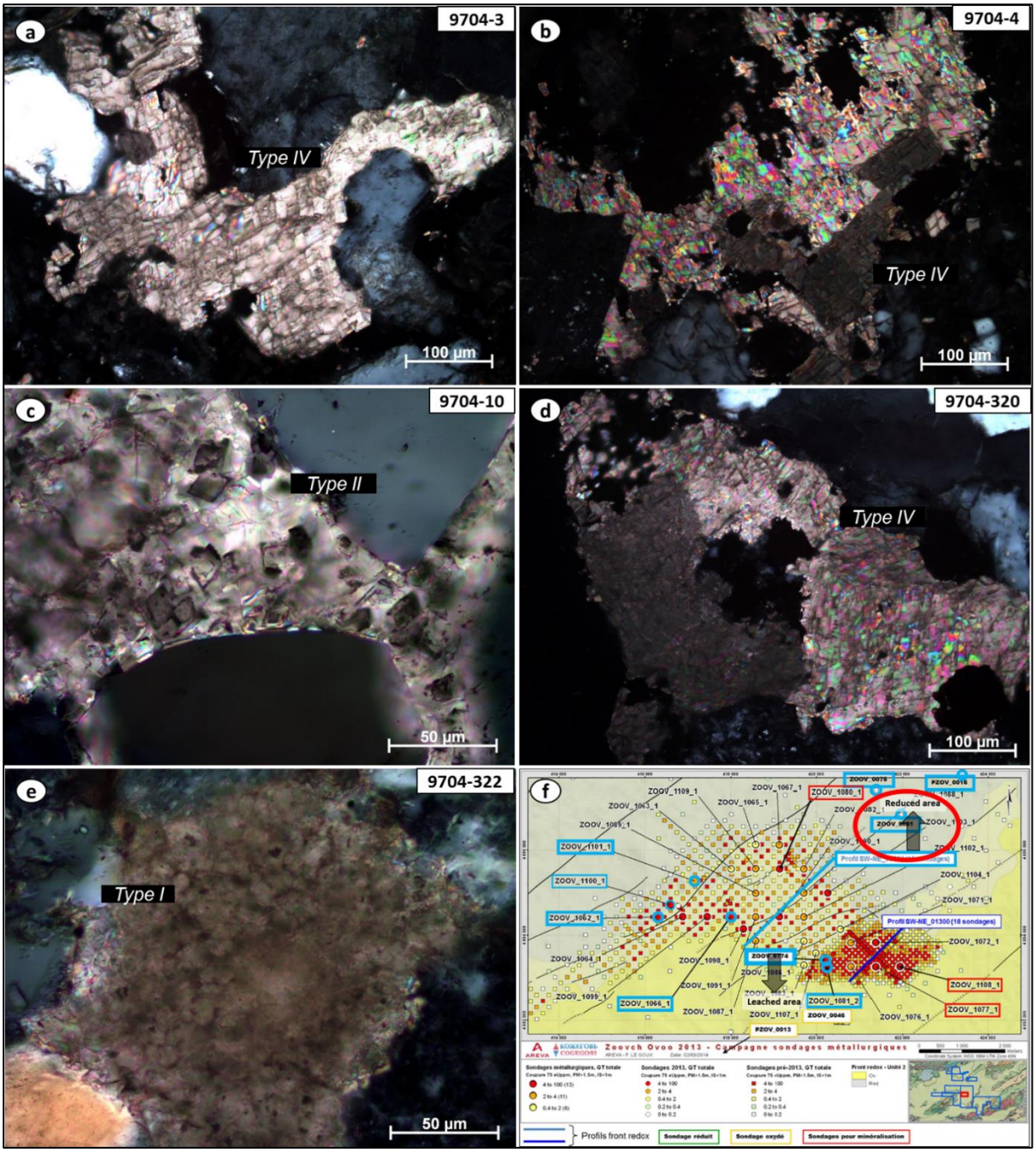

Figure 56: A general overview of the dolomite fabrics recognized in the reduced area of the roll-front. All photographs under LPA. (a, b, d) anhedral dolomite; with undoulous extinction (c) euhedral dolomite with syntaxial cement (poecilitic texture); (e) microcrystalline dolomite, possibly associated to a siderite phase (dark spots) and (f) schematic overview of the Zoovch Ovoo roll-front type deposit in Zuunbayan sub-basin, highlighting in red the location of the new sampling dataset, originating from the reduced area.

Photo-micrographs

Figure 57: A detailed description of a reduced dolomite cemented sandstone (well ZOOV_0081_1) characterized by internal sedimentary structures, laminations and granulometry variations. Different dolomite types were recognized as a function of grain size. In more detail, the microcrystalline (type I) and the euhedral (type II) were recognized in the finer grain size whereas the anhedral (type IV) was recognized in the coarser part of the sandstone.

Sample 9704 - 322**.** All photographs under LPA.

1: The fine sandstone part of the sample is dominated by microcrystalline (type I) dolomite with associated siderite (dark spots inside the dolomite mass).

2: The medium to fine part of the sandstone is dominated my euhedral (type II) dolomite with siderite cores (dark rhombic nuclei of crystals).

3: Finally the medium coarse sandstone is dominated by anhedral (type IV) dolomite.

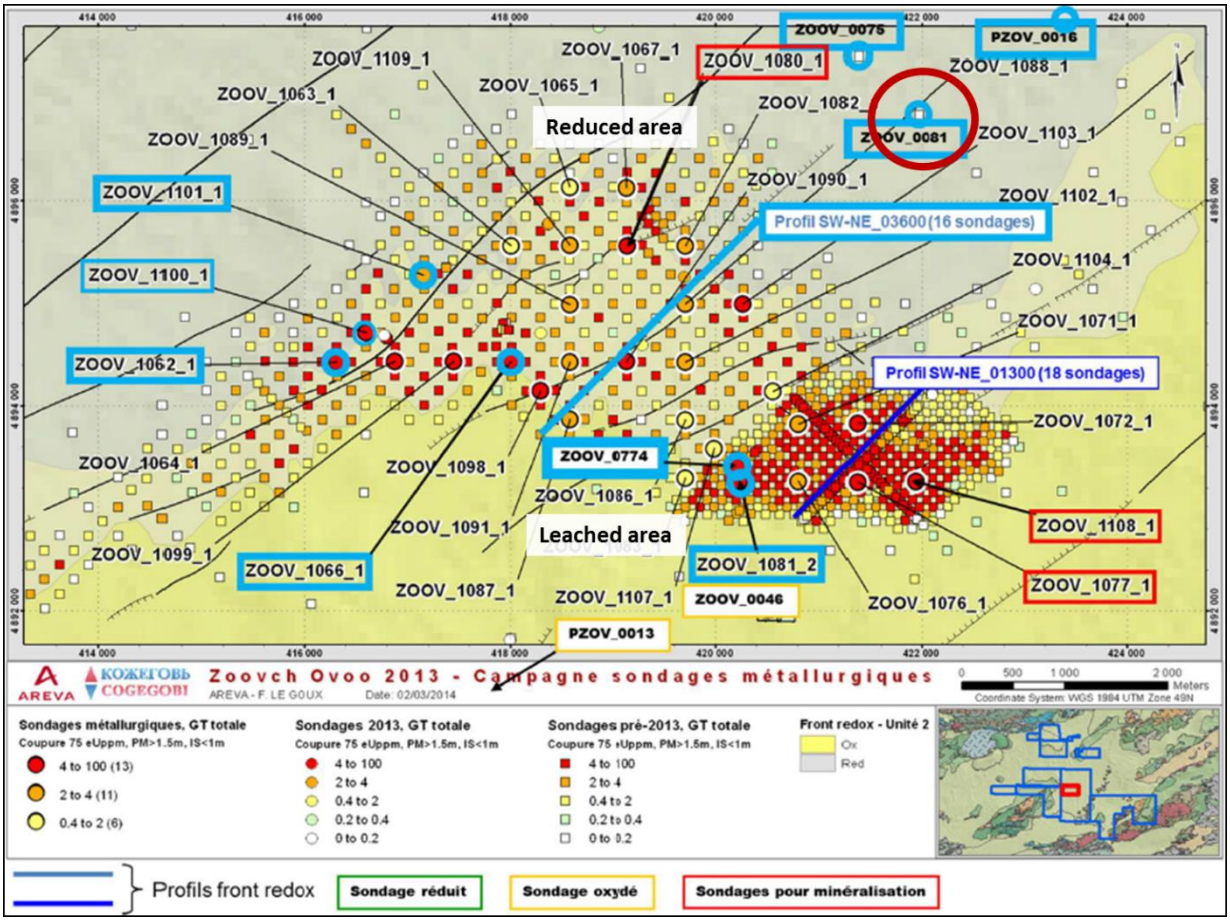

Figure 57: Location of the dolomite cemented sandstone samples from the reduced area of the roll-front, highlighting well ZOOV_0081_1. The dolomite cements recognized are presented in **Figure 57 (continued)**.

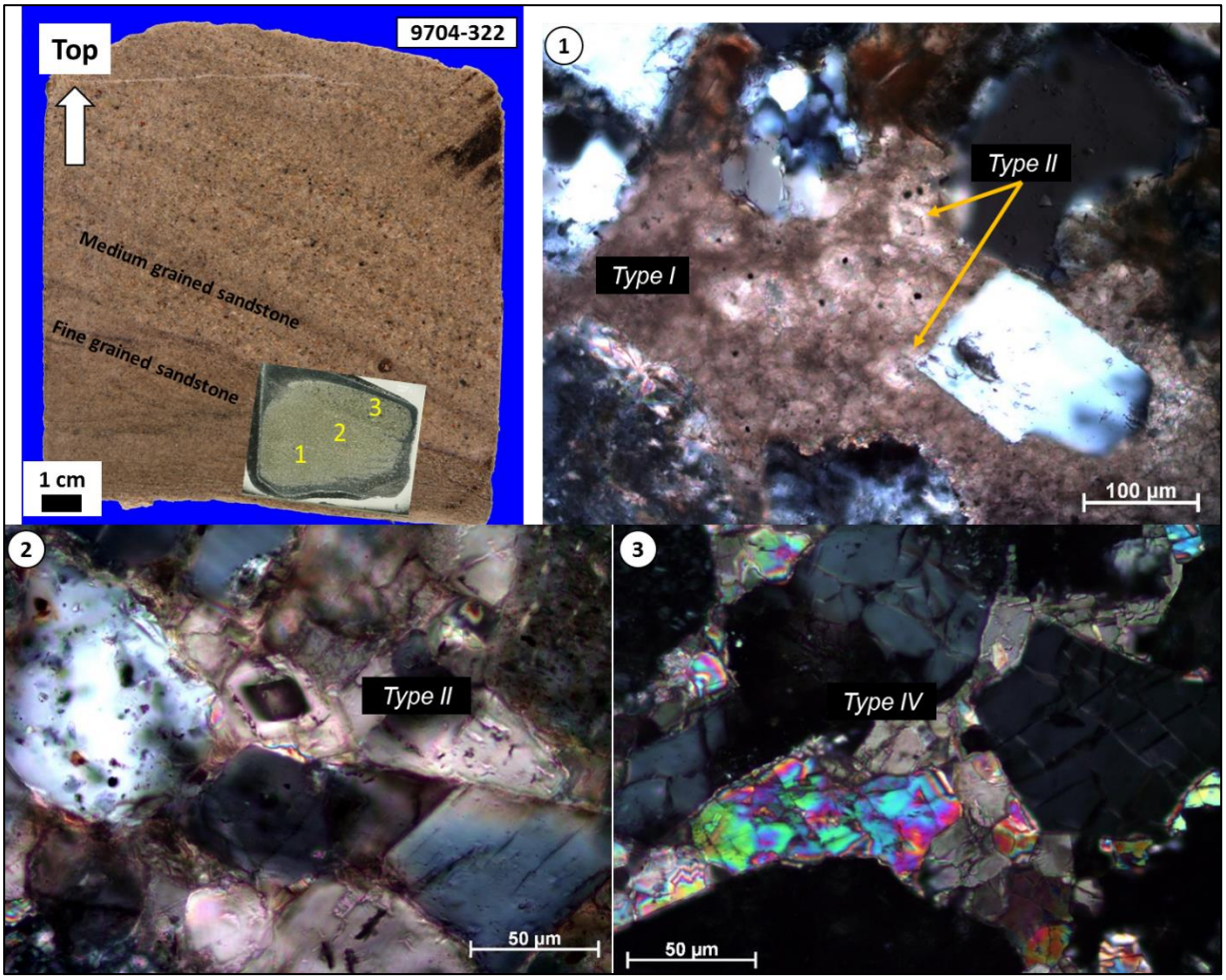

Figure 57 (continued): A closer look of a dolomite cemented sandstone (9704-322) originating from the reduced area of the roll-front (well ZOOV_0081_1), showing oblique planar laminations with visible granulometry interchange. Different dolomite fabrics were recognized as a function of grain size. All micro-photographs under LPA. 1) Microcrystalline (type I) and indices of euhedral (type II) dolomite accounting for the finest granulometric fraction; 2) euhedral (type II) dolomite associated with the discontinuity between the finest and coarsest fractions; 3) anhedral (type IV) dolomite associated to the coarsest fraction.

3.3.2 Petrography of the oxidized dolomite cemented sandstone (post-roll front)

In the leached area at the rear of the roll-front the dolomite phases recognized in the studied samples consider the euhedral (type II) and anhedral (type IV). The special feature of this area is that the dolomite cements are accompanied by Fe-hydroxides and oxides, namely the limonite ($FeO(OH)\cdot nH_2O$), the goethite ($FeO(OH)$) and hematite (Fe_2O_3), respectively.

The dolomite cement appears partially dissolved, affected by the oxidative roll-front waters, resulting in the formation of secondary porosity, while the open pore space is occupied by the newly formed Fe-hydroxides and oxides.

A typical example to study the effect of leaching on dolomite is sample 9704 – 319 from well Zoov_0703_1, presented below in detail.

Photo-micrographs

Figure 58: A typical example of a leached (strongly oxidized) dolomite cemented sandstone.

Sample 9704-319. Pictures (A, B, C) under LPA and (D) under reflected polarized light.

A, B: Open pore space inside euhedral Type II dolomite associated with Fe-hydroxides. The open pores (secondary porosity) are highlighted in blue color. Their irregular shape indicates that the pore space was formerly occupied by other mineral phases, possibly by pyrite or dolomite crystals.

C, D: Partial dissolution of pyrite or euhedral dolomite, creation of secondary porosity and formation of iron hydroxides.

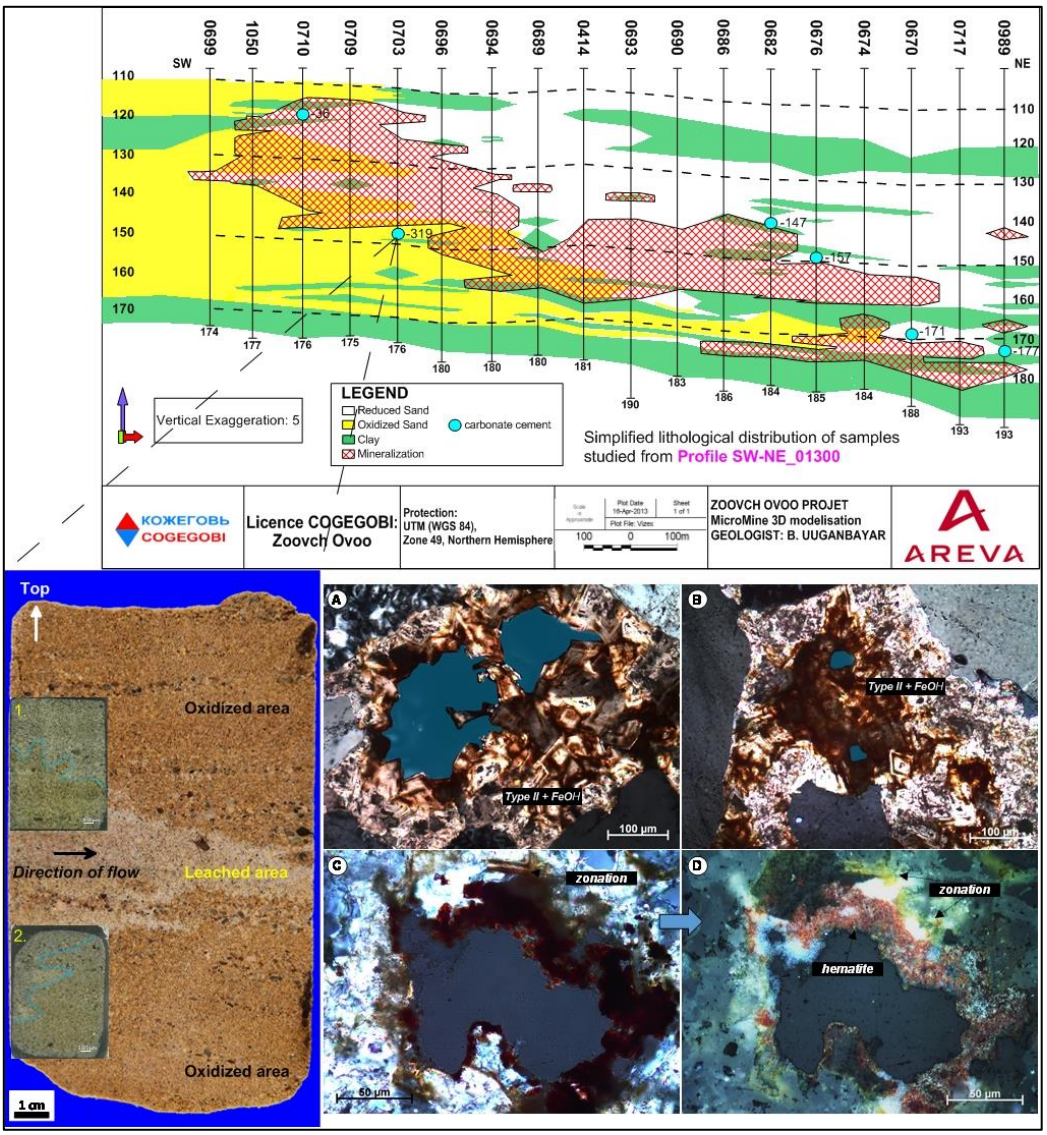

Figure 58: Whole rock sample originating from the leached area (9704-319) highlighting the two thin sections studied. (A, B) examples of a dolomite cemented sandstone from the leached zone, characterized by the dissolution of pyrite or by partial dissolution of dolomite, leading to the formation of Fe-hydroxides, which are concentrated around the secondary porosity; (C, D) Dissolution of pyrite or dolomite, creation of secondary porosity, formation of hematite. It is likely that the destruction of euhedral dolomite is the source of Fe for oxides/hydroxides formation

Photo-micrographs

Figure 59: An example of a dolomite cemented sandstone showing different grain sizes and redox statuses.

Sample 9704-317. All pictures under LPA.

A: Partially oxidized part of the medium to fine sandstone with euhedral (Type II) dolomite and no signs of Fe-hydroxides.

B: Oxidized part of the medium to fine sandstone with euhedral (Type II) dolomite, and Fe-hydroxides. Zone B contains the highest concentration in Fe-hydroxides. This part of the sandstone is as porous as A, C and D2.

C: Partially oxidized medium to fine sandstone with euhedral (Type II) dolomite and few Fe-hydroxides occurrences. This part of the sandstone is the second richest in Fe-hydroxides after zone B.

D1: Reduced part of the medium to fine sandstone with anhedral (Type IV) dolomite and local indices of Fe-hydroxides around open pores (secondary porosity).

D1: Reduced part of the coarse sandstone with gravel containing anhedral (Type IV) dolomite and no Fe-hydroxides. This part of the sandstone shows the least Fe-hydroxides content.

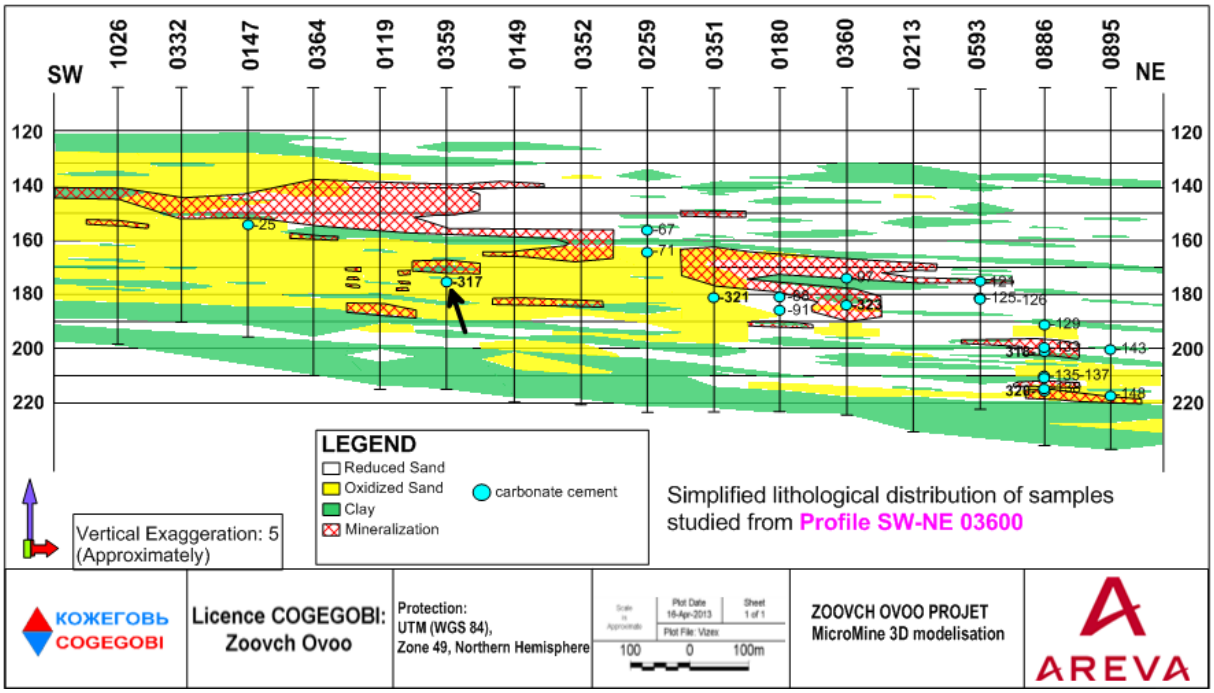

Figure 59: Sample 9704-317 from well Zoov_0359_1 located at Profile SW-NE_03600, contained inside oxidized lithologies; location indicated by the black arrow. The core sample demonstrates two different lithologies, the coarse sandstone with gravels (micro-conglomerate) and the medium to fine sandstone, while some parts are more oxidized showing red to yellow colors and others are reduced with light grey colors. The whole core sample is cemented by anhedral to euhedral dolomite cements that are accompanied by Fe hydroxides, namely goethite and limonite formed by the dissolution of pyrite and dolomite responding to water chemistry changes driver by roll-front water introduction.

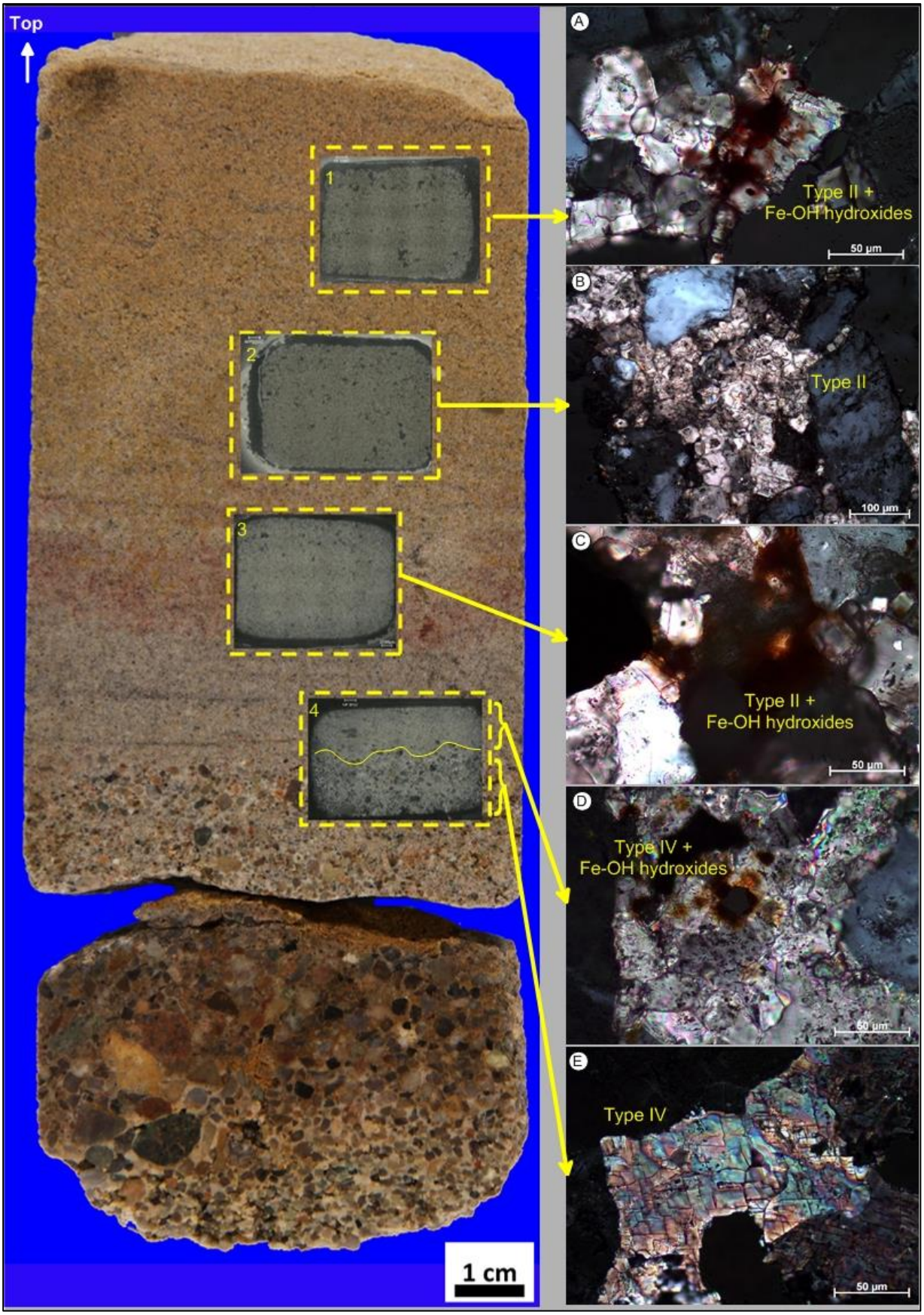

Figure 59 (continued): Whole rock sample originating from the leached area (9704-319) highlighting the presence of anhedral dolomite in the coarser part and the formation of Fe-hydroxides in the oxidized sandstones.

3.4 DISCUSSION ON DOLOMITE FORMATION

The carbonates and in particular the four dolomite fabrics are good indicators of the fluid-rock interaction episodes by showing depletion in REEs and in several trace elements i.e. Fe, Mn, responding to water-rock interactions evolution, while at the same time they are present during the whole history of the deposit, from deposition to post-roll front. Having this in mind the dolomite was used as a tool to uncover the diagenetic history of the deposit.

To begin with, the microcrystalline (type I) dolomite was encountered in two forms. Firstly and more commonly as uniform cement occupying the intergranular porosity binding the sand grains which are not in contact with each other and secondly as individual patches that do not contain any sand grains (Figure 60). The case of having sand grains not in contact could hold two interpretations. In the first case there was rapid chemical carbonate precipitation from an aqueous solution shortly after deposition (a few centimeters or meters of burial depth), therefore the sand grains were not tightly connected. In the second case there was an excess of available carbonate material that led to carbonate crystal overgrowth, while the sandstone host-rock was poorly consolidated causing the sand grains to be pushed aside from each other

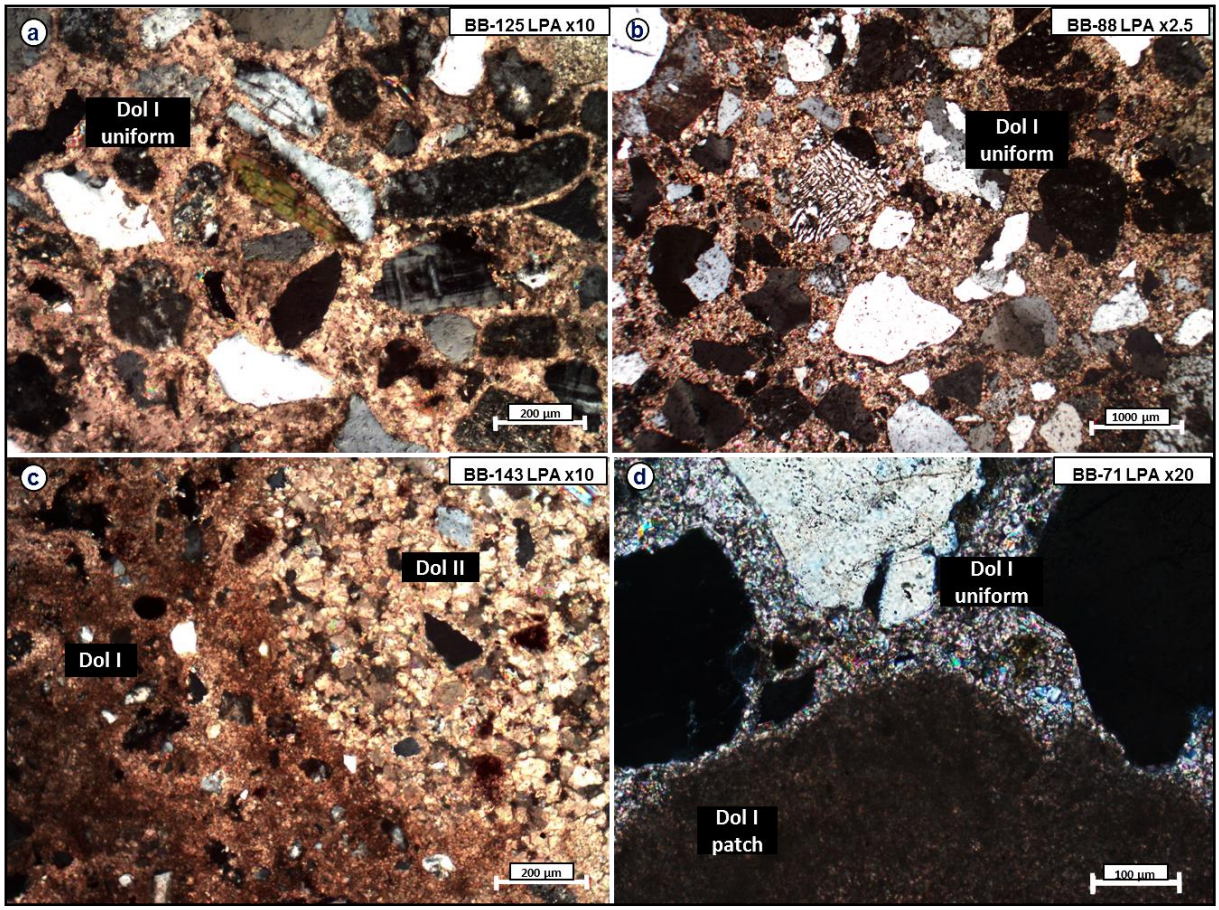

Figure 60: Sand grains not in contact under LPA. Microcrystalline (Type I) dolomite as cement bounding sand grains (a, b). Microcrystalline dolomite and the euhedral (Type II) fabric and an intermediate phase (c). Microcrystalline dolomite as a patch and as uniform cement (d).

In the case when the microcrystalline dolomite is in patchy form there may be a siderite phase associated (Figure 61). The dolomite patches are considered to be the earliest diagenetic dolomite phase and were probably formed during deposition The associated siderite formation implies a Fe reduction event contemporaneous to the patchy dolomite formation. According to Coleman et al. (1993) and Roh et al. (2003) the siderite formation can have biogeochemical origin and can be formed in swamp environments by microbial reduction of Fe(III). The siderite formation is then contemporaneous to the sediment deposition at the salt-march, which could be the case of the highly saline playa lakes, with the surrounding mudflats and swamps (rich in organic matter) of Zoovch Ovoo during the Late Cretaceous period. The formation of saliniferous lake districts in East Asia during that period was favored by the tropical to sub-tropical (semi-arid) climate settings coupled with seasonal monsoons (Chen et al., 2012).

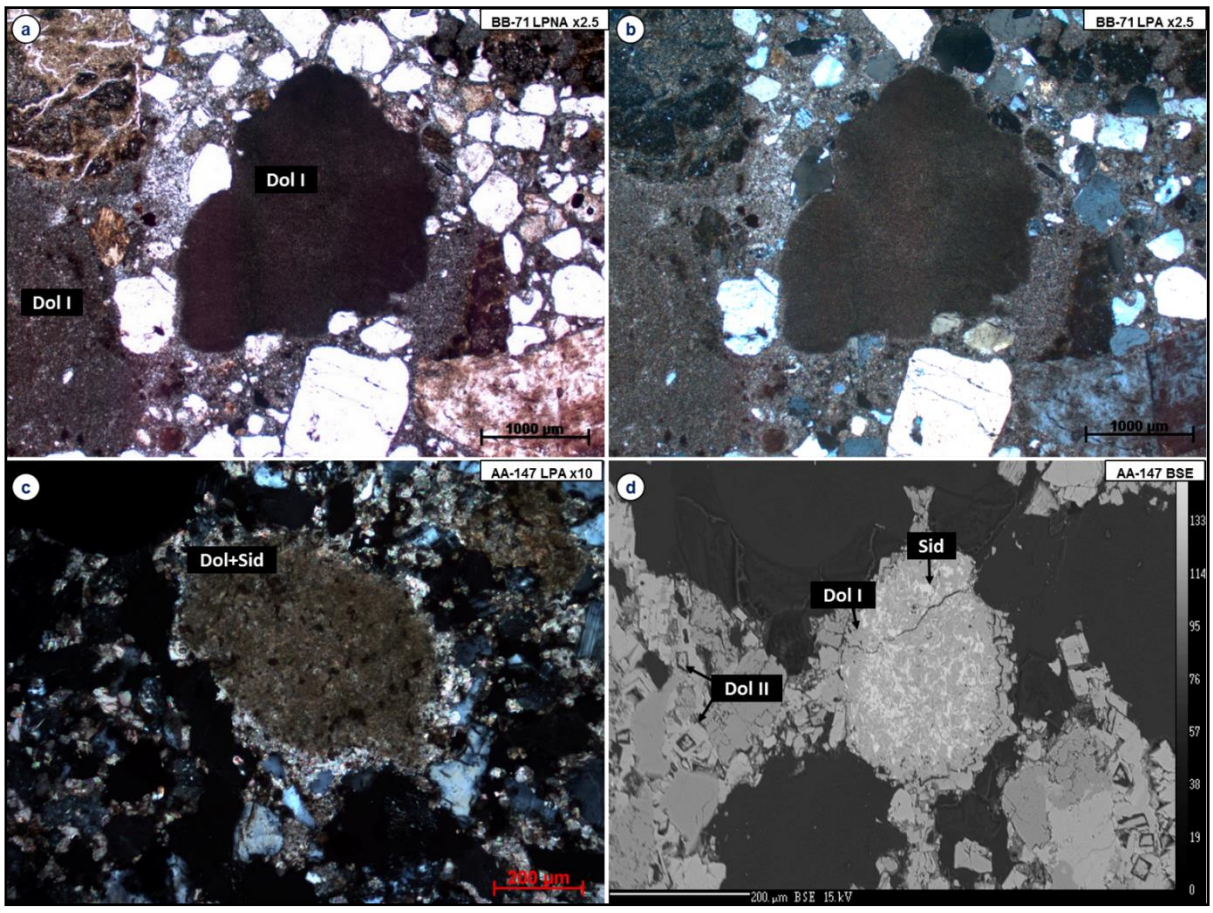

Figure 61: Microcrystalline (Type I) dolomite in patches and in uniform cement without siderite (a, b). In patches with the associated siderite phase (c, d).

In the concept of microbial reduction of Fe(III), the reduction of Fe(III) to Fe(II), in other words of ferric iron to ferrous iron, takes place in anaerobic aquatic environments and is triggered by the oxidation of fermentation products, such as acetate and hydrogen, resulting in the formation of siderite ($FeCO_3$). In more detail, the same bacteria that are responsible for the formation of iron-sulfides, known as sulfate-reducing-bacteria (SRB) are directly reducing Fe(III) through a series of enzymatic reactions. The SRB, termed *Mesophilic* when they thrive at surface

temperatures (20-35ºC that could easily be the case of Zoovch Ovoo during Late Cretaceous), are responsible for the production of ferrous iron, hydroxyl ions and bicarbonate that ultimately lead to the formation of siderite. Those enzymatic reactions are described below step by step:

i. Anaerobic fermentation (decomposition) of organic matter (i.e. glycose) by anaerobic bacteria produces acetic acid.

$$C_6H_{12}O_6 \rightarrow 3CH_3COOH$$

ii. The acetic acid is in chemical equilibrium with acetate anion and hydrogen cation (proton). Above pH of 5.5 the reaction moves to the right (acetic acid converts to acetate ion).

$$CH_3COOH \rightleftharpoons \mathbf{CH_3COO^-} + \mathbf{H^+}$$

iii. Acetate anion is oxidized and the poorly crystalline iron oxide that is made of ferric iron Fe(III) is reduced to ferrous iron Fe(II). Bicarbonate and hydroxyl anions are also produced.

$$4Fe_2O_3 + \mathbf{CH_3COO^-} + 7H_2O \rightarrow 8Fe^{2+} + 2HCO_3^- + 15OH^-$$

iv. The hydrogen that was generated by the anaerobic decomposition of organic matter is used as an electron donor for the metabolism of the SRB. The oxidation of hydrogen coupled to the reduction of Fe(III) favors the precipitation of siderite through the formation of Fe^{2+} and OH^-.

$$Fe_2O_3 + \mathbf{H_2} + H_2O \rightarrow 2Fe^2 + 4OH^-$$

v. Finally Fe(II) reacts with the bicarbonate to form siderite and water.

$$Fe^{2+} + HCO_3^- + OH^- \rightarrow \mathbf{FeCO_3} + H_2O$$

It was already stressed that a pH higher than 5.5 is needed to produce acetate ion. According to multiple laboratory experiments that were performed by Roh et al. (2003), siderite is stable in a Fe-CO_2 aquatic system for specific pH and Eh domains. The thermodynamic stability of siderite at T=25ºC and P=1atm (which could be valid for the Zoovch Ovoo case study), as well as of other phases linked to the Fe biomineralization can be better explained in the Eh/pH equilibrium plot (Figure 62). For instance siderite is a stable phase when pH=7.5/Eh=-0.4 until when pH=10/Eh=-0.55, as the reduction progresses (when more hydrogen is added to the system the redox potential is shifted downwards). Therefore it can be concluded that very soon after burial the pH progressively increases while the Eh decreases and that is clearly imprinted on the siderite formation.

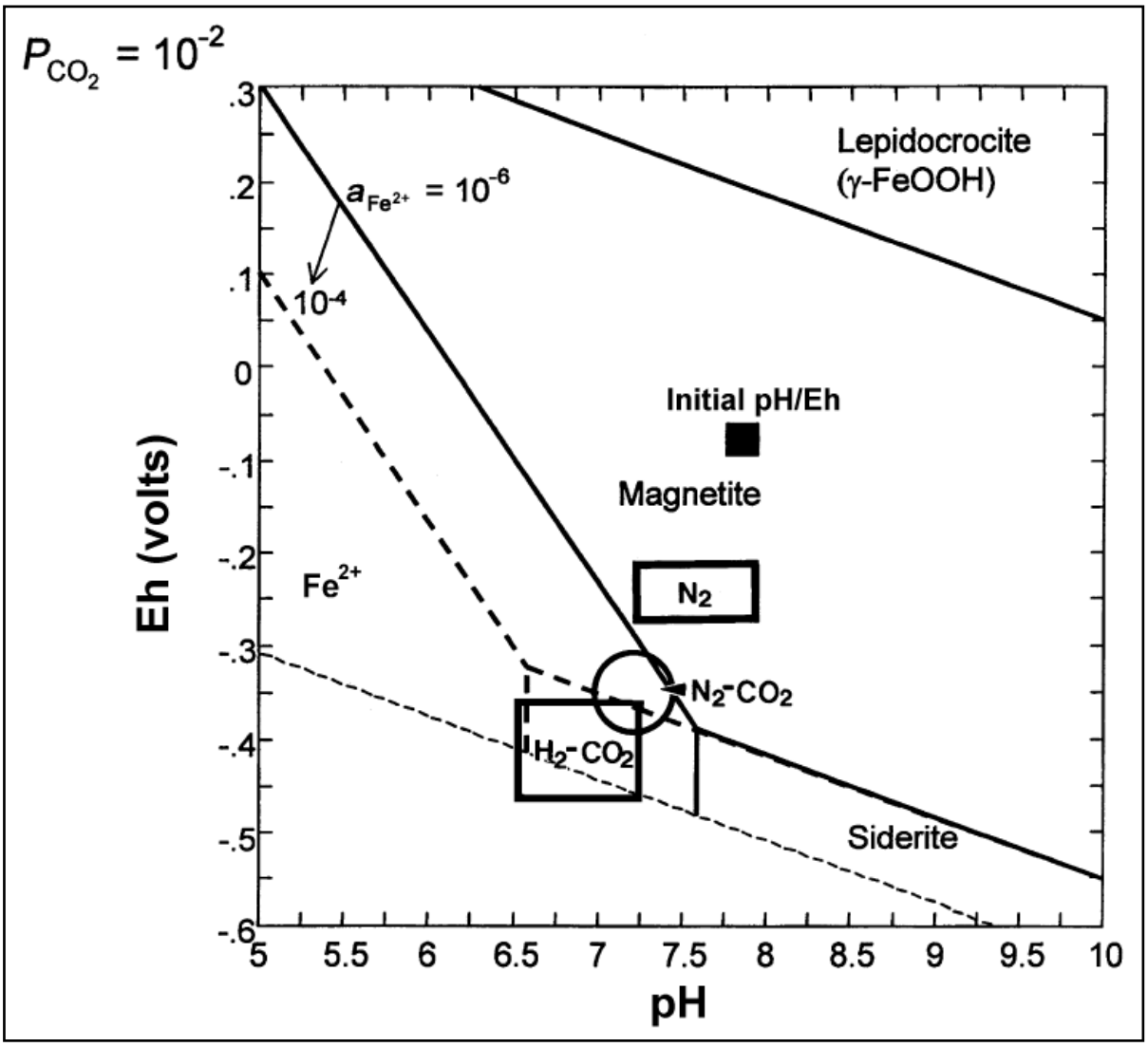

Figure 62: Eh-pH stability fields for iron biomineralization, including siderite in the water-Fe-CO_2 system at 25ºC and 1 atm total pressure (Roh et al., 2003)

Consequently, when the SRB directly reduced the Fe(III) to Fe(II) and siderite was formed there was no actual sulfate reduction taking place, otherwise framboidal pyrite would occur. Another point is that the presence of H_2S, which is needed to form iron-sulfides, hinders siderite formation. Hence, the patchy microcrystalline dolomite with the siderite is earlier diagenetic than the framboidal pyrite, which is the first pyrite type to be formed. It is also noted that pyrite under any form was not found in the samples that contain Type I dolomite. Complementary SEM-BSE photographs on Type I dolomite with the associated siderite phase and the relevant chemical analysis are provided in Figure 63.

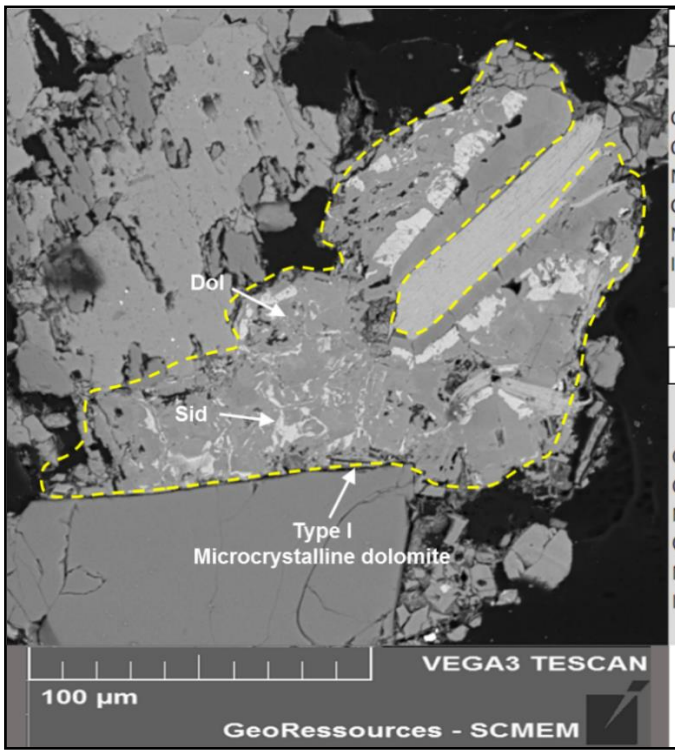

Dolomite

Element	At. No.	Line s.	Netto	Mass [%]	Mass Norm. [%]	Atom [%]
Carbon	6	K-Serie	6177	0.00	0.00	0.00
Oxygen	8	K-Serie	20174	21.08	30.30	50.74
Magnesium	12	K-Serie	14376	9.23	13.27	14.63
Calcium	20	K-Serie	27687	27.53	39.56	26.45
Manganese	25	K-Serie	2928	7.45	10.71	5.22
Iron	26	K-Serie	1403	4.29	6.16	2.96
			Sum	**69.58**	**100.00**	**100.00**

Siderite

Element	At. No.	Line s.	Netto	Mass [%]	Mass Norm. [%]	Atom [%]
Carbon	6	K-Serie	5494	0.00	0.00	0.00
Oxygen	8	K-Serie	33706	23.87	28.96	57.49
Magnesium	12	K-Serie	1099	0.86	1.04	1.36
Calcium	20	K-Serie	4858	4.49	5.45	4.32
Manganese	25	K-Serie	4363	9.79	11.88	6.87
Iron	26	K-Serie	16043	43.42	52.67	29.96
			Sum	**82.43**	**100.00**	**100.00**

Figure 63 (SEM 59AA-147): The Type I fabric depicting the siderite and dolomite phases. The chemistry of each mineral is provided by the table on the right.

In the same sense that not every microcrystalline (Type I) dolomite is associated to a siderite phase, not every euhedral (Type II) dolomite has siderite cores (Figure 64) or siderite zonations (Figure 65).

There were only a few cases where siderite was encountered inside euhedral (type II) dolomite crystals having the typical rhombohedral geometry, although it is possible that polishing caused siderite to be dettached and removed. Roh et al. (2003) showed that the rhombohedral siderite is formed by bacteria of the species *Shewanella* which thrive in estuarine settings at 25ºC (*Mesophilic*). In the case of Zoovch Ovoo, there is no such setting (estuarine or marine influenced) but perhaps the elevated salinity, 20 g/L according to Grizard (2017b), could play a role in the presence of bacteria similar to the *Shewanella algae* that were enduring in the sediment, since there is mixing of two water bodies meteoric/lacustrine exactly as it happens in the estuarine setting, where fluvial water is intermixed with marine.

As was already demonstrated in the C, O stable isotopes chapter, the fact that some surface carbonate occurrences returned $\delta^{13}C$ values close to 0 ‰ as if they were sourced from sea water (Figure 53), could point out that the highly saline playa-lake waters are comparable to marine waters and hence similar micro-organisms to the *Shewanella algae*, could thrive.

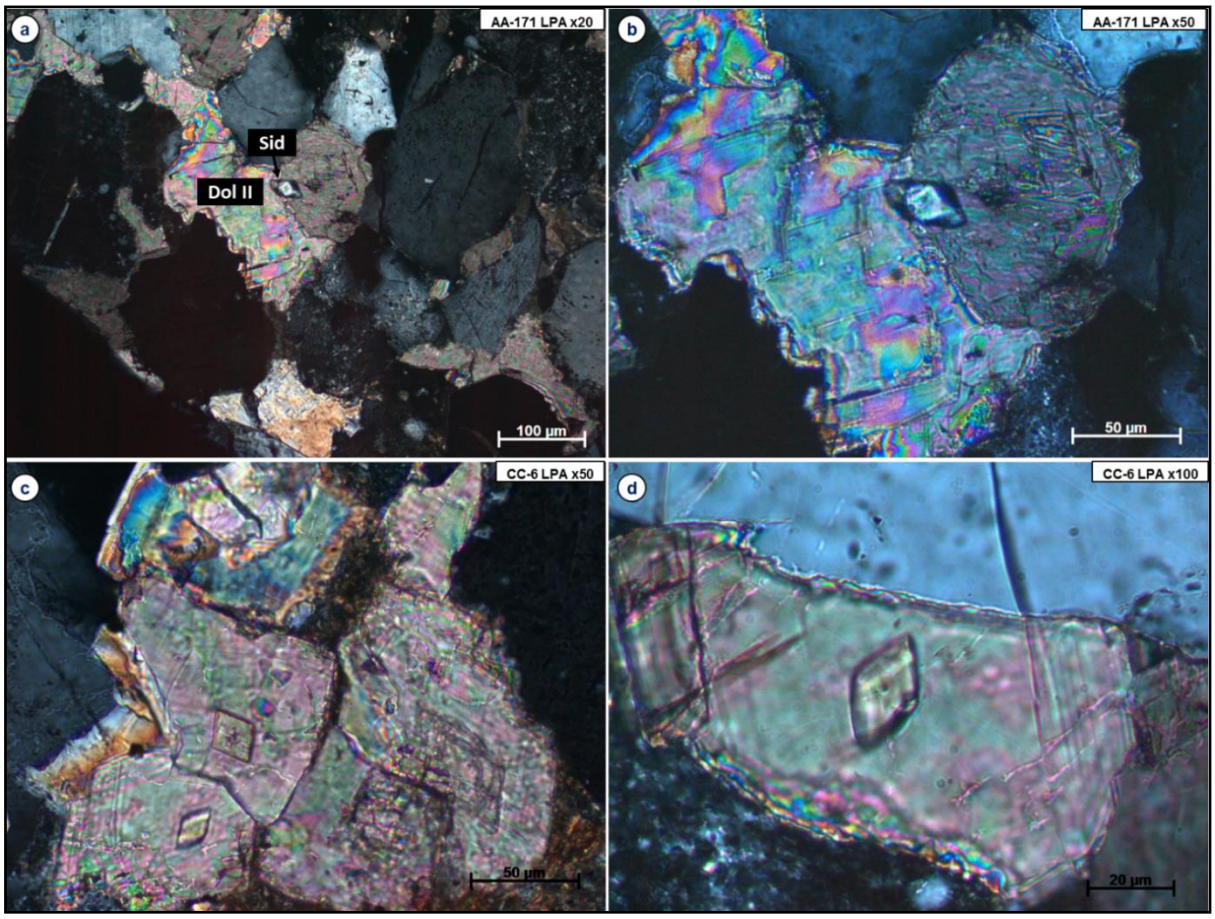

Figure 64: Euhedral (Type II) dolomite of poecilitic texture with siderite core.

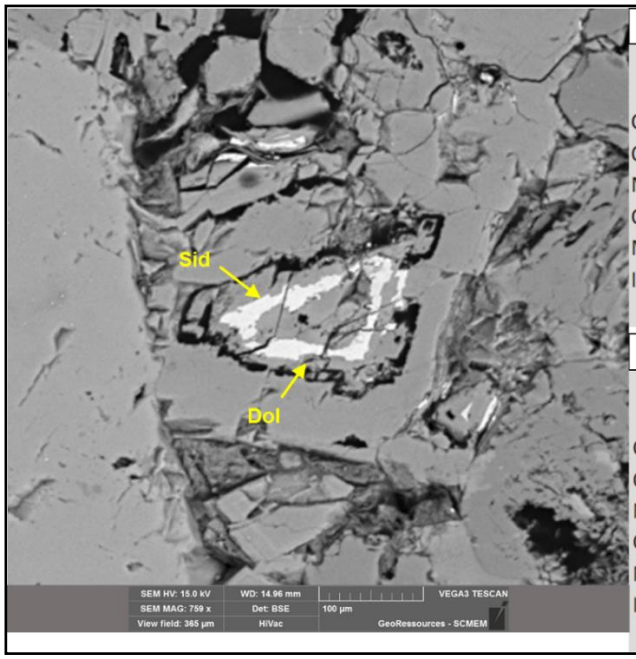

Dolomite

Element	At. No.	Line s.	Netto	Mass [%]	Mass Norm. [%]	Atom [%]
Carbon	6	K-Serie	6177	0.00	0.00	0.00
Oxygen	8	K-Serie	20174	21.08	30.30	50.74
Magnesium	12	K-Serie	14376	9.23	13.27	14.63
Calcium	20	K-Serie	27687	27.53	39.56	26.45
Manganese	25	K-Serie	2928	7.45	10.71	5.22
Iron	26	K-Serie	1403	4.29	6.16	2.96
			Sum	**69.58**	**100.00**	**100.00**

Siderite

Element	At. No.	Line s.	Netto	Mass [%]	Mass Norm. [%]	Atom [%]
Carbon	6	K-Serie	5494	0.00	0.00	0.00
Oxygen	8	K-Serie	33706	23.87	28.96	57.49
Magnesium	12	K-Serie	1099	0.86	1.04	1.36
Calcium	20	K-Serie	4858	4.49	5.45	4.32
Manganese	25	K-Serie	4363	9.79	11.88	6.87
Iron	26	K-Serie	16043	43.42	52.67	29.96
			Sum	**82.43**	**100.00**	**100.00**

Figure 65 (SEM 59AA-147): The Type II fabric depicting the siderite and dolomite chemical zonations.

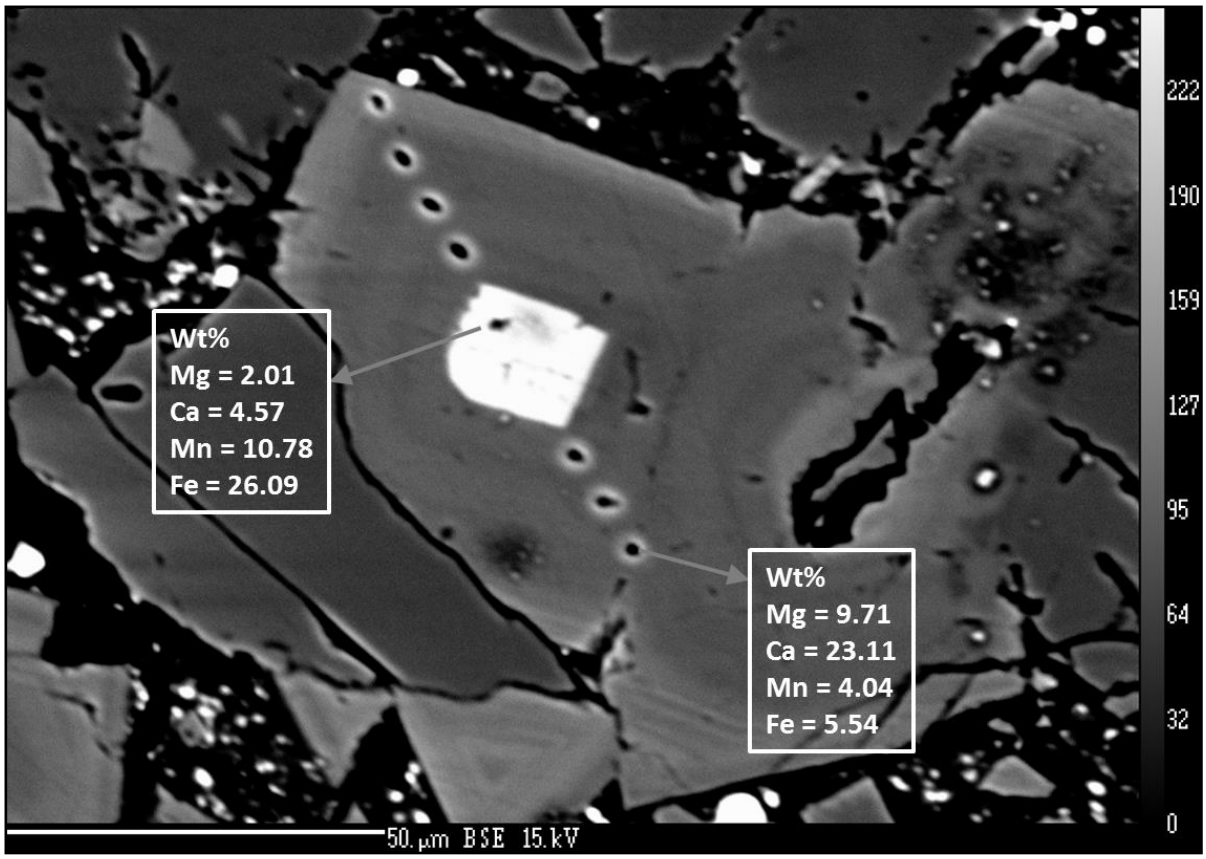

Figure 66 (EMPA 59CC-6): A close view of the siderite core found inside euhedral (Type II) poecilitic dolomite.

As indicated there are at least two episodes of siderite formation since the euhedral (type II) dolomite crystals encountered are respecting the following order: 1) siderite core, 2) euhedral dolomite, 3) siderite zonation and finally 4) euhedral dolomite overgrowth (or poecilitic texture). On the other hand it seems that at a certain moment of the above mentioned sequence the siderite is not stable anymore and iron sulfides are forming instead. Hence, the evolution of the crystal growth of the euhedral (Type II) dolomite should be divided in the part when siderite is stable and in the later part when pyrite becomes the stable iron phase. The exact Eh/pH changes that cause the transition from the siderite to the pyrite stability field depend on the environmental conditions of the system that is studied. Previous studies Mumtaz (1979) mention that the change from siderite to pyrite is linked to increasing pH and decreasing Eh whereas newer studies Burton et al (2006); Lemos et al. (2007) and Burrows et al. (2015) tend to point the opposite.

Nevertheless, it is evident that the overgrowth of euhedral (type II) dolomite is posterior to early diagenesis with respect to the framboidal, as well as to the overgrowth termed concentric pyrite (Figure 67). Hence, the overgrowth of the euhedral (type II) dolomite is post-diagenetic of the first two pyrite generations, the framboid and the overgrowth, meaning that dolomitization of Type II continues even after the second stage of iron sulphide formation.

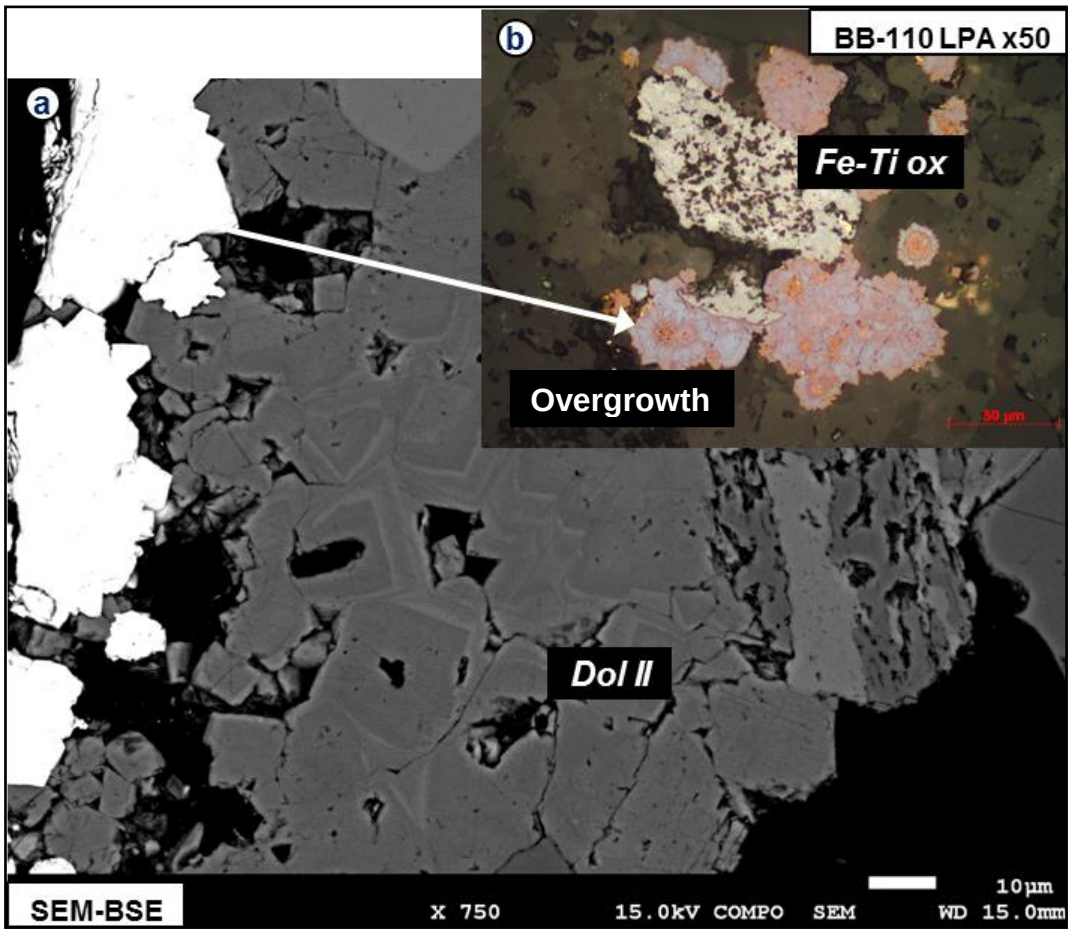

Figure 67: Dolomite Type II postdates framboidal pyrite with concentric overgrowth. In (b) the pyrite and marcasite take orange and azure colors due to oxidation.

To better illustrate the siderite, dolomite, uranium and pyrite relationships chemical maps were constructed by means of EMPA (Figure 68, Figure 69). It was observed that the microcrystalline (type I) dolomite can contain traces of uranium that according to the LA-ICPMS analysis (high precision) are about 300 ppm (0.03 wt%), in sample 59AA-147, which is above the detection limit (10 ppm). The same level of uranium concentration was identified also previously in sample 59BB-71, again inside the microcrystalline texture.

If it is assumed that the early pre-concentration of uranium in the earliest dolomite type is not an analytical artifact then it might have an autochthonous origin. In addition, according to Heijman (1993, 1995) and Roh et al. (2003) the minerals that contain ferrous iron Fe(II) produced by the Fe(III)-reducing bacteria can also chemically reduce other multivalent metals, in this case U(VI).

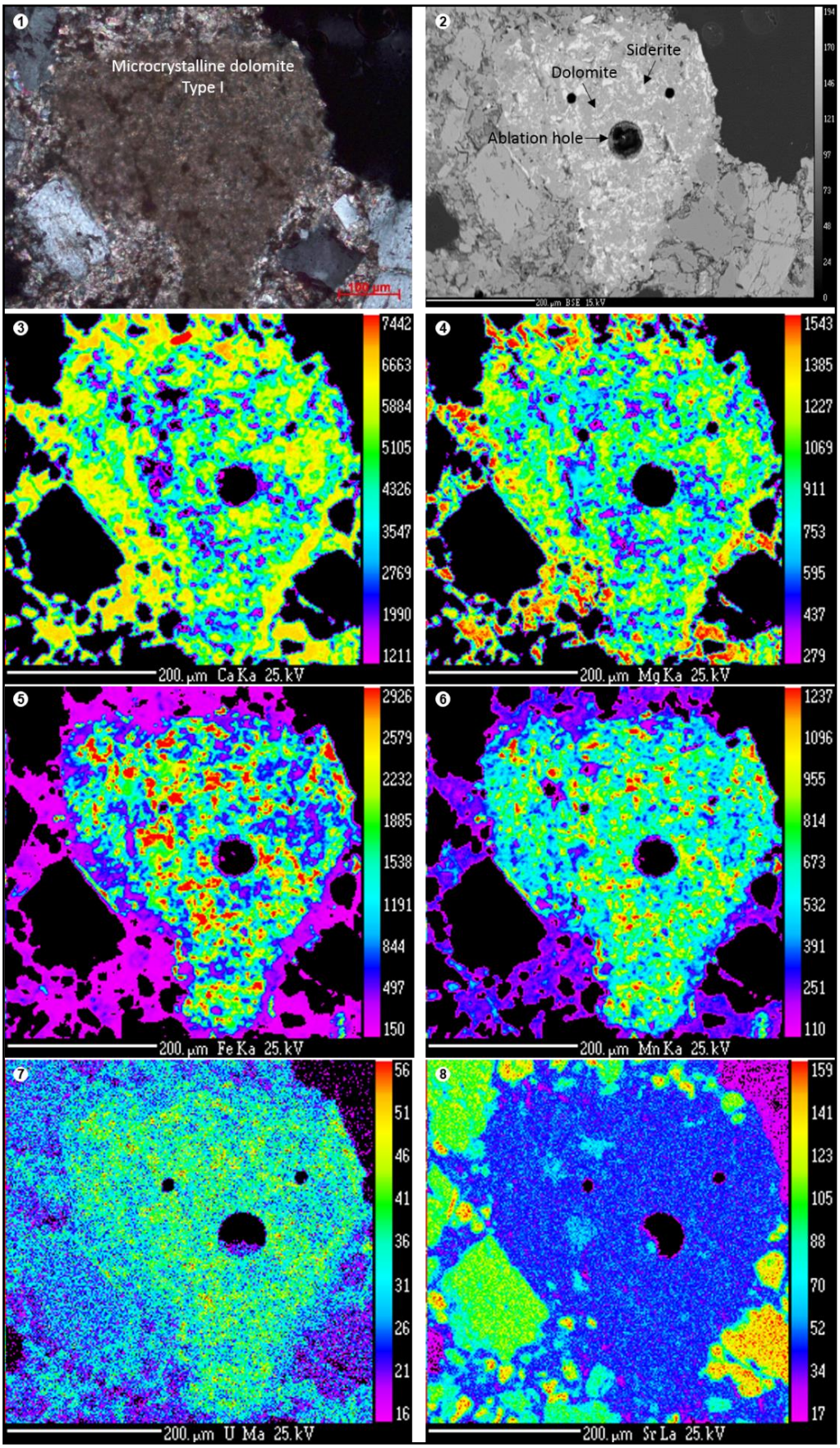

Figure 68 (EMPA 59AA-147): Chemical mapping of the microcrystalline (Type I) dolomite. 1) LPA, 2) BSE, 3-8) EMPA counting Ca, Mg, Fe, Mn, U, Sr. According to LA-ICPMS data the U content can reach 0.03 wt% (300 ppm).

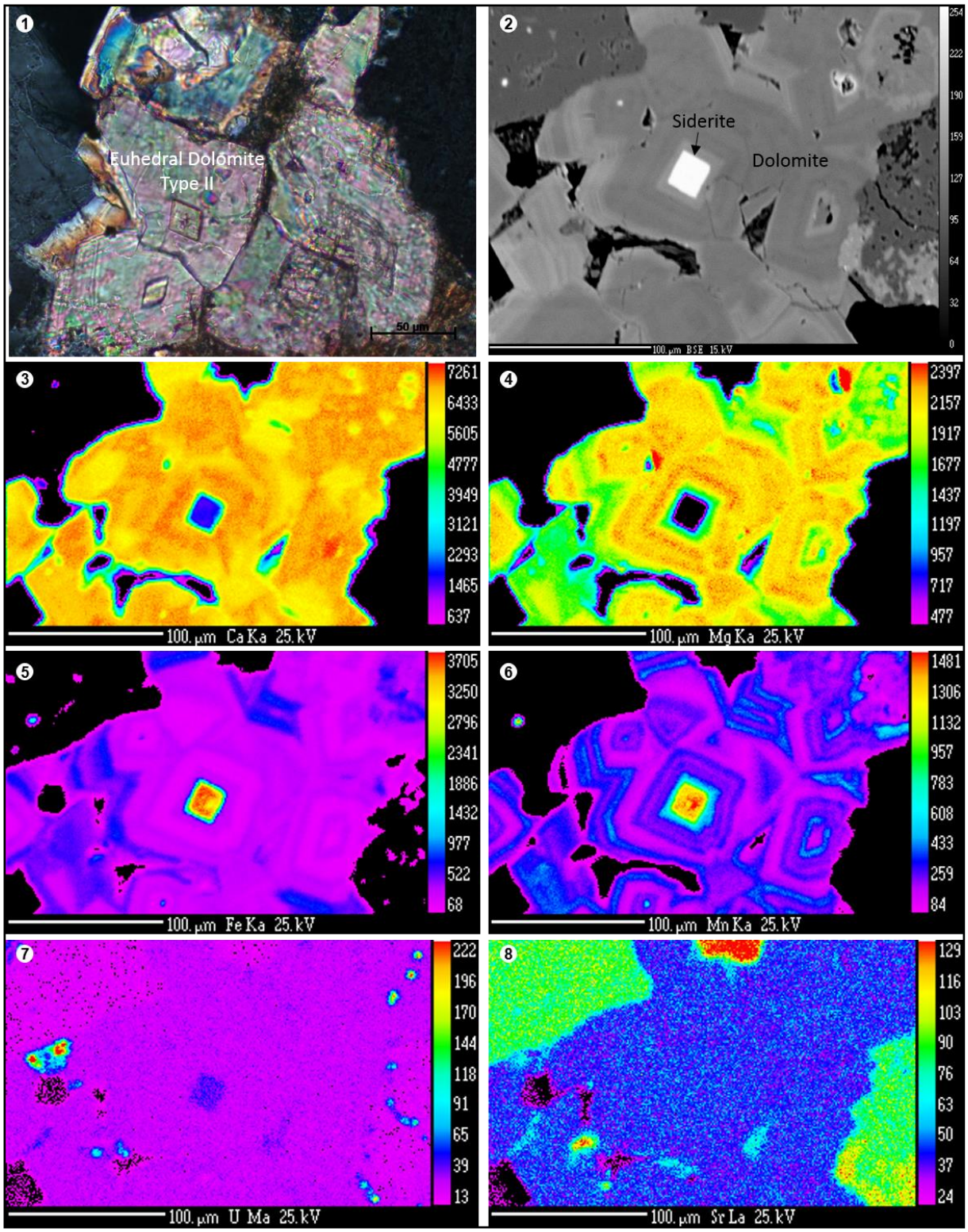

Figure 69 (EMPA 59CC-6): Chemical mapping (EMPA) of the euhedral (Type II) dolomite fabric. 1) LPA, 2) BSE, 3-8) EMPA counting Ca, Mg, Fe, Mn, U, Sr. It is noted that according to LA-ICPMS data the U content can reach 0.3 wt%.

Figure 70 to Figure 72 demonstrate how uranium mineralization is linked to euhedral (Type II dolomite). Uranium precipitates after the formation as well as the overgrowth of the euhedral (Type II) dolomite by filling the available intergranular porosity (a closer look at the chemistry of those elements is available in Figure 70 and Figure 71).

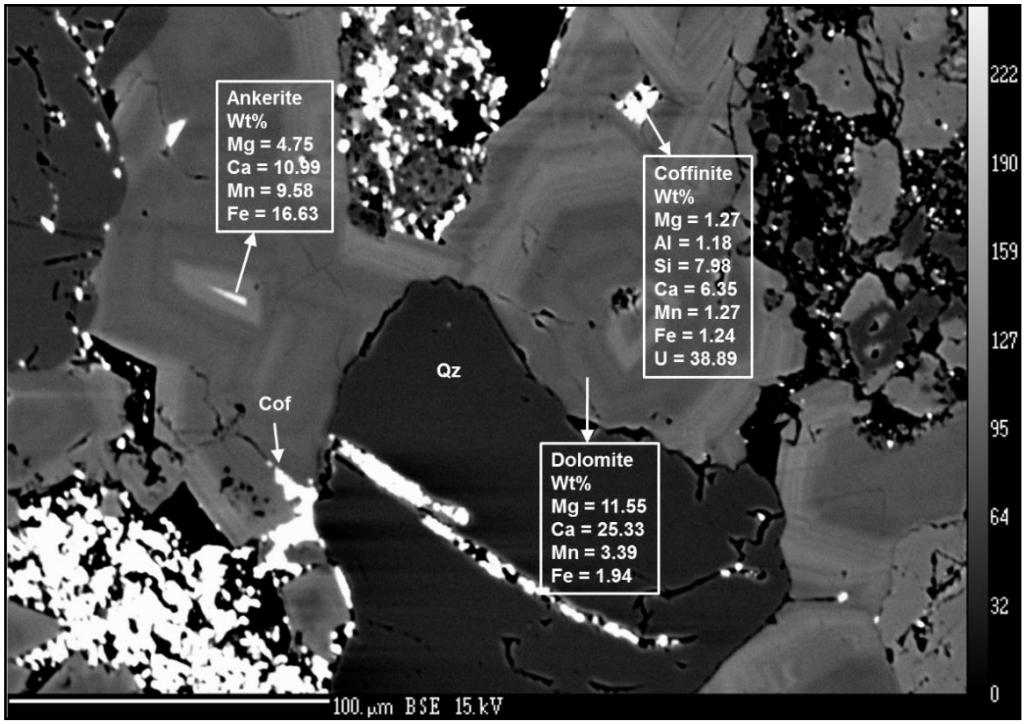

Figure 70 (EMPA 59CC-6): The siderite cores in poecilitic dolomite and the U precipitation in the secondary porosity.

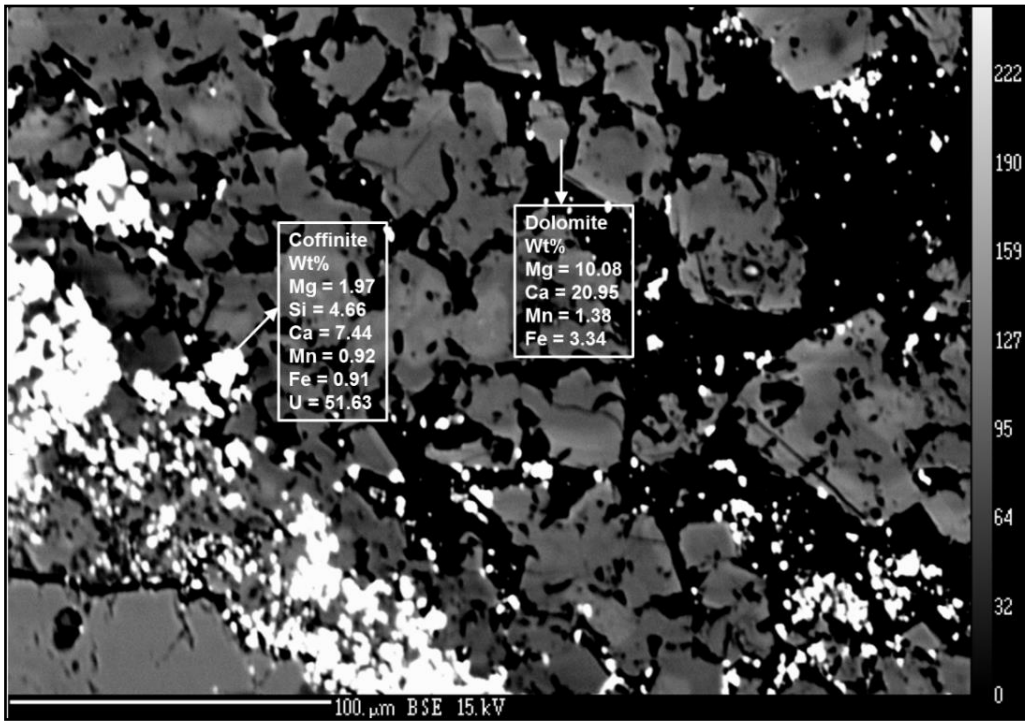

Figure 71 (EMPA 59CC-6): Idiomorphic crystal growth (partial dissolution?) of type II dolomite (poecilitic texture) and coffinite precipitation

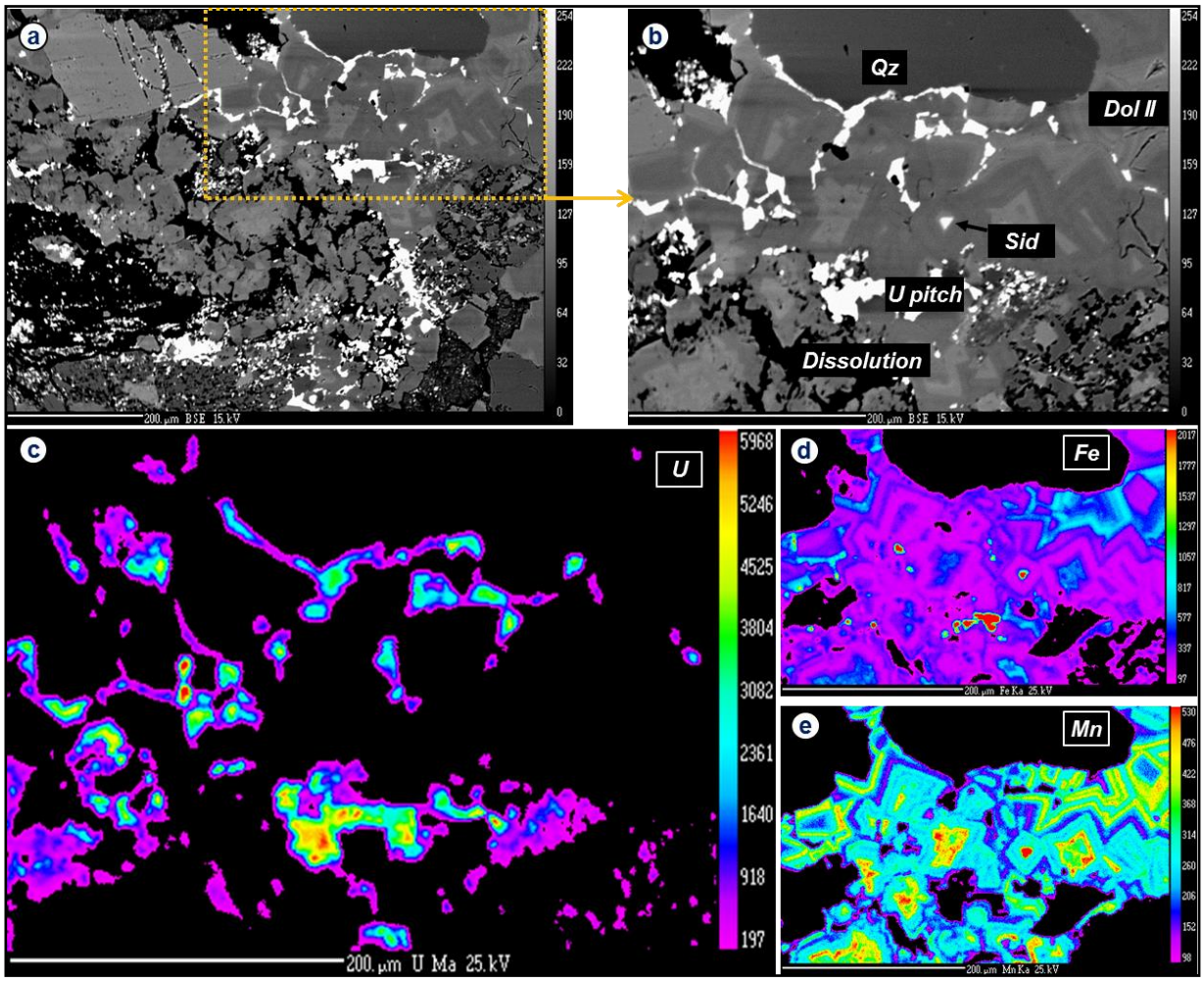

Figure 72 (EMPA 59CC-6): Pitchblende precipitation is post-diagenetic to dolomite Type II.

Furthermore, it was observed that prior to uranium precipitation in a Type II dolomite cemented sandstone, there is partial dissolution of the respective dolomite phase. The uranium bearing fluids are posterior to Type II dolomite, since uranium was found in the intergranular porosity and the secondary porosity created by the dissolved poecilitic dolomite crystals (Figure 70 to Figure 72). It has not been yet demonstrated exactly under which Eh-pH conditions the poecilitic dolomite becomes unstable but it is very possible that the roll-front waters, which have different chemistry than the aquifer that is in chemical equilibrium with the euhedral dolomite, are reacting with this dolomite type and eventually cause its partial dissolution and secondary porosity to be created.

An XRF chemical map of a poecilitic (type II) dolomite cemented sandstone with associated pyrite and organic matter phases is given in Figure 73. Apparently the pyrite comes after the dolomite cement and uranium is the latest phase.

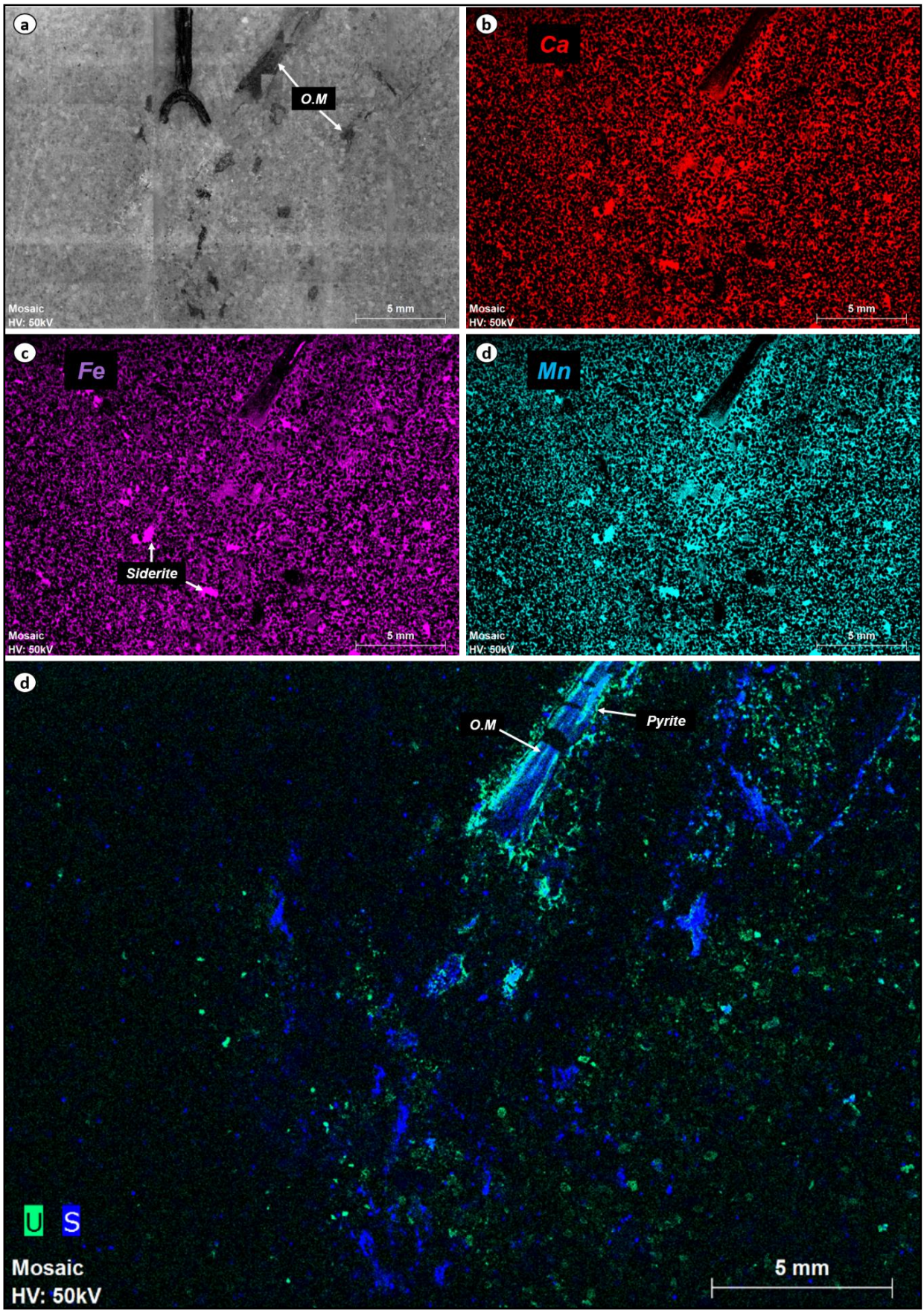

Figure 73 (XRF 59CC-6): XRF chemical mapping cemented sandstone with associated pyrite and organic matter phases. Apparently the pyrite comes after the dolomite cement and uranium is the latest phase.

Later-on after the euhedral (type II) dolomite is dissolved by the roll-front waters, another carbonate phase that is contemporaneous or forming shortly after uranium precipitation, is crystallized. That carbonate phase is termed as subhedral (type III) dolomite. It is very characteristic by its irregular shapes that mimic the precursor fabrics (fabric preserving), by having at least one planar surface left, while the rest are compromised in the case when type II dolomite is the precursor fabric. On the other hand when the precursor is the microcrystalline texture then type III dolomite has larger dolomite crystals of irregular shapes compared to the microcrystalline dolomite. This fabric is also significantly leaner in terms of REEs, Fe and Mn contents. The corresponding chemical map for the subhedral (type III) dolomite can be found in Figure 74, where a recrystallized dolomite phase (type III) is encompassed by microcrystalline (type I) dolomite.

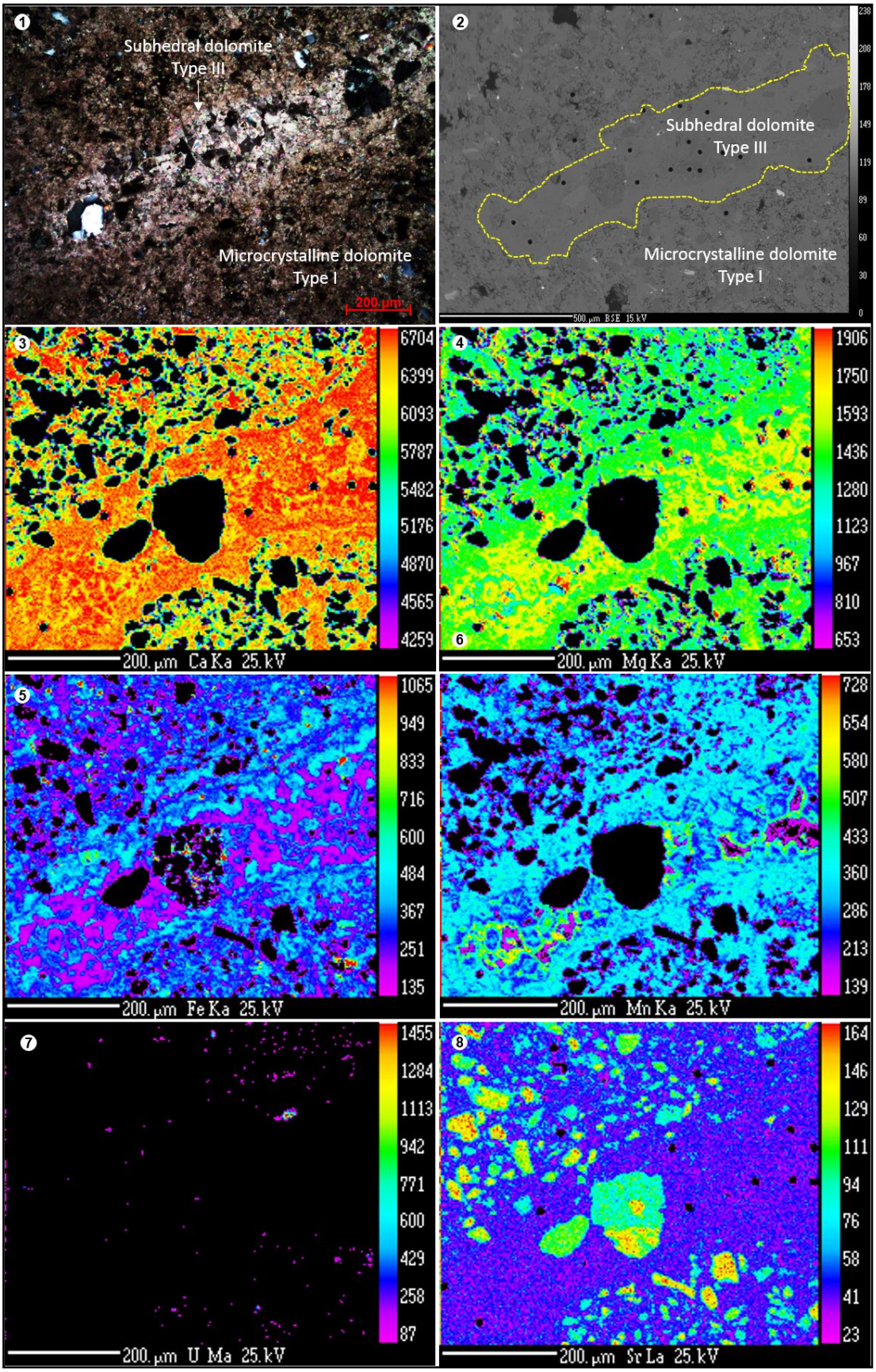

Figure 74 (EMPA 59BB-71): Chemical mapping of the subhedral (Type III) dolomite encompassed by the microcrystalline (Type I) dolomite, 1) LPA, 2) BSE, 3-8) EMPA counting Ca, Mg, Fe, Mn, U, Sr. The dark spots in the middle are quartz grains.

The subhedral (type III) dolomite was found to contain a well-developed pyrite framboid (Figure 75b), therefore there are two possibilities, it is either contemporaneous to dolomite crystal growth or it post-dates the pyrite framboid (the cut of the thin section happened to be located between the pyrite and its support i.e. a detrital grain or organic matter). On the other hand the subhedral dolomite post-dates a cluster of framboidal pyrite with euhedral overgrowth containing uranium (U-Si-P phase) (Figure 75b).

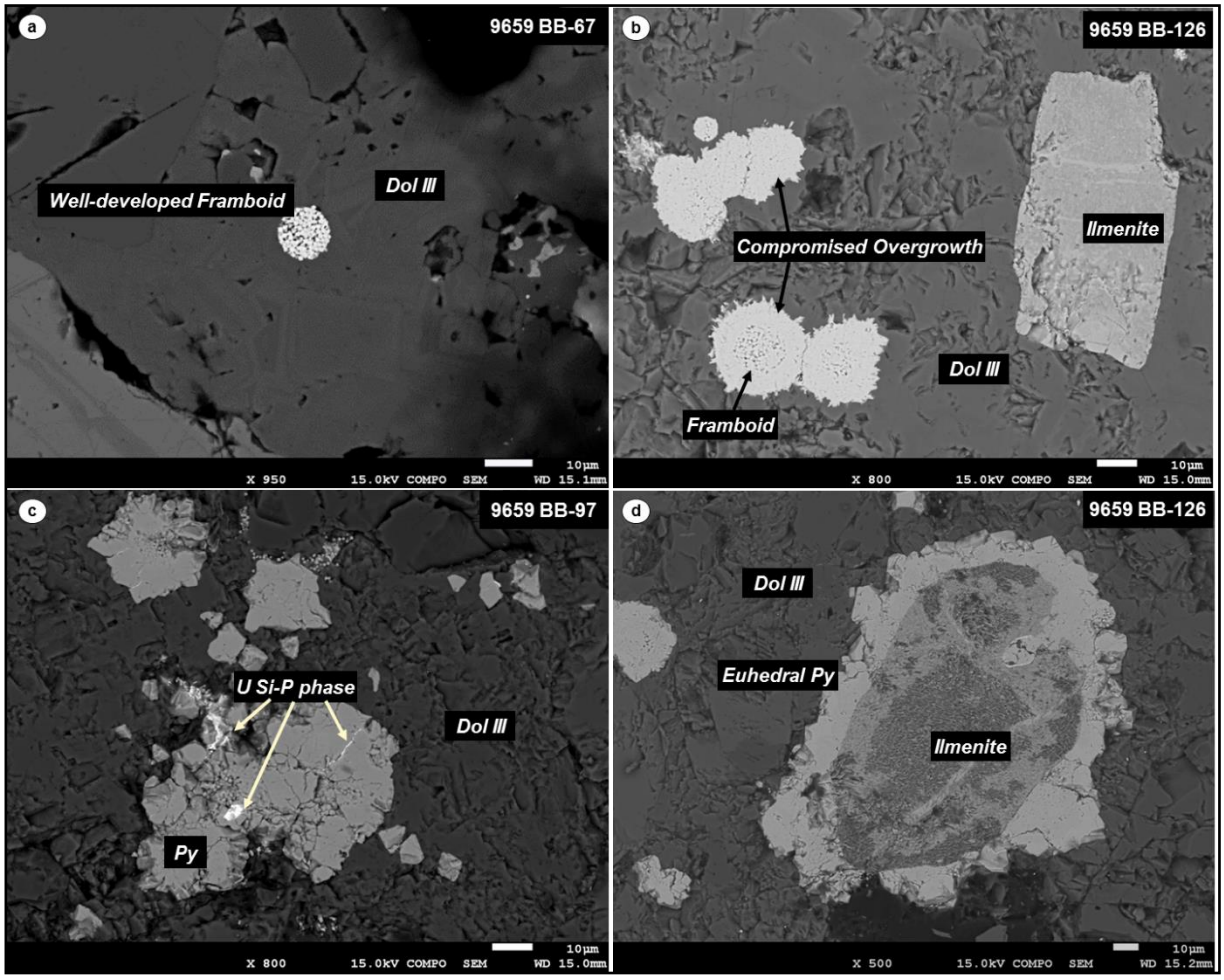

Figure 75 (SEM-EDS): (a) Framboidal pyrite contained inside type III dolomite showing no compromised boundaries; (b) framboidal pyrite (overgrowth) boundaries compromised by type III dolomite; (c) euhedral pyrite carrying U is postdated by dolomite type III (subhedral). As a result the dolomite type III is probably forming contemporaneously to U precipitation from the modified euhedral (type II) dolomite; (d) euhedral pyrite compromised by type III dolomite.

As already stressed, the type III dolomite is formed when the type II dolomite encounters the roll-front waters. It is not clear, whether to place the type III dolomite as a contemporaneous phase or as a phase that follows uranium deposition and that is because until today there are no examples of uranium minerals being contained inside the subhedral dolomite cement, but only when they are accompanied by pyrite. The latest diagenetic dolomite phase is the anhedral (type IV). The corresponding chemical map is found in (Figure 76). There are hardly any zonations left, the fabric seems to fill-in all the available porosity, even the secondary that

is formed by the partial dissolution of feldspars. It does not contain any uranium and it is totally depleted in terms of trace elements (Fe, Mn) and REE.

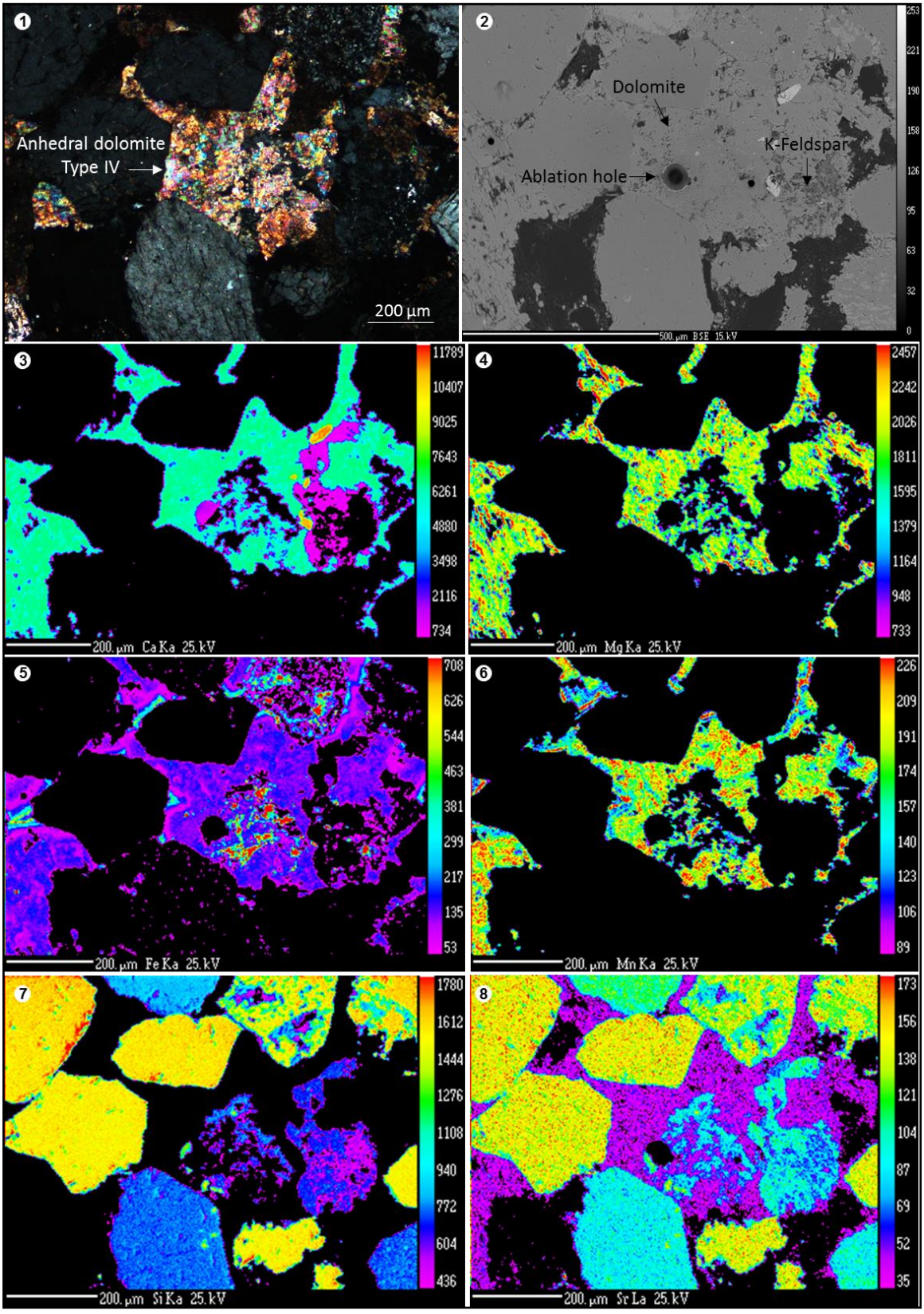

Figure 76 (EMPA 59AA-147): Chemical mapping of the anhedral (Type IV) dolomite. 1) LPA, 2) BSE, 3-8) EMPA counting Ca, Mg, Fe, Mn, Si, Sr.

There are evidences of a quartz cement phase filling the secondary porosity created inside a partially dissolved former Fe-Ti oxide (now Ti oxide), after U deposition and the overall cluster being cemented by the anhedral (type IV) dolomite (Figure 77). The anhedral fabric postdates every other phase i.e. pyrite under every form, uranium and quartz cement. The only phase which is formed after the anhedral dolomite is a new framboidal pyrite phase.

Photo-micrographs

Figure 77: Time relationships of the anhedral (type IV) dolomite with other minerals.

(a) The anatase (TiO_2) is probably a recrystallized Fe, Ti oxide, where the Fe replacement resulted in the formation of secondary porosity that was filled by quartz cement. The whole mineral assemblage is encompassed by dolomite type IV which is therefore later diagenetic;

(b) A close-up of figure (a) showing that Uranium precipitated at the available porosity inside the anatase. The quartz cement filled the rest of the porosity and is thus later diagenetic than uranium;

(c) The well formed framboidal pyrite that shows no overgrowth is a new generation of pyrite that is associated to the crystallization of the dolomite type IV (anhedral) and not to early diagenesis;

(d) Dolomite type IV (anhedral) postdating pyrite cement and a Si-P Uranium phase.

At this point it should be mentioned that there seems to be an affinity between the lithologies and the redox status of the host-rock and the dolomite type that is cementing the rock. This is very important because if predictions on dolomite type are to be made, a correlation with the roll-front activity could occur. It was observed that type I and II dolomite are contained inside reduced carbonate cemented fine sand lithologies (Figure 78). Type III dolomite is hosted inside oxidized fine sandstone lithologies, whereas the roll-front waters seem to have the potential of partially dissolving and recrystallizing the precedent fabric, thus creating secondary porosity (Figure 79 and Figure 80). Finally, type IV (Figure 81) is contained inside oxidized coarse sandstone lithologies and is probably post-diagenetic with respect to uranium precipitation.

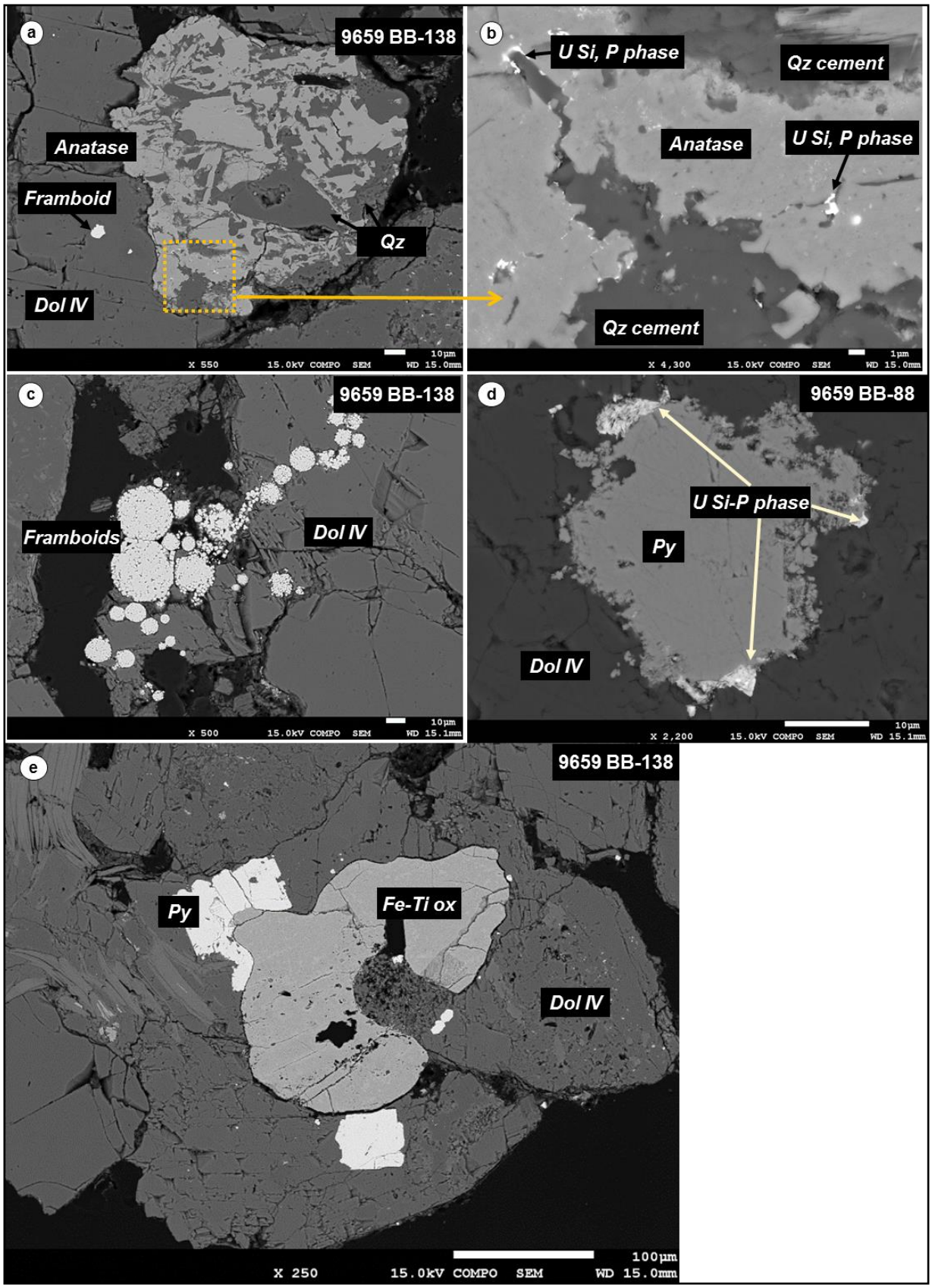

Figure 77 (SEM-EDS): Time relationships of the anhedral (Type IV) dolomite with other minerals.

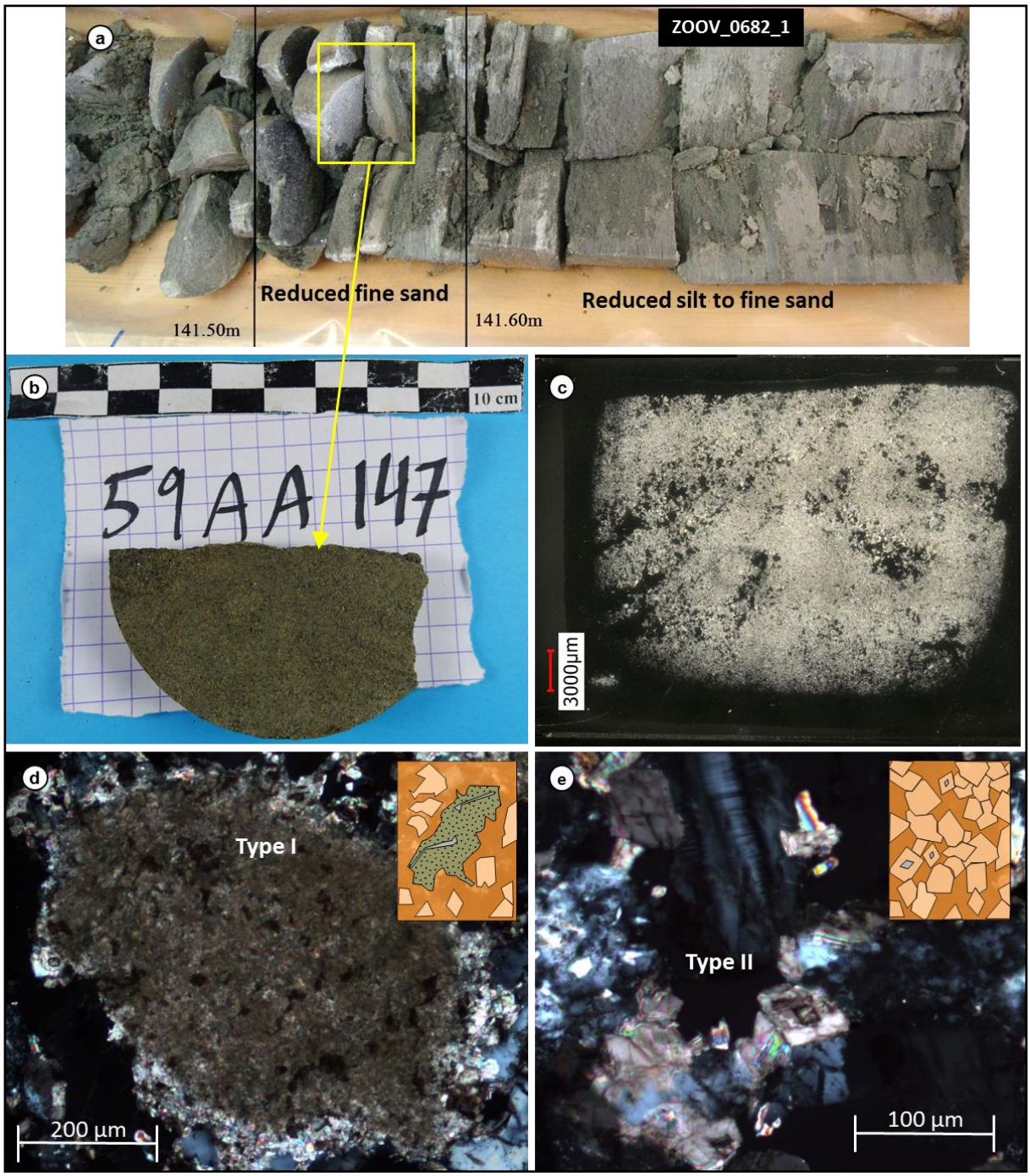

Figure 78: Dolomite cemented reduced fine sandstones that are not affected by the roll-front waters contain only the microcrystalline (Type I) and the euhedral (Type II) dolomite fabrics. (a) Core photograph, (b) sewed hand specimen, (c) thin section under LPA, (d) the microcrystalline dolomite under LPA, (e) the euhedral dolomite under LPA

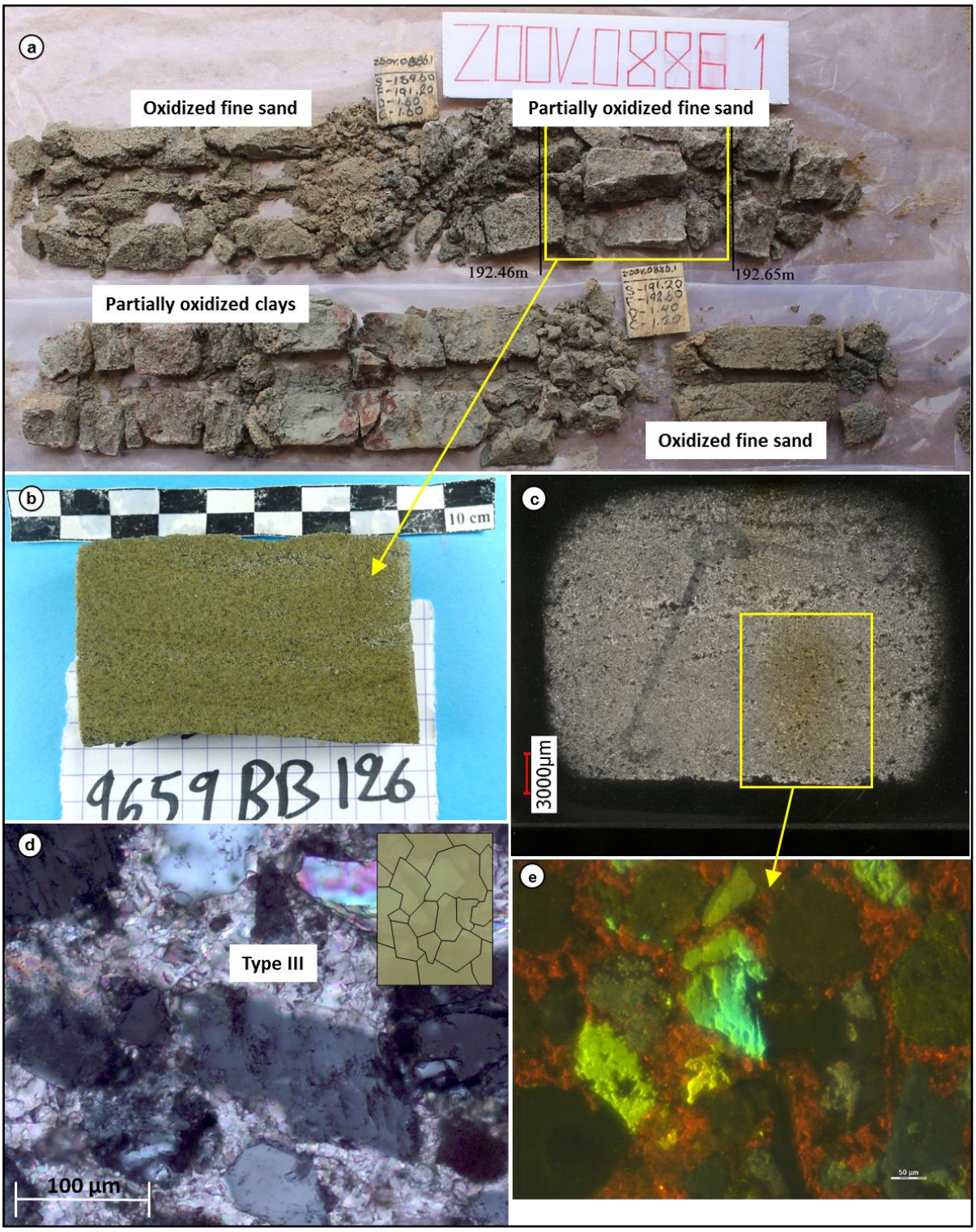

Figure 79: Dolomite cemented partially oxidized sandstones that are affected by the roll-front waters contain subhedral (Type III) dolomite. (a) Core photograph, (b) sewed hand specimen, (c) thin section under LPA, (d) the subhedral dolomite under LPA, (e) the subhedral dolomite under CL

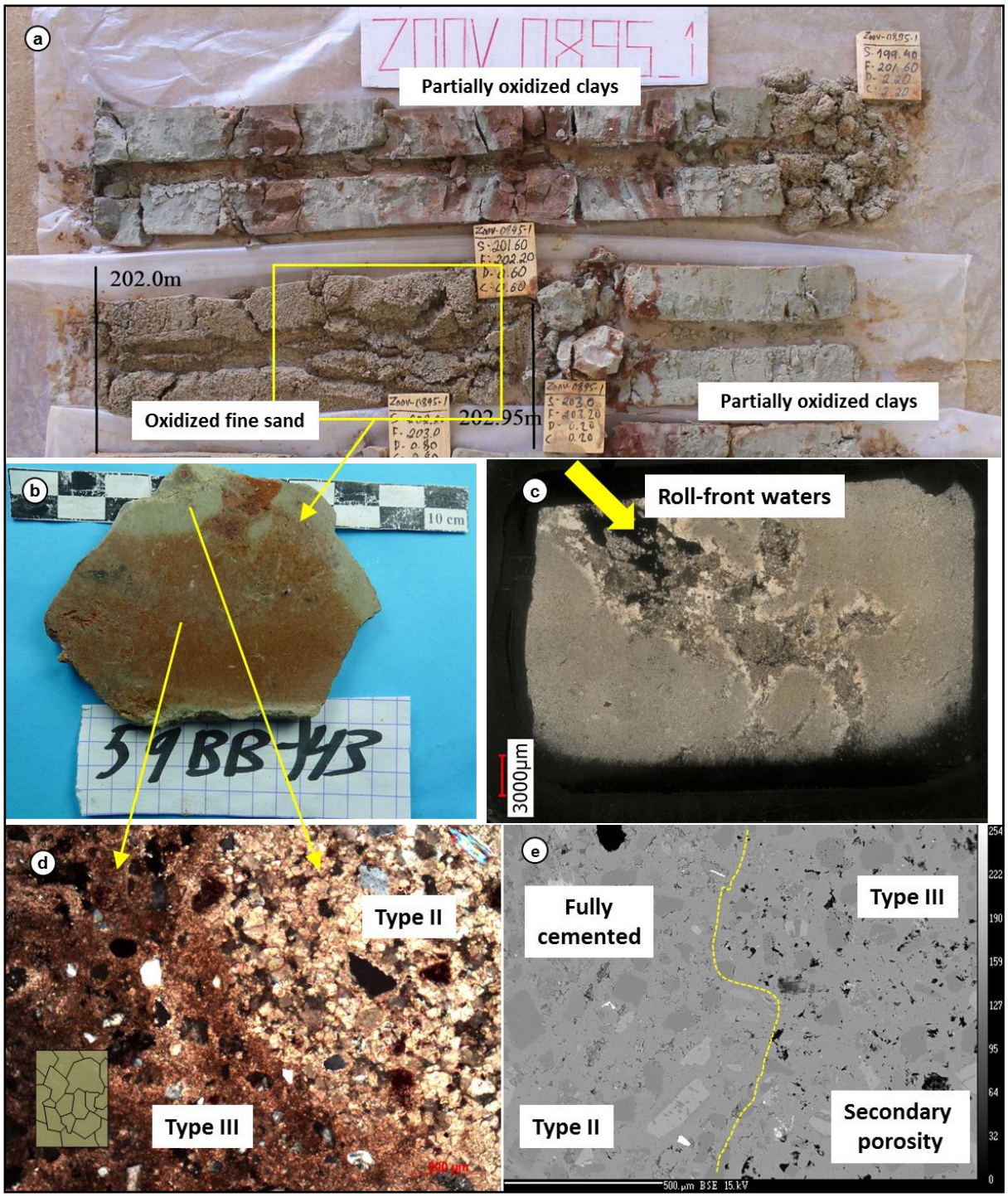

Figure 80: Dolomite cemented partially oxidized sandstones that are affected by the roll-front waters, again containing subhedral (Type III) dolomite. (a) Core photograph, (b) sewed hand specimen, (c) thin section under LPA showing the roll-front waters effect, (d) the subhedral dolomite and the euhedral dolomite under LPA, (e) the same picture as (d) showing that when the roll-front waters cause partial dissolution and recrystallization under BSE.

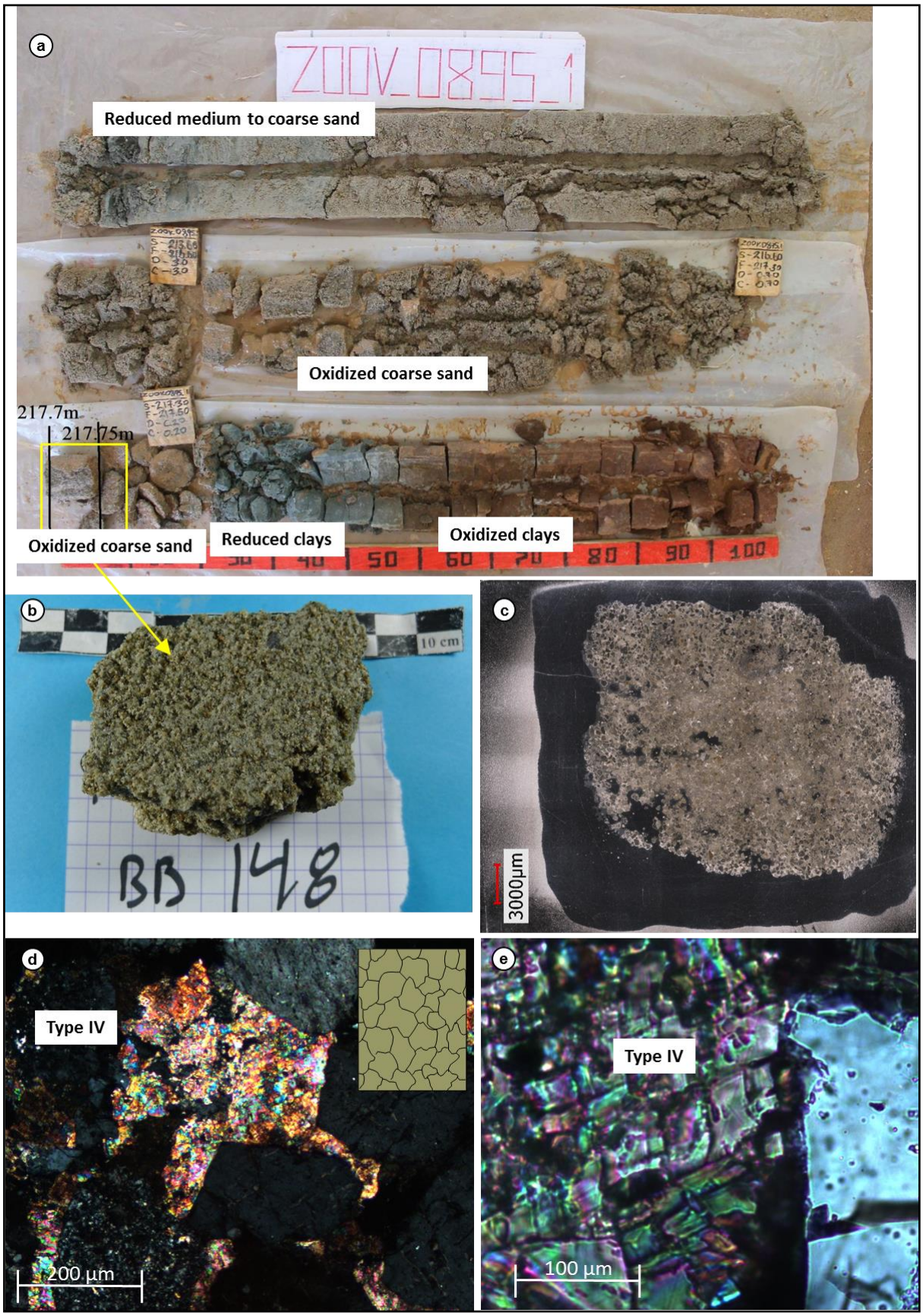

Figure 81: Dolomite cemented sandstones that are fully oxidized by the roll-front waters contain anhedral (Type IV) dolomite. (a) Core photograph, (b) sewed hand specimen, (c) thin section under LPA, (d, e) the anhedral dolomite under LPA showing irregular crystal boundaries and non-planar crystals.

3.5 SYNTHESIS OF THE CARBONATE PARAGENETIC SEQUENCE OF ZOOVCH OVOO AND CONCLUSION

Based on the sedimentology, the petrography and geochemistry of the carbonate cemented sandstone samples studied from the oxidized/leached, U-mineralized and reduced zones of the roll-front, the following conclusions were made:

- **Reduced area (pre-roll-front):** includes types I, II and IV.
- **Roll-front area:** includes types I, II, III and IV (all types).
- **Oxidized and leached area:** includes types III and IV; Types I and II recrystallized to type III.

With respect to the formation of the microcrystalline dolomite, two possible scenarios may be applied (Figure 82). Either primary deposition of dolocrete (Worden and Burley 2003; Cojan, 2010) or early calcite dolomitization due to mixing processes at the fresh-water/saline-water interface, with or without possible organogenic contribution (Humphrey, 2000) linked to the humic-fulvic acids associated to the coals present inside the Zoovch Ovoo sands (Brouand, 2015; this study) or even due to the hydrocarbons linked to the deeper petroliferous formations (Prost, 2004). There is clearly a low P-T diagenetic regime that excludes *a priori* deep burial conditions implying poor mechanical and chemical compaction. Certainly, there are multiple episodes of recrystallized dolomite with fluctuating Ca/Mg and Fe/Mn contents. According to Parize (2015) the depositional environment of the Zoovch Ovoo sands is fluvio-lacustrine with braided rivers, indicating high energy. In general there are very little evidences of biological activity and only in sample BB-71 a late carbonate crystallization phase is interpreted to be filling a former burrow (Figure 37a).

Since calcite was not encountered in Zoovch Ovoo, some calcite samples originating from the surface of East Hongor Tolgoy and Bayangshiree Plateau, were studied in terms of petrography and geochemistry. They should not be considered as the calcite analogue of the Zoovch Ovoo dolomite *sensu stricto* because they were sourced from the overlying formation (Bayangshiree Formation) and in addition it is already known that important regional hydrological differences can occur even inside the same aquifer (Grizard, 2017b). However, by comparing the two carbonate phases, it became clear that the aquifers from which the calcite and dolomite were sourced must have certain differences in chemistry. Yet both calcite and dolomites have precipitated from the same isotopic pool, namely meteoric water.

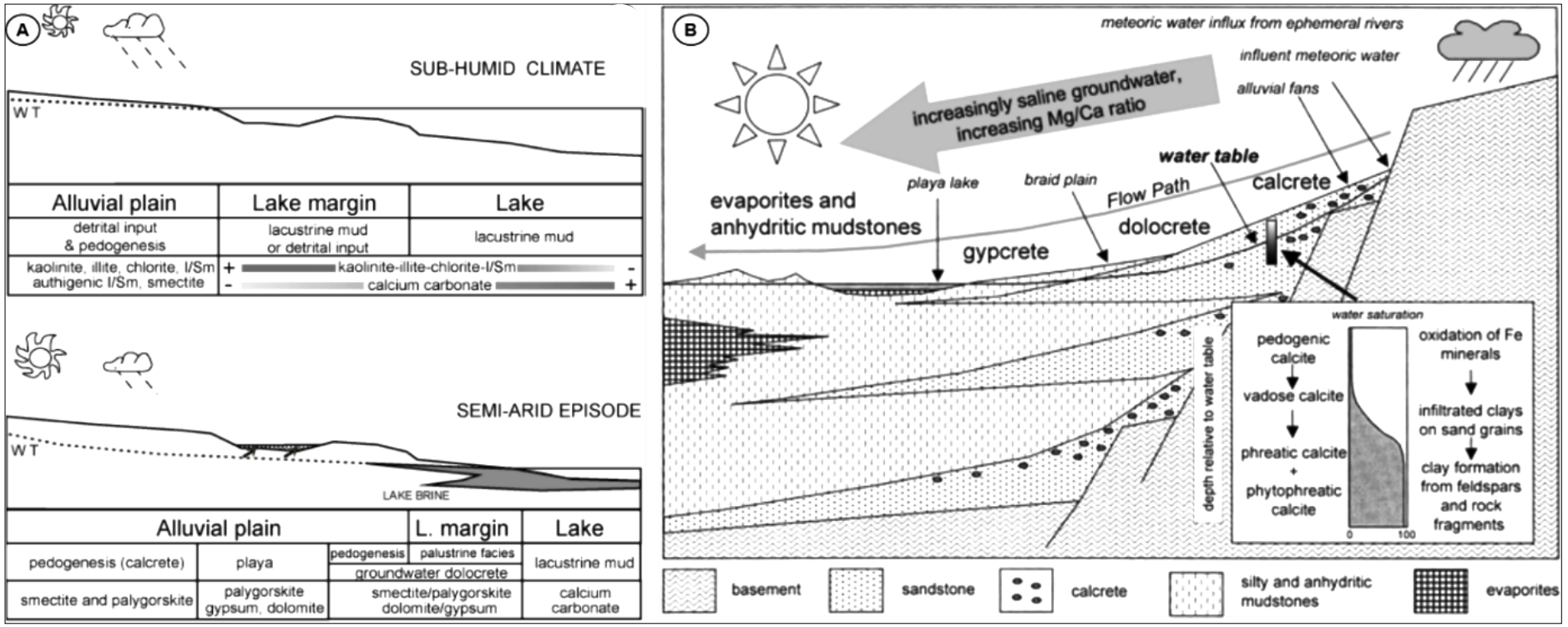

Figure 82: Two general models for primary dolomite deposition in continental settings: 1) the formation of ephemeral continental lakes (playa) during semi-arid episodes around lake mudflats, after Cojan (2010) and 2) the formation of dolocrete due to progressive Ca depletion of meteoric water, after Worden and Burley (2003).

In this framework the microcrystalline dolomite (type I) and euhedral (type II) appear very early in paragenesis, prior to uranium mineralization and they are hence controlled solely by diagenesis. In more detail, the microcrystalline fabric seems to be inherited (formed during deposition) and the euhedral is crystallized from the microcrystalline pool (early diagenesis). On the contrary the anhedral (type IV) is post-diagenetic to uranium mineralization and is always contained in very coarse to micro-conglomerate lithologies. Keeping in mind that the maximum burial depth of Sainshand was about 500 m and that today the reservoirs are located at about 200 m depth, type IV dolomite could be formed during the uplift, as dolomite saturation is re-achieved, after the influence of roll-front waters when the groundwater is re-equilibrated. In this concept, the fluid circulation is enhanced in the very coarse to microconglomerate lithologies that have not yet experienced dolomite cementation. It follows that the subhedral (type III) is possibly contemporaneous to uranium precipitation and stands for the modification of the crystal boundaries of dolomite types I and II, responding to the oxidized roll-front waters. The parts of the reservoir sands that already experienced the roll-front waters, are characterized by the instability of certain diagenetic mineral phases, such as pyrite and dolomite, leading to the creation of secondary porosity and formation of Fe-hydroxides (limonite and goethite). As such, the Fe-hydroxides could have three sources of Fe:

- The oxidation of pyrite.
- The oxidation of siderite that is often associated to the euhedral Type II dolomite.
- The Fe liberated from the dissolved dolomite cement.

The simple mechanism behind the formation of these hydroxides holds that during the oxidation of pyrite and siderite the Fe^{+2} (ferrous iron) is oxidized to Fe^{+3} (ferric iron) and forms as such the Fe-hydroxides, namely the goethite and limonite. To place the above into the paragenetic context a chart summarizing dolomite formation in Zoovch Ovoo is presented below (Figure 83).

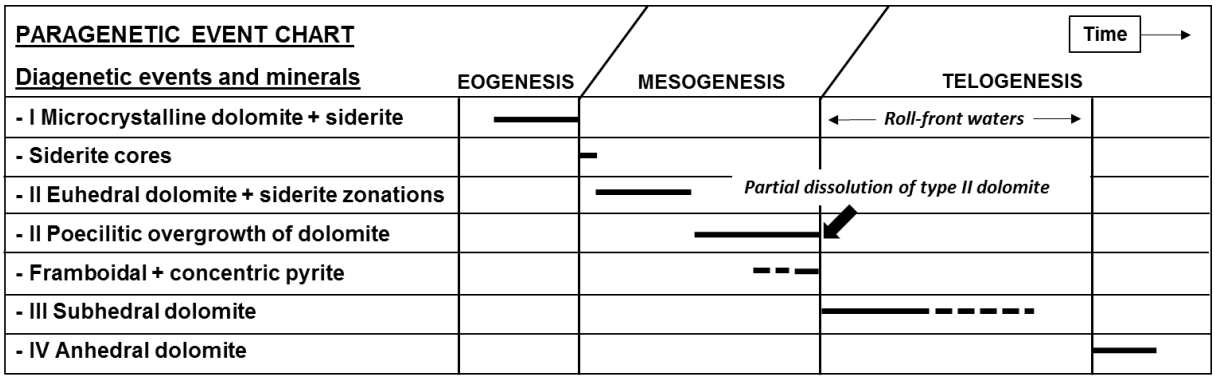

Figure 83: General paragenetic sequence for the carbonate phases identified inside the Sainshand Formation at the roll-front sands of Zoovch Ovoo.

3.5.1 Sedimentological model based on dolomite paragenesis

To place the different carbonate species into a genetic context a synthetic scheme based on the petrographic observations is proposed (Figure 84). As already stressed the earliest dolomite determined in the paragenesis sequence (dolomite I) occurs as detrital grains or as cement in sandstones layers of limited vertical (up to a few decimeters) and lateral extension (no possible correlation between wells). When it appears as cement, it occupies the intergranular porosity of the sand grains which are not in contact with each other indicating low compaction. This feature could hold the following genetic interpretations:

Kearsey et al. (2012) showed that primary microcrystalline dolomite may be formed during pedogenesis as a result of soil bacterial activity. An interplay between diagenesis and pedogenesis in an alluvial/lacustrine setting was presented by Pimentel (2001) to explain how the Mg/Ca ratio can increase progressively and ultimately lead to the dolomitization of pre-deposited pedogenic carbonates lead by two factors. First the concentration levels of Mg increase if there is no available dissolved Si in the system, which would inhibit the formation of Mg-clays (e.g. palygorskite) and secondly the precipitation of calcite results in lower Ca levels; hence the percolating waters become progressively saturated in respect to dolomite. In the model of Díaz-Hernández et al. (2013) the partial dissolution of biological-derived pedogenic calcite was responsible for the formation of dolomite below the petrocalcic soil horizon. The dolomite formation was in part favoured by the evapotranspiration processes of the soil and also by the presence of smectite that retained soil water, promoting Mg incorporation in the carbonate. In the Zoovch-Ovoo area, dolomite I as detrital elements would then be linked to further erosion of pedogenetic layers and transportation before final deposition as rip-up-clasts (Taylor and Machent, 2011) together with other detrital sediments.

Another possibility for the origin of dolomite I as clasts or as cements could be related to dolomite formation in surface evaporative systems. Indeed, Morrow (1982a) for instance proposes dolomite precipitation as a result of rapid chemical carbonate precipitation from a supersaturated (saline) solution shortly after deposition i.e. a few centimeters or meters of burial depth. According to Von der Borch and Jones (1976) and Morrow (1982b) microcrystalline patchy dolomite is often Ca enriched, extremely fine-grained (0.5 to 1µm), amorphous and forms spherular aggregates from direct precipitation in mixing zones of two fluids of different salinities. Such description is quite similar to the Zoovch Ovoo type I dolomite that forms 10 at% Ca enriched spherular aggregates, which according to sedimentological and isotopic data were deposited at a lacustrine-meteoric water interface.

Dolomite I may then be a witness of very early cement formation in the sedimentary systems. This implies early Mg enrichment of surface waters. Worden and Burley (2003) describe the

progressive increase of the Mg/Ca ratio during meteoric water run-off on the surface, leading first to the formation of calcrete and then towards the terminal playa lake to dolocrete. Kuang et al. (2002) made a link between Ca^{2+} enrichment relative to Mg^{2+} in clays and climatic conditions. In their model the degree of aridity has a direct effect on Ca concentration as it has higher transfer ability than Mg due to its larger ionic radius (Sun et al., 2015). Schmidt (1965) suggests that primary microcrystalline dolomite could be formed in similar environments but from an early replacement of aragonite mud before burial. Cojan (2010) and Casado et al. (2014) indicate that significant evaporation of a playa lake during semi-arid episodes causes the abruption of the main lake to smaller hypersaline ponds, where calcrete and dolocrete may be formed.

The intimate association of siderite and dolomite I suggests that they are co-genetic. The presence of siderite implies reducing conditions for Fe during early diagenesis. Such conditions may have been linked to bacterial activity (Coleman et al., 1993; Roh et al., 2003). The type II dolomite which follows dolomite I in the paragenetic sequence is as well associated to siderite indicating continued reducing conditions for iron in absence of reduced sulfur (i.e. bacterial sulfate reduction was not active). Alternating dolomite and siderite zonation in type II dolomite may then indicate fluctuating Eh conditions.

The type I dolomite cement presents the highest concentrations in Mn, while a decrease of several orders of magnitude is observed when considering the paragenetic succession, accompanied by a decrease in Sr to some extent. The REE's concentration follows a similar trend. The petrographic relationships as well as the decrease by some orders of magnitude in Mn and REE between dolomite types are expected for carbonate recrystallization. The same depletion pattern but for calcite cements deposited as well in fluvio-lacustrine settings is recorded in Blamey et al. (2014). The authors proved that late stage calcite that is sourced from a calcite precursor will be four times more depleted in REE and ten times more depleted in Mn during each cycle of dissolution and re-precipitation. Considering the trace elements content of the dolomites cements as well as literature, in the case of Zoovch Ovoo it may be suggested that successive dolomite cements formation underwent at least four cycles of crystallization which is imprinted on their trace element and REE compositions. Such mechanism implies at least partial recycling of the initial dolomite (type I) pool within cemented sandstone layers during progressive diagenesis. It may then be suggested that early sandstone cementation by dolomite could only occur within or nearby layers that recorded input of carbonate rip-up clasts during sedimentation. Localization of dolomite cemented sandstones within the Sainshand formation would then be at least partially controlled by depositional conditions and eventually explain their distribution in space as layers of limited extension. Framboidal pyrite appears in the system only after the end of the poecilitic overgrowth, marking

the onset of bacterial sulfate reduction (BSR) and eventually deeper burial. This may suggest that with on-going cementation, the bacterial community (i.e. mesophilic bacteria) switched from fermentation responsible for siderite formation, to sulfate reduction responsible for framboidal pyrite formation (Roh et al., 2003). In this case, during the overgrowth of type II dolomite (poecilitic texture), the diagenetic waters may have been reducing and have changed from sulfate poor (surface waters, siderite) to sulfate rich (brines, pyrite) with further burial. The poecilitic overgrowth type II dolomite is associated to framboidal pyrite concentric overgrowth which stands for a second pyrite generation, suggesting further burial and continuing reducing conditions. In several cases, partial dolomite dissolution features, post-dating type II cement were documented. This feature was only observed in part of the Sainshand formation were roll-fronts are localized. This is evidenced on a petrographic point of view by deposition of uranium minerals in the newly formed porosity. In sediments that are not leached by the roll-front waters, the type II dolomite does not show any dissolution features. All this information suggests the intrusion of a new water mass in disequilibrium with dolomite, transporting dissolved uranium (in oxidized state i.e. U^{VI}) and thus showing a higher oxidation state than the Sainshand aquifer. Such events may be indicative of intrusion of surface derived waters and may sign the beginning of uplift conditions. Furthermore, in the dolomite paragenetic succession, the dissolution is followed by subhedral type III dolomite formation, characterized by further depletion in Mn and in REE. This dolomite cement generation may be considered as indicative of restoration to dolomite equilibrium condition for waters (background of the hydrological system) after roll-front episodes. The dissolution features as well as type III dolomite are not observed outside of the roll-front area. The type IV (anhedral) cement post-dates all other dolomite cements and marks therefore the latest dolomitization event in the Zoovch Ovoo sub-basin. The type IV dolomite is present within and outside roll-front influenced sediments. It is always contained in medium to very coarse sandstones that have high porosity. Type IV dolomite may characterize equilibrium of diagenetic waters in regards to dolomite during the uplift until most recent times.

Hence, dolomite is used as a tool to mark the burial history of the Zuunbayan sub-basin in relation to the roll-front (Figure 85). By considering Prost (2004) and Graham et al. (2001) it can be estimated that the maximum burial depth for the Sainshand formation was 500-600 m. By taking into account basin modelling by Prost (2004) it may be deduced that the temperature of the formation did not exceed 30-35°C. According to Barker and Pawlewicz (1994), the mean random vitrinite reflectance of kerogen subjected to a maximum temperature of 62°C during burial could not exceed 0.40%. Vitrinite reflectance measurements in the Zoovch Ovoo sands led to %Rr=0.302±0.02. Thus, it may be concluded that the highest temperature experienced by the dolomite cements is estimated at about 40°C.

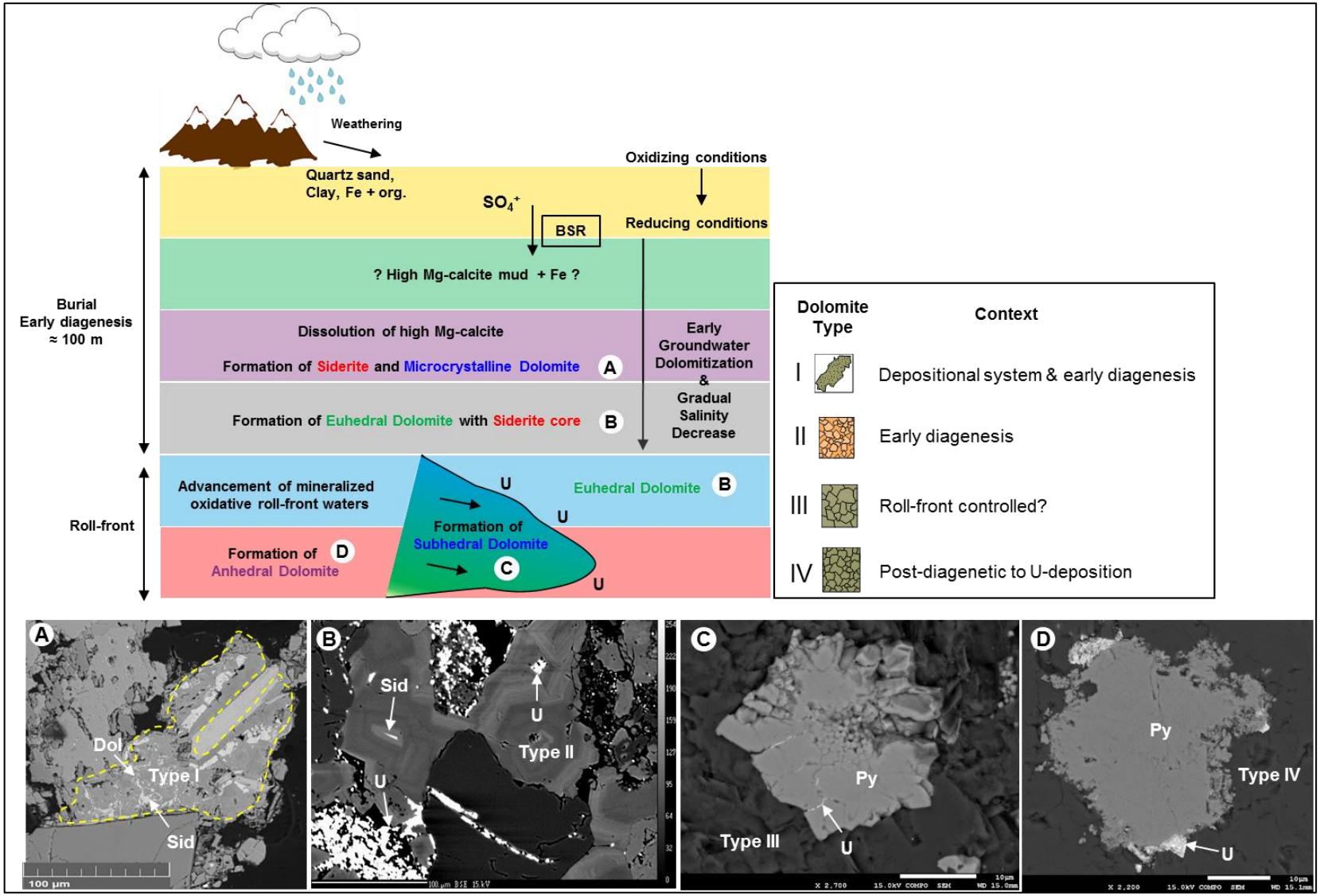

Figure 84: Possible model for dolomite formation in Zoovch Ovoo. When the iron oxide reacts with the O.M it is reduced to Fe^{2+}. When high Mg-calcite? becomes unstable due to higher solubility, siderite is formed instead (Hunken et al. 2010).

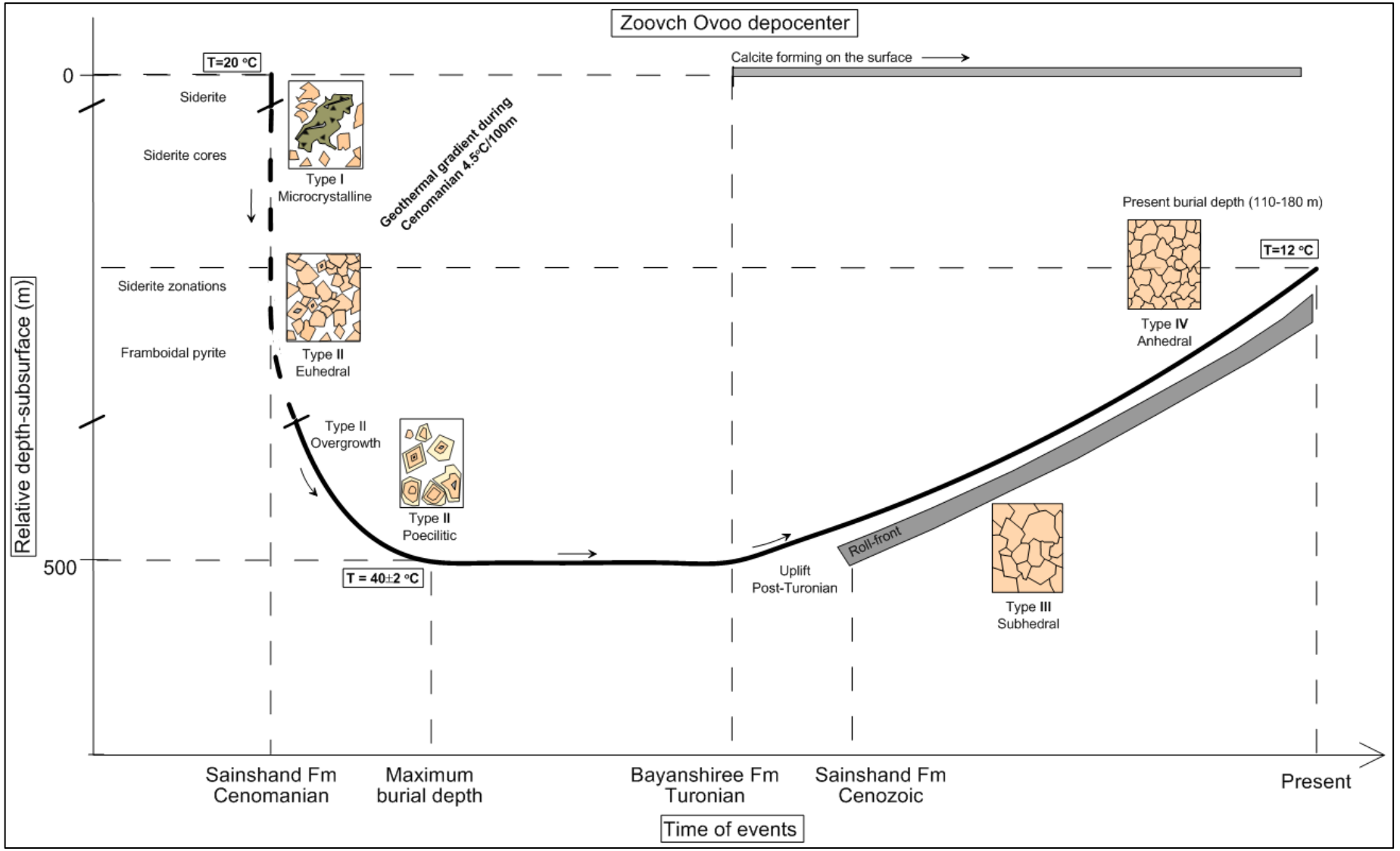

Figure 85: Proposed model for the dolomite cement evolution in Sainshand Formation in Zoovch Ovoo. Surface temperature and geothermal gradient according to Prost (2004). The black arrows indicate the burial pattern.

CHAPTER IV

Organic matter study

4.1 INTRODUCTION

The primary objective of the organic petrography analysis was the identification and determination of the microscopic components of the organic matter, termed macerals. Maceral analysis was thus pursued using an organic petrography microscope equipped with oil-immersion objectives on polished blocks under reflected light and fluorescence mode (blue-light excitation). Vitrinite reflectance measurements were also performed on the same blocks. Scanning electron microscopy equipped with energy dispersive spectroscopy (SEM-EDS) was used as a means to calculate the uranium content of each maceral type. The nomenclature of the organic petrography was based on the ICCP (International Committee for Coal and Organic Petrology) system 1994 - classification of coal organic components (ICCP, 1963, 1971, 1975, 1998, 2001; Sýkorová et al., 2005; Pickel et al., 2017). The maceral classification system used in the present study is presented in Table 5.

The organic matter is contained in the Zoovch sands as coal-clay intraclasts and fragments dispersed inside the mineral matrix or as thin laminas that follow sedimentary bedding. In both cases it can be studied by two methods: either by organic petrography, classifying the different organic components identified using the ICCP classification, or by thin sections, using the nomenclature applied to the palynofacies study as indicated below:

i. The Palynomorphs Group
ii. The Phytoclasts Group
iii. The Amorphous Group (kerogen types I, II, III)

The majority of the organic matter is in general highly altered due to oxidation and weathering, inherited by sedimentation or induced by the roll-front waters. This caused analytical problems, particularly in the vitrinite reflectance measurements. Despite having pursued the VR measurements numerous times and on different samples it was not possible to identify the appropriate maceral surfaces to correctly perform the analysis. Therefore, the presentation of the obtained vitrinite reflectance results will not be discussed. Instead there are other maturity parameters used such as the synthetic vitrinite reflectance calculated from the Tmax of Rock-Eval and basin-modelling data extracted from literature.

Vitrinite reflectance is necessary to adopt the nomenclature of huminite (%R<0.5) or vitrinite (%R>0.5) group macerals when referring to type III kerogens. Since the huminite/vitrinite group classification of macerals depends on the degree of maturity of the organic matter (Suárez-Ruiz et al., 2012), which in this study could not be determined, the nomenclature of the vitrinite group was used conventionally. It is noted that the oxidized character of the macerals would contribute to a suppression of reflectance measurements by at least 0.3%. Having these constraints brought forward the maceral types recognized may be discussed.

The Vitrinite Group macerals consist of degradation products of plant-derived organic substances (cellulose, lignin, proteins) mainly through biodegradation (Taylor et al., 1998). They have typical grey color and reflectance between that of Liptinite and Inertinite. With regards to chemistry they are rich in oxygen and poor in organic carbon compared to the other two maceral groups (van Krevelen, 1993; Stankiewicz et al., 1994; Taylor et al., 1998). Three groups are identified, telovitrinite, vitrodetrinite and gelovitrinite (Sýkorová et al. 2005). The macerals of this group recognized in the present study are:

i. Tellinite and Colloteline (cell-walls).
ii. Corpogelinite (completely filled circular or oval cells).

The Liptinite Group macerals are products of coalification of plant materials, rich in hydrogen, such as spores, pollen, natural resins, leaf cuticles, waxy, fatty or oily organic compounds as well as from bacterial disintegration products of proteins, cellulose and other carbohydrates (ICCP, 1971; Taylor et al., 1998). The typical characteristic of the Liptinite macerals is the very low reflectance and very intense fluorescence colors under blue light excitation. Their optical properties are attributed to their chemical structure, which is composed of aromatic and aliphatic compounds (Diessel, 1992; Stankiewitz et al., 1996; Taylor et al., 1998). The macerals of this group recognized in this study are:

i. Cutinite in few cases (outer coating of leaves, needles or roots).
ii. Resinite (resin, wax, oil, and fat within plant cellular tissues.
iii. Exudatinite (bitumen).

The Inertinite Group macerals derive from the same materials that form those from the Vitrinite Group with the difference that they have undergone a period of intense dehydration and fluctuated oxidation that includes the case of partial combustion (weak oxidation-fusinitization) of the stacked plant debris during periods when it is exposed on the surface above the water-table (Diessel, 1992; Taylor et al., 1998). The typical characteristic of the maceral of that group is the high reflectance as well as the very high oxygen and carbon content compared to the other two maceral groups (ICCP, 2001). The macerals of this group recognized in this study are:

(i) Fusinite (inherited charred material from forest fires).

(ii) Semifusinite (partially combusted).

(iii) Funginite (fungal origin).

iv) Macrinite in few cases (humic material that has been primarily gelified).

Table 5: Maceral classification and kerogen types according to the STOPES-Heerlen system (ICCP, 1993).

Maceral GROUP	Maceral SUB-GROUP	MACERAL	Maceral TYPE	Morphology Description
HUMINITE (<0.5% reflectance) **Kerogen type III**	**Telohuminite**	**Textinite**	A (dark) & B (light)	Cell walls
		Ulminite	Texto-ulminite	Partially fused cell tissue
			Eu-ulminite	Fully fused cell tissue
	Detrohuminite	**Attrinite**		Fragmental cell walls
		Densinite		Attrinite cemented by colloidal humic material – sutures visible
	Gelohuminite	**Gelinite**	Porigelinite	Humic colloids, without specific shape and with pores
			Levigelinite	
		Corpohuminite		Completely filled circular or oval cells
VITRINITE (>0.5% reflectance) **Kerogen type III**	**Telovitrinite**	**Telinite**		Fully or partially fused cell walls
		Collotelinite		Fused, homogenous cell walls without defined cell structure
	Detrovitrinite	**Vitrodetrinite**	Phlobaphinite, Levigelinite or Porigelenite	Disconnected fragments of vitrinite
		Collodetrinite		Fused fragments of vitrinite with no longer discrete boundaries
	Gelovitrinite	**Corpogelinite**		Discrete homogenous vitrinitic bodies representing the infilling of cell lumens
		Gelinite		Maceral of secondary origin. Can occur as cell infilling or as discrete veins
LIPTINITE **Kerogen type I, II**		**Sporinite**		Spore and pollen coats
		Cutinite		Outer coating of leaves, needles, roots
		Resinite		Resins, waxes, oils and fats within plant cellular tissues
		Suberinite		Suberin impregnated cell walls
		Alginite	Telalginite, Lamalginite	Marine and non-marine algae
		Bituminite		Occurs as layers or lenses in marine rocks (cyanobacteria) or sapropelic coals (red-green algae)
		Chlorophyllinite		Turns red under UVL - destroyed fast
	Strictly a bitumen	**Exudatinite**		Veins of bitumen-like material
		Liptodetrinite		Degraded liptinite - structureless
INERTINITE **Kerogen type IV**	Macerals with plant cell structures	**Fusinite**		Charred material from forest fires
		Semifusinite		Partially charred fusinite
		Funginite		Fungal origin (sclerotinite)
	Macerals lacking plant cell structures	**Secretinite**		Fusinized resin-related entities
		Macrinite		Humic material primary gelified
		Micrinite		Microscopic specs within other macerals
	Fragments	**Inertodetrinite**		Small fragments - physical degradation

Plant debris rich in cellulose can be transformed directly to Vitrinite. In low rank (low maturity) coals it is possible to still identify recognizable woody tissue. Within Vitrinite particles it is possible to distinguish two diagenetic processes.

- Biochemical gelification that occurs during the peat and soft brown-coal stages. This process is applicable to the Zoovch Ovoo case.
- Geochemical gelification that affects all the Vitrinite particles in the hard brown coal coalification stage. Due to the high degree of oxidation of vitrinite it is not clear to identify if geochemical gelification has taken place.

The burial diagenesis and biochemical degradation of the organic matter produce gases, organic colloids and acids (Figure 86). Such organic fractions were observed in the case of Zoovch Ovoo. During coalification the organic compounds such as proteins, carbohydrates, lignin and lipids are decomposed down to humic substances. For example the decomposition of peat (immature organic matter), in particular of cellulose and proteins by fungi and bacteria (biochemical activity) results in the formation of humic substances in fluid form. In addition to the decomposition of carbohydrates and lipids, humic-acid molecules can be formed from metabolic products of microorganisms such as phenolic compounds (Borrego and Cook, 2017).

INITIAL MATERIAL	PROCESS	RESPONSE
Oxygen potential		
Aerobic	**aerobic to anaerobic**	**Anaerobic**
COMPOUND GROUPS		
Proteins	strong degradation	hydrolysis to monomers
Carbohydrates	some degradation}followed by repolymerisation	to humic acids to brown coal*
Lignin	degradation but preservation after repolymerization	to humic acids to brown coal*
Lipids cuticles and lipoid coatings, resins spores and pollens	virtually unaltered	report to peat and brown coal*
→		
Plant material	HUMIFICATION (BURIAL AND TIME)	PEAT*——>BROWN COAL* Dispersed organic matter
	Fluids produced	H_2O, H_2S, CO_2 CH_4

Figure 86: Biochemical coalification during vitrinite diagenesis (Borrego and Cook, 2017).

4.2 PHOTO-MICROGRAPHS OF MACERALS OF THE SAMPLES

The macerals identified in the Zoovch Ovoo sands are listed below and are discussed as in (ICCP, 1963, 1971, 1975, 1998, 2001; Sýkorová et al., 2005; Suárez-Ruiz et al., 2012; Pickel et al., 2017):

Photo-micrographs

Figure 87**:** Summary of the macerals identified in the Zoovch Ovoo sands. Polished block photomicrographs under oil-immersion (x50):

Samples: AA-34, AA-154, AA-57, AA-57, AA-133

A: Fusinite with framboidal pyrite.

B: Telovitrinite (telinite) with euhedral pyrite associated to semifusinite. Also Fe-Ti oxide.

C: Very oxidized particle of telovitrinite (collotelinite).

D: Fusinite and fusinite enriched in uranium. Also euhedral pyrite, showing significantly higher reflectance.

E: Fusinite without U-mineralization.

F: Framboidal pyrite at the rim of telovitrinite.

G: Funginite and fusinite with high uranium content.

H: Telovitrinite without U-mineralization.

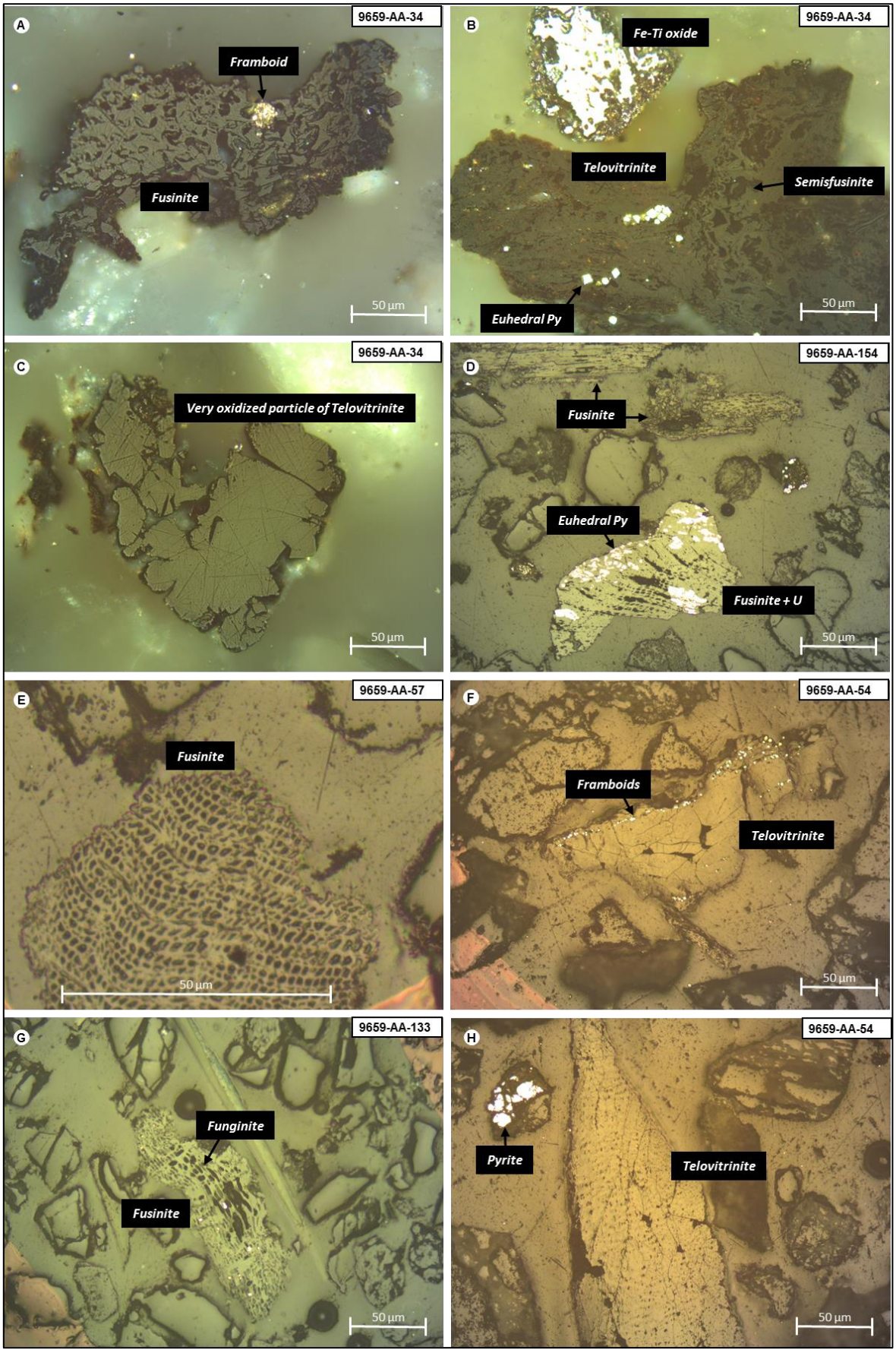

Figure 87: Summary of the macerals identified in the Zoovch Ovoo sands. Polished block photomicrographs under oil-immersion (x50) and reflected light.

4.3 RELATIONSHIP OF ORGANIC MATTER WITH PYRITE

This chapter aims to uncover the genetic mechanism that leads to organic matter epigenization by pyrite (pyritization). Ultimately, the susceptibility to pyrite epigenization for each maceral type contained in the Zoovch Ovoo sands is discussed.

It was observed that organic matter epigenization by pyrite is a function of three variables.

1. Redox status (reduced/oxidized), i.e. vitrinite or inertinite.
2. Textural properties (empty cell-walls, fused cell-walls).
3. Macro-porosity of the maceral (pore space visible under the microscope).

According to petrographic observations the epigenization starts by framboidal pyrite growing inside empty cell-lumens. The framboids continue to grow while their expansion is restricted by the geometry of the cell. If the maceral does not have any cells and is very homogenous (gelified) the pyrite growth, both for framboidal and euhedral, appears to be random although that the borders of the organic particle seem to be more susceptible to epigenization. It is noted that even in full organic matter epigenization the cell-walls (if present) will not be epigenetized, clearly indicating that pyritization is a maceral controlled process. Even pyrite cement will grow in accordance to the geometry of the cell.

Photo-micrographs

Figure 88: Epigenization of pyrite on organic matter in different occasions, presented in order of increasing epigenization.

Samples BB-9, AA-58, BB-134, AA-159 and AA-84.

A: Barren organic matter, inertinite-fusinite cell walls (BSE).

B: Few framboidal pyrite grains inside inertinite-fusinite cell lumens with associated elemental selenium and clays (BSE).

C: Framboidal pyrite associated to pitchblende at the rim and euhedral pyrite along a vitrinite (collotelinite) particle (BSE).

D: Pyrite cement growing inside collapsed cell walls with pitchblende inclusions formed during the euhedral pyrite stage also with pitchblende inclusions. These two pyrite types are actually one generation, but when the pyrite is growing inside cell walls the crystal growth is controlled by the shape of the cell lumen. Hence, instead of euhedral pyrite this time the form is anhedral/cement (BSE).

E: Partially replaced vitrinite particle (reflected light).

F: Fully replaced (reflected light).

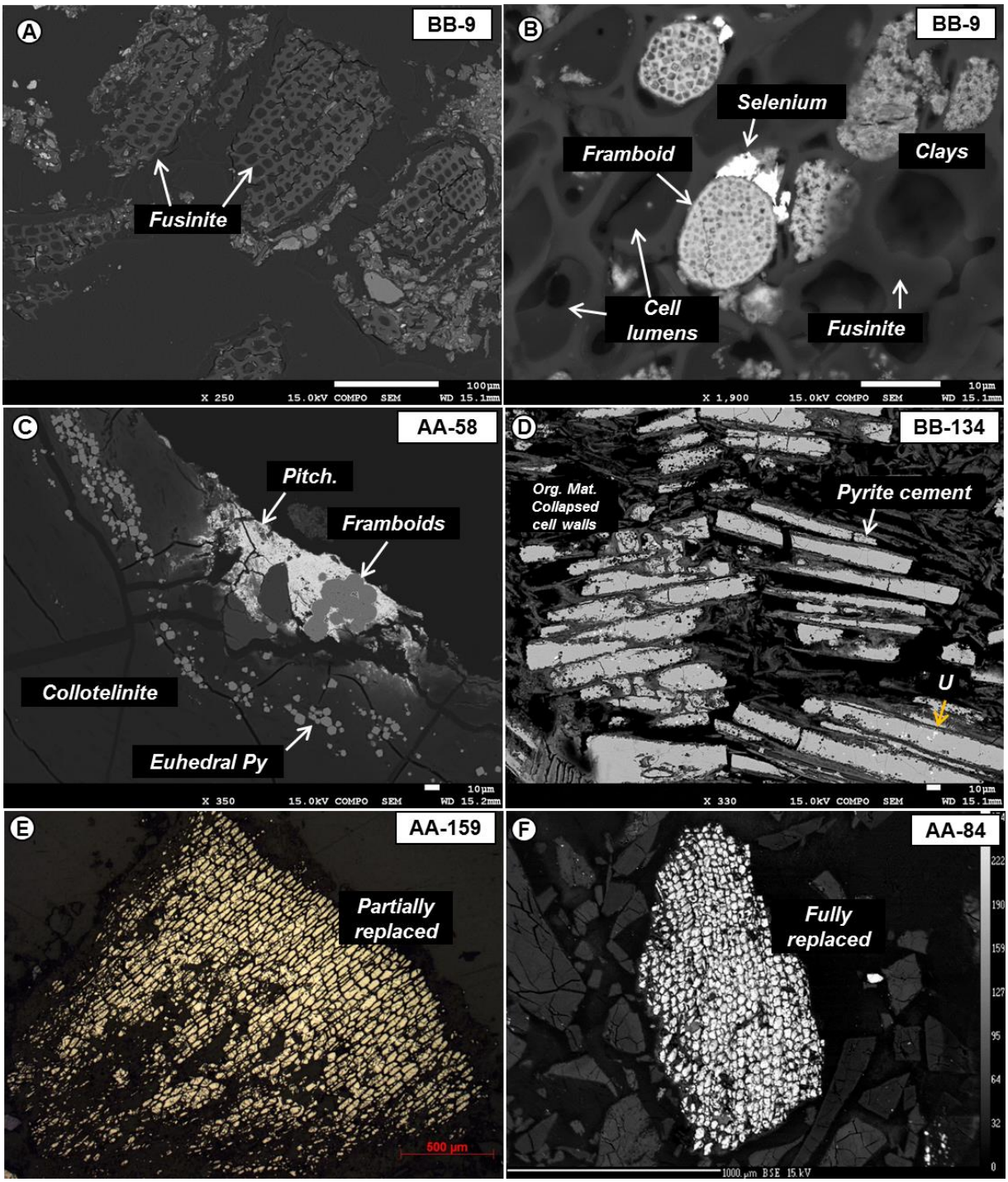

Figure 88: Epigenization of pyrite on organic matter in different occasions, presented in order of increasing epigenization.

4.4 ROCK-EVAL AND VITRINITE REFLECTANCE

All samples studied have very low hydrogen index (S2*100*/TOC), while they show a trend for the oxygen index (S3*100/TOC). The Rock-Eval results for 14 samples are listed in Table 6 and are plotted on Figure 89. As illustrated, an attempt was made to correlate this trend with their uranium content as expressed by radioactivity. However, uranium does not seem to be directly related to the oxygen index. Nevertheless, it is noted that the radioactivity measurements were performed at core scale and they are thus not representing the uranium concentration in the specific organic particles that were analyzed by Rock-Eval.

Table 6: Rock-Eval data for different samples. CPS (counts per second), indicating radioactivity. Background radioactivity 70 cps. The calculated vitrinite reflectance data are named VR.1 for Jarvie et al. (2001) and VR.2 for Jarvie et al. (2018). The negative vitrinite reflectance values (in italix) were not considered in the calculation of the mean value.

Sample	S1 mgHC/g.rock	S2 mgHC/g.rock	TOC(%)	Tmax(°C)	HI	OI	CPS	Calc. VR.1	Calc. VR.2
9704-08	0.01	0.22	1.56	420	14	163	914	**0.40**	**0.42**
9704-9	0	0.07	0.34	428	21	65	132	**0.54**	**0.55**
9704-11	0	0.11	0.67	430	16	57	70	**0.58**	**0.58**
9704-17	0.01	0.17	1.08	418	16	152	90	**0.36**	**0.38**
9704-40	0.01	0.44	2.54	423	17	109	97	**0.45**	**0.47**
9704-47	0.01	0.4	1.53	431	26	121	70	**0.60**	**0.60**
9704-150	0.01	1.34	8.01	340	17	163	76	*-1.04*	*-0.90*
9659A-72	0.03	0.6	3.07	377	20	122	70	*-0.37*	*-0.29*
9659A-116	0.07	0.48	7.29	240	7	220	105	*-2.84*	*-2.55*
9659A-34	0.05	0.3	2.18	410	14	101	70	**0.22**	**0.25**
9659A-62	0.08	0.57	2.41	417	24	134	70	**0.35**	**0.37**
9659A-84	0.06	0.73	17.57	358	4	172	70	*-0.72*	*-0.61*
9659A-151	0.02	0.1	0.38	415	26	97	70	**0.31**	**0.33**
9659A-154	0.04	0.17	3.25	303	5	171	70	*-1.71*	*-1.51*
						Mean	%VR	**0.42**	**0.44**

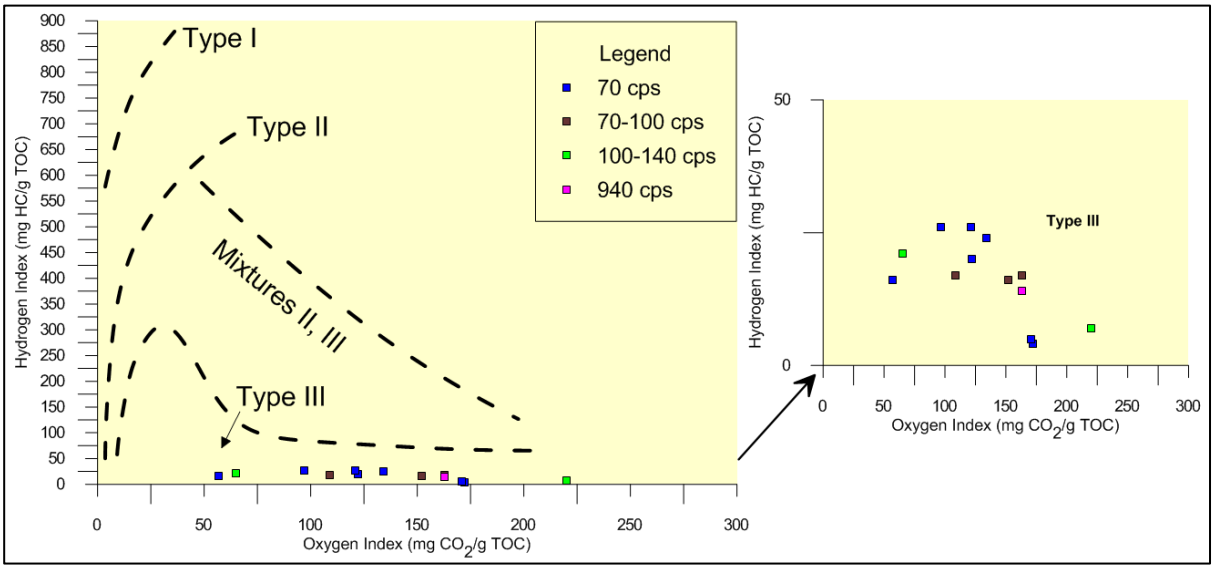

Figure 89: Cross-plot between HI and OI with the samples colored according to their radioactivity (cps-counts per second). All of the samples fall under the Type III (barren) organic matter. Zoomed version is provided on the right part.

Alteration processes that affect the organic matter associated to uranium deposits include weathering (surface), meteoric water influx (leaching by oxygenated waters), bacterial alteration and radiolysis (Landais et al., 1987; Forbes et al., 1988; Landais, 1996). As a result the organic matter shows abnormal values which do not reflect their origin or thermal maturity. In other words the samples display very low HI and progressively higher OI due to radiolysis and probably due to alteration/oxidation processes; Tmax *i.e.* 420-450ºC (Figure 90).

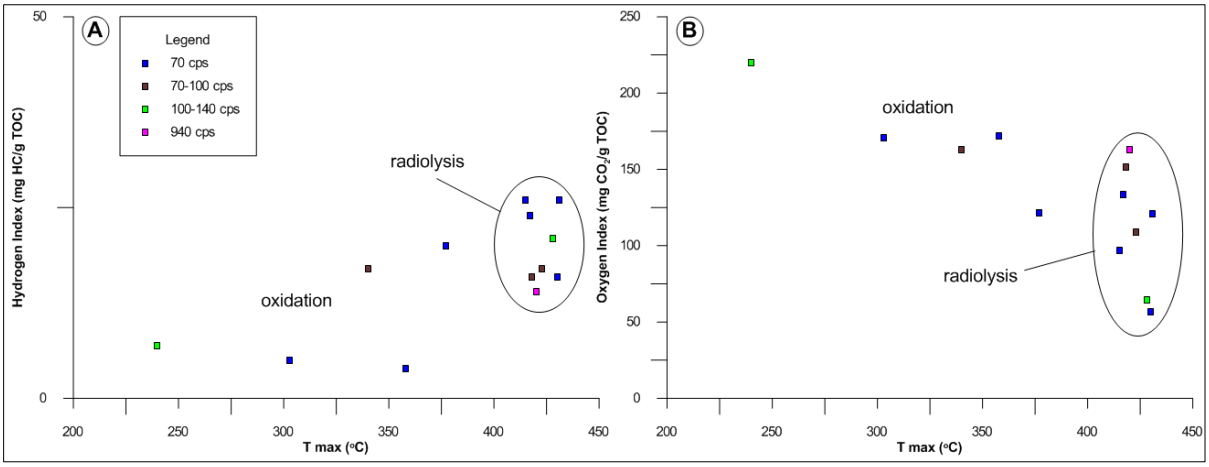

Figure 90: Tmax versus hydrogen index (**A**) and versus oxygen index (**B**) for coal particles associated with the Zoovch Ovoo uranium deposit. Color scale indicates radioactivity measurements of the whole rock.

Despite the abundant type III kerogen in the Zoovch Ovoo sands and the identification of vitrinite particles, it was not possible to correctly measure their reflectance, due to their high degree of oxidation/alteration/weathering (Figure 91), which had implications on the physico-chemical properties of vitrinite and as such the obtained results were not reliable. In general, sandstones contain altered organic matter due to their high porosity, high surface area and the easy access of high Eh waters that can oxidize the organic matter (Suárez-Ruiz et al., 2012). Therefore as stressed before, the nomenclature used for the classification of type III kerogen is conventionally based on the Vitrinite Group.

An attempt was made to calculate the synthetic vitrinite reflectance from Tmax using the formula provided by Jarvie et al. (2001; 2018) and discussed below (in both equations Tmax is expressed in ºC):

Equation 1 -> **Cal. %Ro from Tmax = (0.018 x Tmax) – 7.16**
Equation 2 -> **Cal. %Ro from Tmax = (0.0165 x Tmax) – 6.5143**

Overall, the Rock-Eval results indicate a rather oxidized type III kerogen. The oxidized state refers to altered organic matter, not related to the source or distal transport during sedimentation, but is very likely linked to the roll-front oxidizing waters. This would justify the values for most of the parameters measured by Rock-Eval analysis. Only a small part of the

Tmax appears to return vitrinite reflectance at the level of 0.6%, while most are below 0.5% (Table 6).

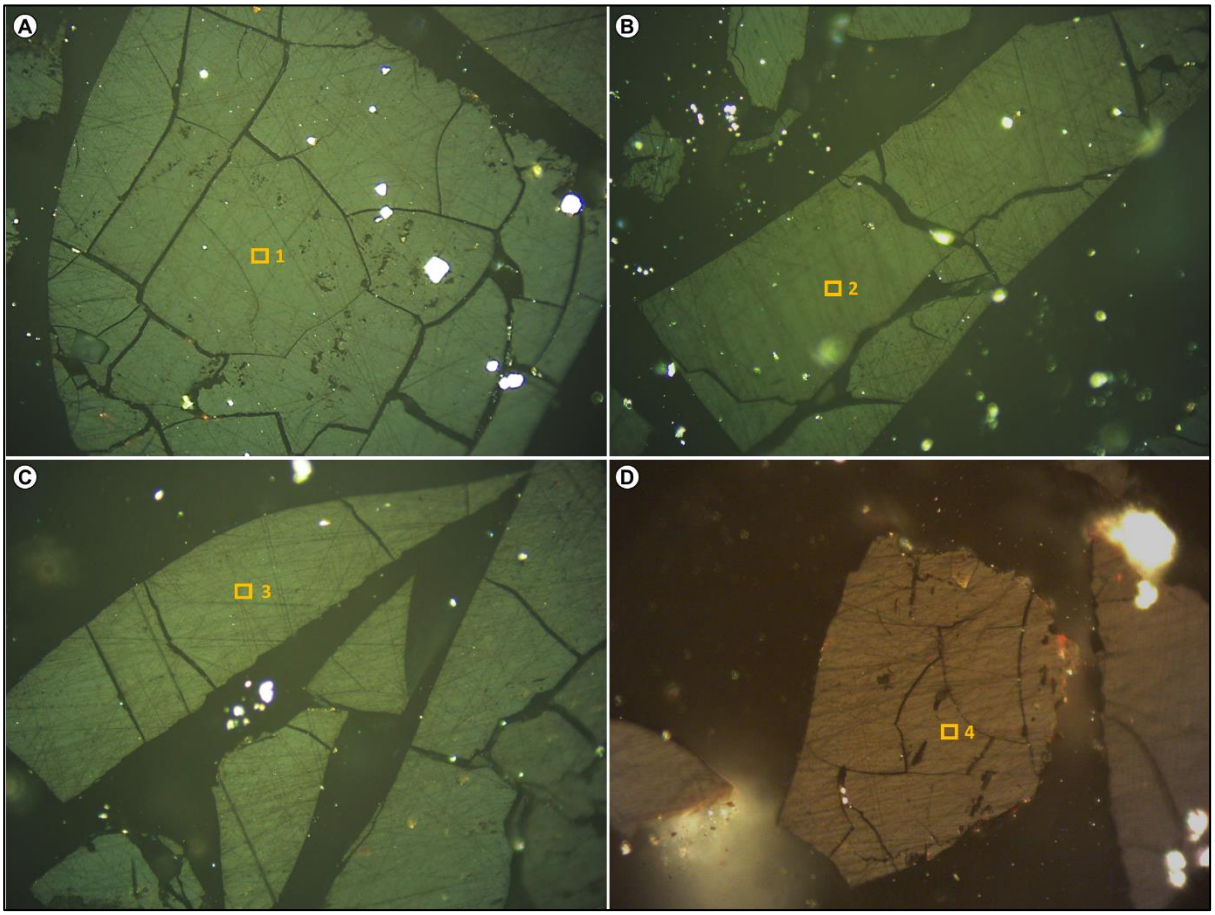

Figure 91: Examples of telovitrinite particles that are highly oxidized/altered/weathered and could thus not be used in the calculation of the vitrinite reflectance. The contrast in brightness is caused by the lamp intensity.

The very low HI<30 mgHC/gC_{org}, could have implications on the synthetic vitrinite reflectance calculation Jarvie et al. (2018). Keeping this constraint in mind, the calculated average vitrinite reflectance from both equations was estimated at 0.43±1%. Deviations higher than 0.05% are not acceptable in VR measurements, but given the very limited ways to discuss the maturity of the organic matter due to the presence of the roll-front system and the limited sampling that was followed, these results are the only way to talk about thermal maturity. Furthermore, data from basin modelling indicate a maximum burial temperature of about 40°C (Prost, 2004; Graham et al., 2001), since:

- Surface temperature in Late Cretaceous 20°C.
- Geothermal gradient, 4.5°C/100m.
- Maximum burial depth 400-500m.

According to Barker and Pawlewicz (1994), the mean random vitrinite reflectance of type III kerogen subjected to a maximum temperature of 62°C during burial could not exceed 0.40%. Thus, it may be concluded that the highest temperature experienced by the organic matter should be lower than 62°C. The high degree of alteration of the organic matter of Zoovch Ovoo would then be responsible for the VR values that exceed 0.4%.

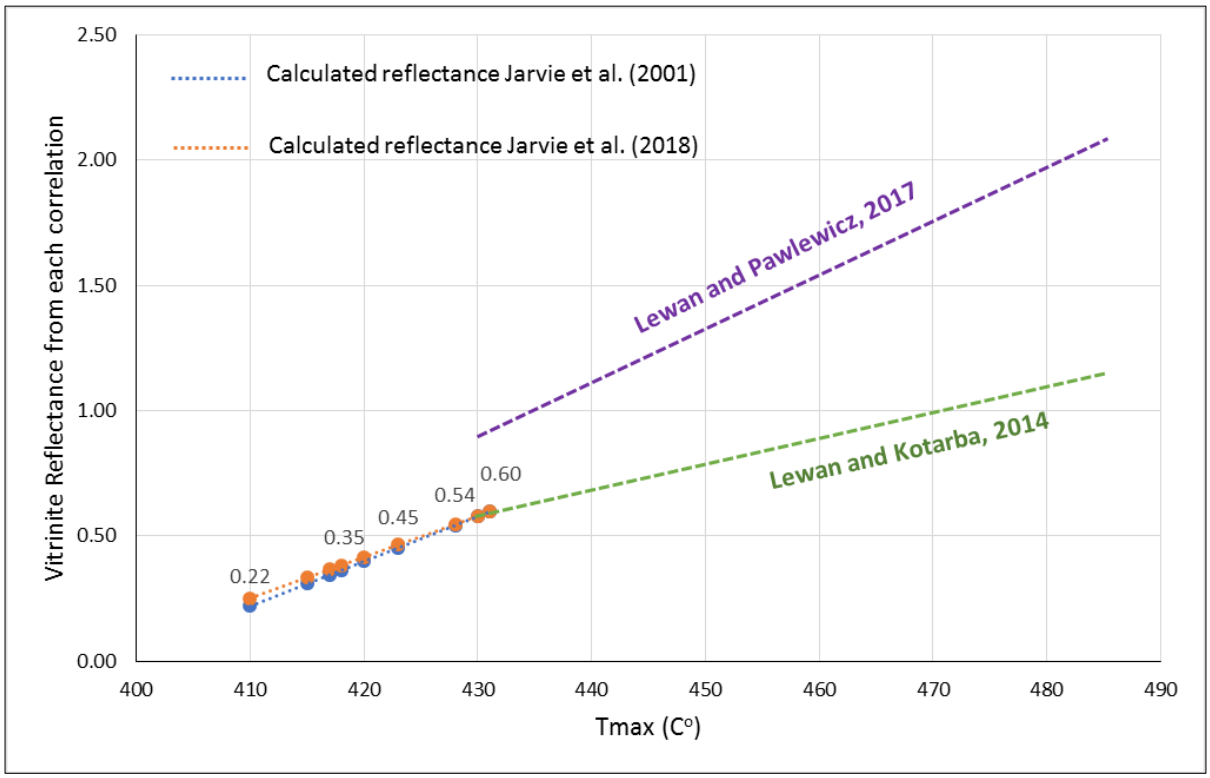

Figure 92: Cross-plot between Tmax and the synthetic vitrinite reflectance calculated from Tmax. The two equation used are discussed in Jarvie et al. (2001; 2018). For comparison the data from Lewan and Kotarba (2014) and Lewan and Pawlewicz (2017) are also indicated.

4.5 MOLECULAR GEOCHEMISTRY

4.5.1 Fourier Transform – Infrared Spectroscopy

The FT-IR spectra is reported in Figure 93 in a sample free of water and mineral matter.

The spectra shows abundant OH bands in the 3620-3200 cm^{-1} and is very lean of aliphatic CH band in the 2950-2850 and 1520-1390 cm^{-1} spectral regions.

The highest peaks are reported for the carboxyl group, in particular for the aromatic C=C and C=O bonds between 1700-1600 and 1300-1000 cm^{-1} spectral regions. Finally, there is clear absence of the aromatic CH bonds at the 900-700 cm^{-1} spectral region.

The abundance of carboxyl functional groups clearly indicates oxidation processes.

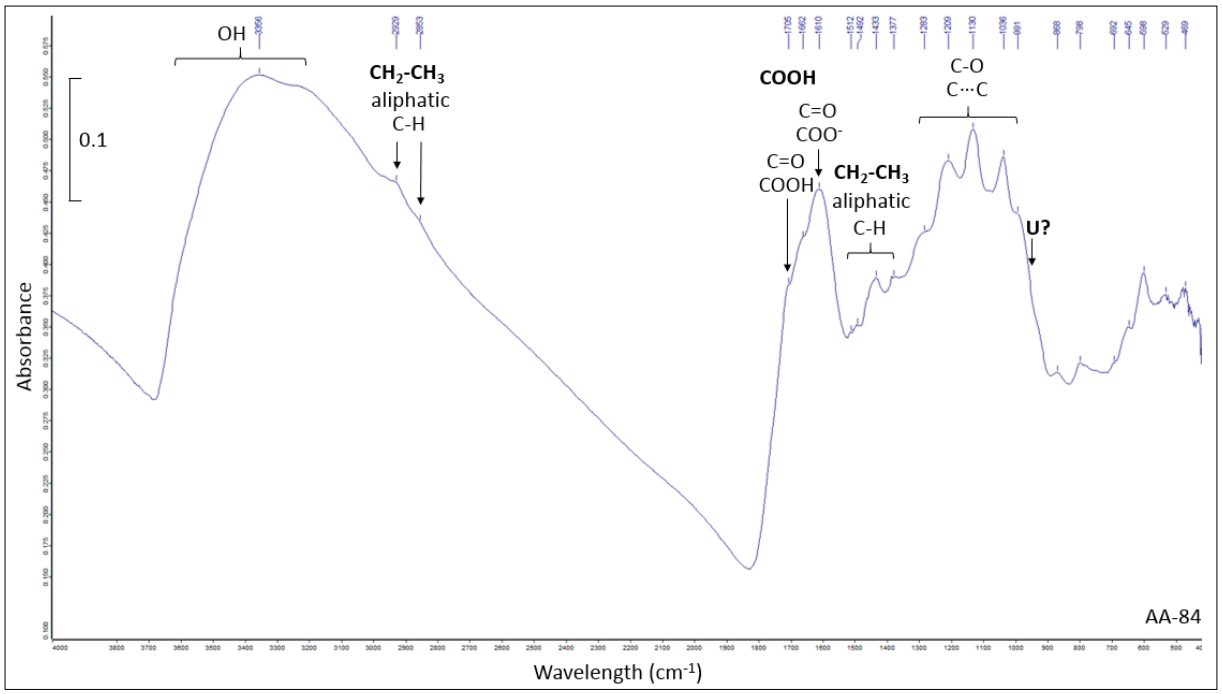

Figure 93: Infrared spectra of coal contained as intraclast in the Zoovch Ovoo sands. The sample is lean of mineral matter. The spectra was enhanced by continuous deconvolution using Lorentz+Gauss algorithms.

4.5.2 Gas analysis

Stable isotope ratios of light hydrocarbons are major diagnostic parameters to evaluate the thermal maturity and the origin of natural gas (Whiticar, 1996). A typical gas chromatogram of the gases collected and analyzed by means of GC-IRMS is presented in Figure 94. The gas is dominated by 92 mol% CO_2 (Table 7). However, other gases are also present, in decreasing order of amount: isobutane, methane, ethane, propane, butane, pentane, iso-pentanes, hexane, isohexanes, isobutene, ethane, propene, butene.

Table 7: Chemical composition of the gases analyzed by means of GC-IRMS.

Component	CO_2	C1	C2	C3	Unsat. iC4	iC4	iC6-ALL
Mol%	91.26	2.55	0.85	n.d	0.33	2.50	2.42

Carbon and hydrogen isotopic measurements were performed on methane, ethane, propane, isobutene, pentanes and hexanes and CO_2. Alkenes as well as nC_4 were in too low abundance to allow isotopic measurements. Carbon isotopic composition are reported in ‰ VPDB and hydrogen isotopic composition in ‰ SMOW.

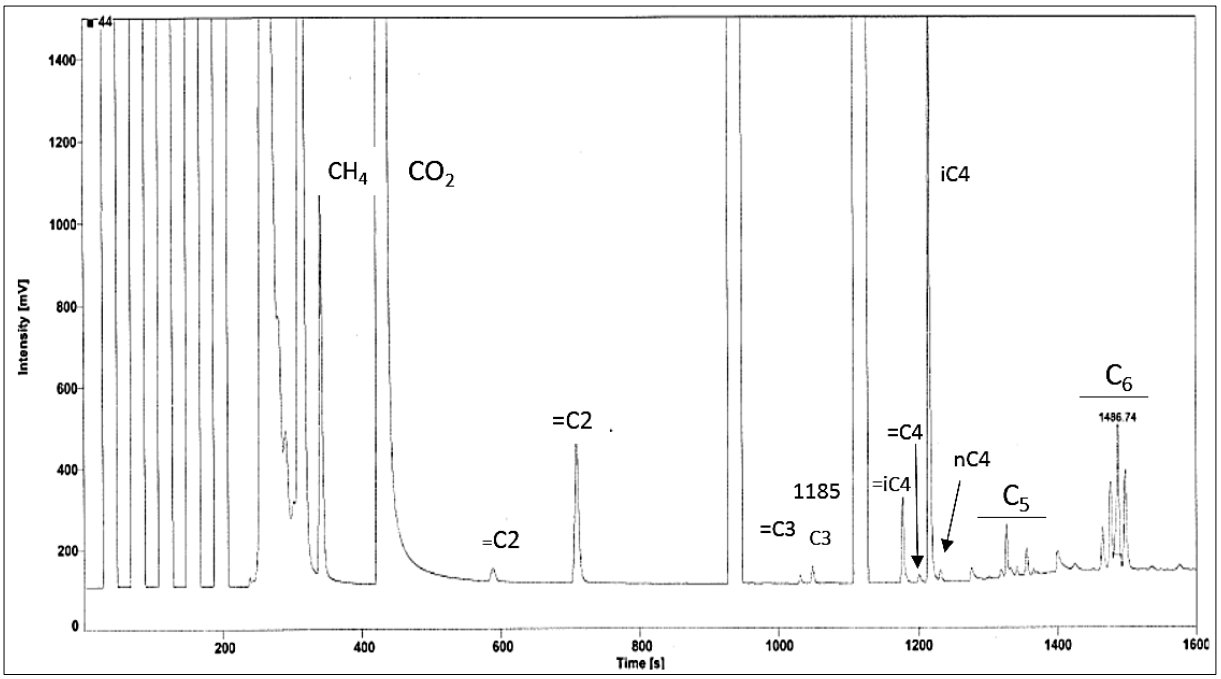

Figure 94: Typical GC-IRMS chromatogram of the gas recovered from the inflated sampling bags, showing CO_2, methane, alkanes/iso-alkanes, alkenes and C1-C6 homologs.

Their results are as follows for $\delta^{13}C$:

- C1 = -70.4 ‰ VPDB
- CO_2 = -49.9 to -51 ‰
- C2 = -46.2 ‰
- C3 = -45.2 ‰
- Unsat. iC4 = -28 ‰
- iC4 = -32.5 ‰
- C6 = -28.7 ‰
- ΣC6 = -27.5 ‰

and for δD:

- C1 = -369 ‰ VSMOW
- C2 = -730 ‰
- iC4 = -158 ‰
- C6 = -148 ‰
- ΣC6 = -141 ‰

The isotopic results are plotted on (Figure 95). Geochemical trends are observed for both $\delta^{13}C$ and deuterium. Moving from light to heavier hydrocarbons, the isotopic values become progressively heavier.

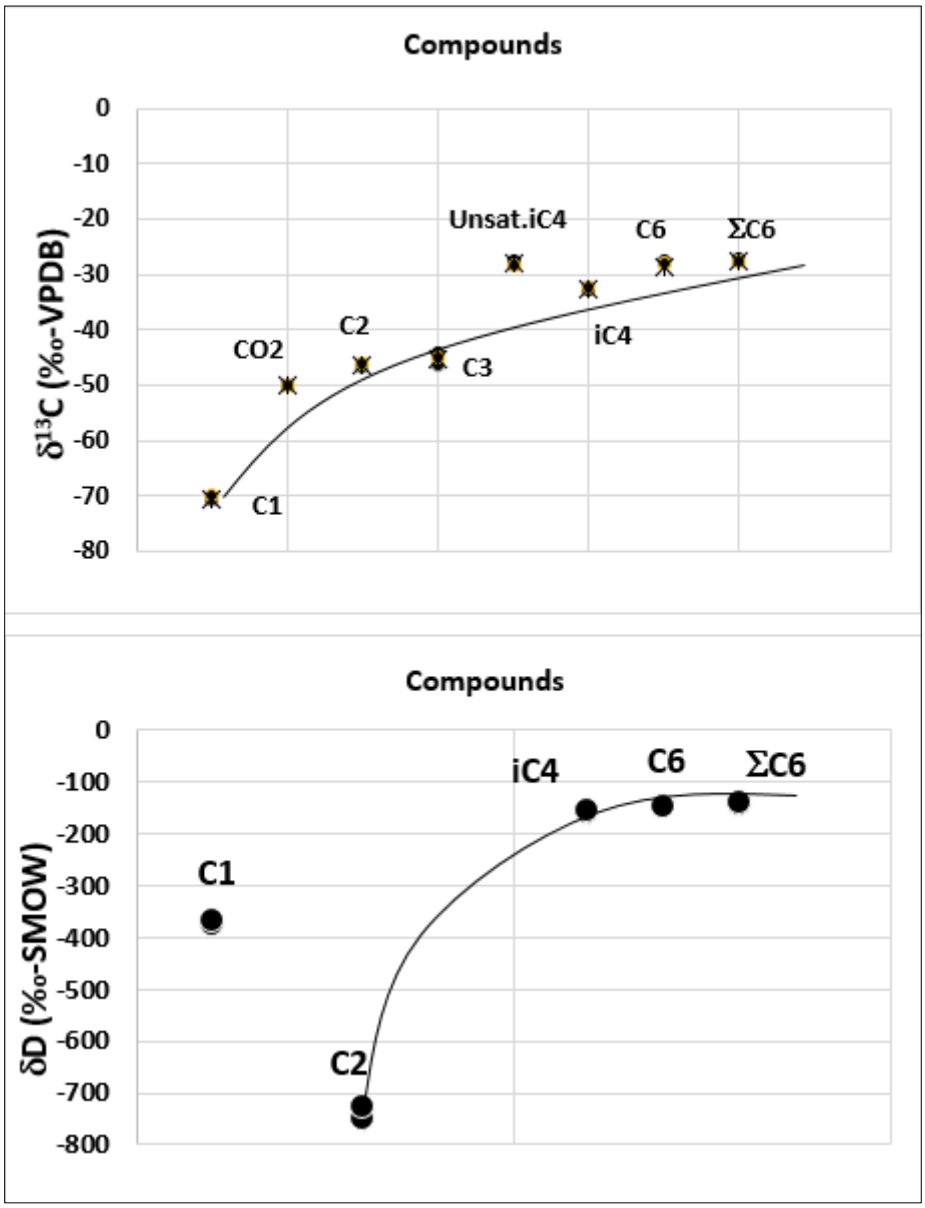

Figure 95: The isotopic composition of the different molecular compounds contained in the gas from the inflated sampling bags. A gradual increase in $\delta^{13}C$ is observed from methane towards ΣC6, from -70.5 to -27.5‰VPDB. Likewise the δD is increasing from -369 for C1 and -730 for C2 to -141‰SMOW for ΣC6.

In the δD vs $\delta^{13}C$ plot (Figure 96; Figure 97) the methane isotopic compositions indicate rather a terrestrial biological origin [**B(t)**]. Schoell (1988) and Whiticar (1990) proposed an interpretation of this diagram in terms of microbial activity. In particular the distribution of the data points may suggest that methane was generated through acetoclastic activity.

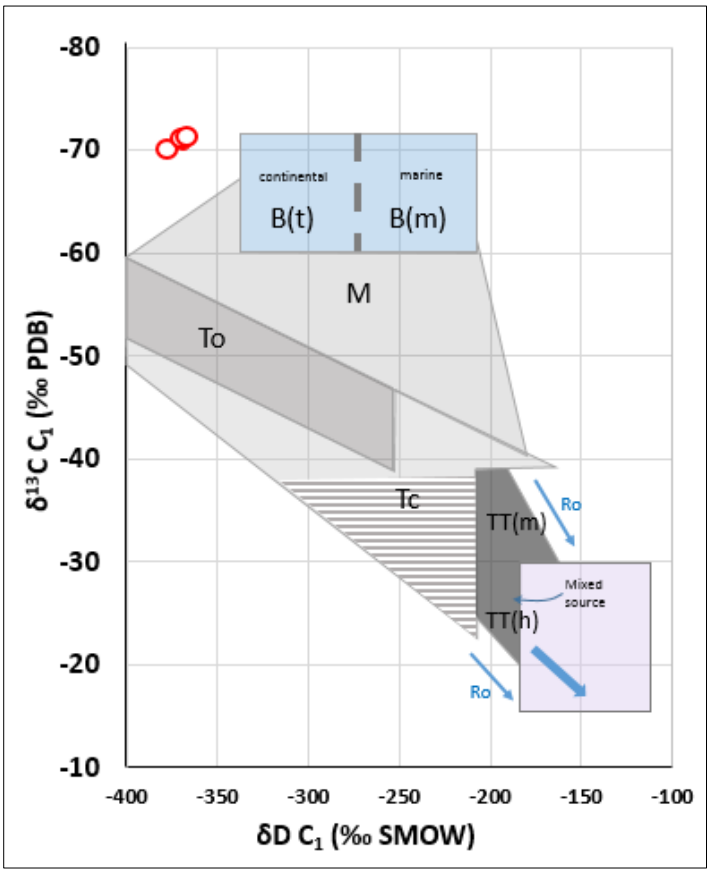

Figure 96: Classification of natural gas by isotopic variation of deuterium and ^{13}C in methane, modified after Schoell (1988). (**B**) biogenic gas, with (**t**) and (**m**) denoting terrestrial and marine environments, respectively; (**T**) associated gases with (**o**) petroleum and (**c**) condensates, respectively; [**TT(m)**] non-associated dry gases from sapropelic liptinitic organic matter; [**TT(h)**] non-associated gases from humic organic matter; (**M**) mixed gases. Initially the plot considered coal gases from NW Germany. Therefore, the reference fields were not fully developed. Therefore it is not clear if the gases from Zoovch Ovoo have a biogenic origin, formed in terrestrial environment [**B(t)**] or are associated to petroleum (**To**).

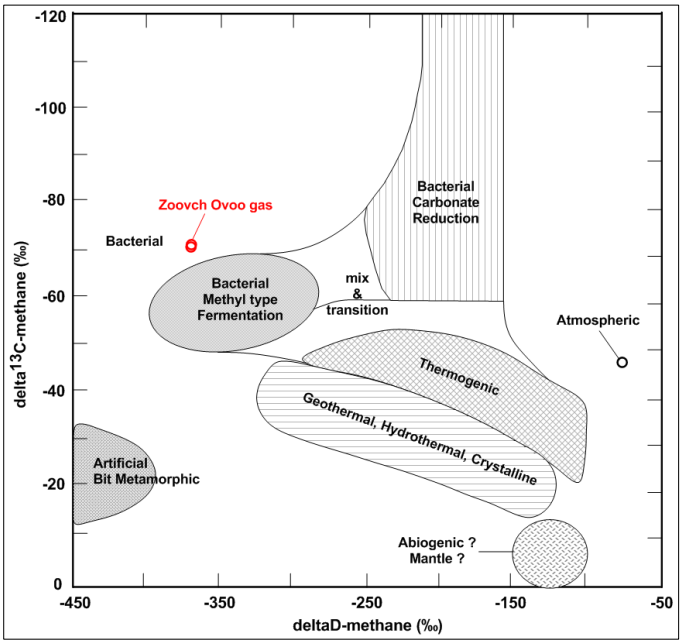

Figure 97: Deuterium versus ^{13}C in methane. The main sources of methane are classified are bacterial, thermogenic and geothermal. Atmospheric and artificial sources are also included. Diagram after Whiticar, 1990.

The diagram for the carbon isotopic compositions of methane vs CO_2 (Figure 98) is based on the equation by Whiticar (1994), to calculate the carbonate isotopic fractionation for biogenic gas of different origins:

$$(1) \qquad \alpha_{CO_2\text{-}CH_4} = \delta^{13}C_{CO_2} + 10^3 / \delta^{13}C_{CH_4} + 10^3$$

This interpretation suggests that methane and CO_2 have the same microbiological origin.

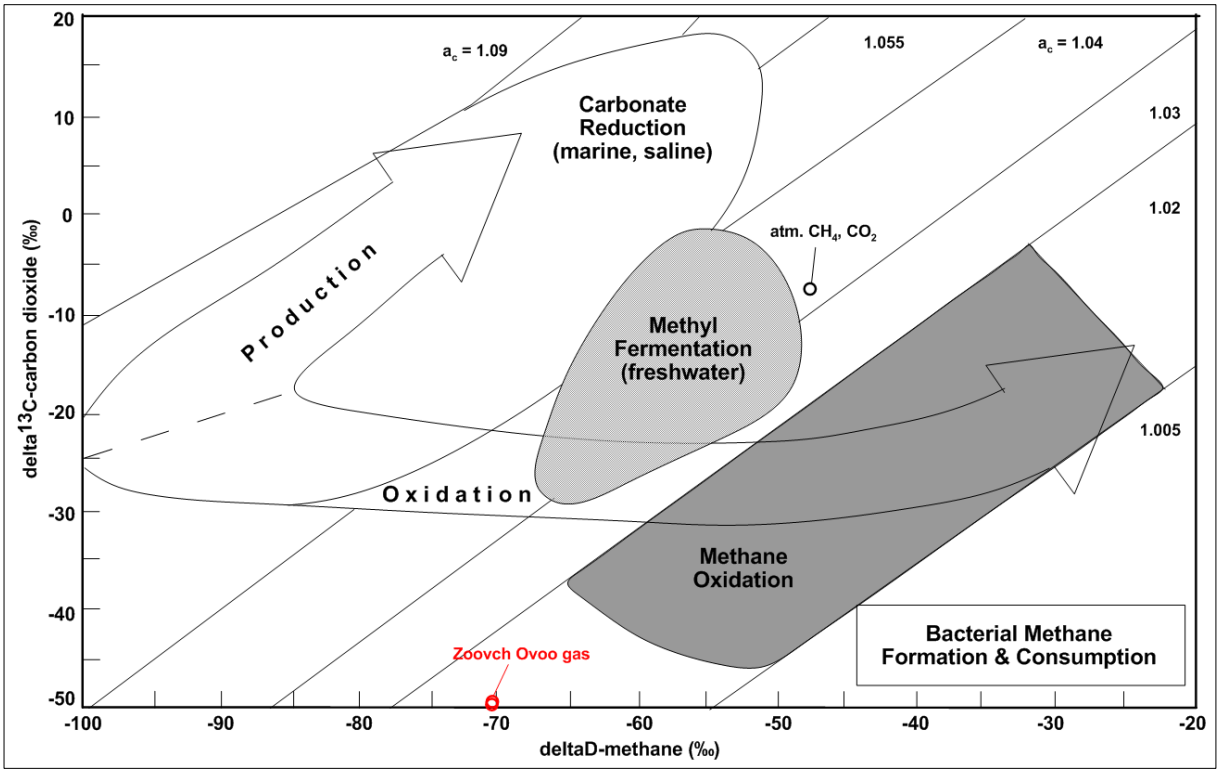

Figure 98: δC^{13} separation plot between methane and carbon dioxide of bacterial natural gas. Production of methane from carbonate reduction is linked to a larger carbon isotopic effect than acetate fermentation and methane oxidation that allows a clear distinction to be made (Whiticar et al., 1986). Reference fields after equation (1).

The comparison of values and evolution of the $\delta^{13}C$ between the C1-C5 hydrocarbons series suggests low thermal maturity for the gas. This is consistent with the predominance of iC4 over nC4.

Considering the Bernard diagram (Bernard et al., 1978) the $C_1/(C_2+C_3)$ ratio and $\delta^{13}C$ suggest a mixing between microbial and thermogenic gases (Figure 99). However, the composition of the C2-C5 fraction of the gas is quite unusual: normal alkanes are accompanied by alkenes while iC4 is strongly dominant over nC_4.

In regards to the high concentration of uranium in the samples, the most probable origin of the alkenes is radiolysis. (Jaraula et al., 2015).

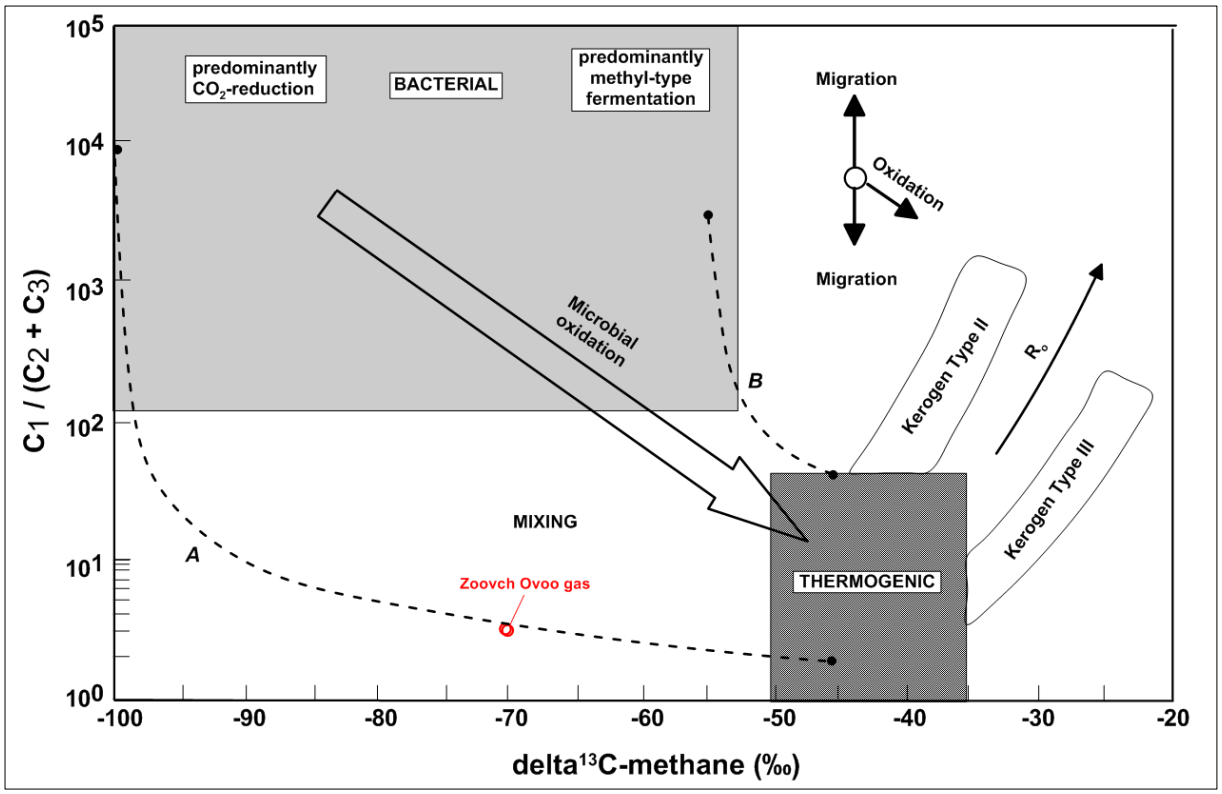

Figure 99: Bernard diagram for natural gas classification, using C1/(C2+C3) (vol%) and the carbon isotopic ratio $\delta^{13}CCH_4$ (Bernard et al., 1978; Faber and Stahl, 1984; Whiticar, 1994). A and B represent mixing lines.

4.5.3 Py-GC-MS

Py-GC/MS chromatograms of sands, silts and clay samples are presented in Figure 100. Gas chromatograms are compared to a well preserved lignite collected in Cretaceous sediments of southeast France. The chromatogram of this reference sample is very typical, with predominant alkene-alkanes doublets, aromatic compounds and oxygenated compounds typical of cellulose and lignin derived molecules (Burgess and Schobert, 1998).

The chromatograms obtained for all the samples of the Sainshand deposit are characterized by the absence of alkene-alkane doublets and by the predominance of aromatic compounds. Since thermal maturity of the formation is estimated to be at the border between diagenesis and catagenesis, thermal alteration is not responsible for this situation. Organic petrography suggests poor preservation of kerogen particles. Therefore sedimentation conditions such as surface oxidation and weathering may be responsible for the molecular composition observed by Py-GCMS. However, uranium rich samples are also degraded by radiolysis or alteration derived from the roll-front waters (Greenwood et al., 2018), which could be again the case for the organic matter in Zoovch Ovoo.

Attempts to correlate the molecular alteration level of samples with their uranium content were made. Unfortunately likewise the Rock-Eval study, this correlation did not succeed.

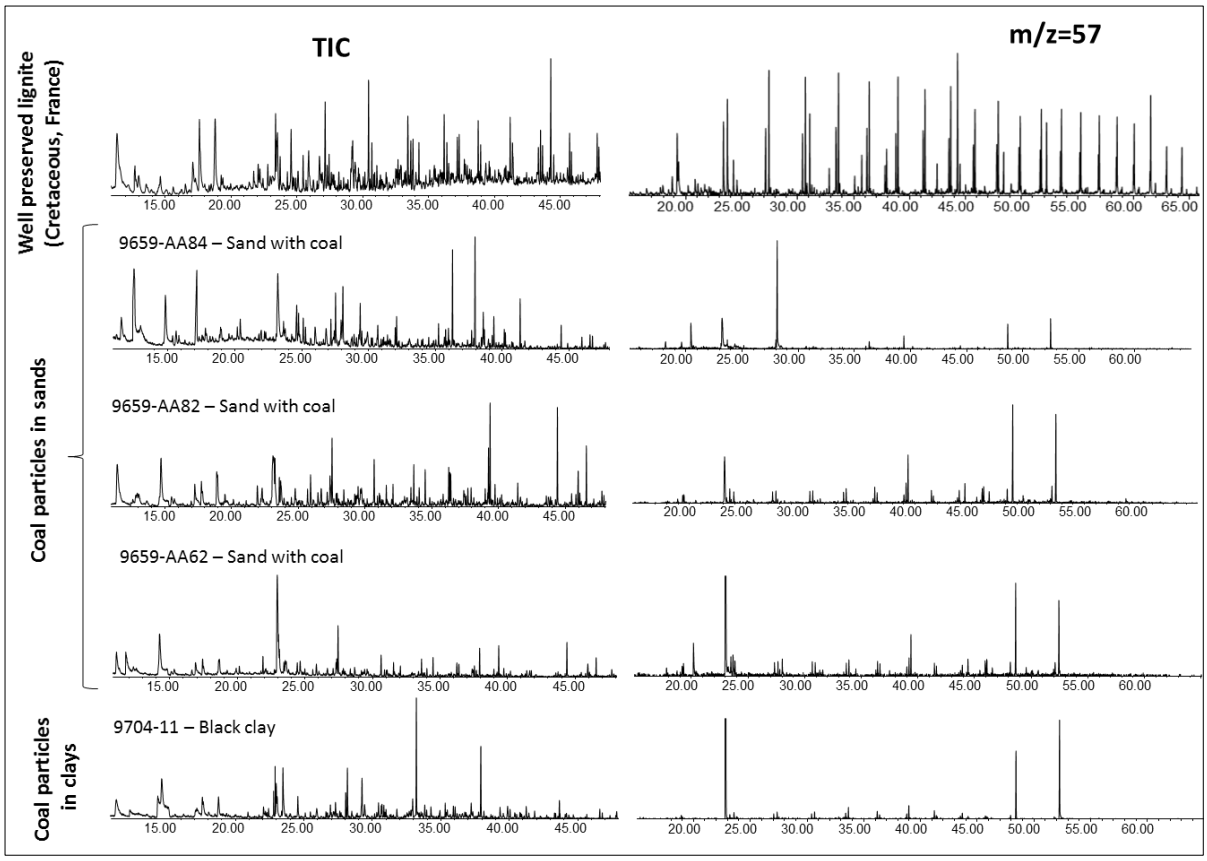

Figure 100: Pyrograms obtained from Py-GCMS (TMAH), showing the molecular composition of kerogen studied (TIC – total ion current).

4.6 TEMPTATIVE INTERPRETATION OF ORGANIC MATTER GEOCHEMISTRY

4.6.1 Molecular geochemistry

Two interpretations can be made about the nature of the kerogen presented in these rocks by considering only the results from Rock-Eval:

i. It is a kerogen at the onset of oil window, between diagenesis and catagenesis stages but never reached gas window, as there is still cutinite and exudatinite which if otherwise would crack to produce liquid hydrocarbons.
ii. It is a kerogen of synsedimentary origin (organic material inherited from forest fires and surface to near-surface oxidation) with very low HI and high OI.

4.6.2 Origin of the gas

As demonstrated, the overall thermal maturity of the Sainshand formation is low, possibly at the onset of the oil window. Thermal generation of gas from type III-IV kerogen is therefore excluded. Isotopic composition of C1 and CO_2 suggest a biologic acetoclastic microbial activity, which is consistent with the presence of numerous facies containing relatively low maturity organic matter. Also, the gas composition is strongly dominated by CO_2. Therefore microbial activity is responsible for most of the gaseous components and for the inflation of the sample bags. Concerning the other hydrocarbons gaseous components and especially in regards to the presence of alkenes, it may be suggested that the C2-C6 fraction of the gas derives from radiolysis of coaly particles.

4.6.3 Radiolytic alteration

Radiolytic degradation causes the consumption of aliphatic CH and aromatic CH bands while the aromatic C=C and C=O bands relatively increase (Colombo et al., 1964; Landais, 1996). As a result the H/C ratio decreases while the O/C increases with increasing U-content (Jaraula et al., 2015).

Consequently, the Tmax and R_o also increase (Forbes et al., 1988). The progressive oxidation of type III kerogen (vitrinite) eventually will lead to type IV (inertinite), first reported as vitrinertinite by Zhang and Rong (2019).

Thermally immature organic matter (%Ro=0.26) was previously reported to have high Tmax (420 ^oC) due to radiolytic phenomena (Greenwood et al., 2018).

From the above it could be concluded that the cases of high Tmax are due to radiolysis (for U rich samples) or oxidation by roll-front fluids.

CHAPTER V

Sulfides study

5.1 INTRODUCTION TO THE SULFIDE STUDY

The functioning of the U-O.M-S system is a key for the understanding of the formation of the U concentrations. Hence, the sulfides were analysed in terms of petrography and crystal-chemistry. On the basis of the petrography of 198 samples (9659 and 9606 studies) of variable lithologies (matrix supported sandstones, sandstones cemented by different dolomite cements and finally mineralized sands), it was concluded that pyrite is by far the main and most abundant sulfide and occurs as several habitus.

5.2 SULFIDE OCCURRENCES IN ZOOVCH OVOO

Pyrite (FeS_2) is the most common sulfide in Zoovch Ovoo. Other sulfides recognized are sphalerite (ZnS) as well as galena (PbS), greenockite/hawleyite (CdS) and acanthite (Ag_2S). Associated phases to sulfides are sulfates i.e. barite ($BaSO_4$) and the selenides, namely clausthalite (PbSe) and stilleite (ZnSe).

5.2.1 Pyrite petrography

The morphological features, the relative abundance as well as the relationship with the organic matter of the different sulfide occurrences identified in the Zoovch Ovoo sands are discussed and presented according to the following order: i) isolated framboids, ii) framboids embedded on organic matter, iii) concentric overgrowth of framboids, iv) framboids embedded within cubic (euhedral) pyrite, v) series of cubic (euhedral pyrite), vi) isolated euhedral pyrite, vii) marcasite on isolated euhedral pyrite and viii) framboidal and euhedral pyrite inside post-uranium dolomite.

The current results confirm the observations described in Brouand (2014; 2015) and Gaudare (2014). According to the latest findings presented in this report, the pyrite, which is the most common sulphide in Zoovch Ovoo, can be classified in at least 9 different categories (not necessarily generations), although in a broad sense there are only the framboids and the single crystals termed euhedral. However, in order to be precise and to uncover the diagenetic history of the sulfides, a detailed approach that considers the relationships with the other diagenetic mineral phases, the transition phases between the framboibal and euhedral pyrite and the grade of organic matter epigenesis by pyrite (pyritization) are to be clearly understood. The morphological features, the relative abundance as well as the relationship with the organic matter of the different sulphide occurrences identified in the Zoovch Ovoo sands are discussed and presented according to the following order:

1. Isolated Framboids
2. Framboids embedded on organic matter
3. Concentric overgrowths of framboids
4. Framboids embedded within cubic (euhedral) pyrite
5. Series of cubic (euhedral) pyrite
6. Isolated euhedral pyrite
7. Marcasite on isolated euhedral pyrite
8. Framboidal and Euhedral pyrite inside anhedral (Type IV) dolomite
9. Other sulfides and associated phases

- Sphalerite (ZnS)
- Galena (PbS)
- Cadmium sulphide i.e. Greenockite or Hawleyite (CdS)
- Acanthite (Ag_2S)
- Barite ($BaSO_4$) and the selenides namely, Clausthalite (PbSe) and Stilleite (ZnSe)

5.2.1.1 Isolated Framboids

Description

Framboibal pyrite, when not associated to organic matter, is encountered very frequently in the studied samples. It can grow inside the intergranular porosity, around Fe-Ti oxides but also independently inside the clay matrix and dolomite cement (excluding type IV dolomite which probably includes a late generation of framboids).

Framboidal pyrite is the first pyrite generation that is crystallized contemporaneously or right after siderite formation. Pyrite framboids can be found isolated (single grains) or in groups of several (polyframboids). They have spherical to sub-spherical shape, variable size that is usually around 10-30 μm, more rarely 40 μm in diameter. They are made of densely packed aggregates of tiny (submicron) pyrite crystals. It was observed that they tend to be densely packed and have well developed spherical shape when they are encompassed by spherical rings (so-called concentric overgrowths), while having sub-spherical shape when the latter is missing.

Photo-micrographs

Figure 101: Examples of isolated framboids.

Samples AA-54, BB-51, BB-134, BB-126 and BB-110 (information on the location of the samples presented, can be found in the end of the pyrite section).

A: Isolated framboid inside clay matrix with the typical size range of 20 μm, the sub-spherical shape is due to the less densely packed pyrite microcrystals (BSE).

B: A typical group of framboids (polyframboids) inside clay matrix, with spherical shape and size that can reach 50 μm. Their boundaries are not very well developed and they show weak packing (RL).

C: Clusters of framboidal pyrite with rings (concentric overgrowths), in the size range of 20-30 μm, with spherical shape and dense packing growing filling intergranular porosity quartz grain (RL).

D: Typical isolated framboid on clay matrix, in the size range of 20 μm with thick overgrowth of 5 μm, spherical and densely packed, later cemented by sphalerite (BSE).

E: Cluster of framboids growing inside microcrystalline dolomite (type I), in the size range of 40 μm. The concentric overgrowth is also visible (RL).

F: Clusters and isolated framboids growing inside euhedral dolomite (type II), in this case around a Fe-Ti oxide. The framboids have well-developed spherical shape and are in the size range of 10 μm while the overgrowth, not easily discriminated, is at the range of 5 μm (BSE).

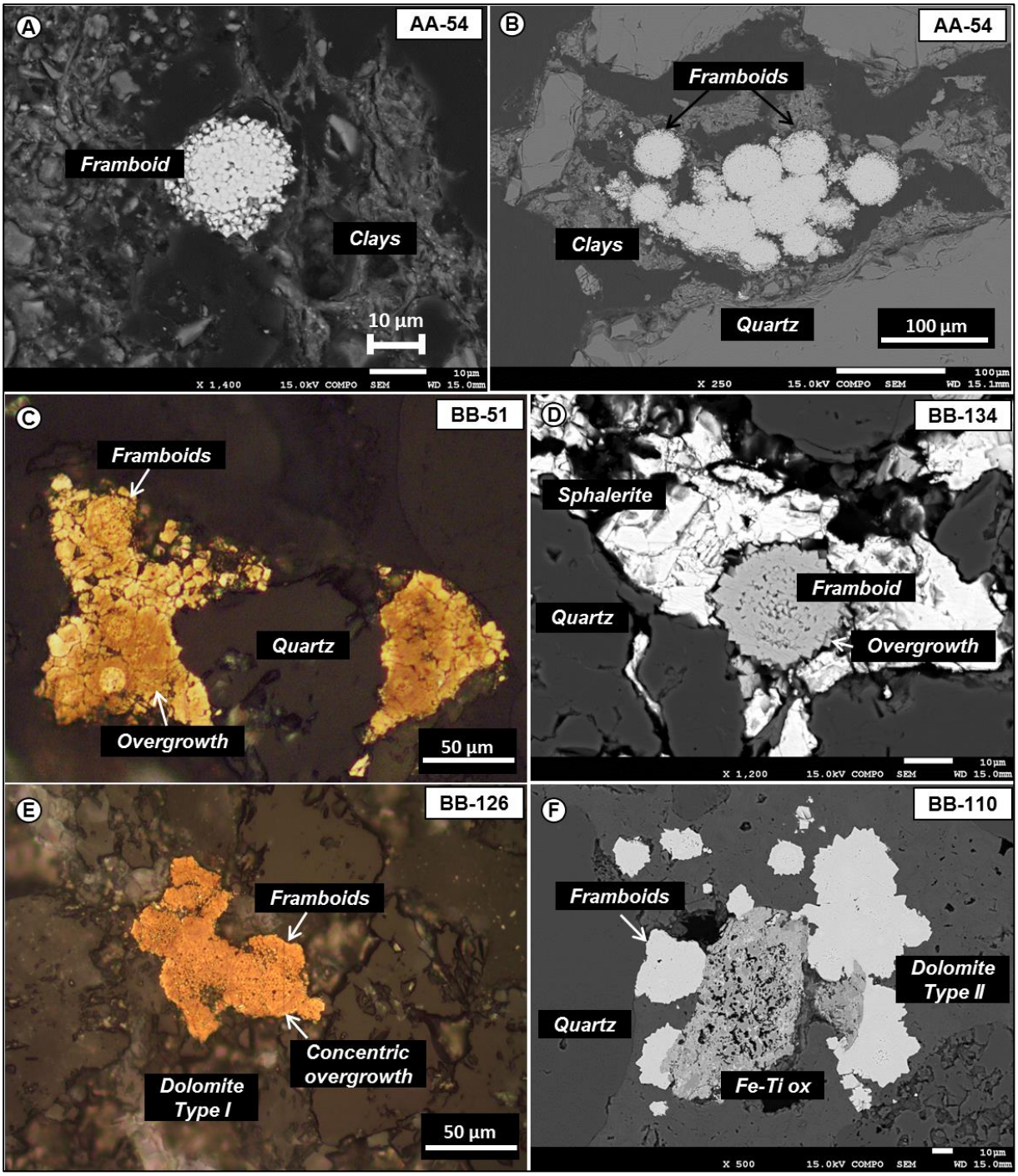

Figure 101: Examples of isolated framboids: (A) framboid in clay matrix; (B) polyframboids in clay matrix; (C) polyframboids with concentric overgrowth in grain-supported sand; (D) framboid with concentric overgrowth inside sphalerite cement; (E) polyframboids with concentric overgrowth inside microcrystalline (type I) dolomite; (F) framboids associated to Fe-Ti oxide, inside euhedral (type II) dolomite.

5.2.1.2 Framboids embedded on organic matter

Description

The framboidal pyrite that is embedded on the organic matter is also very commonly encountered in the Zoovch Ovoo sands. These framboids have similar morphological characteristics with regards to shape and size with the isolated framboids described previously. They have well-developed spherical shape and sizes that fluctuate at the range of 10-30 μm. The difference is that in the case of framboids associated to organic matter, it is possible to find larger sizes i.e. greater than 50 μm, termed pyritospheres.

Photo-micrographs

Figure 102: Examples of framboidal pyrite being embedded in organic matter.

Samples BB-9, CC-25C, CC-6, AA-58, 9606-101 and 9606-143 (location of samples in the end of the chapter).

A: A few sub-spherical framboidal pyrite grains at the range of 10 μm inside inertinite-fusinite cell lumens with associated elemental selenium and clays (BSE).

B: Cluster of framboids and their overgrowths almost totally replacing the organic particle. As a result the framboids and their overgrowths are interconnected and not easily discriminated any more (RL).

C: Framboidal pyrite and spherical pyritosphere of 50 μm size on a telovitrinite particle. There is a preference for the pyrite to grow on the collotelinite, which stands for homogenous cell walls without defined structure over the telinite which refers to partially fused cell walls (RL).

D: Cluster of spherical framboids with overgrowth, from 5 to 15 μm, growing at the rim of telovitrinite later cemented by pitchblende. The consequence is the formation of a pyrite cement (BSE).

E: Pyritospheres (locally > 50 μm) growing at the rim and inside an organic particle. Pyrite grows first in the available space (texto-ulminite) between the gelovitrinite and then inside the latter until full replacement (BSE).

F: Progressive replacement – gradual growing of semi-fused framboidal pyrite grains on organic matter (epigenization).

G: Framboids with concentric overgrowth encompassed by the geometry of the fusinite cell-lumen (RL).

H: Group of sub-spherical framboids (≈50 μm) without overgrowth growing on organic matter (RL).

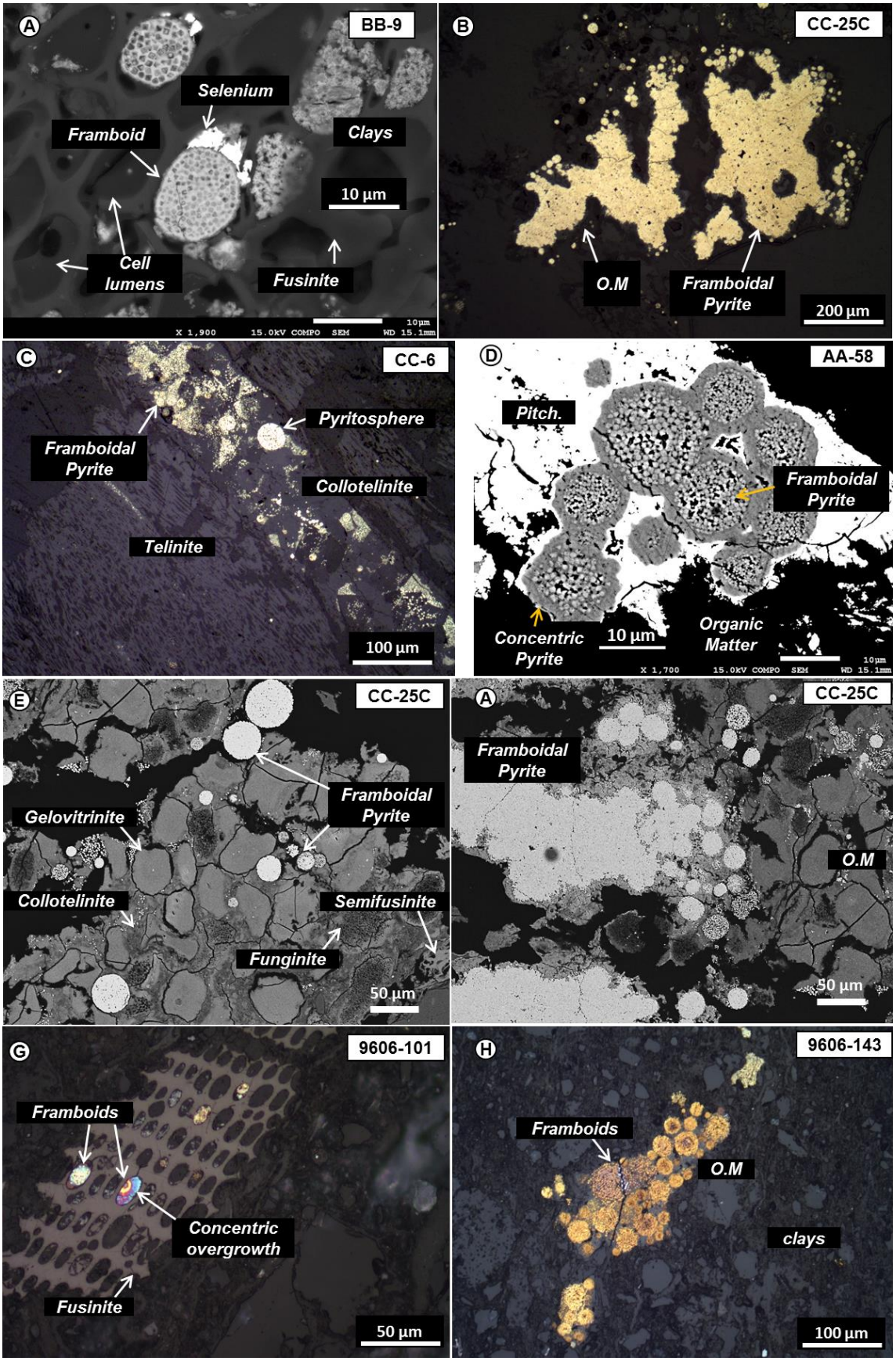

Figure 102: Examples of framboidal pyrite being embedded in organic matter: (A, G) framboid encompassed by O.M cell-walls; (B, H, F) polyframboids replacing O.M; (C, E) Pyritospheres in a telovitrinite particle; (D) Polyframboids and their overgrowths at the rim of a telovitrinite particle associated to pitchblende;

This pyrite type is found inside or at the rim of organic particles, isolated or in groups (polyframboids). Very frequently the cell-lumens are used as nucleation sites and then the crystal size and orientation depends on the geometry of the cell-lumen in a way that a single framboid will fill one cell lumen. The degree of epigenization of pyrite on the organic matter can vary from a few dispersed framboids to full replacement of the organic particle by the framboids and their overgrowths. It was observed that there is a higher affinity between the pyrite and the maceral telocollinite (partially fused cell tissue) compared to the colinite telocolinite (main texture of the cell walls) or corpogelinite (completely filled oval cells). Even in the case when the internal part of the cell walls is empty i.e. fusinite, the framboids use it as nucleation site and grow until they reach the borders of the cell-walls that act as barriers to their further crystal growth.

The frequent association of framboidal pyrite with organic matter up to full replacement suggests that framboids may derive from bacterial activity. Indeed, sulfate reducing bacteria use sulfur from dissolved sulfate as proton source while they oxidize organic matter. As a consequence, reduced sulfate is available for pyrite precipitation while organic carbon is being removed. The spatial replacement of kerogen by pyrite may then start and eventually lead to full epigenization with eventually conservation of the initial organic morphology. Further isotopic analysis of sulfur in pyrite may help to confirm this process and allow more detailed interpretation of pyrite diagenesis.

As epigenization proceeds with increasingly fused framboids, full replacement of organic matter by pyrite may lead to fully pyritized surfaces that may then appear as a cement.

“More examples of pyrite and organic matter relationships, i.e. progressive epigenization of organic matter by pyrite, are discussed in the organic matter chapter”.

5.2.1.3 Concentric overgrowth of framboids

Description

The concentric pyrite is the corona that grows around the framboids as an overgrowth, increasing the cumulative diameter usually by up to 5 μm, clearly marking a new pyrite generation, which in terms of pyrite paragenesis is the second in order. Their internal boundaries (on the framboid side) are discrete and well expressed, whereas their external are somehow diffusive, discontinuous and show irregular crystal growth. This property clearly shows how the space that is available during crystallization affects the development of the concentric pyrite crystals. Obviously the boundaries tend to be more diffusive in the case when there is more available space, whereas they are more rounded in case they are confined. With regards to the organic matter the concentric pyrite accompanies the framboidal pyrite, therefore it can be found anywhere the framboids are, including organic matter.

The oxidation of pyrite on the thin section, results from the contact with the atmospheric air and affects both the framboidal and concentric overgrowth pyrite types, which obtain different orange and blue colors, respectively. As a result, their features can be clearly revealed when working under optical microscopy.

This property was used to better indicate the boundaries of the concentric overgrowths. These pyrite rims are sometimes too thin and amalgamated to the framboidal body to be characterized during electron microprobe analysis or LA-ICP/MS analysis. Therefore their crystal chemistry could not be clearly obtained.

Photo-micrographs

Figure 103: Examples of the concentric pyrite overgrowth in different situations.

Samples BB-106, CC-25C, BB-110 and CC-25B.

A: Cluster of framboids (orange) and their concentric overgrowths (blue) with good interconnection. The assemblage probably grew on an organic particle until full pyrite "epigenesis". The sizes of the framboids are at the range of 20-30 μm and of the concentric pyrite at the range of 5 μm (RL).

B: Elongated cluster of framboids and their overgrowths totally replacing an organic particle. As a result the framboids and their overgrowths are well interconnected (RL).

C: A close view of a spherical framboid (20 μm) with its concentric overgrowth growing on an organic particle. The diffusive external boundaries of the overgrowth are evident (BSE).

D: A close view of an isolated spherical framboid (10 μm) and its overgrowth with the external diffusive boundaries growing on clay matrix (BSE).

E: Overview of pyrite generations growing on clay matrix. Spherical well developed framboidal pyrite (20-30 μm), concentric overgrowth (5 μm) and a new generation, the euhedral (≈30 μm) pyrite (RL). The pyrite generation are described in detail in the next section.

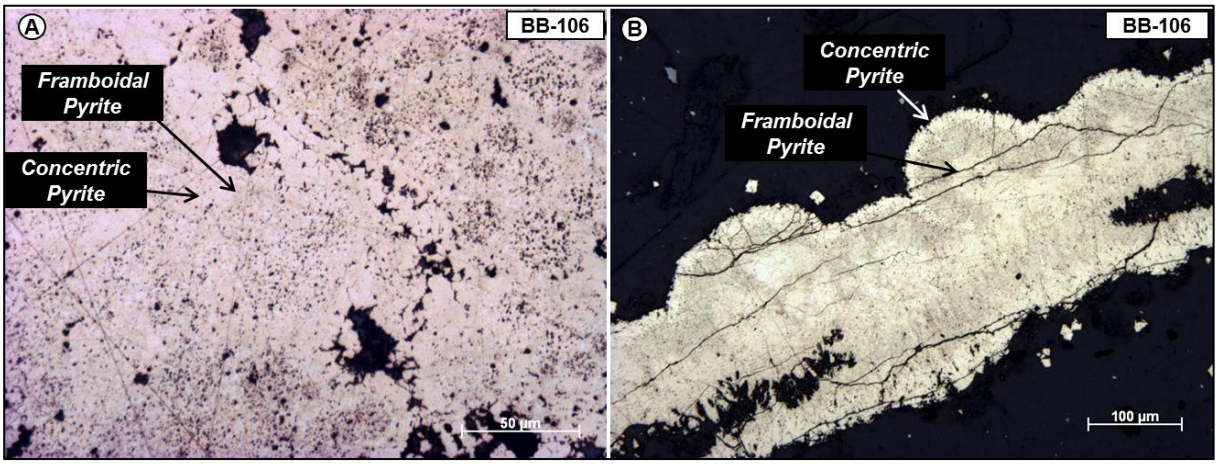

Figure 11: The framboidal pyrite and concentric overgrowth before oxidation. In the next page (pictures A, B) the pyrite is oxidized and the two generations can be better revealed.

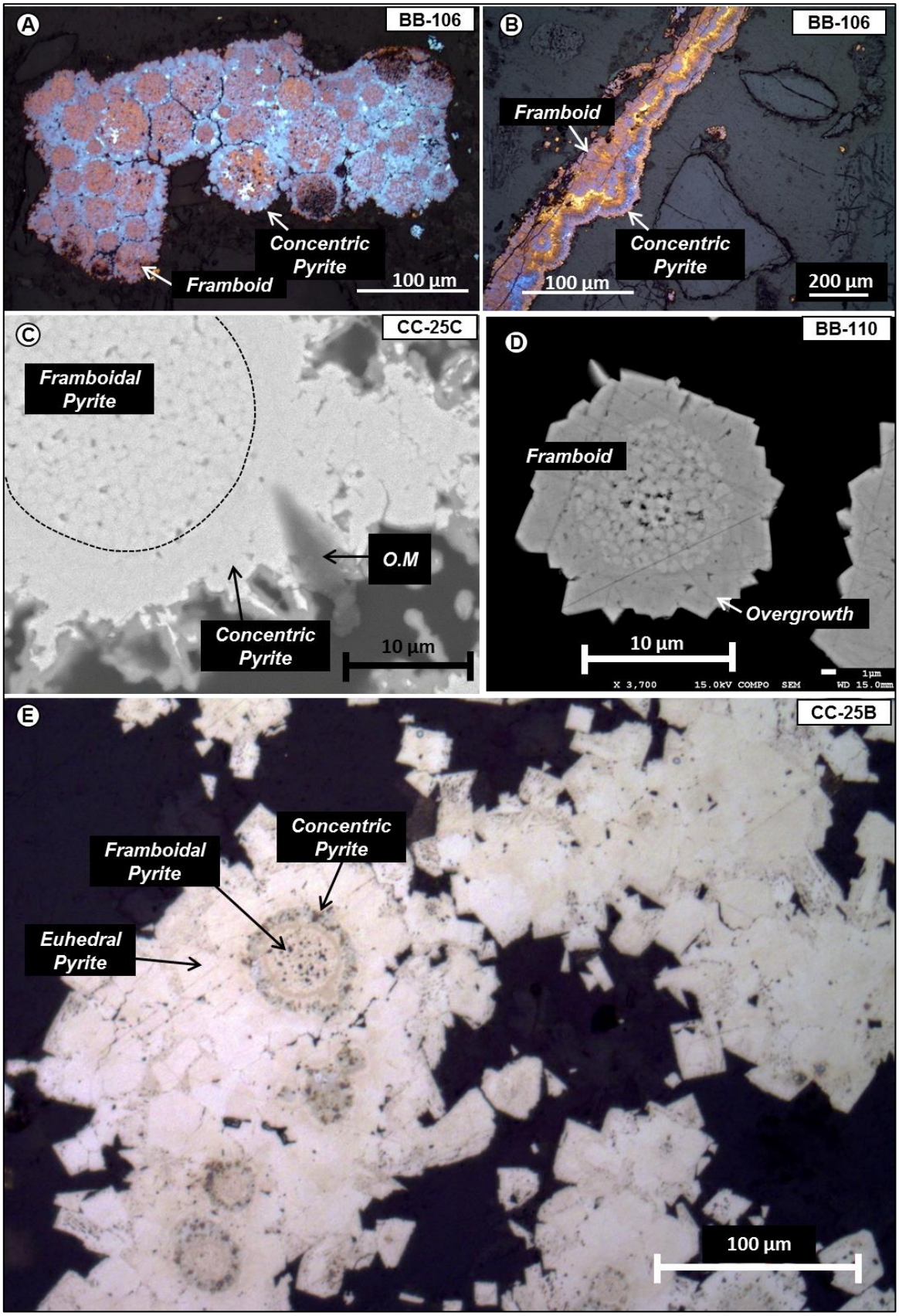

Figure 103 (continued): Examples of the concentric pyrite overgrowth in different situations: (A, B) the same images as in Figure 103, highlighting the two pyrite generations due to differential oxidation; (C) framboidal pyrite encircled by concentric overgrowth growing on organic matter; (D) framboid and overgrowth inside type II dolomite; (E)fFramboid, overgrowth and euhedral pyrite time relationships.

5.2.1.4 Framboids embedded within cubic (euhedral) pyrite

The term euhedral refers to pyrite crystals of cubic shape with sizes at the range of 20-30 μm. Euhedral pyrite is the third generation in the pyrite paragenetic sequence and is found encompassing framboidal pyrite which in turn can be surrounded by the second pyrite generation, the concentric overgrowth. As such it can be found inside the intergranular porosity, clay matrix, dolomite cement or organic matter. The euhedral pyrite can be encountered in three ways: 1) as isolated cubic crystals, 2) as cubic aggregates embedding one or more framboids with concentric overgrowth and 3) as cubic aggregates embedding framboids without the overgrowth.

When the euhedral crystals are growing around framboids they are densely packed and they form aggregates with discriminative crystal boundaries. Looking at those boundaries, it becomes clear that there are zonations, which respond to several generations of euhedral pyrite. Some generations contain uranium in the form of pitchblende as inclusions or as very thin coatings occurring in between the pyrite generations. These successive euhedral generations and their relationships with uranium are presented in Chapter IV.

Photo-micrographs

Figure 104: Examples of framboids being embedded by euhedral pyrite.

Samples AA-54, CC-25B, AA-172A, AA-54 and BB-97.

A, B: Typical example of a pyrite cluster with framboids being embedded by euhedral crystals, located in the intergranular porosity of a matrix supported sandstone. The framboids (20 μm) are densely packed and highly amalgamated with the euhedral grains but they can be still discriminated since they are composed of submicron pyrite crystals. The individual cubic crystals that form the aggregate are at the size of 10 μm (BSE).

C: Again framboids encompassed by euhedral pyrite, this time growing on organic matter, in particular fusinite. Euhedral crystals not associated to framboids are also recognized (BSE).

D: A cluster of framboidal pyrite encompassed by a generation of euhedral pyrite that contains uranium. The cluster is cemented by Type III subhedral dolomite, which is later diagenetic or contemporaneous to uranium formation (more details in Chapter III).

E: Well-developed pyritospheres (15 μm) encompassed by pitchblende, followed by euhedral pyrite (10-15 μm) with pitchblende inclusions. The whole assemblage is within clay matrix where pitchblende is also contained. There appears to be one euhedral pyrite generation (BSE).

F: Group of well-developed framboids (up to 10 µm) encompassed first by concentric overgrowth, then by euhedral pyrite at the size range of 5-10 µm, followed by pitchblende precipitation and another a few µm thick euhedral pyrite generation (BSE).

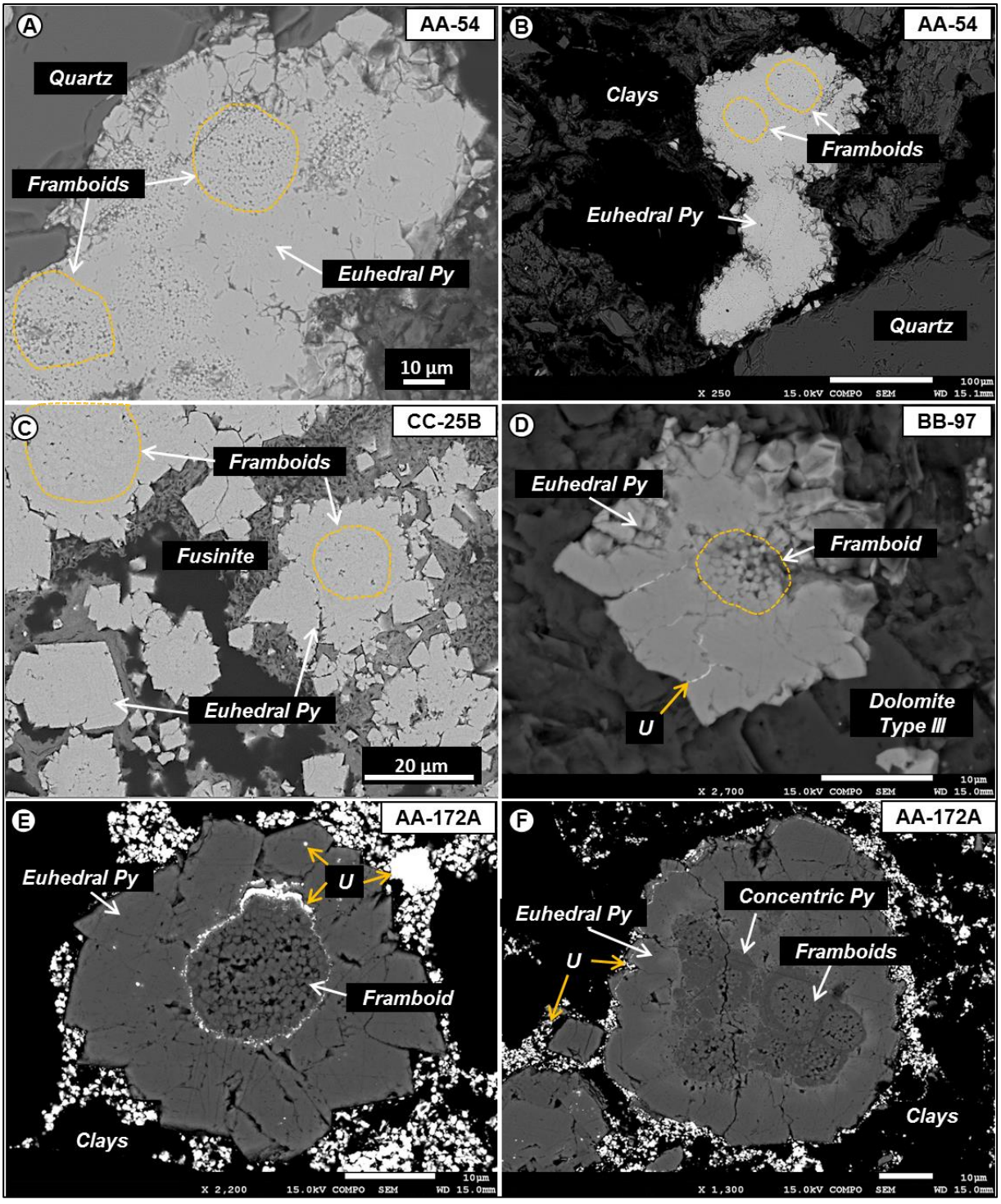

Figure 104: Examples of framboids being embedded inside euhedral pyrite cement.

5.2.1.5 Series (zonations/generations) of cubic (euhedral) pyrite

As was already discussed different generations of euhedral pyrite, mostly on mineralized samples, were recognized. Hence, a euhedral pyrite crystal can be composed from one to up to four generations. These are recognized by their different crystal orientation which causes contrast under the electron microscope. Empty pore space can exist in between two generations. Pitchblende inclusions within the pyrite crystals may also characterize a specific euhedral generation. Thus, euhedral pyrite generations that are earlier diagenetic, contemporaneous and post-diagenetic with regards to uranium precipitation were recognized. Finally, the last generation of euhedral pyrite seems to sometimes have diffusive boundaries.

Photo-micrographs

Figure 105: Examples of euhedral pyrite zonations and their relationships with other diagenetic phases.

Samples BB-134, AA-54, CC-25C, AA-172A, and BB-106 (all photographs taken under BSE).

A: Euhedral crystal at the range of 30-40 μm (Py 1) coated by a second pyrite generation (Py 2) with diffusive boundaries. Empty pore space occurs between the two generations of pyrite. The cluster is contained inside sphalerite cement with pitchblende inclusions.

B: Isolated cubic pyrite composed clearly of two pyrite generations, found inside clay matrix.

C: Cubic pyrite crystal located on organic matter (fusinite) showing four zones of crystallization.

D: Group of well-developed framboids (up to 10 μm) encompassed first by concentric overgrowth, then by two more pyrite generations. Pitchblende is found between the two euhedral generations and around the matrix.

E, F: Framboids coated by pitchblende, encompassed by euhedral pyrite with pitchblende inclusions.

G: Two generations of euhedral pyrite on organic matter with empty pore space in between as in (A).

H: Two pyrite generations growing on clay matrix. The first generation (Py 1) is homogenous and well developed, whereas the next generation (Py 4?) has diffused boundaries and presents pores for which some contain pitchblende.

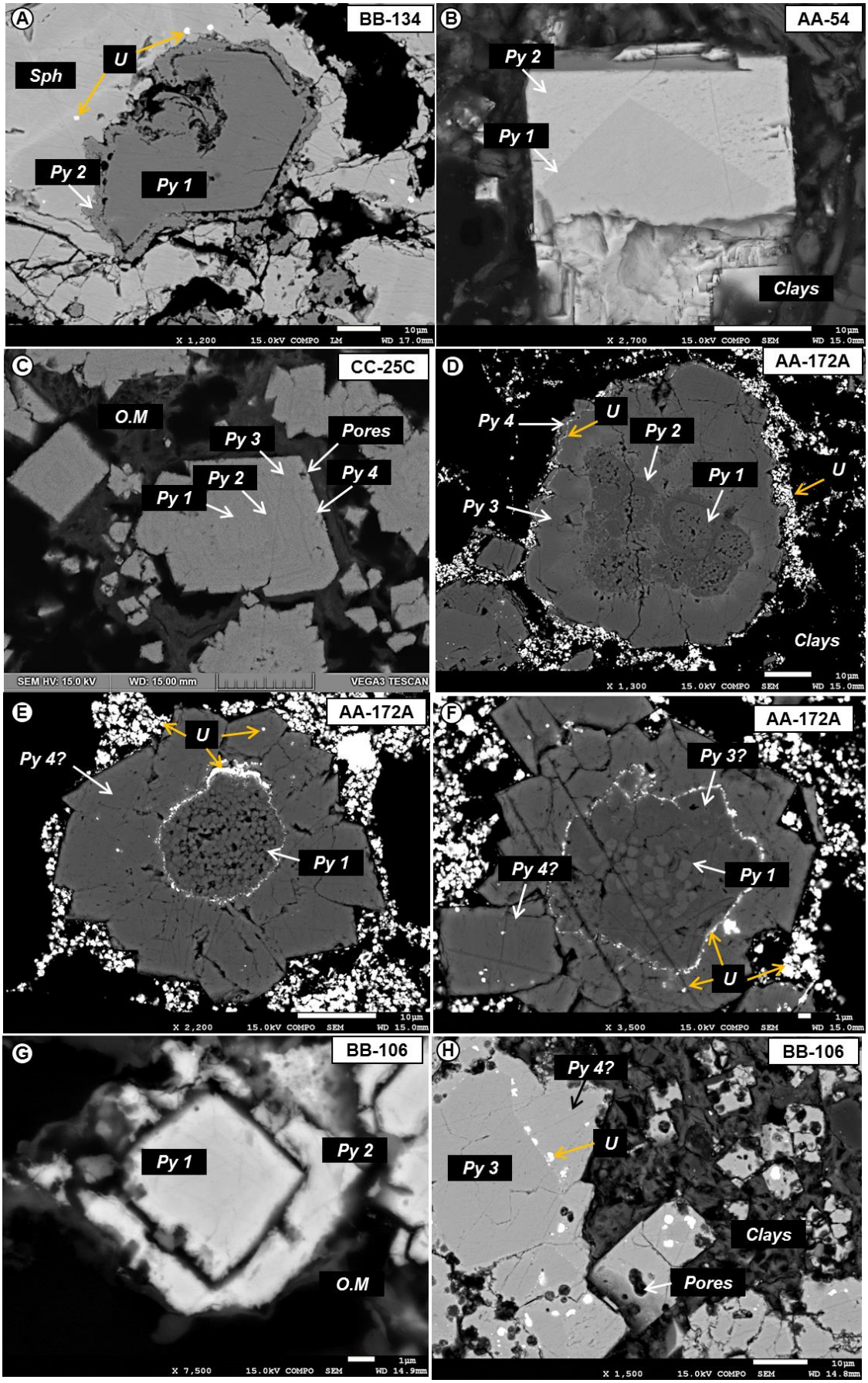

Figure 105: Examples of euhedral pyrite zonations and their relationships with other diagenetic phases. Note that pyrite numbering (Py x) does not correspond to the same pyrite generation in every image.

5.2.1.6 Isolated euhedral pyrite

Isolated euhedral pyrite crystals are commonly found around Fe-Ti oxides and silicates. In case there is enough pore space the pyrite grows as euhedral crystals, whereas when there is not enough space cement is formed instead (anhedral) that does not have any particular crystal shape. Henceforth the term pyrite cement refers to the anhedral pyrite that forms contemporaneously to a certain euhedral pyrite generation.

It was found that particularly large silicate grains, namely quartz and feldspars can contain pyrite inside their secondary porosity (fractures and dissolution pores inherited from sedimentary transport) and even uranium cement. Locally, micas epigenetized by pyrite cement can be found, while the ghost crystals are maintained. One possible explanation could be that when the euhedral crystal growth is confined in space fractures, cell walls or phyllosilicate textures the result is pyrite cement formation, whereas available pore space results in the formation of cubic crystals (euhedra). Pyrite cement bounding together sand grains is also commonly encountered. Cementation starts by cementing a cluster of sand grains and is gradually progressing by cementing adjacent sand grains. This cementation process based on anhedral pyrite growth may be distinguished from the one starting from framboids. Sulfur isotopes may help in the interpretation of these features.

Photo-micrographs

Figure 106: Examples of isolated euhedral pyrite occurrences.

Samples CC-25A, AA-54, BB-126 and BB-67.

A: Pyrite cement inside feldspar fractures (BSE).

B: Euhedral pyrite inside feldspar fracture filled with clays (BSE).

C: Euhedral pyrite at the outer part of the feldspar grain and pyrite cement in the internal part. Uranium cement is also present in between the two pyrite types (BSE).

D: Pyrite cement inside a quartz grain (BSE).

E, F: Euhedral pyrite on ilmenite, cemented by subhedral Type III dolomite (BSE and R.L).

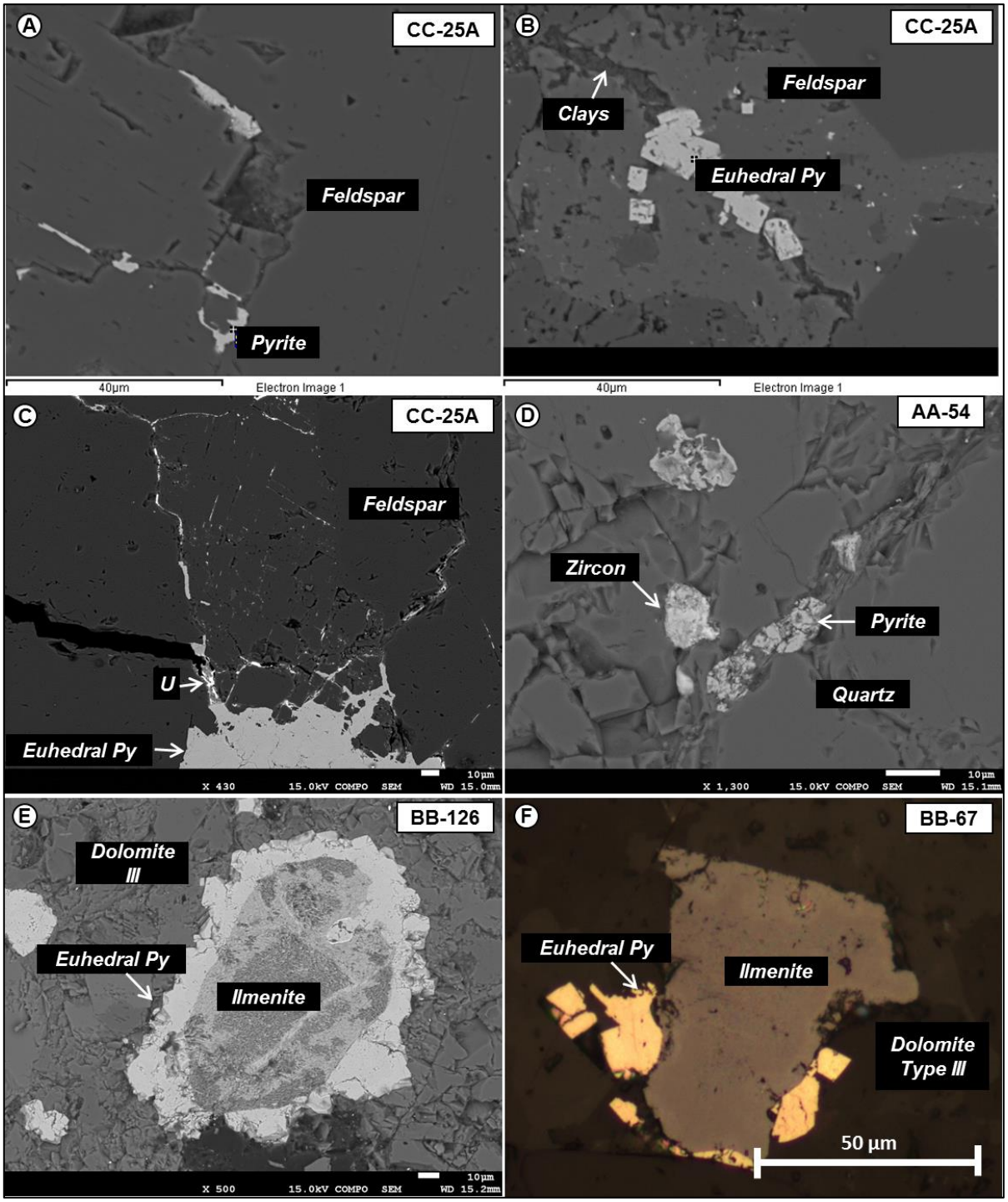

Figure 106: Examples of isolated euhedral pyrite occurrences: Inside the fracture porosity of feldspar, (A) Pyrite cement; (B) euhedral pyrite and clays; (C) uranium and euhedral pyrite. (D) Zircon and pyrite cement inside quartz fracture. (E, F) Euhedral pyrite growing around an ilmenite grain in a dolomite (type III) cemented sandstone.

Photo-micrographs

Samples BB-106, AA-159A, CC-8B, BB-32 and AA-58.

Figure 107: Different degrees of pyrite cementation developed within intergranular pore space.

A, B: Partial cementation of sediment; clusters of pyrite cemented sand grains (RL).

C, D: Partial cemented sand: various density of pyrite microcrystals distribution fills intergranular pore space (RL).

E, F: Full cementation: dense packing of microcrystals fill the pore space of the sandstone (BSE).

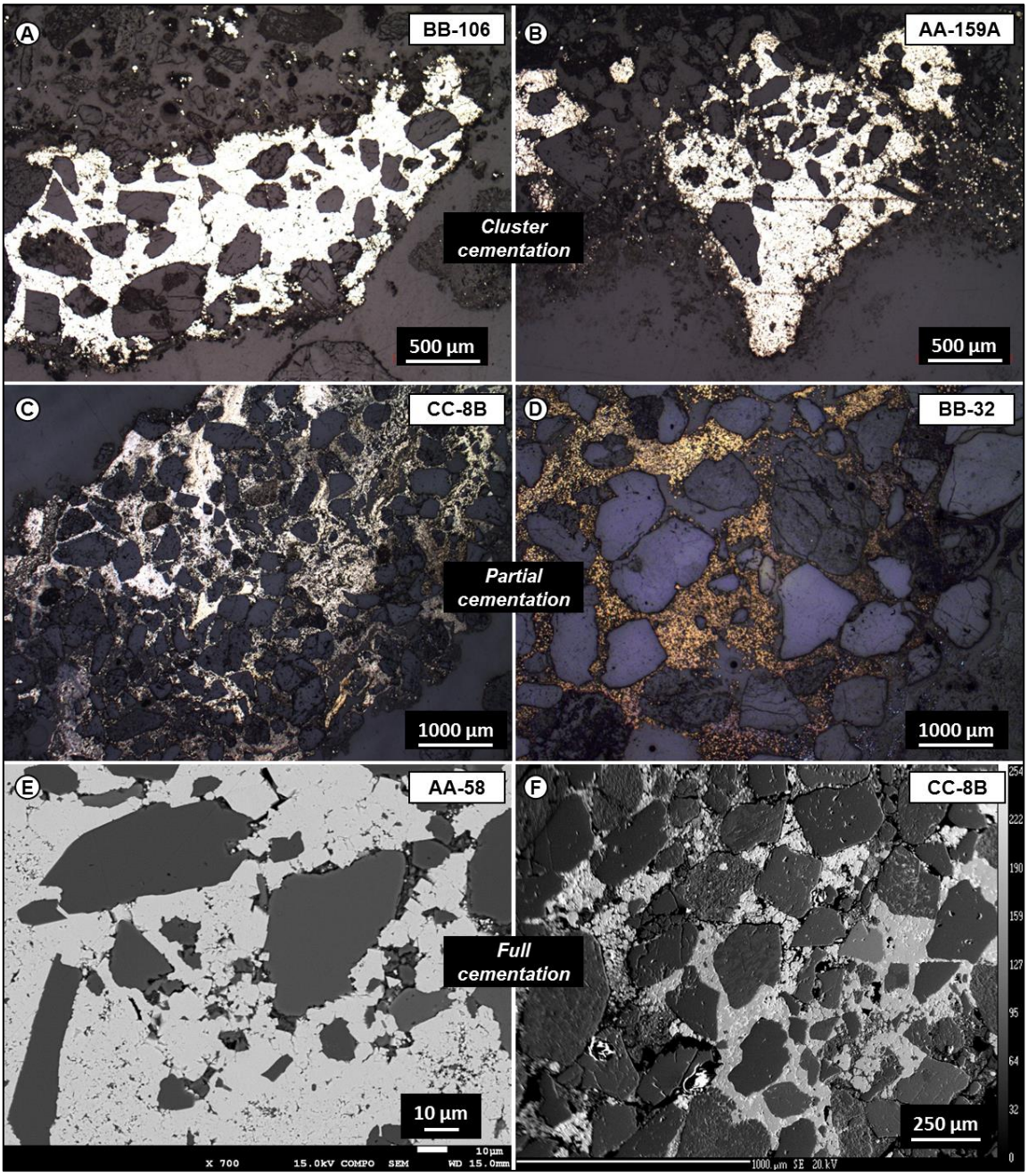

Figure 107: Different degrees of pyrite cementation developed within intergranular pore space.

5.2.1.7 Marcasite on isolated euhedral pyrite

In a single case (Profile SW-NE_01300**,** well ZOOV_0670, sample 9659 AA-172B, depth interval (m) 171,79-171,99) the polymorph marcasite (needle form) could be found around isolated cubic pyrite. Hence, marcasite appears before uranium precipitation. According to mineralogy textbooks it is formed as a response to oxidizing waters. However, marcasite formation requires more investigation.

Photo-micrographs

Figure 108: Examples of marcasite crystals growing around euhedral pyrite cubes.

Sample AA-172B.

A, B: Overview of the euhedral and automorphic pyrite crystals encompassed by the marcasite polymorph. Pitchblende and yellow product are also associated (LR).

C: Higher magnification of the euhedral and automorphic pyrite crystals encompassed by marcasite (LR).

D: A close view of the euhedral and automorphic pyrite having the marcasite polymorph around (BSE).

E: High resolution image of marcasite (RL) – see Figure 211 in APPENDIX I (Figures).

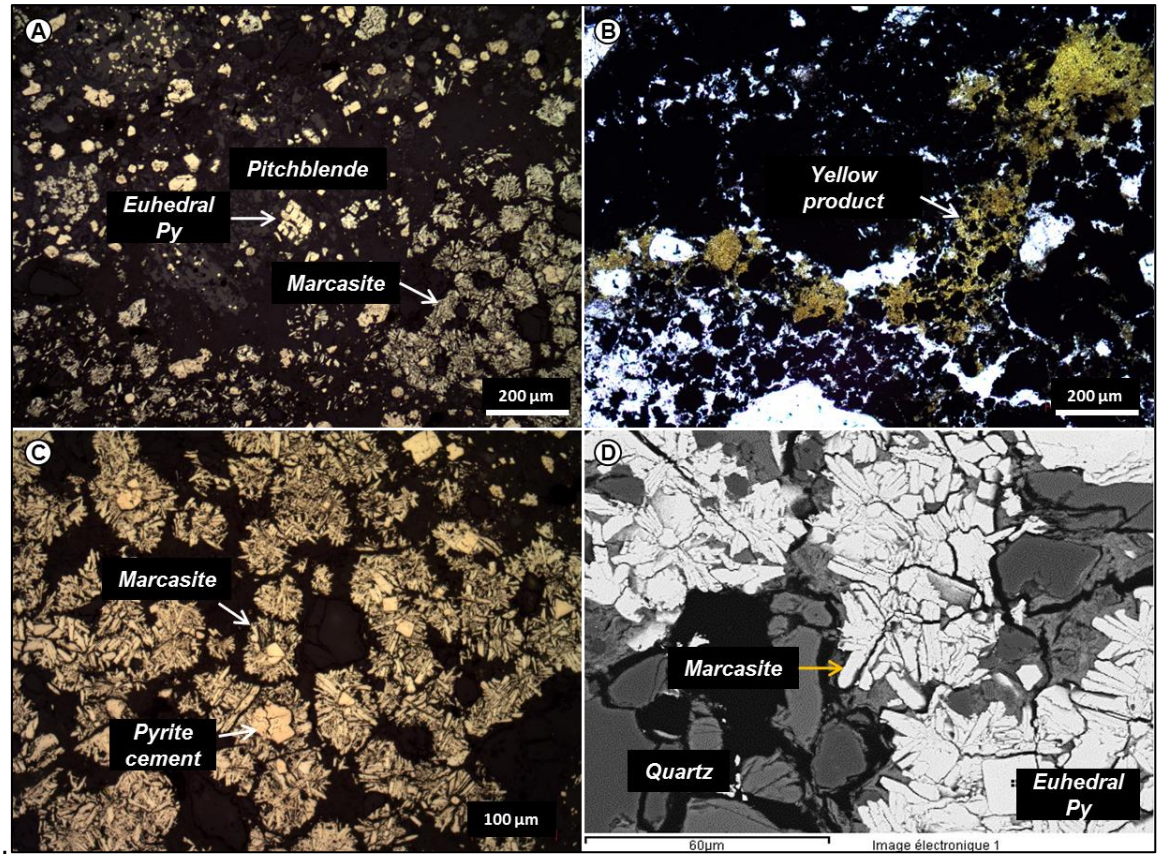

Figure 108: Examples of marcasite crystals growing around euhedral pyrite cubes.

5.2.1.8 Framboidal and Euhedral pyrite inside anhedral (Type IV) dolomite

The framboidal and euhedral pyrite types that are found inside the anhedral (Type IV) dolomite crystals must be a new generation of framboids and euhedral pyrite, respectively, since the anhedral dolomite post-dates uranium formation. These framboids always lack concentric overgrowths and the euhedral crystals are not well developed and they rather appear as pyrite cement.

They were identified only in two cases, listed below:

- Framboids and euhedral in Profile SW-NE_03600, well ZOOV_0886_11a, sample 9659 BB-138, depth interval 215,80-216,10
- Euhedral in Well ZOOV_0391_1_006, sample 9606-72, depth interval 117,35-117,45

Photo-micrographs

Figure 109: Examples of framboids and euhedral pyrite crystals associated to anhedral Type IV dolomite.

Samples 9659BB-138 and 9606-72.

A, B: Framboids at the size range of 5-10 μm without pyrite overgrowth inside anhedral dolomite (LPA, RL)

C: Framboids of variable sizes, from 5-30 μm inside anhedral Type IV dolomite. Different colors of pyrite occur after long-term contact of pyrite with atmospheric contact (RL).

D, E: Framboids of variable sizes, from 5-30 μm inside anhedral Type IV dolomite (BSE).

F: Euhedral pyrite around ilmenite possibly postdated by the growth of the anhedral dolomite, since a certain bending of the euhedral crystal is observed (BSE).

G, H: A close view of the euhedral crystals contained inside anhedral dolomite (LPA, RL).

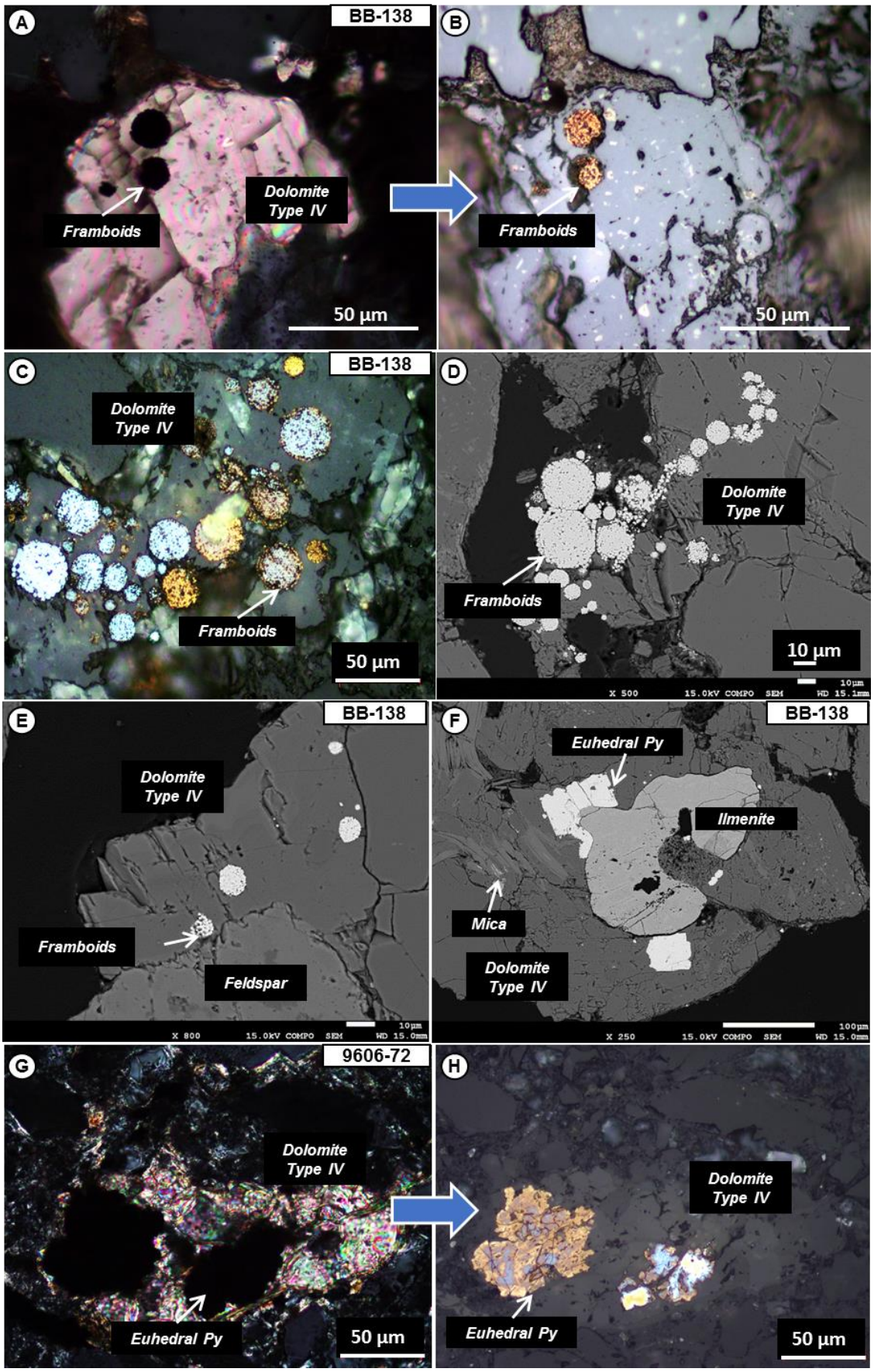

Figure 109: Examples of framboids and euhedral pyrite crystals associated to anhedral Type IV dolomite.

5.2.1.9 Other sulfides (Accessory minerals)

Other sulfides and associated minerals i.e. selenides and sulfates were also identified. These are presented below:

- Sphalerite (ZnS)
- Galena (PbS)
- Cadmium sulfide i.e. (CdS)
- Acanthite (Ag_2S)
- Barite ($BaSO_4$) and
- the selenides namely, clausthalite (PbSe) and stilleite (ZnSe)

Sphalerite is by far the most common sulfide after pyrite and was encountered quite often in mineralized samples. The other sulfides and associated minerals are found in minute quantities and they are most of the times contained in uranium rich samples.

In our database, sphalerite was identified in eight samples presented in **Table 8** below:

Table 8: Samples containing sphalerite indicating well number and depth interval.

Sample ID	Profile	Well	Depth interval (m)
AA-138	SW-NE_01300	ZOOV_0690_12	174,65-174,84
AA-154	SW-NE_01300	ZOOV_0682_7b	160,06-160,16
AA-159	SW-NE_01300	ZOOV_0676_4	172,13-172,23
AA-172A	SW-NE_01300	ZOOV_0670_3	171,79-171,99
BB-134	SW-NE_03600	ZOOV_0886_7	209,40-209,70
CC-6	Punctual Drills	ZOOV_1081_2_3	131,63-131,73
CC-8B	Punctual Drills	ZOOV_1080_1	179,00-179,05
CC-54C	Punctual Drills	ZOOV_1100_6	168,25-168,55

Sphalerite can contain pitchblende as fracture-filling cement or as spherical inclusions of 1 μm size. It definitely postdates the euhedral pyrite that does not contain uranium inclusions but is probably also post-diagenetic with regards to the pyrite that contains uranium inclusions, according to petrographic observations. The petrography of the pyrite with the U-inclusions was presented in chapter 5.2.1.5 Series (zonations/generations) of cubic (euhedral) pyrite and is further discussed here.

Sphalerite is also separated in two categories, the Cadmium rich and the Cadmium poor with the Cd concentration in the first being up to 14 wt% and down to 3 wt% in the latter. However, both sphalerite types contain pitchblende inclusions. In one case, particularly in sample AA-138 presented in the table above, the cadmium sulphide mineral (Greenockite/Hawleyite) was identified.

Photo-micrographs

Figure 110: Examples of sphalerite - euhedral pyrite - pitchblende relationships. All pictures under BSE.

Samples BB-134 and CC-8B.

A: Sphalerite cement post-dating euhedral pyrite without uranium.

B: Sphalerite cement associated to pitchblende. Uranium is filling the fracture in sphalerite and is post-diagenetic.

C: Highly contrasted image. Sphalerite cement with pitchblende inclusions post-dating euhedral pyrite (1) uranium and probably formed contemporaneously to the euhedral pyrite (2) with pitchblende inclusions. The dark-colored sphalerite variety is low in Cd whereas the brighter is richer.

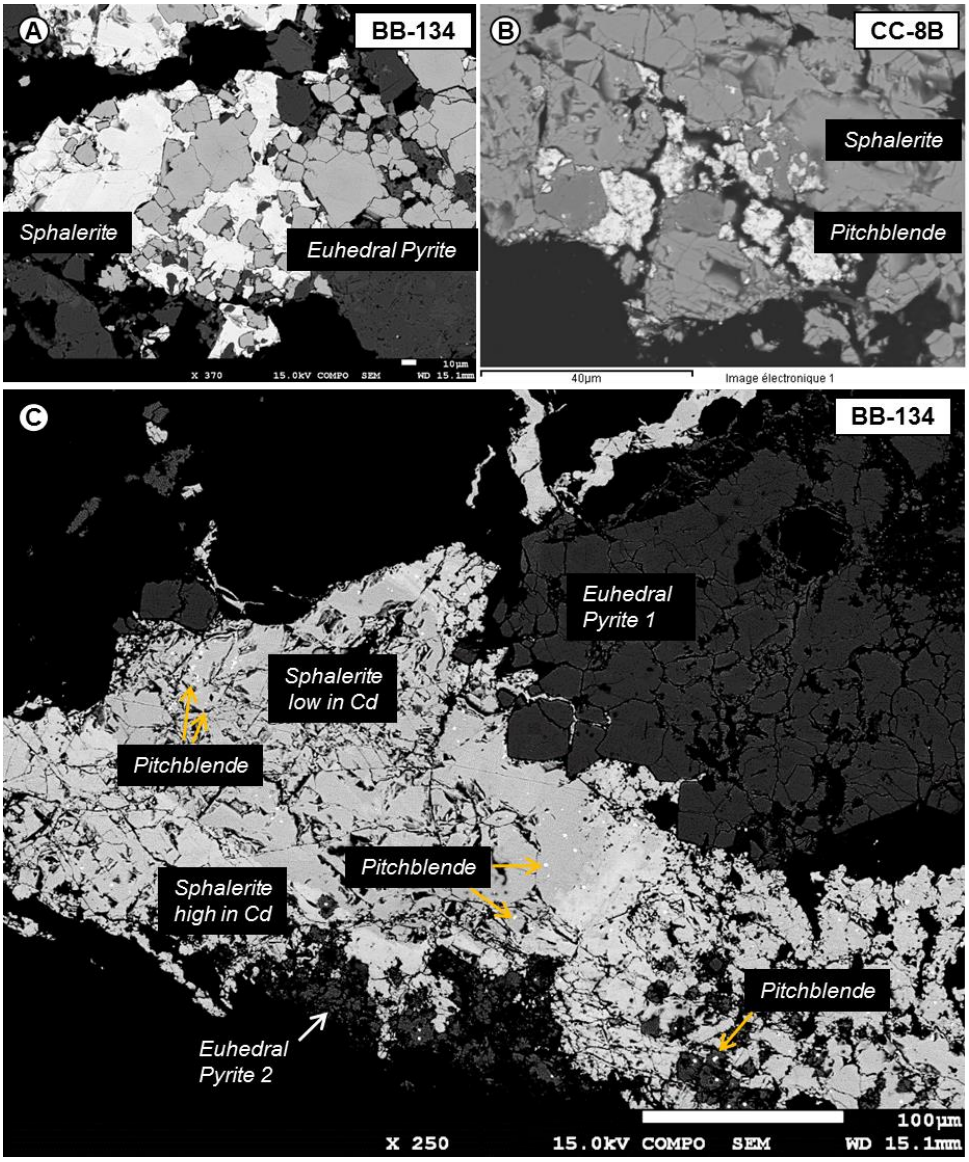

Figure 110: Examples of sphalerite - euhedral pyrite - pitchblende relationships. All pictures under BSE.

Photo-micrographs

Figure 111: Examples of other sulfides and associated minerals recognized in the Zoovch Ovoo sands.

Samples BB-97, AA-138, BB-134 and CC-54C.

A: Barite cement post-dating euhedral pyrite (BSE).

B: A single acanthite occurrence on the surface of a quartz grain inside clay matrix (BSE)

C: Euhedral galena inside intergranular porosity (BSE).

D: Pitchblende cement in clay matrix, containing Greenockite crystals (BSE).

E: Corroded euhedral pyrite associated to coffinitized pitchblende. Clausthalite is also present (BSE).

F: Stilleite assemblage inside clay matrix (RL).

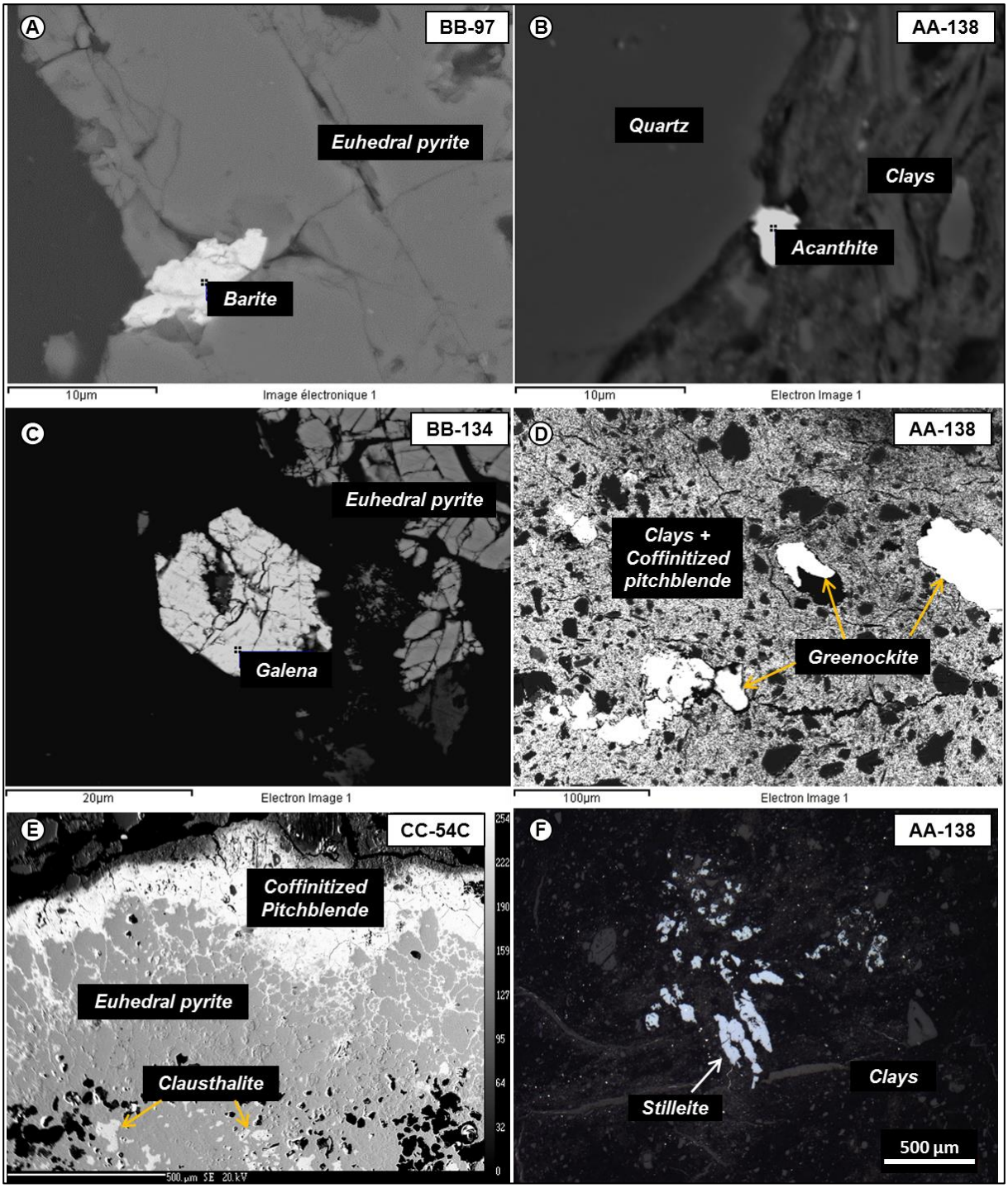

Figure 111: Examples of other sulfides and associated minerals recognized in the Zoovch Ovoo sands.

5.3 SUMMARY OF PYRITE PETROGRAPHY

By studying the petrography of pyrite in the available samples, it was possible to identify different occurrence of crystals, the following:

1. Isolated framboids.
2. Framboids embedded on organic matter (may occur contemporaneously to the isolated framboids).
3. Concentric overgrowth of framboids.
4. Growing of euhedral pyrite. Framboids embedded within cubic (euhedral) pyrite.
5. Isolated euhedral pyrite (may occur contemporaneously to the previous type).
6. Marcasite on isolated euhedral pyrite.
7. Several generations of euhedral pyrite forming zonations. A certain generation is crystallized contemporaneously to pitchblende precipitation.
8. Framboidal and euhedral pyrite inside anhedral (Type IV) dolomite.

Provided that the last category is excluded, since it is not clear if it is new or recycled from others, the pyrite generations can be summarized in Figure 112. It must be noted however that it is very difficult to correlate a given paragenetic stage from one sample to another. The number of successive paragenetic occurrences may vary because not all may have been recorded in samples, or because additional generations of pyrite growth may have occurred.

It may however be proposed that pyrite growth is a characteristic property of the reduced sediment, probably irregular through time and at least partly driven by bacterial activity.

It was possible to understand the paragenesis of pyrite and place the different types into a chronological order. Hence, the various kinds of occurrences may suggest the following paragenetic sequence:

1. Framboidal pyrite (irrespective of associated phases, i.e. organic matter, isolated, clays).
2. Concentric overgrowth of the framboidal pyrite.
3. Euhedral pyrite without pitchblende inclusions.
4. Marcasite around euhedral/anhedral pyrite without pitchblende inclusions.
5. Euhedral pyrite with pitchblende inclusions.
6. Framboidal pyrite post-dating uranium formation.
7. Euhedral pyrite post-dating uranium formation.

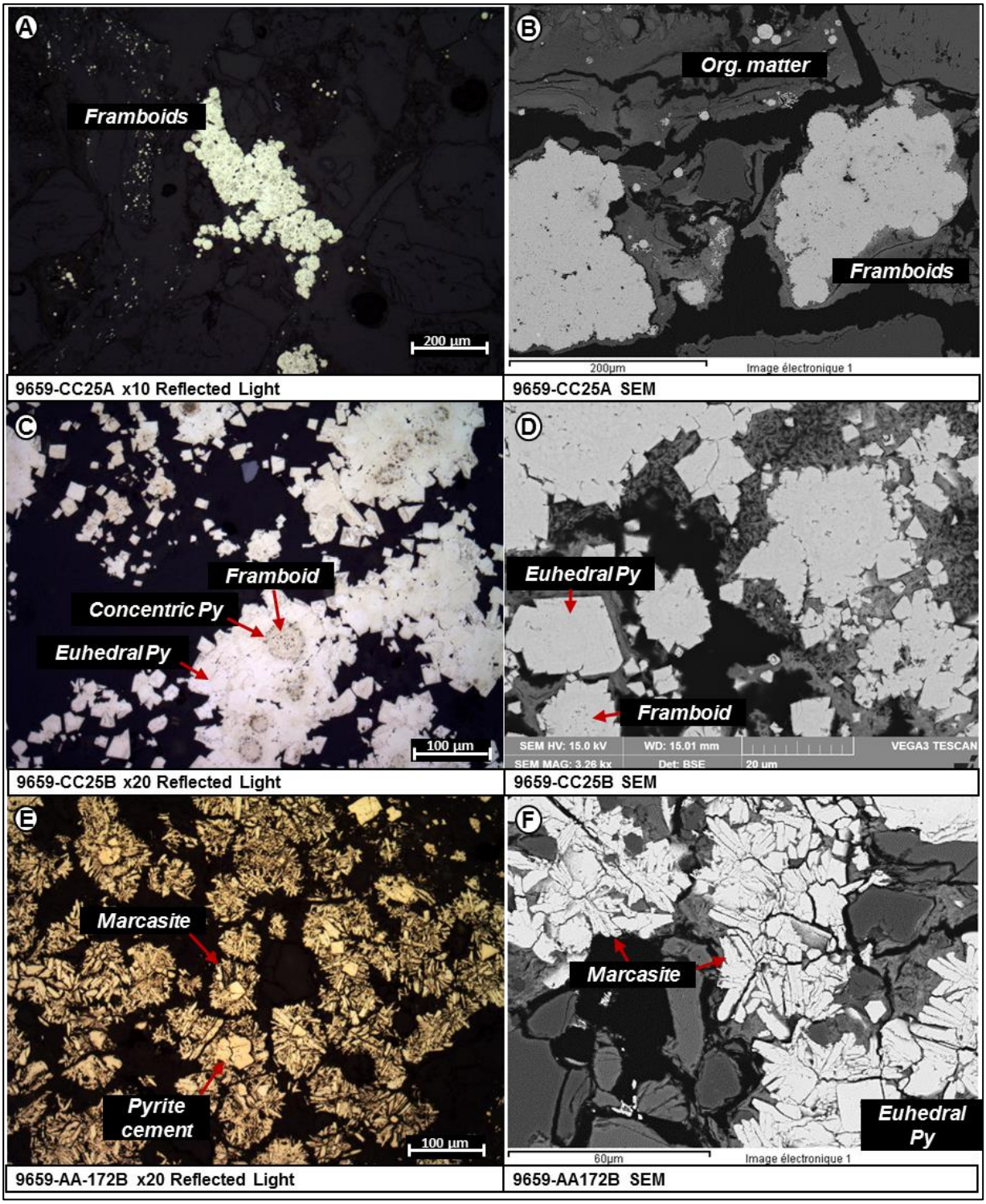

Figure 112: Examples of the most important FeS_2 textures recognized in the Zoovch Ovoo sands. (A) Isolated framboids. (B) Framboids with concentric overgrowth. (C) Framboids with concentric overgrowth, coated by euhedral pyrite. (D) Euhedral pyrite with four zonations (generations). (E, F) Euhedral and automorphic pyrite crystals surrounded by marcasite.

Other sulfides and associated minerals i.e. sulfates and selenides, were also identified. These are namely,

- Sphalerite (ZnS),

- Galena (PbS),
- Cadmium sulphide i.e. greenockite or hawleyite (CdS),
- Acanthite (Ag_2S),
- Barite ($BaSO_4$)
- Clausthalite (PbSe)
- Stilleite (ZnSe).

Special emphasis was put on sphalerite which is contained frequently and in large quantities in mineralized samples, while the rest are encountered rarely forming isolated crystals and are to date of no particular importance.

Due to the complexity of the pyrite occurrences described above, the spatial distribution of pyrite at the roll-front scale was done based on the major critical habitus i.e. framboidal, euhedral and their intermediate phases in the samples where both varieties were observed and finally the polymorph marcasite. These maps are available in Figure 113 and Figure 114. However, the pyrite types appear very mixed on the profiles and clear trends based on their petrography do not occur. It is noted that the spatial distribution of the samples coming from the punctual wells of the 9659 study (prefix CC-) and those from the 9606 study, were not possible to be projected on profiles. Also that a stratigraphic correlation between the different pyrite types projected on Profiles SW-NE_01300 and SW-NE_03600 was not yet elaborated.

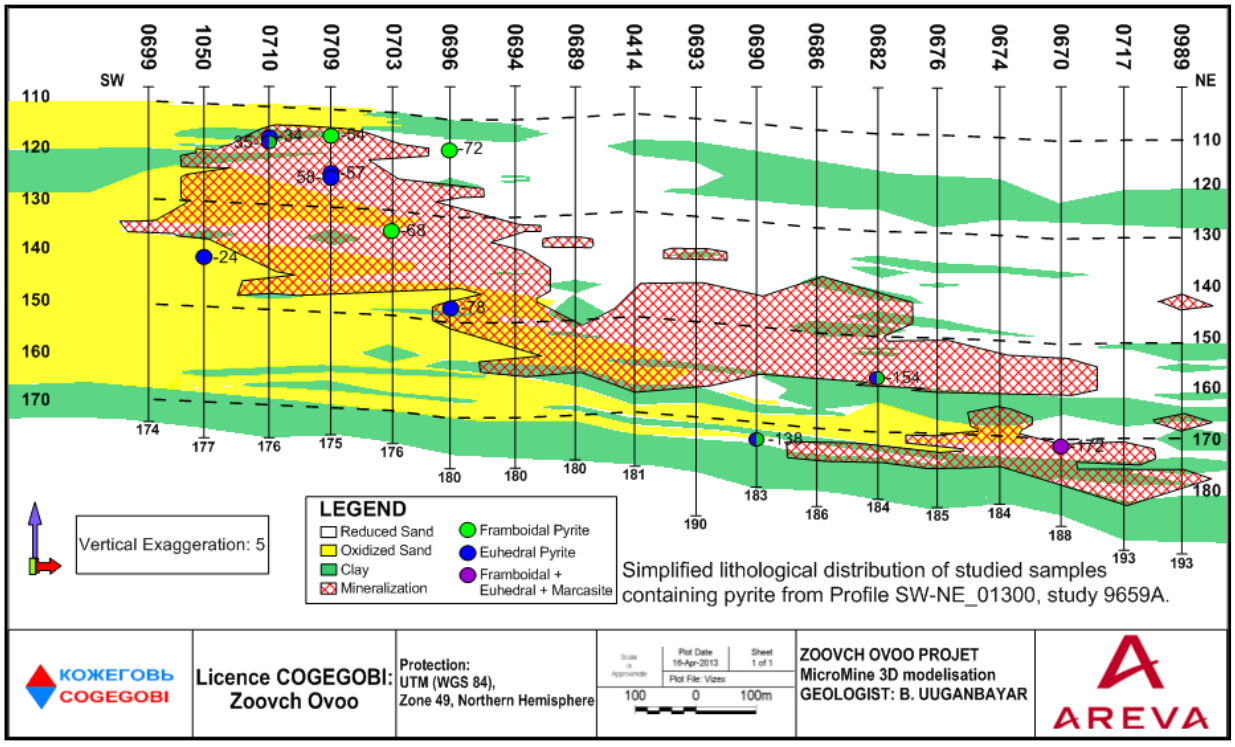

Figure 113: The spatial distribution and the abundance of the different pyrite types encountered along the Profile SW-NE_01300 in Zoovch Ovoo.

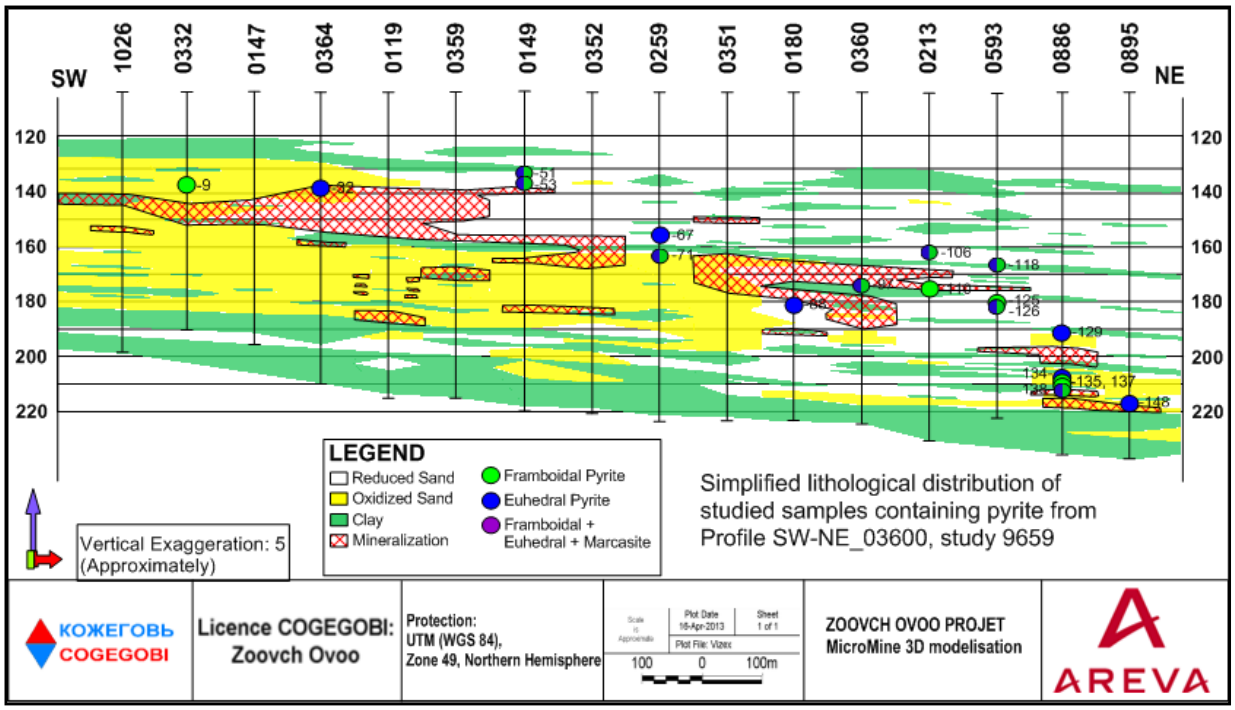

Figure 114: The spatial distribution and the abundance of the different pyrite types encountered along the Profile SW-NE_03600 in Zoovch Ovoo.

5.4 GEOCHEMISTRY OF SULFIDES

The different pyrite occurrences were studied by means of SEM-EDS, EPMA and LA/ICP-MS techniques. The results from the SEM-EDS indicate that certain pyrite phases i.e. the polymorph marcasite and certain euhedral pyrite phases are As enriched. The EPMA is limited to concentrations above 0.01 wt% (100 ppm) and ultimately could not provide with precise information, required for the trace element study. On the other hand by studying the same pyrite occurrences by means of LA/ICP-MS, it was possible to identify several geochemical trends for the following trace elements As, Co, Cd, Ni, V, Zn, Pb, Ag, Mo and Cu. Several plots were constructed from these trace elements. It was observed that the morphology of pyrite i.e. framboidal or euhedral plays minor role on trace element concentration, while in every plot there are always at least two trends visible, the first with pyrite being depleted and the second being enriched in certain trace elements, always irrespective of morphology. All the numerical data can be found in section APPENDIX II (TABLES – numerical data), summary of the LA/ICP-MS study used to construct the trace element plots (Table 27), summary of the EMPA (Table 28) and detailed measurements of the EMPA (Table 29).

5.4.1 Trace elements of Pyrite

Thirteen samples were analysed by means of EMPA to identify the crystal chemistry of the sulfides, mainly of pyrite and in a few occasions sphalerite. To better describe the trace elements, seven of the thirteen samples that were analysed with the EPMA, were also analysed by means of LA-ICP-MS according to the following suite, V, Co, Ni, Cu, Zn, As, Se, Mo, Ag, Cd, Sb, Pb, using four different FeS_2 types standards. The framboidal pyrite, the euhedral pyrite, the marcasite, the euhedral pyrite associated to U cement and a few sphalerite occurrences were used for this study. The concentric pyrite (overgrowth) was not considered as a separate phase from the framboidal due to its very low thickness.

All pyrite occurrences were stoichiometric (Fe:S=1:2) with an acceptable deviation of 0.05 to 0.10 from pyrite stoichiometry (analytical bias). Sometimes when it is in the form of micro-pyrite as a complex inside the organic matter and therefore not visible or if it is associated to U then it is non-stoichiometric. The V and Zn are contained in concentrations up to 200 and 100 ppm, respectively for a few analysis and they are usually below 50 ppm. The Mo concentrations are much diversified. They can be contained from below detection limit to up to 3300 ppm and it is not clear if there is a trend between the different pyrite types with the current number of analyses. With respect to Cu, there is a trend between the framboidal and the other types of pyrite. In some samples Cu was systematically detected on framboids around 1000-3000 ppm but in other samples it was detected below 20 ppm. For the other types of pyrite, Cu is systematically below 100 ppm but it can reach up to 500 ppm. The Se is usually below the

detection limit but in certain cases both in framboidal pyrite and the other types it can reach 2000 ppm. The Cd and Sb are most of the times below 100 ppm. The Pb was detected in many different concentrations up to 6600 ppm, and may correspond partially to radiogenic Pb.

To better illustrate the results from the pyrite study (LA/ICP-MS), certain geochemical plots were constructed. The results were obtained after detailed petrographic analysis of the pyrite habitus, aiming every time to relate the pyrite with other phases, i.e. organic matter, uranium, anhedral dolomite (Type IV) being post-diagenetic to uranium precipitation, sphalerite or marcasite. The pyrite phases that are associated to uranium in this study are:

i. Framboids inside U-replaced organic matter.
ii. Euhedral pyrite surrounded by uranium cement.
iii. Undifferentiated framboids-euhedral pyrite inside uranium cement.
iv. Framboids inside anhedral dolomite (Type IV).
v. Euhedral pyrite inside anhedral dolomite (Type IV).

Other phases that were cross-plotted among the different pyrite phases are:

i. Marcasite.
ii. Euhedral pyrite associated to marcasite.
iii. Sphalerite,

all of which often showing a certain enrichment in trace elements that follows the trend of the uranium associated pyrite.

The five plots that will be presented below are namely:

i. Co vs Cd
ii. Ni+Co vs As
iii. Ni vs V
iv. Zn+Cd vs Pb+Ag
v. Mo+Cu vs V+Ni

Co vs Cd plot

In the Co versus Cd plot (Figure 115) there are about five trends visible:

- First of all the **pyrite**, irrespective of morphology that is not associated to uranium, i.e. isolated or framboids and euhedra related to organic matter, is totally depleted in both Co and Cd.
- On the contrary, the **pyrite** that is associated to uranium shows a progressive enrichment in Co (few ppm to 90 ppm), probably linked to roll-front activity and Cd (few ppm to 5500 ppm).
- The euhedral **pyrite** associated to marcasite is medium rich in Cd (1000-3000 ppm) but is the richest in Co (100-190 ppm).
- In oppose of euhedral pyrite associated to marcasite, the **marcasite** itself is very lean in Cd and Co.
- Finally, the euhedral **pyrite** associated to sphalerite is very lean in Co but can contain up to 10.000 ppm of Cd, which was also the case for sphalerite.

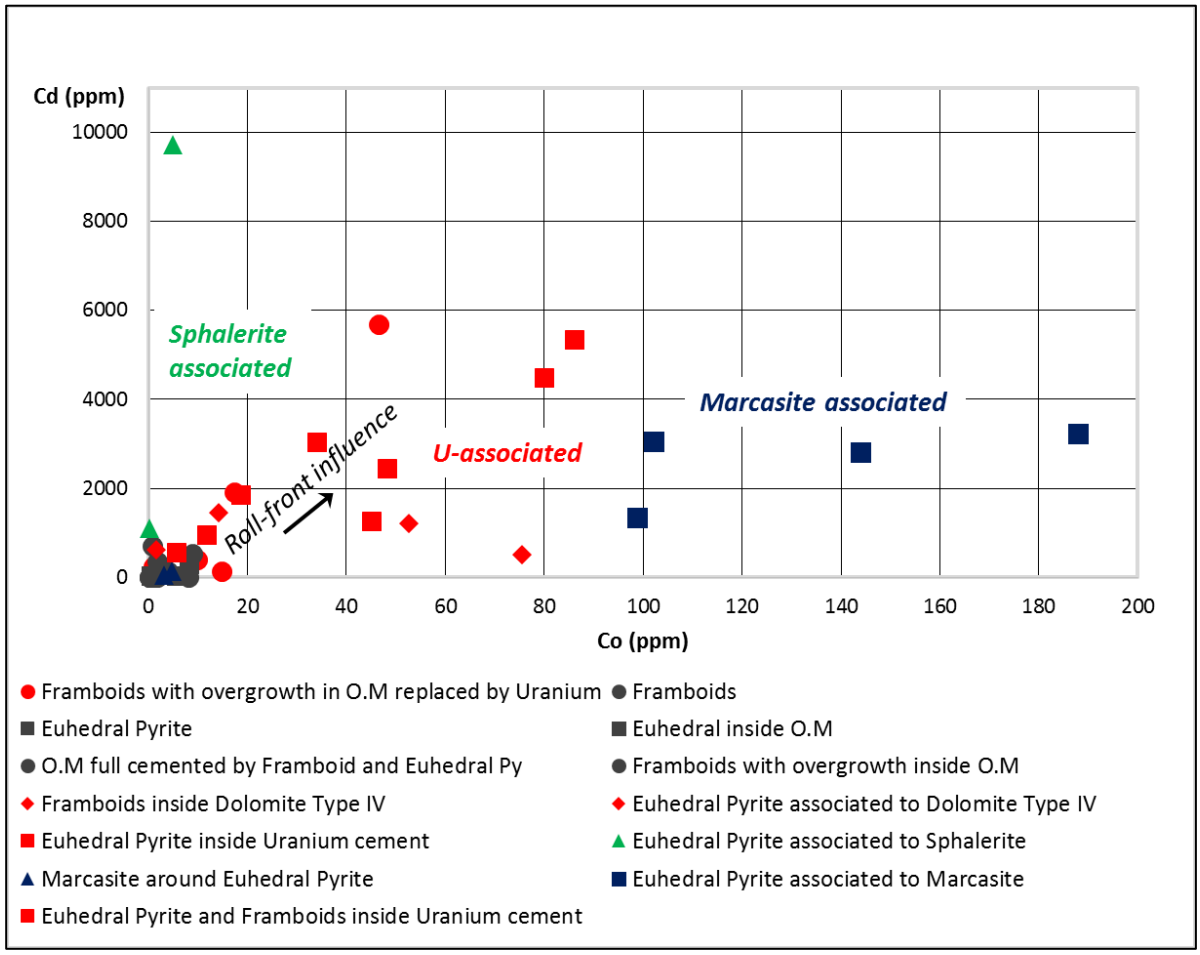

Figure 115: Co versus Cd plot. It is possible to separate the pyrite associated to uranium (in red) that is enriched in Co and Cd whereas the pyrite not linked to uranium (in grey) is depleted. Some framboids that are found inside U-rich organic matter are also richer in Co. Finally, the euhedral pyrite associated to marcasite is enriched in Co while that associated to sphalerite is enriched in Cd.

Ni+Co vs As plot

In the Ni+Co versus As plot (Figure 116) there are two major trends visible:

- First of all the As concentration fluctuates for all pyrite types (plus **sphalerite**) from a few ppm to up to 8000 ppm. Exception is the polymorph **marcasite** which is enriched in As (14.000 ppm).
- Most of the **pyrite** not associated to uranium is plotted at the left hand side with Ni+Co concentration accounting for less than 2000 ppm, although some of them can be as rich as 5000 ppm.
- On the contrary, the **pyrite** that is associated to uranium is plotted at the right hand side with Ni+Co concentration starting from 2000 and reaching up to 30.000 ppm.
- The **marcasite** associated euhedral pyrite has about 8000-10.000 ppm in Ni+Co and 2000 ppm in 2000 ppm in As. The sphalerite associated **pyrite** is at 8000-50.000 ppm in Ni+Co, which is the richest concentration and sphalerite is richer in As than the associated pyrite.

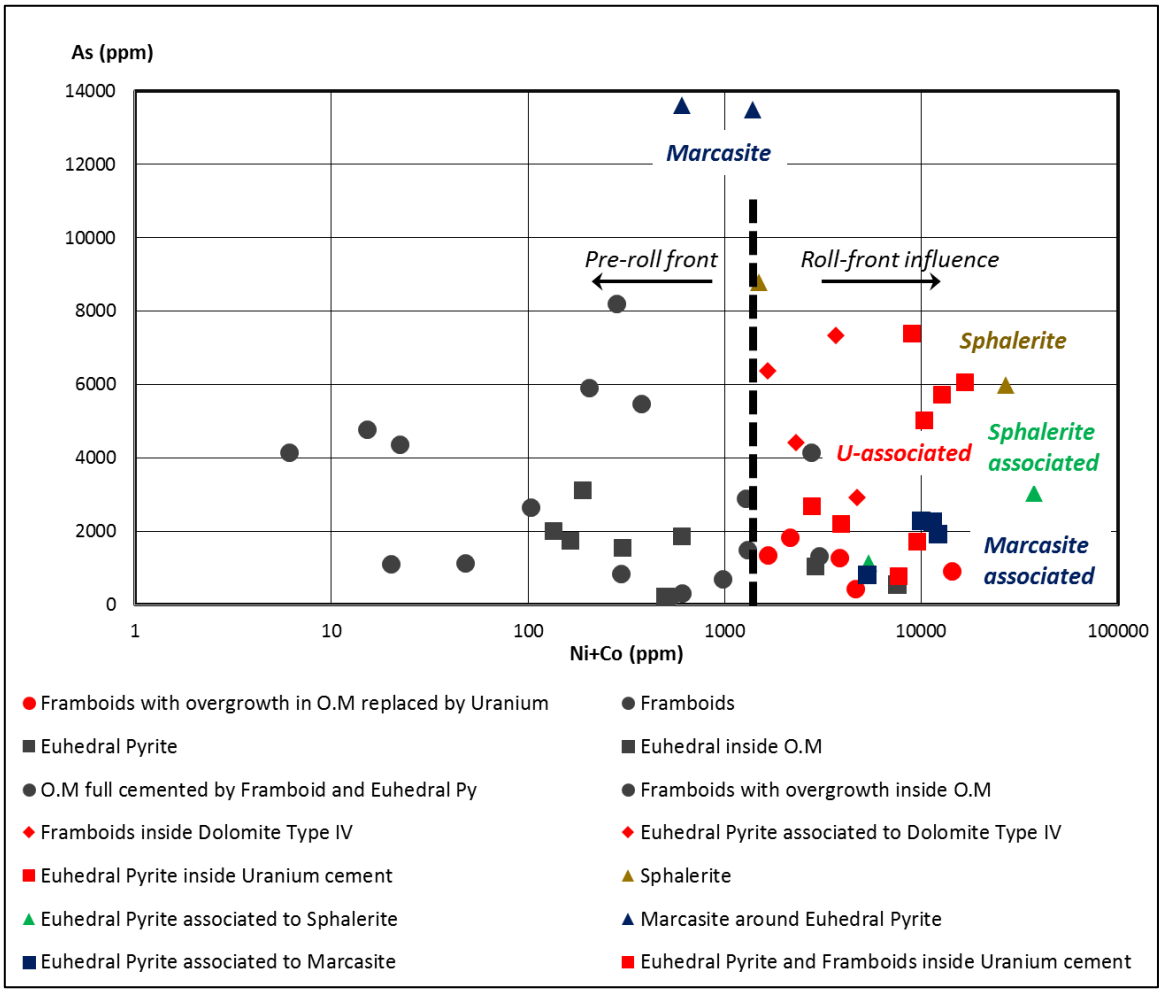

Figure 116: Ni+Co versus As plot for the different pyrite habitus. X axis in logarithmic scale. Red labels: framboidal pyrite with U and euhedral pyrite inside U cement. Grey labels: pyrite not linked to U. Sphalerite and marcasite follow the U-associated pyrite compositions.

Ni vs V plot

In the Ni+Co versus As plot (Figure 117) there are again two major trends visible:

- The first trend at the left side of the dashed line (below 1000 ppm in Ni) concerns the **pyrite** phases not associated to uranium, although locally there are occurrences richer in Ni (up to 8000 ppm). The latter can be transitional or intermixed phases. The V concentration remains constantly lower than 50 ppm.
- The second trend at the right side of the dashed line concerns the **pyrite** associated to uranium (between 1000-11.000 ppm in Ni), the sphalerite associated **pyrite** which is the richest in Ni, the marcasite associated **pyrite** which follows the uranium associated trend and the **marcasite** which fluctuates at the transition zone. With regards to V, the uranium associated **pyrite** can be locally enriched with concentrations up to 220 ppm, while the **sphalerite** is the richest and the marcasite and marcasite associate **pyrite** are totally depleted.

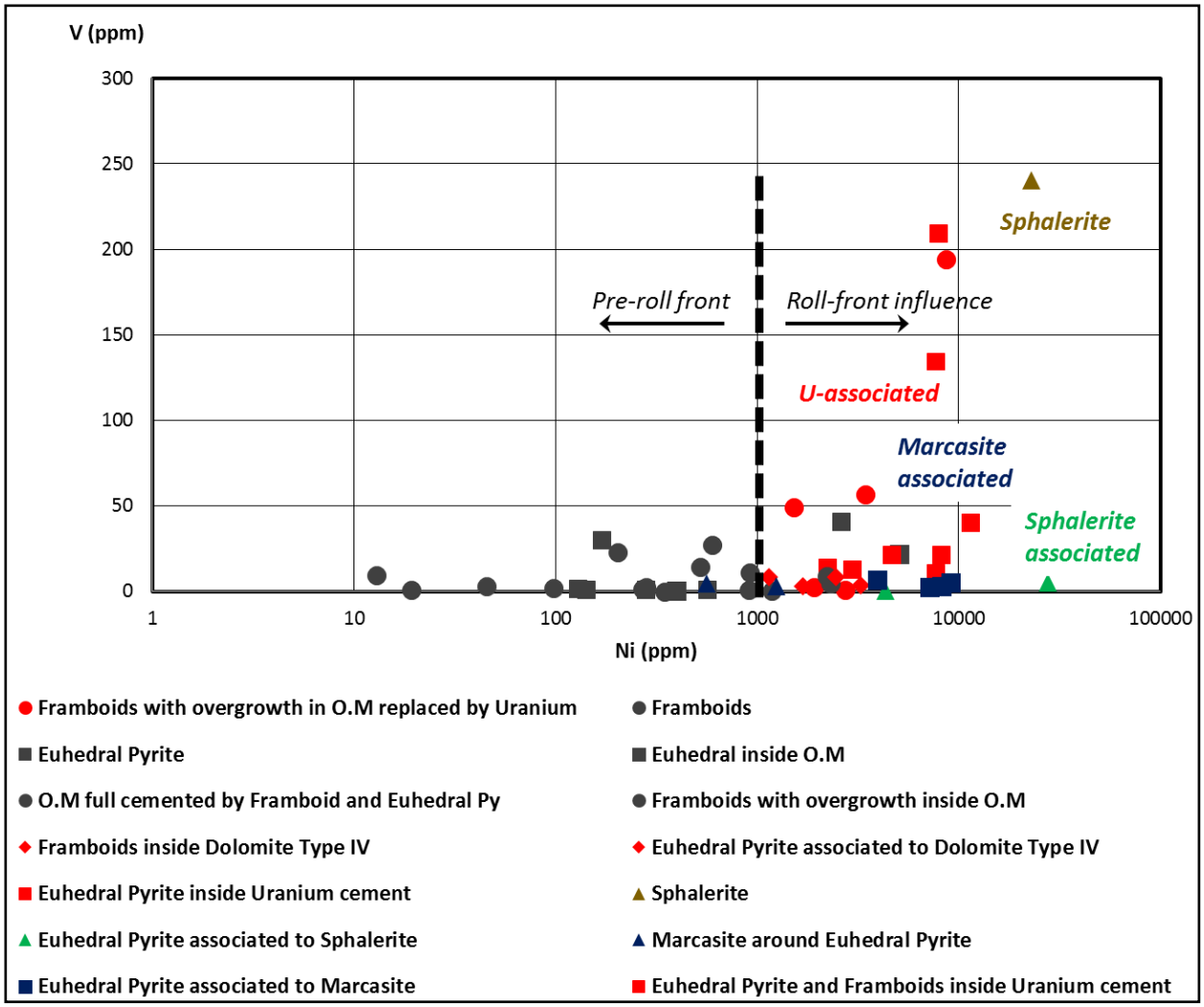

Figure 117: Ni versus V plot for the different pyrite habitus. X axis in logarithmic scale. Red labels: framboidal pyrite with U and euhedral pyrite inside U cement. Grey labels: pyrite not linked to U. Sphalerite and marcasite follow the U-associated pyrite compositions.

Zn+Cd vs Pb+Ag plot

The Zn and Cd as well as the Pb and Ag are elements that are often associated with each other. Hence, they were selected to create the following plot. In the Zn+Cd versus Pb+Ag plot (Figure 118) there are two major trends visible:

- First of all the **pyrite** phases not associated to uranium are either depleted or show a progressive enrichment in Zn+Cd (up to 50 ppm) and Pb+Ag (up to 1350 ppm), which can reflect a transition to the U-associated pyrite phases.
- The U-associated **pyrite** phases are enriched in both Zn+Cd (up to 90 ppm) and Pb+Ag (up to 1600 ppm). The richest U-associated **pyrite** phases it the framboidal pyrite inside dolomite Type IV, while the euhedral pyrite found in the same dolomite is the leanest and is plotted at the barren zone.
- By far the richest pyrite phase is the euhedral **pyrite** associated to marcasite that has concentrations between 120-250 ppm for Zn+Cd and 2000-6500 ppm for Pb+Ag and was thus plotted in a separate plot. On the contrary **marcasite** is plotted at the barren zone.
- The sphalerite associated euhedral **pyrite** is also lean of the respective trace elements.

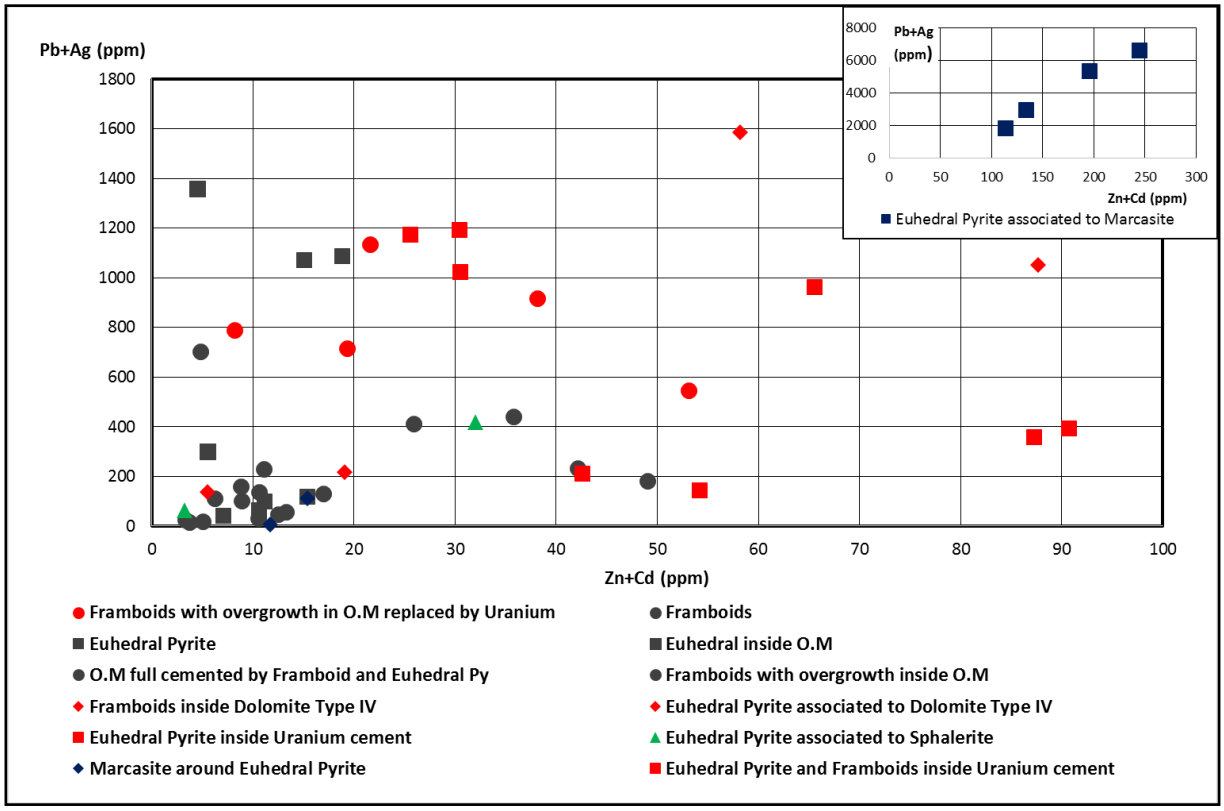

Figure 118: Zn+Cd versus Pb+Ag plot. In general the pyrite associated to uranium (red labels) is enriched in Zn, Cd, Pb and Ag as opposed to the pyrite not associate to uranium phases.

Mo+Cu vs V+Ni plot

In the Mo+Cu versus V+Ni plot (Figure 119) there are again two major trends visible:

- The **pyrite** phases not associated to uranium are plotted at the left side showing a general depletion in Mo+Cu, while for the V+Ni the concentration fluctuates between 20-2000 ppm. Minor exceptions can contain up to 5000 in Mo+Cu.
- The **pyrite** phases that are associated to uranium show similar concentration in V+Ni as the non-associated to U pyrite but are significantly enriched in Mo+Cu (2000-12.000 ppm).
- The **pyrite** associated to marcasite is also enriched in Mo+Cu following the U-associated pattern. On the other hand the **marcasite** is very lean.
- The **pyrite** associated to sphalerite can be very rich in Mo+Cu, locally at 27.000 ppm. In the same sense **sphalerite** can also be very rich 24.000 ppm and in V+Ni, exceeding 100.000 ppm.

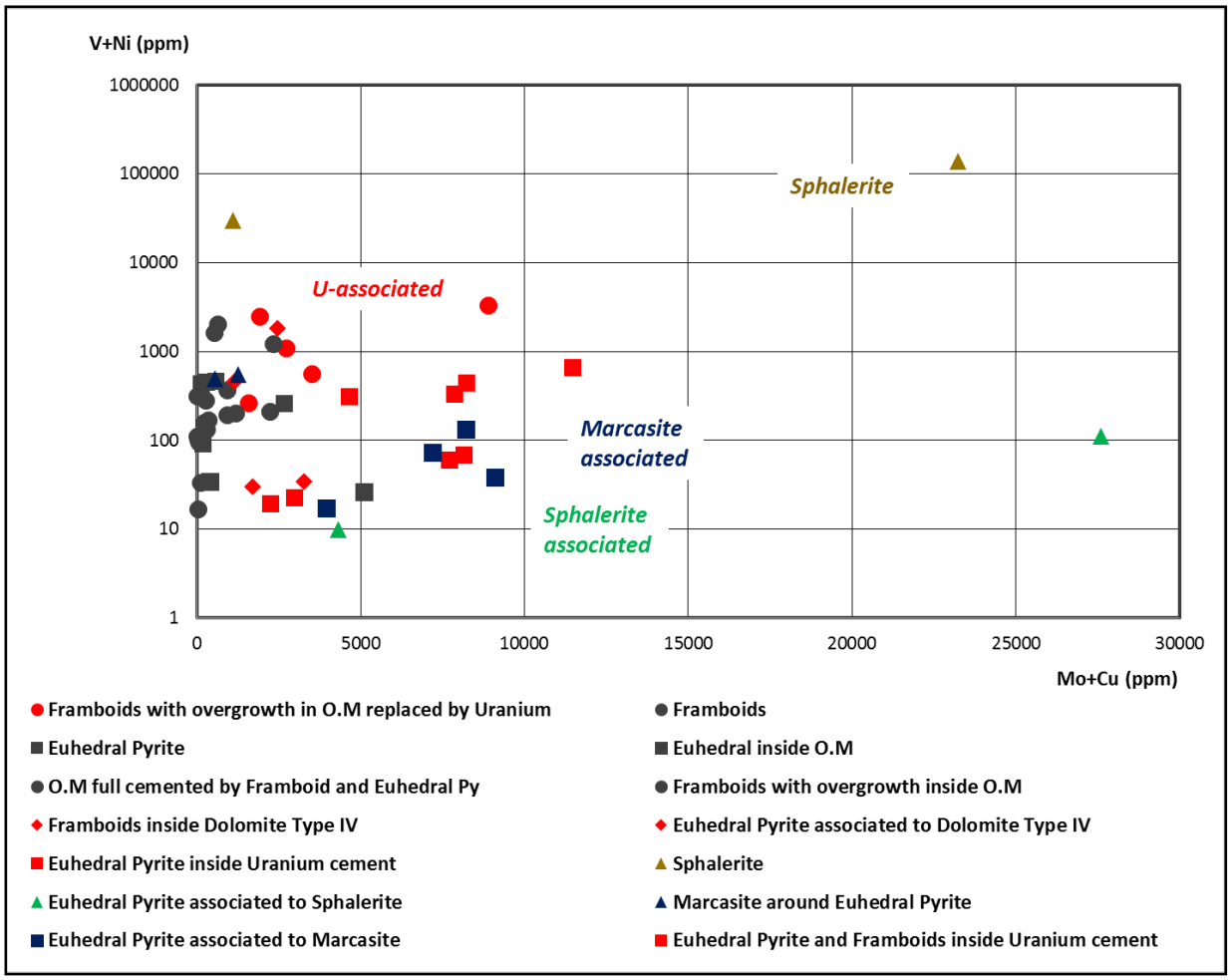

Figure 119: Ni+Co versus As plot for the different pyrite habitus. Y axis in logarithmic scale. In general the pyrite associated to uranium (red labels) is enriched in Mo+Cu as opposed to the pyrite not associate to uranium phases (grey labels). The V+Ni concentration is constant for both pyrite habitus.

5.5 ISOTOPIC CHEMISTRY - $\delta^{34}S$ OF PYRITE

After classifying the pyrite occurrences in terms of petrography and trace element content, it was necessary to perform the isotopic analysis to attempt to establish their paragenesis. Hence, a series of ion probe sessions (SIMS) were dedicated on pyrite isotopic chemistry in order to discover the origin of reduced sulfur. The analyses were performed in collaboration with CRPG Nancy and the Institute Jean Lamour. The samples studied were collected during the sampling campaigns, performed by M. Brouand between 2011 and 2014 at the Zoovch Ovoo site.

In detail, the *in-situ* micrometer scale $\delta^{34}S$ analyses of pyrite were performed in samples according to the pyrite habitus i.e. framboidal, concentric and euhedral as well as to their association to organic matter, marcasite and uranium and finally according to the position in the roll-front as presented in Table 9.

The distribution of the samples is provided in Figure 120. Most samples coming from profile SW-NE_01300 and are contained inside reduced lithologies whereas those coming from profile SW-NE_03600 are contained in “oxidized” lithologies, yet pyrite is still present.

Table 9: Descriptive list of the samples selected for the ion-probe (SIMS) session of $\delta^{34}S$ of pyrite. Background radioactivity at 75 c/s.

DDH Number (well Nº)	Nº PhD 9659	Depth	Redox status	Description	SPPγ (c/s)
Zoov_0709_7	A-54	119,14	reduced	Medium-coarse laminated sand, with organic matter and U-mineralization	1500
Zoov_0709_11	A-58	126,34	reduced		926
Zoov_0670_3	A-172	171,79	reduced	Medium sand with U-mineralization	5379
Zoov_0213_2	B-106	162,05	oxidized	Coarse sand, mineralized organic matter	169
Zoov_0213_1	B-110	175,34	oxidized	Medium-fine carbonate cemented sandstone	75
Zoov_0886_7	B-134	209,40	oxidized	Very coarse sand, mineralized organic matter	541
Zoov_0886_11a	B-138	215,85	reduced	Fine sand with laminae of organic matter / coarse sand	153
Zoov_0774_2	C-25	137,55	reduced	Mineralized organic matter between coarse and fine sand	6177

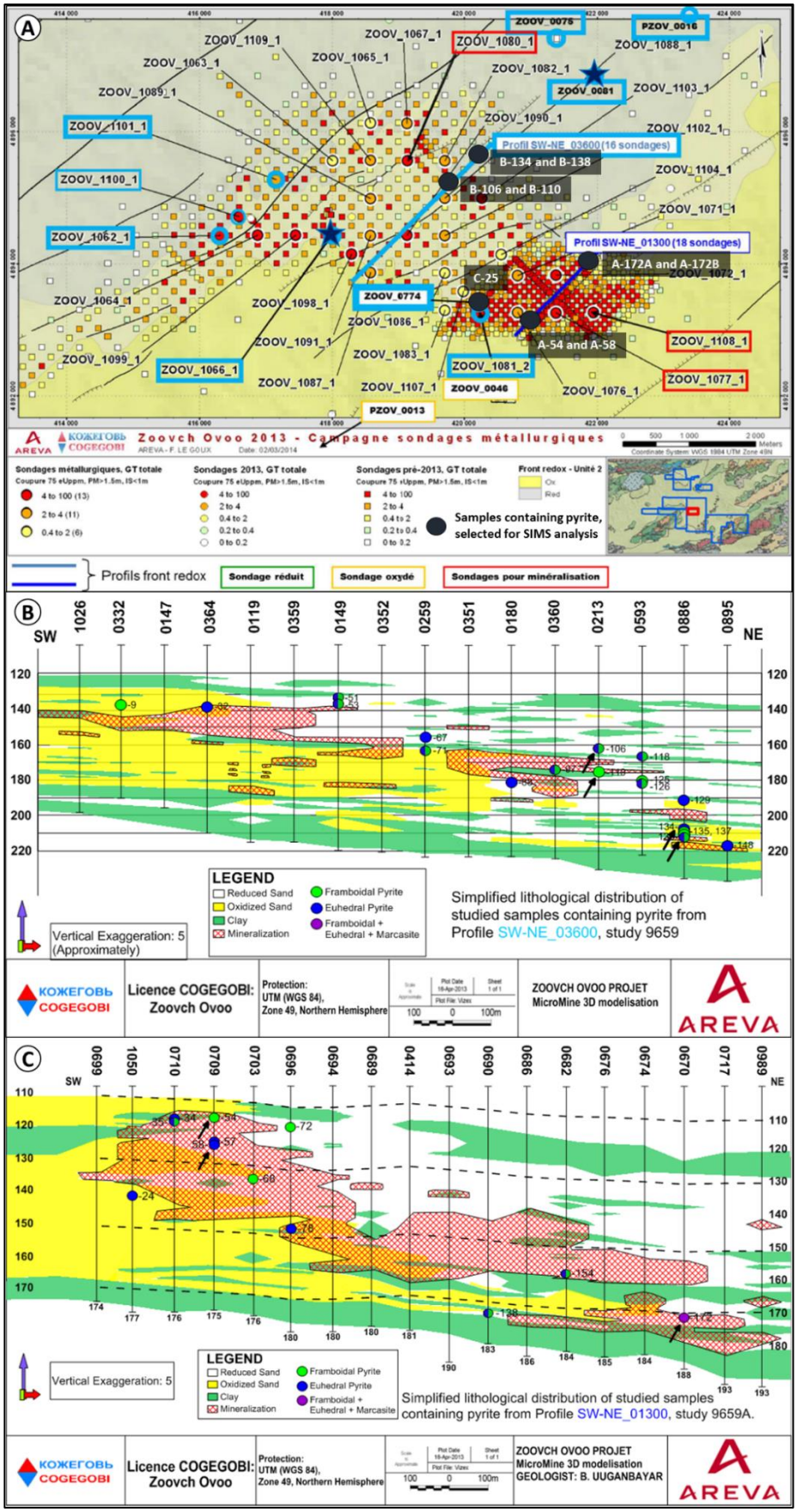

Figure 120: A) Map illustrating the drillings performed in Zoovch Ovoo, the location of the samples containing pyrite that were studied by SIMS is pointed by a black circles and arrows; B) Profile SW-NE_03600 and C) Profile SW-NE_01300.

The whole-rock polished blocks from which thin sections were prepared to be studied by the ion-probe are presented in Figure 121. The micro-photographs of the actual measurements, indicating the position of the beam on pyrite were moved to the APPENDIX I (Figures); Figure 213 to Figure 217. Most of the samples analysed are poorly consolidated sands, with an exception of a dolomite cemented sandstone.

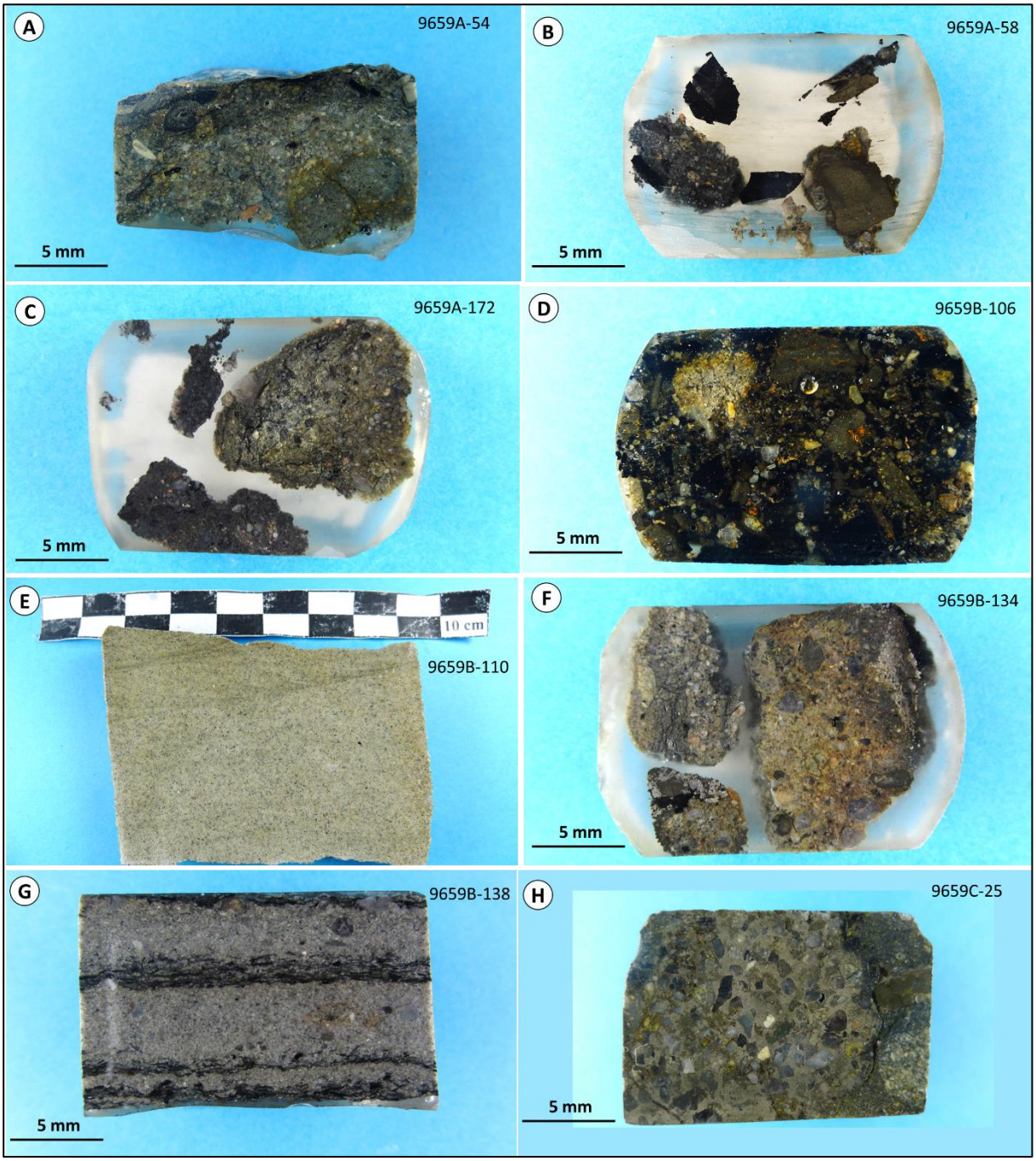

Figure 121: Presentation of the whole rock samples, studied by SIMS for $\delta^{34}S$.

5.5.1 Isotopic composition of $\delta^{34}S$ of pyrite

Detailed information on the pyrite facies contained in each sample with emphasis given on the relationship with the different generations as well as with organic matter and other mineral facies is presented in Table 9. Five of the studied samples contain uranium expressed as oxide, in most cases associated to the respective pyrite facies. As is evident, there is no particular trend between pyrite habitus and U-mineralization.

Table 10: Composition of the samples in terms of pyrite habitus, analyzed by SIMS. With red color the samples that contain relatively high quantity of uranium. Normalized versus in-house standard.

Nº/Morphology Pyrite	A-54	A-58	A-172A	A-172B	B-106	B-110	B-134	B-138	C-25
Isolated Framboids						X			X
Framboids with overgrowth			X						
Isolated Euhedral			X					X	
Euhedral cement	X		X		X		X		
Framboids surrounded by euhedral	X		X						
Euhedral around framboids			X			X			
Clusters of framboidal an euhedral pyrite (unresolved)		X	X						X
Euhedral to anhedral cement embedded in organic matter				X	X		X		X
Marcasite				X					
Euhedral surrounded by marcasite				X					
Framboids embedded in euhedral on organic matter					X				
Framboid embedded in euhedral cement					X				
Framboids in Type IV dolomite								X	

The total spread of all framboid occurrences for $\delta^{34}S$ (n=22) ranges between -40 and +52‰ (mean +6‰) with $\Delta^{34}S$ of 92‰ (Figure 122). Despite the very high spread the isotopic composition of framboidal pyrite is significantly shifted in overall towards the heavy fraction, compared to framboidal pyrite found in other roll-front deposits i.e. Lake Eyre Basin in

Australia from -43 to -18‰ (Ingham et al., 2014), Chu-Sarysu in Kazakhstan from -43 to -18‰ (Lach et al., 2015) and Baxingtu in China from -72 to -6‰ (Bonnetti et al., 2017).

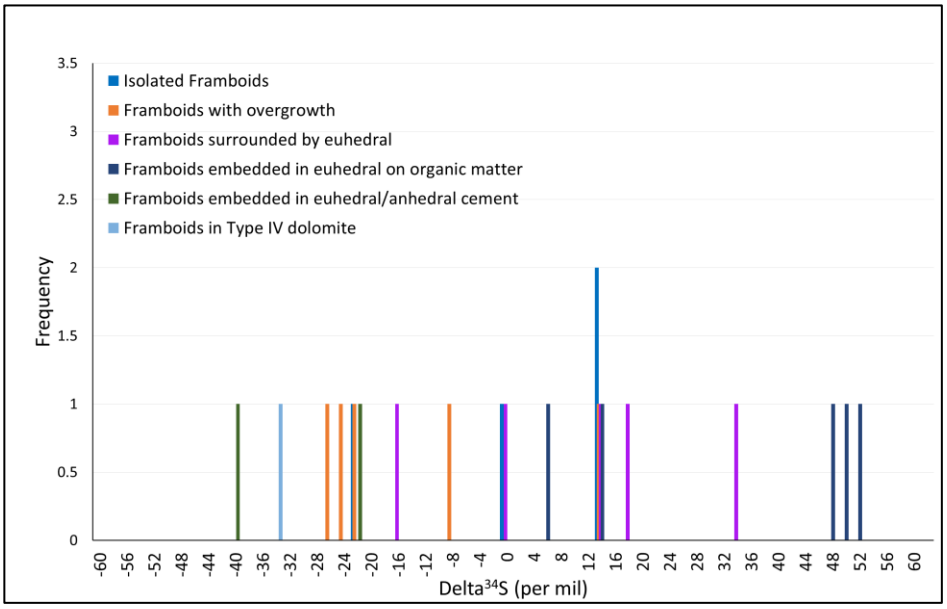

Figure 122: Distribution of $\delta^{34}S$ of framboidal pyrite in different cases with very wide distribution. The heavy end member refer to framboids embedded in organic matter with $\delta^{34}S$ at the range of +50±2‰. On the contrary, the light end member refers to framboids embedded in cubic pyrite to pyrite cement at the range of -31±9‰. Overall the $\delta^{34}S$ concentration is shifted towards the heaviest fraction.

The distribution of $\delta^{34}S$ of euhedral/cement pyrite (n=34) ranges from -50 to +34‰ (mean -8‰) with $\Delta^{34}S$ of 84‰ (Figure 123). Ore stage pyrite fluctuates between -42 and -22‰ (mean -32‰), which clearly indicates biogenic origin as was also reported by Lach et al. (2015) and Bonnetti et al. (2017) for similar deposits. Euhedral is compared to framboidal in Figure 124.

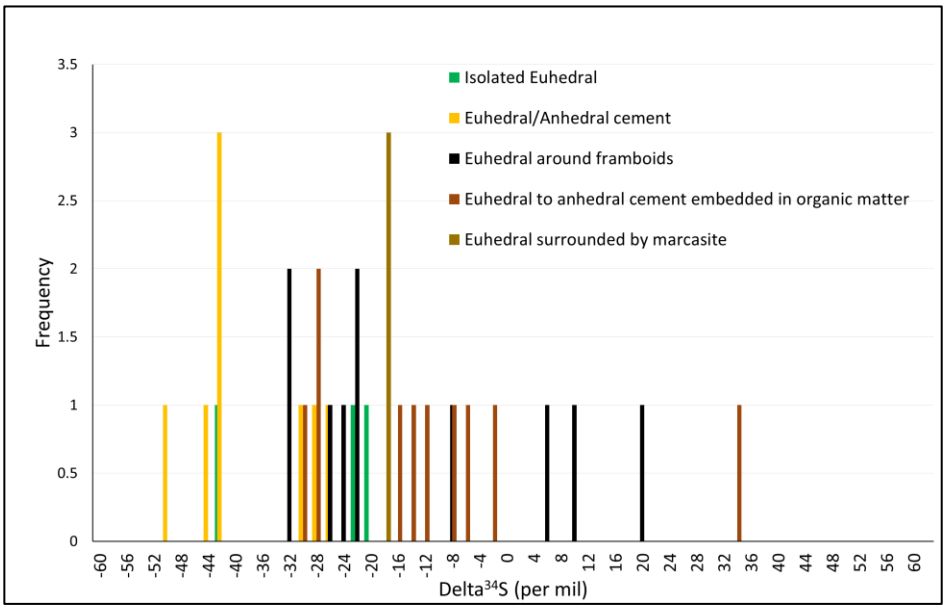

Figure 123: Distribution of the $\delta^{34}S$ of euhedral pyrite associated to other mineral and organic facies. Overall the $\delta^{34}S$ of euhedral pyrite is significantly lighter than framboidal pyrite and is hence shifted towards the lighter fraction. Positive values do exist but they are rarely above +20‰. On average the composition of euhedral pyrite fluctuates at -20±10‰.

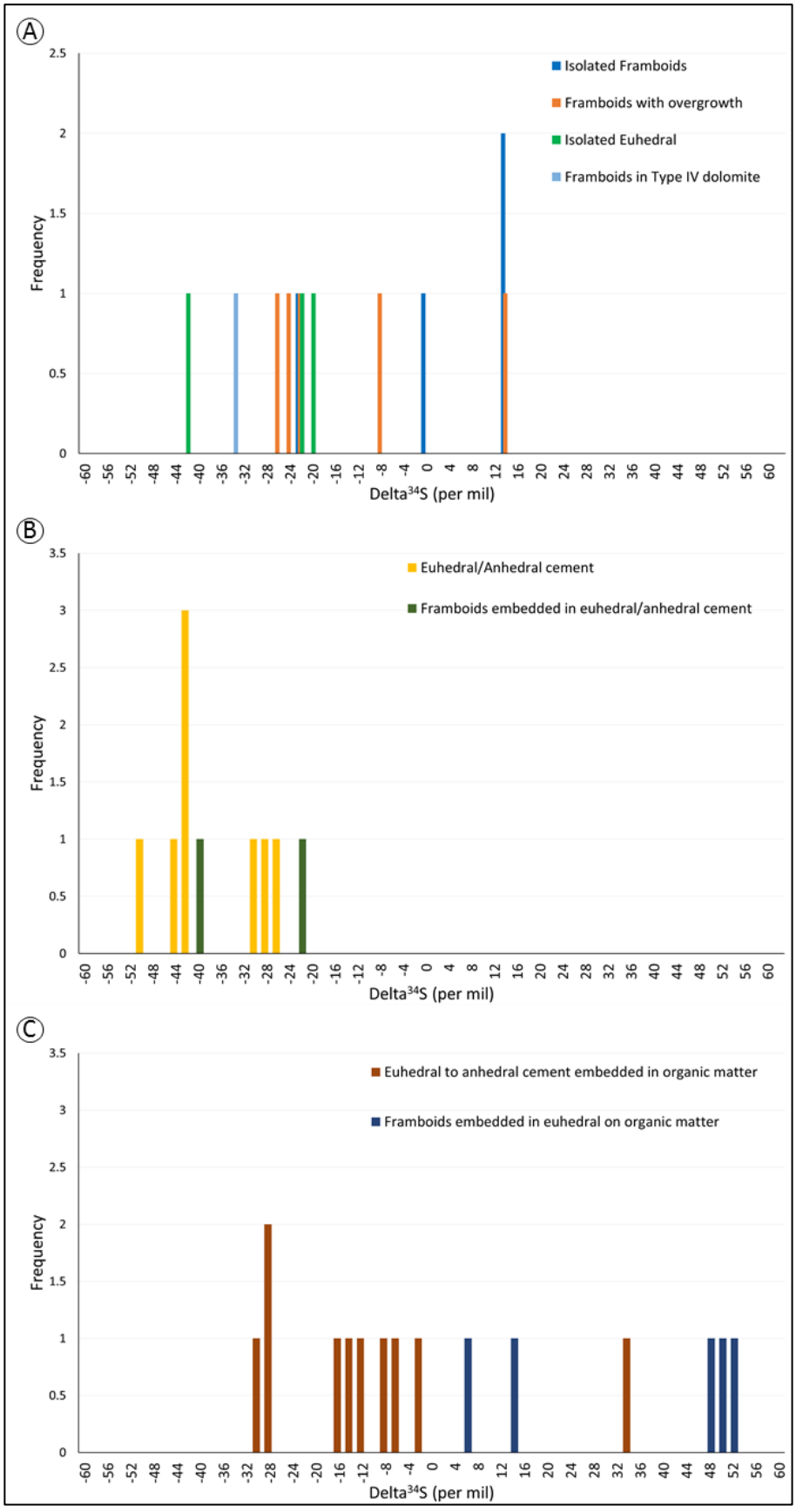

Figure 124: (A) Comparison between the isolated framboids, euhedral and the framboids associated to anhedral dolomite. (B) Comparison between the euhedral/infill cement and the framboids embedded at the center of the latter. (C) Comparison between euhedral and framboidal pyrite embedded in organic matter.

As illustrated in Figure 124 and Figure 125 framboids have in general the tendency to be slighter heavier in $\delta^{34}S$ than euhedral or cement pyrite.

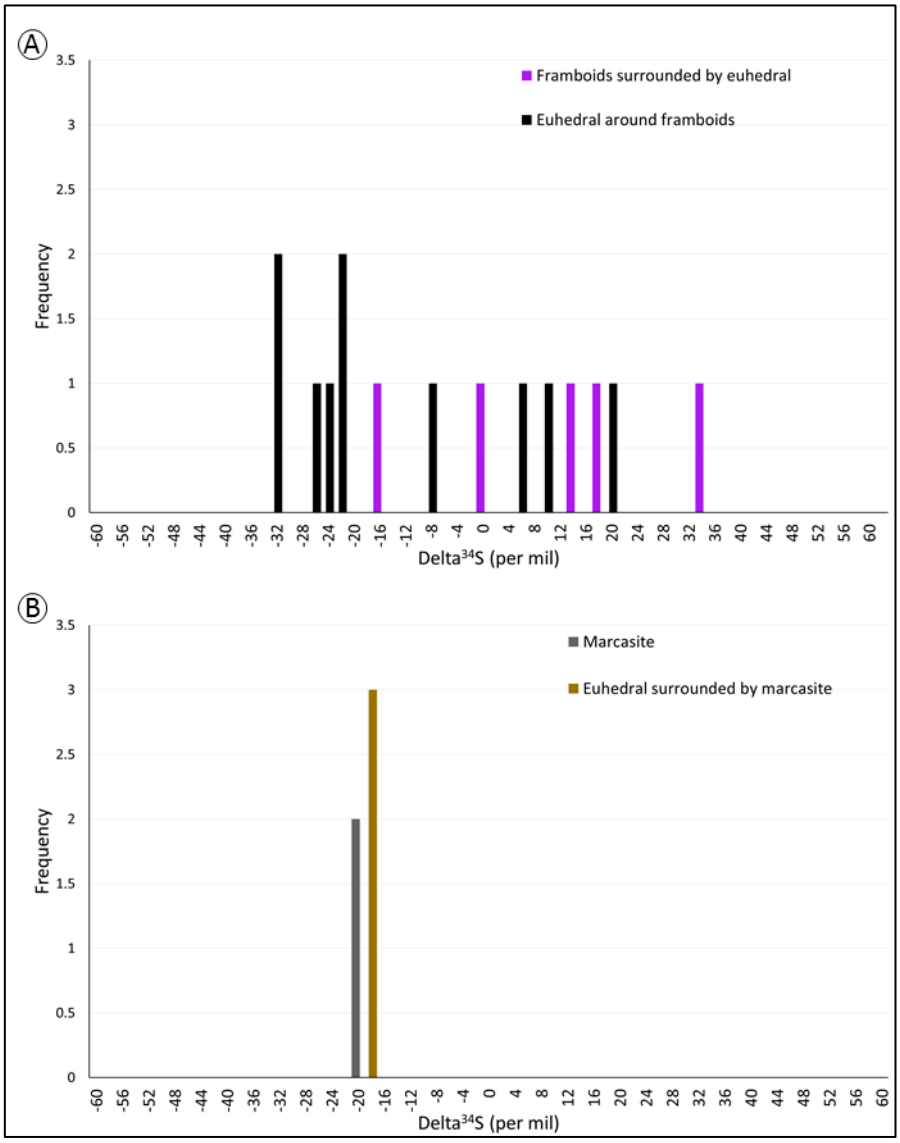

Figure 125: (A) Comparison between framboids surrounded by euhedral pyrite. (B) Comparison between euhedral pyrite surrounded by marcasite

Typically, when framboidal pyrite is embedded within euhedral pyrite it can have very different isotopic composition than its surroundings (Figure 126). In other words, the least complex framboids at the center of the clusters have strong positive isotopic signature from +47 to +49‰, while the surrounding euhedral/cement pyrite are at -6 to -15‰.

This large spread of $\delta^{34}S$ pyrite suggests an evolution of the fluid from isotopically heavy $\delta^{34}S$, with the strongly positive isotopic values of framboids probably linked to sedimentary pyrite (Kohn et al., 1998), to isotopically light $\delta^{34}S$ of euhedral/cement pyrite that is formed during maximum burial and ore stage. It is also noted that ore stage euhedral pyrite has a very typical biogenic signature, therefore bacteria are acting even during uranium ore formation.

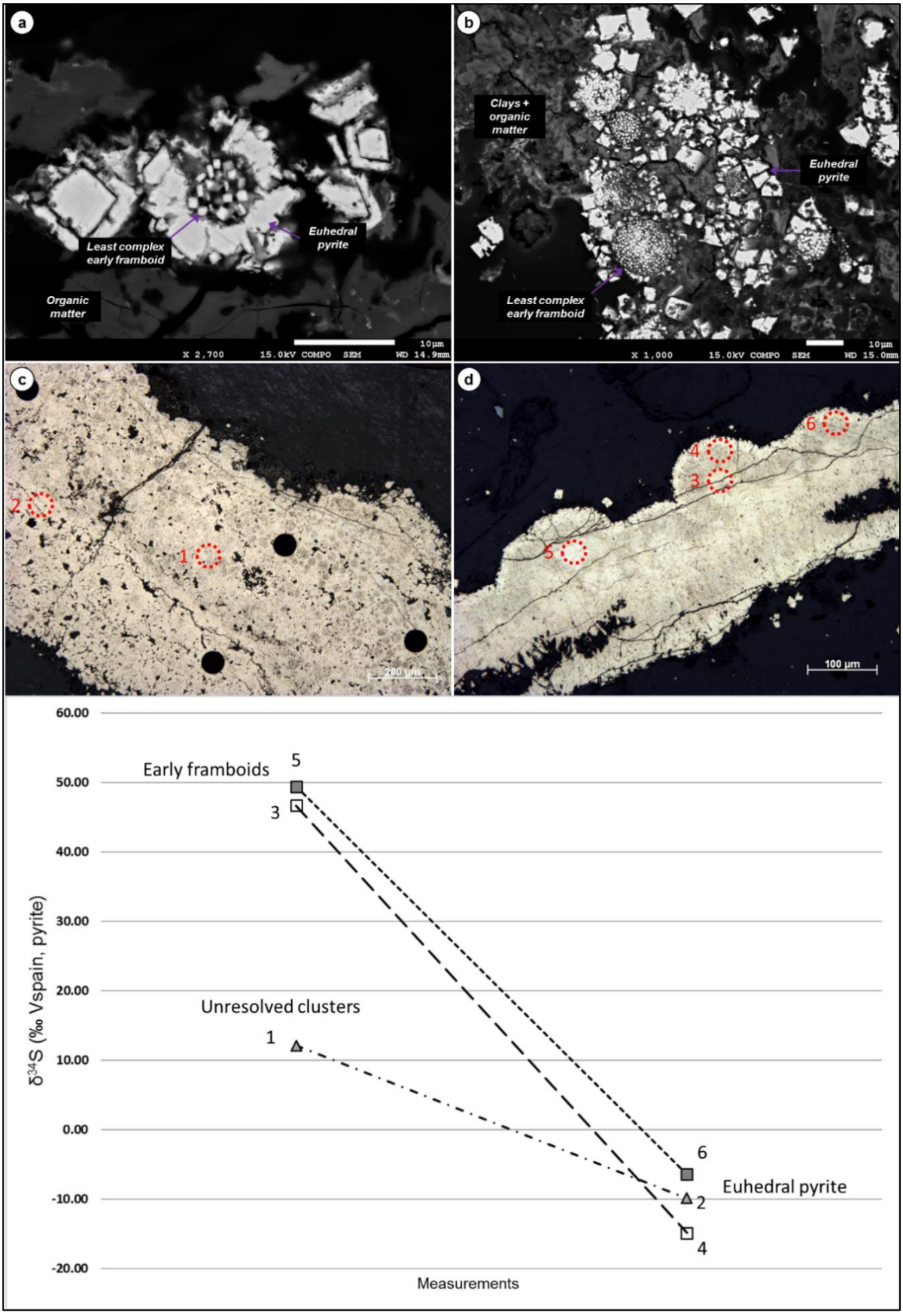

Figure 126: Example of the sulfur isotopic study on pyrite, sample 9659-BB106. The $\delta^{34}S$ of pyrite for least complex framboids is always positive while their overgrowths (concentric rims) and surrounding euhedral pyrite are negative. Pyrite is here associated to organic matter particles.

5.5.2 Comparison between Zoovch Ovoo and Dulaan Uul pyrite isotopic values

Probably the best analogue to compare the isotopic values of $\delta^{34}S$ of pyrite from Zoovch Ovoo is the adjacent roll-front deposit (some km away) of Dulaan Uul, which although has certain differences in terms of diagenetic history and hydrology, is without doubt a case to be considered. The analyses performed by Mercadier (2011) indicate six pyrite types (one being formed during ore stage). Almost similarly to Zoovch Ovoo, the values of the Dulaan Uul range between -59 to +33‰.

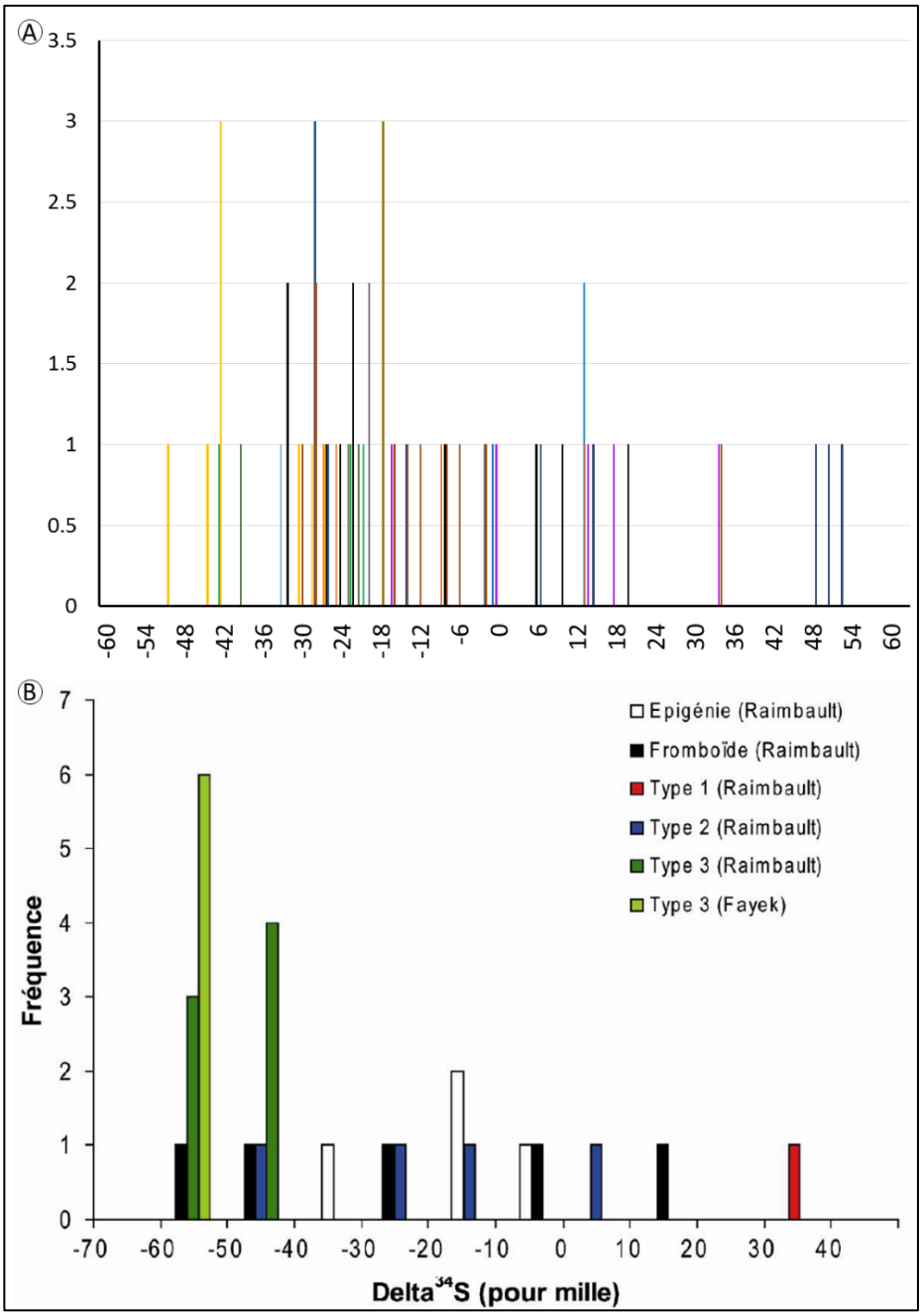

Figure 127: Comparison between the $\delta^{34}S$ of pyrite from (A) Zoovch Ovoo, from this study and (B) Dulaan Uul from Mercadier (2011).

5.6 SUMMARY OF PYRITE GEOCHEMISTRY

The different FeS_2 facies as determined by the petrographic study (Table 11 and Figure 128) were analyzed for both trace elements and isotopic $\delta^{34}S$ values. A response to water chemistry change leads to marcasite formation. Then the roll-front waters are introduced to the system corroding the euhedral pyrite 1. Afterwards, euhedral pyrite 2 is formed, often carrying pitchblende microsized inclusions. Finally, new generations of framboidal and euhedral pyrite are formed inside the anhedral dolomite, due to the re-establishment of anoxic settings and the re-initialization of BSR.

Table 11: Presentation of the paragenetic events associated to the evolution of pyrite. The final generations of framboidal and euhedral pyrite respectively are not clear whether they are newly formed or recycled from previous generations.

PYRITE PARAGENESIS Diagenetic events and minerals	Sedimentation / lowermost part of the lake	Time → Early diagenesis	Roll-front	Late diagenesis
Framboidal pyrite 1		O.M epigenization 1		
Concentric overgrowth				
Euhedral pyrite 1		O.M epigenization 2		
Marcasite				
Euhedral pyrite 2				O.M epigenization 3
Framboidal pyrite 2 (in IV dol.)				
Euhedral pyrite 3 (in IV dol.)				
			Corrosion of Euhedral Pyrite 1	

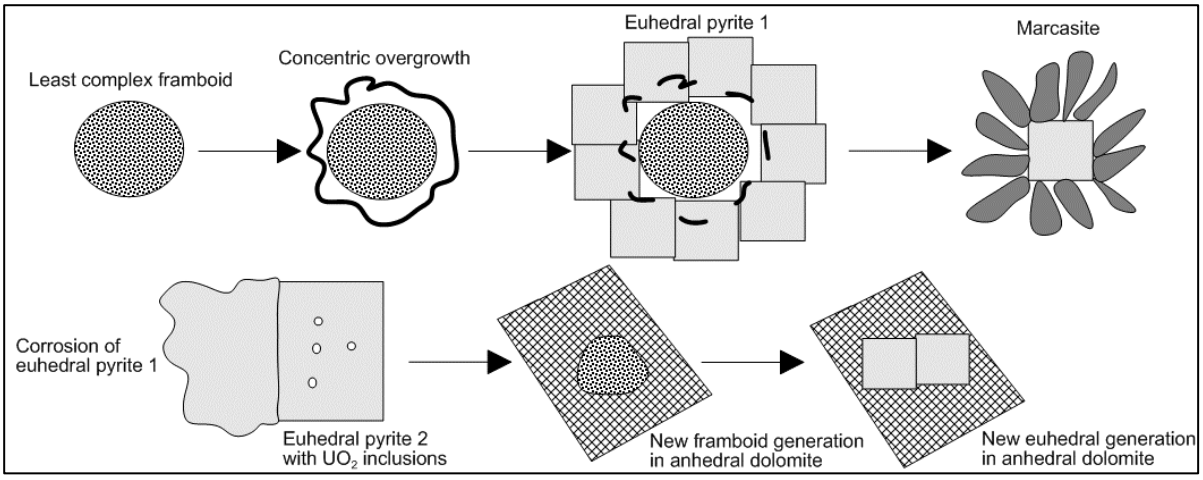

Figure 128: Pyrite paragenesis in Zoovch Ovoo, starting from least complex framboids, passing through concentric rims and the first euhedral pyrite generation.

Striking differences regarding the trace element content between the pyrite types associated to uranium phases and the non-associated, were confirmed. An attempt was made to characterize ore stage pyrite based on trace element concentration. The results were very promising, especially when using Co, Ni, Zn and Mo as indicators. Ore stage pyrite tends to be enriched in these trace elements compared to non-associated pyrite which is very lean.

The pyrite study was concluded with an isotopic study. In particular the $\delta^{34}S$ of the different pyrite occurrences was analyzed in order to understand more about their origin. The results though very diverse, fluctuating in extreme cases between -50 to +50 per mille for $\delta^{34}S$, show that there are more than four pyrite generations, as was previously concluded by petrography. Overall, isolated framboidal pyrite has a preference for positive $\delta^{34}S$ concentrations at the range of 10±5‰, while euhedral pyrite tends to be negative at the range of -18±5‰ (Figure 129). Furthermore large fractionation of the $\delta^{34}S$, at the level of 35±10‰ occurs for the two pyrite types.

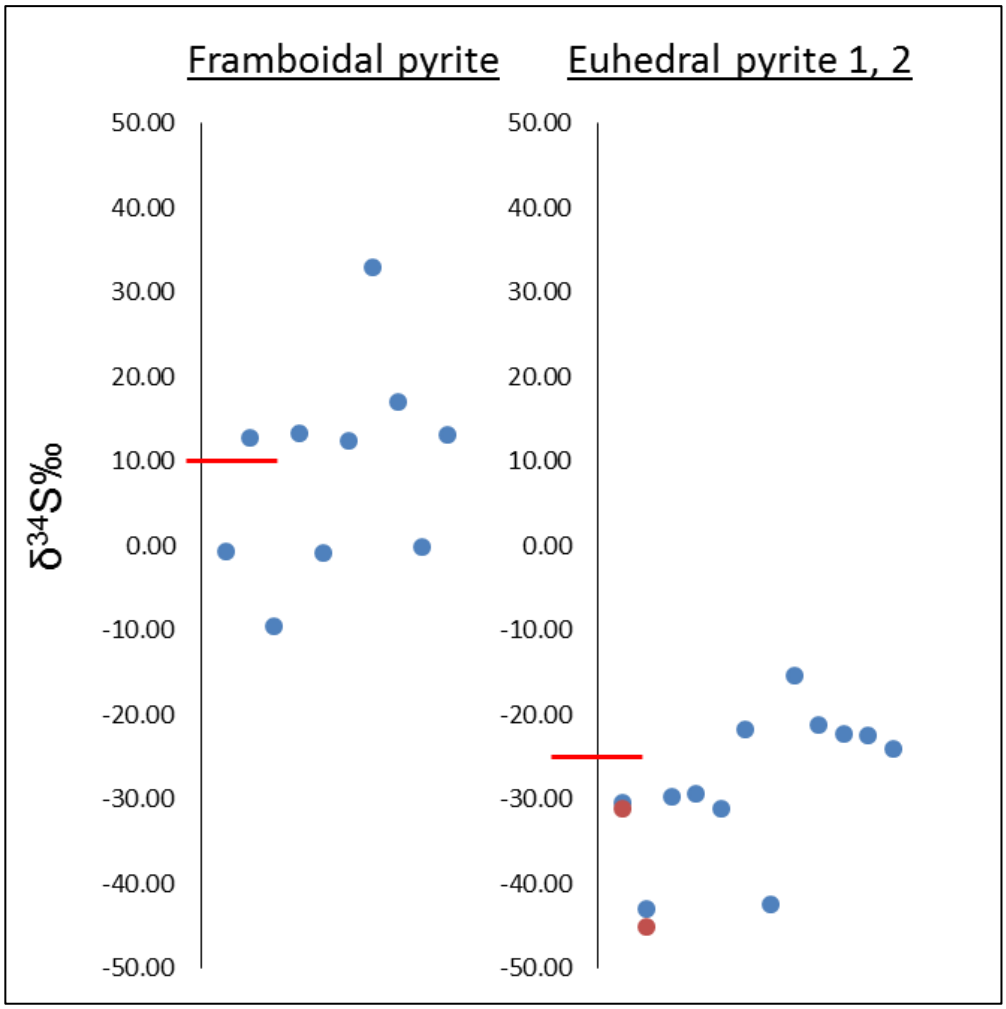

Figure 129: The isotopic values for the $d^{34}S$ on different pyrite occurrences, left for framboidal and right for euhedral pyrite (a few single extreme positive and negative values were excluded due to statistical uncertainty). The results show large fractionation of the $d^{34}S$, at the level of 35±10‰ for the two pyrite types. The U associated pyrite is indicated in red dots.

The gradual fractionation of S from positive to negative values coupled with the geological evolution of Zoovch Ovoo, could indicate that the framboidal pyrite with $\delta^{34}S$ values fluctuating at 20‰ originates from the reduction of evaporites by bacterial sulfate reduction (BSR). The positive $\delta^{34}S$ of framboidal pyrite, in contrast to the usual negative BSR derived pyrite, is due to the initial heavy $\delta^{34}S$ of evaporites, which according to literature usually reaches +20 to

+35‰ (Makhnach et al., 2000). These sulfates may be linked to the depositional environment, but may also be secondary, formed from the mineralizing fluid at later stages of diagenesis. Another possible explanation is that framboidal pyrite is sedimentary (Kohn et al., 1998), especially when dealing with freshwater where only limited quantities of sulfates are available (Berner, 1984).

The euhedral pyrite with negative $\delta^{34}S$ values originates from the further fractionation of the initially positive framboidal pyrite. The positive and negative values are rather reflecting closed vs open fractionation systems. In turn the ^{34}S-depleted euhedral pyrite indicates that it is bacterially derived and that BSR is active during the whole diagenetic history of the deposit and is the unique sulfate reduction process (absence of TSR), even during uranium deposition, since the second euhedral pyrite generation is co-genetic to uranium formation (contains pitchblende inclusions).

For all the above, thermochemical Sulfate Reduction (TSR) is *a priori* excluded in regards to the very low thermal maturity of the studied samples since vitrinite reflectance indicates (%Ro<0.4%), as would be expected for shallow burial and low temperature.

CHAPTER VI

Uranium petrography and crystal chemistry

6.1 INTRODUCTION

The uranium minerals were analysed in terms of petrography and crystal-chemistry. On the basis of 198 samples (9659, 9606, and 9704 studies) of variable lithologies (matrix supported sandstones, sandstones cemented by different dolomite cements and finally heavily mineralized sands). Only two kinds of uranium minerals were recognized. The first and most abundant is uraninite (UO_2) and the second and less common is phospho-coffinite. Uraninite in most cases contains a few percent of silica and phosphorus indicating coffinitization although pure coffinite ($USiO_4$) was not encountered in the studied samples. It was concluded that organic matter and sulfides are the most important agents for uranium trapping. Other phases that are associated to uranium are dolomite, silicates, clays and Fe-Ti oxides.

6.2 URANIUM OCCURRENCES IN ZOOVCH OVOO

The current results confirm the observations described in Brouand (2014; 2015). Uranium crystals are found in three forms. As independent spheres at the size range of 1 μm, as elongated flakes and finally as large aggregates that resemble former organic matter particles, pyrite crystals or Fe-Ti oxides, which were totally replaced by uranium (Figure 130).

Uranium can be contained from very low (0.5 wt%) to very high grades (about 80 wt%) in organic matter, eventually replacing it, while preserving plant l textures. It can be found as isolated inclusions inside sphalerite and in a certain euhedral pyrite generation, dispersed inside clay matrix, deposited in the intergranular porosity of dolomite cemented sandstones or totally replace pyrite cement. It also has the potential of totally replacing Fe-Ti oxides, while preserving the former mineral texture. It is mentioned that there seems to be a late quartz cement phase forming after uranium is deposited inside the Fe-Ti oxides.

6.2.1 Uranium petrography

Based on these observations it was possible to identify 8 different uranium occurrences from the studied dataset. These are described below:

1. U-rich organic matter without any distinguishable U-phase or sulphide, sometimes accompanied by uranium oxides precipitated at the contact of organic matter.
2. Uranium phases “replacing” entirely organic matter.
3. UO_2 inclusions inside euhedral pyrite and sphalerite.
4. U-phases (oxide UO_2 to close to $USiO_4$) replacing entirely pyrite.
5. U-cement diffused in clay matrix.
6. U-cement found within euhedral Type II dolomite.
7. Uranium oxides associated to quartz or replacing Fe-Ti oxides.
8. U-phases within silicates.

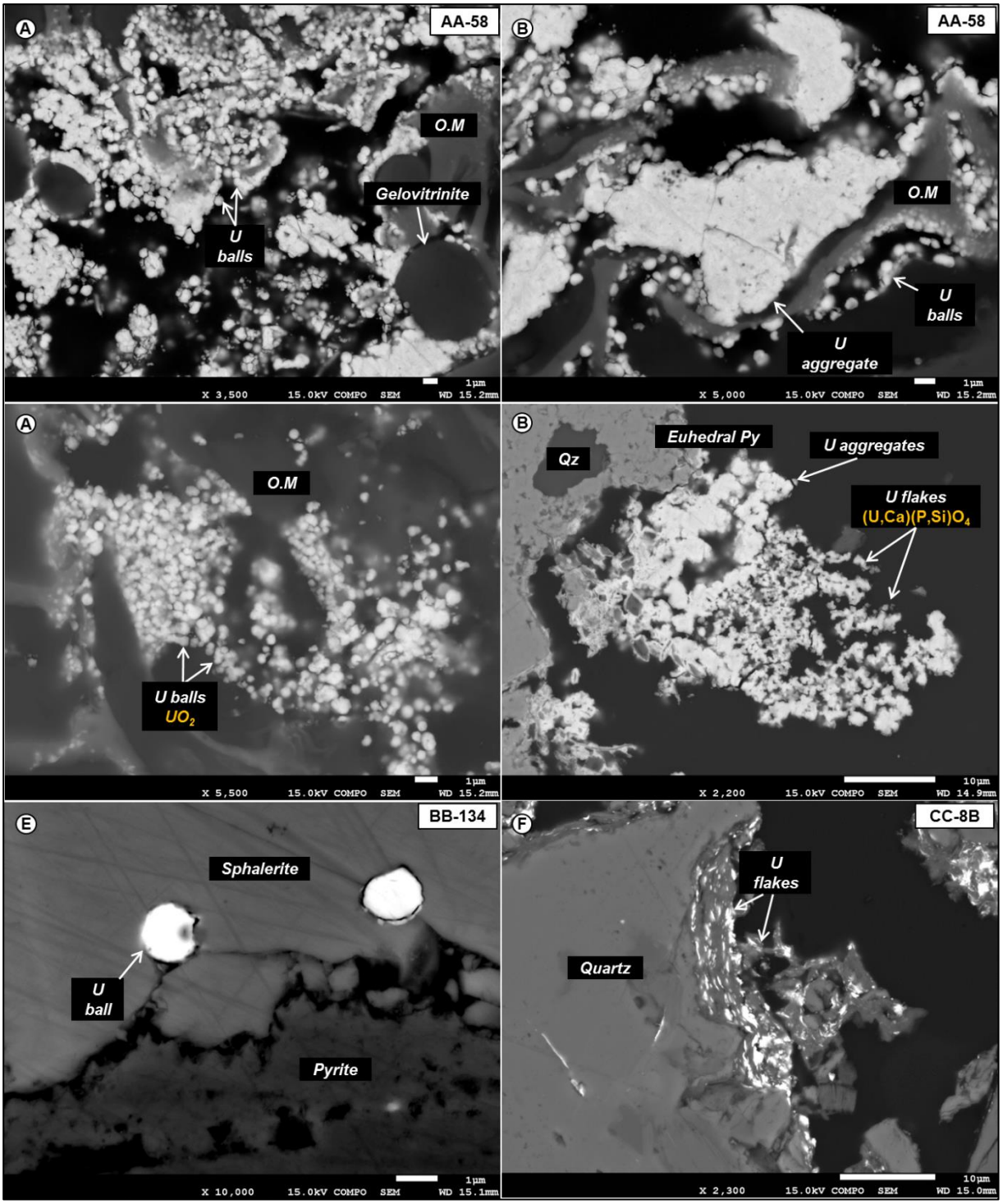

Figure 130: The different forms of uranium (U-cement will be presented independently). (A) Uranium crystals as small spheres (U-balls). It is noted that the maceral gelovitrinite (completely filled cells) appears to be more resilient to U-epigenization. (B) U-balls and their clusters, termed U-aggregate. (C) Disseminated U-balls inside organic matter. (D) Elongated U-crystals termed U-flakes and U-aggregates. (E) U-balls of 1 µm size inside sphalerite cement. (F) U-flakes growing at the rim of a quartz grain.

6.2.1.1 U-rich organic matter without any distinguishable U-phase or sulphide and uranium oxides precipitated at the contact of organic matter.

The organic matter is very commonly associated to uranium. The U grade of the macerals can fluctuate from a few percent up to 50 wt% without any distinguishable U-mineral form. Ultimately “total replacement” of the organic particle is observed by almost pure UO_2 yet still containing some carbon. It has been observed that even a few percent of U inside the organic particles can significantly increase its reflectance.

The U-rich organic matter without any distinguishable phase also contains significant amounts of Ca, Ti, Fe, S, Si and P. The uranium oxides contain often traces of Ca, Ti, Si and P (Fe and S are not in stoichiometric proportions as to be considered as iron sulphide). The uranium oxides associated to organic matter contain as well traces of Ca, Ti, Si and P and have the tendency of precipitating at the contact (rim) of the organic particles, sometimes associated to framboidal and euhedral pyrite. Barren organic particles are very lean in Ca, Si and P. In particular Ca increases proportionally with higher uranium concentration reaching about 2.5 wt% when the organic matter is fully replaced and Si, P increase as coffinitization progresses.

Photo-micrographs

Figure 131: Examples of organic matter associated to uranium, usually not expressed as oxide in the internal part and as oxide at the outer rims of the particle.

Sample AA-84. Polished blocks (created from crushed rock) under BSE mode.

A: Telovitrinite particle with heterogenous uranium concentration. The U-rich areas (2.3 wt% U) show higher reflectance than the U-lean (0.7 wt% U), in this particular vitrinite particle.

B: Telovitrinite particle with U concentration measurements. There is a tendency for U concentration to be higher at the rims of the organic particle, which is often expressed as uranium oxide (UO_2) crystals.

For full linear profile measurements see chapter *6.6 Complementary examples from the Uranium-organic* matter study, Figure 157.

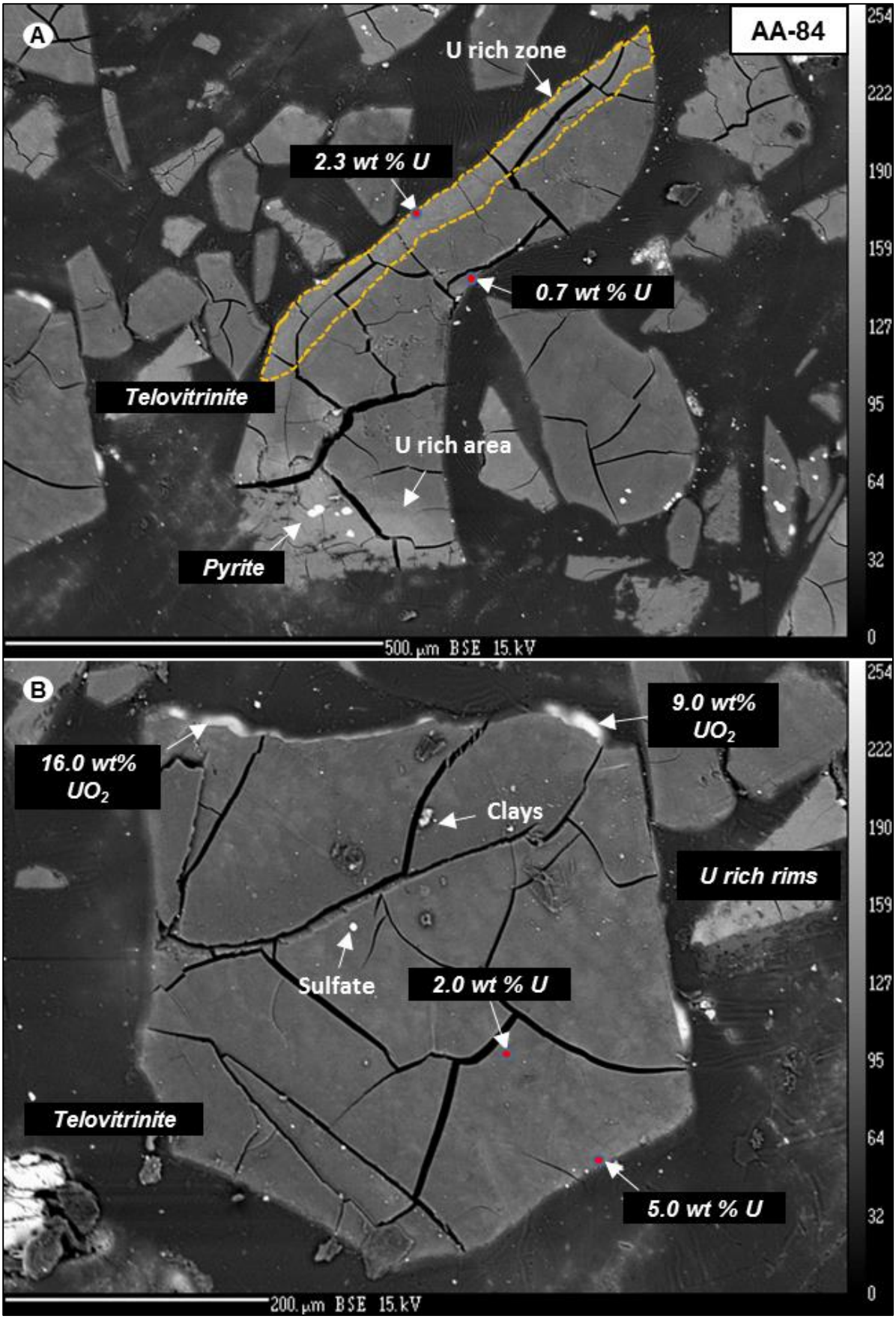

Figure 131: Examples of organic matter associated to uranium, usually not expressed as oxide in the internal part and as oxide at the outer rims of the particle.

Photo-micrographs

Figure 132: Examples of U-organic matter relationships. Uranium occurs at the rim as oxide (UO_2) associated to framboidal and euhedral pyrite and is distributed in the organic matter without being expressed as oxide.

Sample AA-58. (SEM images and semi-quantitative EDS-analyses, concentrations in wt%).

A: Uranium phase (close to UO_2 stoichiometry) at the rim of organic particle and U concentration gradient (along the double arrow) within the particle (no visible mineral), decreasing gradually towards the interior. The brightness (mean Z) is also modified as a function of U concentration under SEM mode.

For full linear profile measurements see chapter 6.6 Complementary examples from the Uranium-organic matter study, *Figure 157.*

B: Uranium phase (close to UO_2) associated to framboidal pyrite with pyrite overgrowth at the rim of a telovitrinite particle.

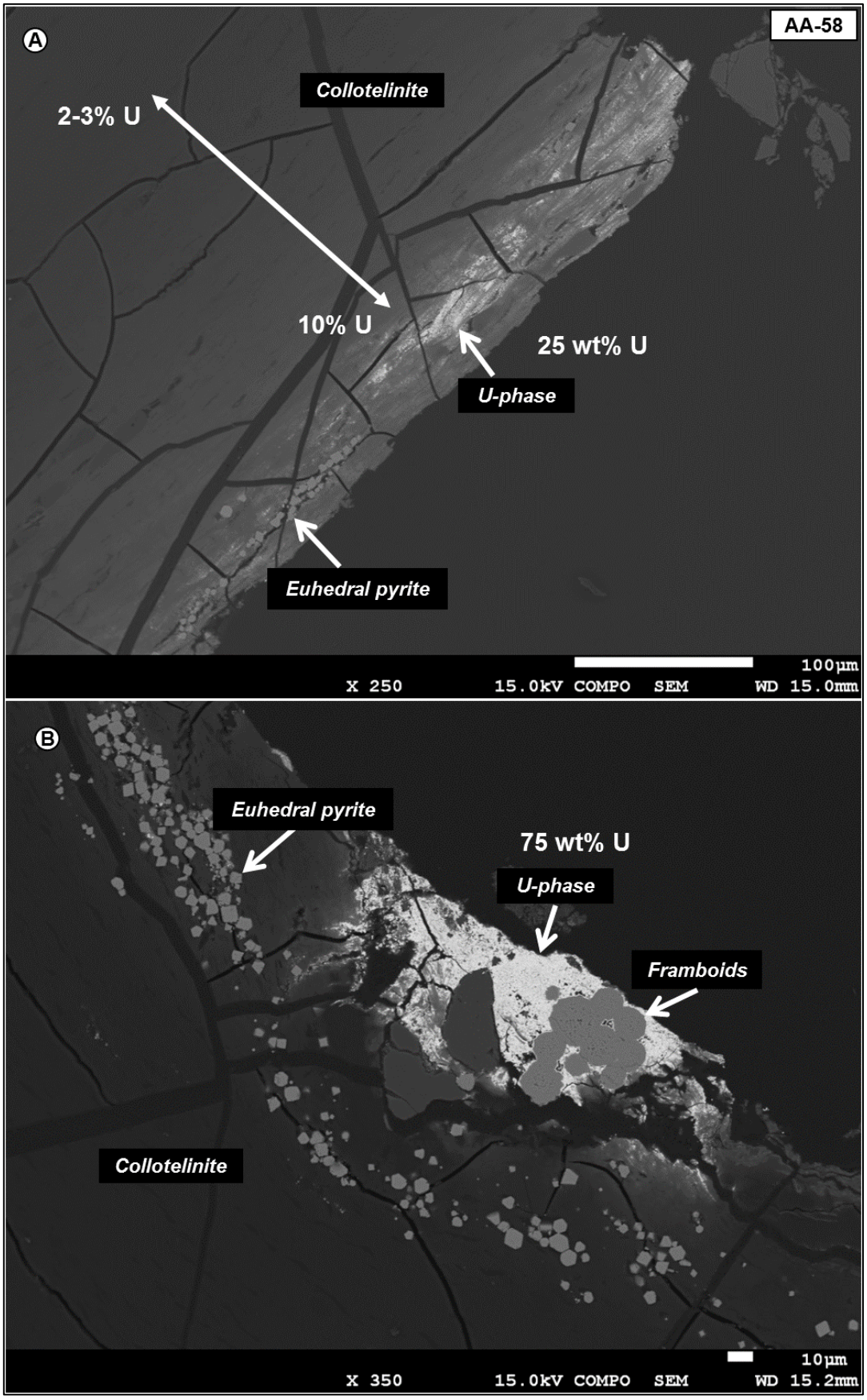

Figure 132: Examples of U-organic matter relationships. Uranium occurs at the rim as oxide (UO_2) associated to framboidal and euhedral pyrite and is distributed in the organic matter without being expressed as oxide.

6.2.2.2 Organic matter particle morphologies preserved as U mineral

Uranium starts to be accumulated gradually on the organic matter by increasing its concentration. According to measurements, uranium can be still not expressed in oxide form even with 50 wt% U concentration in organic matter (except when concentrated at the rims). On the other hand the UO_2 crystals which grew on the expense of organic matter particles contain more than 65 wt% U (hence about 25 wt% carbon). The actual measurements show that the fully replaced organic particles have 75-77 wt% in U concentration.

It is also noted that even in the case of full organic matter replacement, certain textural characteristics of the plant debris are preserved, indicating fine-grained epigenization processes.

Photo-micrographs

Figure 133: Examples of organic matter replaced by uranium. Uranium is expressed in oxide form at the rims of the organic particle and is close to UO_2 stoichiometry.

Samples AA-172B, AA-58. (SEM images and semi-quantitative EDS-analyses).

A, B: Rectangular-shaped telovitrinite particle containing about 65 wt% U, with the cell walls being preserved. Disseminated framboidal and euhedral pyrite are also present inside the U-replace organic particle.

C: Elongated telovitrinite particle at the size range of 400 μm, with fractures and cell walls. The uranium content is 68 wt% and is slightly Ca, Si, P enriched. The remaining organic carbon was estimated to be around 14 wt% calculated by the difference formula (empirical) using SEM-EDS.

D: Collapsed cell walls surrounding a large euhedral pyrite cubic crystal. The uranium epigenesis on the cell walls is at the level of 67 wt%, again enriched in Ca, Si, and P. The remaining organic carbon based on the empirical formula is at the level of 13-14 wt%.

E: Elongated telovitrinite particle composed of smaller pitchblende-epigenetized gelovitrinite particles.

F: Pitchblende precipitation along the fracture in the internal part of a telovitrinite particle. Uranium concentration decreases progressively from 74.6 to 2.5 wt% as a function of increasing distance from the fracture.

For more information on the usage of the empirical formula, see chapter 6.8 The U-organic matter replacement mechanism.

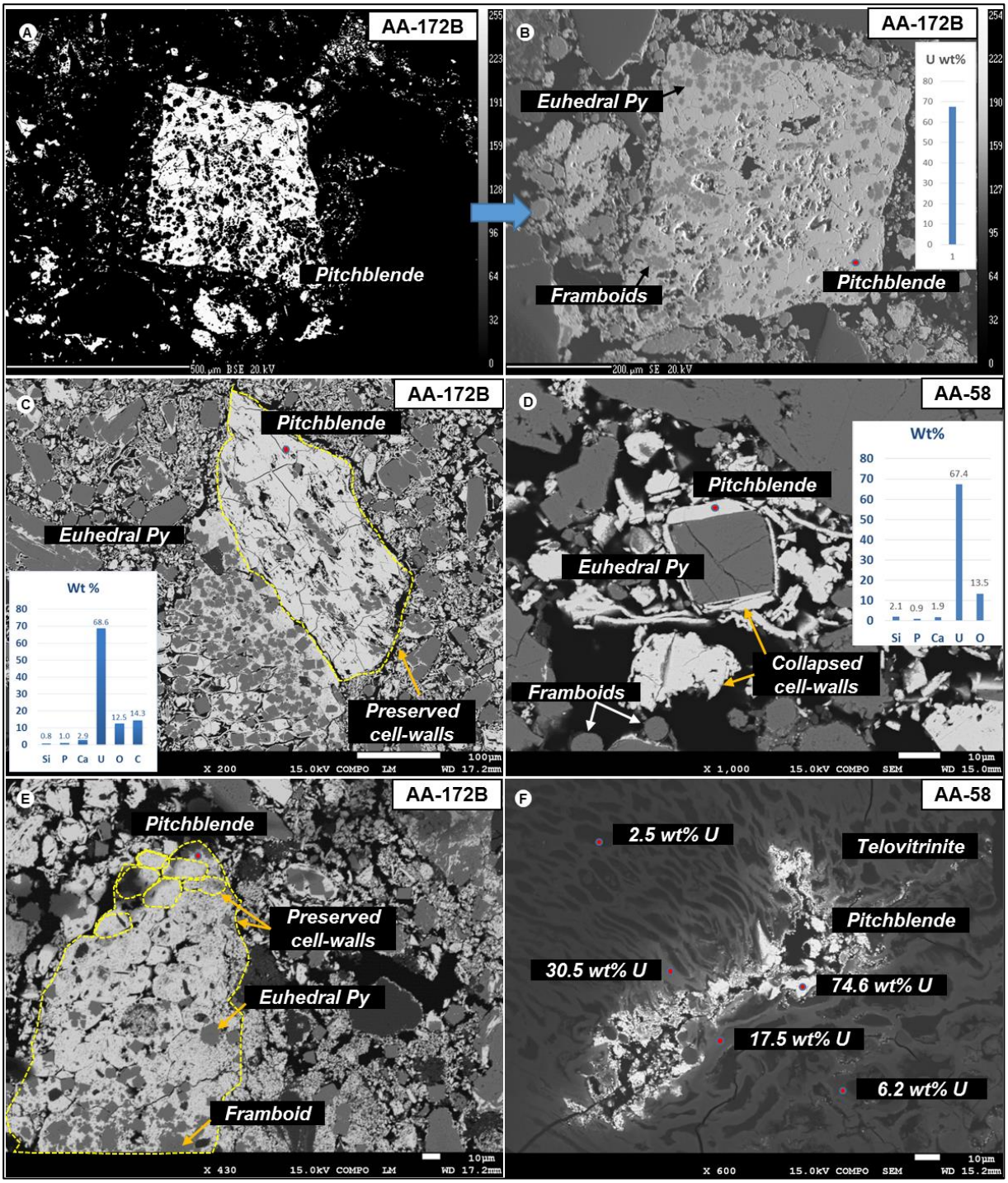

Figure 133: Examples of organic matter replaced by uranium. Uranium is expressed in oxide form at the rims of the organic particle and is close to UO_2 stoichiometry.

6.2.2.3 UO_2 inclusions inside sphalerite and euhedral pyrite

As was described in chapters 5.2.1.4 Framboids embedded within cubic (euhedral) pyrite and 5.2.1.5 Series (zonations/generations) of cubic (euhedral) pyrite, a distinction can be made between euhedral pyrite that contains pitchblende inclusions and euhedral pyrite that is totally lean of uranium. Of course if pyrite is contained inside cell-wall lumens, the evolution of the pyrite crystals is controlled by the geometry of the cell. Therefore, although this pyrite type is chronologically the same as the euhedral pyrite with pitchblende inclusions, it is most appropriate to use the term “anhedral” or “pyrite cement”. To facilitate with petrographic observations, the four different pyrite generations use the abbreviations below:

i. **Py 1** for the first generation, referring to the framboidal pyrite.
ii. **Py 2** for the second generation, which refers to the concentric overgrowth pyrite that encompasses the framboidal pyrite.
iii. **Py 3** for the third generation, referring to the euhedral pyrite that is preceding to uranium formation (termed as pyrite cement or anhedral pyrite in the case it is contained inside organic matter cell-walls).
iv. **Py 4** for the fourth generation, namely for the pyrite cement or anhedral pyrite (formed contemporaneously to the euhedral pyrite, in the case they contain pitchblende inclusions.

With regards to sphalerite, pitchblende can be associated in two ways:

v. As spherical inclusions of 1 μm size in diameter (U formation is contemporaneous to sphalerite).
vi. As cement filling the fractures in sphalerite (in this case U post-dates the sphalerite). This type was already described in the chapter of sulfides (Chapter 5.2.10).

From the above petrographic observations, it is evident that sphalerite is posterior to the euhedral pyrite that does not contain uranium inclusions but is probably also posterior with regards to the pyrite that contains uranium inclusions.

Photo-micrographs

Figure 134: Examples of uranium-sphalerite-pyrite-organic matter relationships.

Samples BB-134, AA-58. (SEM images).

A, B: Framboids (Py 1) with concentric overgrowth (Py 2) coated by pitchblende, followed by euhedral pyrite with pitchblende inclusions, encompassed by uranium rich clays and a close-up of the assemblage.

C: Framboids (Py 1) with concentric overgrowth (Py 2) without U, then euhedral pyrite (Py 3) without U, followed by empty space that based on A, B could be pitchblende that was dissolved,

encompassed by pyrite cement (Py 4) with pitchblende inclusions, all embedded inside sphalerite cement with pitchblende inclusions.

D: A closer view of the spherical pitchblende inclusions of 1 µm size embedded in sphalerite cement.

E, F: Sphalerite with pitchblende inclusions post-dating euhedral pyrite without any uranium (Py 3) and pyrite cement with pitchblende inclusions inside cell-wall lumens (Py 4).

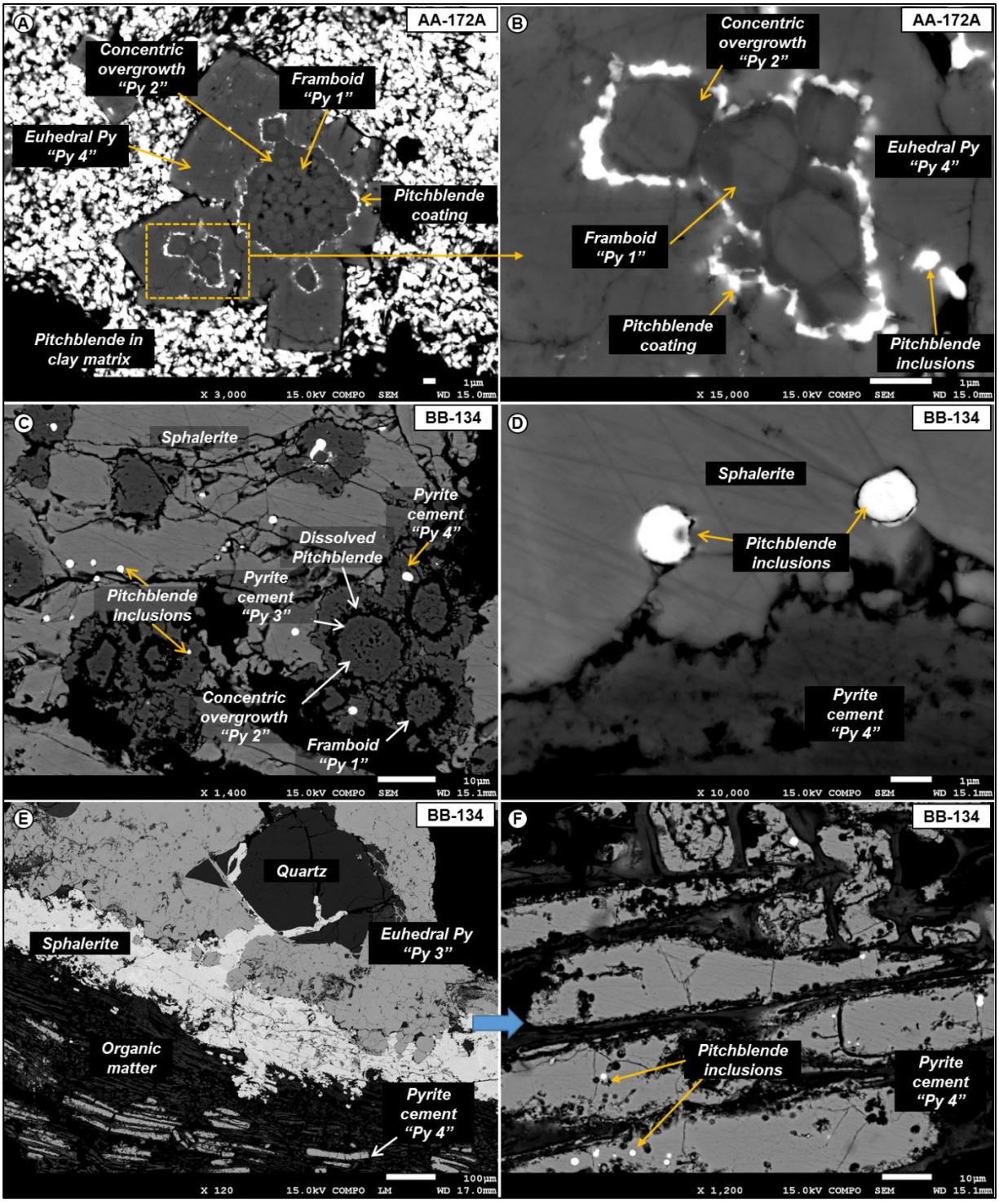

Figure 134: Examples of uranium-sphalerite-pyrite-organic matter relationships.

6.2.2.4 U-phases (oxide UO_2 to $USiO_4$) replacing entirely pyrite

Corrosion of framboids and euhedral pyrite followed by uranium precipitation is frequently observed in the mineralized samples. This feature applies to pyrite that is associated to organic matter but also to pyrite cement that binds together detrital sand grains. In some cases uranium totally replaces organic matter, as well as the associated pyrite and the respective uranium phase is then closer to the phospho-coffinite stoichiometry. In the future these measurements will be populated by studying mineralized samples, in order to identify potential systematic trends.

Not every euhedral and framboidal pyrite is corroded and this triggers the question, why specific pyrite types have corroded rims and open pores in their lattice while others do not. Pitchblende may be contained in the pores of the lattice, which must have been deposited during the growth of the pyrite or during its corrosion from the roll-front waters. This feature leads to the conclusion that the crystallization of pyrite must have been controlled by the chemistry of the roll-front waters and the result was the formation of idiomorphic crystals with pores rather than compacted perfect cubes of the euhedral pyrite generation.

Hence, it could be stressed that the crystallization of the idiomorphic pyrite (pyrite cement) and the precipitation of the pitchblende spheres inside its lattice are “contemporaneous” episodes.

Photo-micrographs

Figure 135: Examples of framboidal and euhedral pyrite followed by uranium precipitation.

Samples: CC.73A, AA-35, AA-78, CC-8B. All pictures taken under BSE.

A: This picture shows within the dotted yellow line, remnant pyrite cement initially made of merging framboids partially replaced by pitchblende. The contact between pitchblende and remaining framboids shows a typical contorted feature, suggesting a dissolution of pyrite contemporaneous to pitchblende deposition.

B: Focus on the contact between the framboidal pyrite cement and pitchblende. Several replacement levels of framboids by pitchblende can be recognized from right to left: fully preserved, framboid grains surrounded by pitchblende, framboid core remnant, almost fully replaced framboid and finally pitchblende cement without recognizable pyrite.

C: Organic matter formerly cemented by euhedral pyrite now almost fully replaced by uranium (about 60 wt% U; hence there is about 15-20 wt% organic carbon remaining). In this particular case the chemistry of the uranium was different, closer to phospho-coffinite stoichiometry.

D: In the lower right half of the picture, detrital grains cemented by pyrite and pitchblende. Note the contorted shape of the interface between pitchblende and pyrite which might be interpreted as a corrosion surface. Upper left corner of the picture: matrix (clays) supported sand.

E: A close view showing the corrosion features of pyrite cement followed by pitchblende precipitation. Note the quartz cement filling a pore and posterior to pitchblende precipitation.

F: Idiomorphic euhedral pyrite crystal growth followed by contemporaneous uranium precipitation inside the available pores. These pores may be interpreted as linked to corrosion stage of pyrite prior to pitchblende deposition.

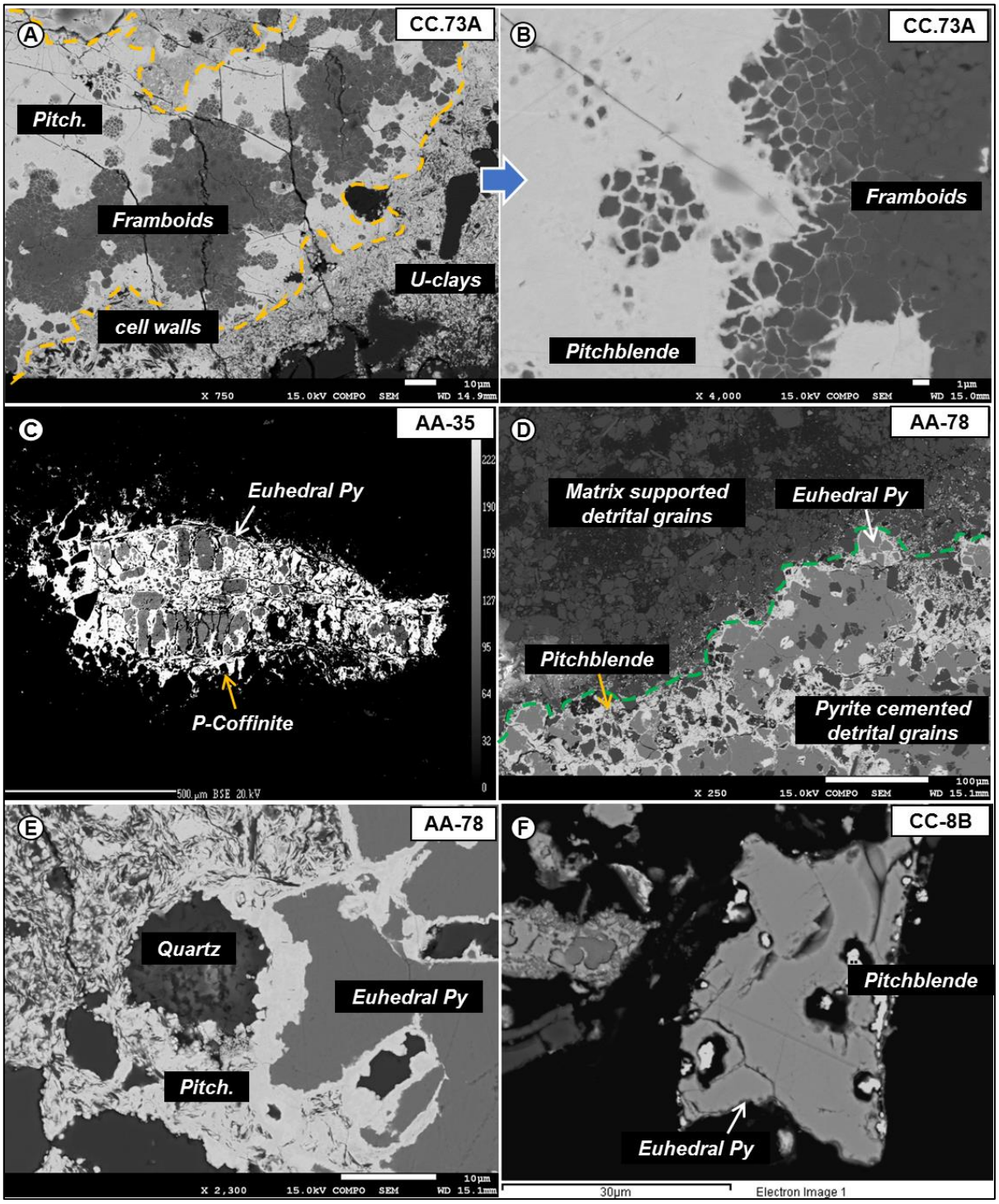

Figure 135: Examples of corroded framboidal and euhedral pyrite replaced by gradually by uranium.

6.2.2.5 UO_2 as cement disseminated in clay matrix

There were cases when uranium in the form of pitchblende to coffinitized-pitchblende precipitated inside the clays. These clays are separated in two categories. Those that were initially the binding phase of the sandstone (matrix) and those secondary that resulted from the alteration (hydrolysis) of feldspars. There is also a third U-clay phase the natro-zippeite/uranopilite (so-called yellow product), which is composed of secondary uranium minerals due to the contact of uranium with the atmospheric air ever since the sample was recovered.

Uranium mineral crystals are disseminated inside the clays, as a result the clays obtain higher brightness (mean Z under SEM-BSE), while maintaining their textural properties. The uranium concentration fluctuates at 30 wt% and contains traces of Ca, Si, and P.

It is difficult to precise the actual chemistry of the U-clays mixture due to the mineralogical complexity and the very small size of individual crystals which avoid acquisition of reliable EDS data. For instance there is definitely a certain interference from the clays when measuring the Si concentration.

Photo-micrographs

Figure 136: Examples of different occurrences of U-rich clays (1).

Samples: AA-138, AA-58, AA-154C, pictures taken under BSE and LPA modes.

A: Uranium (close to phospho-coffinite stoichiometry) enriched clays inside clay matrix associated to euhedral pyrite and stilleite (ZnSe).

B: Matrix supported sandstone showing coffinitized pitchblende associated to euhedral pyrite within the clay.

C: Matrix supported sandstone showing U–clays association as detected by EMPA suggesting the presence of phospho-coffinite at a concentration of about 30 wt%.

D, E: Clays containing 30 wt% U filling pore space between detrital quartz and feldspar. The adjacent pyrite cemented part does not contain uranium.

F: The secondary oxidation of uranium resulting in the mineral natro-zippeite under LPA and BSE modes with the respective EDS spectra.

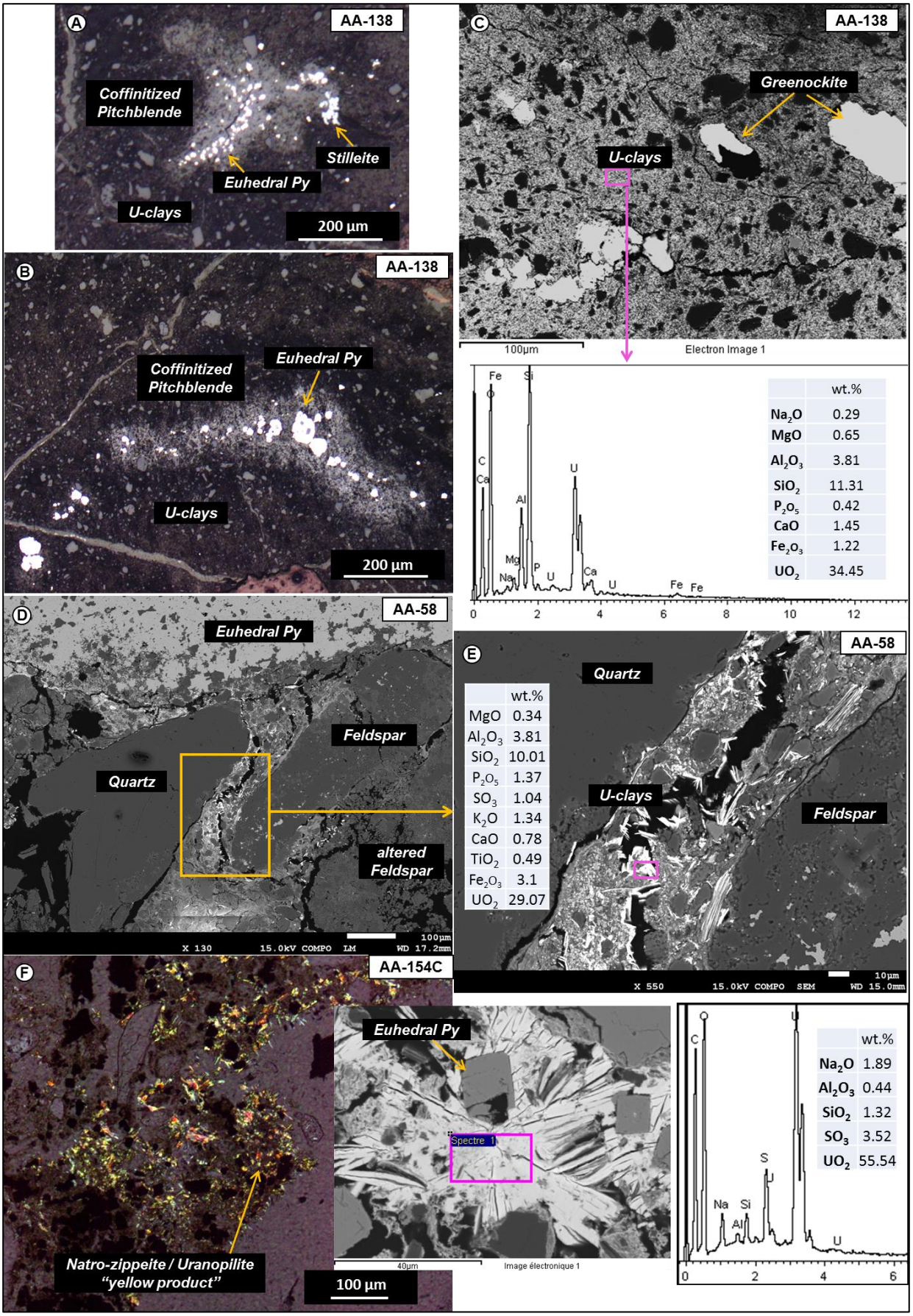

Figure 136: Examples of different occurrences of U-rich clays (1).

Photo-micrographs

Figure 137: Examples of different occurrences of U-rich clays (2).

Sample: AA-58, pictures under BSE mode.

A-E: Different magnifications of the same image, showing clay matrix at the rim of pyrite cemented sandstone. The U minerals here cover the surface of clay crystals, which contain up to 30 wt% U.

Pitchblende-replaced (Fe)-Ti oxides were also identified containing about 5.0 wt% of Ti left.

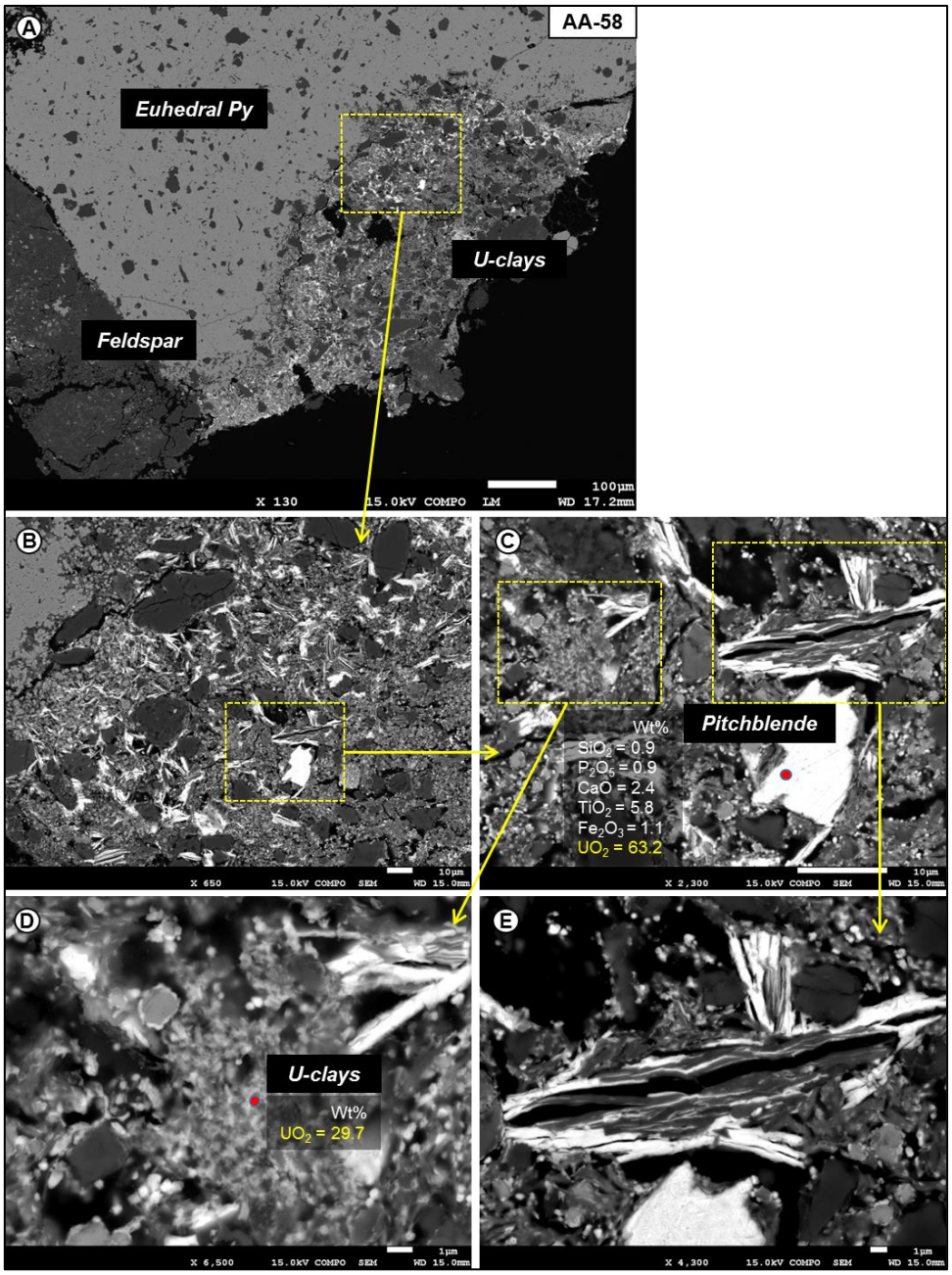

Figure 137: Examples of different occurrences of U-rich clays (2).

6.2.2.6 UO_2 cement within euhedral Type II dolomite

There was only a single case where the euhedral (type II) dolomite was associated to uranium, on the basis of 198 samples, namely from the punctual drills**:**

- Well ZOOV_1081_2_3, sample **9659 CC-6**, depth interval 131,63-131,73 (m).

There uranium precipitated inside the available porosity in between the poecilitic dolomite crystals. The available porosity can be described as in three different occurrences:

1) At the contact of the poecilitic dolomite crystals which did not show perfect interlocking.

2) At the contact between the dolomite detrital silicate grains.

3) Around the idiomorphic dolomite crystals, probably after corrosion.

It is not clear if there was partial dissolution of the poecilitic dolomite or if the crystals grew as such (idiomorphic growth) due to water chemistry interference or due to the lack of available porosity. Hence, the discussion remains open.

Photo-micrographs

Figure 138: Examples of phospho-coffinite located in the porosity around euhedral (Type II) dolomite.

Sample: CC-6, images under BSE mode.

A: Phospho-coffinite/euhedral dolomite/detrital grains relationships. Uranium is located:

i. At the contact of the poecilitic dolomite crystals.
ii. In between the dolomite crystals and detrital grains. Note the presence of siderite within the core of dolomite crystals.

B: Phospho-coffinite located at the available space between the idiomorphic dolomite crystals. The rims of the dolomite crystals appear to be corroded.

C, D: Detailed views of Phospho-coffinite distribution in between idiomorphic crystals of dolomite cement. The contours of some dolomite crystals suggest a dissolution process (bottom of picture D).

Stronger magnification of pictures B, C and D, focusing on the dolomite dissolution aspect are presented in **Figure 139**.

E: Euhedral (Type II) dolomite, organic matter, pyrite and phospho-coffinite relationships. Uranium precipitates at the contact of the poecilitic dolomite crystals, at the contact of the dolomite with the detrital grains (silicates) and around the pyrite inside the organic matter.

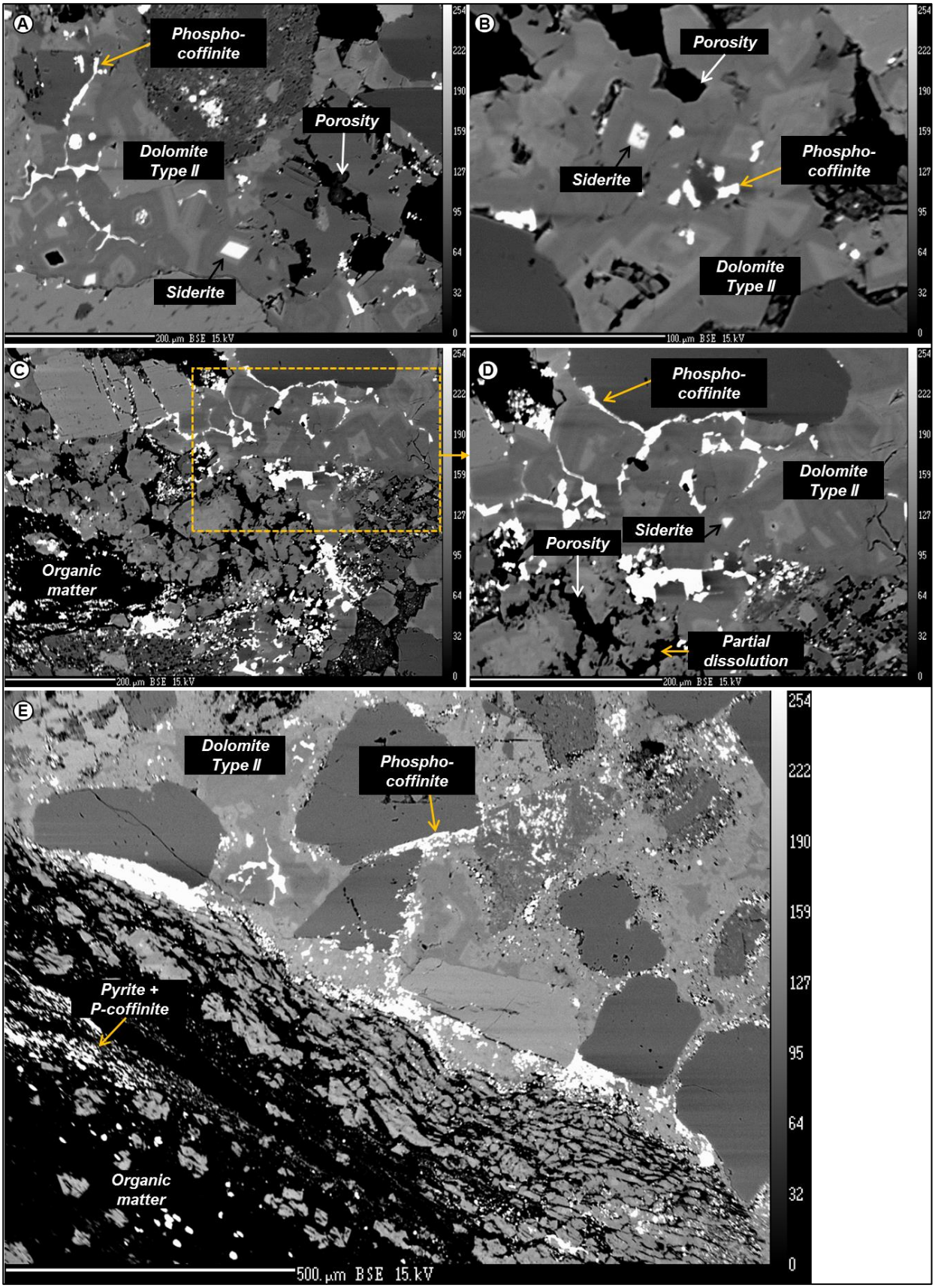

Figure 138: Examples of pitchblende located in the porosity around euhedral (Type II) dolomite.

Photo-micrographs

Figure 139: A close view of the corroded rims previously presented in Figure 138 (B, C and D)

A, B: Partial dissolution taking place around and in the internal area of euhedral dolomite crystals. As a result phospho-coffinite is distributed in the available porosity.

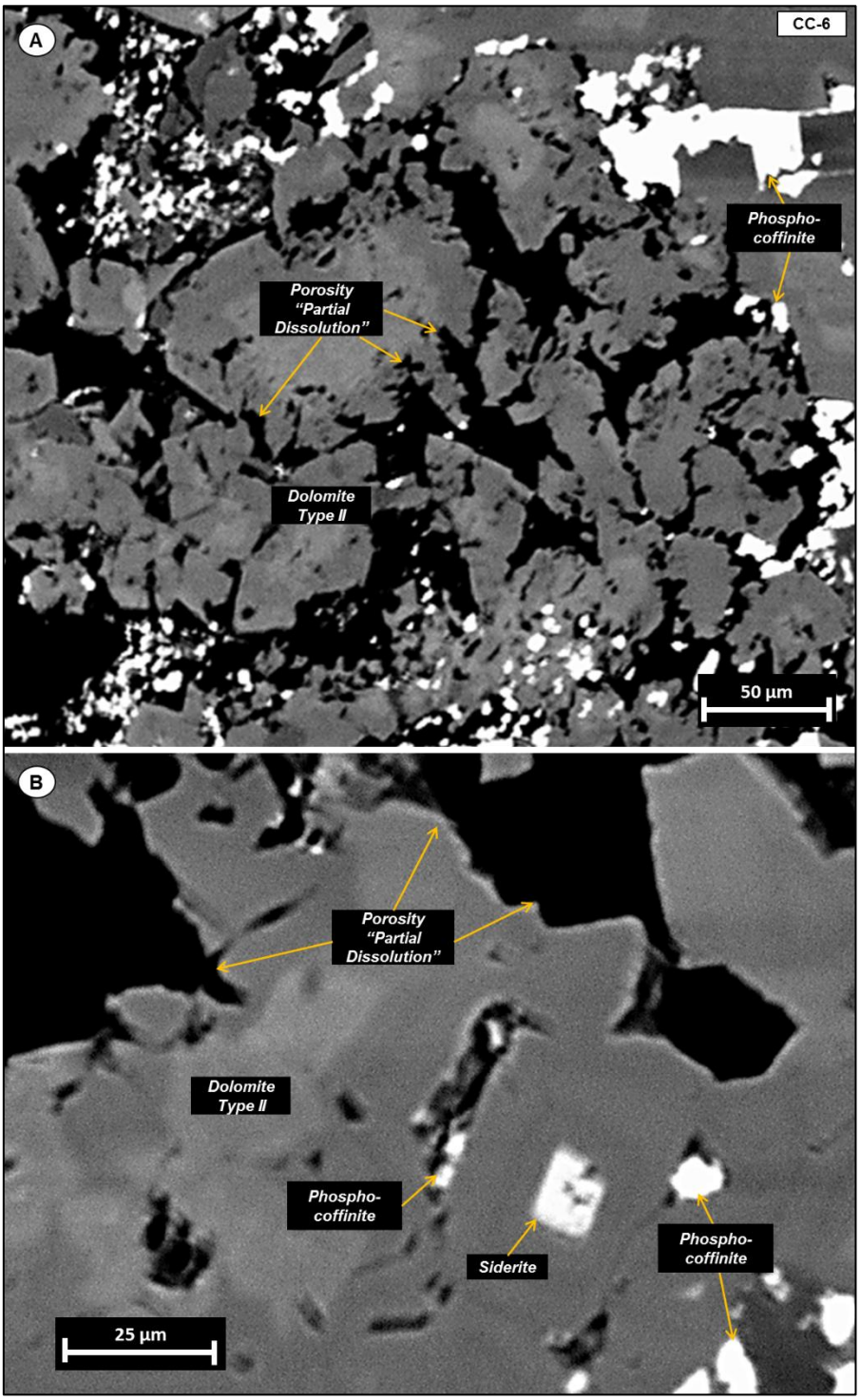

Figure 139: A close view of the corroded rims previously presented in Figure 140 (B, C and D).

Photo-micrographs

Figure 140: Chemical maps (Si, Mg, Fe, Mn, Sr and U detected by EMPA) of the section presented in Figure 138 (picture E).

Map A: Close-up of the dolomite partial dissolution features highlighted by yellow dotted line which allows distinction from the organic matter (both porosity and organic matter have black color).

Map B: Chemical map for silicium, which allows an overview of the silicates. Above of picture quartz, three feldspars are discriminated that are also partially dissolved (top left, bottom right and in the O.M).

Map C: Chemical map for magnesium, focusing on the euhedral (type II) dolomite cement zonations. The porosity in between the well-developed crystals and the siderite cores are now discriminated. The dissolution features with irregular geometry at the bottom left of the picture are also highlighted.

Map D: Chemical map for iron, showing the distribution of the siderite cores. The iron phase that is intermixed with pitchblende in the middle of the picture is probably pyrite, used as substrate for pitchblende growth.

Map E: Chemical map for manganese which clearly shows the distribution of siderite. Manganese is absent from the Fe-U phase in the middle of the picture, which strengthens the assumption that it is pyrite which is associated to uranium.

Map F: Chemical map for strontium used to indicate the porosity. Ideally, all mineral phase plus organic matter contain traces of strontium. Hence, in this case it is evident that there is available porosity in the lower part and the top left part of the image.

Map G: Chemical map for uranium used to indicate the distribution of phospho-coffinite. Practically, uranium fills all available porosity, in between dolomite, in the organic matter and the partially dissolved dolomite and feldspars grains.

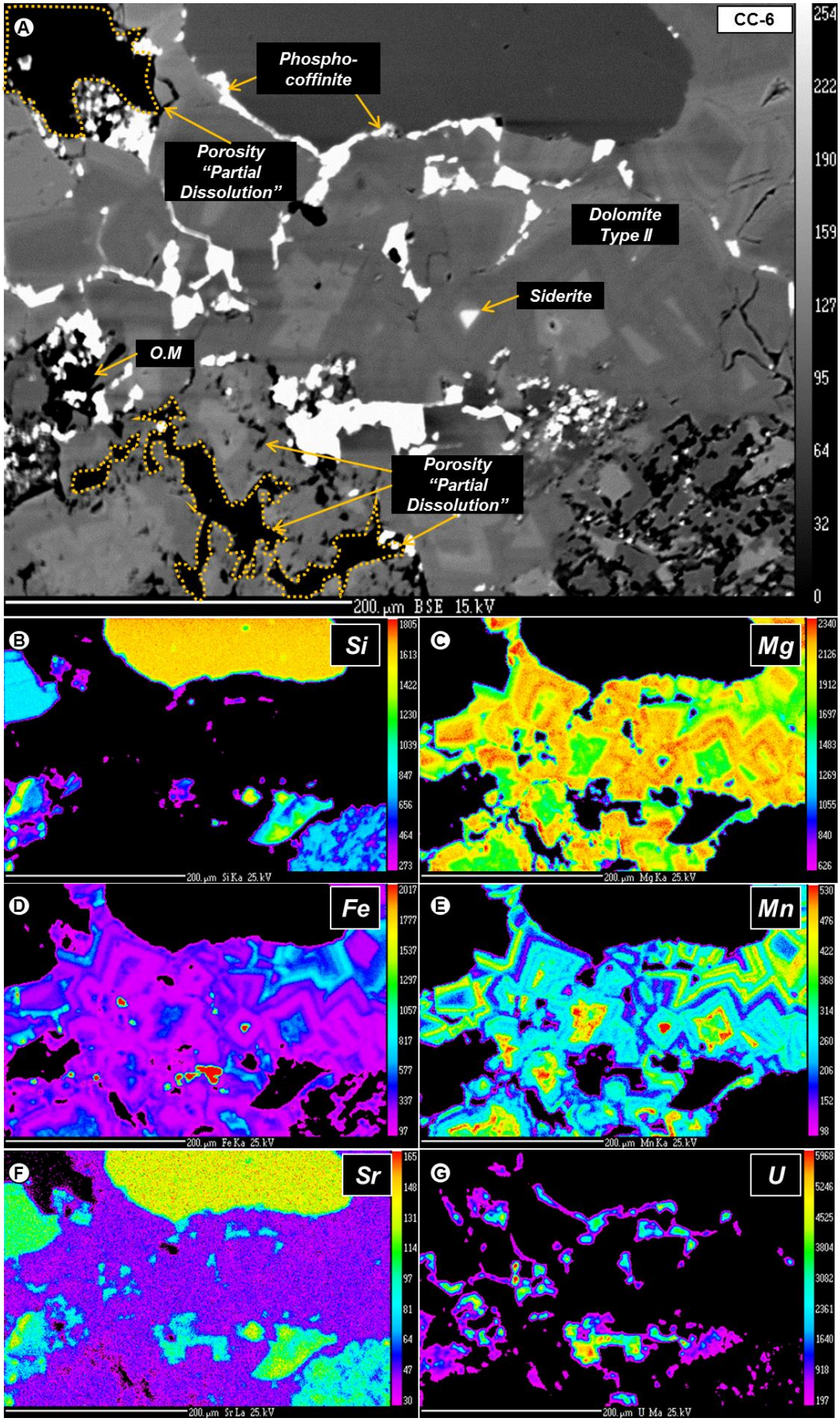

Figure 140: Chemical maps (Si, Mg, Fe, Mn, Sr and U detected by EMPA) of the section presented in Figure 138 (picture D).

Photo-micrographs

Figure 141: Chemical maps (Ca, Mg, Fe, Mn, Na, Si, Sr and U, detected by EMPA) of the section presented in Figure 138 (picture E).

Maps A, B and G: distribution of Ca, Mg and Sr evidencing the distribution of dolomite cement. Dolomite occurs as idiomorphic crystals in between detrital elements, as well as filing pore space inside organic matter particles.

Map C: Distribution of Fe in the dolomite cement as siderite and the organic matter as pyrite.

Map D: Mn distribution helps to differentiate between the pyrite and siderite. There is a single occurrence of siderite located inside dolomite. As a result the bright Fe areas of (picture C) should indicate pyrite.

Map E and F: Na and Si distribution reflect the presence of detrital quartz and feldspar elements.

Map H: The U-phases are mainly distributed at the contact of dolomite with organic matter and irregularly inside the organic matter instead of filling the available empty space.

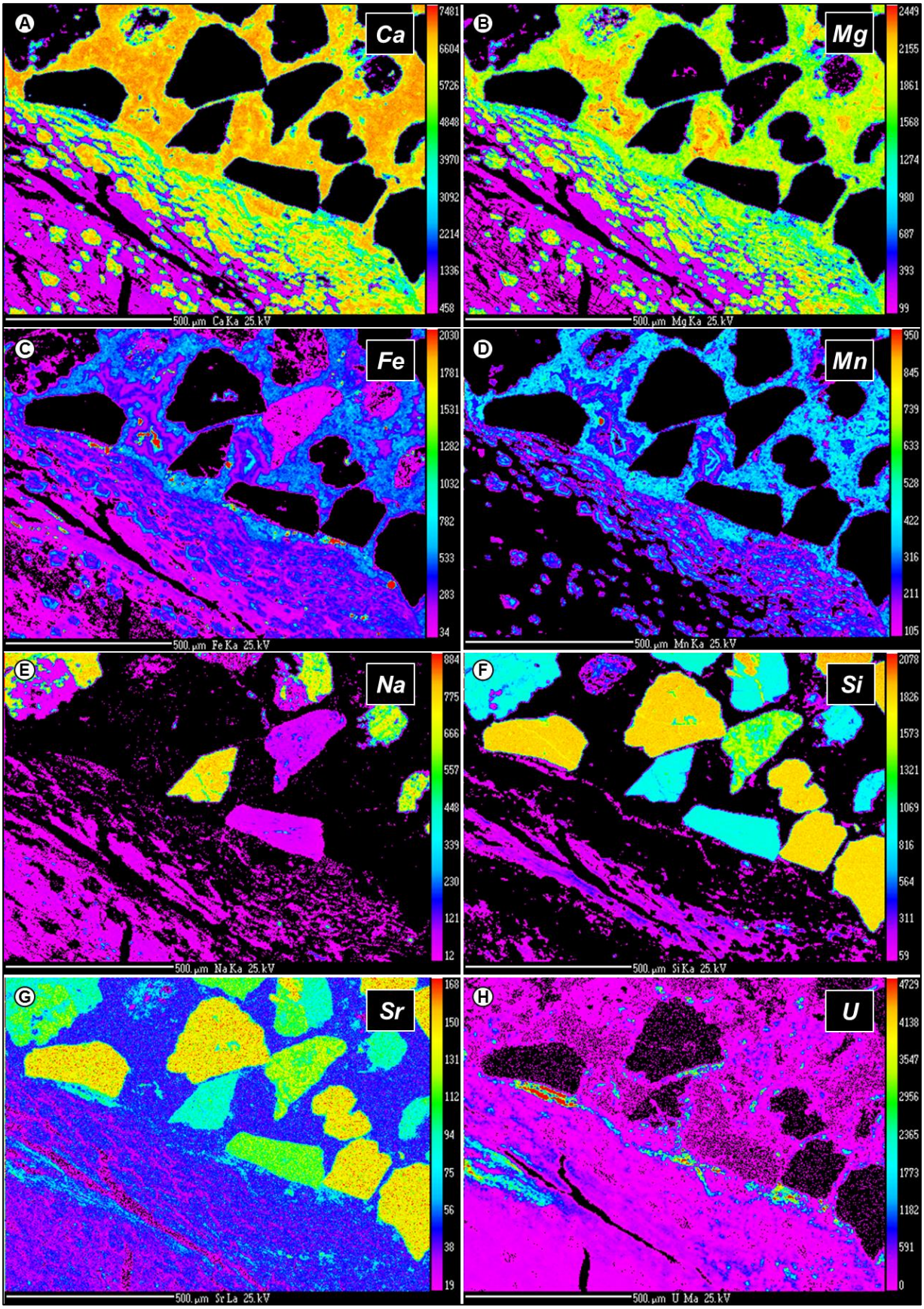

Figure 141: Chemical maps (Ca, Mg, Fe, Mn, Na, Si, Sr and U, detected by EMPA) of the section presented in Figure 138 (picture E).

6.2.2.7 Uranium oxides associated to quartz cement or replacing Fe-Ti oxides

Detrital grains of titanium oxide closely associated to quartz were recognized in two cases, in barren samples coming from the same well:

- Profile SW-NE_03600, well ZOOV_0886_7, sample BB-134, depth interval (m) 209,40-209,70.
- Profile SW-NE_03600, well ZOOV_0886_11, sample BB-138, depth interval (m) 215,85-216,15.

These Ti-oxides quartz clusters are mentioned because uranium was identified inside this association. High magnification shows coffinite located on the surface of titanium oxide fractures cemented by quartz. Quartz cement was also recognized several times in heavily mineralized samples, contained inside uniform pyrite cement with disseminated uranium mineralization. The discussion whether the two different cases of quartz cements are genetically linked, remains open.

It can be suggested that quartz cement comes after a given uranium precipitation episode, not clear which one for the moment, since it was proved that there are at least two UO_2 formation episodes. To go even further, this quartz cement event may belong to the same fluid-rock interaction event that is responsible for the coffinitization of pitchblende. The discussion is left open for the moment as well.

Furthermore, there was a single case where a former titanium oxide was perfectly replaced by pitchblende, without affecting its textural properties, in particular its cleavage.

- Profile SW-NE_01300, well ZOOV_0709_11, sample AA-58, depth interval (m) 126,35-126,55.

The U concentration in this oxide is at the range of 67 wt%, indicating almost perfect replacement.

Photo-micrographs

Figure 142: Examples of a titanium oxide detrital grain associated to quartz cement, U is found in between the titanium oxide and quartz cement. Phospho-coffinite precipitation followed by quartz cement filling a vug in pyrite cement and an almost perfectly pitchblende-replaced titanium oxide mineral.

Samples: BB-138, BB-134, AA-58.

A: Typical detrital grain of titanium-oxide associated to quartz cement, in this case inside anhedral Type IV dolomite cement.

B: Close view of (A) indicating the precipitation of a uranium phase close to the phospho-coffinite stoichiometry, inside the fractured titanium oxide detrital grain, followed by quartz cementation.

C: Another occurrence of the titanium oxide/quartz cement association without uranium and without dolomite cement.

D: The quartz cement inside a pyrite cemented sandstone containing a uranium phase. Again the quartz cement is the latest diagenetic phase.

E: A titanium oxide relic fully replaced by pitchblende.

F: Magnification of (E) to highlight the cleavage preservation and the respective EDS spectra (67 wt%).

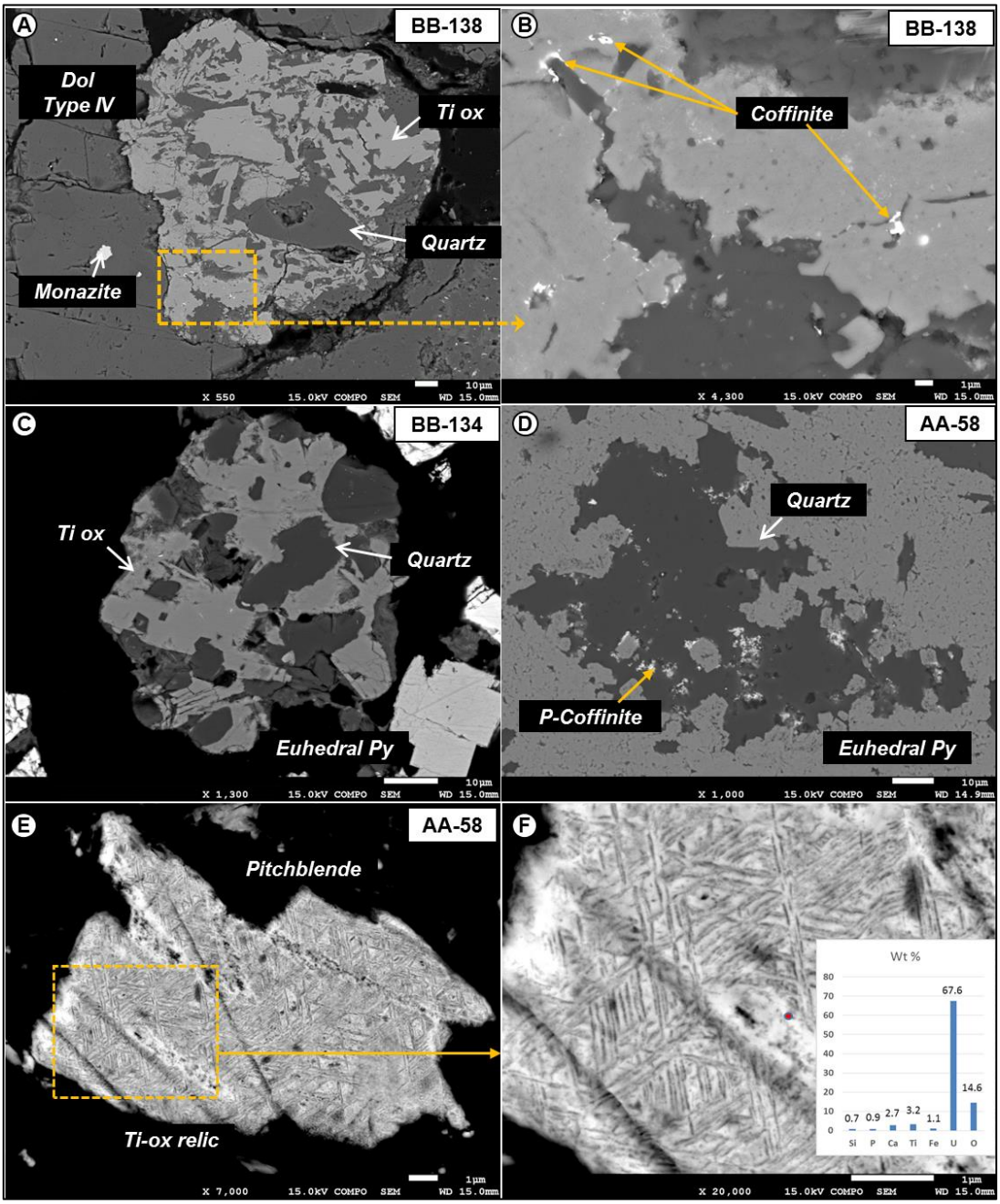

Figure 142: Examples of a titanium oxide detrital grain associated to quartz cement, U is found in between the titanium oxide and the quartz cement. Phospho-coffinite precipitation followed by quartz cement filling a vug in pyrite cement and an almost perfectly replace titanium oxide mineral by pitchblende.

6.2.2.8 U-phases within silicates

Detrital silicate grains of a few micrometers up to 0.5 mm in size can contain associated U-phases inside their fractures and porosity. These silicates can be fractured quartz grains and in most cases porous alkali feldspars showing the common albite/microcline solid solution feature (perthitic texture).

Although this feature is very common, three particular cases are selected as examples and are presented below:

- Profile SW-NE_01300, well ZOOV_0670_3, sample AA-172B, depth interval (m) 171,79-171,99.
- Punctual drill, well ZOOV_1080_1, sample CC-8B, depth interval (m) 179,00-179,05.
- Punctual drill, well ZOOV_1100_6, sample CC-54C, depth interval (m) 168,25-168,55.

The U concentration inside the fractures and pores fluctuates at 55 to 69 wt% in the studied cases. Traces of Si, P, Ca and As are also contained.

Photo-micrographs

Figure 143: Examples of large silicates containing U inside their lattice (fracture porosity).

Samples: CC-54C, AA-172A, CC-8B. Pictures taken under reflected light and BSE mode.

A: The largest alkali-feldspar observed (about half mm in size), with pyrite and pitchblende. The center of the grain presents a better preserved feldspar (the reflectance variation is due to the perthitic texture) than the surrounding which is porous. Porosity may be inherited from the alteration during sedimentary transport of the grain.

B: Alkali-feldspar with pitchblende inside the porosity. Pitchblende is also contained in the clay matrix surrounding the feldspar.

C: Large rounded alkali-feldspar with mineralization in fractures (following the crystal lattice) and pores.

D: Higher magnification of (C) indicating the perthitic texture and the disseminated U-mineralization.

E: Rounded alkali-feldspar detrital grain associated to uranium in fractures and pores.

F: Higher magnification of (C) indicating the feldspar perthitic texture and the disseminated U-mineralization with the respective EDS spectra.

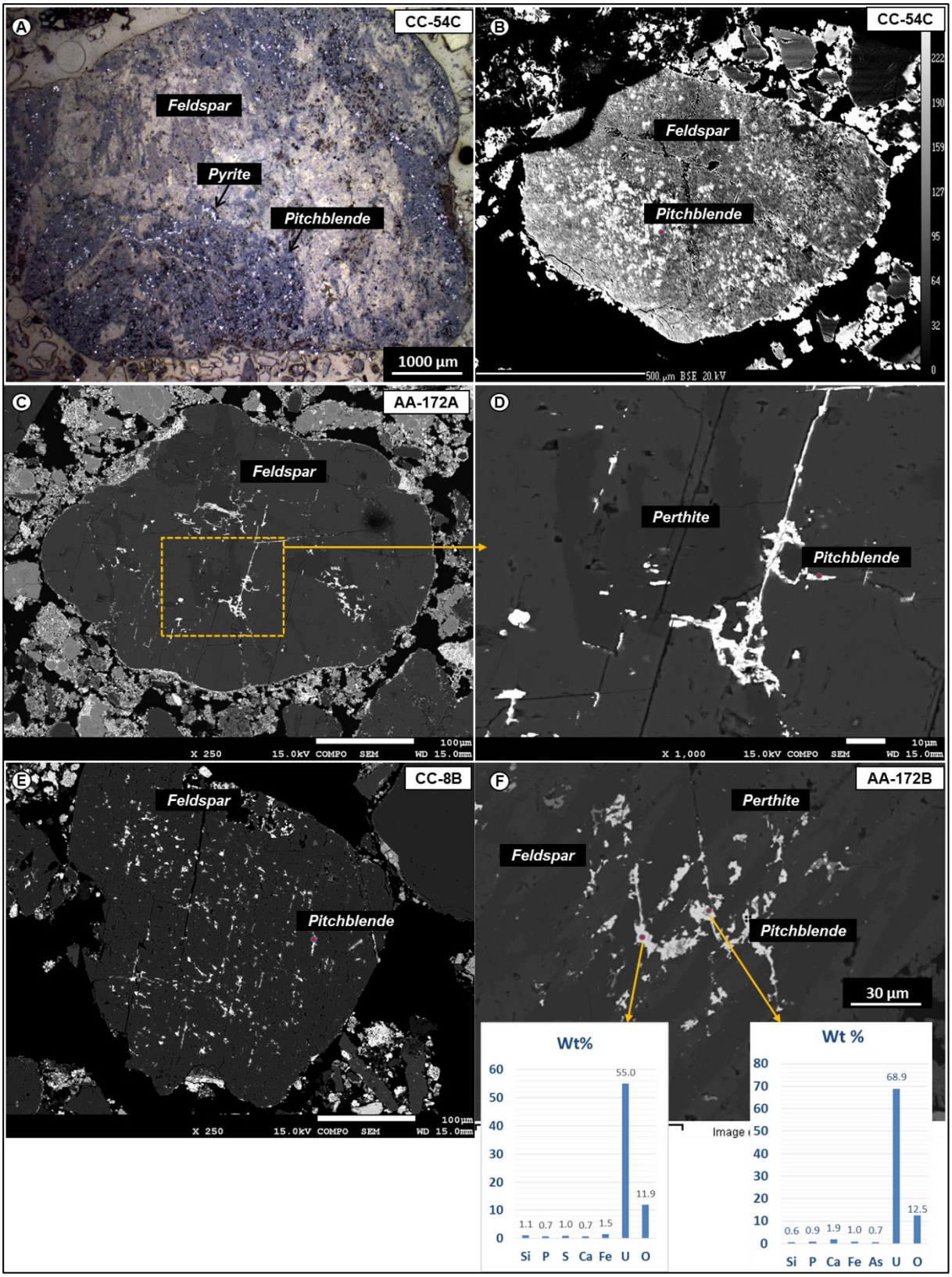

Figure 143: Examples of large silicates containing U inside their lattice (fracture porosity).

6.3 SUMMARY OF URANIUM PETROGRAPHY

By studying the petrography of the available mineralized samples but also of barren samples it was possible to uncover the relationships between uranium and the associated phases namely, organic matter, sulfides, dolomite, silicates, clays and titanium oxides.

Finally, it was possible to identify eight different occurrences of uranium:

1. Organic matter with up to 50 wt% U without not expressed as oxide. Uranium oxides may precipitate at the rims of those U-rich particles. Yet, not clear if it is a U-C association or UO_2 associated to C without mineralogical expression (keeping in mind that dissolved U will occur as UO_2^{2+} in water).
2. Complete replacement of organic matter by uranium. Identified at a 65-70 wt% grade.
3. Pitchblende (uraninite) inclusions in the form of spheres (1 μm) inside certain euhedral pyrite phase, pyrite cement and sphalerite.
4. Pyrite replacement by uranium oxide of (UO_2 to $USiO_4$) chemistry.
5. Uranium in clay matrix as pore filling or as overgrowth of clay crystals.
6. Pitchblende within porosity of euhedral Type II dolomite cement.
7. Uranium oxides preceding quartz cement located in fractures and pores of detrital grains of Fe-Ti oxides, as well as U replacing Fe-Ti oxides.
8. Uranium oxides inside detrital fractured and porous silicate grains, particularly feldspars.

It is concluded that organic matter and sulfides are the most important agents for uranium trapping and that the silicates, clays and Fe-Ti oxides play minor role. Yet, uranium can also be found precipitated in intercrystaline pores of dolomite, as well as in fractures and pores of detrital grains. A quartz cement phase was identified to be post-diagenetic with respect to uranium precipitation and may be involved in coffinitization.

During the petrographic study, the crystal chemistry of the uranium phases was analyzed. It was concluded that there are only two uranium minerals. The first and most abundant is uraninite (UO_2) and the second and less common is phospho-coffinite. Uraninite in most cases contains a few percent of silicium and phosphorus indicating coffinitization although pure coffinite ($USiO_4$) was not encountered in the studied samples. However, systematic trends were not identified.

There was an attempt to project the samples on the respective profiles, namely SW-NE_01300 and SW-NE_03600. Considering that many mineralized samples are coming from the punctual drills (prefix CC-) and these could not be projected on profiles, Figure 144 and Figure 145. Despite the small number of the samples projected it might be suggested that pitchblende is included inside the main mineralization zone and phospho-coffinite bounds the mineralization.

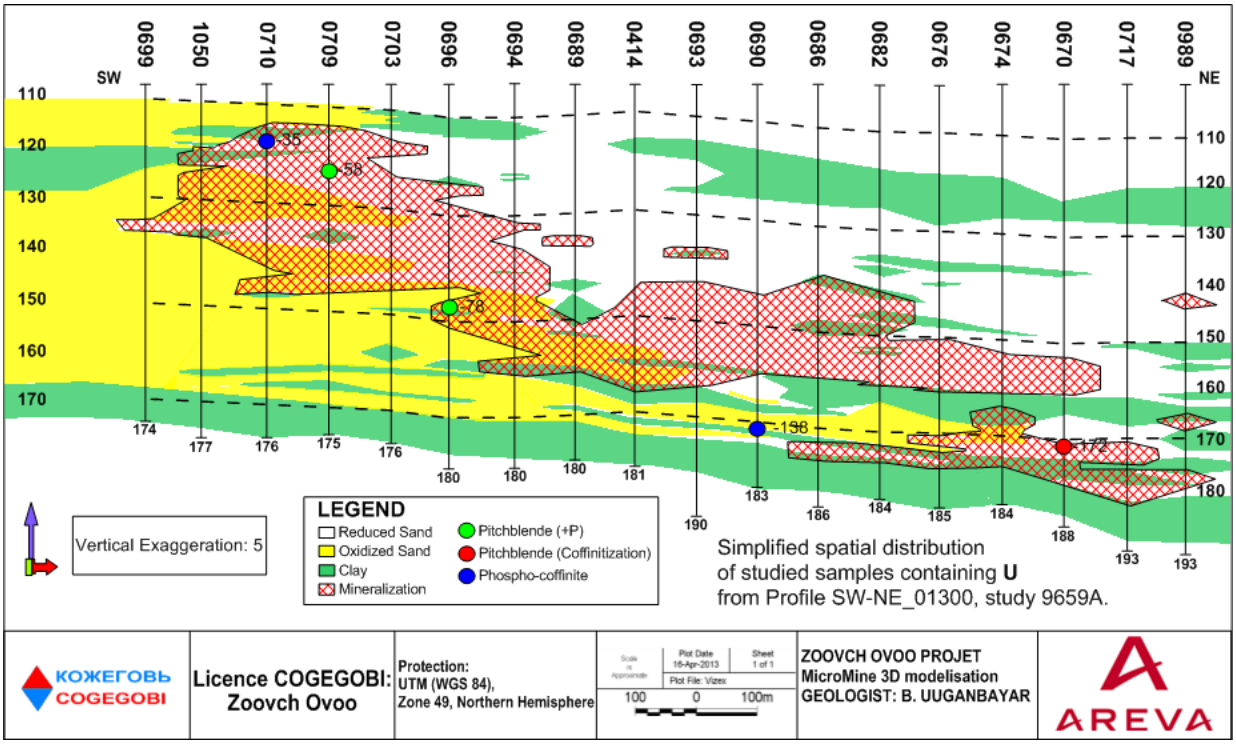

Figure 144: The spatial distribution and the abundance of the different uranium types encountered along the Profile SW-NE_01300 in Zoovch Ovoo.

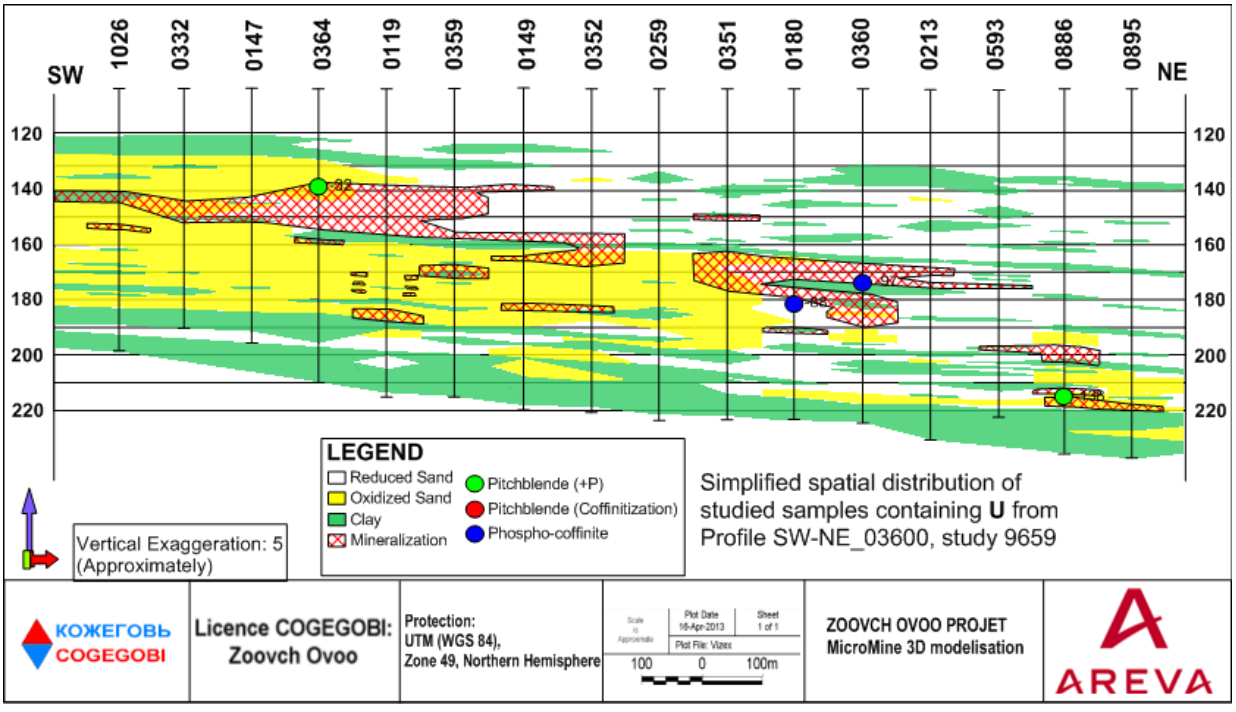

Figure 145: The spatial distribution and the abundance of the different uranium types encountered along the Profile SW-NE_03600 in Zoovch Ovoo.

6.4 CONCLUSIONS FROM URANIUM PETROGRAPHY

Uranium is contained in three forms, as independent spherules and flakes and as aggregates of the previous two categories that lead to the formation of U-cement. According to petrographic observations coupled with geochemical data, there are at least three discrete uranium mineralization episodes, linked to the roll-front activity. Two of them concern the pitchblende formation which occurs at two different times. The first episode takes place right after the first euhedral pyrite generation and the second contemporaneously to the second euhedral pyrite generation; hence pitchblende is found as coating of the first euhedral pyrite generation and as isolated microsize spherules inside the second euhedral pyrite generation. The third uranium generation is differentiated from the previous two due to its chemistry, which this time is close to the phospho-coffinite stoichiometry. This generation seems to be related to organic matter epigenization and is not yet clear if it occurs before or after the pitchblende formation. It was also found that pitchblende experiences a certain coffinitization after its formation and in this sense the phospho-coffinite formation might also be a late diagenetic U-phase. The two different uranium minerals will be further discussed in the next chapter which is focused on uranium geochemistry.

It was also possible to reach to several conclusions based on our study, with regards to the organic matter-pyrite-uranium relationships:

1. Based on observations there are certain organic matter particles that can have a primary very low concentration of U, though not every organic particle contains a primary U content, fluctuating below 0.5 wt%, which is not important in terms of gradient, yet could be important for the imminent charges of uranium that enrich the particle, based on the principle that uranium traps uranium.
2. Pyrite remains were identified inside large pieces of organic matter (400-500 μm) and to a lesser extent in collapsed cell walls that are fully epigenetized by uranium ultimately leading to only traces of pyrite in a “fully replaced” organic particle. The term “fully replaced” was used to indicate about 75 wt% of U and about 10 wt% of organic carbon remaining in an organic particle. As a result several textural characteristics of the plant debris are at all times preserved. Based on the present study it is not definitive if it is the pyrite (in particular the reduced sulfur), the organic carbon or the uranium early concentration inside the organic carbon that plays the major role in uranium reduction and trapping.
3. Pitchblende was identified in the internal part of organic matter particles in cases when fractures (desiccation cracks), which would allow water circulation, were available. In those cases the presence of pyrite was not confirmed. This trend is not systematic and not every fracture can contain uranium, even in heavy mineralized organic particles.

4. Replacement textures of partially dissolved former Fe-Ti oxides are common. The empty space that resulted from the dissolution was occupied by (i) euhedral Type II dolomite crystal growth and (ii) sphalerite cement. In other cases those Fe-Ti oxides were finely replaced by pitchblende, preserving their textural characteristics. The replaced oxide would still contain about 5 wt% in Ti.
5. The Ca, Si and P concentrations are increasing proportionally to U concentration as the organic matter replacement process is evolving. Therefore in the case of full replacement when U will fluctuate around 85 wt% the pitchblende will be accompanied by relative high Si and P, indicating slight coffinitization.
6. The first euhedral pyrite generation that in certain samples plays the role of the binding phase of the detrital grains (pyrite cement not related to organic matter) can be corroded by the roll-front waters, leading in diffused crystal boundaries and diffused pitchblende precipitation.
7. The second generation of “euhedral” pyrite is followed by contemporaneous uranium precipitation inside the available pores of the pyrite clusters. This feature is not corrosion since there are two euhedral pyrite generations side by side while only the late generation is marked by pores and disseminated uranium mineralization. If this feature was not idiomorphic crystal growth but corrosion then both euhedral pyrite generations would have pores. Hence, it could be stressed that there is an interference during the second euhedral pyrite generation resulting in discontinuous euhedral pyrite crystal formation. Contemporaneously uranium precipitates in the available pore space, in between the undeveloped pyrite crystals.
8. Both sphalerite varieties, the Cd rich with 14 wt% and the Cd poor with less than 3 wt%, contain either pitchblende as independent microsize spherules or as fracture-filing cement. The microsize spherules must belong to the first generation of pitchblende and the U-cement which is found perimetrically of sphalerite, to the second.
9. With regards to uranium enriched clays (matrix) with up to 30 wt% U, it may be speculated that the reason for U to have grown on clay surfaces suggests that there was U initially adsorbed and may belong to the same generation of reduced U deposited within the organic matter (with no mineral expression).
10. Poecilitic dolomite crystal growth without perfect interlocking can contain pitchblende among their crystal surfaces (available porosity). Sometimes there were cases where the Type II euhedral dolomite generation had corroded rims followed by pitchblende precipitation. This dolomite phase is pre-diagenetic in regards to pitchblende precipitation and must be unstable in the presence of roll-front waters.
11. Finally, there were cases when quartz cement was recognized. It is post-diagenetic in regards to pitchblende formation and it tends to fill the available vugs inside pyrite

cement, uranium cement and destabilized Fe-Ti oxides with secondary porosity. It is not clear if there is only a single quartz cement episode. The presence of dissolved silica can play an important role for the coffinitization of the pitchblende and phospho-coffinite formation.

6.5 INTRODUCTION TO URANIUM GEOCHEMISTRY

The chemistry of the different uranium occurrences was studied by means of SEM-EDS and EMPA. The results were projected on three plots, namely the U+Ca/Si, the P/Si and the ternary plot of P-Si-U, to summarize and to illustrate the dominant trends among the U-phases.

It was concluded that the uranium mineralization in Zoovch Ovoo is expressed by two uranium minerals, namely and dominantly by pitchblende UO_2 (uraninite) and to a far lesser extent by phospho-coffinite $(U,P)SiO_4$. In some samples the pitchblende was coffinitized and it was hence deviated from the pure uranium dioxide stoichiometry. The presence of other elements, such as Zr, Ti and P in the lattice of the uranium minerals shifts the plotted samples from the pure stoichiometry of the respective minerals. There are no visible trends between pitchblende and phospho-coffinite as in the cases where pitchblende was coffinitized, phosphorus was absent. This concludes to the fact that phospho-coffinite does not descent from pitchblende but stands for an independent uranium generation.

6.5.1 Examples of U-phases used in the computations

Most of the U-phases encountered during the study were not considered in the calculations due to mineralogical complexity and interference of adjacent minerals during the EDS measurement. Most of the measurements that were discarded concerned U-enriched organic matter, since U was not expressed as oxide, even with 50 wt% U. In cases when the silicium content was elevated due to adjacent silicate phases, attention was made on the phosphorus content, which should be proportionally increased. If that requirement was not met or if aluminum was present then there was certainly an interference. When pyrite was associated to the U-phase of interest, then the iron and sulfur contents were removed from the mass and the formula was normalized to the uranium important elements, Si, P, Ca and Ti.

Photo-micrographs

Figure 146: Examples of uranium phases which were used in the computations.

Sample: AA-58 (pictures from SEM-EDS)

A: Slightly coffinitized pitchblende filling a vug inside pyrite cement.

B: Former Fe-Ti oxide, almost fully replaced by pitchblende, inside U-enriched clays (matrix).

C: Former Fe-Ti oxide, replaced by pitchblende, while maintaining the inherited cleavage.

D: Pitchblende as pore-filling cement in the internal fracture system of an organic particle. In certain cases the uranium almost fully replaces the organic matter and the obtained results can be utilized.

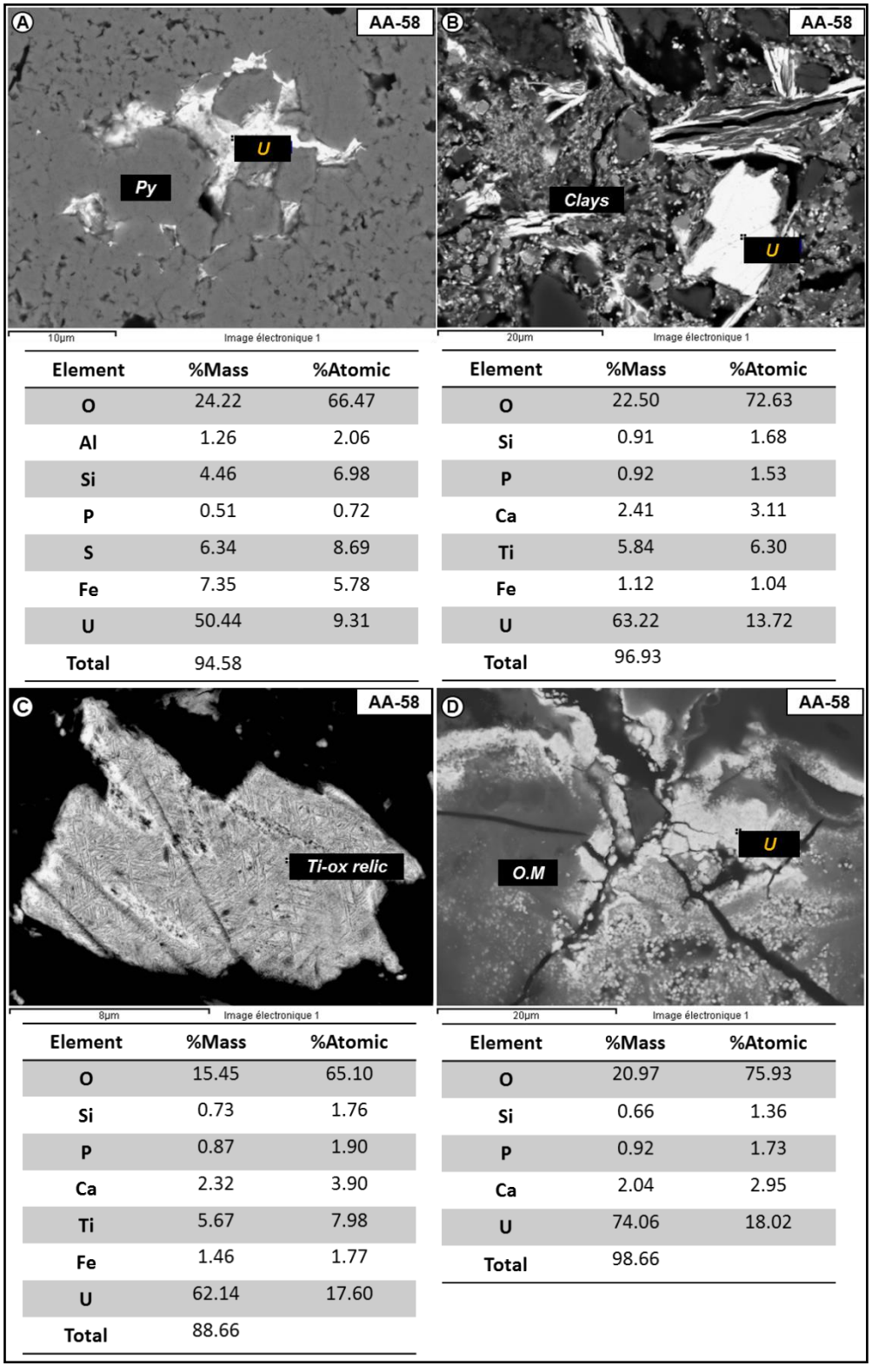

Element	%Mass	%Atomic
O	24.22	66.47
Al	1.26	2.06
Si	4.46	6.98
P	0.51	0.72
S	6.34	8.69
Fe	7.35	5.78
U	50.44	9.31
Total	94.58	

Element	%Mass	%Atomic
O	22.50	72.63
Si	0.91	1.68
P	0.92	1.53
Ca	2.41	3.11
Ti	5.84	6.30
Fe	1.12	1.04
U	63.22	13.72
Total	96.93	

Element	%Mass	%Atomic
O	15.45	65.10
Si	0.73	1.76
P	0.87	1.90
Ca	2.32	3.90
Ti	5.67	7.98
Fe	1.46	1.77
U	62.14	17.60
Total	88.66	

Element	%Mass	%Atomic
O	20.97	75.93
Si	0.66	1.36
P	0.92	1.73
Ca	2.04	2.95
U	74.06	18.02
Total	98.66	

Figure 146: Examples of uranium phases which were used in the computations.

Photo-micrographs

Figure 147: More examples of uranium phases and their limitations for computations.

Sample: AA-58 and AA-78 (pictures from SEM-EDS).

A: Pitchblende filling the porosity between pyrite cement and detrital quartz. This time the associated quartz elevates the Si concentration by about 7 wt%, hence the result is not reliable.

B: Pitchblende filling the porosity inside pyrite cement, used in the computations.

C: Pitchblende flakes associated to clays. The Si content is not affected by the presence of clays.

Figure 148: More examples of uranium phases used in the computations.

A-D: Different magnifications of pitchblende inside pyrite cemented encompassed by the subhedral (Type III) dolomite. This time pitchblende shows coffinitization having elevated Si and P contents.

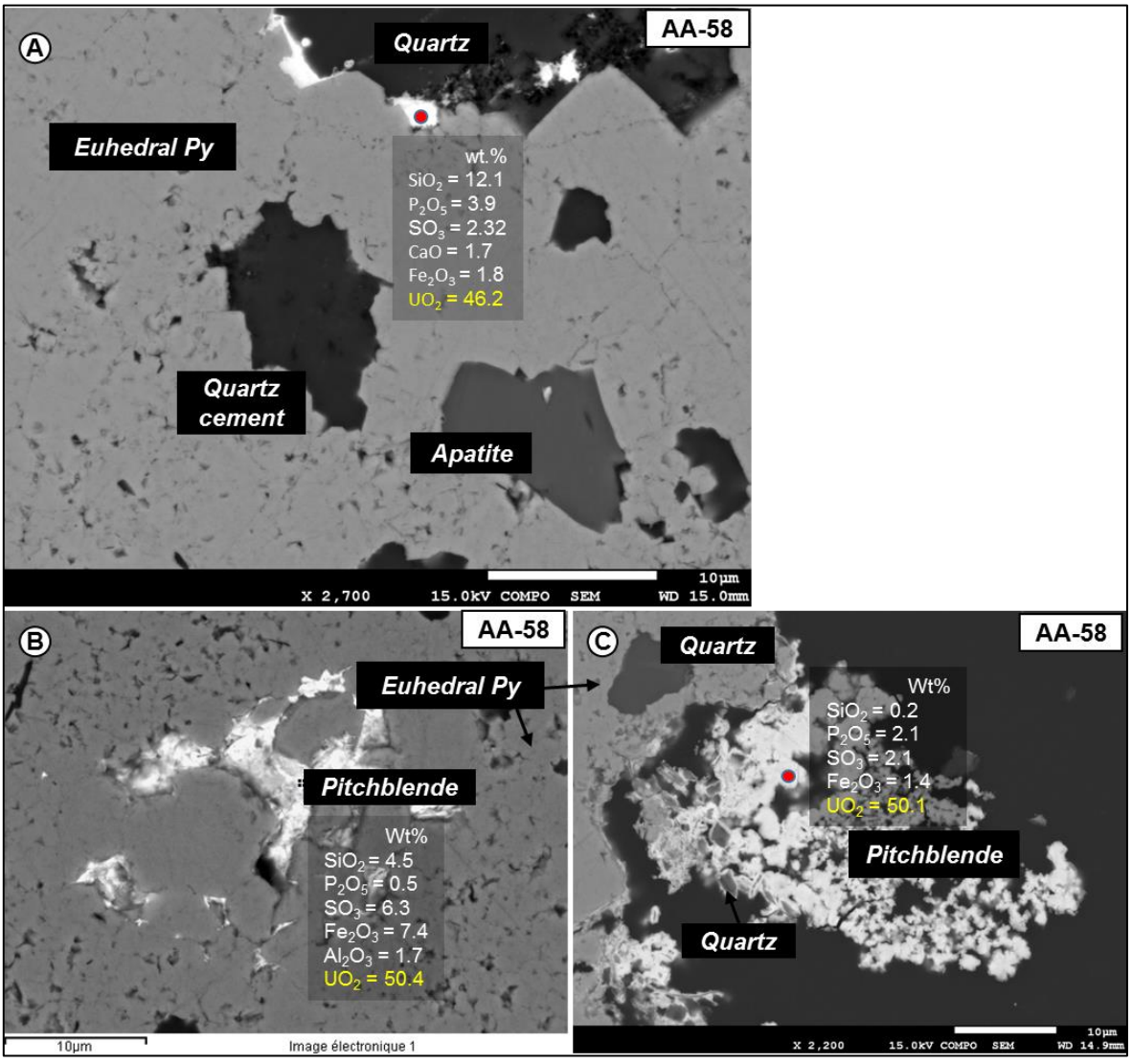

Figure 147: More examples of uranium phases and their limitations in computations.

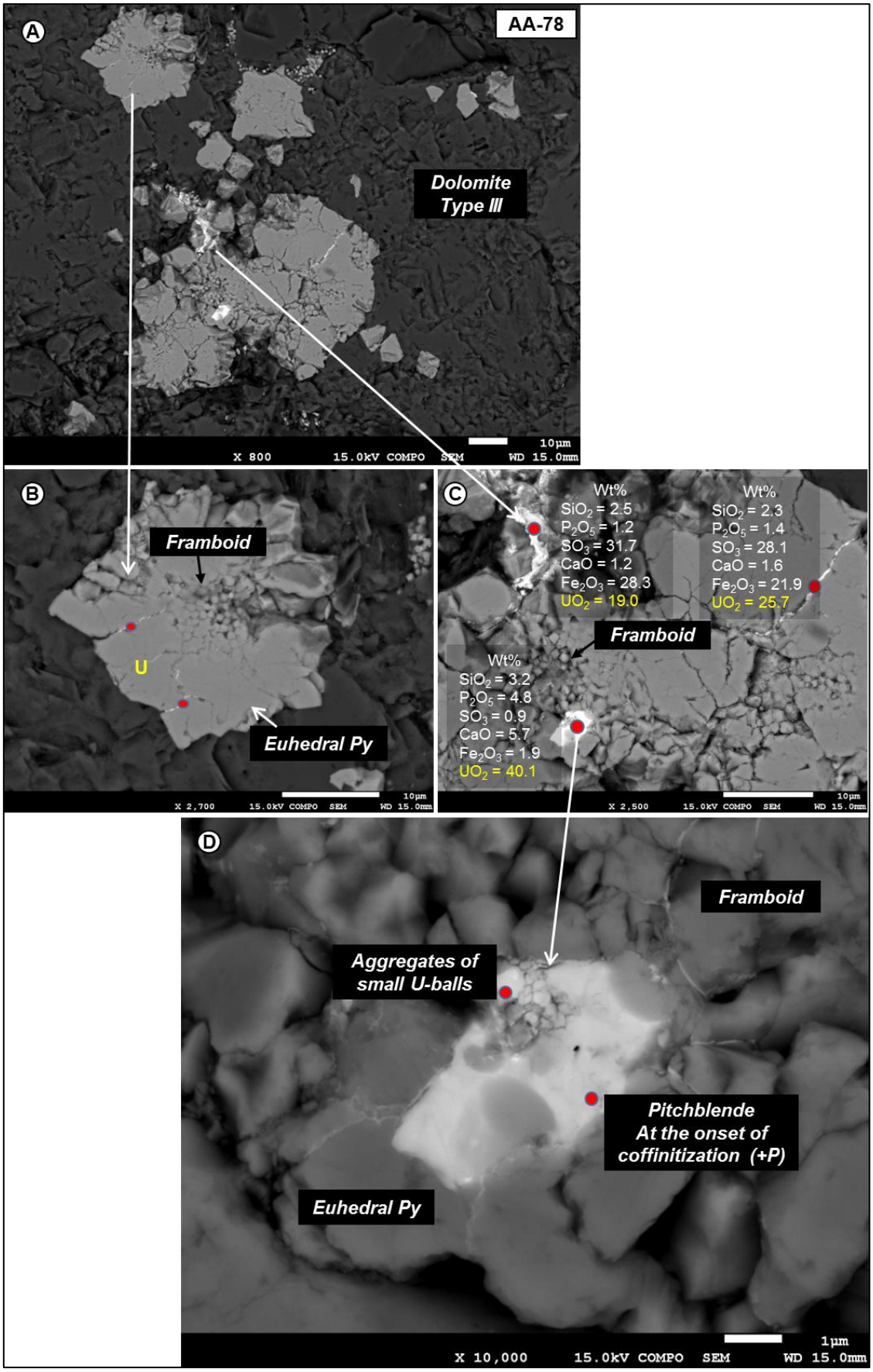

Figure 148: More examples of uranium phases used in the computations.

6.5.1.1 The Si/(U+Ca) plot

This plot (Figure 149) contains measurements from 14 different samples, on assemblages that met the criteria described in the previous chapter.

The trend-line drawn in blue links the end members of pitchblende and coffinite. It is evident that there is a shift from the trend-line, which is due to the presence of other associated elements not used in the pure stoichiometric formula. There are two major groups visible.

1. The first close to the pitchblende domain with some points shifted towards the coffinite domain, indicating increase in silicium; in other words the coffinitization of pitchblende.
2. The second group is closer to the coffinite domain while there is no stoichiometric coffinite.

It appears that the two mineral domains are not related, since most points fall close to the two mineral domains. The U-phases that are plotted close to the pitchblende domain but are less rich in uranium are referring to uranium oxides inside organic matter, hence there is a uranium deficiency due to the presence of remaining organic carbon. Finally, the few spots that are surpassing the 50 wt% in Si were measured inside large silicates, which could therefore be an interference of Si from the feldspars. The exact level of Si in those U-phases is very difficult to be calculated.

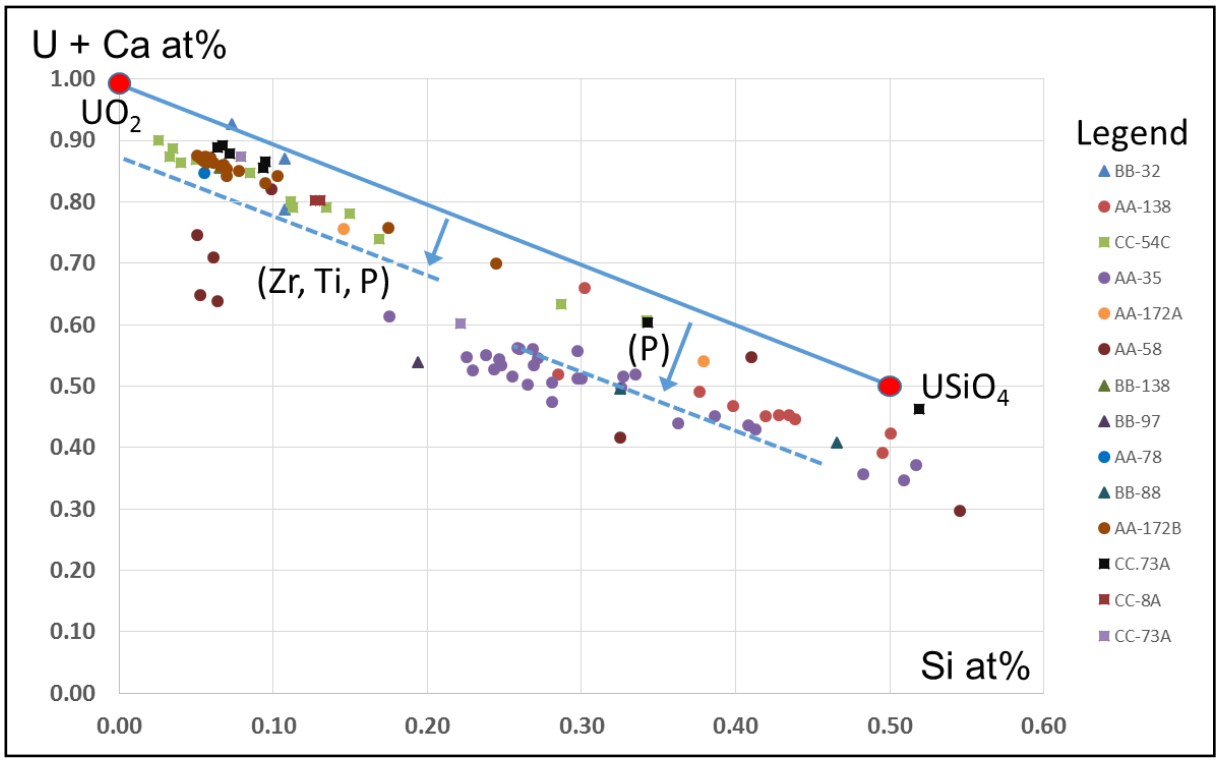

Figure 149: U+Ca versus Si plot expressed in atomic percent, with two distinct compositions of the U phases: one closer to the pitchblende end-member and the other closer to the P-coffinite.

6.5.1.2 The Si/P plot

The same samples plotted in Figure 149 were projected onto a Si/P plot as well (Figure 150).

The trend-lines drawn in blue, link the stoichiometric end members, hence pitchblende and coffinite. It is evident that there are shifts from the trend-lines, which are due to the presence of other associated elements not used in the pure stoichiometric formula. There are two major groups visible.

1. The first group concerns samples with less than 0.10 at% in P and less than 0.20 at% in Si. Locally there are a few samples that have higher than 0.20 at% Si and these indicate that a slight coffinitization of pitchblende has occurred.
2. The second group concerns samples that are close to phospho-coffinite stoichiometry, with P between 0.10 and 0.25 at% and Si between 0.20 and 0.50 at%. There are a few dispersed spots with Si over 0.50 at%, due to interference with associated silicate phases.

Since there are is no trend-line between the pitchblende and phospho-coffinite, the two U-phases must not be not genetically related.

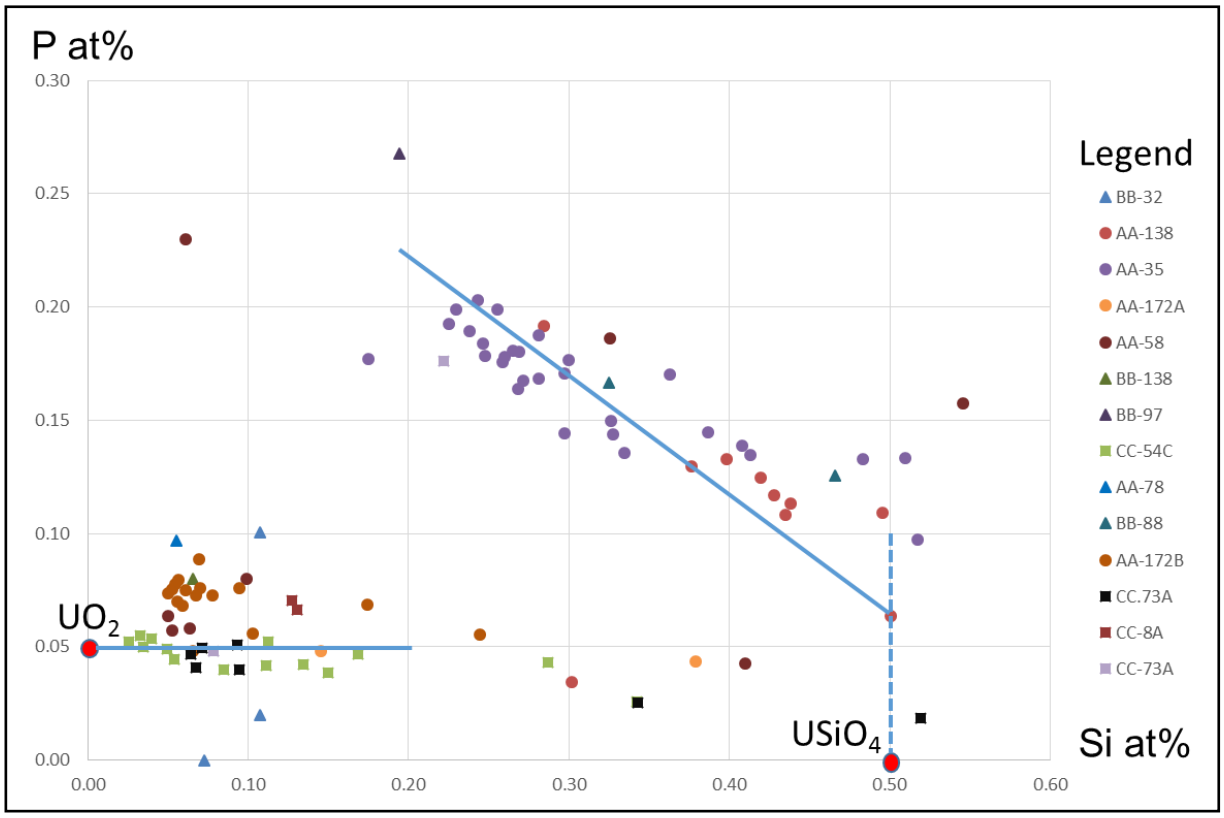

Figure 150: Plot of Si versus P expressed in atomic percent, which shows that the U oxide contains a low P content and a slightly increasing Si contribution (onset of coffinitization). The second example data plot along a trend at decreasing P and increasing Si which can depict the coffinite/P-coffinite solid solution.

6.5.1.3 The (U+Ca)-Si-P ternary diagram

The ternary diagram of P_2O_5-UO_2-SiO_2 was used as a summary of the U-geochemistry (Figure 151). The majority of the samples (9/14) are plotted close to pitchblende stoichiometry, in every case enriched in P which causes a slight deviation from the stoichiometric formula of UO_2. On the other hand much lesser (5/14) are plotted close to the phospho-coffinite stoichiometry, while there is a certain deficiency in P, leading to non-stoichiometric P-coffinite. Pure coffinite is also absent and there is no link between pitchblende and phospho-coffinite indicating that the coffinitization of pitchblende is an independent process. It is also important to note that most of the times the measured U-phases are close to P-coffinite, they are related to organic matter. Examples of the uranium phases that were used for the construction of the ternary diagram are given in Figure 218 and Figure 219.

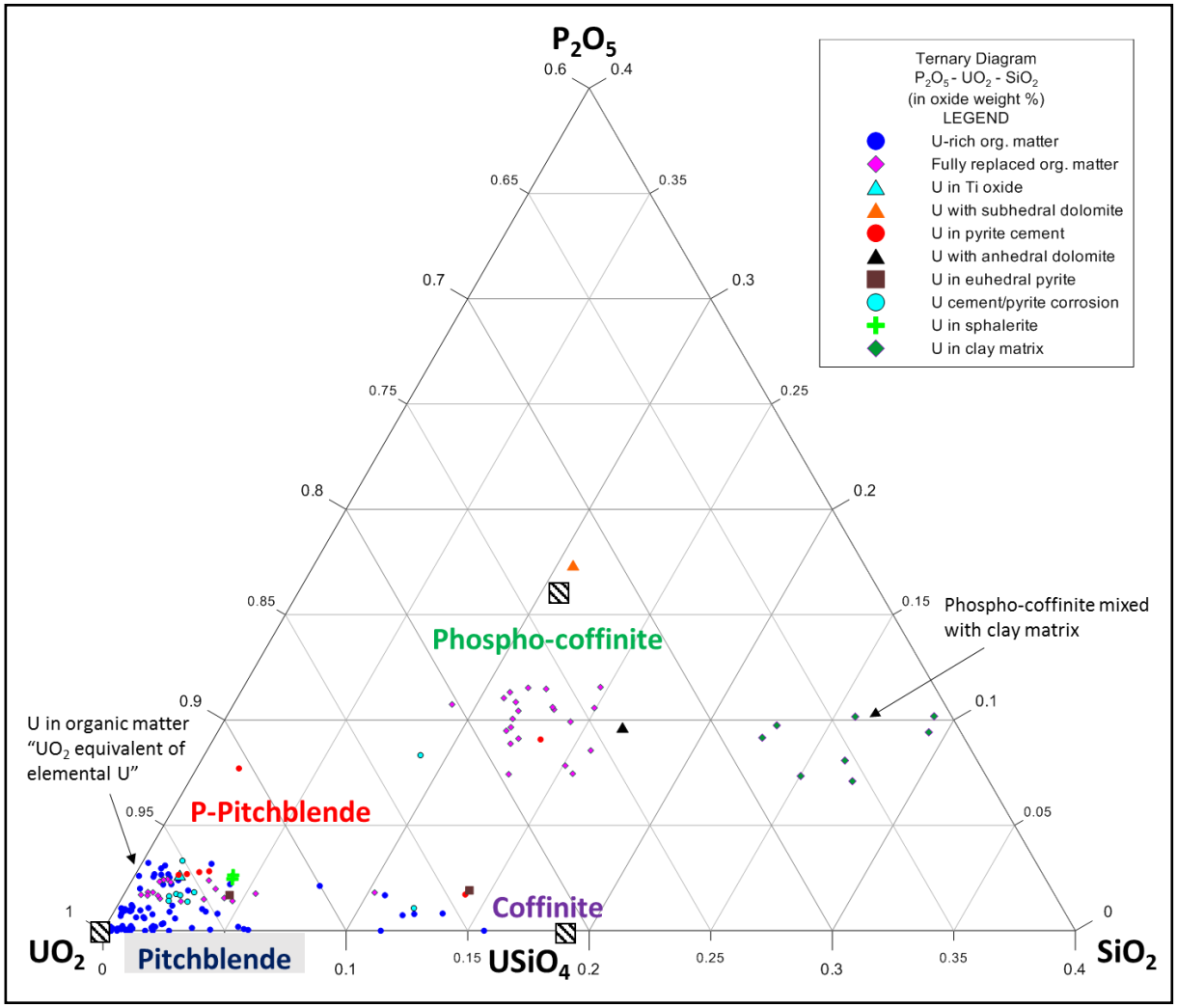

Figure 151: Ternary plot of the P-U-Si, in oxide wt%, indicating the stoichiometric U-mineral domains namely, of Pitchblende, Phosphorus enriched Pitchblende, Coffinite and Phospho-coffinite, used as references.

6.5.2 Uranium ore REE patterns

The REE pattern of the uranium ores hosted in particular type of deposits i.e. roll-front, volcanic related, vein type and others may provide information linked to their genetic mechanism; thus permitting classifications. This approach became possible by studying and comparing the REE patterns of major uranium deposits worldwide for which the genetic mechanism is already known (Mercadier et al., 2011).

The REE content of three samples, the location of which is available on Figure 152 on roll-front scale, hosting uranium as uraninite (UO_2) was studied. Each time uranium was associated to different facies i.e. (A) U-replaced organic matter, (B) U associated to pyrite and (C) U diffused in clay matrix. The REE content was calculated using LA-ICP/MS (Figure 153) and normalized versus chondrite (Anders and Grevesse, 1989). Ultimately the results were compared with the REE patterns as discussed in Mercadier et al. (2011) in order to classify the Zoovch Ovoo type U-deposit.

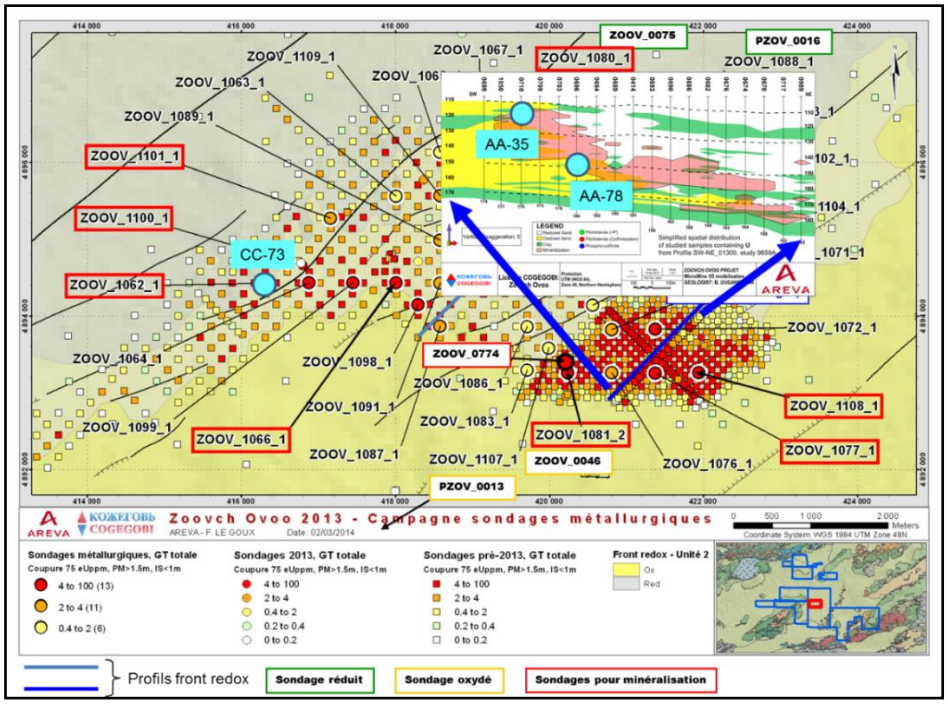

Figure 152: Position of the three U-mineralized samples in the Zoovch Ovoo roll-front.

All the spectra are flat and the REE concentrations range between10^3-10^4 that of chondrite. Sometimes a very small negative anomaly can be seen for Eu as well as a very slight enrichment in HREE. In the synthetic plot (Figure 154) all of the samples presented in Figure 153 are plotted at the same part of the diagram. Half are plotted inside the high salinity fluids field and the other half are plotted closely but outside the proposed reference fields. It is also evident that there is no a link between the uranium oxides from Mongolia and Kazakhstan as indicated. The REE pattern of the uranium oxides is also compared to those of the bulk rock and of dolomite cements (Figure 155).

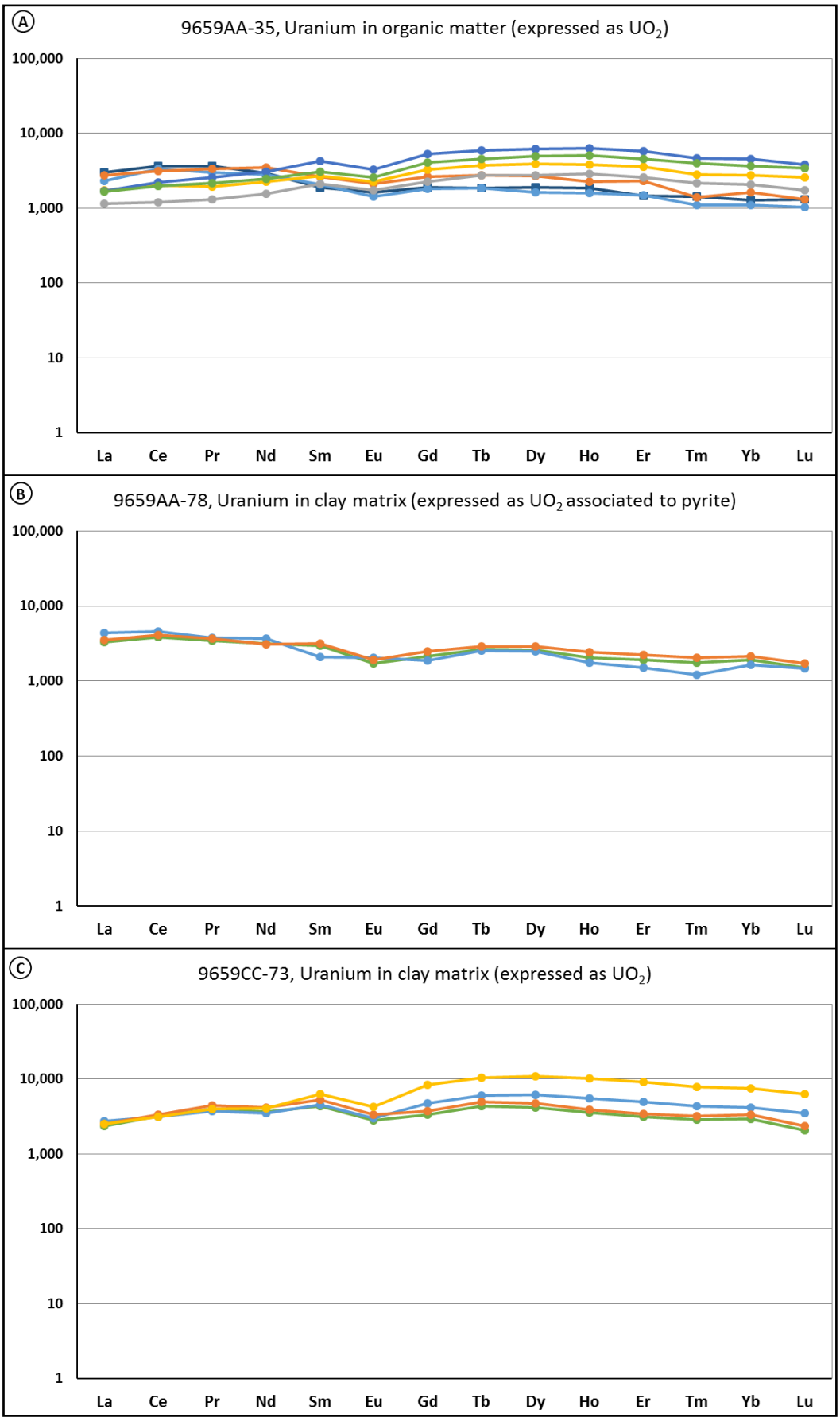

Figure 153: Chondrite-normalized rare earth element patterns for uranium oxides in three different samples.

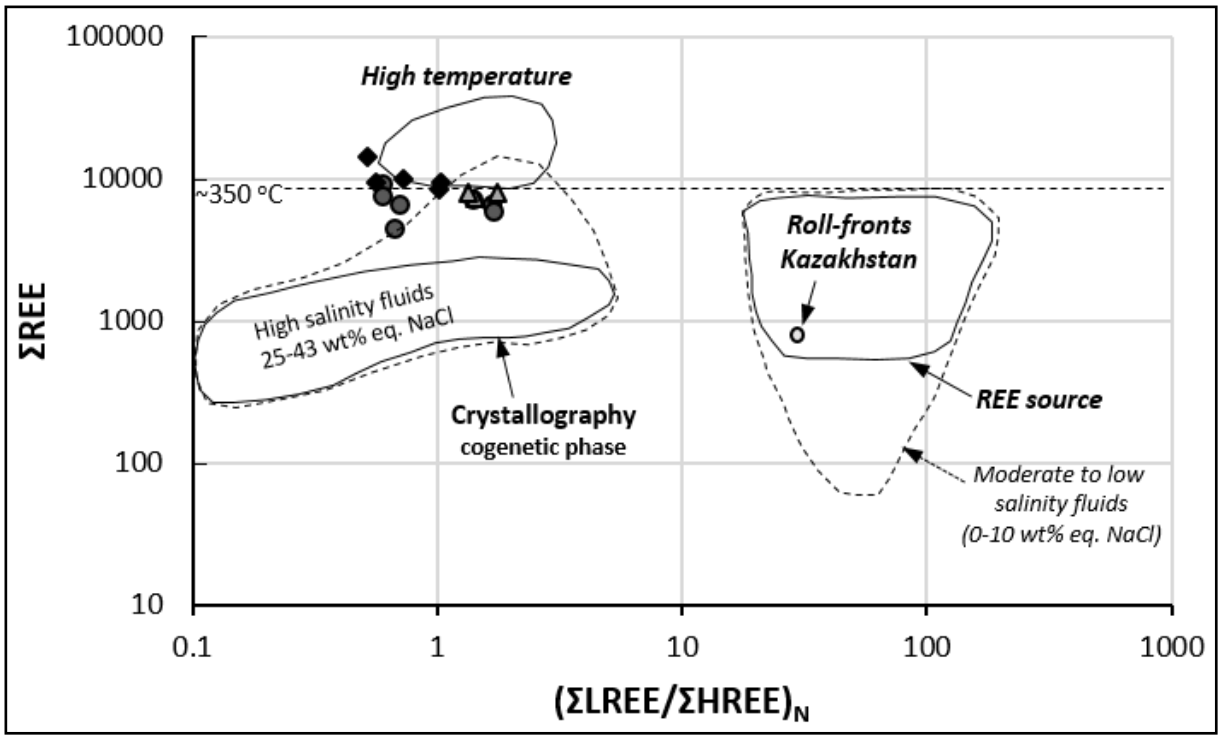

Figure 154: Rare earth element abundance (ΣREE) vs REE fractionation ($(\Sigma LREE/\Sigma HREE)_N$). Reference fields and information on uranium from Kazakhstan roll-front from Mercadier et al. (2011). Dots for sample AA-35, rhombs for sample A-78 and triangles for sample CC-73. All of the samples presented in Figure 153 are plotted at the same part of the diagram. Half are plotted inside the high salinity fluids field and the other half are plotted closely but outside the proposed reference fields. There is clearly not a link between the uranium oxides from Mongolia and Kazakhstan as indicated.

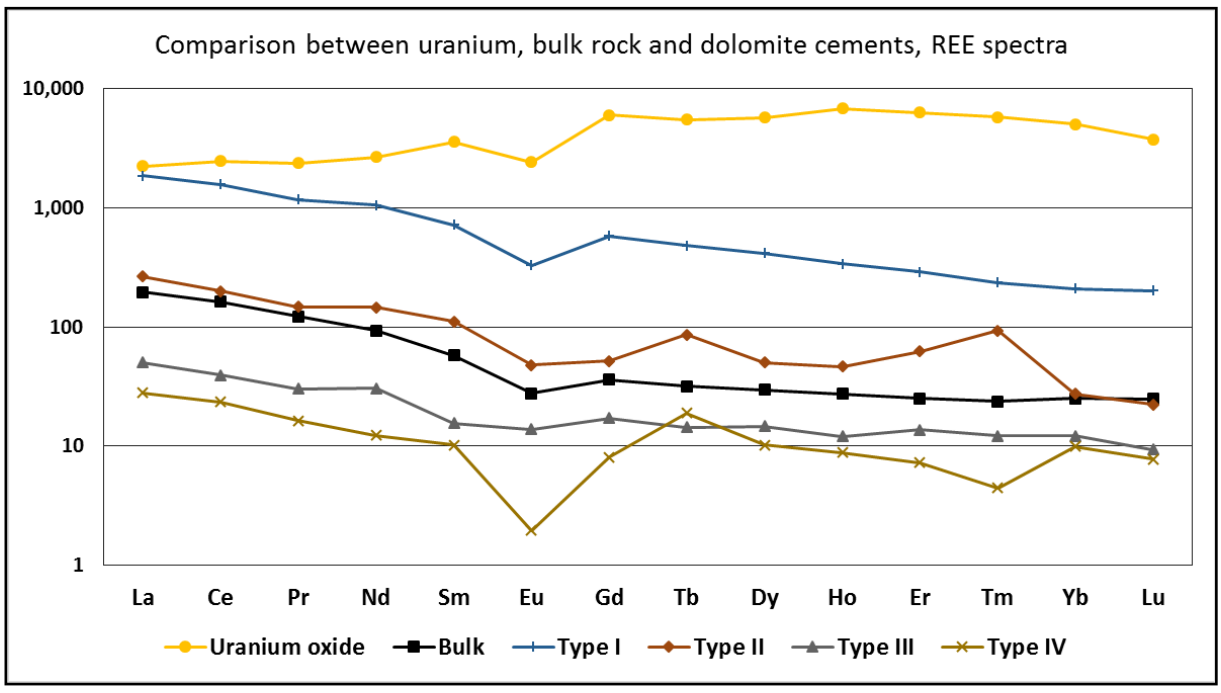

Figure 155: Comparison between the REE concentrations of the uranium oxides, bulk rock and four types of dolomite.

6.6 COMPLEMENTARY EXAMPLES FROM THE URANIUM-ORGANIC MATTER STUDY

Some examples from the uranium-organic matter study were already presented in chapter 6.5.1 Examples of U-phases used in the computations. This chapter contains more analytical data and examples of measurements that were used as complements to the petrography. Although it was observed that even with 50 wt% U in organic matter, uranium can be still not expressed as mineral, there are some limitations. For instance if U precipitates directly at the external rim of an organic particle, or in the internal fracture system, then even with very low concentrations (less than 8.0 wt%) the uranium phase can be expressed as mineral. Furthermore it has been observed that the concentration of U in the organic matter is also controlled by the permeability within the organic matter.

Photo-micrographs

Figure 156: Polished block photographs of telovitrinite macerals taken under BSE and the respective EMPA results for U, Fe, S and Ti.

Samples (AA-58, AA-23).

A) Telovitrinite particle with minor pyrite and Fe-Pb sulfates (probably newly formed). A brighter zone where uranium has higher concentration is distinguished. The overall U concentration is lower than 3.0 wt%. The Fe and S do not follow the pyrite stoichiometry.

B) Uranium is concentrated at the rims of the telovitrinite particle under the form of pitchblende, reaching 15.0 wt%. The profile C-D shows that U concentration is increasing moving from the internal towards the external part.

C) The telovitrinite particle can be separated in two parts, based on the U concentration, with the brighter area always being richer. The overall concentration fluctuates constantly between 0.8-2.5 wt%.

D) Telovitrinite particle with up to 1.4 wt% U, containing euhedral pyrite in fractures and dispersed Fe, S, P and Fe, S, U mixed phases.

E) Iron oxide (probably magnetite) containing native selenium as cement in the middle part and Selenium with Zircon at the right edge.

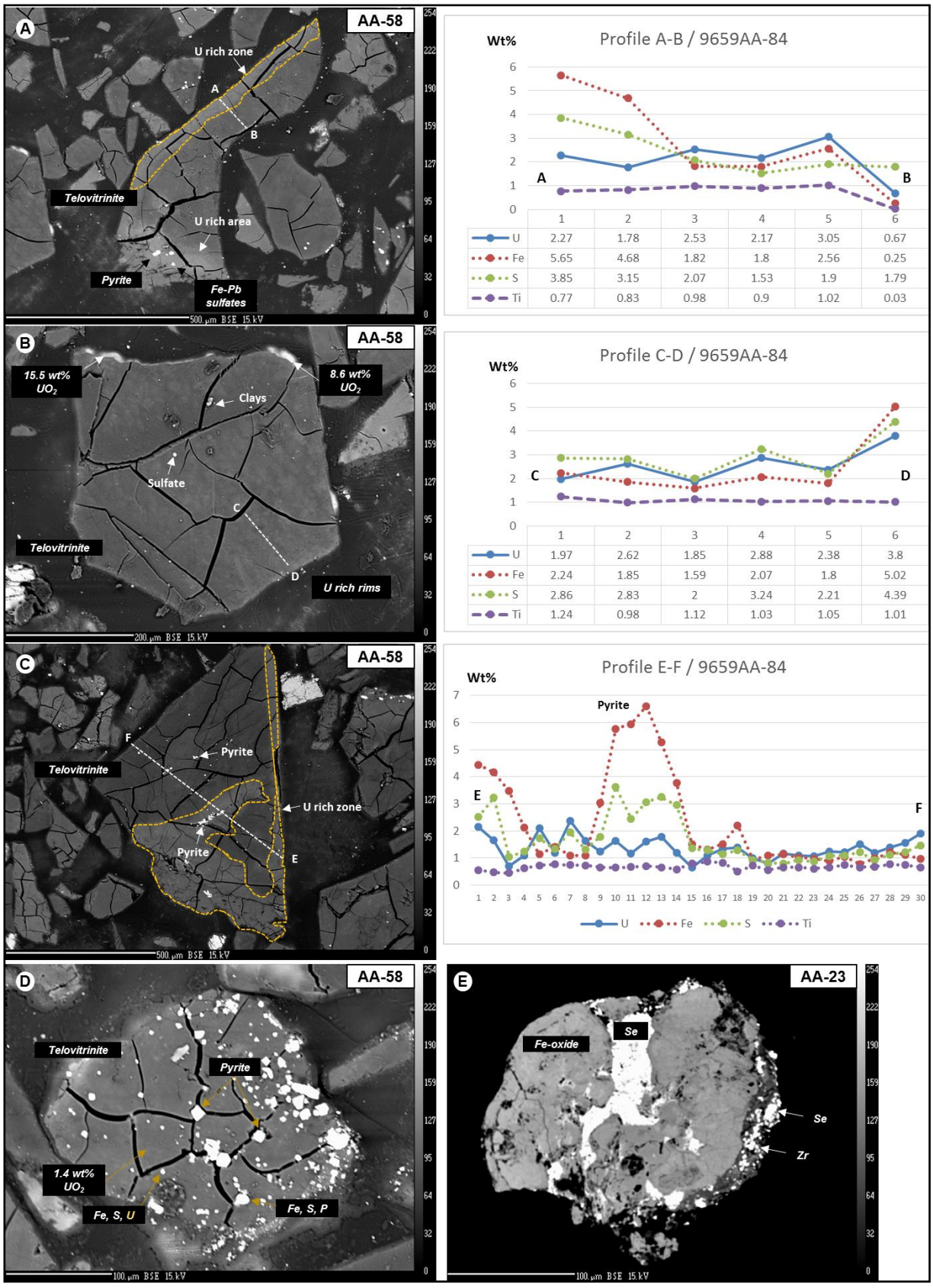

Figure 156: Polished block photographs of telovitrinite macerals taken under BSE and the respective EMPA results for U, Fe, S and Ti.

Photo-micrographs

Figure 157: Thin section photographs of telovitrinite macerals taken under BSE and the respective EMPA results for U, Fe, S and Ti.

A) Pitchblende precipitated at the rim a telovitrinite particle and advanced through using the fracture network. The U concentration fluctuates between 0.5 to 50.0 wt%, while Fe, S and Ti are constantly below 5.0 wt%.

B) Telovitrinite particle with the highest U concentration occurring at the rim, over 40 wt%, gradually decreasing towards the inner part. The Fe, S and Ti concentrations remain constant and are close to zero.

C) High resolution EMPA scanning of a telovitrinite particle with U being located at the rims and internal fractures, 20.0 and 60 wt% U respectively, while the background U concentration of the maceral is constantly below 3.0 wt%.

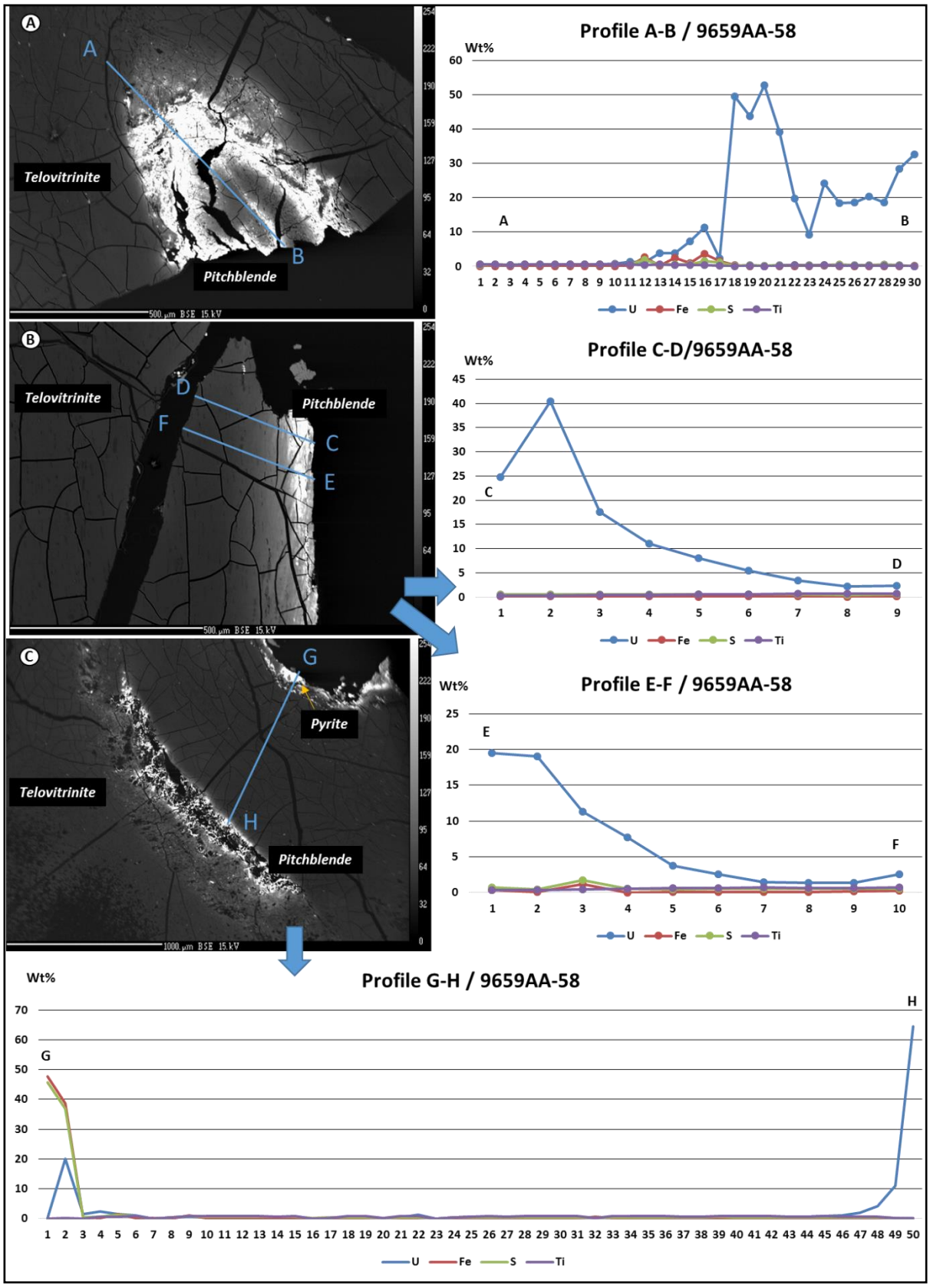

Figure 157: Thin section photographs of telovitrinite macerals taken under BSE and the respective EMPA results for U, Fe, S and Ti.

A few examples of XRF chemical maps on organic matter are provided below (Figure 158 to Figure 160). Chemical maps of U, Fe, Si, S, and their composite maps on a telovitrinite particle (Figure 158). Uranium is concentrated around the particle and in few cases in the internal part due to the presence of fractures. However, the overall U concentration of the particle is very low. Silicium is also found around the particle, probably due to the presence of clays. The Fe and S are concentrated at the rims reflecting pyrite concentration towards the edges and in certain cases interior fractures.

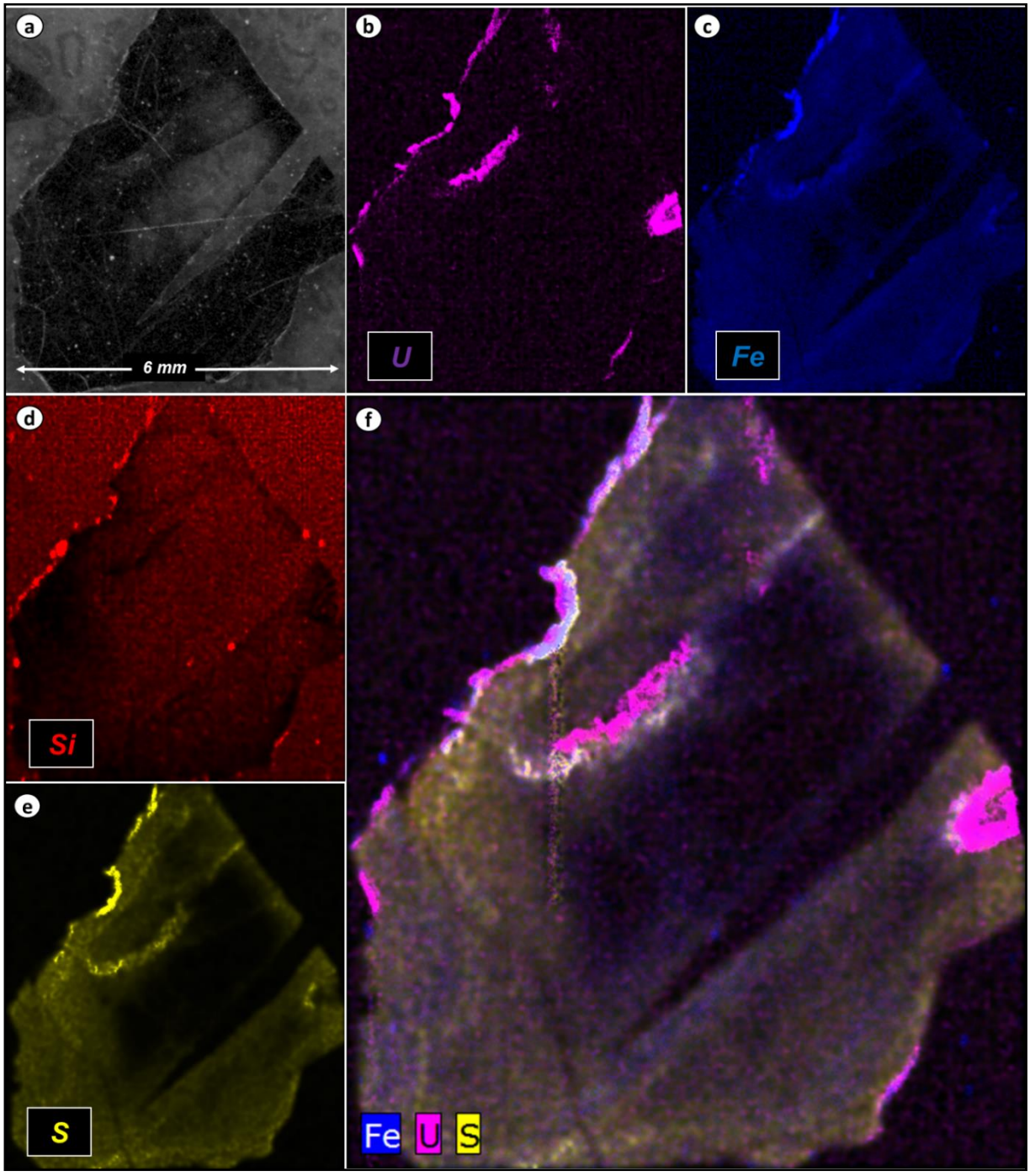

Figure 158 (sample AA-58): XRF chemical mapping of the particle presented in Figure 76 (A, C).

XRF Chemical map of for U, Ti, Fe, S, Ca and their composite map on a telovitrinite particle (Figure 159). Uranium is concentrated only at the rims. There are two concentration zones for calcium that to some extent are in accordance to iron concentration. Titanium has higher concentration towards the one half of the particle. Iron and sulfur seem to be related to small dispersed pyrite crystals inside the organic matter texture i.e. as cell wall infill. Uranium is not associated with these pyrite phases.

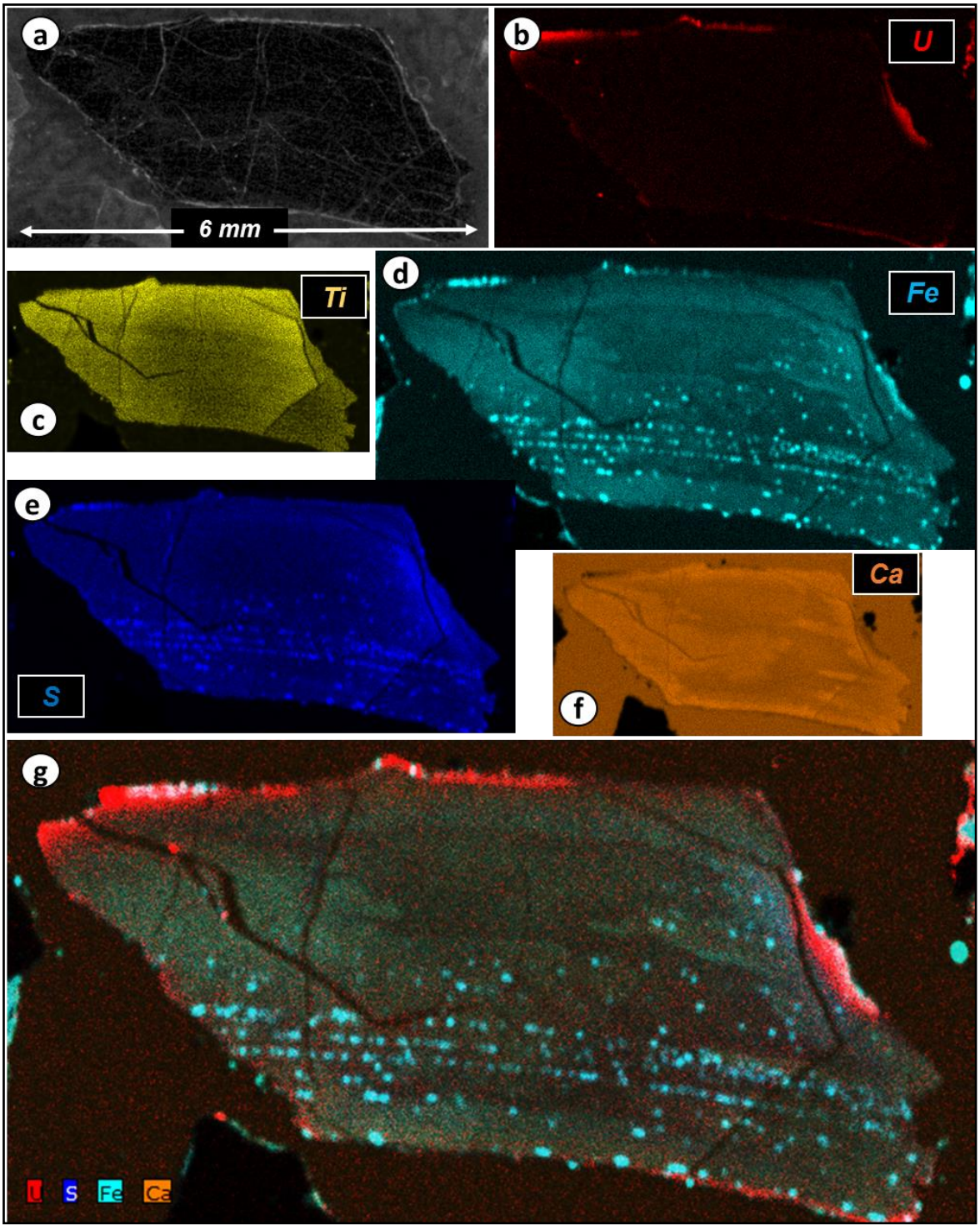

Figure 159 (sample CC-25B): XRF chemical mapping of an external part of a root.

XRF Chemical map of for Ca, Fe, S, U, Ti and their composite maps on a telovitrinite particle (Figure 160). Uranium not expressed as mineral phase (and titanium) is associated to the internal part of the maceral. Sulfur and iron form sulfides at the rim of the particle. Calcium and sulfur seem to be related to gypsum inside the particle.

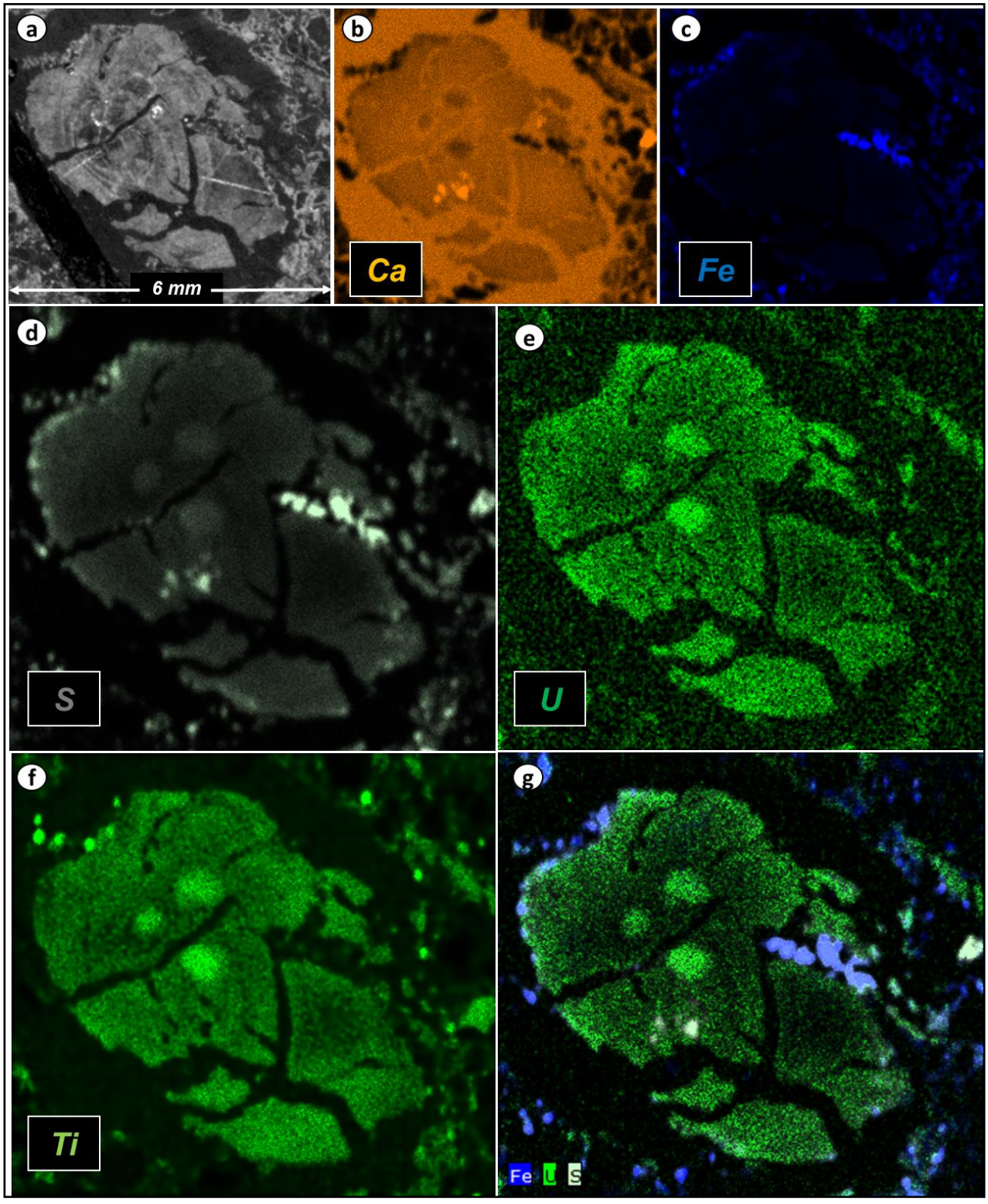

Figure 160 (sample CC-25B): XRF chemical mapping of an internal part of a root.

Finally, a chemical for Ca, Mg, Na, Fe and U from EMPA focusing on a large telovitrinite particle inside a euhedral (Type II) dolomite cemented sandstone was constructed (Figure 161). The Ca and Mg maps show that in addition of the available porosity, dolomite cementation took place also inside the fracture system of the organic particle. The Na map is used to map out the albite. The Fe map is used to identify mainly the location of pyrite, which is concentrated in the area inside the organic matter that is cemented by dolomite. Dispersed pyrite crystals can also be seen in the organic particle. The final map presents the distribution of uranium inside the organic particle, which is concentrated in two areas. At the upper part there is uranium, dolomite and pyrite, while the lower part contains only uranium. Hence, it could be stressed that the presence of pyrite in the organic matter is not necessary for U reduction.

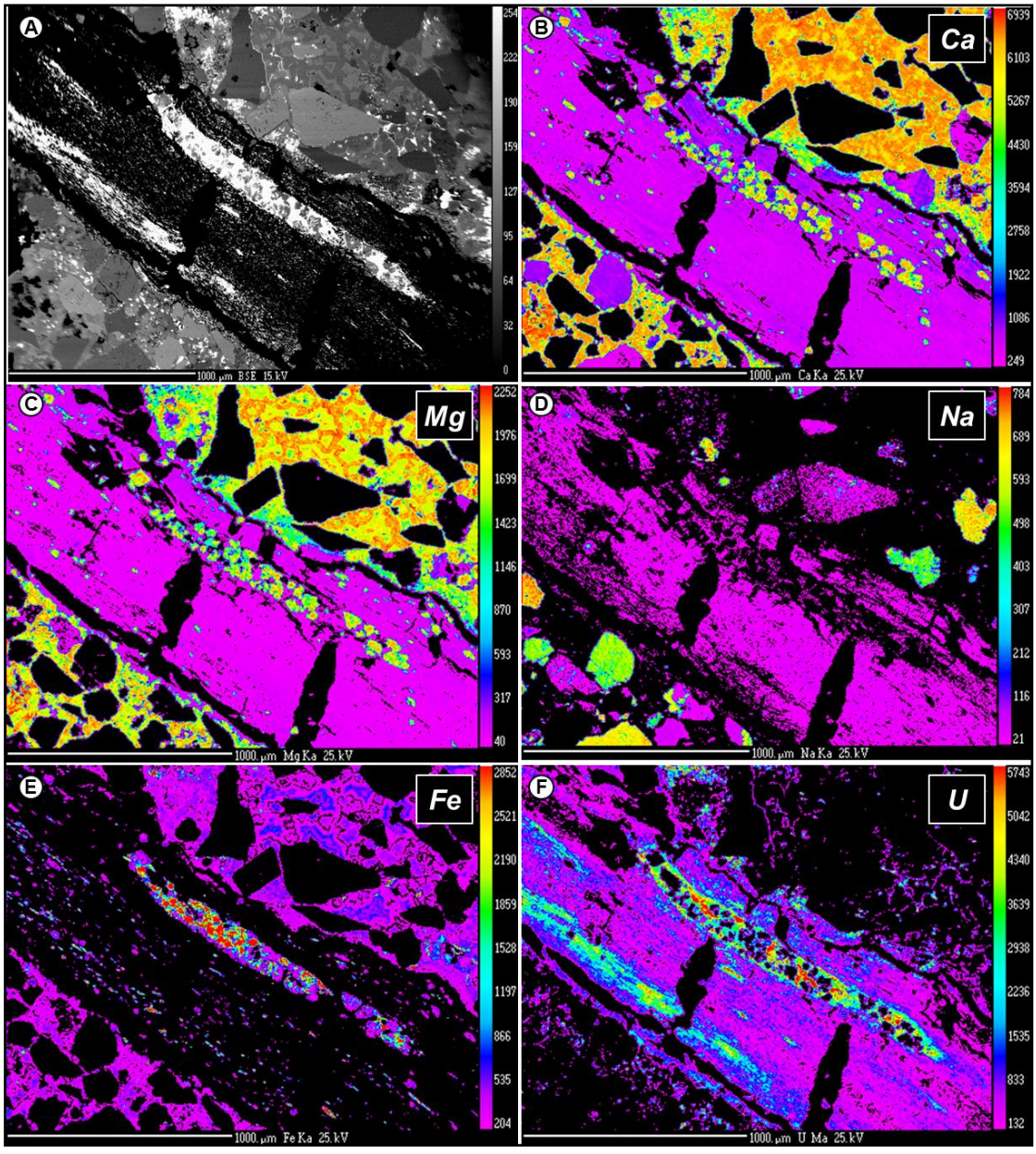

Figure 161 (EMPA CC-25B): XRF chemical mapping of an internal part of a root.

6.7 EVIDENCE FOR LIQUID ORGANIC FRACTIONS (EXUDATINITE) OR BITUMEN/OIL MIGRATED FROM OTHER SEDIMENTS

There were cases where (former) liquid organic matter (exudatinite) was identified. On the basis of 198 thin sections it was identified in very few, particularly in those coming from the 9606 study that were initially studied during the PhD thesis of T. PONS and were re-examined here. It is noted that the chemistry of the former liquid organic matter was not studied yet (i.e. biomarkers) because only thin sections were available.

The liquid organic fractions can be found as:

1. Patches inside the intergranular porosity.
2. Surrounding silicate grains.
3. Impregnating silicate grains.

In the uranium chapter, large feldspar grains carrying U-mineralization were presented. There was a discussion on the nature of the reducing agent for U in those feldspars. There are a few examples of large feldspar grains being susceptible to impregnation by organic fractions. Therefore it could be stressed that the organic carbon contained in the porosity of the feldspars acts as a trap for uranium. The source of those organic matter fluids can be the OM contained in Sainshand Formation (in this case oil windows was reached) or there is H/C migration from other sources e.g. from the oil fields in the vicinity of the uranium reservoir (**Figure 16**).

Photo-micrographs

Figure 162 and **Figure 163:** Examples of unclassified organic matter and liquid organic fractions as identified under thin sections.

Samples from the 9606 study (93, 151B, 85, 88, 26, 69, 109).

A, B: Probably organic matter (RF).

C, D: Liquid organic fractions appear to surround silicate grains (LPNA).

E, F: Liquid organic fractions surrounding a large feldspar grain (RF).

G, H: Overview and close view of the liquid organic fractions impregnating part of the feldspar (LPA).

I, J: Liquid organic fractions in the intergranular space (LPNA).

K, L: Liquid organic fraction surrounding a silicate cluster (LPNA).

M, N: Liquid organic fractions occupying the intergranular porosity (LPA).

O, P: Unclassified organic matter of low plasticity (LPA).

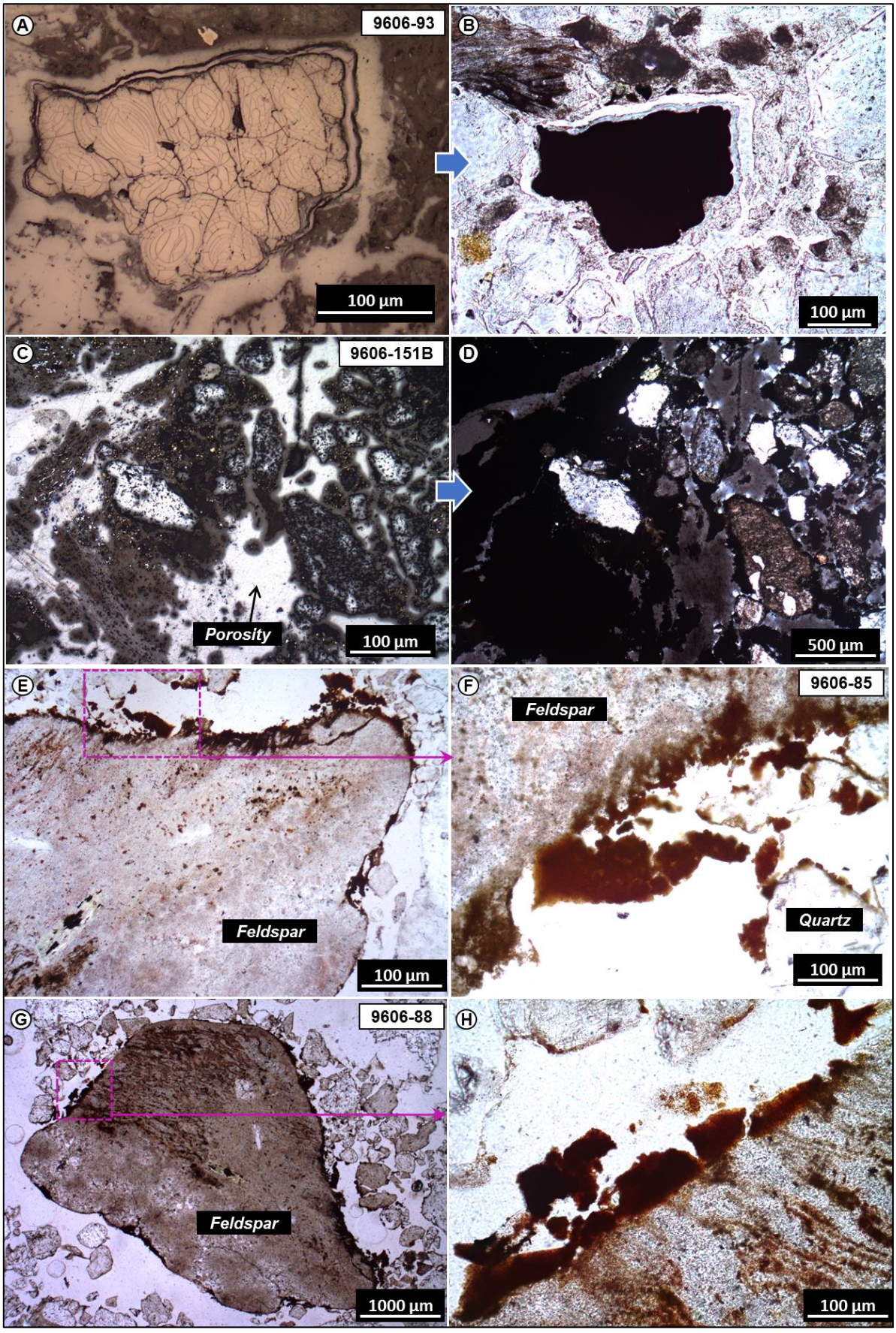

Figure 162: Examples of organic matter and liquid organic fractions (exudatinite or bitumen).

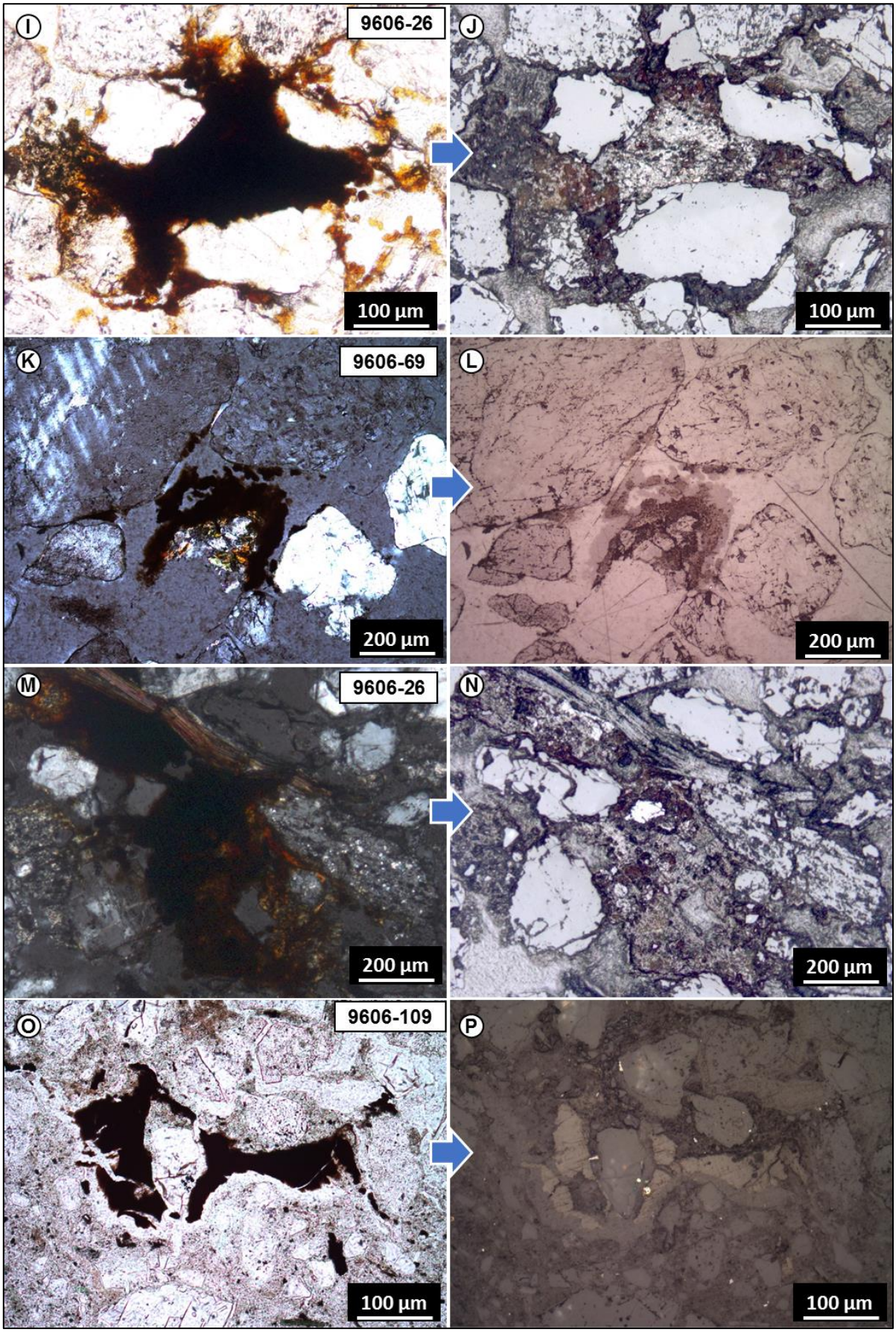

Figure 163: Examples of organic matter and liquid organic fractions (exudatinite or bitumen).

6.8 THE U-ORGANIC MATTER REPLACEMENT MECHANISM

The objective of the present chapter is to explain the function of the uranium-organic matter replacement mechanism. The main idea is to demonstrate how uranium concentration gradually increases in the expense of organic carbon on a given maceral. Since, it was not possible to measure directly the organic carbon using the current analytical tools, the carbon levels were estimated using an empirical formula from the SEM-EDS software. The formula is called “carbon by difference” and is actually a simple subtraction of the wt% of the total elements measured by the EDS, from 100%. For example if all measured elements have a summary of 93 wt% then the organic carbon, which is not included in the 93 wt%, must be about 7 wt%, assuming the volume of sample analyzed is almost totally composed of U and organic matter. Although empirical the formula has a certain validity. An organic carbon particle is mainly composed of carbon and oxygen. Sulfur, nitrogen and hydrogen are also included. Providing that the major elements, such as oxygen and sulfur are measured by the EDS and the concentration of nitrogen and hydrogen is only a few percent, then the calculated carbon can have a standard deviation of less than 2 wt% which is acceptable for the cause of the current study. Another factor to be considered is the macroporosity of the maceral. For example the interinite group macerals often have macroporosity. As was already discussed and is further demonstrated here, the full organic matter replacement occurs when the U concentration reaches 75-77 wt%. According to measurements the level of organic carbon remaining at full replacement is at the level of 5-6 wt% (the rest until 100% is covered by Fe, S, O and minor elements). For instance as presented in Table 30 in the APPENDIX II (TABLES – numerical data) the bulk concentration of other elements associated to the organic matter such as Fe, S and Ti is always below the levels of 1-2 wt%. Based on all the above, the U concentration in a fully replaced organic particle cannot surpass 77 wt%, in which case the organic carbon concentration will be at the levels of 6-7 wt%.

Photo-micrographs

Figure 164: For numerical data see in APPENDIX II (TABLES – numerical data) Table 30.

Sample (9659 AA-154). Polished Block under EMPA.

A: Profile A-B along a telovitrinite particle and distribution along the profile of the U, Fe, S and Ti concentrations, measured from one edge to the other. Uranium is contained constantly in gradients above 67 wt% indicating an almost full replacement. The plot at the bottom left of the figure stands for the remaining organic carbon versus the uranium content. It is evident that there is a linear relationship between the expense of organic carbon and the enrichment in uranium. For instance for 15 wt% remaining carbon, the uranium level will be 68 wt%, while for 10 wt% remaining carbon, uranium will be 74 wt%

B: Profile A-B along a telovitrinite particle and distribution along the profile of the U, Fe, S and Ti concentrations, measured from one edge to the other. Uranium is contained constantly in gradients above 70 wt%. The C content remaining fluctuates at 12-6 wt%. The plot at the bottom right of the figure stands for the remaining organic carbon vs the uranium content, using the data from the Profile C-D.

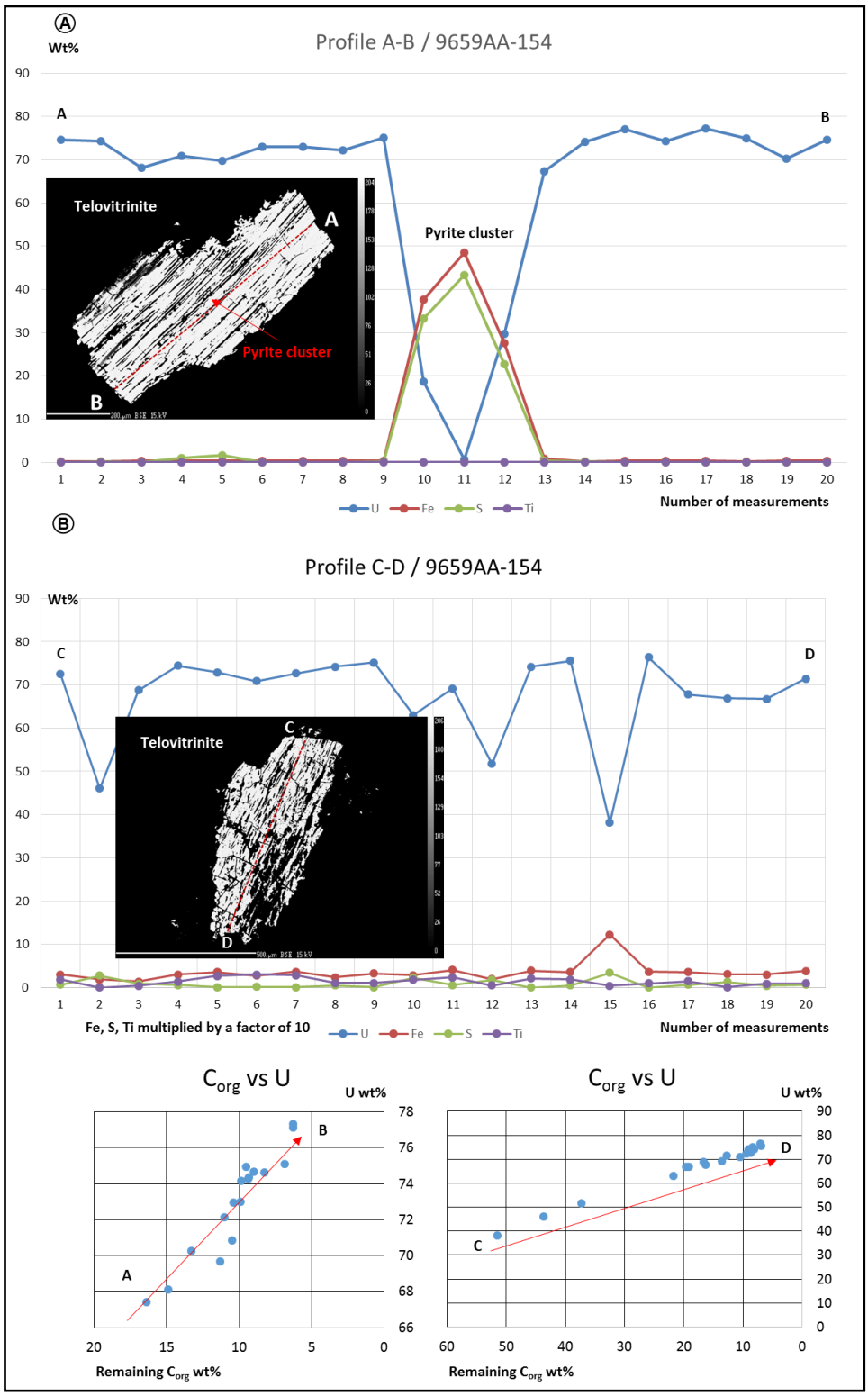

Figure 164: Distribution of U, Fe, S and Ti along Telovitrinite particles.

The data from Profile A-B of Figure 164A and Profile C-D of Figure 164B were plotted on the same diagram (Figure 165). It is immediately recognizable that there is a liner relationship between uranium and organic carbon. Hence, it was possible to find the trend-line and as a result to propose a linear equation of two parameters.

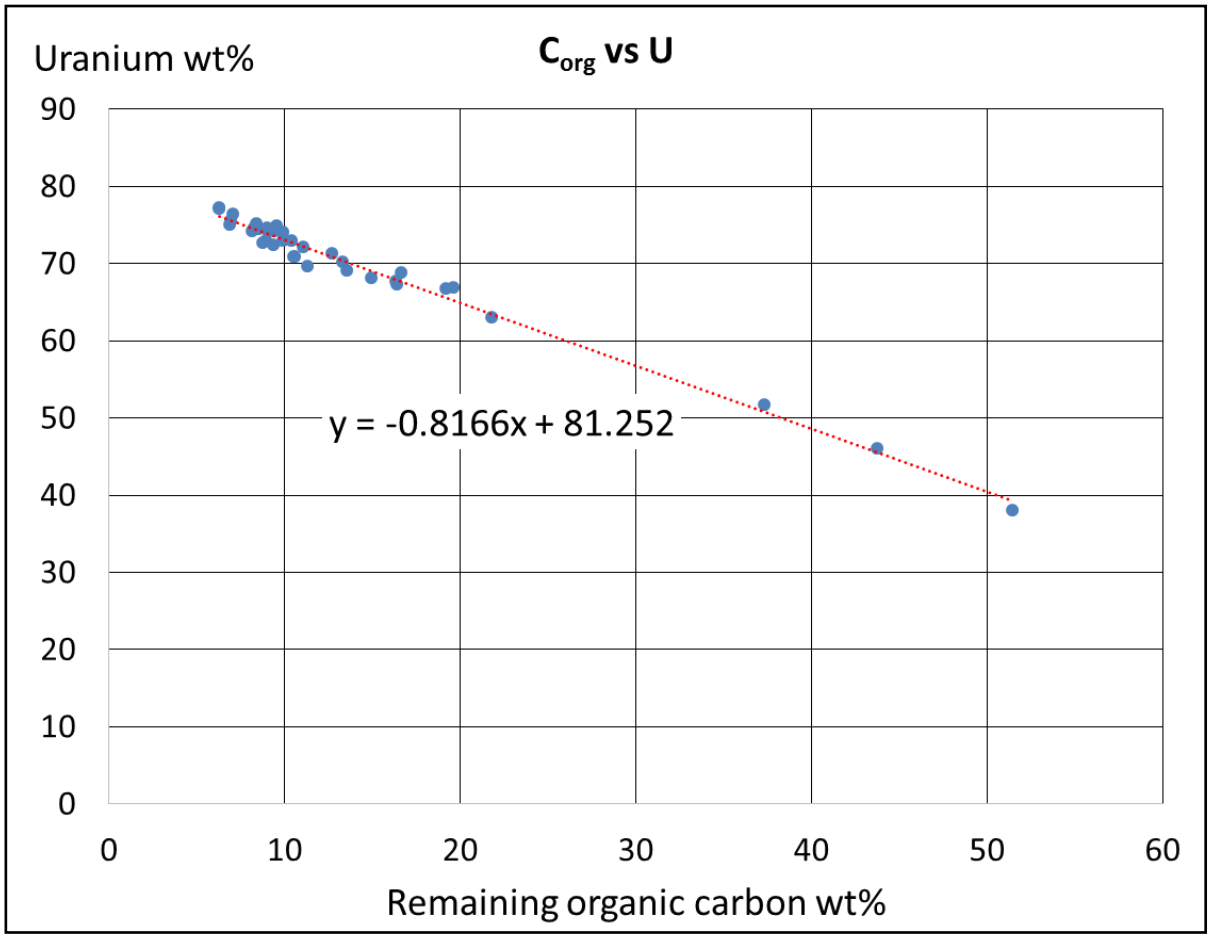

Figure 165: The "remaining organic carbon vs uranium" plot in wt% and the proposed equation.

Based on the above measurements, the following linear equation can be proposed:

$$y = -0.8166x + 81.252$$

Where **y** is the concentration of uranium in wt% and **x** is the remaining organic carbon in wt%.

For instance based on the above formula an organic particle with 15 wt% organic carbon is expected to contain about 69 wt% uranium.

Finally, there was an attempt to find the relationship between maceral type and uranium concentration.

For this demonstration two macerals were selected. A fully replaced telovitrinite particle and a fully replaced funginite particle (Figure 166). Telovitrinite macerals were also presented in

Figure 164. In every case it was concluded that a fully replaced telovitrinite can contain up to 75-77 wt% U while fully replaced funginite macerals are poorer and can contain up to 60 wt% U. Keeping in mind that vitrinite macerals are much richer in organic carbon and hydrogen compared to inertinite macerals, it could be stressed that the maceral type is important for uranium trapping, as a function of permeability and organic carbon content.

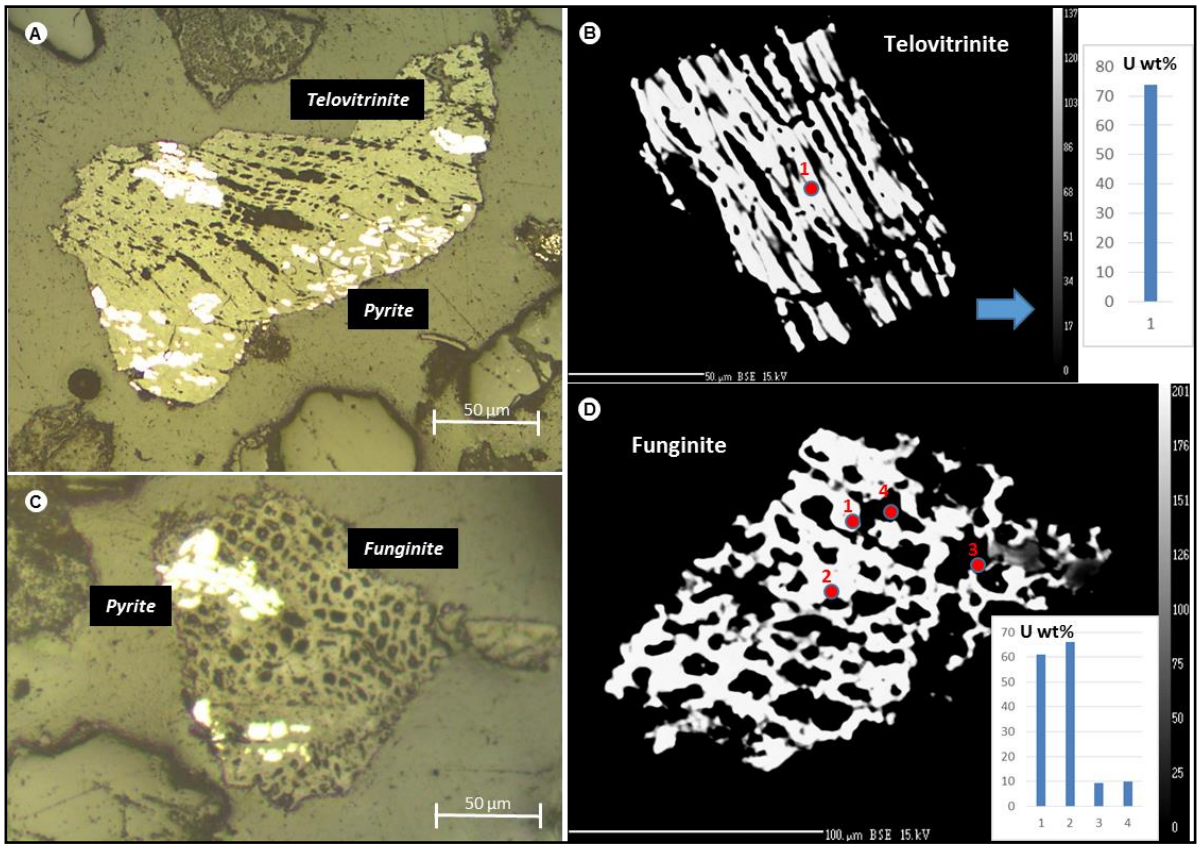

Figure 166: Oil immersion petrography (left) and EMPA (right). (A, B) Telovitrinite with pyrite and more than 70 wt% U content. (C, D) Funginite with pyrite and more than 60 wt% U. It becomes clear than Inertinite can contain high quantities of uranium without the latter being expressed as oxide.

Intentionally left blank

6.9 PHOSPHO-COFFINITE AND COFFINITIZATION

In the current dataset stoichiometric phospho-coffinite was encountered in three samples and in three different cases (Table 12). This chapter is dedicated to explain their chemistry and paragenesis by obtaining high resolution images of uranium-pyrite-dolomite-organic matter relationships.

Table 12: The samples, wells and intervals where pure stoichiometric phospho-coffinite was encountered.

Sample ID	Well	Depth interval (m)
9659AA-35	ZOOV_0710_6	119,40-119,60
9659AA-58	ZOOV_0709_11	126,35-126,55
9659CC-6	ZOOV_1081_2_3	131,63-131,73
9704-8	ZOOV_0738_1	123,00-123,10

Photo-micrographs

Figure 167: Examples of the cases where phospho-coffinite was encountered and the associated diagenetic phases

Sample (9659 AA-35, CC-6, AA-58). Picture A under EMPA and B, C under SEM-EDS.

A: Highly contrasted image, phospho-coffinite replacing gradually euhedral pyrite possibly in a former organic matter particle. In high magnification it is possible to discriminate small framboids building up the euhedral pyrite. Uranium abundance in the assemblage is 85 wt%.

B: Phospho-coffinite cement precipitating inside the porosity of euhedral (Type II) dolomite. The EDS spectra shows that the SiO_2 + P_2O_5 are at the levels of 18 wt%, indicating a very precise stoichiometry for phospho-coffinite. Another element that is always present within the U phases of Zoovch Ovoo is Ca. The presence of Ca, P and Si could indicate sources such as quartz, feldspar and apatite. These elements could become available due to radiolytic damage of silicates.

C: Phospho-coffinite precipitating at the interface between detrital quartz grain and euhedral pyrite cement. Quartz cement (authigenic quartz) is clearly discriminated in the middle of the image filling a vug inside pyrite cement. Phospho-coffinite is formed when U is available in the system as required by the respected stoichiometry, followed by pure quartz cement when the fluid is under-saturated or depleted with respect to U.

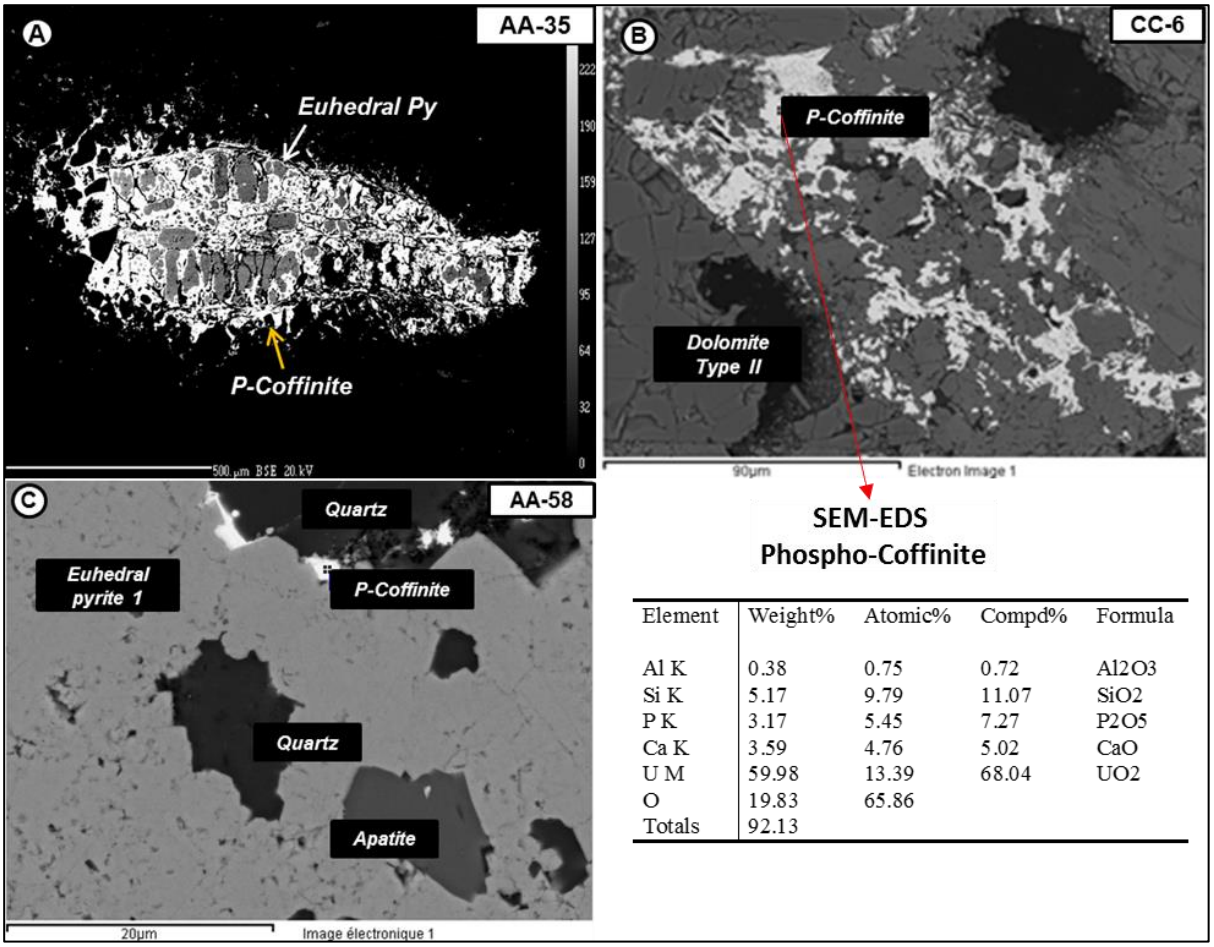

Element	Weight%	Atomic%	Compd%	Formula
Al K	0.38	0.75	0.72	Al2O3
Si K	5.17	9.79	11.07	SiO2
P K	3.17	5.45	7.27	P2O5
Ca K	3.59	4.76	5.02	CaO
U M	59.98	13.39	68.04	UO2
O	19.83	65.86		
Totals	92.13			

Figure 168: Examples of phospho-coffinite associated to other diagenetic phases and the respective EDS spectra. (A) Highly contrasted image of an organic matter particle being firstly replaced by framboidal-euhedral pyrite and then by phospho-coffinite; (B) Phospho-coffinite precipitated inside the euhedral dolomite porosity. (C) Phospho-coffinite precipitated in the intergranular porosity between detrital quartz and pyrite cement; quartz cement and apatite are also featured.

6.10 COFFINITIZATION OF PITCHBLENDE

The EMPA was used to construct chemical maps of U-associated chemical elements in samples where pitchblende was encountered to be at the onset of coffinitization. The main focus was to map the distribution of Si and P with respect to U. Other elements that were mapped are S, Fe, Se, Zn and Ca. The ultimate goal was to establish time-relationships between these elements, keeping in mind that several of them are coming in the system with the roll-front waters. The chemical maps are available in Figure 169. What is presented at Figure 169 is possibly an organic particle which was firstly replaced by pyrite as is evident by the Fe, S distribution (former cell-walls). The roll-front waters are responsible for a series of other elements, first for Se, followed by Zn, Ca, P and ultimately U. Finally, Si is introduced to the system and pitchblende coffinitization commences. It is clearly demonstrated in Figure 169 that Si is the latest element to enter the system, forming a covering layer around the rims of pitchblende.

Photo-micrographs

A possibly former organic particle with corroded pyrite aspects.

A, B: S and Fe forming pyrite prior to the roll-front, *stage 1*.

C: Early stages of roll-front precipitating Se in the system (probably liberated from early pyrite due to corrossion and then re-precipitated), *stage 2*.

D, G: Zn, Ca, P, U are introduced to the system by the roll-front charge, *stage 3*.

H: Si is introduced late in the system and affects the rims of the pitchblende causing coffinitization, *stage 4*.

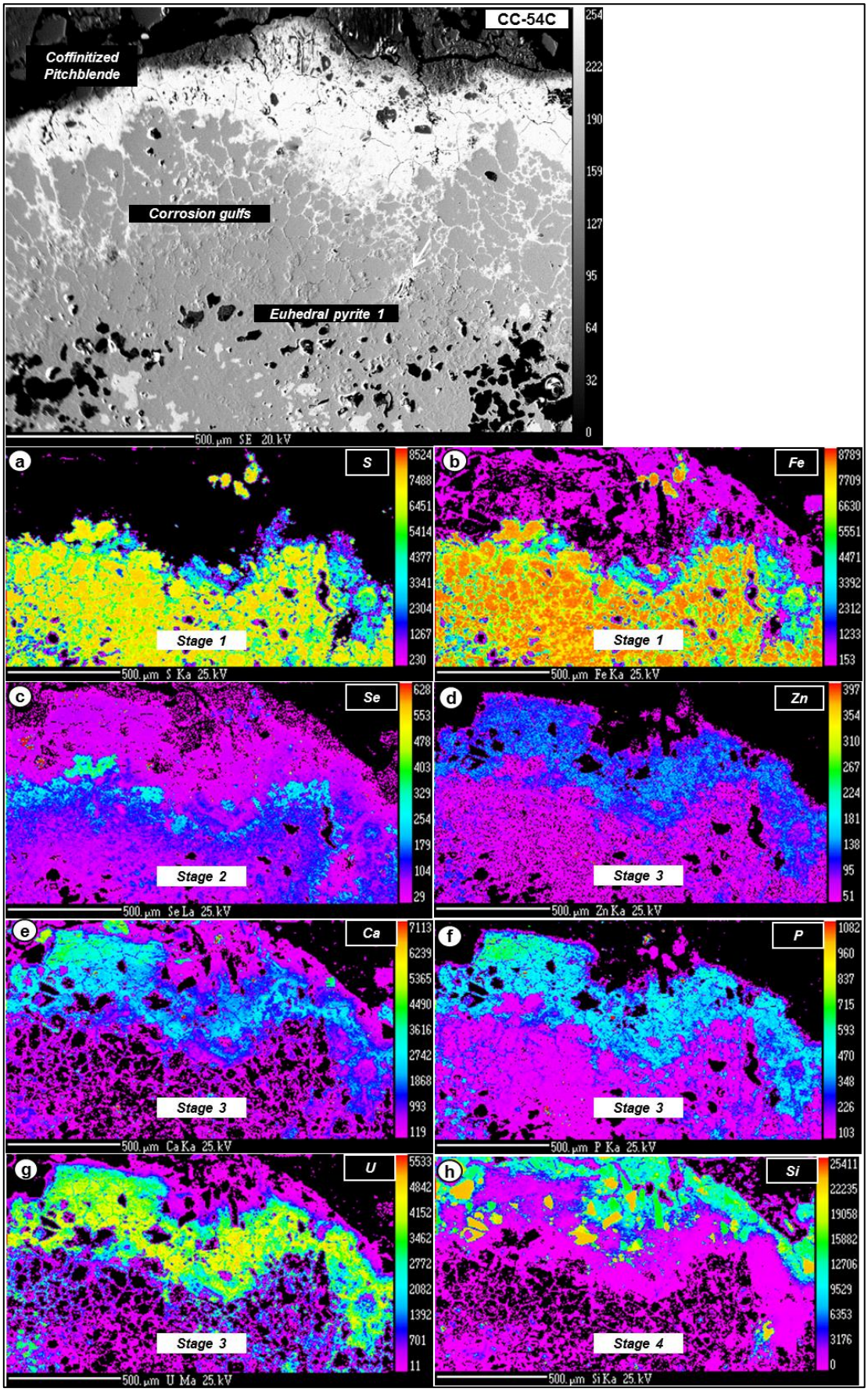

Figure 169: A possibly former organic particle with corroded pyrite aspects and the respective chemical maps performed by EPMA.

6.11 EXAMPLES OF RADIATION DAMAGE ON QUARTZ

Two samples were selected to study the effect of U radiation on quartz grains and the potential formation of damage-rims linked to the emission of alpha particles (He^{++} atoms) caused by the decay of the U^{238} and its daughter nuclides. The first sample carried pitchblende (UO_2) and the second phospho-coffinite ($USiO_4$) mineralization.

Such damage could be pathfinder of past-present of U in the system, based on the following concept. Uranium was once present in an area and was damaging the rims of quartz. Then due to leaching (active roll-front), uranium started to be displaced from that area and subsequently transported downstream, until was totally removed. Hence, upon studying the leached samples it may not be possible to identify any uranium leftovers. On the other hand the radiation damage on quartz will be imprinted; hence this feature can be used to track a roll-front type deposit (Meunier et al., 1990). Indeed halos on quartz grains coated by uranium were observed. These halos start from the surface of the detrital grain and continue towards the interior for about 19-22 μm. The fact that they are always parallel to semi-parallel to the adjacent U minerals outlines that this feature was created after deposition and is not inherited, i.e. created during the presence in the source rock.

Photo-micrographs

Examples of euhedral (Type II) cemented sandstone carrying phospho-coffinite mineralization. Two varieties of detrital quartz were recognized, with blue and orange luminescence, respectively. (Figure 170, sample 9659 – CC6). All pictures under SEM-EDS equipped with CL source.

A, B: Phospho-coffinite occupying the available porosity inside euhedral dolomite, locally replacing framboidal pyrite. The U minerals surround the detrital quartz grains. Under CL, the detrital quartz grains show radiation damage rims, demonstrated by coloration change and the formation of brighter halos compared to the interior part of the grain. The halo has a maximum thickness of 20 μm.

C, D: Phospho-coffinite occupying partly the available porosity of euhedral dolomite, again locally replacing framboidal pyrite. Clear influence of U radiation on the quartz of the orange luminescence, while the blue quartz is not affected by radiation and has far lesser luminescence. Only the face of the orange quartz that is surrounded by U is damaged (maximum depth 20 μm).

E, F: Phospho-coffinite occupying the available porosity inside euhedral dolomite. The U minerals surround the detrital quartz grains. Framboidal pyrite contains a few percent of U. Under CL, it is evident that a halo is created around the quartz grain (maximum penetration

depth 20 µm), which seemed to be initially blue and then altered to orange due to the radiation damage.

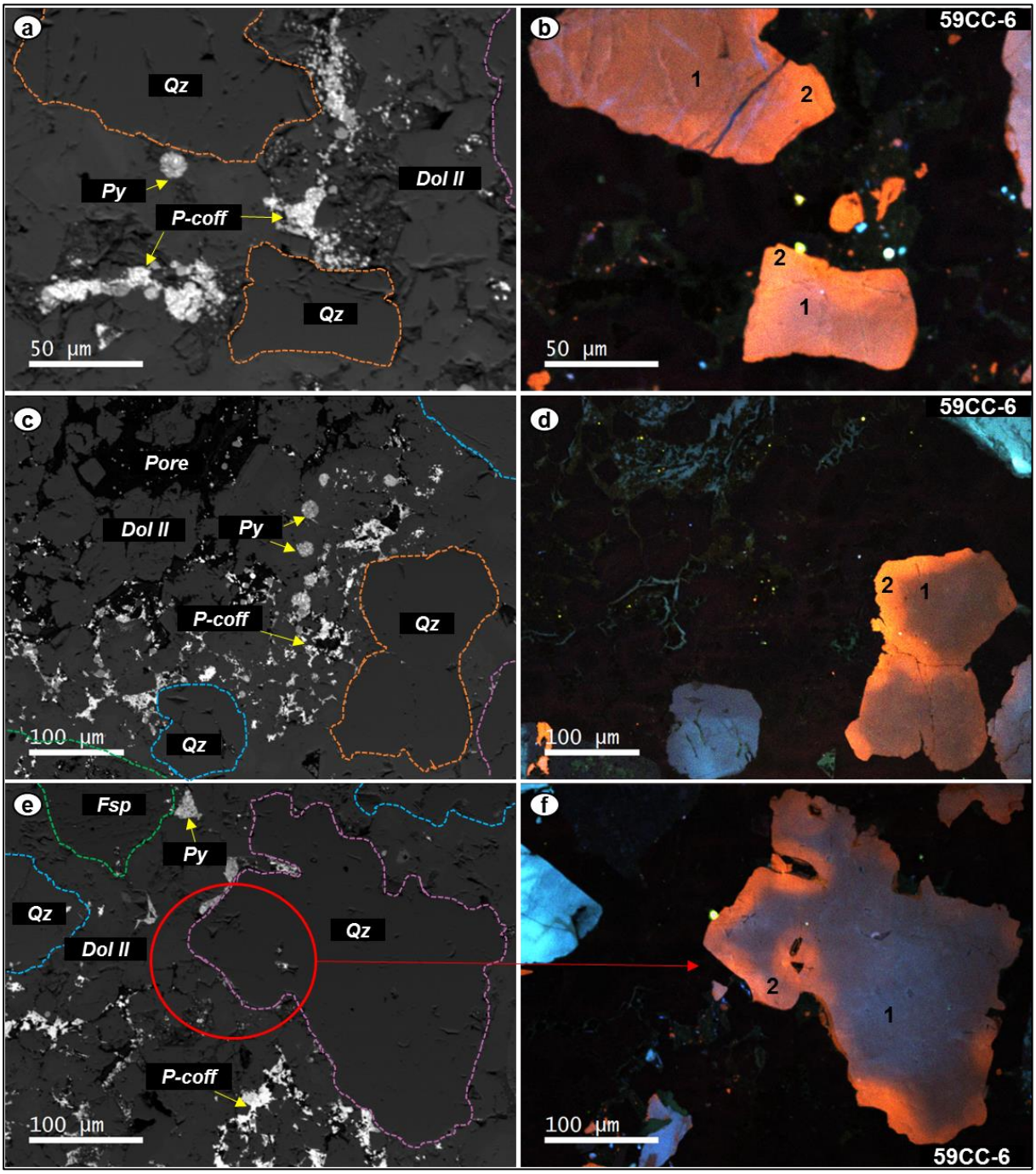

Figure 170: Scanning electron microscopy and corresponding cathodoluminescence images of a dolomite cemented sandstone (sample 9659CC-6) carrying uranium mineralization in particular phospho-coffinite. The study shows that quartz grains that were in contact with U-mineralization experienced radiation damage to their rims, which is evident by the brighter CL. Number (1) indicates the less or unaffected part of the quartz by radiation and number (2) indicates the damage rims.

Photo-micrographs

More examples of radiation damage on quartz rims caused by the presence of phospho-coffinite. The radiation damage is evident due to CL coloration change between the affected rim and the unaffected interior of the grain. When the quartz is monochromatic, the damage rim has brighter luminescence than the interior. On the other hand when the quartz is polychromatic then the interior maintains the inherited color, whereas the rim often switches coloration. For instance in our studied samples we have seen that a blue quartz would acquire orange rims due to radiolysis. Finally, in certain cases we have witnessed texture collapse on quartz grains that were severely damaged by radioactivity (Figure 171, sample 9659 – CC6). All pictures under SEM-EDS equipped with CL source.

A, B: Phospho-coffinite occupying the available porosity inside euhedral dolomite, mixed and replacing partially the pyrite. The U minerals surround the detrital quartz grains. Under CL, the detrital quartz grains have orange luminescence and their rims seem to be affected by the radiation. The large grain on top of the image shows clearly the contrast between the damaged rim and the undamaged interior. In this case the cumulative penetration depth is about 20 μm. The quartz on the left seems has partly destroyed texture and shows a binary coloration, when comparing the interior and the exterior part of the grain. Finally, the small quartz grain in the middle of the image which is fully surrounded by U-mineralization seems to have been totally damaged by radiation, as becomes evident by the very bright luminescence and the yellow core in the very interior of the grain.

C, D: Phospho-coffinite occupying partly the available porosity of euhedral dolomite, again locally replacing framboidal pyrite. The quartz grain on top is fractured and carries mineralization. It is very probable that the texture of this quartz grain has been collapsed due to prolonged radiation damage. The next two quartz grains in the middle and left parts of the image were initially blue and were then altered to orange due to radiation damage. The small grain has been homogenously altered while the larger grain is partly altered, starting from the rim facing primarily the U mineralization and continuing through a depth of 20 μm. Also, the large quartz grain seems to be suffering by some kind of texture collapse, due to radiation damage.

E, F: Large quartz grain with blue luminescence showing radiation damage at the rims that are not in contact with dolomite cement, thus open to fluid circulation and U-minerals precipitation. It is clear that the radiation damage causes the blue quartz to shift to orange luminescence.

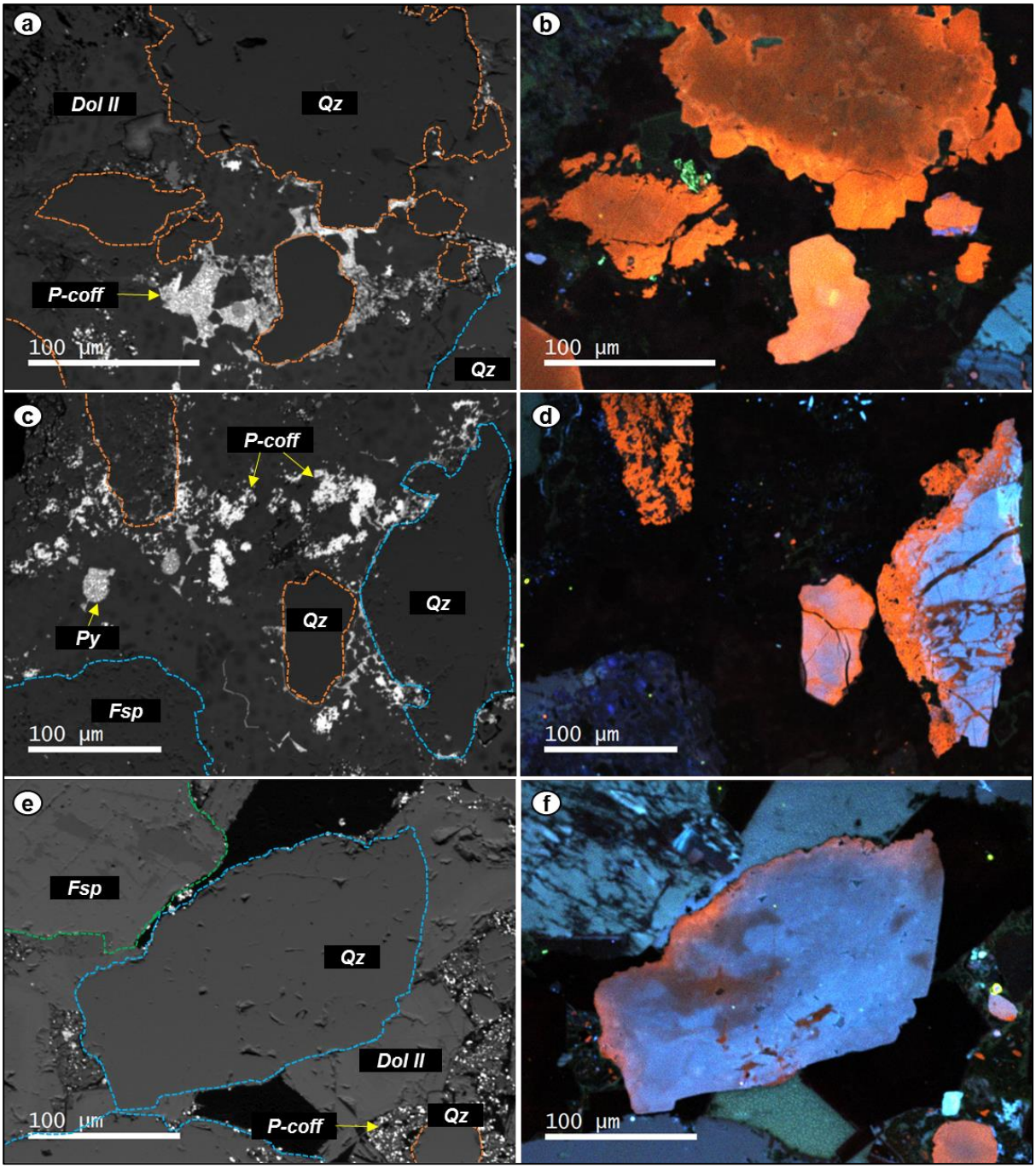

Figure 171: Scanning electron microscopy and corresponding cathodoluminescence images of a dolomite cemented sandstone (sample 9659CC-6) carrying uranium mineralization in particular phospho-coffinite. The study shows that quartz grains that were in contact with U-mineralization experienced radiation damage to their rims, which is evident by the brighter CL. Number (1) indicates the less or unaffected part of the quartz by radiation and number (2) indicates the damaged rims.

6.12 EXAMPLES OF QUARTZ CEMENT FORMATION

It is important to note that quite often we have encountered SiO_2 that appeared to be related to late quartz cementation (newly formed). It was already demonstrated that there are complex clusters of TiO_2 and SiO_2, occasionally carrying U. In those cases the SiO_2 phase was post-diagenetic with regards to U formation. In some cases SiO_2 phases were crystallized inside the pore space of pyrite cement, following U formation.

To understand more about the origin of quartz cement we have selected two samples for the CL study of quartz, with both of them carrying U mineralization. The first carried pitchblende (UO_2) and the second phospho-coffinite ($USiO_4$) mineralization. With regards to the phospho-coffinite mineralization we found quartz overgrowth on certain detrital quartz grains as well as clusters of quartz cement amalgamated with phospho-coffinite. Under cathodoluminescence, the overgrowth quartz is brown and the authigenic quartz is orange with blue zonations. The two examples are summarized below.

Photo-micrographs

Examples of quartz cement formation in a phospho-coffinite mineralized sample. (Figure 172, sample 9659-CC6). All pictures under SEM-EDS equipped with CL source.

A, B: Cluster composed of phospho-coffinite and quartz cement. Under CL, the blue and orange colored part of the cluster indicate SiO_2, whereas the dark colored indicates the uranium phase. The feldspar on the top left is fractured and contains sphalerite microsized spherules. The quartz on the right with the orange luminescence contains newly formed clays inside the fractures.

C, D: Detrital quartz grain of blue luminescence associated to quartz overgrowth at the rim, easily discriminated by the brown color under CL. With a careful look it is possible to recognize internal zonations in the newly formed quartz.

E, F: Zoomed image of (C, D) to highlight the formation of quartz cement (brown color) around the fractured detrital quartz grain (blue color). Again, it is possible to recognize zonations inside the quartz cement.

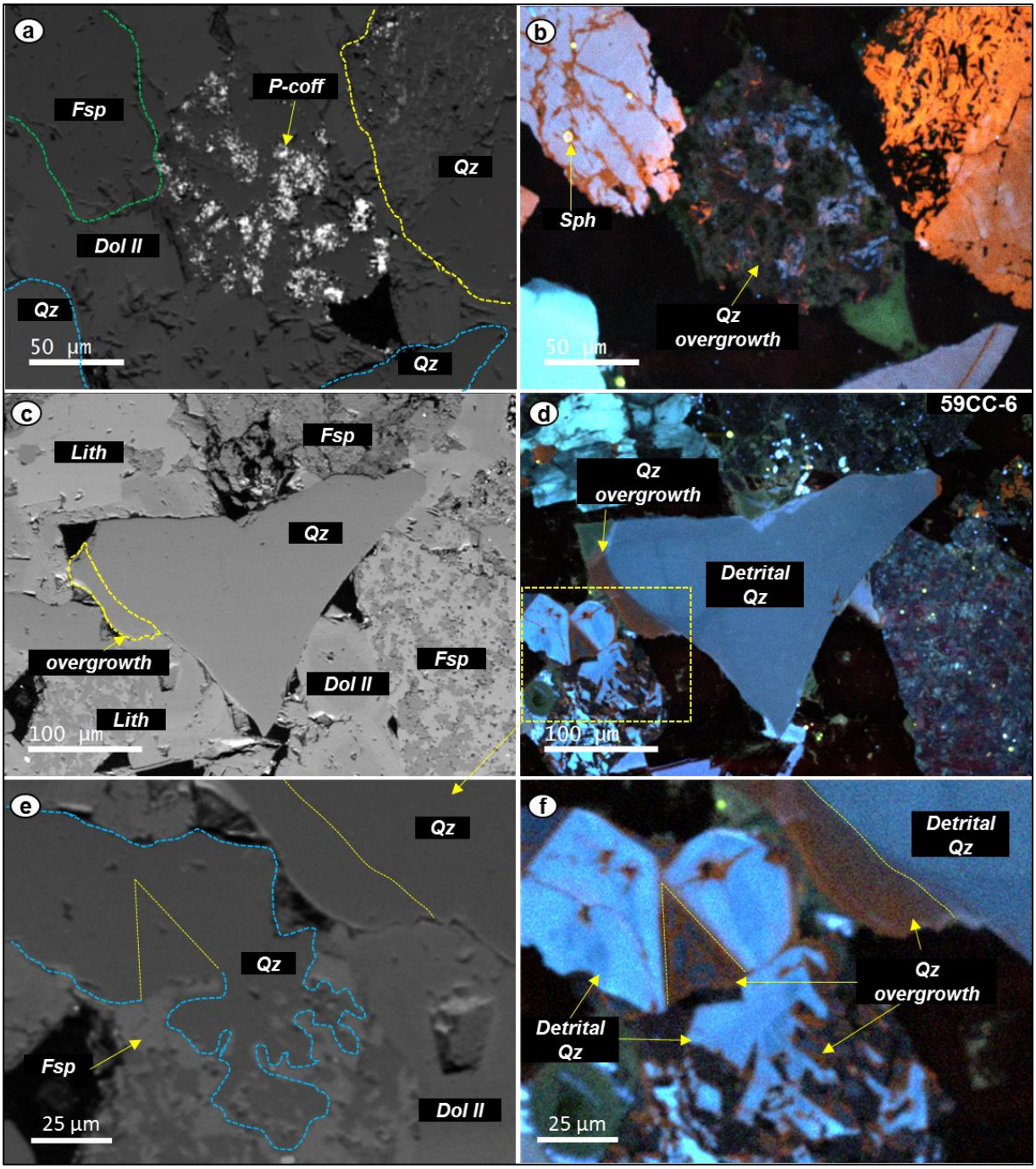

Figure 172: Scanning electron microscopy and corresponding cathodoluminescence images of a dolomite cemented sandstone (sample 9659CC-6) carrying uranium mineralization in particular phospho-coffinite. (A, B) Cluster of phospho-coffinite with quartz cement, sphalerite crystals can be found inside the feldspar. The large orange quartz on the right is fractured and the open space has been occupied by newly formed clays. (C, D) Detrital quartz grain of blue luminescence associated to quartz overgrowth at the rim, easily discriminated by the brown color under CL. (E, F) Zoomed image of (C, D) to highlight the formation of quartz cement (brown color) around the fractured detrital quartz grain (blue color).

Examples of quartz cement, post-dating pitchblende formation inside a pyrite cemented sandstone. The newly formed quartz has bright orange luminescence and shows internal zonations of blue luminescence. The newly formed quartz has irregular shape (crystal boundaries) due to the shape of the associated pitchblende crystals. These properties enable it clearly to be a post-uranium diagenetic episode. (Figure 173, sample 9659 – AA78. All pictures under SEM-EDS equipped with CL source).

Photo-micrographs

A, B: Quartz cement of orange luminescence filling pore space, which can be primary or secondary due to dissolution. The quartz cement shows blue zonations towards the edges.

C, D: Quartz cement of orange luminescence with very discrete zonations that take blue color under CL. The background is pitchblende cement and euhedral pyrite cement.

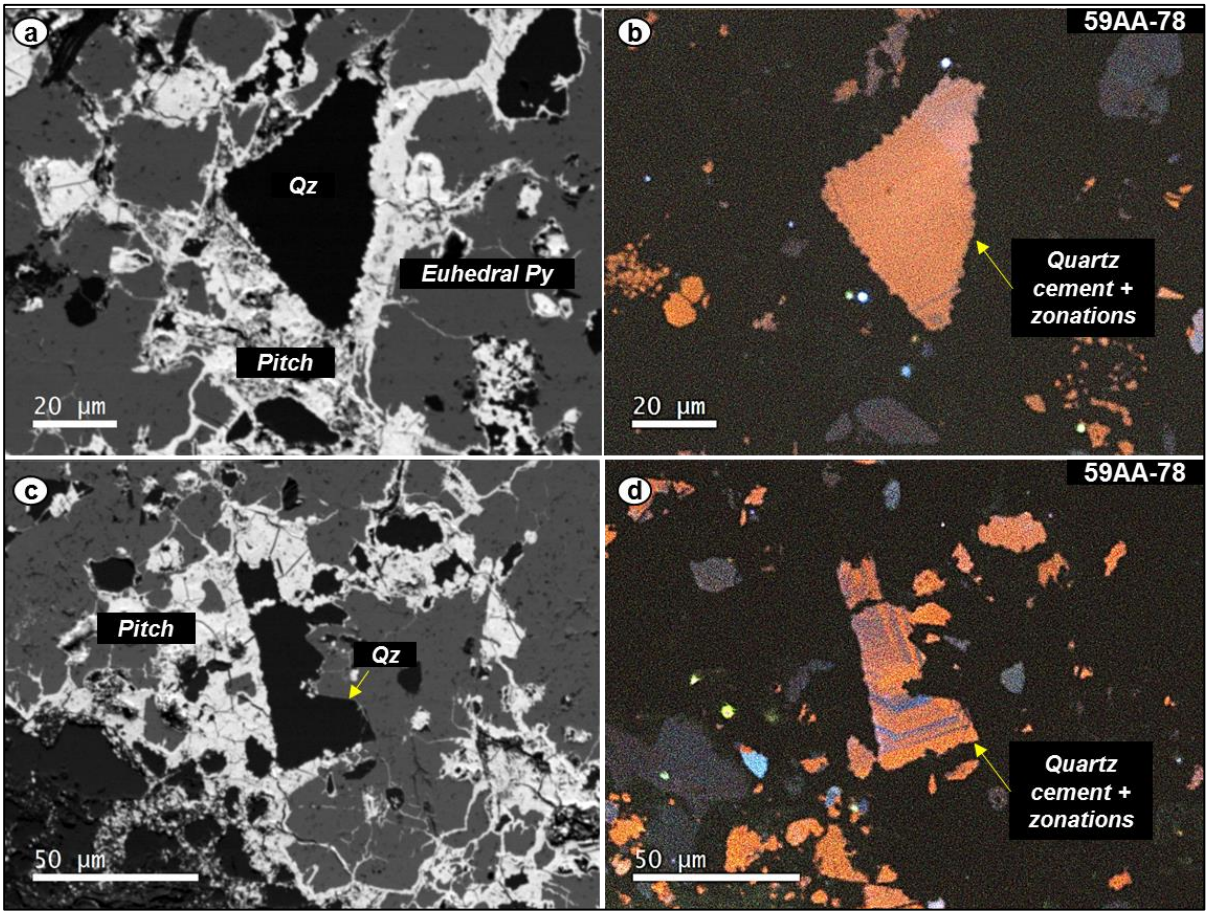

Figure 173: Scanning electron microscopy and corresponding cathodoluminescence images of a dolomite cemented sandstone (sample 9659AA-78) carrying uranium in as pitchblende. (A. B) quartz cement, (C, D) quartz with zonations. It is likely that the zonations reflect minute changes in water chemistry of the formation fluid.

6.13 DISCUSSION ON THE STATUS OF QUARTZ IN THE SANDSTONES FACIES

By using CL it was possible to clearly see the difference between detrital and authigenic (newly formed quartz). Two types of detrital quartz in the Zoovch Ovoo sands were identified. The first has blue and the second orange luminescence.

Quartz cement is late diagenetic and is formed posterior to uranium precipitation. It can be found either as an overgrowth of detrital quartz, in this case characterized by brown luminescence) or as pore-filling cement associated to pitchblende, (characterized by internal zonations of different CL colors). The zonation in quartz cement can be due to minute changes in water chemistry (enrichment in certain trace elements during the authigenic quartz growth).

As a result the effect of radioactivity (alpha-particle bombardment) was clearly imprinted on quartz due to long-term contact with the U mineralization. We have studied two samples, focusing on the different U minerals that are present in Zoovch Ovoo, namely the phospho-coffinite and pitchblende. In the first case we have recognized severe damage of the rims of detrital quartz grains that resulted into coloration change under CL, with the affected rim becoming brighter. In certain cases and on specific grains we have identified texture collapse of the quartz rims. For example a blue luminescent quartz grain can obtain orange luminescent rims after exposure to phospho-coffinite. It is noted that the coloration change on the quartz edges that occurs during transportation (abrasion), before deposition and diagenesis (Krinsley and Tovey, 1978), is not linked to the coloration change that was observed in our case, since only the face of the quartz grain surrounded by U was damaged. The penetration distance of alpha particles was measured to be at the level of 19-20 μm.

To place all the above episodes into the genetic context, we can propose that after pitchblende precipitation, uranium induced radiation damages the quartz grains. The damage induced higher active surface which could have favored quartz radiolysis and to a certain extent Si release. This Si release could have favored: 1) the coffinitization of pitchblende, 2) the precipitation of phospho-coffinite and 3) the precipitation of quartz as both detrital grains overgrowth and as pore filling cement (with internal zonations when a pore is filled with a single quartz crystal). The hydrolysis of feldspars to form clay minerals could also contribute towards the SiO_2 pool, depending on the nature of the clays, Si-rich or Si-poor.

Such scenario would be consistent with the fact that quartz cementation is much localized to the mineralized zones and has never been a major diagenetic feature of the Zoovch-Ovoo formation; hence, unconsolidated sands are predominant compared to sandstones. Nevertheless, this scenario needs still to be confirmed by systematic study.

CHAPTER VII

Synthetic Discussion

7.1 SYNTHETIC OVERVIEW OF DIAGENETIC PHASES

Each of the diagenetic phases, namely the dolomite, pyrite, uranium phases and quartz (authigenic) in addition to the detrital organic matter was studied independently to uncover their origin and significance to the formation of the U-ore deposit.

7.1.1 Dolomite study

Large variations were found among the different dolomite fabrics with respect to the size and geometry of the crystals, which were classified in four types indicating possible recrystallization episodes, starting with: (i) microcrystalline frequently associated to siderite, (ii) euhedral also associated to siderite, (iii) subhedral and (iv) anhedral. Their REE content varied significantly from dolomite I to IV, in particular by a strong depletion in LREE about 30 times, associated with a relative enrichment in HREE. The contrasted precipitation of calcite in Bayanshiree Formation (Turonian) and dolomite cements in Sainshand Formation (Cenomanian) could be attributed to contrasted Mg/Ca ratio of the circulation fluids in the two aquifers. Both carbonates displayed however rather homogenous oxygen and carbon isotopic compositions with $\delta^{18}O$=-10±1‰ (PDB) and $\delta^{13}C$=-7±1‰ (PDB). The $\delta^{18}O$ values were interpreted as typical of meteoric waters quite close of present day waters. The $\delta^{13}C$ values indicated mixed sources that were interpreted as both organic and mineral. All data taken into account, a complete paragenetic succession was constructed highlighting changes in fluid-rock interaction conditions (including roll-front activity). Carbonate cements were thus considered as the best and rather unique geochemical indicators about paleofluid sources and formation conditions.

7.1.2 Pyrite study

Striking differences regarding the trace element content between the pyrite types associated and non-associated with uranium phases, were confirmed. Likewise, large variations occured for their $\delta^{34}S$ values. The results though very diverse, fluctuating in extreme cases between -50 to +50 ‰, showed that there are more than four pyrite generations, which was also concluded by petrography. Isolated framboidal pyrite had a preference for positive $\delta^{34}S$ concentrations at the range of 10±5 ‰, while euhedral pyrite was more negative at the range of -18±5 ‰. The gradual fractionation of S from positive to negative values coupled with the geological evolution of Zoovch Ovoo, could indicate that the framboidal pyrite with $\delta^{34}S$ values fluctuating at 20 ‰ originated from the reduction of evaporites by bacterial sulfate reduction (BSR). In particular the positive $\delta^{34}S$ of framboidal pyrite, in contrast to the usual negative BSR derived pyrite, was due to the initial heavy $\delta^{34}S$ of evaporites, which according to literature can reach 20-50 ‰. These sulfates may be linked to the depositional environment, but may also be secondary, formed from the mineralizing fluid at later stages of diagenesis. The euhedral

pyrite with negative $\delta^{34}S$ values originated from the further fractionation of the initially positive framboidal pyrite. The positive and negative values were rather reflecting closed vs open fractionation systems. In turn the negative S isotopic values of the euhedral pyrite indicated that it is bacterial derived, while BSR is active during the whole diagenetic history of the deposit and is the unique sulfate reduction process (absence of TSR). Since the second euhedral pyrite generation is co-genetic to uranium formation (contains pitchblende inclusions), BSR is active even during uranium deposition.

7.1.3 Uranium study

The uranium ore is expressed as uraninite (UO_2) and less commonly as phospho-coffinite $(U,P)SiO_4$. Calcium is very often present up to 5 wt% in both minerals. The habitus of uranium is as: (i) U-rich organic matter (type III kerogen as detrital elements) with or without any distinguishable U-phase, (ii) UO_2 inclusions inside euhedral pyrite and sphalerite, (iii) U-phases as epigenesis of associated pyrite and sphalerite cement, (iv) U-cement in clay matrix, (v) U-cement within euhedral dolomite, (vi) U-oxides associated to quartz cement, (vii) UO_2 replacing Fe-Ti oxides and (viii) U-phases within porous detrital silicates. Organic matter and sulfides are the most important agents for uranium trapping while clays and Fe-Ti oxides play minor roles. According to petrographic observations coupled with geochemical data, there are at least four major uranium mineralization episodes linked to the roll-front activity. The first episode takes place right after the formation of the first euhedral pyrite on which pitchblende is found as coating. The fixation of U within the detrital organic matter (adsorption and/or complexation) may be contemporaneous to this first stage. The second pitchblende generation precipitated at the same time with the second generation of the euhedral pyrite and of sphalerite, in which it occured as microsized spherules. The third uranium generation was characterized by massive formation of pitchblende acting as cement to the sand grains. Finally, the fourth uranium generation is differentiated by its chemistry which is close to the phospho-coffinite stoichiometry. It was also observed that pitchblende experiences limited coffinitization at a late diagenetic stage. Quartz cement also occurs in samples that carry phospho-coffinite mineralization.

7.2 DETRITAL ORGANIC MATTER AND URANIUM DISTRIBUTION IN SEDIMENTS

7.2.1 Origin of organic matter

According to sedimentological core analysis, peat and coal layers are absent inside the reservoir zone and the organic matter contained in the Zoovch Ovoo sands occurs exclusively as dispersed particles deposited accordingly to sedimentary bedding. Maceral morphology ranges from intact to partially collapsed tissue, indicating that the preservation stage of the maceral is directly linked to the nature of the plant's parts. In particular the well preserved phytoclasts, such as root remains associated to fine grained organic rich lithofacies could be indicative of higher plants which grew within the depositional environment, *e.g.* after no significant transport. In principle, the more distal the source the more fragmented the organic particle reaches the basin (Borrego and Cook, 2017).

The coarse, angular and poorly sorted organic particles are linked to distant transport, within high energy flood-dominated depositional conditions associated to coarse to medium fine grained sand-sized lithologies. The organic matter particles encountered in fine clay layers are better preserved and linked to calm depositional conditions, except if they represent intraclstasts (Figure 174).

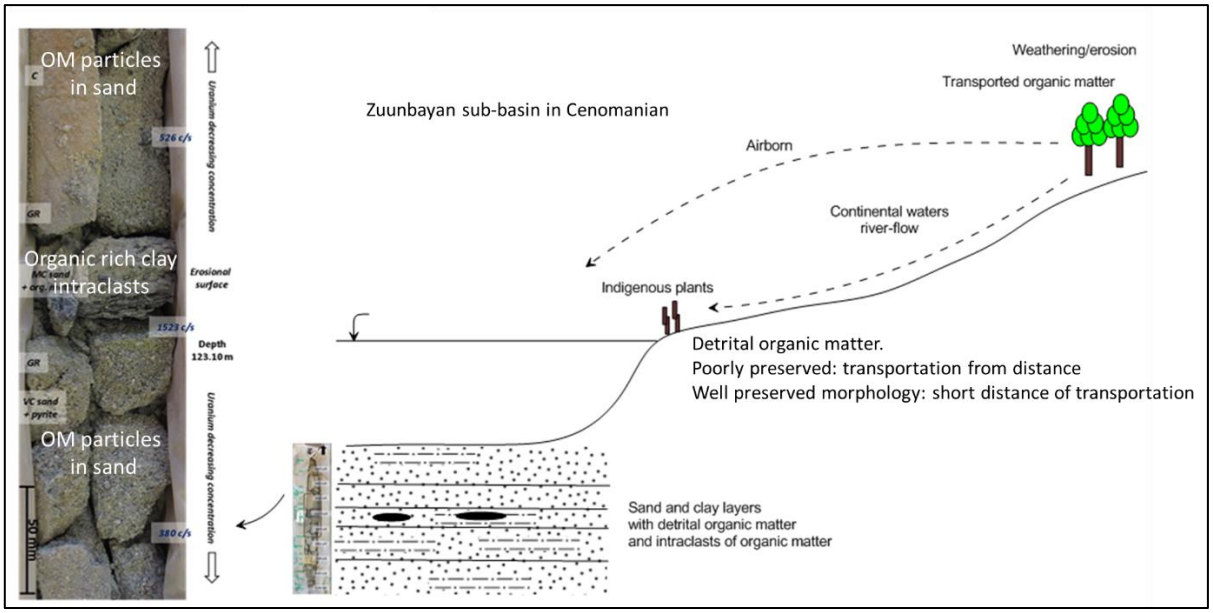

Figure 174: Organic matter is higher-plant derived and reaches the basin as airborn particles or by river-flow. The proximal-distal relationships are reflected by the preservation potential. Organic matter is contained either dispersed in sand and clay layers or can be reworked and redeposited as intraclast alongside clay.

Exudatinite (bitumen) represents an exception, and in this case refers to liquid organic matter formed during vitrinite diagenesis (the coalification process that transforms peat stage material

to higher rank coal Van Krevelen, 1993). It is a secondary product which dervies from the thermal cracking of the primary macerals. Exudatinite is not abundant and when present it was found associated to large silicates (>0.5 mm grain size), located around or inside fracture porosity. It either derives from the maturation of the indigenous organic matter or it is linked to migrated hydrocarbons from adjacent oil basins.

7.2.2 Sedimentological control of O.M and U distribution

Uranium geochemical anomalies as presented in Figure 174 are systematically associated to organic rich layers or intraclast accumulations. The sediments accompanying the anomalies are usually coarse to vey coarse. This feature suggests that the uranium bearing fluid is initially controlled by permeability, migrating along the coarser part of the sand layers and along layer boundaries (erosional surfaces). Detrital organic matter particle accumulations in the vicinity of layers of high permeability will then act as reducing agents to $U^{(VI)}$. Since grain size of the sediments and organic matter distribution are of direct inheritance of the depositional system, it could be suggested that the migration of the U bearing fluids as well as the U trapping by the organic matter at core scale, are under sedimentological control.

7.2.3 U uptake from interstitial waters

Uranium in surficial waters is most often linked to the dissolution of accessory minerals during weathering of the outcropping formations and is transported as uranyl species in oxidizing media (Langmuir, 1978). The processes of uranium-organic matter interactions in shallow buried sediments is complex and involves both processes of complexation and adsorption, followed by reduction of the uranyl ion (Forbes et al., 1988; Landais, 1996; Bone et al., 2017; Cumberland et al., 2018).

The process of chemical adsorption (complexation) was very thoroughly described by Nakashima et al., (1984) and Nakashima (1992). Laboratory experiments showed that the complexation of uranium (without reduction) by the carboxyl groups of terrestrial organic matter is possible, by forming uranyl-carboxyl compounds even at low temperatures (20-45^{o}C). They also showed that $U^{(VI)}$ reduction to $U^{(IV)}$ would require high temperatures (reaching 250^{o}C) and this could be achieved either during late diagenesis or during hydrothermal conditions. However, not all terrestrial organic matter is able to form U-complexes. It must be rich in oxygenated functions, particularly in carboxyl groups. Nakashima (1992) studied two humic substances, one with a vitrinite reflectance of 0.50% (Gardane lignite, Late Cretaceous) and another of 0.34% (Arjuzanx lignite, Late Miocene-Pliocene). The two lignite samples underwent the same laboratory procedure to test their potential to complex U at low temperatures from a U-rich fluid. It was proved that only the lignite of lower reflectance adsorbed uranyl cations UO_2^{2+} without reduction (Nakashima et al., 1999). The complexation of uranyl resulted in pH

increase, decrease of UO_2^{2+} concentration and simultaneous increase in H^{2+} as hydrogen was substituted and hence liberated from lignite by ion exchange. FT-IR analysis revealed that all along uranyl complexation, the carboxylic acids and ketonic groups (C=O) were progressively decreasing, whereas the aromatic groups (C=C and COO^-) were increasing (Stevenson, 1982; Nakashima, 1984). The conclusion was that the abundance of carboxylic functional groups in organic matter plays a major role in uranium complexation.

Another similar case of soluble $U^{(VI)}$ species fixed by lignite of low maturity, resulting to the formation of UO_2^{2+} complexes was reported by Meunier et al. (1990) who studied lignite from the Coutras U-ore deposit, France. Though this lignite was never subjected to elevated temperatures and is rather immature it can contain up to 19 wt% uranium without any distinguishable mineral form.

From the above it could be suggested that the lignite from Arjuzanx (Landes, France; Late Miocene or Pliocene; Nakashima, 1992) as well as the lignite from the Coutras (Gironde, France; Middle Eocene; Meunier et al., 1990) may be considered upon discussing U uptake by the organic matter of Zoovch Ovoo, having a maximum temperature of 40ºC (Graham, et al., 2001; Prost, 2004; Rallakis et al., 2019). The stage of chemical adsorption of uranium without reduction uptaken by organic matter may thus be considered as the earliest stage of U concentration. Though deep burial is *a priori* excluded (epigenetic stage), it is still difficult to know at which time the U-enrichment occurred with the macerals. Therefore, two possible scenarios could apply: i) during sedimentation (syngenetic), or ii) during the shallow to medium burial of the sediments (diagenetic to early catagenetic).

7.2.4 Uranium trapping processes involving O.M at Zoovch Ovoo

Three factors seem to control the epigenization process of the macerals: 1) the permeability around the macerals; 2) the marco-porosity of the macerals (pore network) and 3) their chemical composition. The process is heterogeneous as the organic matter-uranium associations are not a function of the maceral group *i.e.* vitrinite or inertinite and all macerals from the same group have not underwent uranium epigenization.

Among the macerals, telovitrinite (cell-walls) and gelovitrinite (filled cell-walls) show most often high uranium concentration without expression of U minerals (Figure 175). In these macerals, the U concentration is rather homogeneous and reaches 15 to 20 wt%, which is similar to the 19 wt% described in Meunier et al. (1990), but higher than the 5 wt% reported in Douglas et al. (2011) and the 8 wt% in Bonnetti et al. (2017). In particular gelovitrinite can host twice the concentration of U compared to adjacent telovitrinite macerals. This feature is apparently linked to the chemistry of the macerals and could be related to the abundance of carboxylic functional groups known to be responsible for U complexation (Nakashima et al. 1984; Nakashima, 1990;

Cumberland et al. 2018). The U speciation in these macerals could not be determined as no U bearing phase larger than the resolution of SEM (around 0.1 microns) could be observed. Meunier et al. (1990) considers that U dispersed in organic matter occurs under its reduced state $U^{(IV)}$, and is probably under the form of small-sized U-oxides.

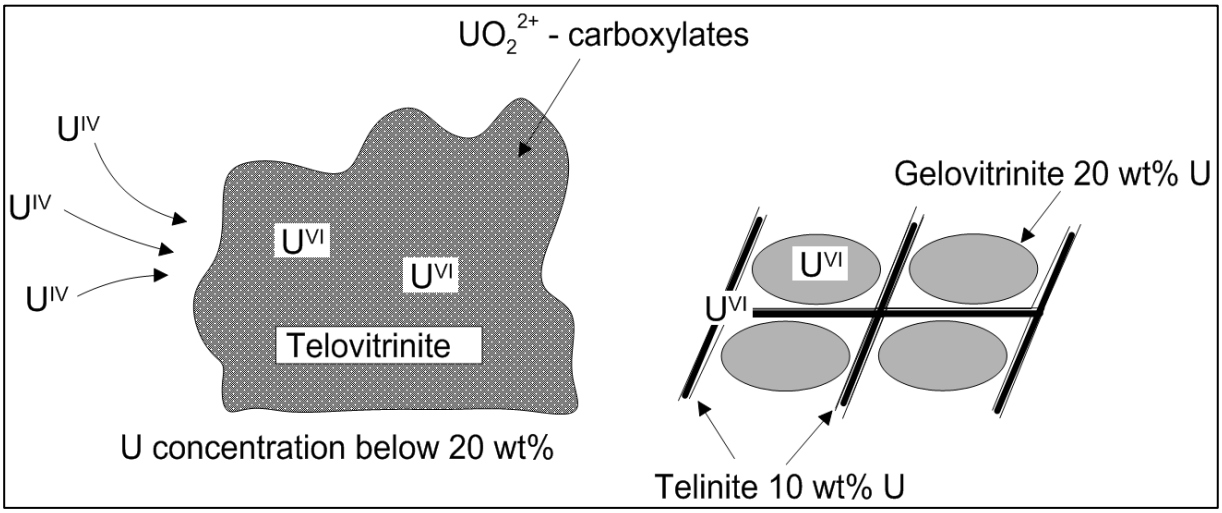

Figure 175: Uranium not expressed as mineral (adsorption). Immature organic matter (peat stage is very efficient in uranium adsorption, which depends on 1) permeability of the macerals (morphology) and 2) carboxylic function content (chemistry).

Direct reduction by organic carbon is also likely to occur (Rouzaud et al., 1979). Nakashima et al. (1984) and Nakashima (1992) suggest that aliphatic hydrocarbons may be involved in the reduction of $U^{(VI)}$. Yet, their experiments suggest that this mechanism is significant at T>120°C, which is not the range of temperatures experienced in the Zoovch Ovoo deposit.

Organic matter of medium thermal maturity like the one encountered in the Zoovch Ovoo deposit can sustain microbiological activity (Lovley et al., 1991; Detmers et al., 2001; Min et al., 2005; Menor-Salván et al., 2010). Especially in the presence of sulfates, sulfate reducing bacteria may be active and generate reduced sulfur species (H_2S, native sulfur; Gruner et al., 1953; Kochenov et al., 1977). These compounds may induce the reduction of the uranyl ion [UO_2^{2+}] to $U^{(IV)}$, although they are not prerequisites for uranium reduction (Spirakis, 1996).

The mechanism of U reduction through biomineralization by bacteria and fungi was previously studied by Lovley et al. (1991) and by Min et al. (2005) in laboratory experiments and in the case of Chinese roll-front systems respectively. Both studies showed that during the initial mineralization stage it is possible for primary uraninite/coffinite to be reduced enzymatically by dissimilatory bacteria, which could use $U^{(VI)}$ as the sole electron acceptor instead of other multivalent metals such as $Fe^{(III)}$. This is because the bacteria thrive in the low temperature environment, using the abundant wood fragments as nutrients and their pores as substrate. In more detail, the complexation of uranium was attributed to the bacterial excreted ligands around their cells, whereas the precipitation to follow was accredited to the redox change

driven by their enzymatic reactions (Gadd, 1996; Suzuki and Banfield, 1999). With respect to fungi the complexation was achieved with nitrogen, whereas the adsorption of uranium occurred at the boundary of their cell-walls, as uranyl hydroxide (Tsezos and Volesky, 1982). According to Min et al. (2005) the progressive accumulation of hexavalent uranium from both bacteria and fungi raises the radioactivity to toxic levels which ultimately poisons the microorganisms. However, uranium concentration continues to increase even at *post-mortem* stage as uranium is accumulated by the negatively-charged sites of the microorganisms' remains through inorganic adsorption. Eventually uranium minerals totally replace the fungi and bacteria that pseudomorphically mimic the inherited biological texture. Therefore, the inflow of SO_4^{2-}, $Fe^{(III)}$, $U^{(VI)}$ and at least three kinds of bacteria during the roll-front activity is responsible for uranium bioreduction (Figure 176).

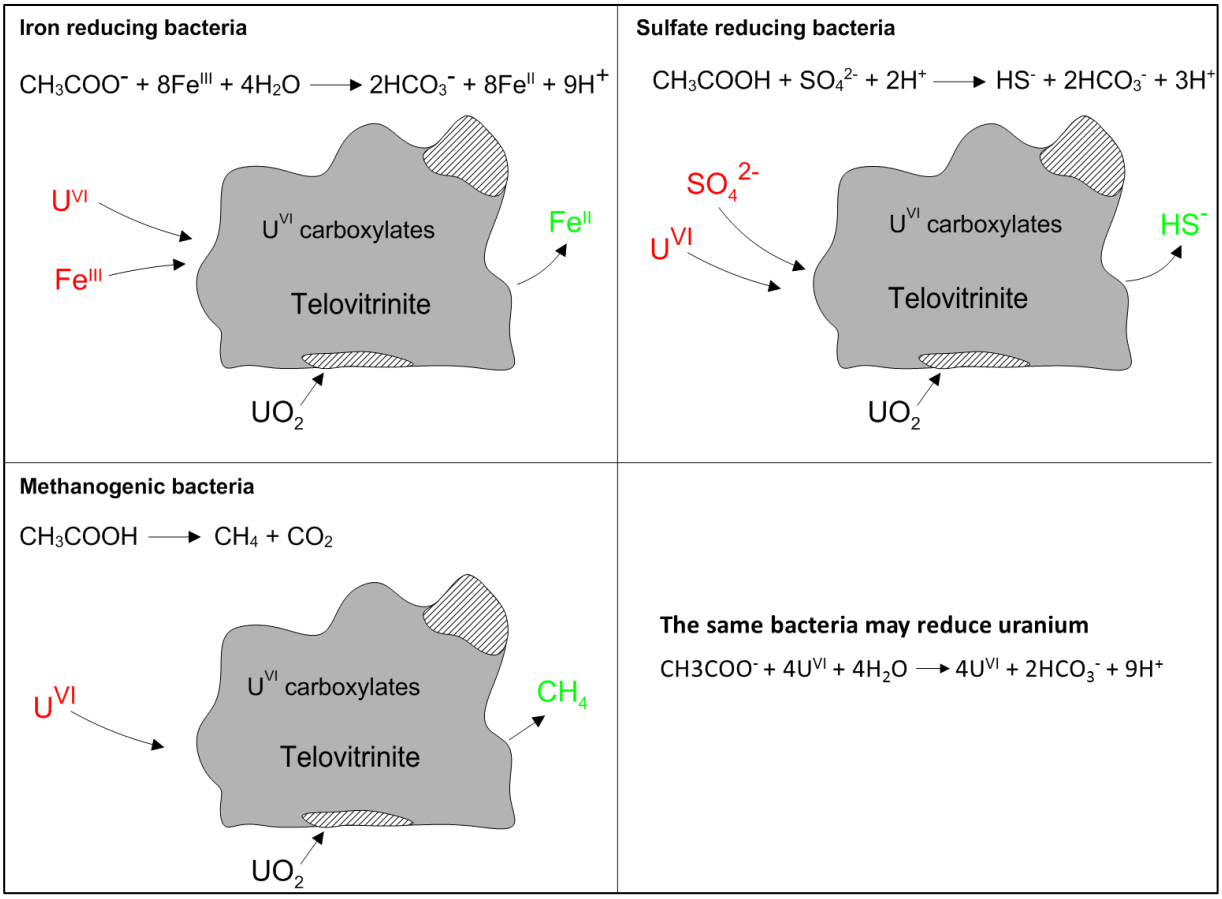

Figure 176: Sulfate and iron reducing bacteria as well as the methanogens are able to enzymatically reduce uranium to form uranium oxides such as pitchblende.

Based on the above it could be suggested that bacterial activity at Zoovch Ovoo may be a major reducing agent for $U^{(VI)}$. Indeed, according to Nakashima et al. (1984); Meunier et al. (1990) and Nakashima (1992), direct reduction of $U^{(VI)}$ by hydrocarbonaceous moieties may be possible only at a coalification stage sufficient to induce the destruction of the carboxyl-uranyl complexes (or experimental temperatures higher than 120°C). Yet, in our study case it is estimated that temperature never exceeded 40°C (Graham et al., 2001; Prost, 2004), while

organic petrography reveals very highly altered/oxidized/weathered OM due to interaction with the oxidizing roll-front waters and radiolysis.

Other studies (Cumberland et al., 2018) mention that it is possible for immature organic matter, such as peat, to scavenge uranium by a factor of 10^4 by groundwater containing uranium at ppb levels (Idiz et al., 1986; Owen and Otton, 1995). In that case $U^{(VI)}$ adsorption was performed by the carboxylic and phenolic groups of the immature organic matter (Warwick et al., 2005; Bryan et al., 2012), while bacteria catalyzed the reduction to $U^{(IV)}$ (Lovley et al., 1991; Spirakis, 1996). In the case of Zoovch Ovoo reduced uranium is observed as UO_2 replacing partially or totally macerals, with partial preservation the original biological woody texture.

Irrespective of maceral composition the organic particles in the Zoovch Ovoo sands can contain high levels of uranium although the adsorption is not uniform. An assemblage of telovitrinite and inertinite macerals, i.e. collotelinite, gelovitrinite and funginite is presented in Figure 177. Some are fully epigenetized by framboidal pyrite, while others contain pyritospheres at a very local scale. As illustrated by the BSE image, the organic particle contains different macerals. Based on the SEM-EDS concentration map, for uranium, gelovitrinite is much richer in uranium compared to texto-ulminite, while it is nearly absent from funginite except for its rims.

The concentrations of U, Fe, S and Ti of the two profiles, namely G-H and I-J are also provided in Figure 177. Profile G-H covered both gelovitrinite and collotelinite macerals and as was also evident from the uranium chemical map, the gelovitrinite contains truly more than double uranium concentration and reaches up to 20 wt%, while at the same the time collotelinite fluctuates between 7-12 wt% U. For certain parts of the profile, the sulfur and iron have the same concentration levels indicating micro-pyrite, whereas in other parts they do not follow the pyrite stoichiometry. Titanium is constant at 0.5 wt%. Profile I-J was performed strictly within a gelovitrinite particle. As is evident uranium is constantly contained between 16-22 wt%. Sulfur and iron are between 4-5 wt% and though they could be compatible with pyrite, no optical expression of sulfide is visible. Titanium is again constant at 0.5 wt%.

Based on the above, it could be concluded that the biodegradation level imposed by bacteria and fungi in each maceral is an important factor for uranium reduction and concentration.

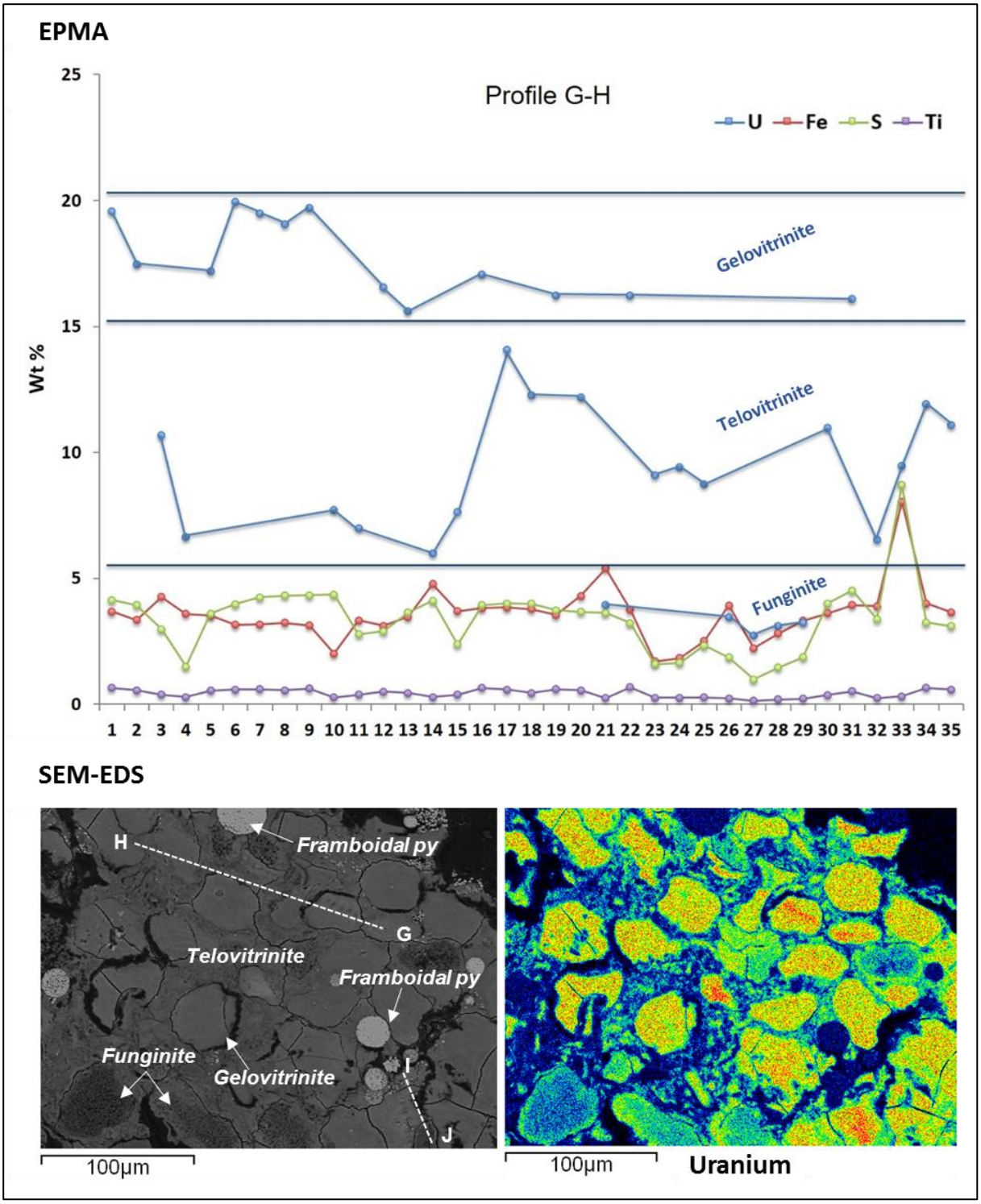

Figure 177*:* Focus in the maceral components, namely, gelovitrinite, telovitrinite and funginite, associated locally to framboidal pyrite and their significance in uranium concentration. The profiles G-H and I-J are also indicated. The SEM-EDS map for uranium shows that gelovitrinite is the richest maceral followed by telovitrinite and finally funginite. In some cases, certain gelovitrinite particles are particularly enriched in U (red areas). Profile G-H clearly demonstrates that the composition of uranium in gelovitrinite is more than double compared to the telovitrinite background, reaching 19 wt%. Sulfur concentration is for most of the times higher than for iron and only in few cases indicates the presence of pyrite (50-50 Fe, S in wt%). All particles are very lean of titanium which fluctuates below 1 wt%. Profile I-J was performed on a single gelovitrinite particle and as such it clearly shows that uranium concentration is constant and between 16-22 wt%. Sulfur and iron are also constant and at the same levels, which could indicate nano-pyrite. Titanium is constantly below 1 wt%.

Finally, to illustrate the successive stages of uranium-organic matter epigenization a sketch drawing was conceived (Figure 178). Apparently the process is not the same for porous and non-porous macerals, as far as macro-porosity is concerned *i.e.* cavities in cellular wall structures. Hence, two different pathways are proposed. In the case of macerals with limited macro-porosity, for instance telovitrinite with fully fused cell-walls, the epigenization starts by the rims and by internal fractures, if any are present. Uranium concentration reaches about 40-45 wt% with progressive accumulation which results in the formation of uranium. The progressive accumulation continues until the particle is fully replaced. In case of macerals with preserved cell-structure *i.e.* telinite and funginite the epigenization will be more uniform and uranium oxides greater than 1 micron will precipitate when the concentration reaches 40-45 wt%. When an organic particle is composed of different macerals, pores in between the different macerals enhance fluid penetration resulting in a more homogenous epigenization. In addition, it was observed that certain macerals *i.e.* gelovitrinite will accumulate uranium in greater amounts than collotelinite or fusinite. Gelovitrinite is an exception that has very low porosity due to its origin.

Therefore, the presence or absence of cell-structure of the maceral is another factor that plays a major role in fluid circulation and to such extent to uranium accumulation.

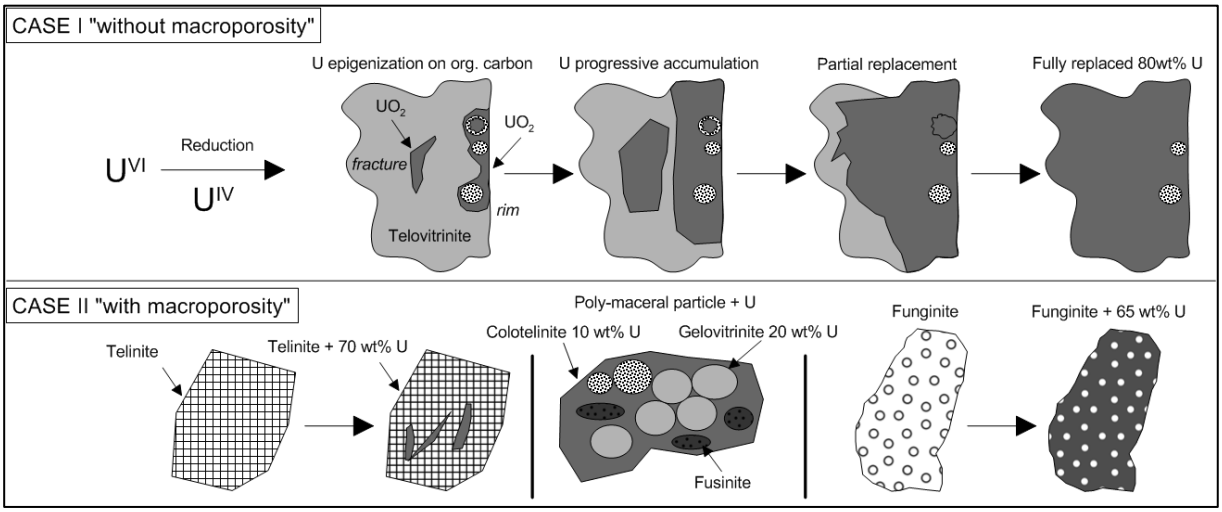

Figure 178: Graphical representation of the organic matter epigenization by uranium in five steps. Uranium is carried in solution as U(VI) until it encounters a reducing agent i.e. organic carbon or pyrite and it is reduced U(IV). When uranium is reduced by organic carbon it can be concentrated around internal fractures or at the rims of the maceral as uranium oxide. From the rim where U is expressed as oxide towards the interior where U is accumulated but not yet expressed, there is a linear decreasing concentration gradient. Eventually the replacement process keeps up, leading primarily to partial and progressively to full replacement. The latter case refers to organic particles with up to 75-80 wt% uranium, while organic carbon is almost destroyed. One of the main aspects of this replacement process is that the fully replaced organic particle maintains its textural characteristics although organic carbon is no longer present.

7.2.5 Uranium sources and initial conditions

Several hypotheses can be made for the sources of uranium. However, none of these is conclusive as there are not enough evidence to support each. The first question to be asked is when does uranium first appear in the system? One way to answer this question is to try to identify the level of uranium in organic matter since deposition. If there is uranium pre-ore uranium enrichment (preconcentration) then it is imperative that U-enriched organic particles are identified outside the roll-front area. In this scenario, organic matter may trap $U^{(VI)}$ by adsorption from the time of deposition until the roll-front starts (Figure 179). However, with the proviso that limited samples from the areas outside the roll-front were studied, it is proposed for the moment that no significant U content is found in sediments outside the roll-front area. The second question is, where does uranium come from? One possibility is from the granitic, metamorphic and volcanic basement rocks outcropping in the regional area and another from the volcanic ash/glass that covers Sainshand Formation.

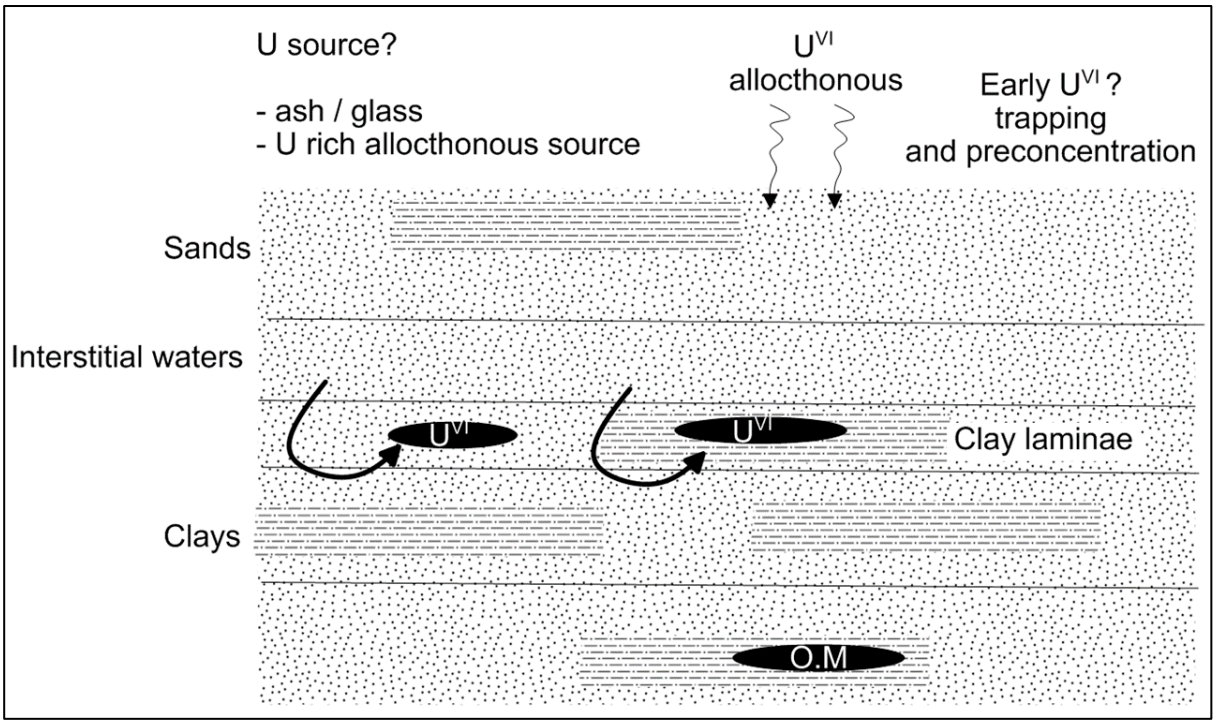

Figure 179: There are several candidates for the uranium source and time of trapping. If uranium is early in the system (preconcentration), then the organic matter trapping (adsorption) must occur soon after sedimentation. If not, then there must be other sources that release uranium after burial, such as leached volcanic ash/glass or interstitial waters carrying U from another U-rich source i.e. metamorphic or granitic rocks.

Since there was very limited number samples with organic matter from the area outside the roll-front, samples from the mineralized area were studied in detail. A good example to understand the possibility of uranium preconcentration is given in Figure 180 and Figure 181. The sedimentology and petrography of the studied sample was already discussed in Figure. This sample is about an intraclast of clay and organic matter contained between coarse to very

coarse sand layers. The organic matter contains between 7.6 and 13.1 wt% U without mineral expression (Figure 180).

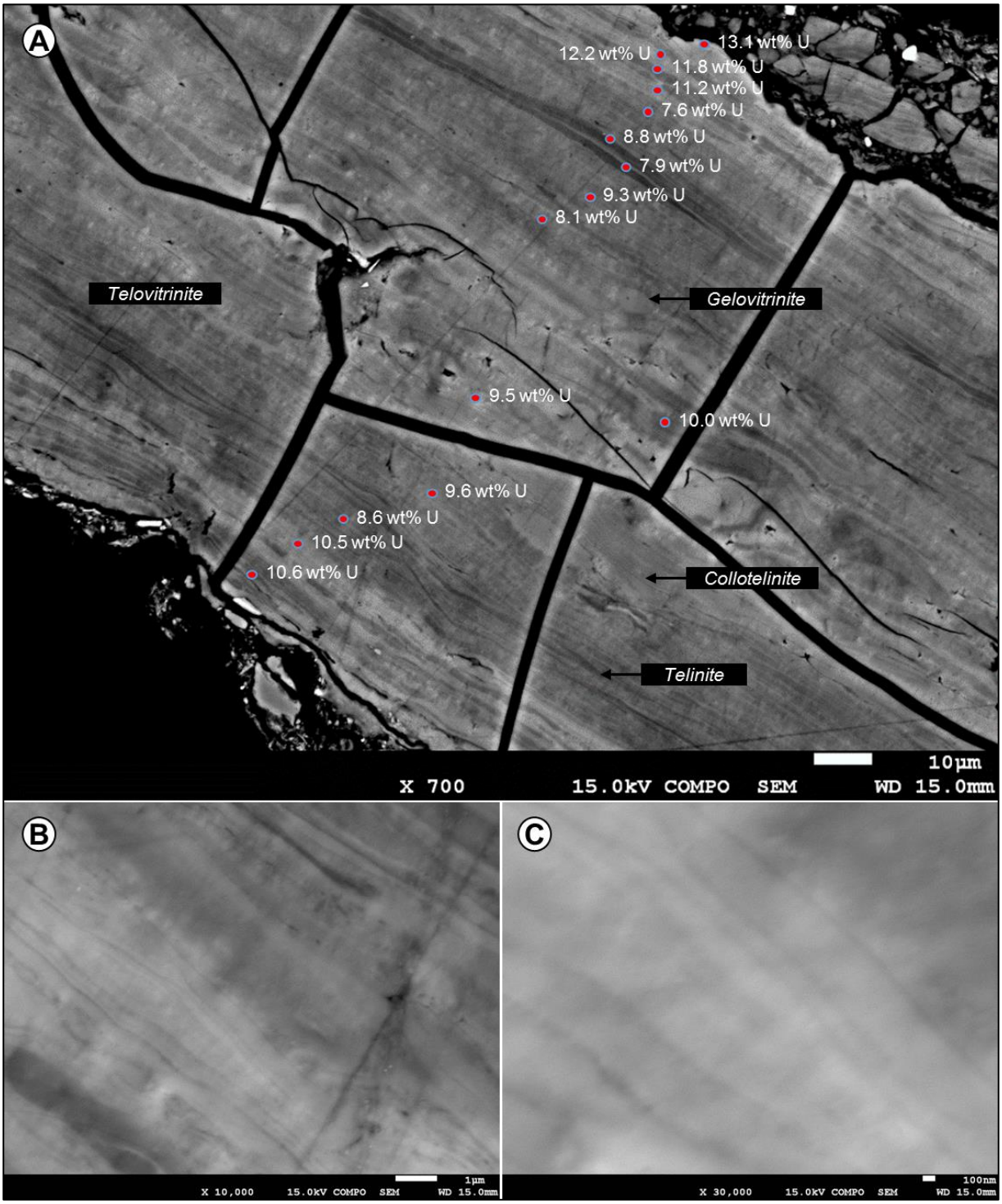

Figure 180: SEM-EDS analysis of a telovitrinite particle from sample 9704-8 (clay and organic matter intraclast in very coarse grained mineralized sand). Three macerals can be discriminated, telinite, collotelinite and gelovitrinite. (**A**) Point measurements across the particle focusing on the areas of different brightness. The uranium content is uniform fluctuating between 7.9-13.1 wt%. (**B,C**) High magnification of the bright areas of the telohuminite particle. Uranium distribution is not uniform in this scale. Yet, it is not clear if uranium is adsorbed as uranyl ion or is reduced as oxide. Concentration maps for the above presented organic particle are provided in Figure 180.

As was explained in the previous chapter, uranium adsorption by macerals depends on the abundance of carboxylates, the level of biodegradation and finally the porosity/permeability. As presented in Figure 181 and Figure 180 uranium is concentrated preferably in the softer parts of the organic particle, in particular in gelovitrinite and collotelinite macerals. On the contrary the harder parts i.e. telinite contains lesser amounts by an order of 3-5 wt%. Sulfur is nearly following the same pattern with uranium. Iron and titanium are contained at constant levels, with the local high concentrations of the latter indicating pyrite. Calcium is many times contained in pitchblende in Zoovch Ovoo and magnesium is mostly associated to clays; both concentrations are constant and insignificant. Finally, aluminum and silica are totally absent.

As was presented in in Figure the coarse sand in contact to the organic matter/clay intraclast layer, contains uranium expressed as phospho-coffinite associated to clays and pyrite around silicates. Knowing that phospho-coffinite mineralization is secondary, this feature may be an indication of uranium preconcentration in the organic matter.

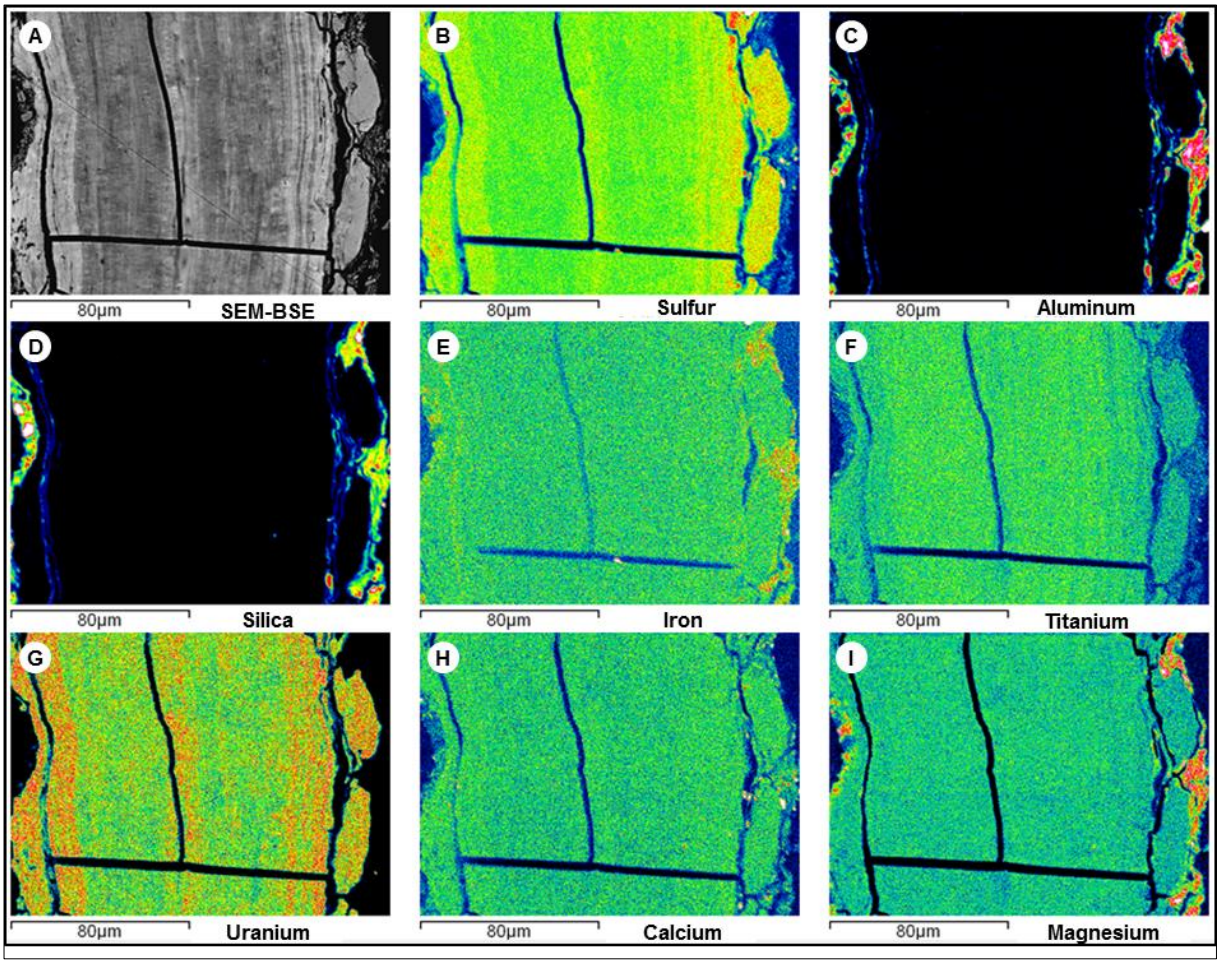

Figure 181: SEM-EDS concentration maps for a series of elements on a telohuminite particle (A), in sample 9704-8 (clay and organic matter intraclast in very coarse grained mineralized sand). The contrast in mean Z in (A) is a result of differential uranium concentration (adsorbed or reduced?) in the maceral components of the particle. This is evident since the bright zonations that appear in (A) are in accordance to (G) which is a concentration map for uranium. The telovitrinite particle is composed of respective telinite and collotelinite macerals. The latter appears to contain uranium in higher quantities.

7.2.6 Iron and sulfur in organic matter particles

The relative amounts of Fe and S are following roughly the stoichiometry of pyrite although iron sulfides are not always visible on SEM images and micro-XRF maps. However, significant shifts in stoichiometric relationships are observed (Figure 182) and confirmed by the micro-XRF maps, where some parts of the macerals are enriched in Fe and others in S. Meunier et al. (1990) also referred to iron and sulfur organic compounds contained in natural organic matrix that were not linked to iron sulfides. Dichloromethane extraction of the samples followed by gas chromatography-mass spectrometry allowed to identify the presence of elemental sulfur. Its presence may be linked to sulfate reducing bacteria. Yet, the redox state of iron (when not associated to sulfur) in the organic matter of the studied samples is not easy to determine. However, in regards to the reducing environment (organic matter, reduced species of sulfur, $U^{(IV)}$ minerals) it is highly probable to be $Fe^{(II)}$. Like the reduced sulfur species, $Fe^{(II)}$ may arise from microbial activity (reduction of $Fe^{(III)}$ carried together with $U^{(IV)}$ by the mineralizing fluid). When associated in stoichiometric proportions, iron and sulfur may reflect the presence of the amorphous phases, which are precursors to pyrite as disordered mackinawite of formula $Fe_2(HS)_4$ (Davison et al., 1998) or Fe_3S_3 $(H_2O)_6$ (Theberge and Luther, 1987), ordered mackinawite, and greigite Fe_3S_4 (Rickard, 1995; Wolthers et al., 2005; Bura-Nakić, 2009). This might explain the absence of identified pyrite crystals in the organic matter. Compositions consistent with pyrite stoichiometry may indeed be indicative of microcrystals. Excess of iron or sulfur in the analysis may be linked to $Fe^{(II)}$ carboxylates as well as S^0 adsorbed to organic matter.

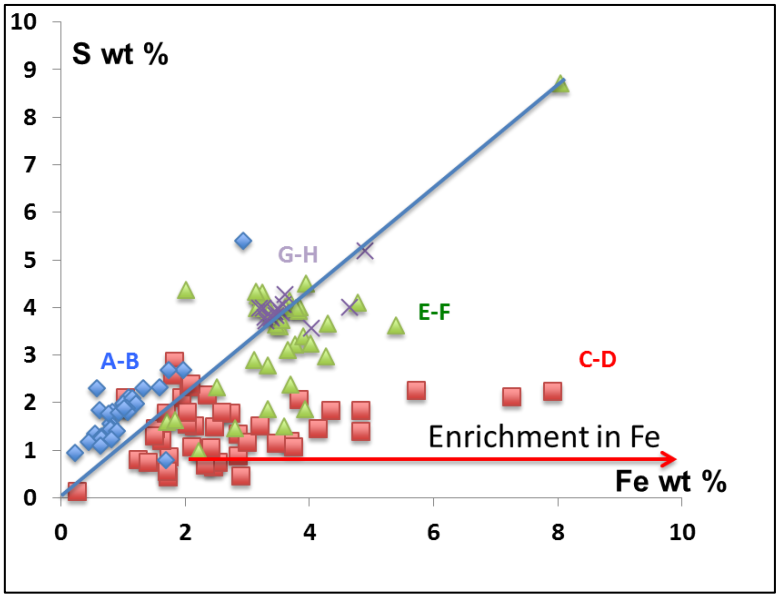

Figure 182: S-Fe plot for the organic matter analyses carried out along different profiles on U-rich macerals, in particular AB and C-D on a root fragment and E-F and G-H on vitrinite nodules (gelovitrinite), and distribution along the profile of the U, Fe, S and Ti concentrations.

7.3 EVOLUTION PATHWAYS OF THE PYRITE PHASES

As was already demonstrated the framboidal and euhedral pyrite phases indicate by definition two distinct generations. There was an attempt to understand the pathways that lead from the least complex microframboids to framboids, then to polyframboids and finally to cubic crystals. According to Sawlowicz (1993) there are three pathways that can explain the transition from framboids to euhedral pyrite crystals and this transformation occurs due to crystal surface energy minimization. These evolution pathways are presented in Figure 183. In this model, there are first scarce or compacted rounded pyrite grains that are rearranged to micro-size euhedral grains (due to lower surface energy), then grow in size by adding an outer ring, which is then amalgamated with the main body, ending up in a perfect cubic pyrite crystal.

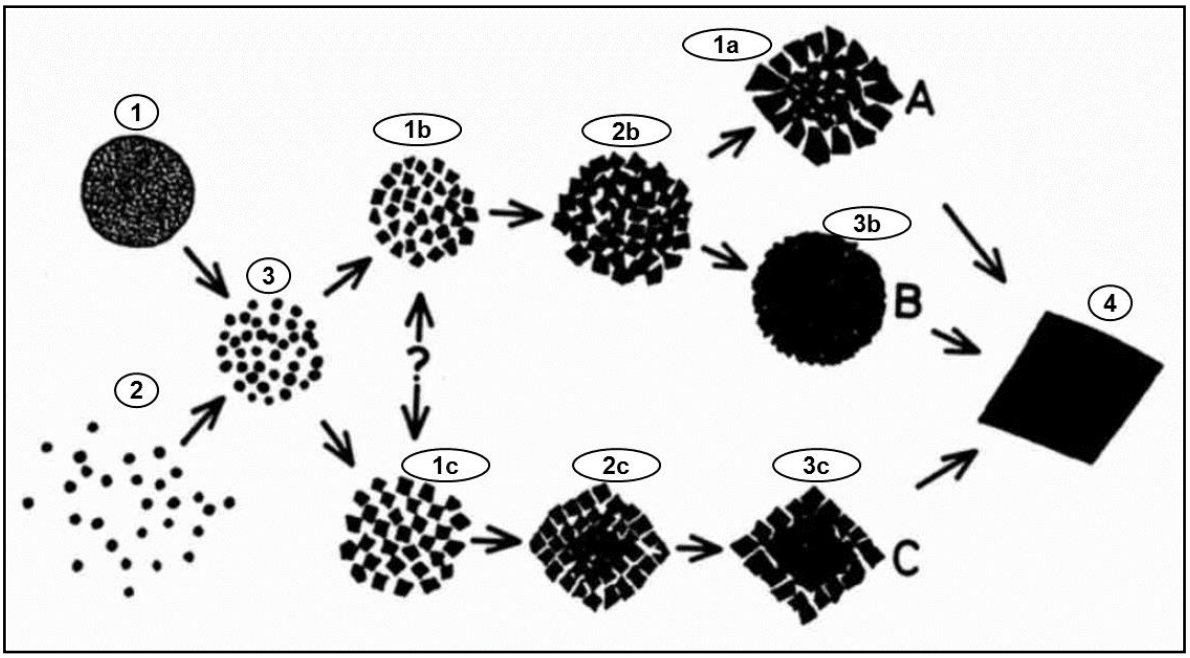

Figure 183: Graphical representation of the three pathways that could lead to euhedral pyrite formation starting from framboids (Sawlowicz, 1993). Certain numbers were added on each pyrite phase to better correlate with the current database.

Numbers were added on Figure 183 in order to correlate the graphical representation with the current findings of the pyrite study (Figure 185). It is noted that some of the very early stages were not identified.

Photo-micrographs

Figure 184: Examples of different pyrite types showing the pathways from framboidal to euhedral pyrite.

A: Large rounded pyritospheres, possibly of the first generation (1).

B: Least complex microframboid (1b); **C:** Compacted microframboid (2b).

D: Pyritosphere with an outer ring (1a); **E:** Embedded framboids (3b) in euhedral mass (4).

E: Group of framboids with overgrowth (2c);

F: Angular overgrowth, one step before the transformation to cubic pyrite (3c).

G: Perfect euhedral crystal consisting of small cubes, previously forming angular clusters of framboids with concentric overgrowth (4).

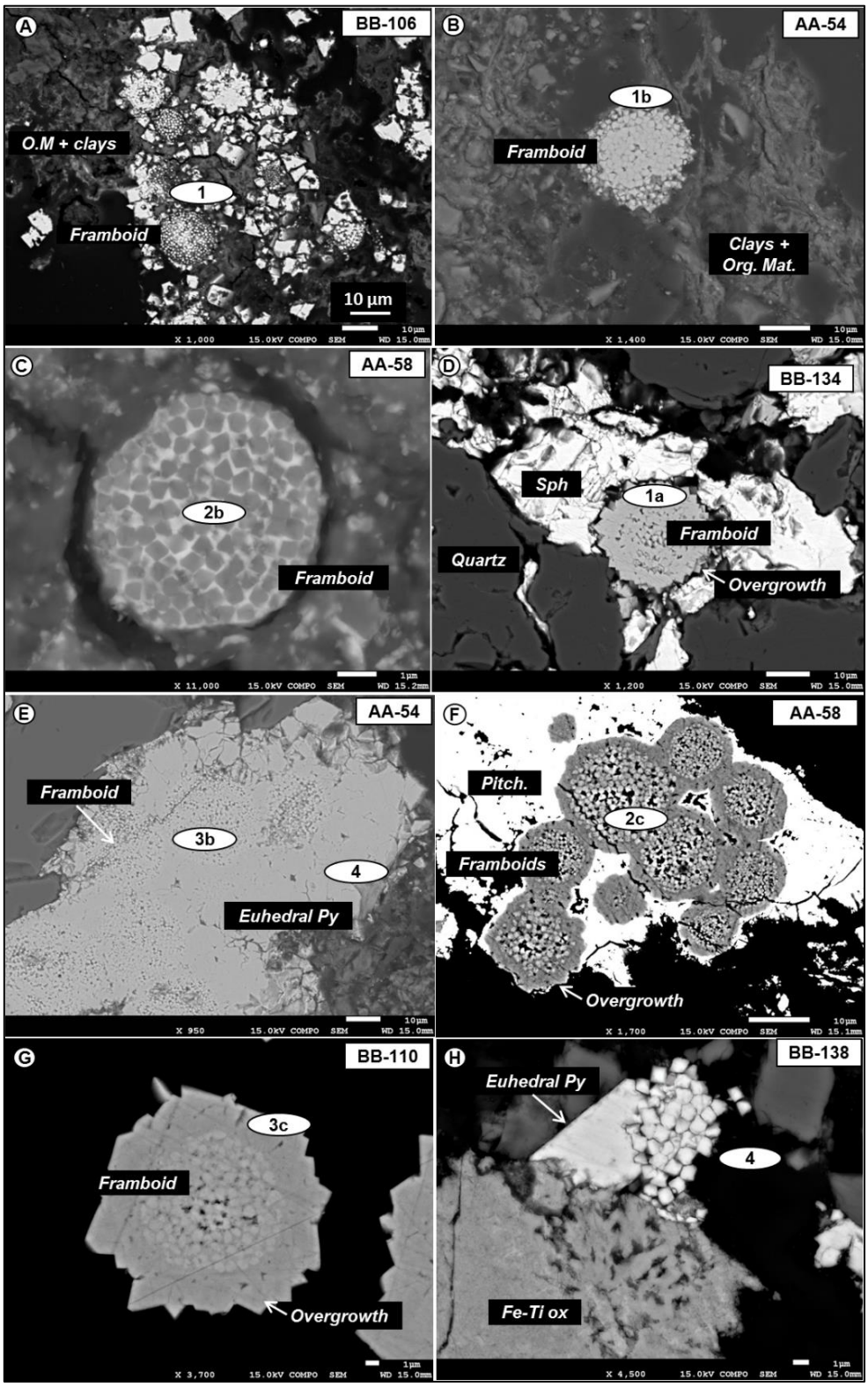

Figure 185: Examples of different pyrite types showing the pathways from framboidal to euhedral pyrite.

7.4 ORIGIN OF FRAMBOIDAL PYRITE

The term framboidal pyrite or framboids refers to microscopic spheroidal to sub-spheroidal clusters of equidimensional and equimorphic microcrystals. These microcrystals have a specific internal microarchitecture (Ohfuji and Rickard, 2005b). The framboidal texture mostly occurs in pyrite and is the main pyrite texture to be found in nature, for instance:

i. in sedimentary rocks (Love and Amstutz, 1966; Hallbauer, 1986; Sassano and Schrijver, 1989),
ii. in recent marine and freshwater sediments (Sweeney and Kaplan, 1973; Perry and Pedersen, 1993),
iii. in anoxic water columns (e.g. Ross and Degens, 1974; Wilkin et al., 1996; Suits and Wilikin, 1998).

The microbial processes in sediments regulate the source of the sulfur that essentially derives from the sulfate-reduction by prokaryotes (Berner, 1984), with simultaneous production of other pyrite textures. According to Berner (1969) the first synthesis of framboids is related to abiological processes. Ohfuji and Rickard (2005a, b) demonstrated how these uncommon self-assembled structures can be produced by inorganic processes.

The origin of framboidal pyrite and the reason why it is the main pyrite texture in nature are two of the major questions that are still under debate. Their size in diameter usually ranges between 1 to 250 μm (Dill and Kemper, 1990; Sawlowicz, 2000), but are often at the range of 10 μm (Love and Amstutz, 1966; Rickard, 1970; Wilkin et al., 1996). In recent sediments, pyrite can occur as discrete microcrystalline grains without defined shape that can be equidimensional and equimorphic, occasionally with regular organization resembling the framboids (Bertolin et al., 1995; Jiang et al., 2001; McKay and Longstaffe, 2003). In more detail the interior of the framboidal pyrite in recent sediments is not solid but instead is composed of distinct densely packed microcrystals. According to Ohfuji and Rickard (2005b) framboidal pyrite in nature can be expressed in two types based on their internal structure which can be ordered or disordered. The ordered framboids refer to homogenous and microcrystals evenly oriented with either cubic close packing or icosahedral packing (Ohfuji and Akai, 2002). The disordered are composed of microcrystals that are randomly oriented.

Framboidal pyrite can occur also in environments that are harsh for the development of microorganisms, for instance in volcanic rocks with high temperature (Love and Amstutz, 1966) or even in hydrothermal ores (England and Ostwald, 1993) and can be synthesized abiogenically. Thus, self-organisation of framboidal microcrystals is achieved abiologically. Extreme pyrite supersaturations are required in order to successfully synthesize framboidal pyrite so that the rate of crystal growth is smaller than the rate of pyrite nucleation. Pyrite is

highly insoluble and requires high supersaturations to initiate nucleation, which can be achieved via multiple ways that vary the reaction conditions. It was proven experimentally that the Eh in a closed system can increase progressively by saturating in elemental sulfur, oxygen or by elevating the temperature. The reaction that leads to the formation of framboidal pyrite is controlled by physical and mechanical parameters. For example S(0) can produce locally high concentrations and temporarily form polysulfide ions, while oxygen can also provide with restricted increased concentrations. At the same time the constant supply of nutrients strengthens the fast growth of large framboidal crystals. In cases that the crystal growth of the framboidal pyrite microcrystals is limited, the nutrient supply must have been lower than the rate of the crystal growth that would also reflect a change in the hydrodynamics of the system (Ohfuji and Rickard, 2005b).

7.5 SUMMARY OF PYRITE GEOCHEMISTRY

7.5.1 Trace element behavior

Pyrite plays a very significant role as uranium reducer in Zoovch Ovoo. Sphalerite is also reducing uranium but its abundance is much more limited. Pyrite was divided in four different generations that can become six if the two pyrite generations that are related to the anhedral (type IV) dolomite are included. Sphalerite is as well divided in two generations. Emphasis is put on the euhedral pyrite generations 1 and 2 that stand for pre-ore and ore-stage euhedral pyrite.

The first euhedral generation is genetically related to the previous pyrite generations, hence euhedral 1 is formed gradually from framboids their concentric overgrowths if present. This transformation is caused in order for the crystal to minimize its surface energy and become more stable (Sawlowicz, 1993). The genetic relationship is known because many times pyrite clusters of embedded framboids were found in the central part of euhedral crystals. The timing of formation of the first euhedral pyrite genetration is clearly set before the roll-front. Sometimes marcasite can be interpolated in between the first and second euhedral pyrte generations. As such marcasite is the last pre-roll-front iron disulfide. All four pre-roll-front iron disulfides are characterized by a depletion in certain trace elements, namely in Cd, Co, Ni and to a lesser extent in V, Zn, Mo and Cu, relative to the second euhedral generation that is formed during ore-stage. Marcasite is very enriched in As compared to all other iron disulfides. According to Savage et al. (2000); Lowers et al. (2007) and Ingham et al. (2014) reduced arsenic (As^{-1}) is incorporated in the iron disulfide lattice by substituting sulfur. It could be thus proposed that As is scavenged due to low sulfur availability during the final stage of iron disulfide formation before the roll-front waters recharge.

The enrichment in certain trace elements in ore-stage pyrite could hold two interpretations. Either the roll-front waters that also bring uranium in the system are leaching these elements from host lithologies i.e. a combination of mafic rocks (Co, Ni; Goldschmidt, 1954; Clark et al., 2004), granitic rocks (Mo; Blevin et al., 1996) and organic rich black shales (As, V; Brumsack, 2006) that were not available in Cretaceous, hence absent from pre-roll-front pyrite or the concentration of these trace elements in late stage sulfides is due to the redistribution of pyrite (dissolution and recrystallization) with the evolution of the roll-front (Ingham et al., 2014), since these elements are also contained in the pre-roll-front pyrite generations. According to the tectonic history of the basin, Sainshand Formation was deposited during the post-rift stage and there was only minor tectonic activity from Cenomanian and on. As such, it is unlike that important deformation episodes took place that brought to the surface other than the existing basement rocks. In this framework the trace element redistribution scenario seems to be more accurate. With respect to native Se found in relation to organic matter, Ingham et al. (2014) proposed that Se is being scavenged from the dissolution of pre-ore pyrite or ideally from other Se-bearing minerals. Indeed, in Zoovch Ovoo reservoir there are selenides, such as clausthalite (PbSe) and stilleite (ZnSe), which could potentially be a source for Se. Hematite has also precipitated during late-stage events.

Above the distinction in trace element concentration between the two euhedral pyrite generations, there are two more aspects that can be used for their discrimination. First only the ore-stage euhedral pyrite may contain pitchblende microsize inclusions. Secondly, only the ore-stage pyrite will be stable, in well-developed cubic crystals at the presence of roll-front waters, while the first euhedral pyrite generation will be corroded through a series of abiogenic chemical reactions (Figure 187). The phenomenon of ore-stage sulfides not being replaced by uranium mineralization was detected and described by Bonnetti et al. (2017) in their study of the Baxingtu roll-front deposit in NE China.

7.5.2 Significance of sulfur isotopic composition

Sulfur isotopes in uranium roll-front deposits can help to distinguish between biogenic and abiogenic pyrite and as a result to decipher the redox mechanisms (Hough et al., 2019). As demonstrated above the Zoovch Ovoo roll-front is controlled by bacteria (iron reducing, sulfate reducing and methanogens).

The gradual fractionation of ^{34}S from positive to negative values coupled with the geological evolution of Zoovch Ovoo, could indicate that the framboidal pyrite with $\delta^{34}S$ values fluctuating at 20‰ originates from the reduction of evaporites by bacterial sulfate reduction (BSR). The positive $\delta^{34}S$ of framboidal pyrite, in contrast to the usual negative BSR derived pyrite, is due to the initial heavy $\delta^{34}S$ of evaporites, which according to literature usually reaches +20 to

+35‰ (Makhnach et al., 2000). In contrast sulfur from intrusive rocks display $\delta^{34}S$ close to zero (Ohmoto and Goldhaber, 1997), hence this source is not providing S for framboidal pyrite. These sulfates may be linked to the depositional environment, but may also be secondary, formed from the mineralizing fluid at later stages of diagenesis. Framboidal pyrite is probably sedimentary (Kohn et al., 1998) formed from the limited dissolved sulfates in freshwater (Berner, 1984).

The euhedral pyrite with negative $\delta^{34}S$ values originates from the further fractionation of the initially positive framboidal pyrite. The positive and negative values are rather reflecting closed versus open fractionation systems. In turn the ^{34}S-depleted euhedral pyrite indicates that it is bacterial derived and that BSR is active during the whole diagenetic history of the deposit and is the unique sulfate reduction process (absence of TSR), even during uranium deposition, since the second euhedral pyrite generation is co-genetic to uranium formation (pitchblende bearing).

For all the above, thermochemical sulfate reduction (TSR) is *a priori* excluded in regards to the very low thermal maturity of the studied samples and the low vitrinite reflectance ($\%R_o$<0.4%), as would be expected for shallow burial and low temperature.

There are examples from other roll-front deposits of the world that demonstrate similar values for the $\delta^{34}S$ of pyrite. In particular:

1. The deposit from Pepegoona and Pannikan (Lake Eyre Basin-South Australia) with $\delta^{34}S$ from -43.9 to +32.4‰ (Ingham et al., 2014).
2. The deposit from Lost Creek and Willow Creek Mine Unit 10 (Wyoming-USA) with $\delta^{34}S$ from -68.1 to +142.8‰ and from -48.1 to +68.2‰, respectively (Hough et al., 2019).

The first study concluded that there is possibly no direct relationship between the $\delta^{34}S$ isotopic composition of pyrite and U mineralization. Yet, the same authors suggest that the roll-front waters may have an effect on the inherited $\delta^{34}S$ from the dissolution of pre-ore pyrite.

The second study mentions that the $\delta^{34}S$ fractionation of about 210.9‰ indicates a closed system, whereas a $\delta^{34}S$ fractionation of about 116.3‰ indicates an open system. The Zoovch Ovoo fractionation of $\Delta^{34}S$ is about 100‰. To contrast with the fractionation of Lost Creek and Willow Creek Mine Unit 10, the data and plot from Hough et al., 2019 were cross-plotted with the data from Zoovch Ovoo (Figure 186).

Based on the above, the fractionation of Zoovch Ovoo is pointing towards an open system. However, it is also very likely that the fractionation of 100‰ could indicate a semi-open/semi-closed system, with limited fresh water recharge during the history of the reservoir.

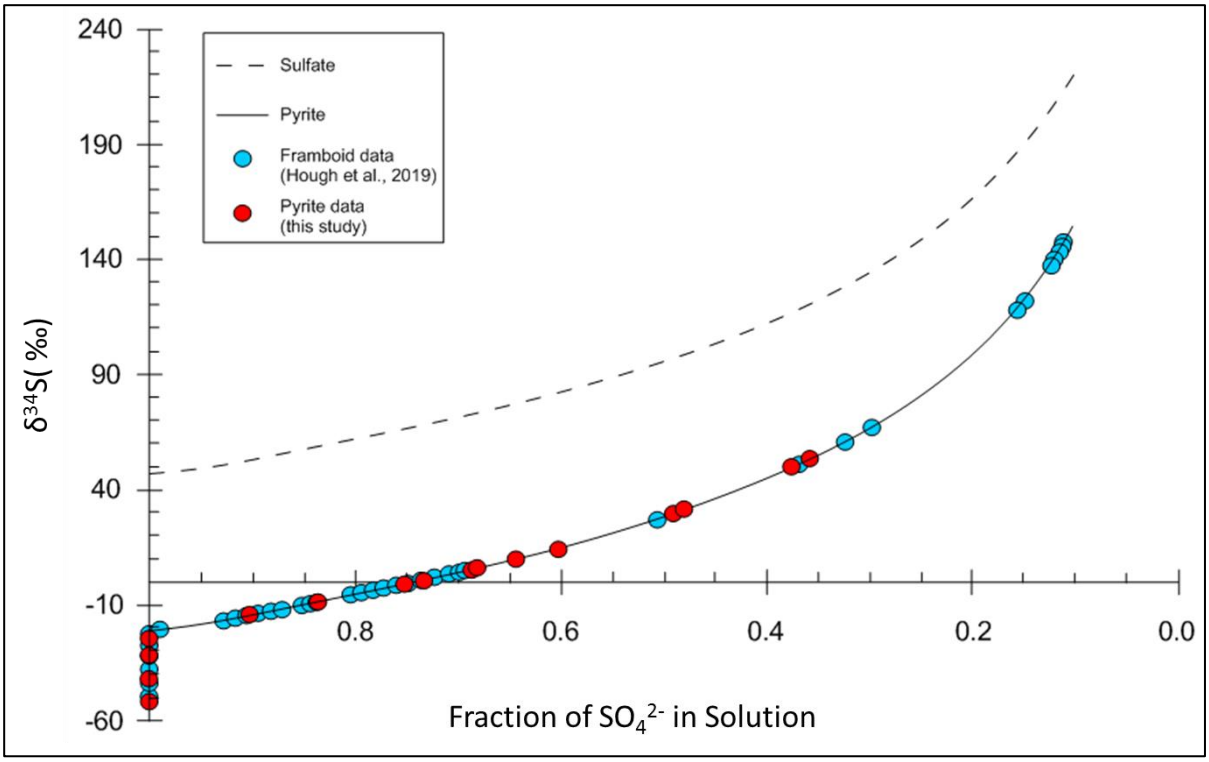

Figure 186*:* The Rayleigh fractionation model of framboidal pyrite at Lost Creek (LC) from Hough et al., 2019 (blue dots), crossplotted with the results of this study (red dots). The dashed line models $\delta^{34}S$ value of sulfate in solution with progressive sulfur depletion. The solid black line is the $\delta^{34}S$ value of pyrite produced at a specific level of depletion. According to the authors, the data correspond to 88.5% depletion of solution sulfate. The fractionation from Lost Creek is higher by about 100‰ than Zoovch Ovoo.

7.5.3 Uranium trapping processes involving pyrite at Zoovch Ovoo

Pyrite is a major uranium reducer in roll-front systems. Pyrite can be oxidized biogenically by ferro-oxidizing bacteria and abiogenically under semi-oxic conditions. In a roll-front the redox interface is build by ferro-oxidizing bacteria, responsible for the oxidation of pre-ore pyrite and by sulfate-reducing bacteria that reduce sulfate to form ore-stage pyrite (Descostes et al., 2010; Hough et al., 2019). In addition, organic matter serves as a nutrient for the bacteria if present. Afterwards, ore-stage pyrite can reduce U(VI).

The abiogenic redox model that also reduces hexavalent uranium is described through the equations presented in Figure 187. Ore stage pyrite is stable in the presence of U-rich waters in oppose to pre-ore stage pyrite which is susceptible to dissolution by the oxidizing waters, producing reduced sulfur (HS^-) and reduced iron (Fe^{2+}) that in turn reduce hexavalent uranium (Wilkins et al., 2006). In detail there are many metastable phases that occur from the oxidation of pyrite. The sulfur species that are generated include thiosulfate ($S_2O_3^{2-}$) and sulfite (SO_3^{2-}) that form H_2S and SO_4^{2-} (Hough et al., 2019).

The main difference between the biogenic and abiogenic redox model is that there is great abundance of pyrite in the ore-zone in the first case, whereas in the second the ore-zone is gradually depleted due to the continuous removal of sulfate.

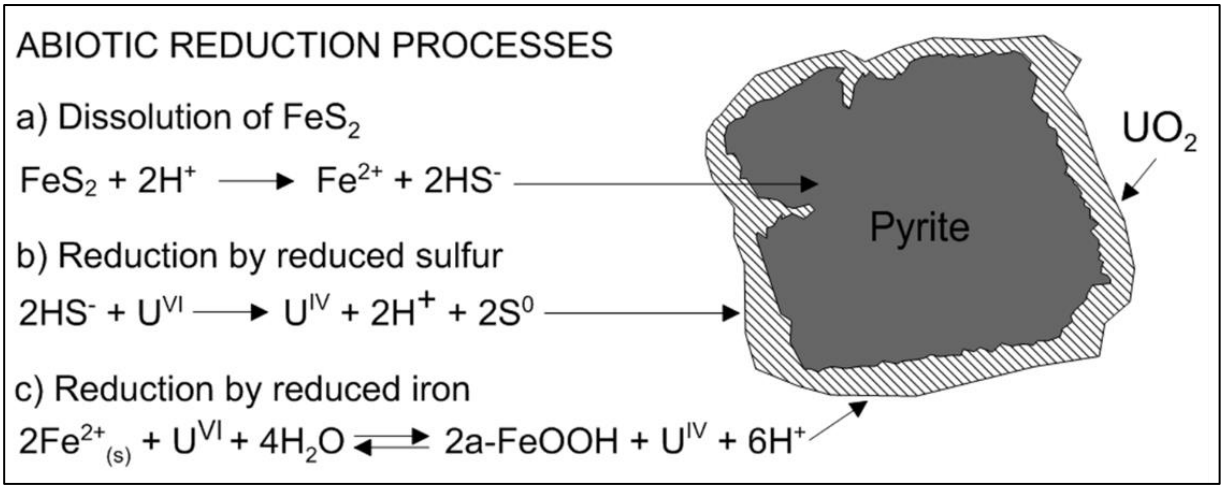

Figure 187: Abiogenic redox model for pyrite dissolution and uranium reduction. (a) Pyrite is first partially dissolved; (b) Uranium is reduced from reduced sulfur and (c) by reduced iron.

7.6 SUMMARY OF PYRITE PETROGRAPHY AND GEOCHEMISTRY

The crystal chemistry of each pyrite type was determined and the results were plotted on several geochemical diagrams in an attempt to identify potential trends for the different pyrite phases, namely the framboidal, the euhedral and the marcasite (polymorph). The concentric pyrite (overgrowth) was not considered as a separate phase from the framboidal due to its thickness being lower than the diameter of the analytical beams. At the first place, there was an attempt to find differences between the pyrite types based only on their morphology. Petrography thus allows to consider pyrite habitus succession in terms of progressive crystal growth (as proposed by Sawlowicz et al., 1993; Figure 183 and Figure 185). Yet, no clear classification can be made between pyrite habitus (i.e. framboidal or euhedral) and trace element concentration. From a different perspective, the pyrite phases which were associated to uranium, irrespective of their petrographical characteristics, were always enriched in certain trace elements i.e. Co, Ni, Cd, Mo, Cu, Pb and As and the pyrite which was not associated to U-mineralization, was always depleted or less enriched for the same elements.

In addition, the pyrite phases associated to the marcasite and sphalerite but also sphalerite follow the U-associated pyrite trend. On the contrary the polymorph marcasite is As enriched and follows most of the times the pyrite phases which are not associated to U-mineralization.

As was already presented certain pyrite phases are co-genetic to uranium precipitation and are systematically enriched in several trace elements. From all the above it could be suggested

that trace element geochemistry of pyrite may help in identifying those influenced by the roll-front waters.

All the analysed pyrite occurrences were stoichiometric (Fe:S=1:2) and had an acceptable deviation of 0.05 to 0.10 from pyrite stoichiometry (analytical bias). Sometimes when it is in the form of micro-pyrite as a complex inside the organic matter and therefore not visible or if it is associated to U then it is non-stoichiometric.

Striking differences regarding the trace element content between the pyrite types associated to uranium phases and the non-associated, were confirmed. An attempt was made to characterize ore stage pyrite based on trace element concentration. The results were very promising, especially when using Co, Ni, Zn and Mo as indicators. Ore-stage pyrite tends to be enriched in these trace elements compared to non-associated pyrite which is very lean. To confirm the enrichment of ore-stage pyrite the analyses were repeated in a sample that hosts both species (Figure 188).

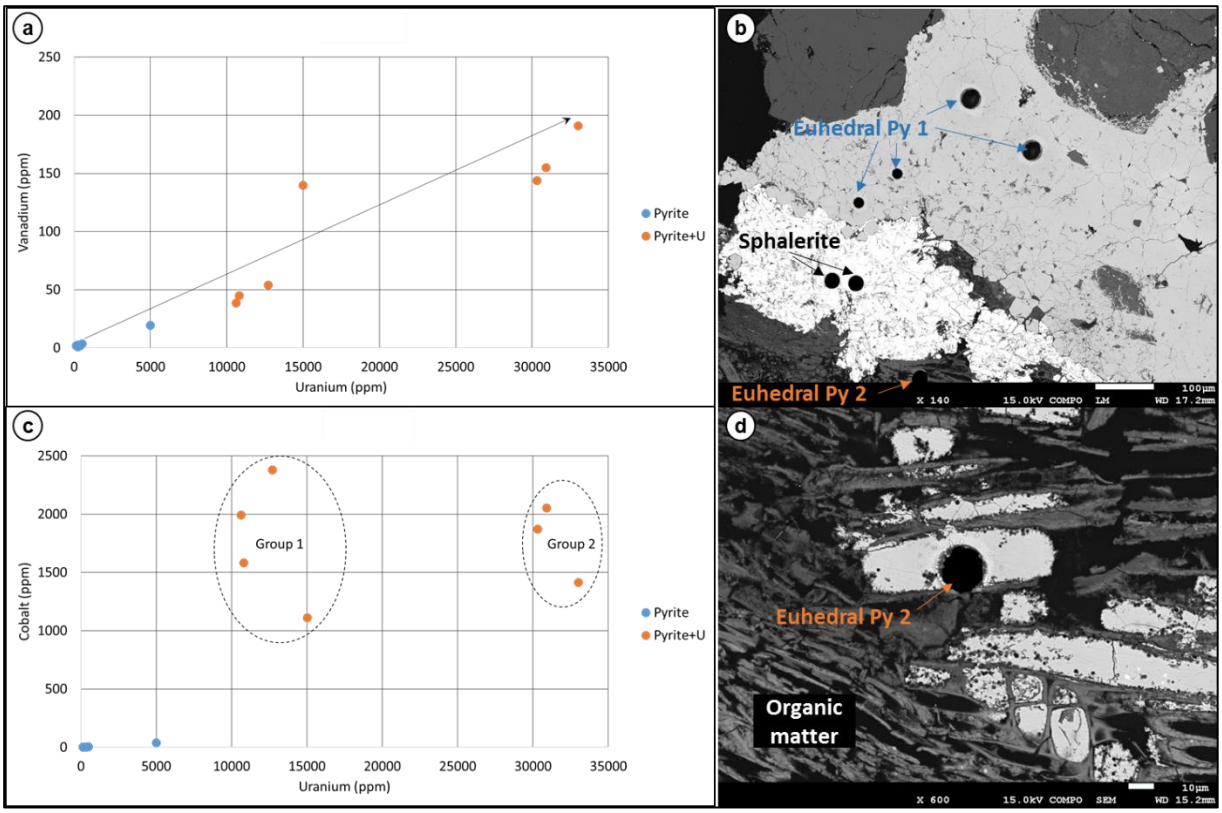

Figure 188: Examples from the LA-ICP/MS study: (a) U vs V plot and (c) Co vs U plot. (b, d) under SEM-EDS show the locations of the ablations first on the euhedral pyrite 1 (blue) lean of U and then on the euhedral pyrite 2 (with pitchblende inclusions).

As illustrated the first euhedral pyrite generation (pyrite 1) is very lean of trace elements and U, reaching a maximum of 5000 ppm in U, whereas the concentration of U in the second euhedral pyrite generation (pyrite 2) fluctuates at 10.000 – 34.000 ppm. In more detail and with respect to the U vs V plot we see a linear progressive enrichment for both elements. On the other hand according to the U vs Co plot, the Co content remains constant at the levels of 1100

– 2400 ppm despite the enrichment in U. According to Fischer and Stewart (1961) and Parnell et al. (2018) the enrichment in elements such as Cu, Co and V indicate more oxidizing conditions because these elements are mobile at high Eh. Indeed, according to petrography pyrite 2 contains pitchblende inclusions, which indicate that this pyrite type was formed during the presence of roll-front waters to the system, which by definition have higher Eh than aquifer water.

The pyrite study was concluded with an isotopic study. In particular the $\delta^{34}S$ of the different pyrite occurrences was analyzed in order to understand more about their origin. The results though very diverse, fluctuating in extreme cases between -50 to +50 per mille for $\delta^{34}S$, show that there are more than four pyrite generations, as was previously concluded by petrography. Overall, isolated framboidal pyrite has a preference for positive $\delta^{34}S$ concentrations at the range of 10±5‰, while euhedral pyrite tends to be negative at the range of -18±5‰ (Figure 129). Furthermore large fractionation of the $\delta^{34}S$, at the level of 35±10‰ occurs for the two pyrite types.

7.7 SUMMARY OF URANIUM GEOCHEMISTRY

Based on the measurements performed on 14 U-mineralized thin sections but also by studying a number of polished blocks, it was possible to identify the mineralogy of uranium and the relationship with organic matter. In Zoovch Ovoo uranium is dominantly expressed as pitchblende (uraninite), slightly enriched in phosphorus, in certain cases experiencing coffinitization. Secondly uranium is expressed as phospho-coffinite that was found to be mostly associated to organic matter. The full replacement of organic matter by uranium occurs when U reaches about 77 wt% in vitrinite macerals and 65 wt% in inertinite macerals. Uranium can be expressed in oxide form at the rims of organic particles even with less than 10 wt% concentrations, while in the internal part even with 50 wt% it can remain unexpressed. Based on the SEM-EDS and EPMA systematic measurements it was possible to propose an equation for the organic matter replacement process.

7.8 TECTONIC SCENARIO AND MINERAL PARAGENESIS OF ZOOVCH OVOO

The complete paragenetic sequence that covers the whole mineral paragenesis of Zoovch Ovoo as was identified by petrographic observations is summarized in Figure 189. In this model Zoovch Ovoo is an endorheic basin (terminal lake) during Cenomanian with saline waters due to seasonal water input and evaporation cycles. As the depocenter was developed during the post-rift stage, uplift and erosion cycles take place from Cenomanian and on (thermal cooling phase). The accommodation space created in Zoovch Ovoo in Cenomanian is not linked to

tectonics but it probably results from sediment deflation. Based on the burial model from Prost (2004), the total uplift is estimated at 300 m maximum.

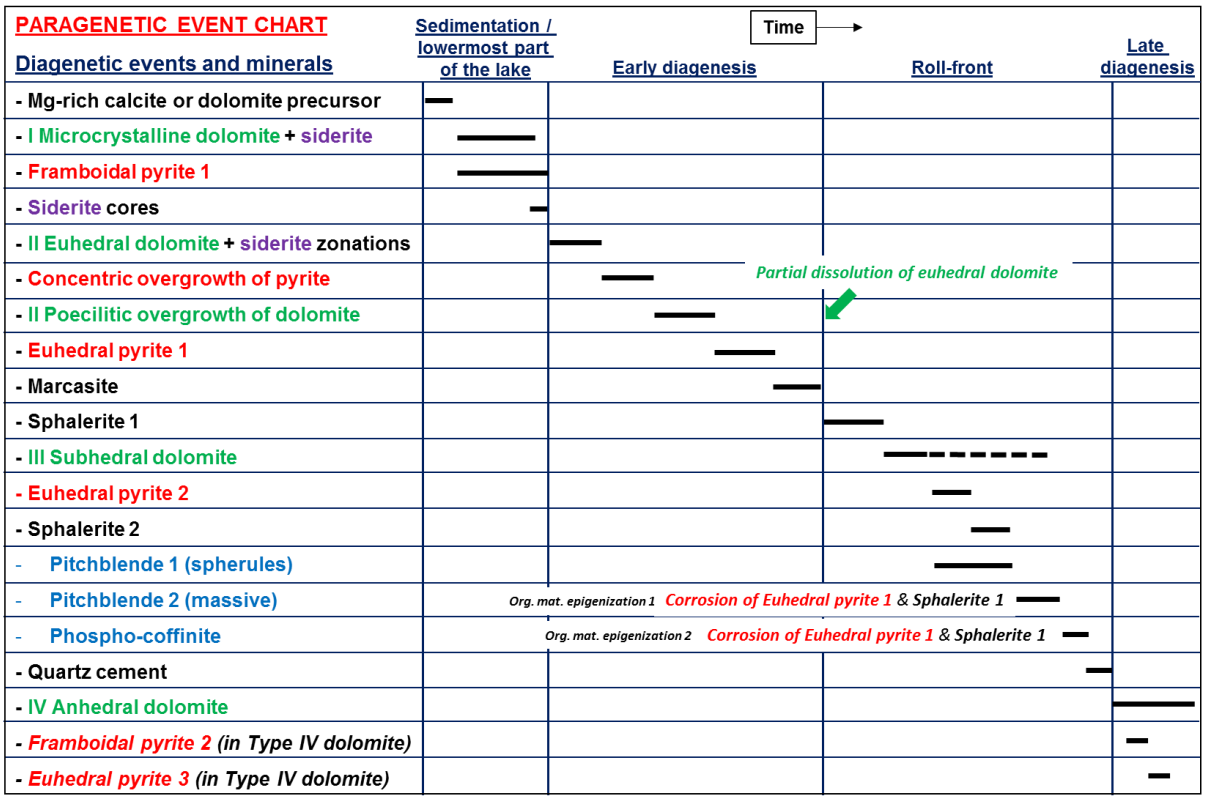

Figure 189: The complete paragenesis of the diagenetic phases encountered in the Zoovch Ovoo sands. The last two phases namely, the framboidal pyrite 2 and the euhedral pyrite 3, stand for new pyrite phases and are still under debate, whether they stand for newly formed pyrite or if they are recycled from previous generations.

Early diagenetic stage

The Zoovch Ovoo sediments indicate a fluvio-lacustrine setting under semi-arid climate with rather seasonal water input (Parize, 2015). Based on the conclusions from the dolomite study there was very probably no calcite precursor to the microcrystalline (type I) dolomite, instead there was primary dolomite deposition as dolomicrite. The organic matter is detrital and has two sources, one distal and one proximal, which is suggested by the preservation status of the organic particles, respectively.

To begin with, dolomite types I and II were formed during early diagenesis since they are associated to siderite and framboidal pyrite that were as well formed early during shallow burial, upon the establishment of reducing conditions that favored BSR, which made reduced iron and reduced sulfur available. The overgrowths of pyrite and dolomite as well as the formation of the first euhedral pyrite generation and of marcasite were also formed during this stage, with the latter being the response to water chemistry changes, particularly of acidic conditions (Anthony et al., 2003).

Effect of roll-front waters

The first sphalerite generation is prior to U precipitation in the diagenetic sequence, although possibly Zn arrives with the roll-front waters. The second ZnS generation is co-genetic to U precipitation. This is known because the first generation can be replaced by uraninite while the second contains pitchblende microsize inclusions.

The partial dissolution of the dolomite due to the reactivity with the roll-front waters is responsible for the formation of secondary porosity and consequently of subhedral (type III) dolomite. The roll-front has also an effect on the first euhedral pyrite causing corrosion and U-replacement. On the contrary both the second euhedral pyrite and sphalerite generations are co-genetic to the first uranium episode, since both of them contain pitchblende inclusions (pitchblende 1). The first uranium episode refers to the incipient stages of U precipitation followed by the second uranium episode, which refers to massive introduction of U to the system (pitchblende 2). During the second U episode, pitchblende tends to be accumulated as follows:

i. As uranium oxides at the rims of the organic particles (UO_2) and then with cryptocrystalline form and with decreasing concentration gradients towards the interior of the particle. The accumulation of U leads ultimately to the full replacement of the organic particle.
ii. As uniform cement inside clay matrix, preferably on parts that were previously pyrite cemented.
iii. In the intergranular porosity between the detrital grains or in the secondary porosity caused by dolomite dissolution.
iv. Finally by corroding and replacing the first pyrite and sphalerite generations as well as the pyrite associated to organic matter.

The direct long term contact of detrital grains i.e. quartz, feldspars and micas with pitchblende cement is responsible for the formation of pleochroic halos around these minerals that are visible under cathodoluminescence. Such processes were already demonstrated by pioneer works (Meunier et al., 1990). These halos are caused by prolonged alpha-particle bombardment on the silicate mineral surface; a process known as radiation damage.

Eventually, pitchblende mineralization will be dissolved and redistributed further in the roll. However, the radiation damage will be permanent, hence the silicate relics will provide evidence that pitchblende cement was previously present.

Late diagenetic stage

The late diagenetic stage is characterized by the formation of anhedral dolomite, precipitated from formation fluids very lean in REE. The strong negative Eu anomaly of anhedral dolomite

(Fowler and Doig, 1983) and the newly formed framboidal and euhedral pyrite found inside their lattice, indicate reducing conditions. This is in oppose to the oxidizing conditions that prevail during the input of the roll-front waters. One possible explanation could hold that the system was uplifted and the reducing settings were re-initialized (BSR). Therefore, these elements are regarded as post roll-front. Furthermore, type IV dolomite cement was confirmed in sediments originating from the area outside the roll-front. It is therefore suggested that anhedral dolomite is totally disconnected from the roll-front influence. In addition the fact that anhedral dolomite is uniquely found in coarse to micro-conglomeritic lithologies indicates that it is linked to horizons of high permeability, which is in contrast to dolomite type I and II that are found in sediments of finer grain size. This supports the scenario that the formation of type IV dolomite is sourced from aquifer waters, totally lean of REE that percolate through the remaining non-cemented sands of high permeability. It also indicates that the aquifer waters are in equilibrium with dolomite.

During late diagenesis there is local phospho-coffinite cementation. The chronology of uranium mineralization events is possible by studying the respective samples under cathodoluminescence. In particular, radiation halos were identified in quartz grains that were not in conformity with phospho-coffinite cement. Keeping in mind that direct contact is needed between uranium minerals and quartz for alpha particles to be able to penetrate the mineral lattice, this feature suggests the following paragenetic events. Pitchblende cement was deposited all around detrital grains. Pitchblende was dissolved later and redistributed further away to the front. Next, when the fluid was saturated with respect to Si, phospho-coffinite was formed and occupied the available porosity that was already covered in part by dolomite overgrowth after pitchblende dissolution. Hence, the radiation halos do not follow the distribution of phospo-coffinite. Finally, upon depleting the fluid in uranium, quartz cement (authigenic quartz) was formed locally instead.

7.9 SEDIMENTOLOGICAL/BURIAL DIAGENESIS MODEL

Conceptual graphical representations were developed to address the mineral paragenesis from Cenomanian to Turonian and finally to Tertiary that is similar to present day (Figure 190, Figure 191 and Figure 192). The diagenetic evolution of dolomite and pyrite is used to describe the fluid-rock interactions in each geologic period. The Zoovch Ovoo depocenter was a fluvio-lacustrine system with deltas and seasonal water input (Figure 190). The sources that were providing the basin with sediments were the volcanic, metamorphic and granitic outcrops in the south, as petrography revealed minerals that are typical of these sources i.e. pyroxene, zircon, tourmaline, ilmenite, anatase and lithic elements with myrmekite-granophyric and doleritic textures. However, it is not clear if uranium was carried in solution at the time of

deposition of Sainshand Formation, which has implications in the U preconcentration scenario. Organic matter is definitely of detrital origin and in particular derived from higher plants. The differential preservation status of the DOM points towards a scenario of at least two sources, a proximal for the well-preserved (vitrinite) and a distal for the oxidized (inertinite). Dolomite was formed at the surface as microcrystalline mud cementing parts of the underwater sand dunes without a particular pattern. The hypothesis of primary dolomite formation is explained by high Mg/Ca ratios. During surface run-off the water is progressively depleted in Ca as calcite and gypsum are formed. By the time the water reaches Zoovch Ovoo, it is saturated in respect to dolomite, hence dolomite mud is deposited. During evaporation/recharge cycles the dolomite cemented layers are exposed and are eroded and redistributed in near-parts of the basin during flooding events. Likewise, intraclasts of mud and organic matter are redistributed in other parts of the basin.

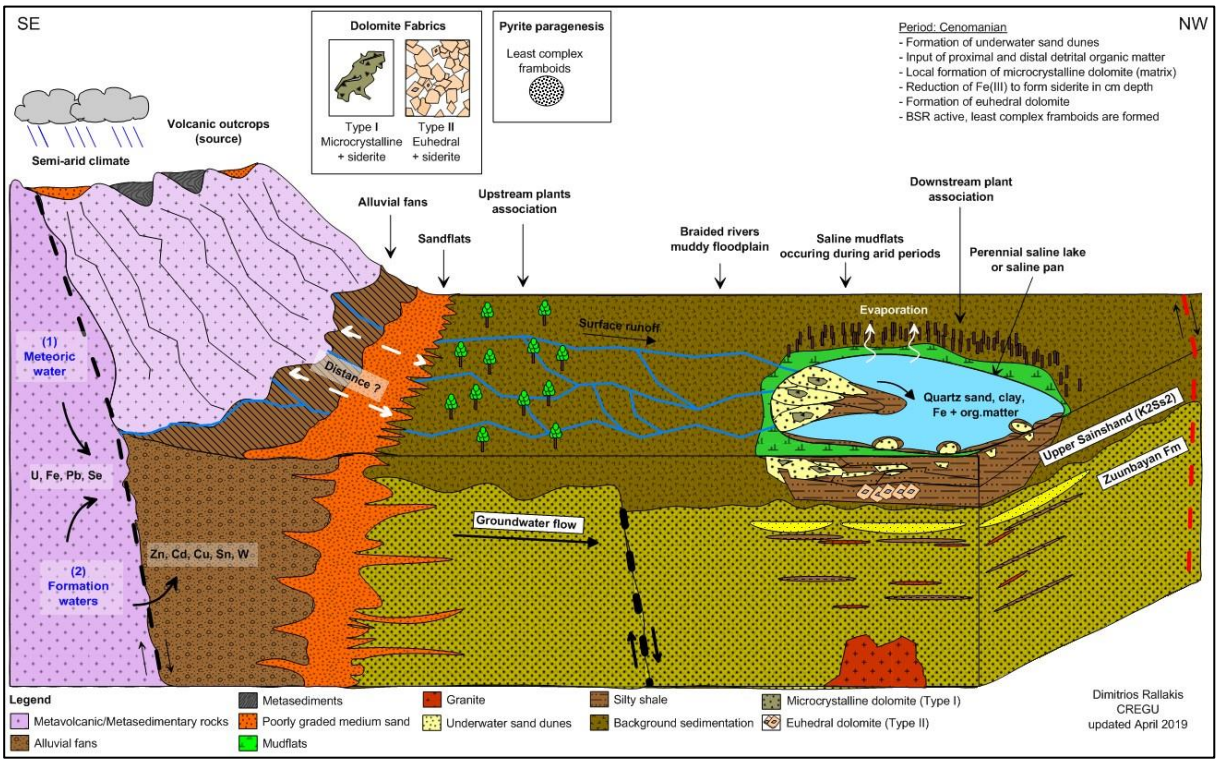

Figure 190: Conceptual model of the regional area around Zoovch Ovoo depocenter during Cenomanian (Sainshand Fm), illustrating a fluvio-lacustrine system coarse sands and varves. The climatic conditions that prevailed during Cenomanian were semi-arid, favoring evaporation-recharge cycles. In this model, microcrystalline dolomite is formed near-surface due to high Mg/Ca ratios. Height of the outcrops not in scale.

Euhedral dolomite is formed after burial out of the microcrystalline mud due to thermodynamics (to minimize surface energy). Siderite and framboidal pyrite are formed by bacteria as part of their metabolism through iron reduction and BSR, while the availability of reduced sulfur in the system, besides pCO_2, controls the formation of siderite.

Later, during Turonian, the Bayangshiree Formation is deposited, made up of silty clays with minor sand input. These features are sedimentologically interpreted as typical of meandric river systems (Figure 191). The Sainshand Formation reaches maximum burial depth (about 500 m). Euhedral dolomite continues to grow by adding syntaxial cement (overgrowth) until the maximum burial depth (maximum temperature 40ºC). Groundwater flow is bringing in the system additional SO_4^{2-} that is used by BSR leading to the next pyrite generations, namely the concentric overgrowth and euhedral pyrite 1 (pre-ore). By the time of these events, calcite is forming on the surface (Bayangshiree Formation).

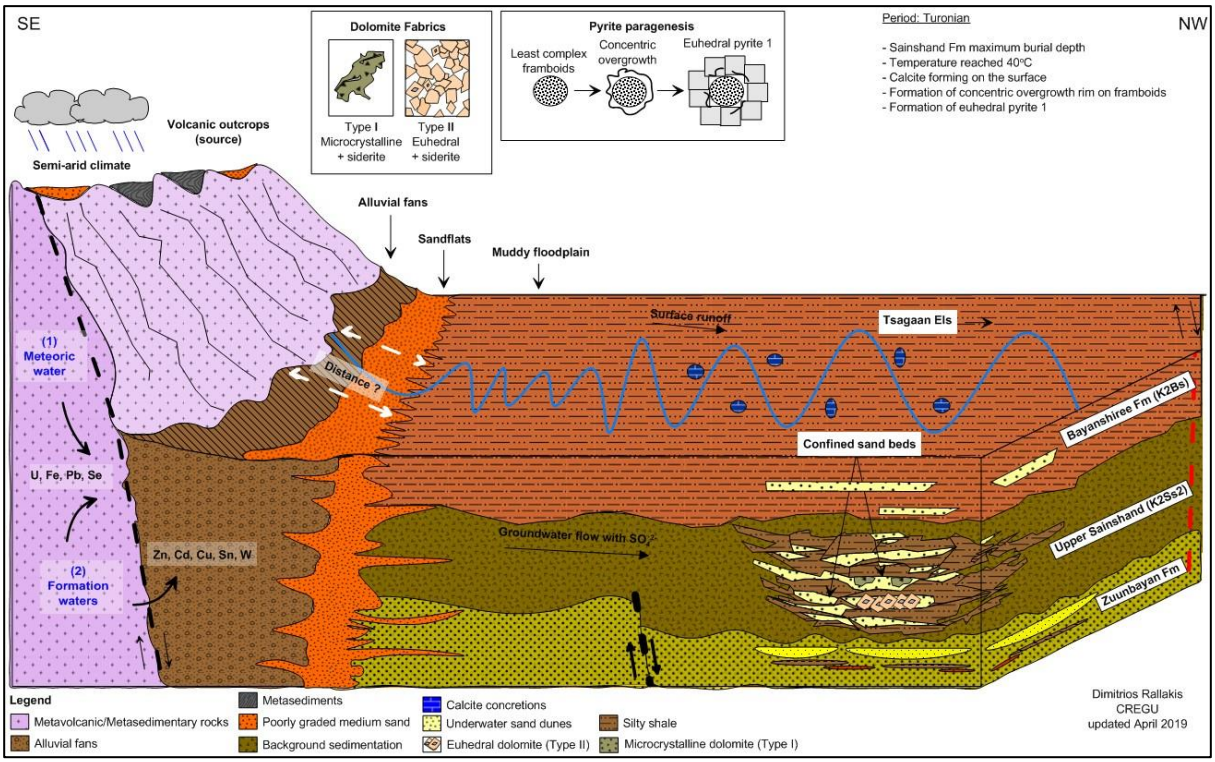

Figure 191: Conceptual model of the Zoovch Ovoo depocenter during Turonian (Bayangshiree Fm), consisting of silty clays and minor sand input. Bayangshiree Fm was dominated by meandric river systems. Calcite was formed on the surface in oppose to the dolomite of Sainshand Fm. Height of the outcrops not in scale.

The rifting phase in East Gobi Basin was ceased at the end of Early Cretaceous (Figure 192). From Cenomanian and on, the sedimentary sequence in Zoovch Ovoo experiences uplift and erosion (estimated at 300 m at maximum), entering the thermal cooling phase. In addition during Tertiary, the Zuunbayan fault system is reactivated with strike-slip movement. These local tectonics could be responsible for opening the system, allowing meteoric waters to percolate through Zuunbayan Formation, carrying $U^{(VI)}$, $Fe^{(III)}$, SO_4^{2-} and bacteria.

Marcasite is formed locally responding to the Eh and pH changes of water. Dolomite types I and II are affected by the oxidizing waters and they are partially dissolved and recrystallized to type III (subhedral). Uranium is adsorbed by organic matter and is also complexed to form uranyl-carboxylates. It is also reduced to $U^{(IV)}$ and forms pitchblende that is associated to

organic matter, pyrite, titanium oxides and silicates. With respect to organic matter, it is the bacteria that are responsible for reducing uranium to form pitchblende. This is envisaged because there is no other mechanism that could explain uranium reduction at 40°C, besides bioreduction. Euhedral pyrite 1 reduces $U^{(VI)}$ as this pyrite generation is founded corroded/replaced by pitchblende. Euhedral pyrite 2 is isochronous to pitchblende formation as it contains UO_2 microspheres and is not affected by the oxidizing waters.

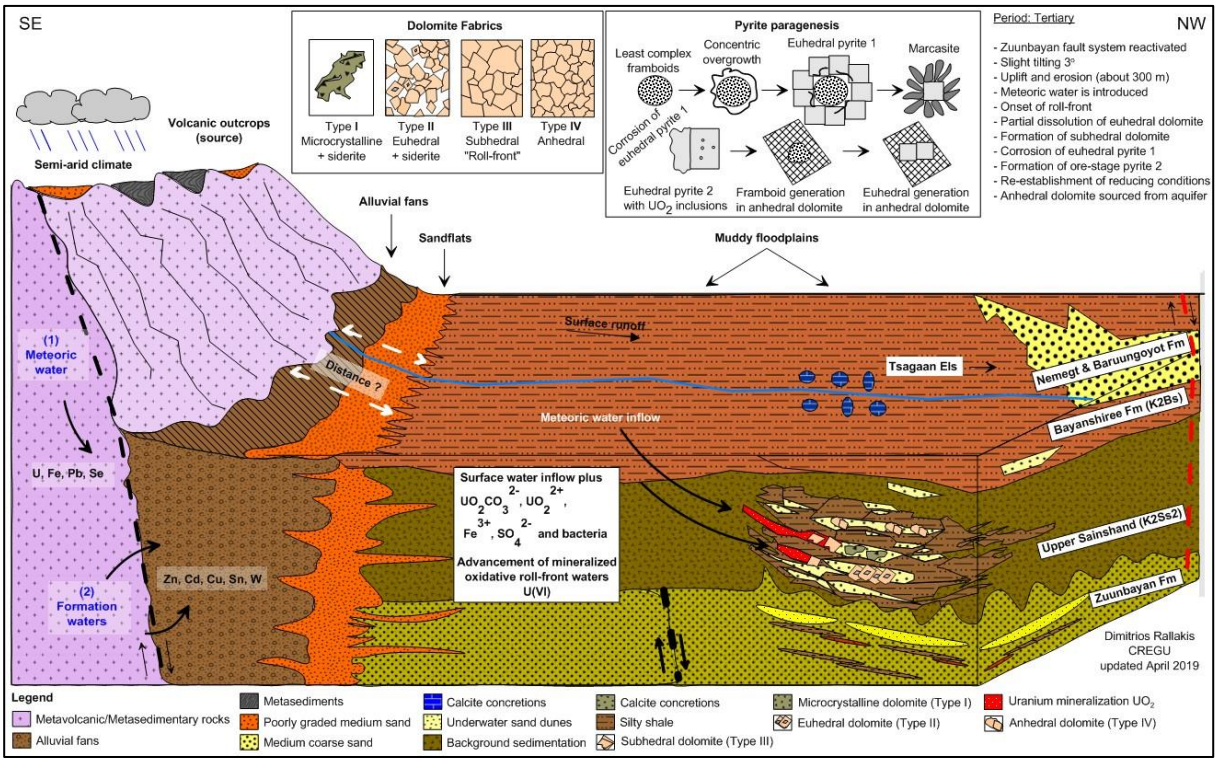

Figure 192: Conceptual model of the Zoovch Ovoo regional area during Tertiary. Cenozoic sediments on the surface are very scarce. Slight tilting of Sainshand Fm due to Cenozoic strike-slip fault activity cause meteoric water rich in U to enter the system. Height of the outcrops not in scale.

With progressive uplift, parts of the roll-front are cut off and reducing conditions are re-established. The aquifer waters that are saturated in respect to dolomite percolate through the uncemented sand layers, particularly through the coarser units, hence the anhedral (type IV) dolomite cement is precipitated. There are two pyrite types (framboidal and euhehdral) that are formed very locally and are associated strictly to the anhedral dolomite. Since their isotopic signature but also their morphology is different than the early framboids these are regarded as a new generation. As the roll-front system is active, diagenetic phases such as uranium minerals and sulfides are dissolved and redistributed further away. The empty space created is uptaken by newly formed mineral phases such as iron hydroxides/oxides, dolomite type III or IV, phospho-coffinite and quartz cement.

7.10 METALLOGENIC MODEL OF THE ZOOVCH OVOO DEPOSIT

There are arguments which may come forward to sustain the role of bacteria in the formation of the Zoovch Ovoo U deposit. Bacteria play the major role on uranium reduction similarly to sulfate and iron reduction and they appear to be present during the whole diagenetic history of the deposit.

Roll-front setting

The Zoovch Ovoo reservoir (Upper Sainshand – K2Ss2 unit) was never subjected to high temperature or deep burial conditions. The maximum temperature reached was 40^{o}C, and the maximum burial depth was 500-600m (Prost, 2004; Graham, 2001). Petrographic analysis did not confirm any hydrothermal minerals or alterations. The organic matter contained in Zoovch Ovoo is immature and according to vitrinite reflectance data it is still in early stage (%R_r<0.4). This has implications for uranium complexation. According to Nakashima (1992) uranyl ions can be complexed very efficiently on peat-stage (low maturity lignite) organic matter particles when in low temperature (<50^{o}C) and that peat itself can concentrate U by a factor of 10.000 from groundwater that contains ppb levels of uranyl ions (Cumberland, 2018 and references therein). On the contrary lignite-stage organic matter is less efficient. This is due to the fact that peat is richer in carboxyl functional groups than lignite. Uranyl-carboxyl complexation may explain the high concentration of U in organic matter without visible mineralogical expression as was discussed in Chapters 7.2.3 and 7.2.4. In complexed form, uranium remains in U(VI) state. Higher temperatures are required to decompose the uranyl-carboxyl complexes (>180 ^{o}C), in particular for the decarboxylation of peat, following the reduction of U(VI) to U(IV) by organic carbon and the precipitation of uraninite (Meunier et al., 1990; Nakashima, 1992). However, as discussed these temperatures are excluded in the case of Zoovch Ovoo.

So the question that comes forward is, if peat can trap very high quantities of uranium but the latter remains in U(VI) state at low temperatures, then what is the mechanism behind uranium reduction on organic matter? Apparently, the only process that could reduce uranium in near-surface temperatures is bioreduction (Lovley et al., 1991). Through a series of enzymatic reactions, it is possible for certain types of bacteria to use multivalent metals as electron acceptors to maintain their metabolism (Rackley, 1972; Huang, 1978). Bacteria would then reduce multivalent metals *e.g.* Fe^{3+} or U^{6+} to form pyrite (marcasite or mackinawite as intermediate phase) and uraninite/coffinite, respectively as observed in Zoovch Ovoo or even non-crystalline U(IV) as described by Bhattacharyya et al. (2017). Organic matter would play a central role in the metallogenic system since it would concentrate uranium by adsorption or complexation, but also be a source of nutrients to sustain bacterial activity responsible for metal reduction.

Fe(III) and sulfate in the oxidizing part of the roll front

Meteoric waters bearing iron, sulfate and uranium percolate downdip through the permeable sandy horizons of the reservoir as illustrated in Figure 193. In the case of Zoovch Ovoo, sulfate could derive from the dissolution of sulfates (gypsum or celestite formed at the surface during evaporation), as was concluded by the strong positive $\delta^{34}S$ isotopic values (Figure 186). Dissolved ferrous iron, Fe(II), derive from the dissolution of micas (Figure 25) and ilmenite (Figure 26) that according to petrography are very abundant in the reservoir formations. Both Fe(II) and sulfates might also derive from the dissolution of updip pre-ore pyrite, a phenomenon eventually enforced by the activity of microorganisms like *Thiobacillus ferooxidans* present in the percolating surface waters (Rackley, 1972).

The iron bearing waters are “deferrized” by both the oxidation of ferrous iron by dissolved oxygen and the activity of *Thiobacillus ferooxidans* (Stumm and Lee, 1961), leading to the precipitation of ferric iron, Fe(III), and the formation of minerals such as hydroxides (goethite/limonite) and oxides (hematite), discussed in Figure 58 and Figure 59. When these waters come in contact with reduced clay layers (initially grey in color), Fe(III) minerals are deposited and the clay layers turn in part red due to oxidation (Figure 21).

Origin of pyrite and its role in the uranium ore formation

The petrographic and geochemical study of pyrite demonstrated that several generations of pyrite are formed at the interface between the oxidized and reduced part of the roll (discussed in Chapter V). This questions the origin of reduced iron and sulfur. As already described above, dissolution of phylosilicates (e.g. biotite) and ilmenite may provide Fe(II). The Fe(II) may eventually arise from the reduction of Fe(III) by bacteria like the genus *Desulfovibrio* (Rackley, 1972)*;* yet Fe(III) is not an easily soluble species (Schwertmann, 1991)*.* The same bacterial strains will be able to reduce sulfates (the dominant sulfur source) into sulfides (Rackley, 1972), producing intermediate valence species of sulfur (such as S_2^-, HS^- , H_2S, S_0; Chapter 7.2.4). Reduced iron would then react with HS^- leading thus to the formation of bacterial derived pyrite (as evidenced by the strong sulfate isotopes fractions described in Chapter 5.5). This process results in pH increase allowing subhedral (type III) dolomite, typical of roll-front activity (Chapter III) to precipitate.

Petrographical data (Chapter VI) show that pyrite is replaced by UO_2. Indeed, (Chapter 7.5.3) pyrite may reduce uranium even at ambient temperature (Wersin et al. 1994; Eglizaud et al., 2006; Du et al., 2011). According to the same authors the interaction between pyrite and U(VI) is a two-step process: first U(VI) is adsorbed on the solid surface of the pyrite crystal and next the redox reaction is initiated. Reduced uranium can be found either sorbed or precipitated as $UO_{2+x(s)}$ ($0<x<2$), according to Eglizaud et al. (2006) and references therein.

The Fe(II) as well as the reduced sulfur are both considered in literature (Wersin, 1994; Eglizaud, 2006; Boyanov, 2007; Hua, 2008; Boonchayaanant et al., 2010; Du et al., 2011) as being able to reduce U(VI). Yet, the exact role of each species is still under debate and may vary accordingly to physical and chemical conditions [e.g. crystalline vs aqueous Fe(II); reduction rate of U(VI) is dependent on acidic pH while adsorption is not].

Late pyrite will continue to precipitate together with UO_2. This ore-stage pyrite contains UO_2 microsize inclusions and is much more resilient in corrosion by the roll-front waters compared to pre-ore stage pyrite (Figure 105). Other sulfides *i.e.* sphalerite that is abundant in Zoovch Ovoo, have similar behavior as late pyrite.

Late processes

During the late stages of the roll-front activity, pitchblende often experiences coffinitization. In addition to coffinitization the phosphorus content of the uranium minerals is also increasing, ultimately leading to phospho-coffinite formation in which P_2O_5 and SiO_2 account for 18% of the total oxide mass of U,P(SiO_4). Phosphorus may also be linked to bacterial activity. Indeed, previous studies (Gächter and Meyer, 1993; Hutchens et al., 2006; Bonnetti et al., 2015) have shown that microorganisms are responsible for the release of P from organic compounds as well as from the dissolution of apatite during BSR, using P for their metabolism. Apatite is an accessory mineral that is very often encountered in Zoovch Ovoo. Thus, based on literature its contribution to the P-pool must not be neglected.

Bacterial communities as control of the chemical trap at Zoovch Ovoo.

From the preceding discussion it appears that bacteria are essential in the control of the redox reaction in the roll-front of Zoovch-Ovoo. They are implied in:

- the direct reduction of U(VI) to U(IV) by dissimilatory bacteria which could use U(VI) as the sole electron acceptor instead of other multivalent metals such as Fe(III). Such mechanism may lead to the formation of uraninite (as described in Chapter VI) or as biogenic non crystalline U(IV)/biofilms (Bhattacharyya et al., 2017).
- the reduction of sulfate into sulfur species (e.g. S^{2-}, HS^-, H_2S, S_0) leading to the formation of amorphous iron sulfides (mackinawite), marcasite and pyrite, the latter being essential as redox trap for U.
- the analysis of gases desorbed from the Zoovch Ovoo rock samples revealed the presence of bacterially derived methane, indicating extant activity of methanogens.
- the formation of CO_2, which is 98% of the gas desorbed from the rock samples. The isotopic composition of the CO_2 observed is evidence of the existence of aerobic bacteria (e.g. sustaining on the acetoclastic biochemistry) which would be active in the oxidizing part of the roll-front.

- The geochemistry of phosphorous available for phospho-coffinite formation.

Easily accessible organic matter with high degradation potential (as for peat) is necessary to sustain bacterial biochemical reactions. The uranium ore deposit at Zoovch Ovoo is primarily controlled by the distribution of the detrital organic matter in the sedimentary system as well as by the permeability network allowing the input of Fe, S, U and micro-organisms. These conditions are actually met by the sandy facies containing detrital organic matter and this would explain why uranium is systematically associated to organic matter particles or to pyrite present in the same facies.

The rather shallow aquifers probably underwent a nearly continuous bacterial activity which is responsible of many chemical features and processes controlling the U and sulfide precipitation. However, main uranium deposition events occur since the beginning of exhumation when enhanced fluid movement sustain roll-front activity. The latter displaces and combines the ingredients of the biochemical trap, allowing progressive enrichment in uranium through time. Based on the current data three main mineralization events took place in Zoovch Ovoo (Figure 189).

Synthetic metallogenic model for Zoovch Ovoo

Considering all the preceding discussion, a metallogenic model for uranium precipitation and associated phases may be proposed (Figure 193). In this model there is no significant uranium preconcentration. Hexavalent uranium is carried in solution by the high Eh meteoric waters and is trapped upon contact with organic matter, organic matter/bacteria association, sulfides (mostly pyrite), dissolved sulfur species, Fe-Ti oxides and clays containing reduced iron and adsorbed native sulfur.

Trapping mechanisms include, complexation (i.e. uranyl-carboxyl complexes), adsorption (i.e. hexavalent uranium adsorbed on the surface of an organic or clay particles), reduction by bacterial activity to uraninite or non-crystalline U(IV) or by pyrite.

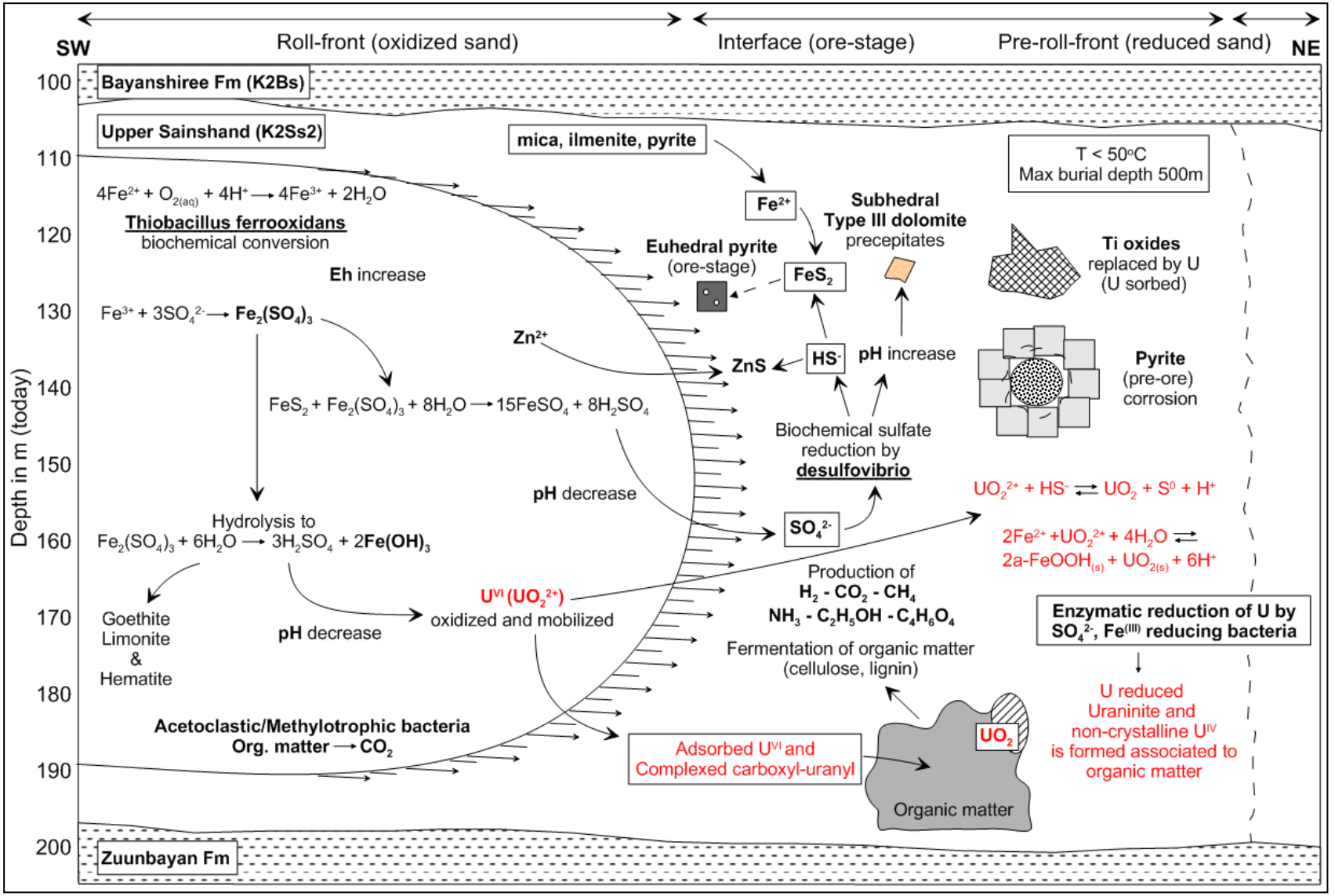

Figure 193: The metallogenic model for uranium formation and associated diagenetic phases in Zoovch Ovoo. The overall thickness of the reservoir is at maximum 100 m. Inspired by Rackley (1972); Eglizaud et al. (2006); Hua et al. (2008).

7.11 COMPARISON OF ZOOVCH OVOO WITH OTHER ROLL-FRONT DEPOSITS FROM KAZAKHSTAN AND CHINA

A summary of the main geological features important for the metallogenic model for each roll-front type uranium deposit of China (Bayinwula, Nuheting, Baxingtu) and Kazakhstan (Chu-Sarysu), contrasted to Zoovch Ovoo (Mongolia), is provided below (Table 13). The roll-fronts of Kazakhstan in the Chu-Sarysu basin are today among the most important uranium producers in the world and they could therefore serve as a good analogue for comparison with the Zoovch Ovoo deposit in East Gobi Basin.

The Chu-Sarysu basin contains four uranium roll-front type deposits, the Inkai, Muyunkum, Karamurun and Zarechnoe. The sedimentary sequence has Late Cretaceous to Paleogene age. The Zuunbayan basin contains the Zoovch Ovoo deposit where the sedimentary sequence has Middle Jurrassic to Tertiary age. In Chu-Sarysu the U-reservoir is separated in three mineralized horizons with ages ranging from Paleocene to Middle Eocene. In Zoovch-Ovoo the mineralization is confined uniformely in a Cenomanian horizon about 100m thick.

In Chu-Sarysu the mineralization event was initiated by tectonic activity associated to orogenesis between Late Pliocene and Quaternary. In Zoovch Ovoo the mineralization event was probably initiated due to tectonic activity during the post-rift basin stage and the development of left lateral strike-slip faults in Cenozoic. In both cases the result was the change of the hydrodynamic regime which allowed oxidizing waters carrying U(VI) to enter the system. Likewise, the maximum burial temperature did not exceed 40-50°C and the burial depth 500-700m in both basins. The uranium mineralization is represented by uraninite, coffinite and phosphor-coffinite in Chu-Sarysu and by uraninite and phospho-coffinite in Zoovch Ovoo.

The detrital organic matter in Chu-Sarysu is common although there are evidences that gases and oil from the Permian petroliferous formations, migrated in the reservoir and acted as the main uranium reducers. Zoovch Ovoo is very different. It contains abundant detrital organic matter where bacteria are responsible for uranium reduction, while there is very little evidence to support the migration of organic fluids from the petroliferous formations tha lie underneath the reservoir zone. With respect to pyrite, there are many similarities in terms of pyrite generations and isotopic values. In Chu-Sarysu the values of $\delta^{34}S$ fluctuate between -66.2 to +36.2 ‰ and in Zoovch Ovoo between -40 to +52 ‰. The high spread clearly indicates BSR.

The reservoirs in both cases are made of sediments that are locally cemented by carbonates. In the case of Chu-Sarysu the major carbonate phase is calcite and is attributed to the lateral movement of the aquifers, which are recharged by meteoric waters, while there are very few traces of dolomite. In the case of Zoovch Ovoo, the only phase is dolomite, which was primarily formed on the surface and was then recrystallized following a diagenetic trend, while there is

clearly absence of calcite. The U-mineralization in Chu-Sarysu is mostly associated to pyrite embedded in calcite cement which poses problems for *in-situ* recovering processes. On the other hand, in Zoovch Ovoo the U-mineralization is not associated to dolomite cemented layers. In some occasions dolomite crystals were found dissolved/recrystallized upon interaction with the roll-front waters.

Table 13: Table comparing Zoovch Ovoo with other roll-front deposits from Central Asia U Province.

Geological Features	**Zoovch Ovoo (Mongolia)**	**Bayinwula (China)** Bonnetti et al., 2015a	**Nuheting (China)** Bonnetti et al., 2015b	**Baxingtu (China)** Bonnetti et al., 2017	**Chu-Sarysu (Kazakhstan)** Munara, 2012
Host Formation/age	Late Cretaceous Sainshand Formation	Early Cretaceous Saihan Formation	Late Cretaceous Erlian Formation	Late Cretaceous Yaojia Formation	Paleogene Karatau Formation
Reservoir Lithology	Lacustrine (underwater) sand dunes	Channel sandstones	O.M rich lacustrine mudstones	Medium to Fine grained channel sandstones	Continental silicoclastic formations
Uranium source	Volcanic tuff on top of reservoir?	Pre-concentration in Fe-Ti oxides and possibly organic matter	Pre-concentration in clay matrix, sulfates,	Pre-concentration in Fe-Ti oxides, organic matter, clays, volcanic tuff	Pre-concentration in organic matter possible
Uranium minerals	Uraninite, Phospho-coffinite	Phospo-coffinite	Uraninite, coffinite	Uraninite, coffinite	Phospho-coffinite, Uraninite
Uranium reducers	Organic matter, pyrite, Fe-Ti oxides, other sulfides	Pyrite and probably organic matter	Pyrite, organic matter, O.M rich mudstones	Sulfides and organic matter	Pyrite, organic matter, fluids
Organic matter kerogen type	Type III and IV, limited II	Type III and IV	Type III and IV, limited II	Type III and IV	Type III (H/C hypothesis)
Pyrite types	Framboids, overgrowth, euhedral, cement in organic matter, in clays, in dolomite and around Fe-Ti oxides	Framboids and cement	Framboids, euhedral, cement	Mainly framboids and then euhedral and cement	Framboids, concentric, euhedral and cement
$\delta^{34}S$ of pyrite	Framboids -40 to +52‰, euhedral and cement from -42 to -22‰	-30.5 to -7.5‰	n/a	-72.0 to -6.2‰	-66.2 to +36.2‰
Role of microbes	BSR, U bioreduction	BSR	BSR	BSR, U bioreduction	BSR

CHAPTER VIII

Conclusions and Perspectives

8.1 CONCLUSIONS

Very high levels of uranium concentration were found in the detrital organic matter of the Cretaceous sands from the Zoovch Ovoo deposit in Mongolia. Such concentrations have never been reported to occur in the other roll-front U deposits from the large uranium province of Central Asia which extends from Kazakhstan to China and Mongolia. This peculiarity asked the question of the role of the organic matter in the uranium deposit.

Petrographic as well as geochemical investigation of the maceral particles allows to propose the following:

- Organic matter present at Zoovch Ovoo is land plant derived and occurs as detrital particles concentrated into clay layers, clay intraclasts or sandy laminae. Biological features of particles are more or less preserved depending on their transportation (proximal or distal origin). Its thermal maturity is very low (peat to lignite stage).
- Maceral particles show high concentration (up to 20 wt%) of U not expressed as oxide (detectable under SEM). It is very likely that $U^{(VI)}$ is adsorbed as uranyl-carboxyl groups. The organic matter particles have therefore captured U from circulating fluids at low temperature (T<40°C). It is not yet clear if the trapping occurred during sedimentation (pre-concentration stage) or during the roll-front events or both.
- The land plant particles concentrated microbiological activity which triggered biodegradation, iron as well bacterial sulfate reduction. The absence of detectable pyrite crystals in the organic matter despite the presence of Fe and S in often non FeS_2 stoichiometric proportions suggests the presence of other forms of sulfur, such as amorphous FeS phase (e.g. mackinawite) and/or elemental sulfur.
- The distribution of UO_2 in the organic particles seems to be linked to porosity/permeability of the organic structure which may be a control of fluid accessibility to the macerals. Organic matter particles can be fully replaced by UO_2 with partial preservation of organic structure (suggesting an epigenesis).
- As burial diagenesis is too low to consider reduction of $U^{(VI)}$ by carbonaceous moieties, it is suggested that microorganisms are mainly responsible for the reduction of $U^{(VI)}$, either directly through their physiological activity or by providing reduced sulfur (which is an efficient reducing agent for $U^{(VI)}$. $Fe^{(II)}$ carboxylates may also be considered as possible reducing agent (Boyanov et al., 2007).

From this study it may therefore be concluded that at least two controls of different scales can be considered for the Zoovch Ovoo uranium deposit:

- At the scale of the sedimentary particles, organic matter plays a capital role on uranium deposition as it acts as a uranium trap through complexation and sustains the $U^{(VI)}$ reduction mechanism into UO_2 through biological activity.
- At the scale of the sedimentary deposit, organic matter distribution as well as the permeability network allowing the circulation of uranium bearing fluids are controlled by the sedimentary architecture.

With respect to the dolomite study the following conclusions could be made:

- The petrographical and geochemical study of cements in the Sainshand Formation of the Zoovch Ovoo area allowed to identify four dolomites types. The three of the four dolomite cement types, namely the type I, II and IV were recognized within all cemented sandstone layers. On the other hand, dissolution features followed by type III dolomite were only recognized as linked to roll-front. As such, it was possible to build a scenario for dolomite evolution with type I probably being formed very early during initial diagenetic conditions, followed by type II linked to burial diagenesis, type III linked to a change in water chemistry composition due to roll-front activity and finally type IV (post-diagenetic) linked to uplift. Considering published basin modelling, as well as vitrinite reflection measurements, it is estimated that the dolomite cement paragenesis does cover a burial history from surface to a maximum depth of 500-600m with a maximum temperature of 40°C.
- By comparing the isotopes from the dolomite in depth with the calcite from the surface it was concluded that they were precipitated from the same oxygen isotopic pool, namely meteoric water. It was also concluded that the aquifer waters from which the calcite and dolomite were formed have probably the same origin, but must have certain differences in chemistry, due to the difference in burial and host formation (Bayanshiree and Sainshand formations). The magnesium needed for high Mg/Ca ratio of saline waters to allow precipitation of exclusively dolomite cements may be sourced from the erosion of the basic volcanic rocks of the regional outcrops.
- Within the unconsolidated sands succession of the Sainshand formation in the Zoovch Ovoo area, the scarce occurrence of carbonate cemented facies provided a unique opportunity to reconstruct a relative chronological succession from early to burial diagenesis conditions. They are also among the rare indicators available to documents fluid-rock interactions as most detrital mineral have remained unchanged since sedimentation.

There are many similarities between the Zoovch Ovoo deposit and regional deposits from the Central Asia Uraniferous Province (Table 13):

- Firstly, all deposits contain the same type of U-mineralization, uraninite/pitchblende and coffinite to phospho-coffinite.
- Secondly, all deposits are dominated by detrital organic matter of type III and IV kerogen, while there is always absence of evidence that could justify hydrocarbons contributing to the formation of the uranium deposits.
- Pyrite is always formed after BSR and in particular, the same petrographic type of pyrites are identified, framboids, concentric overgrowth, euhedral.
- The role of bacteria in the formation of the deposit is considered in at least one more case other than Zoovch Ovoo.

The main differences between the compared cases is in the uranium preconcentration hypothesis. In every deposit there are different candidates i.e. Fe-Ti oxides, organic matter, clay matrix, sulfates and volcanic tuff, which could indicate totally different uranium sources.

8.2 PERSPECTIVES

The analytical work and the interpretations that were made have advanced the knowledge for the Zoovch Ovoo metallogenic system. However, new questions arose and further study is now required.

- Due to the limited number of the uraniferous samples studied, the paragenesis of uranium minerals may be incomplete. It is proposed that more relevant work is done to validate the current results.
- The origin of U is to date ambiguous. It is not clear if the U source is autocthonous i.e. from the volcanic ash on top of the reservoir or from the granitic-metamorphic-volcanic outcrops of the region. In addition the timing of U trapping is unknown, consequently there is no evidence to conclude if there was uranium pre-concentration in the organic matter or not.
- The role of microorganisms in the formation of the deposit is undisputed. A microbiological study could identify the bacteria species as well as the types of the biological functions that acted.
- The knowledge of the local tectonic system is limited. The reason that the roll-front activity commences in relation to tectonics is not clear. It is also not clear if the shifts in the tectonic setting played a role in changing the hydrogeological setting and in flushing in oxidizing waters.
- Also, this study was concluded without Transmission Electron Microscopy (TEM) observations and Extended X-ray Absorption Fine Structure (EXAFS) measurements. Both techniques are necessary in order to understand the status of uranium in relation to organic matter, i.e. adsorbed, complexed or reduced.

REFERENCES

AKHTAR, S., YANG, X., PIRAJNO, F. (2017). Sandstone type uranium deposits in the Ordos Basin, Northwest China: A case study and an overview. Journal of Asian Earth Sciences 146, 367-382.

ALFIMOVA, N.A., FELITSYN, S.B. and MATRENICHEV, V.A. (2011). Mobility of Cerium in the 2.8-2.1 Ga Exogenous Environments of the Baltic Shield: Data on Weathering Profiles and Sedimentary Carbonates. Lithology and Mineral Resources, 2011, Vol. 46, No. 5, pp. 397-408.

ANDERS, E., GREVESSE, N. (1989). Abundances of the elements – Meteoritic and solar. Geochimica et Cosmochimica Acta, vol. 53, pp. 197-214.

ANTHONY, J.W., BIDEAUX, R.A., BLADH, K.W. NICHOLS, M.C. (2003). Eds., Handbook of Mineralogy, Mineralogical Society of America, Chantilly, VA 20151-1110, USA. http://www.handbookofmineralogy.org/.

AUBAKIROV, KH. B. (1998). On the deep origin of ore-forming solutions in the uranium deposits in platform sequence of depressions (with Chu-Sarysu Province as an example). Geology of Kazakhstan 2(354), pp. 40-47.

BARBIER, M., LEPRETRE, R., CALLOT, P.J., GASPARRINI, M., DANIEL, J.M., HAMON, Y., LACOMBE, O. and FLOQUET, M. (2012). Impact of fracture stratigraphy on the paleo-hydrogeology of the Madison Limestone in two basement-involved folds in the Bighorn basin. (Wyoming, USA). Tectonophysics 576-577, pp. 116-132.

BARKER, C.E. and PAWLEWICZ, M.J. (1994). Calculation of Vitrinite Reflectance from Thermal Histories and Peak Temperatures. A comparison of Methods. pp. 216-229. In: MUKHOPADHYAY, P.K. and WALLACE, G.D. (1994). Vitrinite Reflectance as a Maturity Parameter. Applications and Limitations. ACS Symposium Series, 570, 294 p.

BAU, M. and MÖLLER, P. (1992). Rare earth element fractionation in metamorphogenic hydrothermal calcite, magnesite and siderite. Mineralogy and Petrology, 45(3), pp. 231-246.

BERNARD, B.B., BROOKS, J.M., SACKETT, W.M., (1978). Light hydrocarbons in recent Texas continental shelf and slope sediments. Journal of Geophysical Research, 83, 4053–4061.

BERNER, R.A. (1969). The synthesis of framboidal pyrite. Economic Geology, 64, pp. 383-384.

BERNER, R.A. (1978). Sulfate reduction and the rate of deposition of marine sediments. Earth and Planetary Science Letters, 37, pp. 492-498.

BERNER, R.A. (1984). Sedimentary pyrite formation and update*. Geochimica et Cosmochimica Acta, 48, pp. 605-615.

BERTOLIN, A., FRIZZO, P., RAMPAZZO, G. (1995). Sulphide speciation in surface sediments of the Lagoon of Venice: a geochemical and mineralogical study. Marine Geology, 123, pp. 73– 86.

BHATTACHARYYA, A., CAMPBELL, K.M., KELLY, S.D., ROEBBERT, Y., WEYER, S., BERNIER-LATMANI, R., BORCH, T. (2017). Biogenic non-crystalline U(IV) revealed as major component in uranium ore deposits. Nature communications, 8, doi.10.1038/ncomms15538

BONE, E.S., DYNES, J.J., CLIFF, J., BARGAR, J. (2017). Uranium (IV) adsorption by natural organic matter in anoxic sediments. Proceedings of the National Academy of Sciences of the United States of America, pp. 711-716.

BONNETI, C., CUNEY, M., MALARTRE, F., MICHELS, R., BOURLANGE, S., LIU, X., PENG, Y., YANG, J. (2013) The Bayinwula Roll Front-Type Uranium Deposit, Erlian Basin, NE. China. Conference paper, 12th SGA biennial meeting - Mineral deposit research for a high-tech world, August 2013.

BONNETTI, C., CUNEY, M., MALARTRE, F., MICHELS, R., LIU, X., PENG, Y. (2015a). The Nuheting Deposit, Erlian Basin, China: Synsedimentary vs Diagenetic Uranium Mineralization. Ore Geology Reviews, 69, pp. 118–139. doi.org/10.1016/j.oregeorev.2015.02.010

BONNETTI, C., CUNEY, M., MICHELS, R., TRUCHE, L., MALARTRE, F., LIU, X., YANG, J. (2015b). The Multiple Roles of Sulfate-Reducing Bacteria and Fe-Ti Oxides in the Genesis of the Bayinwula Roll Front-Type Uranium Deposit, Erlian Basin, NE China. Economic Geology, V. 110, pp. 1059-1081.

BONNETTI, C., LIU, X., ZHAOBIN, Y., CUNEY, M., MICHELS, R., MALARTRE, F., MERCADIER, J., CAI, J. (2017). Coupled uranium mineralization and bacterial sulphate reduction for the genesis of the Baxingtu sandstone-hosted U deposit, SW Songliao Basin, NE China. Ore Geology Reviews, 82, pp. 108-129.

BORREGO, A.G., COOK, A. (2017). Humic Macerals: Vitrinite/Inertinite, Chapter 9, In: 10th ICCP Training Course on Dispersed Organic Matter. Integrating transmitted and reflected light microscopy, GFZ, Potsdam, Germany, 276 p.

BOULÈGUE, J. (1981). Simultaneous Determination of Sulfide, Polysulfides and Thiosulfat as an Aid to Ore Exploration. Developments in Economic Geology, 15, pp. 21-36. doi.org/10.1016/0375-6742(81)90053-4

BRYAN, N.D., ABRAHAMSEN, L., EVANS, N., WARWICK, P., BUCKAU, G., WENG, L., VAN RIEMSDIJK W.H. (2012). The effects of humic substances on the transport of radionuclides: recent improvements in the prediction of behaviour and the understanding of mechanisms, Applied Geochemistry, 27 (2), pp. 378-389.

BROUAND, M. (2014). – Compte-rendu de mission. Pétrographie – Secteur de Zoovch Ovoo. 12-27 avril 2014. Mongolie. CR AREVA-Mines DGS Nº AMS-DGS-TEC-PM-CRM-0004. 21 pp.

BROUAND, M. (2015). Caractérisations minéralogiques et géochimiques des faciès et minéralisations uranifères de Zoovch Ovoo (Mongolie). Janvier 2015. Rapport technique AMS-DGS-TEC-PM-RT-0018. 71 pp.

BRUMSACK H.J. (2006). The trace metal content of recent organic carbon-rich sediments: Implications for Cretaceous black shale formation. Palaeogeogr. Palaeoclimatol. Palaeoecol. 232, 344-361.

BLAMEY, N.J. F., AZMY, K., BRAND, U. (2014). Provenance and burial history of cement in sandstones of the Northbrook Formation (Carboniferous), western Newfoundland, Canada: A geochemical investigation. Sedimentary Geology, 299. (2014), 30-41.

BLEVIN P.L., CHAPPELL B.W. AND ALLEN C.M. (1996). Intrusive metallogenic provinces in eastern Australia based on granite source and composition. Trans. R. Soc. Edinb. Earth Sci. 87, 281-290.

BOONCHAYAANANT, B., GU, B., ORTIZ, M.E., CRIDDLE, C.S. (2010). Can microbially-generated hydrogen sulfide account for the rates of U(VI) reduction by a sulfate-reducing bacterium?. Biodegradation, 21, pp.81-95.

BOYANOV, M.I., O'LOUGHLIN, E.J., RODEN, E.E., FEIN, J.B., KEMNER, K.M. (2007). Adsorption of Fe(II) and U(VI) to carboxyl-functionalized microspheres: The influence of speciation on uranyl reduction studied by titration and XAFS. Geochimica et Cosmochimica Acta, 71, pp. 1898–1912.

BURA-NAKIC, E., VIOLLIER, E., JÉZÉQUEL, D., THIAM A., CIGLENECKI, I. (2009). Reduced sulfur and iron species in anoxic water column of meromictic crater Lake Pavin (Massif Central, France). Chemical Geology, 266, pp. 311-317.

BURGESS, C.E., SCHOBERT, H.H. (1998). Relationship of coal characteristics determined by pyrolysis /gas chromatography/mass spectrometry and nuclear magnetic resonance to liquefaction reactivity and product composition. Energy and Fuels, 12, pp. 1212-1222.

BURROWS, J.E., PETERS, S.C., CRAVOTTA, C.A. (2015). Temporal geochemical variations in above- and below-drainage coal mine discharge. Applied Geochemistry, vol. 62, pp. 84-95.

BURTON, E.D., BUSH, R.T., SULLIVAN, L.A. (2006). Sedimentary iron geochemistry in acidic waterways associated with coastal lowland acid sulfate soils, Geochimica et Cosmochimica Acta, vol. 70, 22, pp. 5455-5468.

CAI, C.F., LI, H.T., QIN M.K., LUO, X.R., WANG, F.Y., OU, G.X. (2007). Biogenic and petroleum-related ore-forming processes in Dongsheng uranium deposit, NW China. Ore Geology Reviews 32, 262-274.

CAO, B.F., BAI, G.P., ZHANG, K.X., HE, B. (2016). A comprehensive review of hydrocarbons and genetic model of sandstone-hosted Dongsheng uranium deposit, Ordos Basin, China. Geofluids, 16, pp. 624-650.

CARDON, O., LE GOUX, F., SALABERT, J. (2015). Prospection d'uranium en Mongolie: découverte majeure dans le désert de Gobi [Uranium exploration in Mongolia: important discovery in the Gobi Desert]. Revue Générale Nucléaire, vol. 47, pp. 12-19.

CASADO, A.I., ALONSO-ZARZA, A.M., LA IGLESIA, Á. (2014). Morphology and origin of dolomite in paleosols and lacustrine sequences. Examples from the Miocene of the Madrid Basin. Sedimentary Geology, vol. 312, pages 50-62, ISSN 0037-0738.

CHEN, H.B., XU, G.Z., WANG, J.P., LI, W.H., ZHAO, X.G. (2006). Mineralization characteristics of Diantou uranium deposit in the southern margin of Ordos and in comparison with Dongsheng uranium deposit. Acta Geologica Sinica 80, 724-732 (in Chinese with English abstract).

CHALLINOR, J.M. (1995). Characterization of wood by pyrolysis derivatization-gas chromatography/mass spectrometry. Journal of Analytical and Applied Pyrolysis, 35, 93–107.

CHEN, R.Y., LUO, X.R., CHEN, Z.K., YU, J., YANG, Y. (2006). Restoration of burial history of four periods in Ordos Basin. Acta Petrolei Sinica 27, 43-47 (in Chinese with English abstract).

CHEN, J., ZHAO, P., WANG, C., HUANG, Y., CAO, K. (2012). Modelling East Asian climate and impacts of atmospheric CO_2 concentration during the Late Cretaceous (66 Ma). Paleogeography, Paleoclimatology, Palaeoecology, vol. 385, 190-201.

CLARK, C., GRGURIC B., SCHMIDT, M.A. (2004). Genetic implications of pyrite chemistry from the Palaeoproterozoic Olary Domain and overlying Neoproterozoic Adelaidean sequences, northeastern South Australia. Ore Geology Reviews, 25, pp. 237-257.

COLEMAN, M.L., HEDRICK, D.B., LOVLEY, D.R., WHITE, D.C. and PYE, K. (1993). Reduction of Fe(III) in sediments by sulphate-reducing bacteria. Letters to Nature, vol. 361, pp. 436-438.

COLOMBO, U., SIRONI, G., DENTI, E. (1964). A geochemical investigation upon the effects of ionizing radiation on hydrocarbons. Journal of the Institute of Petroleum, 50, pp. 125-132.

COJAN, I. (2010). Les évènements globaux au travers des plaines d'inondation ou le fil d'ariane des systèmes fluviatiles. Géologie appliquée. Université Pierre et Marie Curie-Paris VI.

CUMBERLAND, S.A., ETSCHMANN, B., BRUGGER, J., DOUGLAS, G., EVANS, K., FISCHER, L., KAPPEN, P., MOREAU, J.W. (2018). Characterization of uranium redox state in organic-rich Eocene sediments. Chemosphere, 194, pp. 602-613.

CUNEY, M. and KYSER, K. (2009). Recent and not-so-recent developments in uranium deposits and implications for exploration, MAC Short Course Series, Vol 39, 271 pp.

DAHLKAMP, F.J. (1993). Uranium Ore Deposits, Berlin Heidelberg: Springer-Verlag, 460 pp.

DAHLKAMP, F.J. (2009). Uranium Deposits of the World: Asia, Berlin Heidelberg: Springer-Verlag, 493 pp.

DAVISON, W., BUFFLE, J., DEVITRE, R. (1998). Voltammetric characterization of a dissolved iron sulfide species by laboratory and field studies. Analytical Chimica Acta, 377, pp. 193-203.

DAWSON, G.K.W., GOLDING, S.D., BOREHAM, C.J. and MERNAGH, T. (2013). Authigenic carbonates as natural analogues of mineralisation trapping in CO2 sequestration. Cooperative Research Centre for Greenhouse Gas Technologies, Canberra, Australia, CO2CRC Publication Number RPT13-4602. 75pp.

DESCOSTES, M., SCHLEGEL, M.L., EGLIZAUD, N., DESCAMPS, F., MISERQUE, F., SIMONI, E. (2010). Uptake of uranium and trace elements in pyrite (FeS_2) suspensions. Geochimica et Cosmochimica Acta, 74, pp. 1551-1562.

DETMERS J., BRÜCHERT V., HABICHT K. S., KUEVER J. (2001). Diversity of sulfur isotope fractionations by sulfate-reducing prokaryotes. Applied Environmental Microbiology, 67, pp. 888-894.

DÍAZ-HERNÁNDEZ., J.L., SÁNCHEZ-NAVAS, A., REYES, E. (2013). Isotopic evidence for dolomite formation in soils. Chemical Geology, vol. 347, pp. 20-33.

DIESSEL, C.F.K. (1992). Coal-bearing Depositional Systems. Springer-Verlag, Berlin. 721 pp.

DILL, H., KERNER, E. (1990). Crystallographic and chemical variations during pyritization in the upper Barremian and lower Aptian dark claystones from the Lower Saxonian Basin (NW Germany). Sedimentology, 37, pp. 427-443.

DOTT, R. H. JR. (1964). Wacke, greywacke and matrix-What approach to immature sandstone classification?. Journal of Sedimentary Petrology, vol. 34, No. 3. pp. 625-632.

DOUGLAS, G.B., BUTT, C.R.M., GRAY, D.J. (2011). Geology, geochemistry and mineralogy of the lignite-hosted Ambassador palaeochannel uranium and multi-element deposit, Gunbarrel Basin, Western Australia. Mineralium Deposita, 46, pp. 761-787.

DU, X., BOONCHAYAANANT, B., WEI-MIN, W., FENDORF, S., BARGAR, J., CRIDDLE, C.S. (2011). Reduction of Uranium(VI) by Soluble Iron(II) Conforms with Thermodynamic Predictions. Environmental Science & Technology, American Chemical Society, 45, pp. 4718-4725.

EGLIZAUD, N., MISERQUE, F., SIMONI, E., SCHLEGEL, M.L., DESCOSTES, M. (2006). Uranium (VI) interaction with pyrite (FeS_2): chemical and spectroscopic studies. Migration 2005, Avignon, France, pp. 651-656. DOI : 10.1524/ract.2006.94.9-11.651

ENGLAND, B.M., OSTWALD, J. (1993). Framboid-derived structures in some Tasman fold belt base metal sulphide deposits, New-South-Wales, Australia, Ore Geology Reviews 7, pp. 381-412.

ESPITALIE, J., DEROO, G., MARQUIS, F. (1985). Rock-eval pyrolysis and its applications. Oil Gas Sci. Technol. -Rev IFP 40–6, 755–784.

FABER, E., STAHL, W. (1984). Geochemical surface exploration for hydrocarbon in North Sea. AAPG, 68, pp. 363-386.

FRIEDMAN, I. and O'NEIL, J.R. (1977). Compilation of stable isotope fraction factors of geochemical interest. In: FLEISCHER, M. (Ed), Data of Geochemistry, sixth edition, pp. 440-1212 United States Geological Survey Professional Paper.

FORBES, P., LANDAIS, P., BERTRAND, P., BROSSE, E., ESPITALIÉ, J., YAHAYA, M. (1988). Chemical transformations of type-III organic matter associated with the Akouta uranium deposit (Niger): Geological implications. Chemical Geology, 71, pp. 267-282.

FOWLER, A.D., DOIG, R. (1982). The significance of europium anomalies in the REE spectra of granites and pegmatites, Mont Laurier, Quebec. Geochimica et Cosmochimica Acta, 47, pp. 1131-1137.

FISCHER, R.P., STEWART, J.H. (1961). Copper, vanadium and uranium deposits in sandstone. Their distribution and geochemical cycles. Economic Geology, 56, pp. 509-520.

FRAZIER, S.W., NOWACK, K.O., GOINS, K.M., CANNON, F.S., KAPLAN, L.A., HATCHER, P.G. (2003). Characterization of organic matter from natural waters using tetramethylammonium hydroxide thermochemolysis GC-MS. Journal of Analytical and Applied Pyrolysis, 70, 99–128.

GÄCHTER, R., MEYER, J.S. (1993). The role of microorganisms in mobilization and fixation of phosphorus in sediments. Hydrobiologia, 253, pp. 103-121.

GADD, G.M. (1996). Influence of microorganisms on the environmental fate of radionuclides. Endeavour, 20, pp. 150-156.

GAUDARE, L. (2014). Etude pétrographique par comptage de points des séries de lames minces 9659A, 9659B et 9659C (Zoovch Ovoo, Mongolie). 28 Août 2014. Rapport technique AMS-DGS-TEC-PM-RSTG-0001. 64 pp.

GOLDSCHMIDT V. M. (1954). Geochemistry. The Clarendon Press, Oxford, p. 730.

GRANGER, H.C.; WARREN, C.G. (1969). Unstable sulfur compounds and the origin of roll-front type uranium deposits. Economic Geology, 64 (2), pp. 160-171.

GRAHAM, S.A., HENDRIX, M.S. JOHNSON, C.L., BADAMGARAV, D., BADARCH G., AMORY, J., PORTER, M., BARSBOLD, R., WEBB, L.E., and HACKER B.R. (2001). Sedimentary record and tectonic implications of Mesozoic rifting in southeast Mongolia. Geological Society of America Bulletin, vol. 113, pp. 1560–1579.

GREENWOOD, P.F., SHAN, C., HOLMAN, A.I., GRICE, K. (2018). The composition and radiolysis impact on aromatic hydrocarbons in sedimentary organic matter from the Mulga Rock (Australia) uranium deposit. Organic Geochemistry, 123, pp. 103-112.

GRIZARD, P. (2017a). AREVA, Personal communication, Map of localities of calcite samples in Zuunbayan sub-basin.

GRIZARD, P. (2017b). Fonctionnement hydrogéologique et hydrochimique du bassin crétacé de Tsagaan Els (Dornogobi, Mongolie). Thèse de doctorat, PSL Research University, Paris, 371 pp.

GRUNER, J.W., GARDINER, L., SMITH, D.K (1953). Studies relating to the origin and distribution of uranium deposits on the Colorado Plateau. Annual Report for July 1, 1952 to March 31. Division of Raw Materials, Washington 25, D.C., 58 p.

HAN, X.Z., ZHANG, Z.L., YAO, C.L., LI, X.D., LI, S.X., MIAO, A.S., YANG, J.X., (2008). Discussion on metallogenic model for sandstone-hosted uranium deposits in northeastern Ordos Basin. Mineral Deposits 27, 415-422 (in Chinese with English abstract).

HALLBAUER, D.K. (1986). The mineralogy and geochemistry of Witwatersrand pyrite, gold, uranium and carbonaceous matter. In: Anhaeusser, C.R., Maske, S. (Eds.), Mineral Deposits of Southern Africa. Geological Society of South Africa, pp. 731-752.

HARSHMAN, E.N. (1972). Geology and uranium deposits, Shirley Basin area, Wyoming. Report. USGS Numbered Series, 745, 82 p. DOI: 10.3133/pp745

HATCHER, P.G., CLIFFORD, D.J. (1994). Flash pyrolysis and in situ methylation of humic acids from soils. Organic Geochemistry, 21, 1081–1092

HEIJMAN, C.G., HOLLIGER, C., GLAUS, M.A., SCHWARZENBACH, R.P., ZEYER, J. (1993). Abiotic Reduction of 4-Chloronitrobenzene to 4-Chloroaniline in a Dissimilatory Iron-Reducing Enrichment Culture. American Society for Microbiology, vol. 59, no. 12, pp. 4350-4353.

HEIJMAN, C.G., GRIEDER, E., HOLLIGER, C., SCHWARZENBACH, R.P. (1995). Reduction of Nitroaromatic Compounds Coupled to Microbial Iron Reduction in Laboratory Aquifer Columns. Environ. Sci. Technol., 29, pp. 775-783.

HEUMANN, J.M., JOHNSON, L.C., WEBB, L.E., TAYLOR, P.J., JALBAA, U., MINJIN, C. (2014). Total and left–lateral displacement across the East Gobi Fault Zone, southern Mongolia: Implications for timing and modes of polyphase intracontinental deformation. Earth and Planetary Science Letter (392), pp. 1-15.

HOEFS, J. (2009). Stable Isotope Geochemistry, 6th ed. Springer-Verlag, Heidelberg, Berlin, New York, 285 p.

HOUGH, G., SWAPP, S., FROST, C., FAYEK, M. (2019). Sulfur Isotopes in Biogenically and Abiogenically Derived Uranium Roll-Front Deposits. Economic Geology, v. 114, no. 2, pp. 353-373.

HUA, B., DENG, B. (2008). Reductive immobilization of uranium (VI) by amorphous iron sulfide. Environmental Science & Technology, 42, pp. 8703-8708.

HUANG, W.H. (1978). Geochemical and Sedimentologic Problems of Uranium Deposits of Texas Gulf Coastal Plain. vol. 62, 6, pp. 1049-1062.

HUANG, XIAN-FANG., LIU, DE-CHANG., DU, LE-TIAN., ZHAO, YING-JUN. (2005). A new sandstone type uranium metallogenetic type—'structure—oil, gas type'. In: JINGWEN, M., BIERLEIN, F.P. (eds), Mineral Deposit Research: Meeting the Global Challenge. Proceedings of the Eighth Biennial SGA meeting, Beijing, China, August 2005, 265–268.

HUMPHREY, J.D. (2000). New Geochemical Mixing-Zone Dolomitization at Golden Grove, Barbados. Journal of Sedimentary Research, vol. 70, No. 5, pp. 1160-1170.

HUNKEN, N. M., BJØRLYKKE, K. & NIELSEN, J. K. (2010). Carbonate Sediments, Chapter 5, pp. 141-200. In: BJØRLYKKE, K. (2010). Petroleum Geoscience: From sedimentary environments to Rock Physics, DOI 10,1007/978-3-642-02332-3_5, Springer-Verlag Berlin Heidelberg, 508 p.

HUTCHENS, E., VALSAMI-JONES, E., HAROUIYA, N., CHAÏRAT, C., OELKERS, E.H., McELDONEY, S. (2006). An Experimental Investigation of the Effect of Bacillus megaterium on Apatite Dissolution, Geomicrobiology, 23(3), pp. 177-182.

IDIZ, E.F., CARLISLE, D., KAPLAN, I.R. (1986). Interaction between organic matter and trace metals in a uranium rich bog, Kern County, California, U.S.A, Applied Geochemistry, 1, 573-590.

INGHAM, E.S., COOK, N.J., CLIFF, J., CIOBANU, C.L., HUDDLESTON, A. (2014). A combined chemical, isotopic and microstructural study of pyrite from roll-front uranium deposits, Lake Eyre Basin, South Australia. Geochimica et Cosmochimica Acta, 125, pp. 440-465.

INTERNATIONAL ATOMIC ENERGY AGENCY (IAEA) and NUCLEAR ENERGY AGENCY (NEA). (2018). Uranium 2018: Resources, production and Demand, NEA No. 7413, © OECD 2018, pp. 462.

INTERNATIONAL COMMITTEE FOR COAL PETROLOGY (ICCP), 1963. International Handbook of Coal Petrography, 2nd Edition. CNRS. Academy of Sciences of the USSR, Paris, Moscow.

INTERNATIONAL COMMITTEE FOR COAL PETROLOGY, (ICCP), 1971. International Handbook of Coal Petrography, 1st Supplement to 2nd Edition. CNRS, Paris.

INTERNATIONAL COMMITTEE FOR COAL PETROLOGY, (ICCP), 1975. International Handbook of Coal Petrography, 2nd Supplement to 2nd Edition. CNRS, Paris.

INTERNATIONAL COMMITTEE FOR COAL PETROLOGY (ICCP), 1993. International Handbook of Coal Petrography, 3st Supplement to 2nd Edition. University of Newcastle U, Tyne (England).

INTERNATIONAL COMMITTEE FOR COAL AND ORGANIC PETROLOGY, (ICCP), 1998. The new vitrinite classification (ICCP System 1994). Fuel 77, 349–358.

INTERNATIONAL COMMITTEE FOR COAL AND ORGANIC PETROLOGY, (ICCP), 2001. The new inertinite classification (ICCP System 1994). Fuel 80, 459–471.

ITTERBEECK, J.V., HORNE, D.J., BULTYNCK, P., VANDENBERGHE, N. (2005). Stratigraphy and palaeoenvironment of the dinosaur-bearing Upper Cretaceous Iren Dabasu Formation, Inner Mongolia, People's Republic of China, Cretaceous Research, Volume 26, Issue 4, August 2005, Pages 699-725.

JARAULA, C.M.B., SCHWARK, L., MOREAU, X., PICKEL, W., BAGAS, L., GRICE, K. (2015). Radiolytic alteration of biopolymers in the Mulga Rock (Australia) uranium deposit. Applied Geochemistry, 52, pp. 97-108.

JAIRETH, S., McKAY, A., LAMBERT, I. (2008). Association of large sandstone uranium deposits with hydrocarbons. Australian Government, Geoscience Australia, 89, 6 p.

JARVIE, D.M., CLAXTON, B.L., HENK, F., AND BREYER, J.T. (2001). Oil and Shale Gas from the Barnett Shale, Ft. Worth Basin, Texas, AAPG National Convention, June 3-6, 2001, Denver, CO, AAPG Bull. Vol. 85, No. 13 (Supplement), 100 p.

JARVIE, D.M. (2018). Correlation of Tmax and measured vitrinite reflectance. TCU Energy Institute. Available online: http://www.wildcattechnologies.com/application/files/9915/1689/1979/Dan_Jarvie_Correlation_of_Tmax_and_measured_vitrinite_reflectance.pdf

JEANNEAU, L., DENIS, M., PIERSON-WICKKMANN, A.C., GRUAU, G., LAMBERT, T., PETITJEAN, P. (2014). Sources and transfer mechanisms of dissolved organic matter during storm and inter-storm conditions in a lowland headcatchment: constraints from high-frequency molecular data. Biogeosciences Discussions 12, 3349– 3379.

JIANG, W.-T., HORNG, C.-S., ROBERTS, A.P., PEACOR, D.R. (2001). Contradictory magnetic polarities in sediments and variable timing of neoformation of authigenic greigite. Earth and Planetary Science Letters, 193, pp. 1-12.

JIAO, Y.Q., WU, L.Q., RONG, H., PENG, Y.B., MIAO, A.S., WANG, X.M. (2016). The relationship between Jurassic coal measures and sandstone-type uranium deposits in the northeastern Ordos Basin, China. Acta Geologica Sinica 90, 2117-2132.

JIAO, Y.Q., WU, L.Q., RONG, H., ZHANG, F., YUE, L., TAO, Z.P., SUN, Y.H. (2018). Geological modeling of uranium reservoir: The geological foundation of revealing the metallogenic mechanism and solving “Remaining Uranium”. Earth Science 43, 3568-3583 (in Chinese with English abstract).

JONES, G.E., STARKEY, R.L. (1962). Some necessary conditions for fractionation of stable isotopes of sulfur by *Desulfovibrio desulfuricans*, in Biogeochemistry of sulfur isotopes. Symposium: Yale Univ., Dept. Geology, pp. 61-79.

JOHNSON, C.L. (2004). Polyphase evolution of the East Gobi basin: sedimentary and structural records of Mesozoic-Cenozoic intraplate deformation in Mongolia. Basin Research (16), 79-99.

JOHNSON, C.L. and RITTS, B.D. (2012). Plate interior poly-phase basins. In: BUSBY, C. and AZOR PEREZ, A. (2012). Tectonics of Sedimentary Basins: Recent Advances. Wiley, Hoboken, ISBN: 9781444347135, pp. 567-582.

KEARSEY, T., TWITCHETT, R. J. AND NEWELL, A. J. (2012). The origin and significance of pedogenic dolomite from the Upper Permian of the South Urals of Russia. Geological Magazine, 149 (2), pp. 291-307.

KENDALL, C. and McDONNELL, J.J. (1998). Isotope Tracers in Catchment Hydrology, Elsevier Science B.V., Amsterdam. pp. 51-86.

KITAYAMA, Y., THOMASOT, E., O'NEIL, J., WING, B. (2012). Sulfur-and oxygen-isotopes, constraints on the sedimentary history of apparent conglomerates from the Nuvvuaggittuq Greenstone Belt (Nuvanik, Quebec). Earth and Planetary Science Letters, 355, pp.271-282.

KOCHENOV, A.V., KOROLEV, K.G., DUBINCHUK, V.T., MEDVEDEV, Y.L. (1977). Experimental data on precipitation of uranium aqueous solution. Geochemistry International, 14, pp. 82-87.

KOHN, M.J., RICIPUTI, L.R., STAKES, D., ORANGE, D.L. (1998). Sulfur isotope variability in biogenic pyrite: Reflections of heterogeneous bacterial colonization?. American Mineralogist, 83, pp. 1454-1468.

KÖSTER, M.H. and GILG, H.A. (2015). Pedogenic, palustrine and groundwater dolomite formation in non-marine bentonites (Bavaria, Germany). Article in Clay Minerals 50 (2), pp. 163-183.

KRINSLEY, D.H., TOVEY, N.K. (1978). Cathodoluminescence in quartz sand grains. Scanning Electron Microscopy, SEM Inc. AMF O'Hare, IL60666, Chicago, pp. 887-894.

KUANG, S.P., XU, Z., SHANG, S.S., MA, Z.D. (2002). Applying geochemistry to research into Meso-Cenozoic climate: discussion on Jurassic climatic change in Sichuan Basin, China. Qingdao Institute of Chemical Technology. 3(1):4-9.

KUZNETSOV, S.I., IVANOV, M.V., LYALIKOVA, N.N. (1963). Introduction to geological microbiology (P.T. Broneer, trans. from Russian): New York, McGraw-Hill Book Co., 252 p.

LACH, P., CATHELINEAU, M., BROUAND, M., FIET, N. (2015). In-situ isotopic and chemical study of pyrite from Chu-Sarysu (Kazakhstan) roll-front uranium deposit. Procedia Earth and Planetary Science, 13, pp. 207-210. doi.org/10.1016/j.proeps.2015.07.049

LAGNY, P., MICHEL, J.C., VIRLOGEUX, D., CAPUS, G., CUNEY, M., BRUNETON, P. (2010). Géologie des principaux types de gisement, In: Géochronique NO 113. (2010). Magazine des Géosciences: L'uranium, Mars 2010, 68 pp.

LANDAIS, P., CONNAN, J., DEREPPE, J.M., GEORGE, E., MEUNIER, J.D., MONTHIOUX, M., PAGEL, M., PIRONON, J., POTY, B. (1987). Alterations of the organic matter, a clue for uranium ore genesis. Uranium, 3, 307–342.

LANDAIS, P. (1996). Organic geochemistry of sedimentary uranium ore deposits. Ore Geol. Reviews, 11, pp. 33-51.

LANGMUIR, D. (1978). Uranium solution-mineral equilibria at low temperatures with applications to sedimentary ore deposits. Geochimica et Cosmochimica Acta, 42, pp. 547-569.

LAMB, M.A. and BADARCH, G. (1997): Paleozoic sedimentary basins and volcanic-arc systems of southern Mongolia: New stratigraphic and sedimentologic constraints: International Geology Review, v. 39, p. 542-576.

LE GOUX, F., BANZRAGCH, T.O., DELAUNAY A., NYAMDORJ, B.I., JAQUES, E., KORSHUNOV, A., PARIZE, O. and BROUAND, M. (2015). The Major Gobi Uranium Deposits, Upper Cretaceous East Gobi Basin, Mongolia: Geodynamical and Mineralogical Key Parameters of Uranium Ore Geology. In: Mineral Resources in a Sustainable World, 13th SGA Biennial Meeting 2015, vol. 5, 1815-1818.

LEMOS, V.P., LIMA da COSTA, M., LEMOS, R.L., GOMES de FARIA, M.S. (2007). Vivianite and siderite in lateritic iron crust: an example of bioreduction. Quim. Nova, vol. 30. no. 1, available online http://www.scielo.br/scielo.php?pid=S0100-40422007000100008&script=sci_arttext

LEWAN, M. D., KOTARBA, M.J. (2014). Thermal maturity limit for primary thermogenic-gas generation from humic coals as determined by hydrous pyrolysis: Bulletin, v. 98, pp. 2581-2610.

LEWAN, M.D., PAWLEWICZ, M.J. (2017). Reevaluation of thermal maturity and stages of petroleum formation of the Mississippian Barnett Shale, Fort Worth Basin, Texas, AAPG Bull., v. 101, no. 12, pp. 1945-1970.

LI, W.H., XU, G.Z. (2006). Relationship between late reformation and formation of sandstone type uranium ore in Ordos Basin. Journal of Earth Sciences and Environment 28, 19-23 (in Chinese with English abstract).

LIU, D.L., SUN, X.R., LI, Z.S., TANG, N.A., TAN, Y. and LIU, B. (2006). Analysis of carbon and oxygen isotope on the Ordovician dolostones in the Ordos Basin. Natural Gas Geoscience 20(1):44-49.

LIU, J.H., SHI, W.J., SUN, Z.X. (2007). A study of the formation process and ore prospecting indicators of the sandstone type uranium deposits in the light of uranium series isotopes. Acta Geoscientica Sinica 28, 39-42 (in Chinese with English abstract).

LOVE, L.G., AMSTUTZ, G.C. (1966). Review of microscopic pyrite. Fortschritte der Mineralogie 43, pp. 273-309.

LONGERICH H.P., JACKSON S.E. and GÜNTHER D. (1996). Laser Ablation Inductively Coupled Plasma, Mass Spectrometric Transient Signal Data Acquisition and Analyte Concentration Calculation. Journal of Analytical Atomic Spectrometry, vol. 11, p. 899-904.

LOVLEY, D.R., PHILLIPS, E.J.P., GORBY, Y. A., LANDA, E.R. (1991). Microbial reduction of uranium. Nature, 350, pp. 413-416. doi:10.1038/350413a0

LOWERS, H.A., BREIT, G.N., FOSTER, A.L., WHITNEY, J., YOUNT, J., UDDIN, M.N., MUNEEM, A. (2007). Arsenic incorporation into authigenic pyrite, Bengal Basin sediment, Bangladesh, Geochimica et Cosmochimica Acta, 71, pp. 2699-2717.

MACK, G.H., COLE, D.R., GIORDANO, T.H., SCHAAL, W.C. & BARCELOS, J.H. (1991). Palaeoclimatic controls on stable oxygen and carbon isotopes in the caliche of the Abo formation (Permian), south central, New Mexico, USA. Journal of Sedimentary Petrology, vol. 61, pp. 458-472.

MAKHNACH, A., MIKHAJLOV, N., KOLOSOV, I., GULIS, L., SHIMANOVICH, V., DEMENEVA, O. (2000). Comparative analysis of sulfur isotope behavior in the basins with evaporites of chloride and sulfate types. Sedimentary Geology, 134, pp. 343-360.

MASON, S.L., FILLEY, T.R., ABBOTT, G.D. (2012). A comparative study of the molecular composition of a grassland soil with adjacent unforested and afforested moorland ecosystems. Organic Geochemistry, 42, 1519–1528.

MASUDA A., NAKAMURA N., and TANAKA T. (1973). Fine structure of mutually normalized rare-earth patterns of chondrites, Geochimica et Cosmochimica Acta, 37, pp. 239-248.

McKAY, J.L., LONGSTAFFE, F.J. (2003). Sulphur isotope geochemistry of pyrite from the upper Cretaceous Marshybank Formation, Western Interior Basin. Sedimentary Geology 157, pp. 175-195.

McLENNAN, S.M. (1989). Rare Earth Elements in Sedimentary Rocks: Influences of Provenance and Sedimentary Processes. Reviews in Mineralogy and Geochemistry, 21, 169-200.

MENOR-SALVAN C., TORNOS, F., FERNANDEZ-REMOLAR, D., AMILS, R (2010). Association between catastrophic paleovegation changes during Devonian-

Carboniferous boundary and the formation of giant massive sulfide deposits. Earth and Planetary Science Letters, doi:10.1016/j.epsl.2010.09.020.

MERCADIER, J. (2011). Uranium et oxydo-réduction : signification des marqueurs minéralogiques des altérations liées au dépôt de l'uranium et processus de dépôt associés. Post-doctorat, G2R-CREGU (Nancy), 333 p.

MERCADIER, J., CUNEY, M., LACH, P., BOIRON, M.C., BONHOURE, J., RICHARD, A., LEISEN, M., KISTER, P. (2011). Origin of uranium deposits revealed by their rare earth element signature. Terra Nova, 23, No.4, pp.264-268.

MEUNIER, J.D., SELLIER, E., PAGEL, M., (1990a). Radiation damage rims in quartz from uranium bearing sandstones. Journal of Sedimentary Petrology, 60, pp. 53-58.

MEUNIER, J.D., LANDAIS, P., PAGEL, M. (1990b). Experimental evidence of uraninite formation from diagenesis of uranium rich organic matter. Geochimica et Cosmochimica Acta, 54, pp. 809-817.

MEYERHOFF, A.A. and MEYER, R.F. (1987). Geology of heavy crude oil and natural bitumen in the USSR, Mongolia, and China. In: MEYER, R. F, ed., Exploration for heavy crude oil and natural bitumen: AAPG Studies in Geology 25, pp. 31-101.

MIKHAILOV, V.V. and PETROV, N.N. (1998). Age of exogene uranium deposits in south and south-east Kazakhstan according to the lead-isotope study. Geology of Kazakhstan 2(354), pp. 63-70

MIN, M., XU, H., CHEN, J., FAYEK, M. (2005). Evidence of uranium biomineralization in sandstone-hosted roll-front uranium deposits, northwestern China, Ore Geology Reviews, Volume 26, Issues 3–4, July 2005, Pages 198-206.

MORROW, D.W. (1982a). Diagenesis 1. Dolomite – Part 1: The Chemistry of Dolomitization and Dolomite Precipitation. Geoscience Canada, vol. 9, Number 1. pp. 5-13.

MORROW, D.W. (1982b). Diagenesis 2. Dolomite – Part 2: Dolomitization Models and Ancient Dolostones. Geoscience Canada, vol. 9, Number 2. pp. 95-107.

MÖLLER, P. (1983). Lanthanoids as a Geochemical Probe and Problems in Lanthanoid Geochemistry Distribution and Behaviour of Lanthanoids in Non-Magmatic-Phases, Systematics and the properties of the Lanthanides. Springer, pp. 561-616.

MUMTAZ. A.A. (1979). Geochemistry and mineralogy of namurian sediments in the Pennine basin, England. PhD thesis, University of Sheffield, 507 p.

MUNARA, A. (2012). Formation des gisements d'uranium de type roll : approche minéralogique et géochimique du gisement uranifère de Muyunkum (Bassin de Chu-Sarysu, Kazakhstan). Thèse soutenue le 9 Juillet 2012, PhD Univ. H. Poincaré Nancy. 327p.

NAKASHIMA, S. (1992). Complexation and reduction of uranium by lignite. Science of the Total Environnent, 117-118, pp. 425-437.

NAKASHIMA, S., DISNAR, J.R., PERRUCHOT, A., TRICHET, J. (1984). Experimental study of mechanisms of fixation and reduction of uranium by sedimentary organic matter under diagenetic or hydrothermal conditions. Geochimica et Cosmochimica Acta, 48, pp. 2321-2329.

NAKASHIMA, S., DISNAR, J.R., PERRUCHOT, A. (1999). Precipitation Kinetics of Uranium by Sedimentary Organic Matter under Diagenetic and Hydrothermal Conditions. Economic Geology, 94, pp. 993-1006.

NIU, L., HUANG, S., YANG, G. (1995). The characteristics of uranium mineralization and genesis of Nuheting uranium deposit in Erlian Basin, Inner Mongolia. China Nucl. Sci. Technol. Rep. 1995–00 (in Chinese with English abstract).

OHFUJI, H., AKAI, J. (2002). Icosahedral domain structure of framboidal pyrite. American Mineralogist, 87, pp. 176-180.

OHFUJI, H., RICKARD, D. (2005a). Experimental syntheses of framboids—a review. Earth-Science Reviews, 71, pp. 147-170.

OHFUJI, H., RICKARD, D., BUTLER, I.B. (2005b). Environmental controls of pyrite texture development from aqueous solutions at 25-160°C – an experimental study. Abstracts for Annual Meeting of the Mineralogical Society of Japan.

OHMOTO, H., GOLDHABER, M.B. (1997). Sulfur and carbon isotopes. In: Barnes, H. L. (Ed.), Geochemistry of hydrothermal ore deposits, 3rd edition, Wiley, New York, pp. 517-611.

OWEN D.E., OTTON J.K. (1995). Mountain wetlands: efficient uranium filters-potential impacts. Ecological Engineering, 5, pp. 77-93.

PARIZE, O. (2013). Le remplissage de la dépression de Tsagaan Els et les dépôts fluviatiles associés (Crétacé moyen, Bassin de Zuunbayan). Implication stratigraphiques et sédimentologiques sur le gisement de Zoovch Ovoo – Synthèse des résultats 2012-2013. Octobre 2013, édition décembre 2014. Rapport technique AMS-DGS-TEC-SDYRT-0008, (Poster AMS-DGS-TEC-SDY-RT-0008_PosterZoovchA1_2013).

PARIZE, O. (2015). Le remplissage de la dépression de Tsagaan Els et les dépôts fluviatiles associés (Crétacé moyen, Bassin de Zuunbayan). Implication stratigraphiques et sédimentologiques sur le gisement de Zoovch Ovoo – Synthèse des résultats 2012-2013. Octobre 2013, édition décembre 2014. Rapport technique AMS-DGS-TEC-SDYRT-0008, (Poster AMS-DGS-TEC-SDY-RT-0008_PosterZoovchA1_2013).

PARNELL, J., PEREZ, M., ARMSTRONG, J., BULLOCK, L., FELDMANN, J., BOYCE, A.J. (2018). Geochemistry and metallogeny of Neoproterozoic pyrite in oxic and anoxic sediments, Geochemical Perspectives Letters, pp. 12-16.

PEARCE N.J.G., PERKINS W.K., WESTGATE J.A., GORTON M.P., JACKSON S.E., NEAL C.R. AND CHENERY S.P. (1997). A compilation of new and published major and trace

element data for NIST SRM 610 and NIST SRM 612 glass reference materials. Geostandards and Geoanalytical Research, vol. 21, pp. 101-114.

PEARSON, M.J., NELSON, C.S. (2005). Organic geochemistry and stable isotope composition of New Zealand carbonate concretion sand calcite fracture fills. New Zealand Journal of Geology and Geophysics, vol. 48, pp. 395-414.

PERRY, K.A., PEDERSEN, T.F. (1993). Sulphur speciation and pyrite formation in meromictic ex-fjords. Geochimica et Cosmochimica Acta 57, pp. 4405-4418.

PETROV N.N. (1998). Les gisements épigénétiques du Kazakhstan. Géologie du Kazakhstan, 2(354): pp. 22-39. (trans. from Russian).

PETTIJOHN, F.J., POTTER, P.E. and SIEVER, R. (1987). Sand and Sandstone, 2nd ed., New York, Springer-Verlag, 533 pp

PIMENTEL, N.L.V. (2002). Pedogenic and early diagenetic processes in Palaeogene alluvial fan and lacustrine deposits from the Sado Basin (S Portugal). Sedimentary Geology, vol. 148, pp. 123-138

PICKEL, W., KUS, J., FLORES, D., KALAITZIDIS, S., CHRISTANIS, K., CARDOTT, B.J., MISZ-KENNAN, M., RODRIGUES, S., HENTSCHEL, A., HAMOR-VIDO, M., CROSDALE, P., WAGNER, N. (2017). Classification of liptinite - ICCP System 1994. International Journal of Coal Geology, 169, pp. 40-61.

PIRANJO, F., SELTMANN, R., YANG, Y. (2011). A review of mineral systems and associated tectonic settings of northern Xinjiang, NW China. Geoscience Frontiers, vol. 2, pp. 157-185

PONTOLILLO, J. & STANTON, R. W. (1994). Coal petrographic laboratory procedures and safety manual II. Open-file Report 94-631. U.S Department of Interior Geological Survey. 74 p.

PROST, G.L. (2004). Tectonics and hydrocarbon systems of the East Gobi basin, Mongolia, AAPG Bulletin, vol. 88, No. 4, pp. 483-513.

RACKLEY, R.I. (1972). Environment of Wyoming Tertiary Uranium Deposits. The American Association of Petroleum Geologists Bulletin, v. 56. No. 4. Pp. 755-774.

RALLAKIS, D., SIAVALAS, G., OSKAY, R.G., TSIMIKLIS, D., CHRISTANIS, K. (2013). Maturity of dispersed organic matter in bituminous formations of the Ionian zone (Epirus region, NW Greece). Proceedings of the 13th International Congress, Chania, Greece.

REINHOLDT, M. (2016). Réactions minérales et mobilité de l'U et du ^{226}Ra en contexte d'exploitation minière par In Situ Recovery du test expérimental de Dulaan-Uul (Mongolie): rapport final de l'étude postdoctorale de Marc REINHOLDT (Université de Poitiers) – Internal report

REYNOLDS, R.L., GOLDHABER, M.B., CARPENTER, D.J. (1982). Biogenic and Nonbiogenic Ore-Forming Processes in the South Texas Uranium District: Evidence form the Pana Maria Deposit. Economic Geology. vol. 77. pp. 541-556.

REYNOLDS, R.L., GOLDHABER, M.B. (1978). Origin of a South Texas roll-type uranium deposit: I. Alteration of iron-titanium oxide minerals. Economic Geology 73:1677–1689.

RICKARD, D. (1977). Kinetics of pyrite formation by the H_2S oxidation of iron(II) monosulphide solutions between 25 °C and 125 °C: the rate equation. Geochimica et Cosmochimica Acta, 61, pp. 115-134.

RICKARD, D., GRIFFITH, A., OLDROYD, A., BUTLER, I.B., LOPEZ-CAPER, E. MANNING, D.A.C., APPERLEY, D.C. (2006). The composition of nanoparticulate mackinawite, tetragonal iron (II) monosulfide. Chemical Geology, 235, pp. 286-298.

RITTS, B.D., HANSON, A.D., DARBY, B.J., NANSON, L., BERRY, A. (2004). Sedimentary record of Triassic intraplate extension in north China: Evidence from the nonmarine NW Ordos Basin, Helan Shan and Zhuozi Shan. Tectonophysics 386, 177-202.

ROH, Y., ZHANG, C.L., VALI, H., LAUF, R.J., ZHOU, J. and PHELPS, T.J. (2003). Biogeochemical and environmental factors in Fe biomineralization: magnetite and siderite formation. Clay and Clay Minerals, vol. 51, No. 1, 83-95.

ROSS, D.A., DEGENS, E.T. (1974). Recent sediments of the Black Sea. In: Degens, E.T., Ross, A. (Eds.), Black Sea—Geology, Chemistry, and Biology, AAPG Mem., 20, pp. 183-199.

ROUZAUD, J.N., OBERLIN, A., TRICHET, J. (1979). Interaction of uranium and organic matter in uraniferous sediments. In: Douglas, A.G., Maxwell, J.R., Advances in Organic Geochemistry, Eds.; Pergamon Press: Oxford, UK, 1979, pp. 505-516.

SANCHEZ, A.G. (2010). Relation entre les failles, la migration d'hydrocarbures et les minéralisations d'uranium en Mongolie de l'Est. Rapport de Master 2 Professionnel au sein d'AREVA NC. Université de Montpellier 2, Master BGAE, Spécialité Géosciences, Parcours Réservoirs Géologiques, 52 pp.

SANCHEZ, A.G. (2011). Dynamique de bassin et rôle du système pétrolier sur les minéralisations d'uranium. Définition des indices de surface pour l'établissement de guides d'exploration. Compte-rendu bimensuel, Thèse, 1r année, 6 pp.

SANFORD, R. (1994). Hydrogeology of Jurassic and Triassic wetlands in the Colorado Plateau and the origin of tabular sandstone uranium deposits. U.S. Geol. Surv. Prof. Paper 1548.

SASSANO, G.P., SCHRIJVER, K. (1989). Framboidal pyrite: early-diagenetic, late-diagenetic, and hydrothermal occurrences from Acton Vale quarry, Cambro-Ordovician, Quebec. American Journal of Science 289, pp. 167-179.

SAVAGE, K.S., TINGLE, T.N., O'DAY, P.A., WAYCHUNAS, G.A., BIRD, D.K. (2000). Arsenic speciation in pyrite and secondary weathering phases, Mother Lode Gold District, Tuolumne County, California. Applied Geochemistry, 15, pp. 1219-1244.

SAWLOWICZ, Z. (1993). Pyrite framboids and their development: a new conceptual mechanism. Geologische Rundschau, 82(1), pp. 148-156.

SAWLOWICZ, Z. (2000). Framboids: from their origin to application. Polska Akademia Nauk – Oddział W Krakowie, Prace Mineralogiczne, 88, 80 pp.

SENSULA, B., BOETTGER, T., PAZDUR, A., PIOTROWSKA, N. and WAGNER, R. (2006). Carbon and oxygen isotope composition of organic matter and carbonates in recent lacustrine sediments. Geochronometria, vol. 25, pp. 77-94.

SCHEFFER, C., TARANTOLA, A., VANDERHAEGHE, O., RIGAUDIER, T., PHOTIADES, A. (2016). CO_2 flow during orogenic gravitational collapse: Syntectonic decarbonation and fluid mixing at the ductile-brittle transition (Lavrion, Greece), Chemical Geology, vol. 450, pp. 248-263.

SCHMIDT, V. (1965). Facies, diagenesis, and related reservoir properties in the Gigas Beds (Upper Jurassic), northwestern Germany: in PRAY, L. C. AND MURRAY, R. C., Dolomitization and Limestone Diagenesis: Society of Economic Paleontologists, Mineral Special Publication, vol. 13, pp. 124-168.

SCHOELL, M. (1988). Multiple origins of methane in the Earth. Chemical Geology, 71, pp. 1-10.

SCHOLLE, P.A. and ULMER-SCHOLLE, D.S. (2003). A Color Guide to the Petrography of Carbonate Rocks: Grains, textures, porosity, diagenesis, AAPG memoir, vol. 77, 474 pp. DOI: 10.1306/M77973

SCHWERTMANN, U. (1991). Solubility and dissolution of iron oxides. Plant and soil, 130, pp. 1-25.

SPIRAKIS, C. (1996). The role of organic matter in the formation of uranium deposits in sedimentary rocks. Ore Geology Reviews, 11, pp. 53-69.

STANKIEWICZ, B.A., KRUGE, M.A. AND CRELLING, J.C. (1994). Geochemical characterization of maceral concentrates from Herrin No. 6 coal (Illinois Basin) and Lower Toarcian Shale kerogen (Paris Basin): Bulletin Des Centres De Recherches Exploration-Production, Special Publication 18, p. 237-251.

STANKIEWICZ, B.A., KRUGE, M.A. AND MASTALERZ, M. (1996). A geochemical study of macerals from a Miocene lignite and an Eocene bituminous coal, Indonesia. Organic Geochemistry, 24, pp. 531-545.

STEVENSON, F.J. (1982). Humus, Chemistry. Genesis, Composition, Reactions; John Wiley and Sons: New York, NY, USA, 443 pp.

STUMM, W., LEE, G.F. (1960). The chemistry of aqueous iron. Schweizerische Zeitschrift für Hydrologie, 22(1), pp. 295-319.

SUÁREZ-RUIZ, I., FLORES, D., MENDONÇA FILHO, J.G., HACKLEY, P.C. (2012). Review and update of the applications of organic petrology: Part 1, geological applications. International Journal of Coal Geology, 99, pp. 54-112.

SUESS, E. and WHITICAR, M.J. (1989). Methane-derived CO_2 in pore fluids expelled from the Oregon subduction zone. Palaeogeography, Palaeoclimatology, Palaeoecology: vol. 71, pp. 119-136.

SUITS, N.S., WILIKIN, R.T. (1998). Pyrite formation in the water column and sediment of a meromictic lake. Geology, 26, pp. 1099–1102.

SUN, G., YIN, J., ZHANG, S., LU, X., ZHANG, S. and SHI, J. (2015). Diagenesis and sedimentary environment of Miocene series in Eboliang III area. Environmental Earth Science: vol. 74, pp. 5163-5179.

SUZUKI, Y., BANFIELD, J.F. (1999). Geomicrobiology of Uranium, chapter 8. In: Burns, P.C., Finch, R. (1999). URANIUM: Mineralogy, Geochemistry and the Environment, Reviews in Mineralogy, 38, 673 p.

SÝKOROVÁ, I., PICKEL, W., CHRISTIANIS, K., WOLF, M., TAYLOR, G.H., FLORES, D., 2005. Classification of huminite—ICCP System 1994. International Journal of Coal Geology 62, 85–106.

SWEENEY, R.E., KAPLAN, I.R. (1973). Pyrite framboid formation: laboratory synthesis and marine sediments. Economic Geology, 68, pp. 618–634.

TAYLOR, G.H., TEICHMULLER, M., DAVIS, A., DIESSEL, C.F.K., LITTKE, R., ROBERT, P. (1998). Organic Petrology. Gebrüder Borntraeger, Berlin. 704 pp.

TAYLOR, K. and MACHENT, P.G. (2011). Extensive carbonate cementation of fluvial sandstones: An integrated outcrop and petrographic analysis from the Upper Cretaceous, Book Cliffs, Utah. Marine and Petroleum Geology. pp. 1461-1474.

THEBERGE, S., LUTHER, G.W. (1987). Determination of the electrochemical properties of a soluble aqueous FeS species present in sulfide solutions. Aquatic Geochemistry, 3, pp. 191-211.

TRAYNOR, J.J. and SLADEN, C. (1995). Tectonic and stratigraphic evolution of the Mongolian People's Republic and its influence on hydrocarbon geology and potential: Marine and Petroleum Geology, v. 12, p. 35-52.

TSEZOS, M., VOLESKY, B. (1982). Biosorption of uranium and thorium, Biotechnology Bioengineering, 23, pp. 583-604.

VAN KREVELEN, D.W. (1993). Coal: Typology – Chemistry – Physics – Constitution, 3rd ed. Elsevier, The Netherlands, 979 pp.

VON DER BORCH, C.C and JONES, J. B. (1976). Spherular modern dolomite from the Coorong area, South Australia. Sedimentology, vol. 23, pp. 587-591.

WANG, J., CAO, Y., LIU, K., LIU, J., XUE, X. & XU, Q. (2016). Pore fluid evolution, distribution and water rock-interactions of carbonate cements in red-bed sandstone reservoirs in the Dongying Depression, China. Marine and Petroleum Geology, vol. 72, pp. 279-294.

WARWICK, P., EVANS, N., HALL, A., WALKER, G., STEIGLEDER, E. (2005). Stability constants of U(VI) and U(IV)-humic acid complexes. Journal of Radioanalytical and Nuclear Chemistry, 266(2), pp. 179-190.

WENTWORTH, C.K. 1922. A scale of grade and class terms for clastic sediments. Journal of Geology. 30:377-392.WORDEN, R.H. & BURLEY, S.D. (2003). Sandstone diagenesis: the evolution of sand to stone, Sandstone Diagenesis: Recent and Ancient. International Association of Sedimentologists, 44 pp. ISBN: 978-405-10897-3.

WERSIN, P., HOCHELLA, M.F., PERSSON, P., REDDEN, G., LECKIE, J.O., HARRIS, D.W. (1994). Interaction between aqueous uranium (VI) and sulfide minerals: Spectroscopic evidence of sorption and reduction. Geochimica et Cosmochimica Acta, 58(13), pp. 2829-2843.

WORDEN, R.H. and BURLEY, S.D. (2003). Sandstone diagenesis: the evolution of sand to stone, Sandstone Diagenesis: Recent and Ancient. International Association of Sedimentologists, 44 pp. ISBN: 978-405-10897-3.

WHITICAR, M.J., FABER, E., SCHOELL, M. (1986). Biogenic methane formation in marine and freshwater environments: CO_2 reduction *vs.* acetate fermentation–Isotope evidence. Geochimica et Cosmochimica Acta, 50, pp. 693-709.

WHITICAR M.J. (1990). A geochemical perspective of natural gas and atmospheric methane. Organic Geochemistry, 16, pp. 531-547.

WHITICAR, M.J. (1994). Correlation of Natural Gases with their Sources: Chapter: 16: Part IV. Identification and Characterization. AAPG Special Volumes, Oil—Methodology and Concepts, pp. 261-283, In: M 60: The Petroleum System—From Source to Trap.

WHITICAR, M.J. (1996). Stable isotope geochemistry of coals, humic kerogens and related natural gases. International Journal of Coal Geology, 32, pp. 191-215.

WILKIN, R.T., BARNES, H.L., BRANTLEY, S.L. (1996). The size distribution of framboidal pyrite in modern sediments: an indicator of redox conditions. Geochimica et Cosmochimica Acta, 60, pp. 3897-3912.

WILKINS, M.J., LIVENS, F.R., VAUGHAN, D.J., LLOYD, J.R. (2006). The impact of Fe(III)-reducing bacteria on uranium mobility. Biogeochemistry, 78(2), pp. 125-150.

WOLTHERS, M., CHARLET, L., VAN DER LINDE, P., PICKARD, D., VAN DER WEIJDEN, C. (2005). Surface chemistry of disordered mackinawite (FeS). Geochimica et Cosmochimica Acta, 69, pp. 3469-3481.

XIANG, W.D., FANG, X.H., LI, T.G., CHEN, X.L., PANG, Y.Q., CHENG, H.H. (2005). Geology and origin of the Dongsheng uranium deposit in the Ordos Basin, north China. Mineral Deposit Research: Meeting the Global Challenge. Germany: Springer 1, 327-330.

XIANG, W.D., FANG, X.H., LI, T.G., CHEN, X.L., PANG, Y.Q., CHENG., H.H. (2006). Metallogenic characteristics and model of Dongsheng uranium deposit in Ordos Basin, north China. Uranium Geology 22, 257-266 (in Chinese with English abstract).

XING, X.J., LIU, Y.Q., LI, W.H., GONG, B.L. (2008). Sandstone diagenesis and uranium mineralization of the Zhiluo Formation in the Diantou area, southern Ordos Basin. Acta Geoscientica Sinica 29, 179-188 (in Chinese with English abstract).

XIE, X., MINGCAI, Y., WANG, C., LI, L., SHEN H. (1989). Geochemical reference samples GSD 9-12, GSS 1-8, GSR 1-6, Geostandards and Geoanalytical Research, vol. 13, pp. 83-179.

XUE, C. J., CHI, G. X., XUE W. (2011). Effects of hydrocarbon generation on fluid flow in the Ordos Basin and its relationship to uranium mineralization. Geoscience Frontiers, v. 2, p. 439–447.

YANG, X.Y., LING, M.X., SUN, W.D., LUO, X.D., LAI, X.D., LIU, C.Y., MIAO, J.Y., SUN, W. (2009). The genesis of sandstone-type uranium deposits in the Ordos Basin, NW China: constraints provided by fluid inclusions and stable isotopes. International Geology Review 51, 422–455.

YAZHIKOV, V. (1996). Uranium raw material base of the Republic of Kazakhstan and prospects of using in situ leach mining for its development. In: In Situ leach uranium Mining. Proceedings of IAEA Technical Committee Meeting, Almaty, Kazakhstan, September 1996.

YUE, L., JIAO, Y., Wu, L., RONG, H., XIE, H., WANG, Q., YAN, Q. (2019). Selective crystallization and precipitation of authigenic pyrite during diagenesis reservoir sandbodies in Ordos Basin. Ore Geology Reviews, vol. 107, pp. 532-545.

ZAMMIT, C.M., BRUGER, J., SOUTHAM, G., REITH, F. (2014). In situ recovery of uranium – the microbial influence. Hydrometallurgy, vol. 150, pp. 236-244. DOI: 10.1016/j.hydromet.2014.06.003

ZHANG, R., DING, W. (1996). Discussion on geological characteristics of Nuheting type uranium deposit and the relation between oil and gas-bearing water and uranium metallogenesis. Galaxy of Research Achievements of Uranium Geology of China. Bureau of Geology, CNNC, Beijing, pp. 205–214

ZHANG, Z.L., HAN, X.Z., LI, S.X., YAO, C.L., ZHAO, Y.A. (2010). Sedimentary facies of the lower part of Middle Jurassic Zhiluo Formation in northeastern Ordos Basin and its controls on uranium mineralization. Journal of Palaeogeography 12, 749-758 (in Chinese with English abstract).

ZHANG, F., JIAO, Y.Q., WU, L.Q., RONG, H., WANG, L.H. (2018). Relations of uranium enrichment and carbonaceous debris within the Daying uranium deposit, northern Ordos Basin. Journal of Earth Science, DOI: 10.1007/s12583-017-0952-0.

ZHANG, F., JIAO, Y., WU, L., RONG, H., WANG, L., ZHANG, Z. (2019). In-situ analyses of organic matter maturation heterogeneity of uranium-bearing carbonaceous debris within sandstones: A case study from Ordos Basin in China. Ore Geology Reviews, DOI: https://doi.org/10.1016/j.oregeorev.2019.03.021.

ZHAO, H.G., OU, G.X. (2006). The relationship between depositional system and ore-formation of sandstone-type uranium deposits in Dongsheng area, Ordos basin. Uranium Geology 22, 136-98 (in Chinese with English abstract).

ZHAO, Y.Y. and ZHENG, Y.F. (2013). Geochemical constraints on the origin of post-depositional fluids in sedimentary carbonates of the Ediacaran system in South China. Precambrian Research, vol. 224, pp. 341-363.

ZHU, M., WU, R., LIU, X., NIE, F., YU, D. (2012) Geologic setting of interformational-braided-channel type sandstone uranium deposits in north china, 2012 IAEA conference.

PUBLICATION ON URANIUM ORGANIC MATTER RELATIONSHIPS

THE ROLE OF ORGANIC MATTER ON URANIUM PRECIPITATION IN ZOOVCH OVOO, MONGOLIA

Minerals **2019**, *9*(5), 310; https://doi.org/10.3390/min9050310

The role of organic matter on uranium precipitation in Zoovch Ovoo, Mongolia

Dimitrios Rallakis [1], Raymond Michels [1,*], Marc Brouand [2], Olivier Parize [2] and

Michel Cathelineau [1,*]

[1] Université de Lorraine, CNRS, CREGU, GeoRessources Laboratory, rue Jacques Callot, F-54506 Vandoeuvre-lès-Nancy, France; dimitrios.rallakis@univ-lorraine.fr (D.R.)

[2] ORANO Mining, Tour AREVA, place Jean Millier 1, 92084, Courbevoie, France; marc.brouand@orano.group (M.B); olivier.parize@orano.group (O.P)

***** Correspondence: raymond.michels@univ-lorraine.fr (R.M); michel.cathelineau@univ-lorraine.fr (M.C); Tel.: +33-372-745-561 (R.M); +33-372-745-543 (M.C)

Received: 10/4/2019; Accepted: 9/5/2019; Published: date

Abstract: The Zoovch Ovoo uranium deposit is located in East Gobi Basin, Mongolia. It is hosted in the Sainshand Formation, a Late Cretaceous siliciclastic reservoir, lower part of the post-rift infilling of the Mesozoic East Gobi Basin. The Sainshand Formation corresponds to poorly consolidated medium-grained sandy intervals and clay layers deposited in fluvial-lacustrine settings. The uranium deposit is confined within a 60-80 m thick siliciclastic reservoir inside aquifer driven systems assimilated to roll-fronts. As assessed by vitrinite reflectance (%Rr<0.4) and molecular geochemistry, the formation has never experienced significant thermal maturation. Detrital organic matter (type III and IV kerogens) is abundant in the Zoovch Ovoo depocenter. In this framework uranium occurs as: (i) U-rich macerals without any distinguishable U-phase under SEM observation, and containing up to 40 wt% U; (ii) U expressed as UO_2 at the rims of large (several millimeters) macerals and (iii) finally U-oxides replacing partially to entirely macerals, while preserving the inherited plant-texture. Uranium is thus accumulated gradually in the macerals through an organic carbon-uranium epigenization process in respect of the maceral chemistry and permeability. Most macerals are rich in sulfur and to a lesser extent in Fe, and frequently Fe and S contents do not fit the stoichiometry of pyrite, although pyrite also occurs as small inclusions within the macerals. The organic matter appears thus as a major redox trap for uranium in this kind of geological setting.

Keywords: Roll-front, uranium, organic matter, Late Cretaceous, East Gobi Basin, Mongolia

1. Introduction

Organic carbon is considered as an important uranium reducer in sedimentary uranium ore deposits [1-6]. Several mechanisms may account for uranium fixation by low maturity lignite and reduction during its burial history. It is possible for uranium to be adsorbed by carboxyl groups, to form organo-uranyl compounds, by means of cation exchange at ambient conditions or without cation exchange when exposed to heat [7]. It is noted however that adsorption may

not be accompanied by $U^{(VI)}$ reduction [8-10]. With increasing thermal maturity, U adsorption may co-exist with reduction reactions and finally at higher temperatures [11,12] reduction of $U^{(VI)}$ is predominant.

It is therefore proposed that in geological environments U may be trapped by peat or lignite without reduction at low temperature (lignite stage [13,14]), while at later diagenetic stages (catagenesis, metagenesis stages of coalification) U reduction will prevail. The reduction mechanism of $U^{(VI)}$ may occur through the dehydrogenation of aliphatic and hydroxyl hydrocarbonaceous moieties [9,7]. Subsequently two protons (H^+) are liberated from the organic matter and two oxygens are fixed during the formation of UO_2 [15,16,12]. Roll-front systems are ideal cases to study the organic matter-uranium relationships, as uranium and iron-sulfur bearing phases are dissolved and then re-precipitated along a physical-chemical front which affects progressively sands or sandstones, frequently rich in detrital organic matter [17,18]. Central Asia hosts three important roll-front provinces: i) the Chu-Sarysu basin in Southern Kazakhstan where large scale U roll-front system of tens of kilometers are exploited [19-21]; ii) the sedimentary basins hosting U roll-fronts, in particular the Yili, Tuha, Ordos and Erlian basins in North-East and North China [22-25]; iii) the East Gobi Basin in Mongolia, with the Zoovch Ovoo and Dulaan-Uul U-ore deposits [26]. The Zoovch Ovoo deposit provides a unique opportunity to study the organic matter-uranium relationships, as the host formation is richer in organic matter more than most of other deposits. The macerals were thus studied in detail, in particular their textural relationships with uranium phases and sulfides, as well as the spatial distribution of U, Fe and S in maceral grains. The objective was to understand the role of organic matter in uranium trapping and reduction.

2. Geological Setting

The roll-front system of the Zoovch Ovoo U-ore deposit is hosted in the Cenomanian Sainshand Formation which thickness ranges from 100 to 350 m [26]. It can be separated into respective sub-units that reflect different cycles of lacustrine and alluvial sedimentation setting up an association of conglomerates, sands, silts and clays [27]. In particular the sand dunes of the flood-dominated braided delta inside the lacustrine realm serve as uranium reservoirs (**Figure 1**). The Sainshand Formation is overlaid by the Late Cretaceous (Turonian-Santonian) Bayanshiree Formation, consisting mainly of reddish to greyish shales with minor input of sandstones with meandering channel-shape geometry [28,29,26]. The Late Cretaceous lacustrine coarse clastic units, namely the Santonian-Campanian Baruungoyot Formation and the Campanian-Maastrichtian Nemegt Formation occur only sporadically. Finally, Tertiary and Quaternary sediments are undifferentiated with granular sizes from very fine to coarse, and top-up unconformably the Late Cretaceous strata [30].

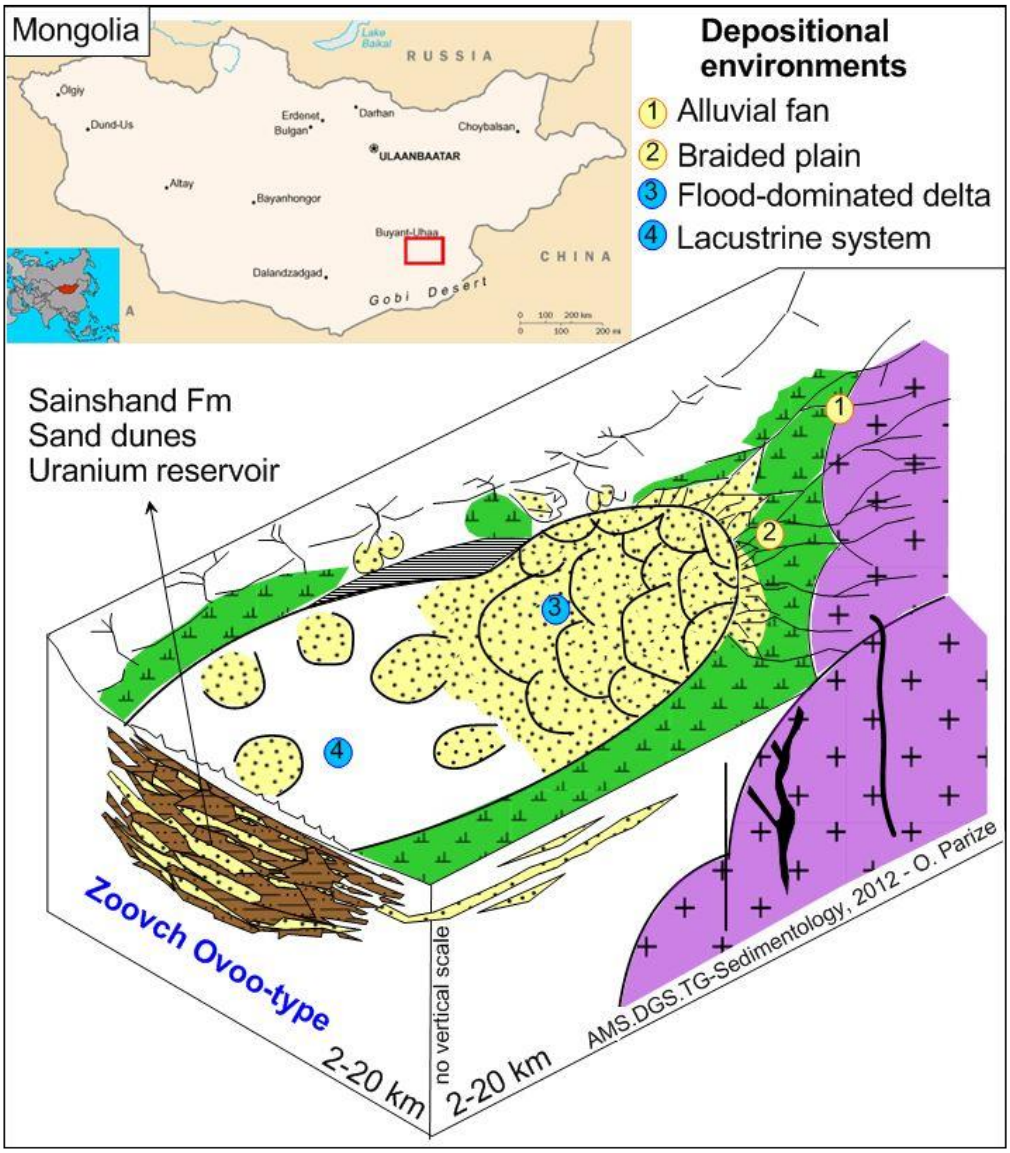

Figure 1. Location map of the study area and depositional model of the Zoovch Ovoo depocenter in Cenomanian [26]. Sedimentary depositional systems are fluvio-lacustrine with alluvial fans, braided rivers and deltas. The sands of Sainshand Formation are the host-rock for uranium mineralization.

3. Materials and Methods

The current study was carried out on core samples recovered during the exploration campaigns conducted by COGEGOBI, from 2011 to 2017, in Zoovch Ovoo. Samples were recovered by the roll-front area, within Sainshand Formation at depths between **Figure 2**. Coal layers are lacking inside the reservoir zone and the organic matter occurs as detrital particles deposited in accordance with the sedimentary bedding structures. The coarse, angular and poorly sorted organic particles are reworked, linked to distant transport within high energy depositional settings and associated to fine to coarse grained sands. Organic matter particles encountered in fine clay (organic rich) layers are better preserved and linked to low energy depositional settings under less oxygenated conditions. The well preserved phytoclasts, such as root

remains associated to fine grained organic rich lithofacies could be indicative of higher plants which grew within the depositional environment setting and did not undergo any significant transport.

3.1. Petrography

3.1.1 Optical Microscopy

Polished thin sections (~30 µm thick) were studied using optical microscopy in transmitted and reflected light modes, with objectives to describe the morphology and the nature of the different types of uranium mineralization encountered along the redox front.

3.1.2. Scanning Electron Microscopy

A PHILIPS XL30 Scanning Electron Microscope (SEM), equipped with an energy dispersive spectrometer using a Si-(Li) semi-conductor detector, coupled with a HITACHI S-4800 scanning electron microscope (SEM) was used in order to establish the mineral paragenesis and to identify the main uranium bearing phases, and their composition using EDS analyses.

3.1.3. In Situ Analysis

The Electron Probe Micro-analysis (EPMA) of uranium cements was performed using a CAMECA SX100 at SCMEM (Service Commun de Microscopie Electronique) Nancy. The calibration was made using natural and synthetic oxides or alloys (orthoclase, albite, $MnTiO_3$, wollastonite, hematite and olivine). The analytical conditions were: 10 nA current, accelerating voltage of 15 kV, 10 s counting time for (K, Na, Ca), 20 s for (Al, Fe, Mn), 40 s for (Mg). The accelerating voltage was raised from 15 kV to 25 kV to amplify the detection limit in particular when investigating the uranium-organic matter relationships.

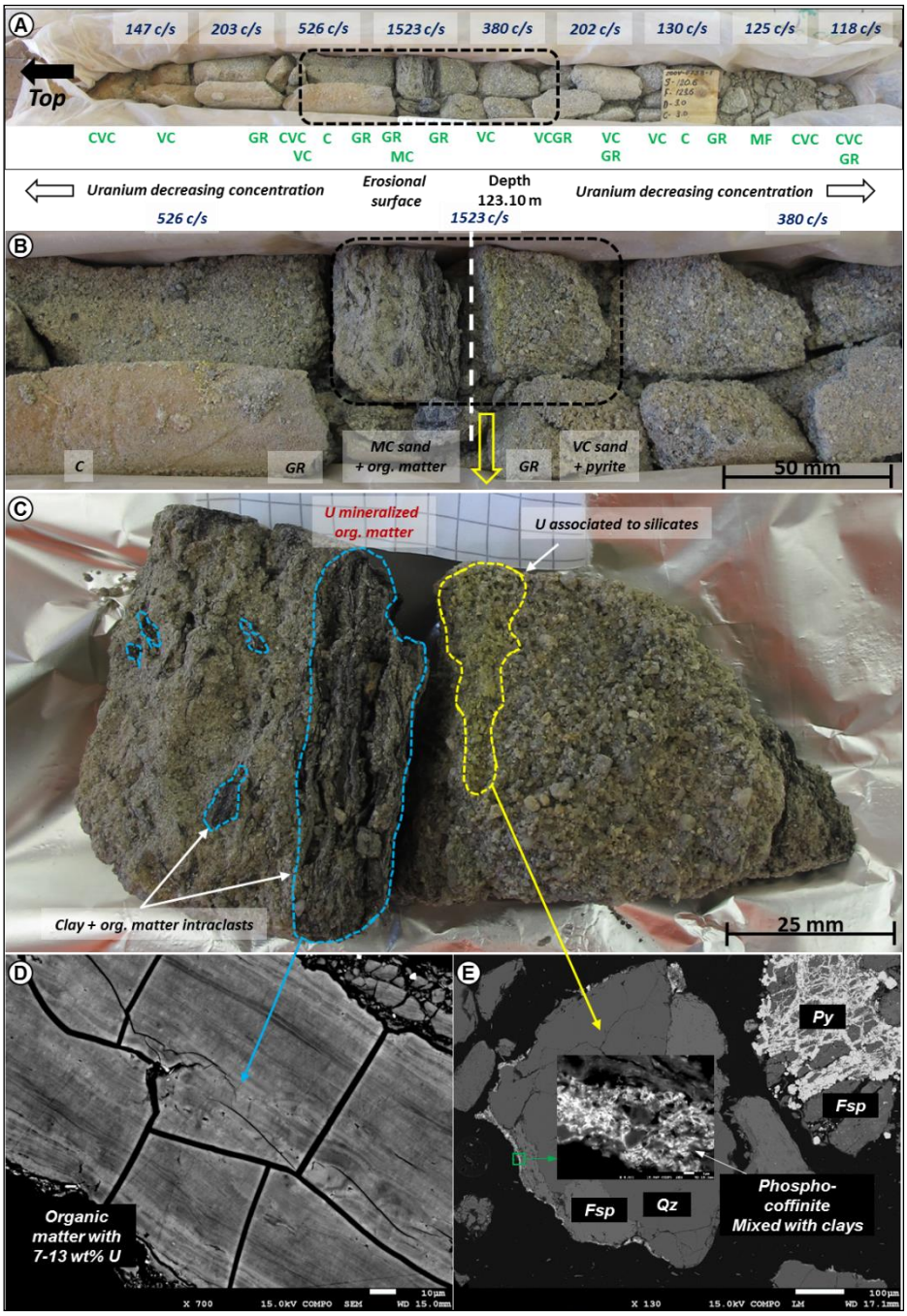

Figure 2. Abbreviations: GR (granules); CVC (coarse to very coarse sand), VC (very coarse sand), C (coarse sand), MC (medium coarse sand), Fsp (feldspar), Qz (quartz), Py (pyrite); (**A**) Drill-core recovered from 123.20 m depth targeting the U-reservoir, Sainshand Formation; Gamma ray spectroscopy measurements, presented in blue, were performed in contact with the rock unit with a step distance of 10 cm, expressed in c/s (counts per second); (**B**) Two upward-fining sequences are distinguished, starting with granules and ending with medium coarse sand in both cases. The sequences are separated by an erosional surface and followed by coarse deposits containing intraclasts of silty clay and organic matter; (**C**) A zoomed image of (B) highlighting the areas of organic matter and of higher uranium concentration. The intense bright yellow color reveals an oxidation of U-ores in contact with air. Uranium concentration is the highest at the contact with the erosional surface; (**D**) Organic matter particle containing between 7-13 wt% uranium, without mineral expression; (**E**) Silicate grains coated by phospho-coffinite intermixed with clays; (D, E images under SEM/BSE mode).

3.1.4. Organic Petrography

Polished blocks were prepared from the organic matter rich samples and studied by means of oil-immersion petrography. The samples were initially screened for their organic matter content, either forming thin laminae following the sedimentary bedding or as coal rich clay intraclasts and phytoclasts (plant remains) inside the poorly consolidated sands or carbonate cemented sandstones. Consequently, the organic matter was mechanically sorted and recovered from the sand and sandstone samples. The material was then grossly hand-crushed using agate mortar, to prevent the production of fine-grained particles. The detailed methodology followed for the preparation of the polished blocks as well as for the polishing were based on [31].

The random vitrinite reflectance (Rr%) was measured on polished blocks on surface of 1 mm in diameter, mounted on epoxy resin according to ISO 7404-2 [32]. A Zeiss (Axio Imager D1M) microscope equipped with oil-immersion objectives with 50x magnification was used. The vitrinite reflectance was conducted following ISO 7404-5 [33]. The reflectance measurements were made on huminite using spinel (%R=0.420) as a standard and a photomultiplier tube (PMS) coupled to SpectraVision A.S&Co software.

3.1.5. Micro X-ray Fluorescence Mapping

Micro-XRF mapping was obtained using the Bruker-Nano M4 Tornado instrument. This system has a Rh X-ray tube with a Be side window and polycapillary optics giving an x-ray beam with a diameter of 25-30 µm on the sample. The X-ray tube was operated at 50 kV and 200 µA. X-rays are detected by a 30 mm^2 xflash® SDD with an energy resolution of <135 eV at 250,000 cps. All analyses were carried out at 2 kPa vacuum. Semi-quantitative maps were generated for major elements such as U, Fe, S and Ti.

4. Results

4.1. Organic Matter Sedimentology

Organic matter occurs as disseminated detrital particles (dispersed organic matter-DOM) within poorly consolidated coarse sand to clay lithologies. For instance, organic detrital particles can be found: 1) dispersed within poorly sorted sand layers with no visible internal structure; 2) concentrated into laminae of well-structured fining upward layers or bottom sets of dunes/mega ripples; 3) associated with clay rich intra-clasts located at the base of sandy layers and 4) dispersed within silt to clay rich layers.

Two typical samples of uranium enriched layers are presented in **Figure 2**. Maximum SSPγ counts/second (1523 c/s) are recorded at the erosional surface located beneath a base of layer rich in organic matter and clay. SSPγ counts/second decrease downward or upward this limit.

Uranium is concentrated inside underwater dune sediments (pebbles made of clay/detrital organic matter intraclasts, gravel and sand) that represent the base of the delta foreset slope. After burial, the oxidizing mineralized fluids are advancing through the well sorted coarse sandy to microconglomeratic deposits. The high energy depositional conditions during the formation of these sequences explain the absence of the fine fractions, which implies high permeability.

4.2. Organic Petrography

In organic petrography, the term vitrinite is used to distinguish between the organic matter that has reached a certain coalification stage in contrast to huminite that refers to peat material of very low maturity and poor gelification. Hence, considering the petrographic features of the macerals, the low burial depth (<500 m) [30] and the very low vitrinite reflectance measurements in the Zoovch Ovoo sands (%Rr=0.302±0.02), it can be concluded that the type III kerogen never reached the thermal maturity needed to be accredited as vitrinite. Therefore, since the organic matter is still in peat stage, the nomenclature that was used to describe the type III kerogen macerals belongs to the huminite group [34]. The macerals that were recognized during the organic petrography study are presented in **Figure 3** and discussed below.

4.2.1. Huminite Macerals

Most commonly telohuminite sub-group macerals such as textinite (intact and well-preserved cell-walls with open cell-lumens), ulminite (massive/homogenized structured huminite particles with minor open cell-lumens) and finally texto-ulminite (intermediate phase of textinite and ulminite with collapsed walls and partly open cell-lumens filled occasionally by gelified material), were recognized. Also attrinite (fragmental cell walls) is often encountered as well as corpohuminite (structureless bodies filling cell lumens) inside telohuminite macerals.

4.2.2. Inertinite Macerals

The inertinite group macerals were also very systematically encountered. In particular fusinite (charred material/charcoal from forest fires and less often tissues with strongly bonded oxygen) and semifusinite (either partially charred material from forest fires as fusinite or humic material that was partially oxidized by biochemical activity before or right after shallow burial). Finally, funginite (material of fungal origin) and inertodetrinite (fragments) were also very abundant.

4.2.3. Liptinite Macerals

Their abundance is very limited and they are not systematically present, compared to the huminite and inertinite group macerals. They were recognized under blue-light excitation (500 nm) as they obtain yellowish fluorescence. The only liptinite maceral recognized was cutinite which stands for the outer walls of the leaves, stems and other aerial parts of plants. As such

this maceral is resistant to degradation during sedimentary transport. Exceptionally solid bitumen (bituminite) may be found around silicates or inside the fracture porosity of large detrital grains. With respect to the preservation status of the macerals, both opaque and non-opaque, biostructured and non-biostructured (banded and pitted) phytoclasts were recognized; classified according to [35].

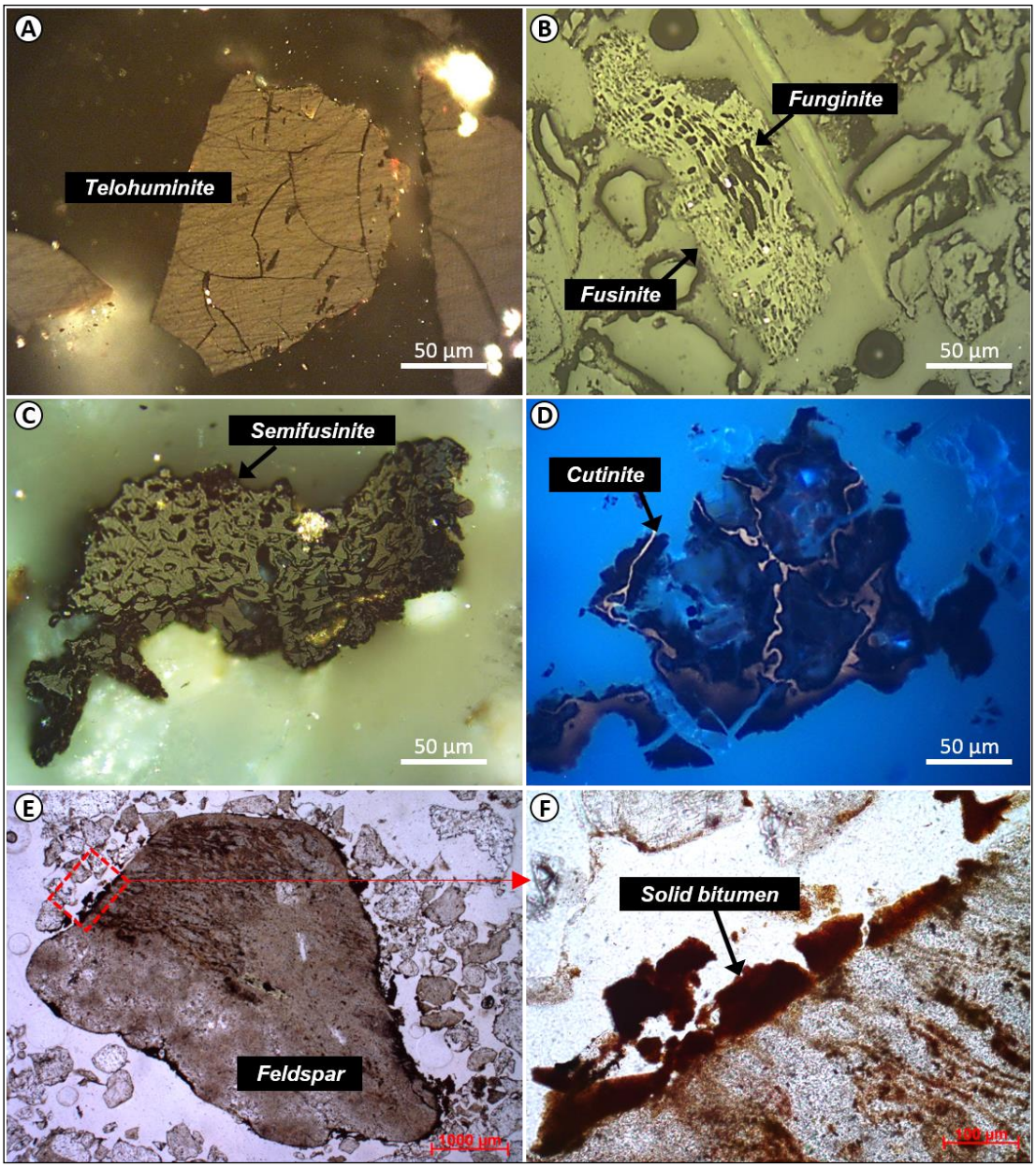

Figure 3. Presentation of the organic particles (macerals) recognized in the Zoovch Ovoo sands. (**A**, **B**, **C**) polished blocks under oil-immersion indicating telohuminite/telovitrinite, fusinite and funginite and finally semifusinite; (**D**) fluorescence mode on thin section indicating cutinite; (**E**, **F**) plain light on thin section showing solid bitumen penetrating and concentrating along the rims and fractures of a porous feldspar.

4.3. Petrography of Organic Matter-Uranium Associations and Mineral Geochemistry

Uranium mineral phases were studied in samples of variable lithologies, *e.g.,* matrix supported sandstones, sandstones cemented by dolomite as discussed in [36], and then analyzed by EPMA (**Table 1**). Two phases were identified: uraninite and coffinite, sometimes occurring together. Uraninite forms independent spheres at a minimum size range of 1 μm, while Ca-P-rich coffinite occurs as elongated flakes of 1-2 μm size (**Figure 4**). Aggregates of the previous two oxides are also common. In both minerals, Ca, Si, P, Zr and Ti are found in significant concentrations. The U+Ca versus Si binary plot (**Figure 4**) shows that data points distribute in between the two end-members. The most abundant U mineral is uraninite (UO_2), slightly deviated from the stoichiometric formula due to P, Zr and Ti enrichment. The second and less common is Ca-P-rich coffinite [$(U,Ca)(P,Si)O_4$]. Pure coffinite is absent.

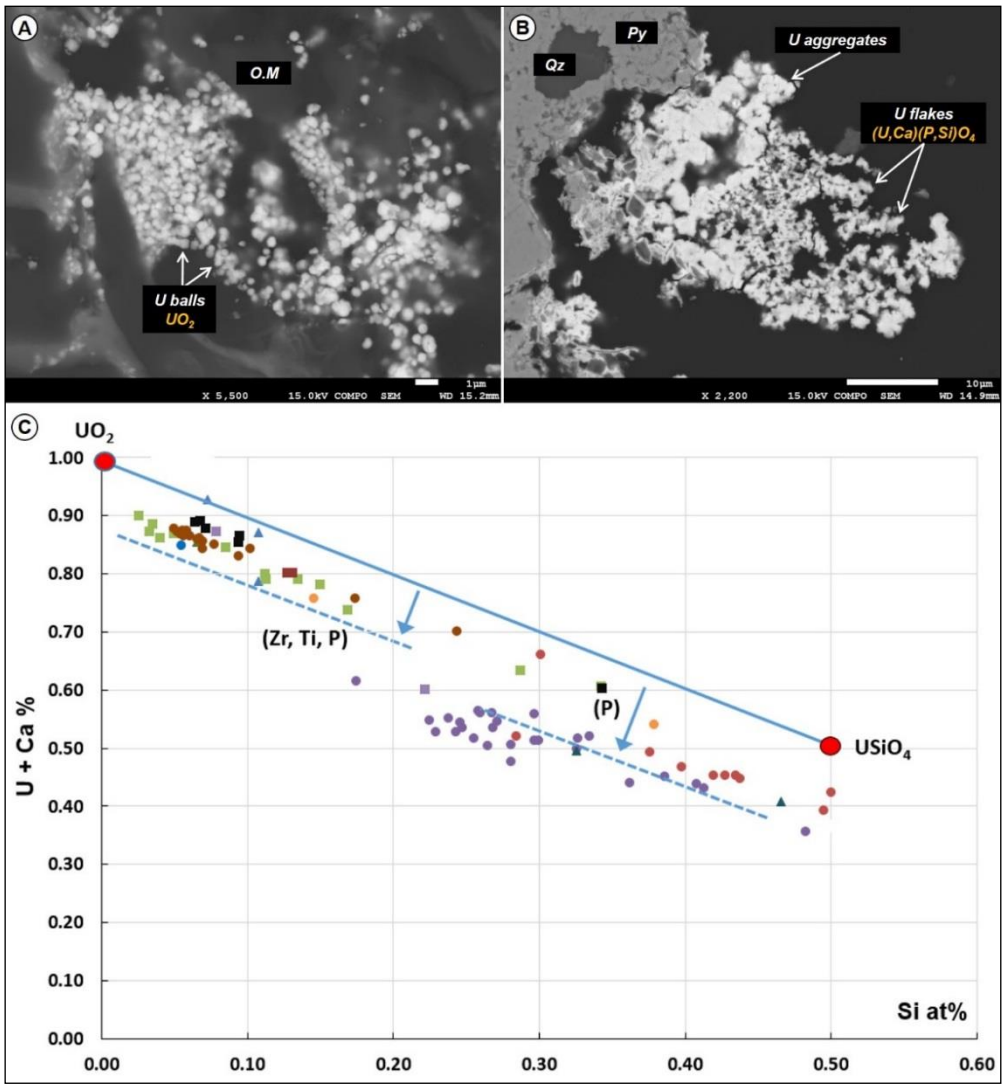

Figure 4. (A) Ternary plot of the P-U-Si, in wt% oxide, indicating the stoichiometric U-mineral domains of uraninite, phosphorus enriched uraninite, coffinite and phospho-coffinite, used as references (data from EPMA); (B) SEM images of uraninite (U-spheres) associated to organic matter and (C) Ca-P-coffinite (U-flakes) associated to pyrite. Aggregates of both U-minerals are also indicated.

Table 1. Most representative values and close to the end-members for uraninite and Ca-P-coffinite. Data obtained from EPMA.

Oxides mass%	**Uraninite**		**Coffinite**	
UO_2	76.28	76.48	61.92	56.58
SiO_2	1.20	1.30	6.65	12.69
P_2O_5	2.06	2.18	6.23	7.40
CaO	3.58	3.39	4.00	5.67
Total	83.12	83.35	78.80	82.34

With the help of SEM-EDS and micro-XRF it was possible to identify three different cases of uranium-organic matter associations, which are presented below.

4.3.1. U-rich Organic Matter Without any Distinguishable U-Phase

The organic particles in the Zoovch Ovoo sands can contain high concentrations of uranium. As illustrated by, the BSE image illustrates an assemblage of telohuminite and inertinite macerals, *i.e.,* texto-ulminite, corpohuminite and funginite **Figure 5**. Half of the macerals are fully epigenetized by framboidal pyrite, while the remaining contain pyritospheres at a very local scale. Based on the SEM-EDS chemical maps, corpohuminite is much richer in sulfur than texto-ulminite, while it is nearly absent from funginite except for its rims. Iron content is constant in both huminite group macerals while it is absent from funginite. Uranium shows higher concentration in corpohuminite. Titanium is always present at a rather low concentration. In addition, some disseminated Ti-oxides grains were identified.

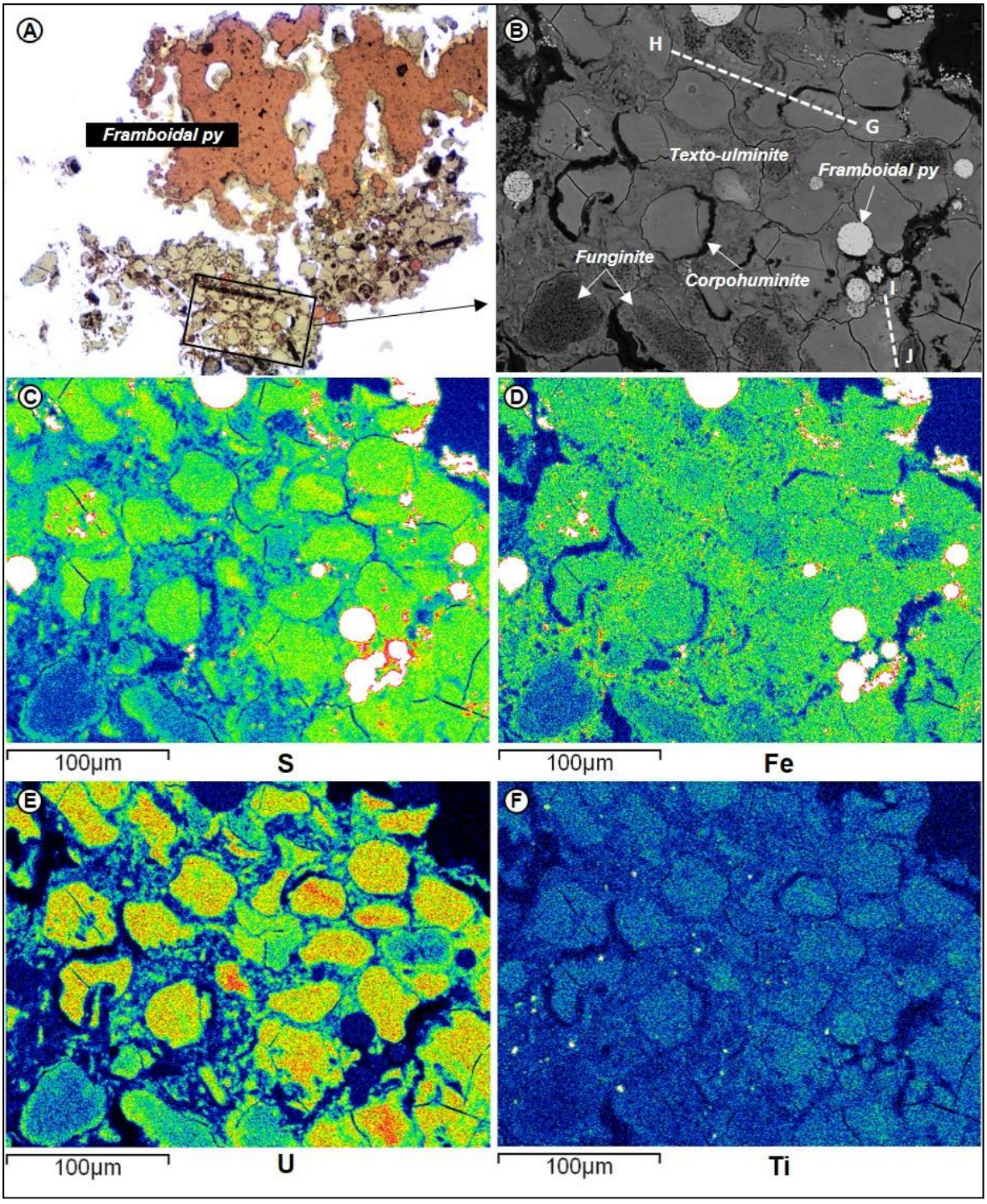

Figure 5. Organic matter relationship to U, Fe, S, Ti. The macerals corpohuminite, texto-ulminite and funginite are locally associated to framboidal pyrite (images **A**-**B,** under reflected light and SEM mode, respectively). U concentration profiles G-H and I-J of Figure 6 are also indicated. The SEM-EDS maps for S, Fe, U and Ti (images **C**-**F**) suggest that sulfur and iron are present in all particles, showing a preference for corpohuminite, then for texto-ulminite and finally for funginite. Likewise, the uranium concentration follows the same preference pattern. In some cases, certain corpohuminite particles are particularly enriched in U. Titanium is mainly dispersed at low concentration in macerals but is also contained as microsized Ti-oxides.

The concentrations of U, Fe, S and Ti of the two profiles G-H and I-J of **Figure 5**b, are presented in **Figure 6**. Profile G-H interests both corpohuminite and texto-ulminite macerals and shows that the corpohuminite contains up to 20 wt%, while texto-ulminite U concentration fluctuates between 7 and 12 wt%. For certain parts of the profile, S and Fe concentrations vary together and indicate the presence of pyrite micro-crystals. In other parts S and Fe they are not perfectly correlated. Titanium concentration is nearly constant around 0.5 wt%. Profile I-J was performed strictly within a corpohuminite particle: U ranges between 16 and 22 wt% U, sulfur and iron between 4-5 wt% with no visible optical expression of sulfide.

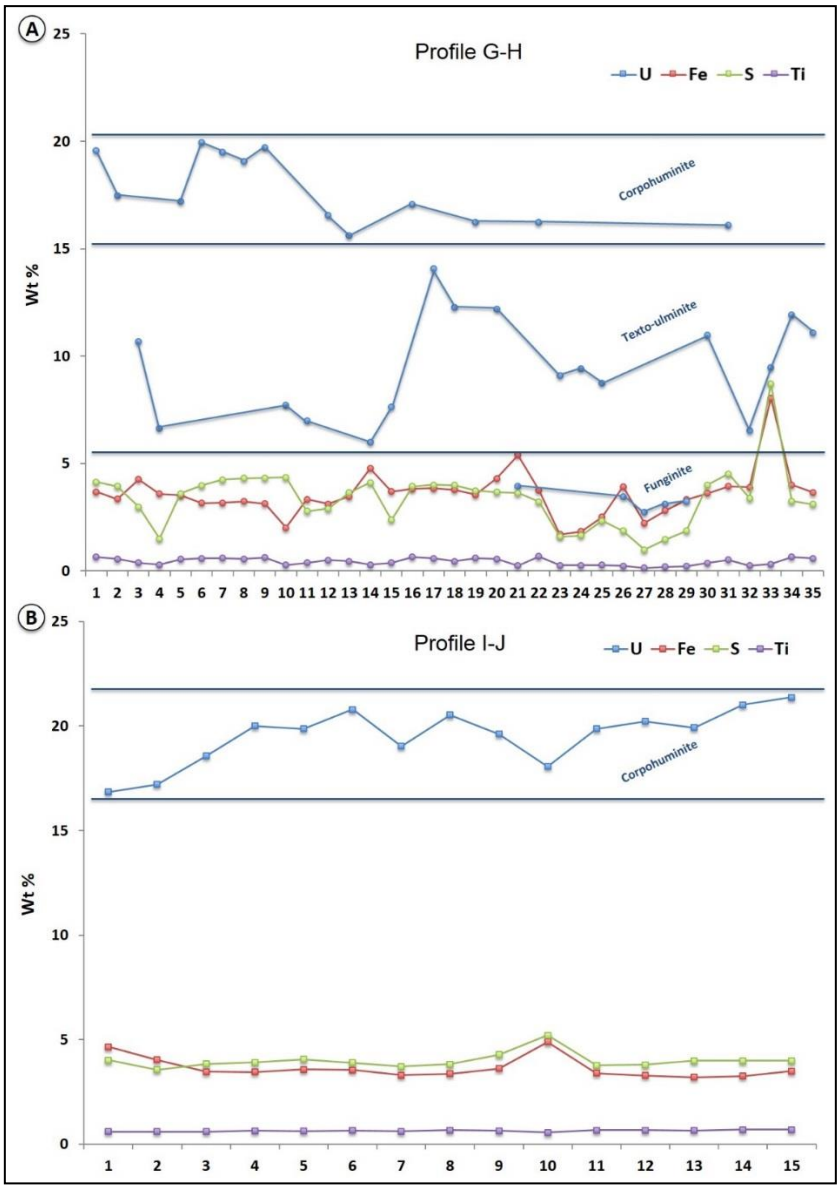

Figure 6. The profiles G-H and I-J presented in Figure 5. Profile G-H indicates that the composition of uranium in corpohuminite is more than double compared to the texto-ulminite background, reaching 19 wt%. Sulfur and iron concentrations are not perfectly correlated and several datapoints show antagonistic behavior. Profile I-J was performed on a single corpohuminite particle and shows that uranium concentration is between 16-22 wt%. Sulfur and iron are sub-constant and correlated, which could be related to pyrite nanocrystal inclusions. Titanium is sub-constant and around 1 wt% for both profiles.

A binary plot for S and Fe (**Figure 7**) was constructed from the profiles G-H and I-J **Figure 5** and **Figure 6**, with the reference stoichiometry lines for pyrite (FeS_2) and amorphous FeS (*e.g.,* mackinawite). Profile G-H that refers to the transition between corpohuminite and texto-ulminite particles, shows Fe concentration between 1.8 and 8.0 wt% while S fluctuates between 1.0 and 8.5 wt%. Most of the data points plot away from the pyrite composition reference line by approximately 2.0 wt% Fe. Few data points correspond to a slight enrichment in S from the reference line by a maximum of 1.5 wt%. Hence, although some data points distribute along the pyrite stoichiometry line, there are clear deviations in the data point distribution from FeS_2 line towards the FeS line. In the profile I-J that refers to corpohuminite, Fe concentration varies between 3.2 and 4.9 wt%, whereas S is between 3.5 and 5.1 wt%. Most of the data points are tightly plotted and close to pyrite stoichiometry line, which could indicate the presence of nanometric (<0.1 micron) pyrite inclusions similarly to the data obtained on the profile G-H.

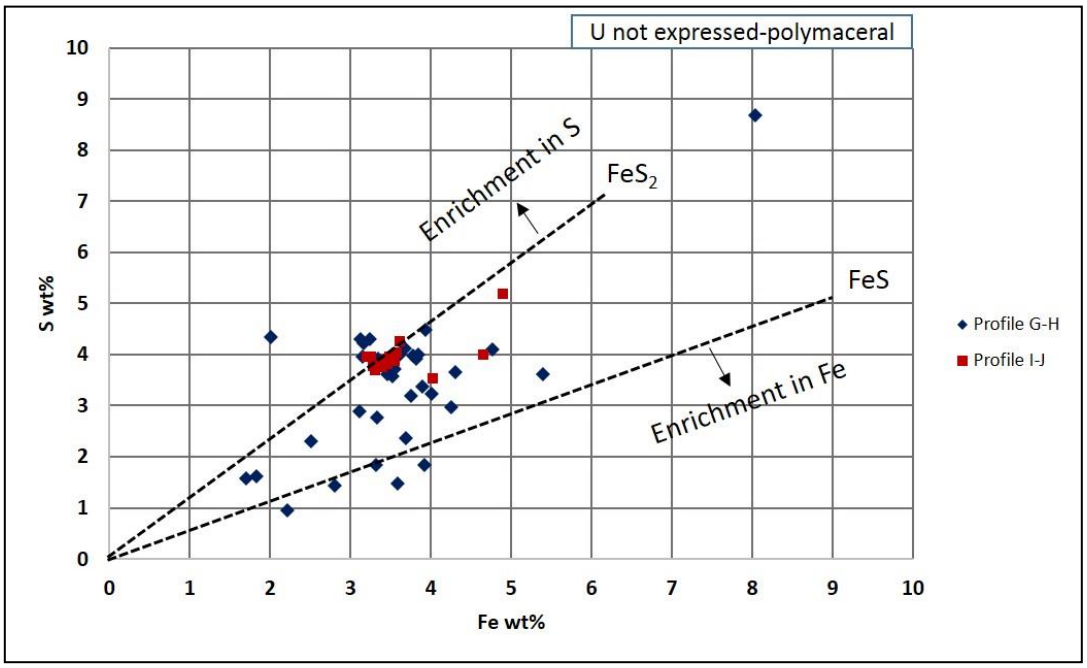

Figure 7. S-Fe binary plot, illustrating profiles G-H and I-J presented in Figure 5..

A root structure composed of telohuminite macerals, particularly textinite to texto-ulminite was also analyzed (**Figure 8**). The concentrations of U, Fe, S and Ti along the profile A-B of the root structure is presented in **Figure 8**C. The U concentrations are between 10 and 20 wt%. Sulfur concentrations fluctuate slightly around 2.5 wt% but can reach 5.5 wt%, whereas iron is less than sulfur by approximately 1 wt%. Titanium is contained below 1.0 wt%. Profile C-D refers to the external part of the root. In this profile (not presented), the U concentration fluctuates between 15.0 and 3.0 wt%. Titanium reaches at maximum 1.2 wt%.

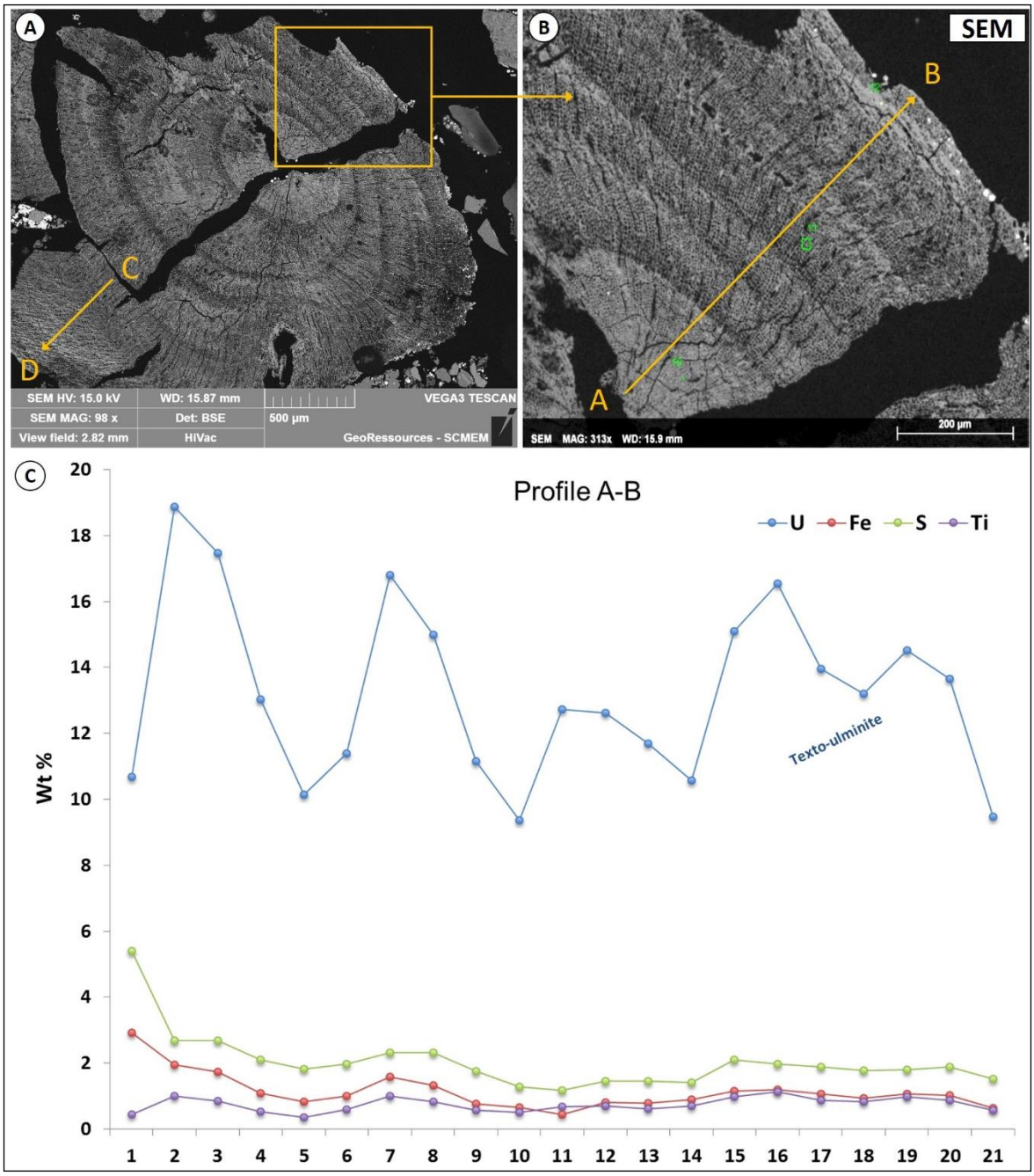

Figure 8. (A) View of a well preserved root structure (telohuminite), typical of the organic matter contained in the Zoovch Ovoo sediments and the associated X-Ray microfluorescence maps; (**B**) Zoomed image of a part of the root highlighting the EPMA profile (A-B) for U, Fe, S, Si, Ti respectively. **(C**) According to the EPMA profile A-B performed on a root structure (texto-ulminite), S and Fe are always present inside the particle, whereas their stoichiometry does not indicate pyrite. Titanium is also present in minute quantities (<1 wt%). Uranium concentration fluctuates between 10-19 wt%.

Sulfur and Fe concentrations along profiles A-B and C-D are projected on a binary plot (**Figure 9**). Fe-S data for the internal part (A-B) of the root are very close to pyrite stoichiometry. The external profile (C-D) shows a trend enriched in Fe from 1 to 8 wt% while S fluctuates between 0.5 and 2.8 wt%. Data points from both profiles indicate an enrichment in S up to 1 wt%

compared to pyrite stoichiometry, while Fe enrichment may exceed mackinawite stoichiometry in profile C-D.

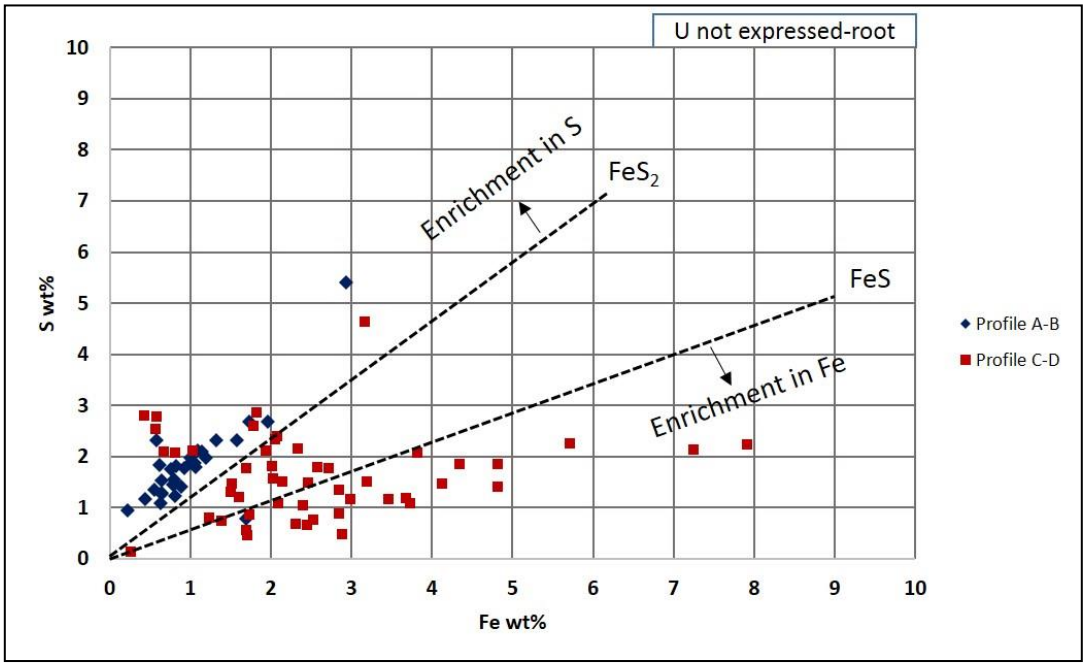

Figure 9: S-Fe wt% composition plot derived from the EPMA measurements along profiles A-B and C-D presented in Figure 8. Profile A-B was performed on the internal part of the root structure, whereas C-D in the external. For the internal part the data points in blue distribute close to the pyrite line, with a slight relative sulfur enrichment. For the external part, most data points in red indicate significant Fe enrichment at constant S concentration.

4.3.2. Uranium Oxides Precipitated at the Contact of the Organic Particle

UO_2 infillings occur most frequently around organic matter particles or within maceral micro-fractures as confirmed by micro-XRF maps (Figure 10A, B). In the particle presented in Figure 10A, uranium concentration is rather low, and there are two distinct distributions of Fe and S: a) as pyrite micro-inclusions, observed under reflected light microscopy and confirmed by micro-XRF, and b) as zones enriched either in Fe or S with the two elements not correlated (Figure 10 C and D). In Figure E, and F other examples of U phases distributed at the rim of organic particles are shown. Sometimes when a telohuminite particle has large open pore spaces or fractures in the interior, uranium can as well precipitate there as oxide (Figure 10H).

In more detail the U concentration along the fracture in the internal part of a telohuminite particle is typical of UO_2 and in the maceral, it decreases gradually to 2 wt% from the fracture. It can be noted that a few percent (*i.e.,* 3-5 wt%) of U inside the organic particles can significantly increase the average atomic number (Z) under BSE mode. The heterogeneous distribution of Z in an organic particle reveals thus the U distribution.

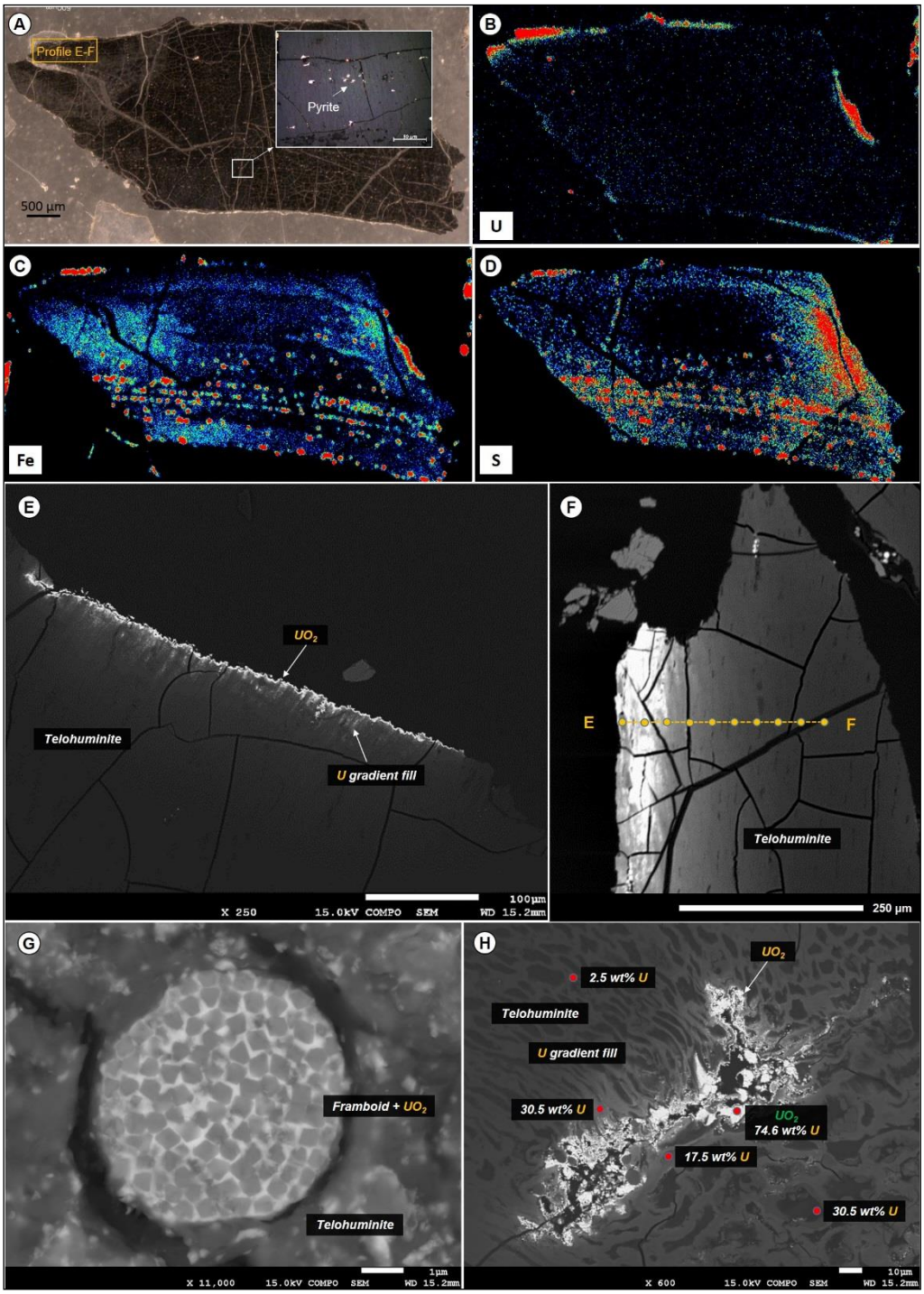

Figure 10: Telohuminite particle and the associated X-Ray microfluorescence maps; (**A**) Overview of the particle under reflected light, showing the EPMA profile position E-F for U, Fe, S and Ti respectively and a zoomed image showing the presence of pyrite. (**B, C**, **D**) the XRF maps for U, Fe and S. Uranium is concentrated around the rims in high concentration and is much less abundant towards the interior of the particle. (**E**) BSE image showing uranium oxide precipitate (in this case UO_2) at the rim of a telohuminite particle; (**F**) The same association in higher magnification, coupled with an EPMA measurements profile (E-F) (10 points), from the rim to the interior of the maceral particle. (**G**) Uranium cement inside framboidal pyrite; (**H**) Uraninite precipitation along a fracture in the internal part of a telovitrinite/telohuminite particle. Uranium concentration decreases progressively from 74.6 to 2.5 wt% as a function of increasing distance from the fracture.

The distribution of U, Fe, S and Ti for profile E-F covers a distance of about 300 µm from the rim where there is UO_2 expression towards the interior where there is no mineral expression for U (**Figure 11**). Uranium concentration reaches about 20 wt% in the organic particle without being expressed as a visible phase and about 40 wt% when it is expressed as uraninite/Ca-P-coffinite. Sulfur, Fe and Ti are constantly below 0.5 wt%.

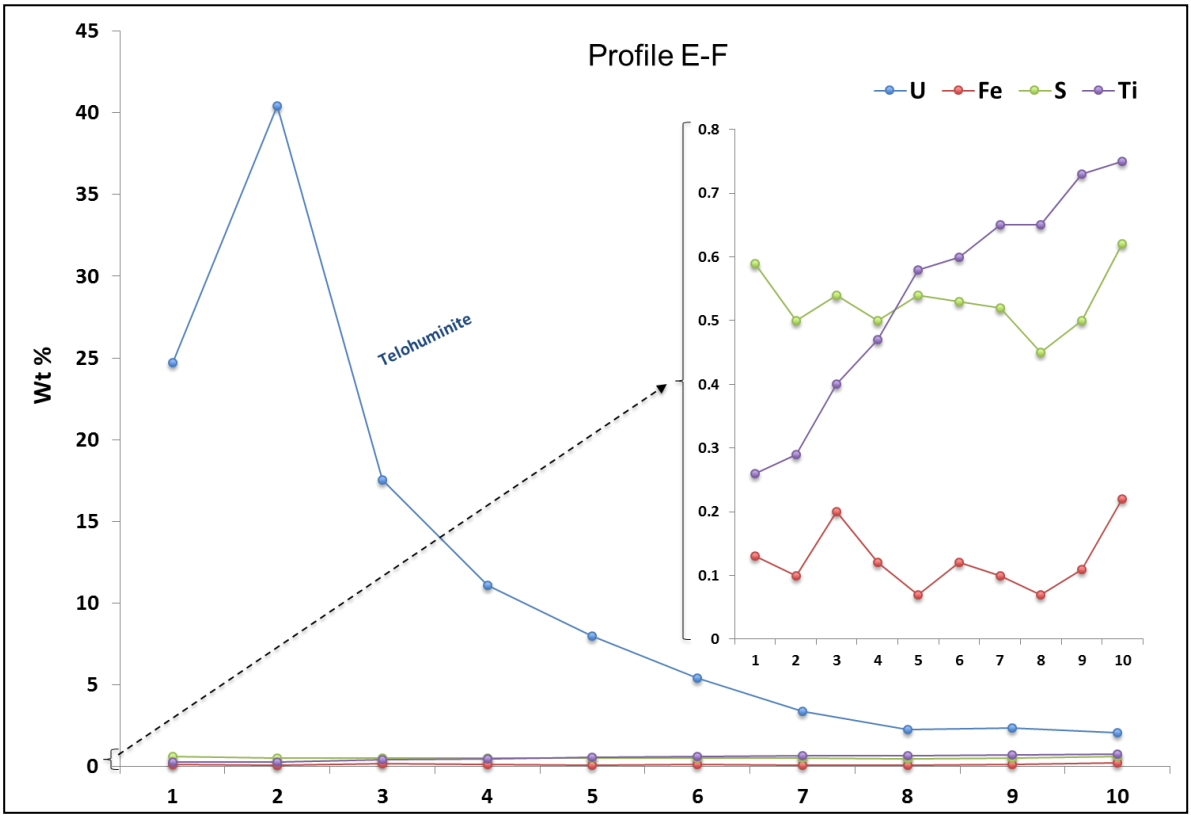

Figure 11. Profile E-F was performed on a telohuminite particle with uranium expressed as UO_2 at the rims. U concentration starts at 25 wt% at the rim. As shown in Figure 10F the first point was measured on a part of the particle where UO_2 is not expressed as uraninite. The next spot was measured on a part where U is expressed as uraninite and hence the concentration is raised to 41 wt%. Afterwards the U-concentrations decrease proportionally as a function of increasing distance from the particle rim. The Fe and S concentrations are respectively at 0.1 wt% and 0.5wt% (detection limit of 0.1%) as shown in the upscaled part of the graph. Titanium concentration is increasing from the rim towards the interior of the particle, from 0.26 to 0.75 wt%.

In the binary plot of S and Fe (**Figure 12**) it is clearly demonstrated that the telohuminite particle associated to U expressed as oxide at the rims is almost depleted for both sulfur and iron, though they are plotted very close to pyrite stoichiometry.

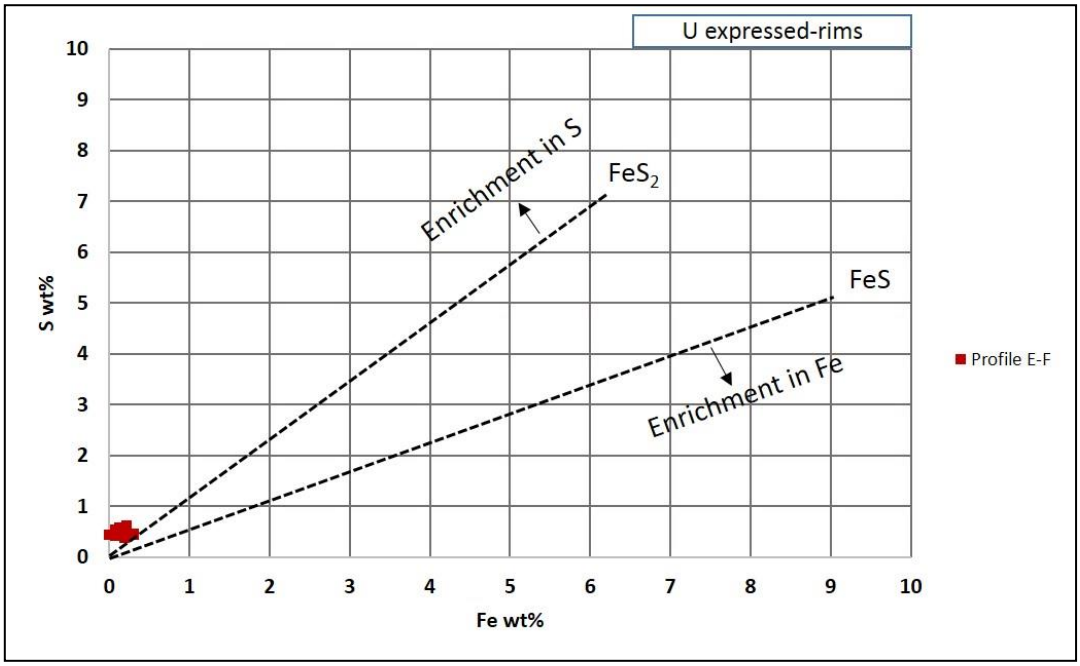

Figure 12: EPMA S and Fe concentrations measurements of profile E-F performed on a telohuminite particle (eu-ulminite) plotted into the S vs Fe wt%, S and Fe are always below 1 wt%, slightly enriched in S. Reference lines refer to the stoichiometry of FeS_2 (pyrite) and FeS (i.e. mackinawite).

4.3.3. Uranium Phases Replacing Entirely Organic Matter

The UO_2 crystals progressively replace almost entirely the organic carbon of the macerals. According to the *in situ* SEM-EDS analyses the macerals can contain more than 65 wt% U that corresponds to mix analysis of UO_2 and OM with approximately 20 wt% carbon. Fully replaced organic particles have 75-77 wt% U (**Figure 13**) with an additional few percent of Ca, Si and P.

It is also noted that even in the case of full organic matter replacement, some textural characteristics of the plant debris are preserved *i.e.,* cell walls and desiccation cracks, indicating fine-grained epigenization processes. Very often disseminated framboidal and euhedral pyrite are also present inside the U-replaced organic particle. Collapsed cell walls (attrinite) sometimes surrounding euhedral pyrite crystals can also be fully replaced by U, reaching 67 wt%, while becoming enriched in Ca, Si, and P. With progressive U epigenesis even the macerals with minor permeability are replaced.

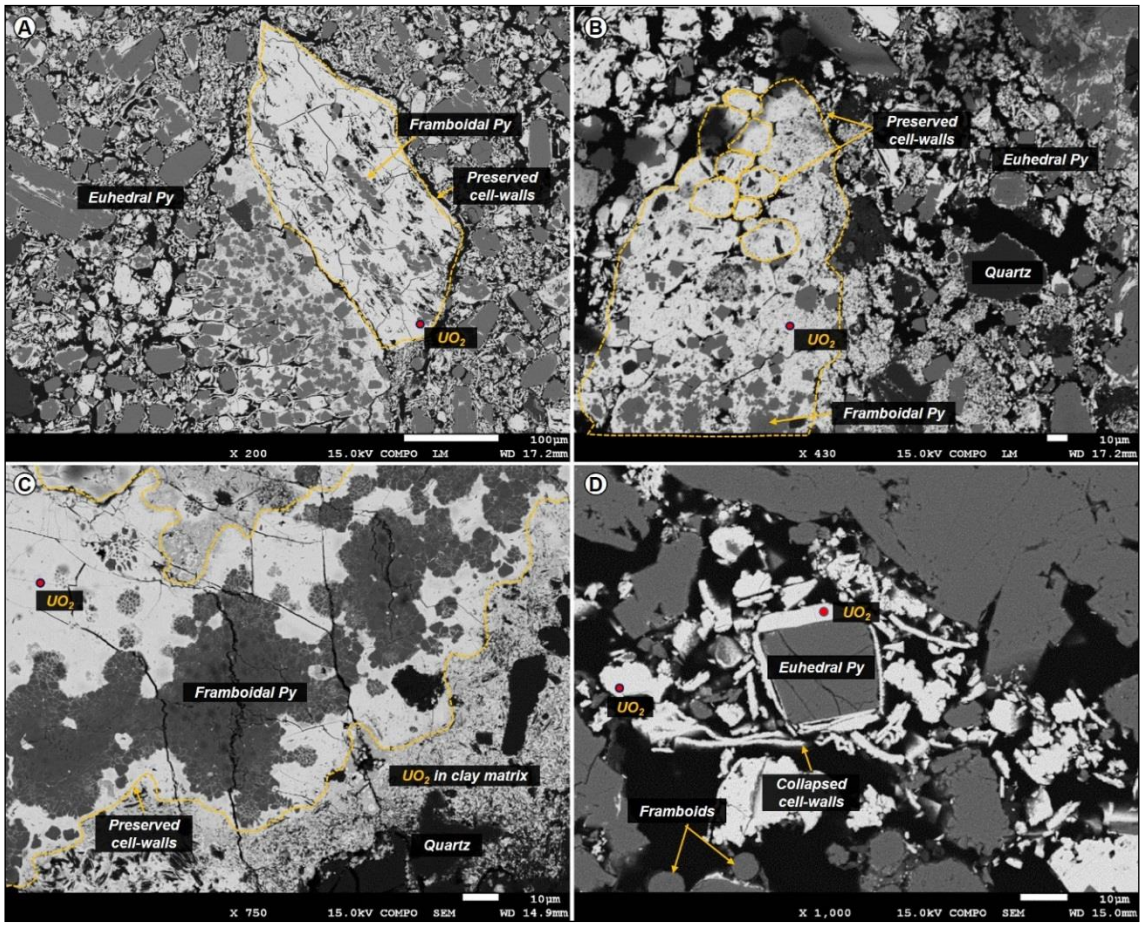

Figure 13: Examples of organic matter replaced by uranium, which is expressed in oxide form at the rims of the organic particle with a composition close to UO_2 stoichiometry (as measured under SEM-EDS mode); (**A**) Telohuminite particle at the size range of 400 µm, with the textural characteristics (cell walls and desiccation cracks) still visible; (**B**) Elongated gelohuminite particle composed of smaller epigenetized corpohuminite particles; (**C**) A fully uranium cemented organic particle associated to framboidal pyrite which shows features of corrosion and replacement by uranium. The cell-walls of the particle are preserved even after replacement. The particle is surrounded by U-rich clay matrix; (**D**) Collapsed cell walls structures (attrinite) surrounding a large euhedral pyrite crystal.

5. Discussion

5.1. Detrital Organic Matter and U Distribution in Sediments

5.1.1. Origin of Organic Matter

According to sedimentological core analysis, peat accumulation and coal layers are absent inside the reservoir zone. The organic matter contained in the Zoovch Ovoo sands occurs as detrital particles deposited accordingly to the sedimentary bedding structures. Maceral analysis indicates that the organic particles are of higher plant origin and can be found in either reduced (huminite group macerals) or oxidized (inertinite group macerals) state. The coarse, angular and poorly sorted organic particles are linked to distant transport (reworked), within high energy flood-dominated depositional conditions associated to coarse to medium sized lithologies (coarse to medium fine grained sands). Organic matter particles encountered in fine clay layers

are better preserved and linked to calm depositional conditions. The well preserved phytoclasts, such as root remains associated to fine grained organic rich lithofacies could be indicative of higher plants which grew within the depositional environment, *e.g.,* after no significant transport. Maceral morphology ranges from intact to partially collapsed tissue, indicating that there are more than one organic matter sources and that the preservation stage of the maceral is directly linked to the distance from those sources. In principle, the more distal the source the more fragmented/oxidized the organic particle reaches the basin [37]. Hence, it could be proposed that there are two main potential sources, a proximal for the well-preserved huminite group macerals and a distal for the angular lath-shaped inertinite group macerals.

Bituminite represents an exception and refers to liquid organic matter formed during vitrinite diagenesis i.e. the coalification process that transforms peat stage material to higher rank coal [38]. Bituminite is not abundant and when present it was found located around or inside fracture porosity of large silicates grain (>0.5 mm size).

5.1.2. Uranium Uptake from Interstitial Waters

Dissolved uranium in surficial waters results generally from the dissolution of accessory minerals during weathering of the outcropping formations and is transported as uranyl species in oxidizing media [39]. The processes of uranium-organic matter interactions in shallow buried sediments is complex and involves both processes of complexation and adsorption, followed by reduction of the uranyl ion [16,4,41,8].

The process of chemical complexation was thoroughly described by [7,11]. Laboratory experiments showed that the complexation of uranium (without reduction) by the carboxyl groups of terrestrial organic matter is possible, by forming uranyl-carboxyl compounds even at low temperatures (20-45°C). They also showed that $U^{(VI)}$ reduction to $U^{(IV)}$ would require high temperatures (reaching 250°C) and this could be achieved either during late diagenesis or during hydrothermal conditions. However, not all terrestrial organic matter is able to form U-complexes. It must be rich in oxygenated functions, particularly in carboxyl groups. [7] studied two humic substances, one with a vitrinite reflectance of 0.50% (Gardane lignite, Late Cretaceous) and another of 0.34% (Arjuzanx lignite, Late Miocene-Pliocene). The two lignite samples underwent the same laboratory procedure to test their potential to complex U at low temperatures from a U-rich fluid. It was proved that only the lignite of lower reflectance adsorbed uranyl cations UO_2^{2+} without reduction [42]. The complexation of uranyl resulted in pH increase, decrease of UO_2^{2+} concentration and simultaneous increase in H^+ as hydrogen was substituted and hence liberated from lignite by ion exchange. FT-IR analysis revealed that all along uranyl complexation, the carboxylic acids and ketonic groups (C=O) were progressively decreasing, whereas the aromatic groups (C=C and COO-) were increasing

[43,11]. The conclusion was that the abundance of carboxylic functional groups in organic matter plays a major role in uranium complexation.

Another similar case of soluble $U^{(VI)}$ species fixed by lignite of low maturity, resulting to the formation of UO_2^{2+} complexes was reported by [12] who studied lignite from the Coutras U-ore deposit, France. Though this immature lignite was never subjected to elevated temperatures it can contain up to 19 wt% uranium without any distinguishable visible form.

From the above it could be suggested that the lignite from Arjuzanx (Landes, France; Late Miocene or Pliocene; [7]) as well as the lignite from the Coutras (Gironde, France; Middle Eocene; [12]) could be used as direct analogues of the Zoovch Ovoo case, since they both demonstrate the same low level of maturity and have trapped uranium at low temperatures, between 20-45°C (maximum burial temperature at Zoovch Ovoo is estimated at 40°C according to [28,30,37]. The stage of chemical complexation of uranium without reduction uptaken by organic matter may be considered as the earliest stage of U concentration. Though deep burial is a priori excluded in Zoovch Ovoo, it is still difficult to know at which time the U-enrichment of macerals occurred. Hence, there are two possible stages: i) during sedimentation (syngenetic), or ii) during the shallow burial of the sediments (early diagenetic).

5.1.3. Uranium Trapping Processes Involving Organic Matter at Zoovch Ovoo

Three factors seem to control the epigenization process of the macerals: 1) the permeability around the macerals; 2) the porosity of the macerals and 3) their chemical composition. The process is heterogeneous as the organic matter-uranium associations are not a function of the maceral group *i.e.,* huminite/vitrinite or inertinite and all macerals from the same group have not undergone uranium epigenization.

Among the macerals, texto-ulminite (cell-walls) and corpohuminite (filled cell-walls) show most often high uranium concentration without expression of a visible U phase. In these macerals, the U concentration is rather homogeneous and reaches 15 to 20 wt%, which is similar to the 19 wt% described in [12], but higher than the 5 wt% reported in [44] and the 8 wt% in [45]. In particular corpohuminite can host twice the concentration of U compared to adjacent texto-ulminite macerals. This feature is apparently linked to the chemistry of the macerals and could be related to the abundance of carboxylic functional groups known to be responsible for U complexation [11,42,8]. The U speciation in these macerals could not be determined as no U bearing phase larger than the resolution of SEM (around 0.1 microns) could be observed. [12] considers that U dispersed in organic matter occurs under its reduced state $U^{(IV)}$, and is probably under the form of small size U-oxides.

Direct reduction by organic carbon is also likely to occur [46]. [11,7] suggest that aliphatic hydrocarbons may be involved in the reduction of $U^{(VI)}$. Yet, their experiments suggest that this

mechanism is significant at T>120°C, which is not the range of temperatures experienced in the Zoovch Ovoo deposit.

Organic matter of low thermal maturity like the one encountered in the Zoovch Ovoo deposit can sustain microbiological activity [47-50]. Especially in the presence of sulfates, sulfate reducing bacteria may be active and generate reduced sulfur species *i.e.* H_2S/native sulfur [51,52].

Another possibility of U reduction is the mechanism of biomineralization (by bacteria and fungi), previously studied by [47] and by [49] in laboratory experiments and in the case of Chinese roll-front systems respectively. Both studies showed that during the mineralization stage it is possible to enzymatically reduce U into uraninite/coffinite by dissimilatory bacteria, which could use $U^{(VI)}$ as the sole electron acceptor instead of other multivalent metals such as $Fe^{(III)}$. Amorphous UO_2 may be the result of such processes. Indeed, besides complexation and sorption, a third mechanism was recently proposed by [53]: the formation of $U^{(IV)}$ biofilms which evolve into biogenic non-crystalline $U^{(IV)}$ compounds. Thus, using EXAFS spectroscopy data, these authors revealed the role of microorganisms in the reduction of $U^{(VI)}$ and the formation of disseminated $U^{(IV)}$ in organic matter which acts as nutrient and a trap

For Zoovch Ovoo, the successive stages of uranium-organic matter epigenization are summarized in (**Figure 14**). Most values for uranium concentration in organic matter range from 10-20 wt%. In that case that the speciation of U is not known and the crystal size lower than 0.1 µm. It was also observed that when the concentration reaches 40-45 wt%, UO_2 minerals are systematically present. The epigenization process is not the same for porous and non-porous macerals, hence two different pathways are proposed. In the case of non-porous macerals, for instance texto-ulminite with fully fused cell-walls (**Figure 10**), the epigenization starts by the rims and internal fractures, if any are present. In the case of porous macerals, *i.e.,* textinite (**Figure 8**) and funginite (**Figure 5**) the epigenization will be more pervasive. The progressive accumulation continues until the particle is fully replaced (about 78 wt% U).

When an organic particle is composed of different macerals, pores in between the different macerals enhance fluid penetration resulting in a more homogenous epigenization, similarly to what was described by [12]. In addition, it was observed that certain macerals *i.e.* corpohuminite (**Figure 5**) will accumulate uranium in greater amounts than texto-ulminite or fusinite.

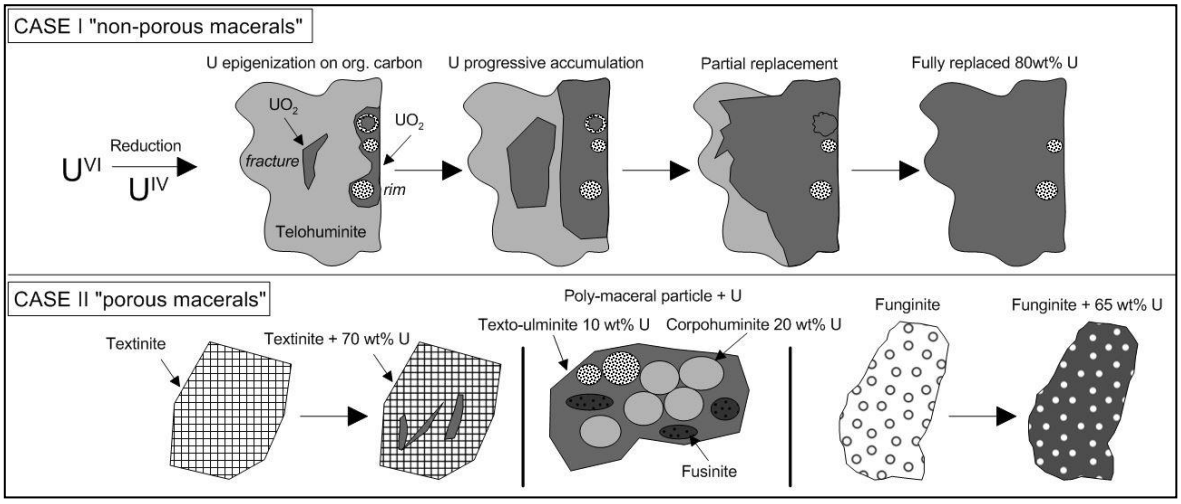

Figure 14. Graphical representation of the organic matter epigenization by uranium. Uranium is carried in solution as $U^{(VI)}$ until it encounters a reducing agent and becomes $U^{(IV)}$. When uranium is reduced in the presence of macerals it can be concentrated around internal fractures or at the rims of the maceral as uranium oxide. There is a linear decreasing concentration gradient from the rim where U is expressed as oxide towards the interior where no mineral form is visible. Eventually the replacement process keeps up, leading primarily to partial and progressively to full replacement (i.e. organic particles with up to 78 wt% uranium). One of the main aspects of this replacement process is that the fully replaced organic particle maintains its textural characteristics although organic carbon is no longer present.

5.1.4. Iron and Sulfur in Organic Matter Particles

The relative amounts of Fe and S are following approximatively the stoichiometry of pyrite although iron sulfides are not always visible on SEM images and micro-XRF maps. However, significant shifts in stoichiometric relationships are observed (**Figure 7**) and confirmed by the micro-XRF maps where some parts of the macerals are enriched in Fe and other in S. [12] also referred to iron and sulfur organic compounds contained in natural organic matrix that were not linked to iron sulfides. Dichloromethane extraction of the samples followed by gas chromatography-mass spectrometry allowed to identify the presence of elemental sulfur. Its presence may be linked to sulfate reducing bacteria. Yet, the redox state of iron (when not associated to sulfur) in the organic matter of the studied samples is not easy to determine. However, in regards to the reducing environment (organic matter, reduced species of sulfur, $U^{(IV)}$ minerals) it is highly probable to be $Fe^{(II)}$. $Fe^{(II)}$ may originate from the dissolution of detrital grains (*e.g.,* biotite) or may arise from microbial activity (reduction of $Fe^{(III)}$ carried together with $U^{(IV)}$ by the mineralizing fluid).

Thus, when associated in stoichiometric proportions, iron and sulfur may reflect the presence of the amorphous phases, which are precursors to pyrite as disordered mackinawite of formula $Fe_2(HS)_4$ [54] or Fe_3S_3 $(H_2O)_6$ [55], ordered mackinawite, and greigite Fe_3S_4 [56-58], as illustrated on **Figure 7**. This might explain the absence of identified pyrite crystals in the organic matter. Compositions consistent with pyrite stoichiometry may indeed be indicative of

microcrystals. Excess of iron or sulfur in the analysis may be linked to $Fe^{(II)}$ carboxylates as well as S^0 adsorbed to organic matter.

5.1.5. Sedimentological Control of Organic Matter and Uranium Distribution

Uranium geochemical anomalies as presented in **Figure 2** are systematically associated to organic rich layers or intraclast accumulations. The sediments accompanying the anomalies are usually very coarse to coarse. This feature suggests that the uranium bearing fluid is initially controlled by permeability, migrating along the coarser part of the sand layers (and along layers boundaries *e.g.,* erosional surfaces). Detrital organic matter particle accumulations in the vicinity of these highly permeable layers will then act as trap and participate to the complexation and reduction processes to $U^{(IV)}$ as explained above. Since grain size of the sediments and organic matter distribution are of direct inheritance of the sedimentary depositional system, it could be suggested that the migration of the U bearing fluids as well as the U trapping by the organic matter are under sedimentological control at core scale.

6. Conclusions

Very high levels of uranium concentration (a few percent up to 78 wt%) were found in the detrital organic matter of the Cretaceous sands from the Zoovch Ovoo deposit in Mongolia. Such concentration levels have never been reported to occur in the other roll-front U deposits from the large uranium province of Central Asia which extends from Kazakhstan to China and Mongolia. This peculiarity asked the question of the role of the organic matter in the uranium deposit.

Petrographic as well as geochemical investigation of the maceral particles allows to propose the following:

Organic matter present at Zoovch Ovoo is land plant derived and occurs as detrital particles concentrated into clay layers, clay intraclasts or sandy laminae. Biological features of particles are more or less preserved depending on their transportation (proximal or distal origin). Its thermal maturity is very low (peat to lignite stage; $\%R_r$=0.3).

Maceral particles show high concentration (up to 20 wt%) of U not expressed as oxide (detectable under SEM). It is very likely that $U^{(VI)}$ is adsorbed as uranyl-carboxyl groups. The organic matter particles have therefore captured U from circulating fluids at low temperature (T<40°C). It is not yet clear if the trapping occurred during sedimentation (pre-concentration stage) or during the roll-front events or both.

The land plant particles concentrated microbiological activity which triggered biodegradation, iron as well bacterial sulfate reduction. The absence of detectable pyrite crystals in the organic matter despite the presence of Fe and S in often non FeS_2 stoichiometric proportions suggests

the presence of other forms of sulfur, such as amorphous FeS phase (*e.g.*, mackinawite) and/or elemental sulfur.

The distribution of UO_2 in the organic particles seems to be linked to porosity/permeability of the organic structure which may be a control of fluid accessibility to the macerals. Organic matter particles can be fully replaced by UO_2 with partial preservation of organic structure (suggesting an epigenesis).

As burial diagenesis is too low to consider reduction of $U^{(VI)}$ by carbonaceous moieties, it is suggested that microorganisms are mainly responsible for the reduction of $U^{(VI)}$, either directly through their physiological activity or by providing reduced sulfur (which is an efficient reducing agent for $U^{(VI)}$. Furthermore, $Fe^{(II)}$ carboxylates may also be considered as possible reducing agent [59]. The $U^{(IV)}$ speciation can be better understood by using EXAFS. Thus, it is necessary to identify the potential presence of biogenic non-crystalline $U^{(IV)}$ compounds within the macerals.

From this study it may therefore be concluded that at least two controls of different scales can be considered for the Zoovch Ovoo uranium deposit:

At the scale of the sedimentary particles, organic matter plays a capital role on uranium deposition as it acts as a uranium trap through complexation and sustains the $U^{(VI)}$ reduction mechanism into UO_2 through biological activity.

At the scale of the sedimentary deposit, organic matter distribution as well as the permeability network allowing the circulation of uranium bearing fluids are controlled by the sedimentary architecture.

Author Contributions: Conceptualization, D.R, R.M and M.C.; Methodology and Data Curation, D.R, R.M and M.C.; Validation, M.B and O.P.; Writing—Original Draft Preparation, D.R.; Writing—Review & Editing, D.R., R.M., M.B., O.P. and M.C.

Funding: This work was performed and funded in the research framework between ORANO Mining and CREGU (*Centre de Recherches sur la Géologie des Matières Premières Minérales et Energétiques*), in the Laboratory of GeoRessources in Nancy, France.

Acknowledgments: We are grateful to COGEGOBI's geological team for the hospitality and the equipment provided during the field work as well as for taking care of the shipping of the samples from Mongolia to France. People from the laboratory of GeoRessources, in particular Andreï Lecomte and Olivier Rouer are acknowledged for the crystal chemistry analyses and the manipulation of the analytical means. The MicroXRF used is an equipment co-funded by ICEEL (Carnot institute)-CREGU-Labex Resources 21 (reference ANR-10-LABX 21-LABEX

RESSOURCES 21) and FEDER. Finally, the authors would like to help both anonymous reviewers for improving this manuscript.

Conflicts of Interest: The authors declare no conflict of interest.

References

1. Nash, J.T.; Granger, H.C.; Adams, S.S. Geology and concepts of genesis of important types of uranium deposits. *Economic Geology,* **1981**, *75*th Anniversary Volume, pp. 63-116. doi.org/10.5382/AV75.04
2. Meunier, J.D.; Landais, P.; Monthioux, M.; Pagel, M. Oxidation reduction processes in the genesis of the uranium-vanadium tabular deposits of the Cottonwood Wash mining area (Utah, USA): evidence from petrological study and organic matter analysis. *Bulletin de Minéralogie*, **1987**, *110*, pp. 145-156.
3. Landais, P.; Connan, J.; Dereppe, J. M.; George, E.; Meunier, J.D.; Monthioux, M.; Pagel, M.; Pironon, J.; Poty, B. Alterations of the organic matter, a clue for uranium ore genesis. *Uranium*, **1987**, *3*, pp. 307-342.
4. Landais, P. Organic geochemistry of sedimentary uranium ore deposits. *Ore Geology Reviews*, **1996**, *11*, pp. 33-51. doi.org/10.1016/0169-1368(95)00014-3
5. Spirakis, C.S. The roles of organic matter in the formation of uranium deposits in sedimentary rocks. *Ore Geology Reviews*, **1996**, *11*, pp. 53-69. doi.org/10.1016/0169-1368(95)00015-1
6. Cuney, M. Ore deposits, **2007**, In: *Encyclopedia of Geochemistry*. Springer International Publishing AG, **2016**, 13p. DOI: 10.1007/978-3-319-39193-9_126-1.
7. Nakashima, S. Complexation and reduction of uranium by lignite. *The science of the Total Environment*, **1992**, *117/118*, pp. 425-437. doi.org/10.1016/0048-9697(92)90108-5
8. Cumberland, S.A.; Etschmann, B.; Brugger, J.; Douglas, G.; Evans, K.; Fisher, L.; Kappen, P.; Moreau, J.W. Characterization of uranium redox state in organic-rich Eocene sediments. *Chemosphere*, **2018**, *194*, pp. 602-613. doi.org/10.1016/j.chemosphere.2017.12.012
9. Anderson, R.F. Redox behavior of uranium in an anoxic marine basin, *Uranium*, **1987**, *3*, pp. 145-164.
10. Goldhaber, M.B.; Hemingway, B.S.; Mohagheghi, A.; Reynolds, R.L.; Northrop, H.R. Origin of coffinite in sedimentary rocks by a sequential adsorption-reduction mechanism. *Bulletin de la Société de l'industrie Minérale*, **1987**, *110*. pp. 131-144. doi.10.3406/bulmi.1987.7975
11. Nakashima, S.; Disnar, J.R.; Perruchot, A.; Trichet, J. Experimental study of mechanisms of fixation and reduction of uranium by sedimentary organic matter under diagenetic or hydrothermal conditions. *Geochim. Cosmochim. Acta*, **1984**, *48*, pp. 2321-2329. doi.org/10.1016/0016-7037(84)90228-X
12. Meunier. J.D.; Landais, P.; Pagel, M. Experimental evidence of uraninite formation from diagenesis of uranium-rich organic matter. *Geochim. Cosmochim. Acta*, **1990**, *54*, pp. 809-817. doi.org/10.1016/0016-7037(90)90375-U
13. Van Krevelen, D.W. Coal. Typology – Chemistry – Physics – Constitution. 1st ed., Elsevier, **1961**, Amsterdam, The Netherlands, 514p.
14. Tissot, B.P.; Welte D.H. Petroleum formation and occurrence. 2nd ed., Springer-Verlag, **1984**, Berlin Heildelberg, New-York, 699p.
15. Adreyef, P.F.; Chumachenko, A.P. Reduction of uranium by natural organic substances. *Geokhimiya*, **1964**, *1*, pp. 12-22.
16. Forbes, P.; Landais, P.; Bertrand, P.; Brosse, E.; Espitalié, J.; Yahaya, M. Chemical transformations of type-III organic matter associated with the Akouta uranium deposit (Niger): Geological implications. *Chemical Geology*, **1988**, *71*. pp. 267-282. doi.org/10.1016/0009-2541(88)90054-X

17. Granger, H.C.; Warren, C.G. Unstable sulfur compounds and the origin of roll-front type uranium deposits. *Economic Geology*, **1969**, *64* (2), pp. 160-171.
18. Boulègue, J. Simultaneous Determination of Sulfide, Polysulfides and Thiosulfat as an Aid to Ore Exploration. *Developments in Economic Geology*, **1981**, *15*, pp. 21-36. doi.org/10.1016/0375-6742(81)90053-4
19. Petrov N.N. Les gisements épigénétiques du Kazakhstan. *Géologie du Kazakhstan*, **1998**, *2*(354): pp. 22-39. (en russe).
20. Munara, A. Formation des gisements d'uranium de type roll : approche minéralogique et géochimique du gisement uranifère de Muyunkum (Bassin de Chu-Sarysu, Kazakhstan). *Thèse* soutenue le 9 Juillet **2012**, PhD Univ. H. Poincaré Nancy. 327p.
21. Lach, P.; Cathelineau, M.; Brouand, M.; Fiet, N. In-situ isotopic and chemical study of pyrite from Chu-Sarysu (Kazakhstan) roll-front uranium deposit. *Procedia Earth and Planetary Science*, **2015**, *13*, pp. 207-210. doi.org/10.1016/j.proeps.2015.07.049
22. Cai, C.; Dong, H.; Li, H.; Xiao, X.; Ou, G.; Zhang, C. Mineralogical and geochemical evidence for coupled bacterial uranium mineralization and hydrocarbon oxidation in the Shashagetai deposit, NW China. *Chem. Geol.,* **2007**, *236*, pp. 167-179. doi.org/10.1016/j.chemgeo.2006.09.007
23. Zhu, M.; Wu, R.; Liu, X.; Nie, F.; Yu, D. Geologic Setting of Interformational Braided Channel Type Sandstone Uranium deposits in North China, Available online: East China Institute of Technology, **2012** https://www.slideshare.net/monatom/05-xiaodong-liu-geologic-setting-of-interformationalbraidedchannel-type-sandstone-uranium-deposits-in-north-china
24. Yue, S.; Wang, G. Relationship between the hydrogeochemical environment and sandstone-type uranium mineralization in the Ili basin, China. *Applied Geochem*, **2011**, *26*, pp. 133-139. doi.org/10.1016/j.apgeochem.2010.11.010
25. Bonnetti, C.; Cuney, M.; Malartre, F.; Michels, R.; Liu, X.; Peng, Y. The Nuheting Deposit, Erlian Basin, China: Synsedimentary vs Diagenetic Uranium Mineralization. *Ore Geology Reviews*, **2015**, *69*, pp. 118–139. doi.org/10.1016/j.oregeorev.2015.02.010
26. Le Goux, F.; Banzragch, T.O.; Delaunay A.; Nyamdorj, B.I.; Jaques, E.; Korshunov, A.; Parize, O.; Brouand, M. The Major Gobi Uranium Deposits, Upper Cretaceous East Gobi Basin, Mongolia: Geodynamical and Mineralogical Key Parameters of Uranium Ore Geology. In: Mineral Resources in a Sustainable World, *13th SGA Biennial Meeting* **2015**, *5*, pp. 1815-1818.
27. Dahlkamp, F.J. Uranium Deposits of the World: Asia, Berlin Heidelberg: Springer-Verlag, **2009**, 493p.
28. Graham, S.A.; Hendrix, M.S.; Johnson, C.L.; Badamgarav, D.; Badarch G.; Amory, J.; Porter, M.; Barsbold, R.; Webb, L.E.; Hacker B.R. Sedimentary record and tectonic implications of Mesozoic rifting in southeast Mongolia. *Geological Society of America Bulletin*, **2001**, *113*, pp. 1560–1579. doi.org/10.1130/0016-7606(2001)113<1560:SRATIO>2.0.CO;2
29. Johnson, C.L. Polyphase evolution of the East Gobi basin: sedimentary and structural records of Mesozoic-Cenozoic intraplate deformation in Mongolia. *Basin Research*, **2004**, *16*, pp. 79-99. doi.10.1046/j.1365-2117.2003.00221.x
30. Prost, G.L. Tectonics and hydrocarbon systems of the East Gobi basin, Mongolia, *American Association of Petroleum Geologists Bulletin*, **2004**, *88*, No. 4, pp. 483-513. doi.org/10.1306/11150303042
31. Pontolillo, J.; Stanton, R.W. Coal petrographic laboratory procedures and safety manual II. Open-file Report 94-631. *U.S Department of Interior Geological Survey*, **1994**, 74 pp. https://pubs.usgs.gov/of/1994/0631/report.pdf
32. (ISO) 7404-2, International Organization for Standardization. Methods for the Petrographic Analysis of Coals - Part 2: Methods of Preparing Coal Samples, International Organization for Standardization, Geneva, Switzerland, **2009**. 12 pp.
33. (ISO) 7404-5, International Organization for Standardization. Methods for the Petrographic Analysis of Coal - Part 5: Methods of Determining Microscopically the

Reflectance of Vitrinite, International Organization for Standardization, Geneva, Switzerland, **2009**, 14 pp.
34. Sýkorová, I.; Pickel, W.; Christanis, K.; Wolf, M.; Taylor, G.H.; Flores, D. Classification of huminite – ICCP System 1994: *Int. J. Coal Geol.*, **2005**, *62*, pp. 85-106. doi.org/10.1016/j.coal.2004.06.006
35. International Committee for Coal and Organic Petrology (ICCP). **2011**. ICCP training course on Dispersed Organic Matter, Impressão: Pleninagem, ISSN No 978-989-8265-67-8, 322p.
36. Rallakis, D.; Michels, R.; Brouand, M.; Parize, O.; Cathelineau, M. Dolomite cements in Cenomanian continental sand deposits: time evolution and significance (Zoovch Ovoo, U-deposit, East Gobi Basin, Mongolia), *Journal of Sedimentary Research*, **2019**, (under review).
37. Borrego, A.G.; Cook, A. Humic Macerals: Vitrinite/Inertinite, Chapter 9, In: *10th ICCP Training Course on Dispersed Organic Matter. Integrating transmitted and reflected light microscopy*, **2017**, GFZ, Potsdam, Germany, 276 p.
38. Van Krevelen, D.W. Coal. 3rd Edition, *Elsevier Science Publishers*, **1993**, Amsterdam.
39. Langmuir, D. Uranium solution-mineral equilibria at low temperatures with applications to sedimentary ore deposits. *Geochim. Cosmochim. Acta*, **1978**, *44*, pp. 1753-1766. doi.org/10.1016/0016-7037(78)90001-7
40. Forbes, P.; Landais, P.; Bertrand, P.; Brosse, E.; Espitalié, J.; Yahaya, M. Chemical transformations of type-III organic matter associated with the Akouta uranium deposit (Niger): Geological implications. *Chemical Geology*, **1988**, *71*, pp. 267-282. doi.10.1016/0009-2541(88)90054-X
41. Bone, E.S.; Dynes, J.J.; Cliff, J.; Bargar, J. Uranium (IV) adsorption by natural organic matter in anoxic sediments. *Proceedings of the National Academy of Sciences of the United States of America* (PNAS), **2017**, *114*, pp. 711-716. doi.10.1073/pnas.1611918114
42. Nakashima, S.; Disnar, J.R.; Perruchot, A. Precipitation Kinetics of Uranium by Sedimentary Organic Matter under Diagenetic and Hydrothermal Conditions. *Economic Geology*, **1999**, *94*, pp. 993-1006. doi.org/10.2113/gsecongeo.94.7.993
43. Stevenson, F.J. Humus, chemistry. Genesis, composition, reactions. *John Wiley and Sons*, **1982**, New York, p. 443.
44. Douglas, G.B.; Butt, C.R.M.; Gray, D.J. Geology, geochemistry and mineralogy of the lignite-hosted Ambassador palaeochannel uranium and multi-element deposit, Gunbarrel Basin, Western Australia. *Mineral Deposita*, **2011**, *46*-7, pp. 761–787. doi.org/10.1007/s00126-011-0349-4
45. Bonnetti, C.; Liu, X.; Zhaobin, Y.; Cuney, M.; Michels, R.; Malartre, F.; Mercadier, J.; Cai, J. Coupled uranium mineralization and bacterial sulfate reduction for the genesis of the Baxingtu sandstone-hosted U deposit, SW Songliao Basin, NE China. *Ore Geology Reviews*, **2017**, *82*, pp. 108-129. doi.org/10.1016/j.oregeorev.2016.11.013
46. Rouzaud, J.N.; Oberlin, A.; Trichet, J. Interaction of uranium and organic matter in uraniferous sediments, In: *Advances in Organic Geochemistry*, **1979**. (eds. A. G. Douglas and J. R. Maxwell), Pergamon Press, pp. 505-516. doi.org/10.1016/0079-1946(79)90133-2
47. Lovley, D.R.; Phillips, E.J.P.; Gorby, Y. A.; Landa, E.R. Microbial reduction of uranium. *Nature*, **1991**, *350*, pp. 413-416. doi:10.1038/350413a0
48. Detmers, J.; Schulte, U.; Strauss, J.; Kuever, J. Sulfate Reduction at a Lignite Seam: Microbial Abundance and Activity. *Microb. Ecol.*, **2001**, *42*(3), pp. 238-247. doi.10.1007/s00248-001-1014-8
49. Min, M.; Xu, H.; Chen, J.; Fayek, M. Evidence of uranium biomineralization in sandstone-hosted roll-front uranium deposits, northwestern China. *Ore Geol. Rev.*, **2005**, *26*, pp. 198-206. doi.org/10.1016/j.oregeorev.2004.10.003
50. Menor-Salván, C.; Tornos, F.; Fernández-Remolar, D.; Amils, R. Association between catastrophic paleovegetation changes during Devonian-Carboniferous boundary and

the formation of giant massive sulfide deposits. *Earth Planet. Sci. Lett.*, **2010**, *299*, pp. 398-408. doi.org/10.1016/j.epsl.2010.09.020
51. Gruner, J.W. Syntheses of uranium minerals at room and elevated temperatures. *Am. Mineral.*, **1953**, *38*, 342.
52. Kochenov, A.V.; Korolev, K.G.; Dubinchuk, V.T.; Medvelev, Y.L. Experimental data on the conditions of precipitation of uranium from aqueous solutions. *Geochem. Int.*, **1977**, *14*, pp. 82-87.
53. Bhattacharyya, A.; Campbell, K.M.; Kelly, S.D; Roebbert, Y.; Weyer, S.; Bernier-Latmani, R.; Borch, T. Biogenic non-crystalline $U^{(IV)}$ revealed as major component in uranium ore deposits. *Nature communications*, **2017**, *8*, doi.10.1038/ncomms15538
54. Davison, W.; Buffle, J.; Devitre, R. Voltammetric characterization of a dissolved iron sulfide species by laboratroy and field studies, *Anal. Chim. Acta*, **1998**, *377*, pp. 193-203. doi.org/10.1016/S0003-2670(98)00334-1
55. Theberge, S.; Luther, G.W. Determination of the electrochemical properties of a soluble aqueous FeS species present in sulfide solutions. *Aquat. Geochem.*, **1987**, *3*, pp. 191-211. doi.10.1023/A:1009648026806
56. Rickard D.; Griffith, A.; Oldroyd, A.; Butler, I.B.; Lopez-Caper, E.; Manning, D.A.C.; Apperley, D.C. The composition of nanoparticulate mackinawite, tetragonal iron (II) monosulfide. *Chem. Geol.*, **2006**, *235*, pp. 286-298. doi.org/10.1016/j.chemgeo.2006.07.004
57. Wolthers, M.; Charlet, L.; van Der Linde, P.; Rickard, D.; van Der Weijden, C. Surface chemistry of disordered mackinawite (FeS). *Geochim. Cosmochim. Acta*, **2005**, *69*, pp. 3469-3481. doi.org/10.1016/j.gca.2005.01.027
58. Bura-Nakić, E.; Viollier, E.; Jézéquel, D.; Thiam, A.; Ciglenečki, I. Reduced sulfur and iron species in anoxic water column of meromictic crater Lake Pavin (Massif Central, France). *Chem. Geol.*, **2009**, *266*, pp. 311-317. doi.org/10.1016/j.chemgeo.2009.06.020
59. Boyanov, M.I.; O'Loughlin, E.J.; Roden, E.E.; Fein, J.B.; Kemner, K.M. Adsorption of Fe(II) and U(VI) to carboxyl-functionalized microspheres: The influence of speciation on uranyl reduction studied by titration and XAFS. *Geochim. Cosmochim. Acta*, **2007**, *71* (8), pp. 1898–1912. doi.org/10.1016/j.gca.2007.01.025

APPENDIX I (FIGURES)

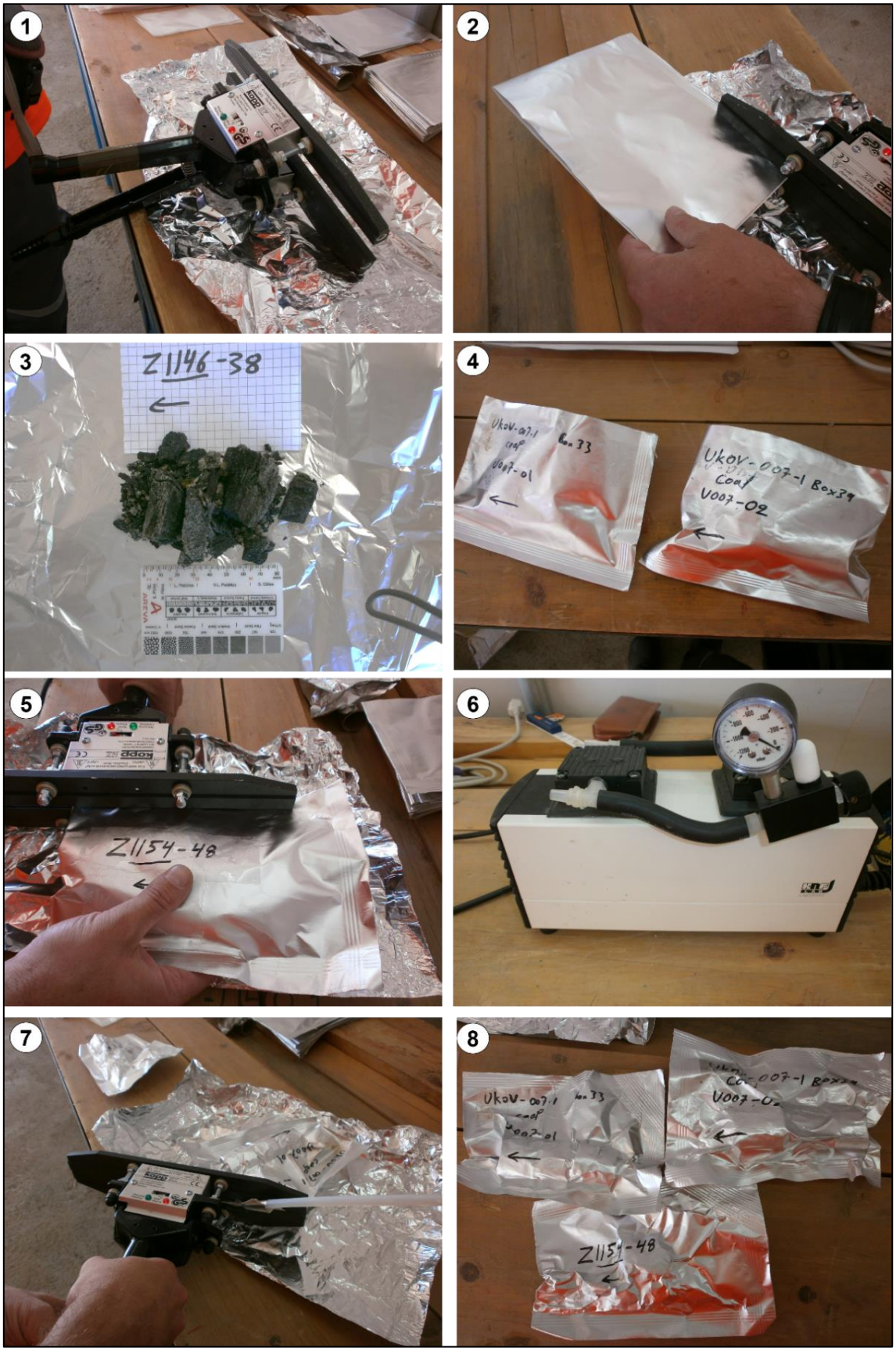

Figure 194: Step-by-step methodology followed for the sampling of the organic matter from the drill-cores.

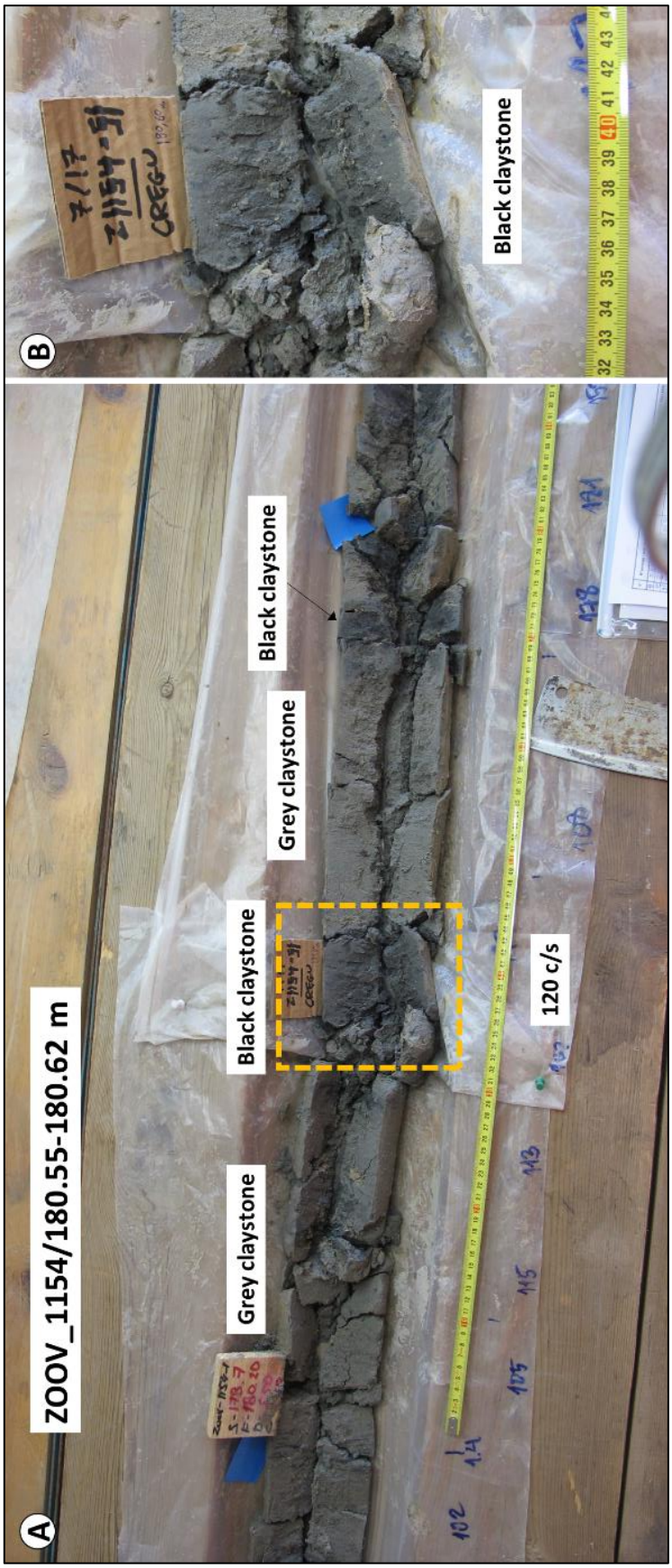

Figure 195: Core photograph of well ZOOV_1154, interval 180.55-180.62m, highlighting sample Z1154-51 and radioactivity measurement. The sequence is represented by alternating black and grey claystone beds. The thermo-sealed bag containing sample Z1154-51 was for a great part inflated after 8 month storage under vacuum.

Fabric	Sample	La	Ce	Pr	Nd	Sm	Eu	Gd	Tb	Dy	Ho	Er	Tm	Yb	Lu
Type (I)	AA-147	173,4	126,1	96,1	81,2	60,8	37,8	53,3	48,2	43,1	41,0	42,8	33,4	35,3	26,0
	AA-171	1865,0	1579,1	1174,8	1048,1	721,6	328,6	579,9	482,0	417,1	338,8	288,1	236,0	209,9	202,4

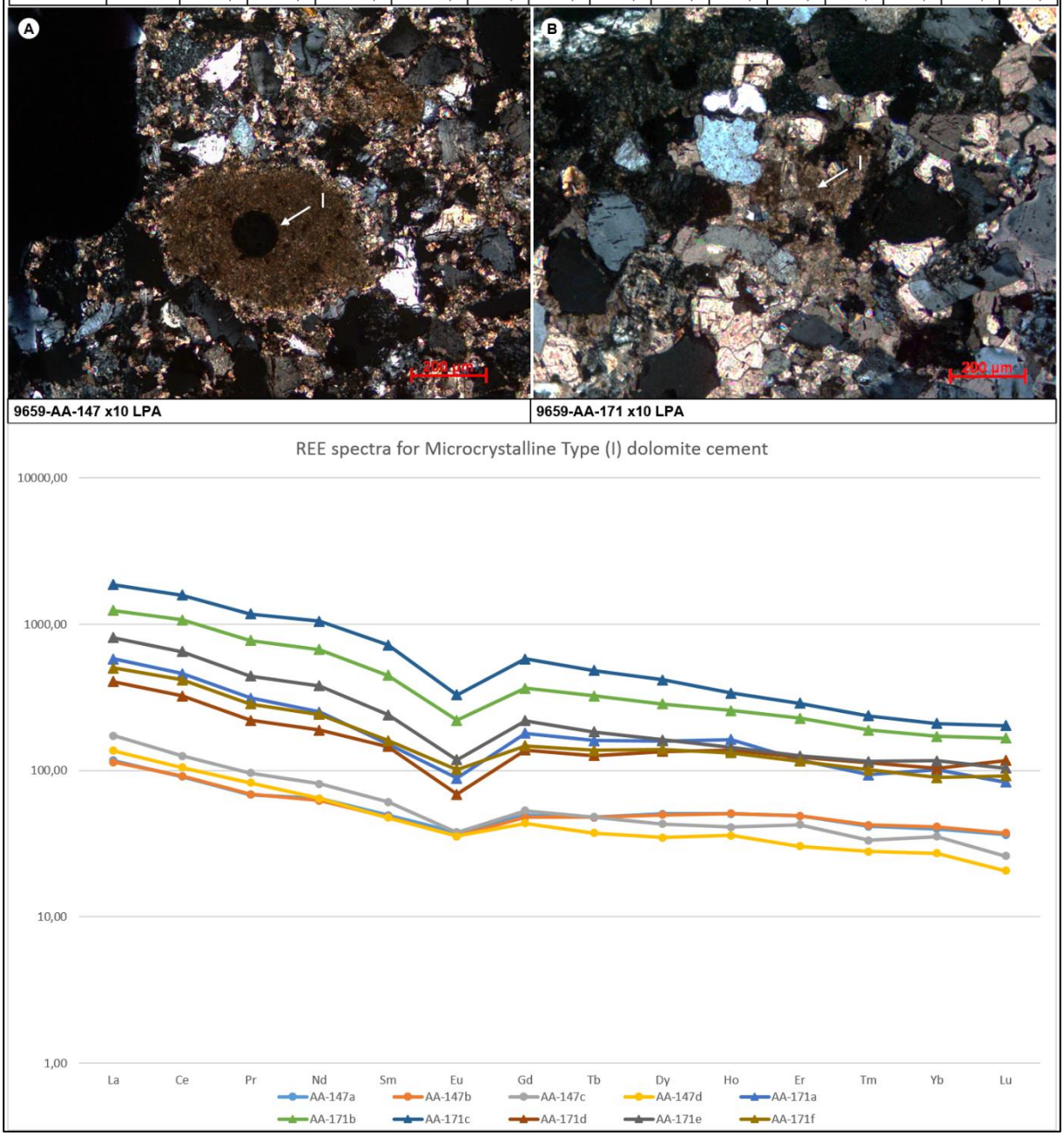

Figure 196: REE spectra for two different varieties of the microcrystalline fabric showing an overall high REE content. The values fluctuate between 120 to 1800 times the chondrite. The spectra is fractionated and LREE enriched, measured on samples AA-147 (A) and AA-171 (B).

Fabric	Sample	La	Ce	Pr	Nd	Sm	Eu	Gd	Tb	Dy	Ho	Er	Tm	Yb	Lu
Type (II)	AA-157	264,1	199,0	147,6	146,6	110,8	48,0	51,8	85,9	50,4	46,5	62,5	92,7	27,3	22,7
	AA-171	143,0	132,0	91,8	85,3	73,6	40,7	69,9	74,8	75,6	72,7	61,1	48,9	46,3	33,0

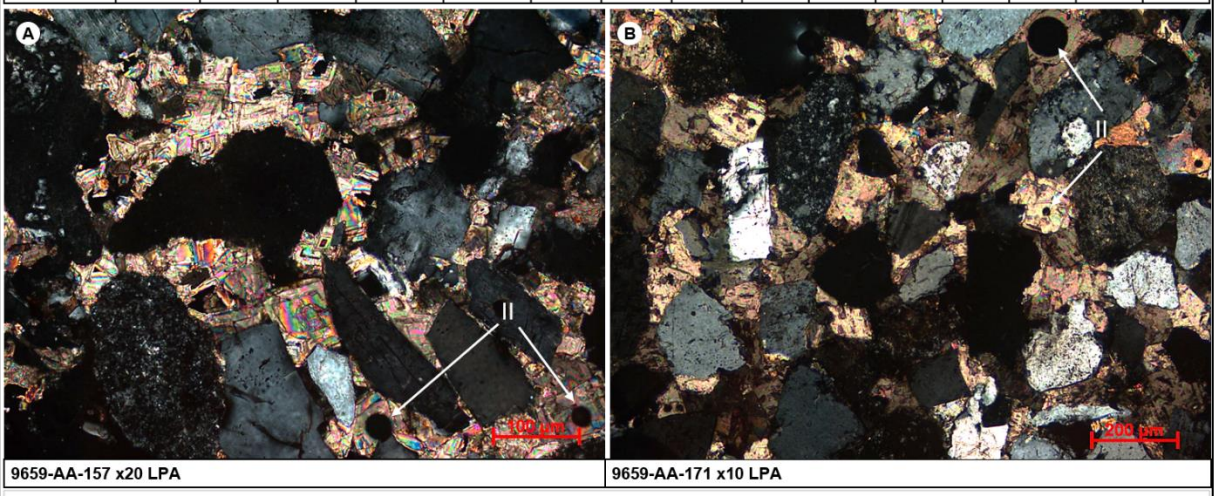

9659-AA-157 x20 LPA | 9659-AA-171 x10 LPA

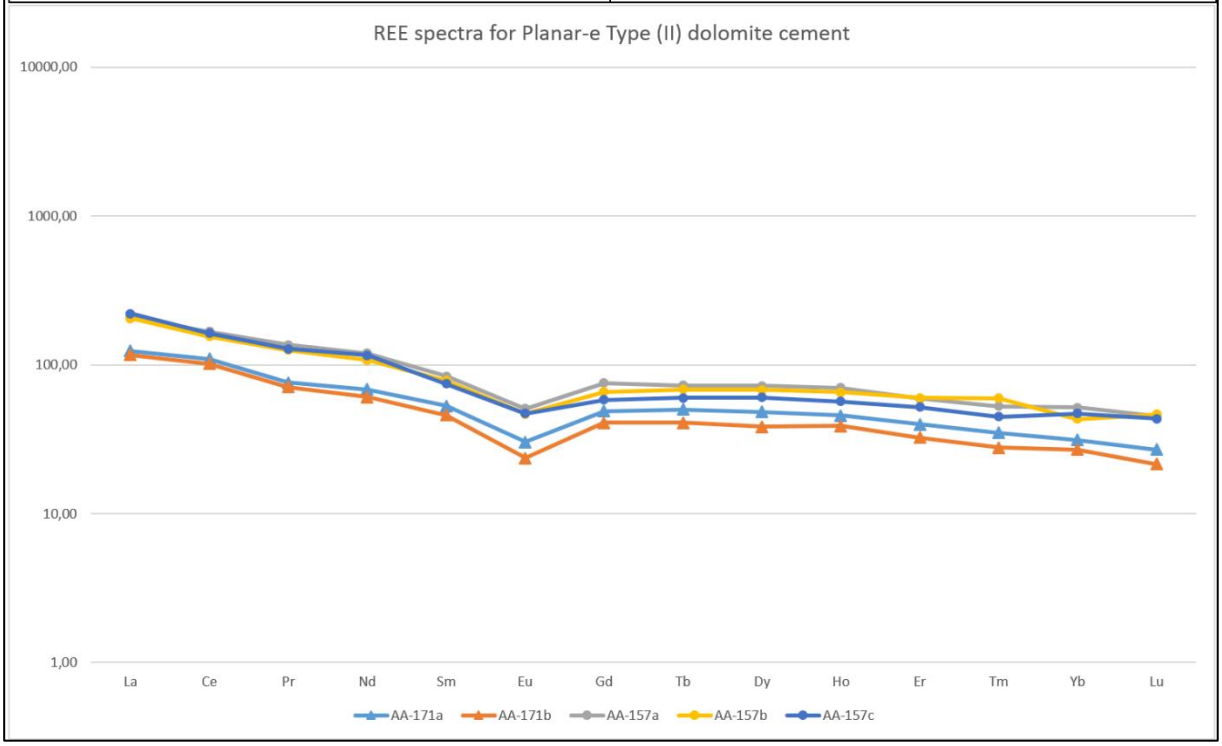

Figure 197: REE spectra for the euhedral-rhombohedral (planar-e) fabric. The spectra of this dolomite cement is less fractionated than the spectra of the microcrystalline fabric. The values fluctuate between 120 to 450 times the chondrite, measured on samples AA-157 (A) and AA-171 (B).

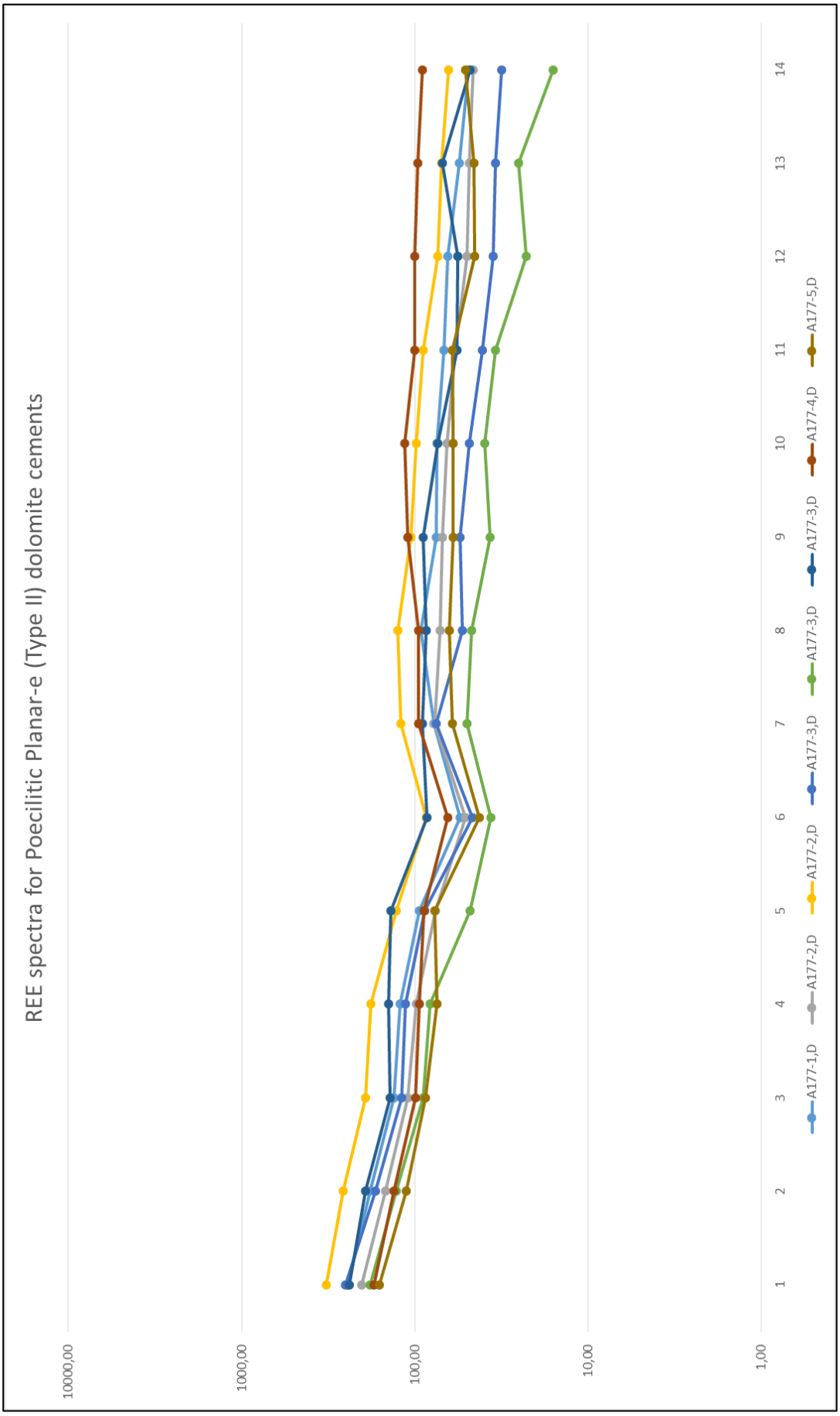

Figure 198: Overview of measurements performed on poecilitic planar-e dolomite crystals for sample AA-177.

Fabric	Sample	La	Ce	Pr	Nd	Sm	Eu	Gd	Tb	Dy	Ho	Er	Tm	Yb	Lu
Type (III)	BB-91	69,62	50,08	34,81	31,29	27,70	17,76	21,11	22,99	21,54	23,44	19,81	17,81	18,14	16,26

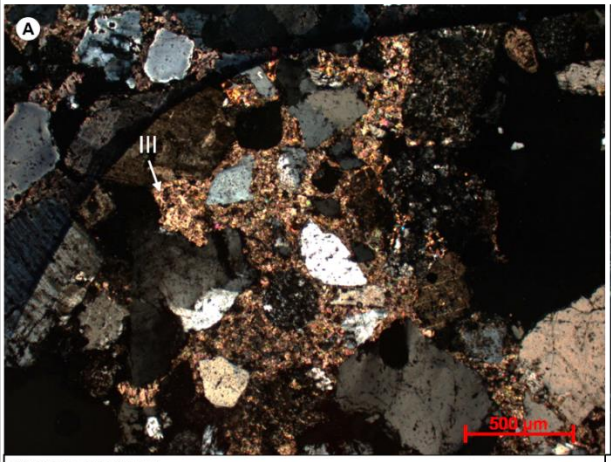

9659-BB-91 x5 LPA

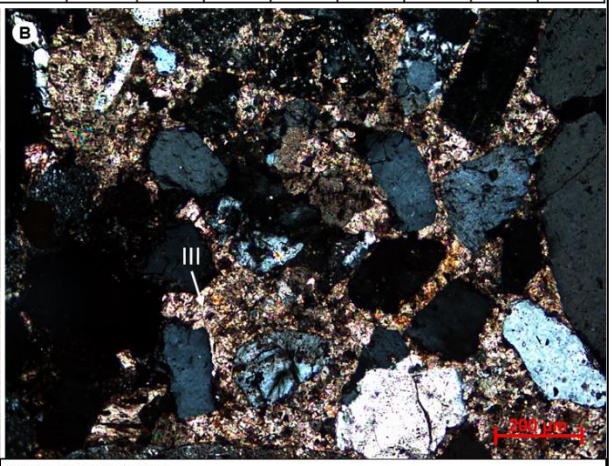

9659-BB-91 x10 LPA

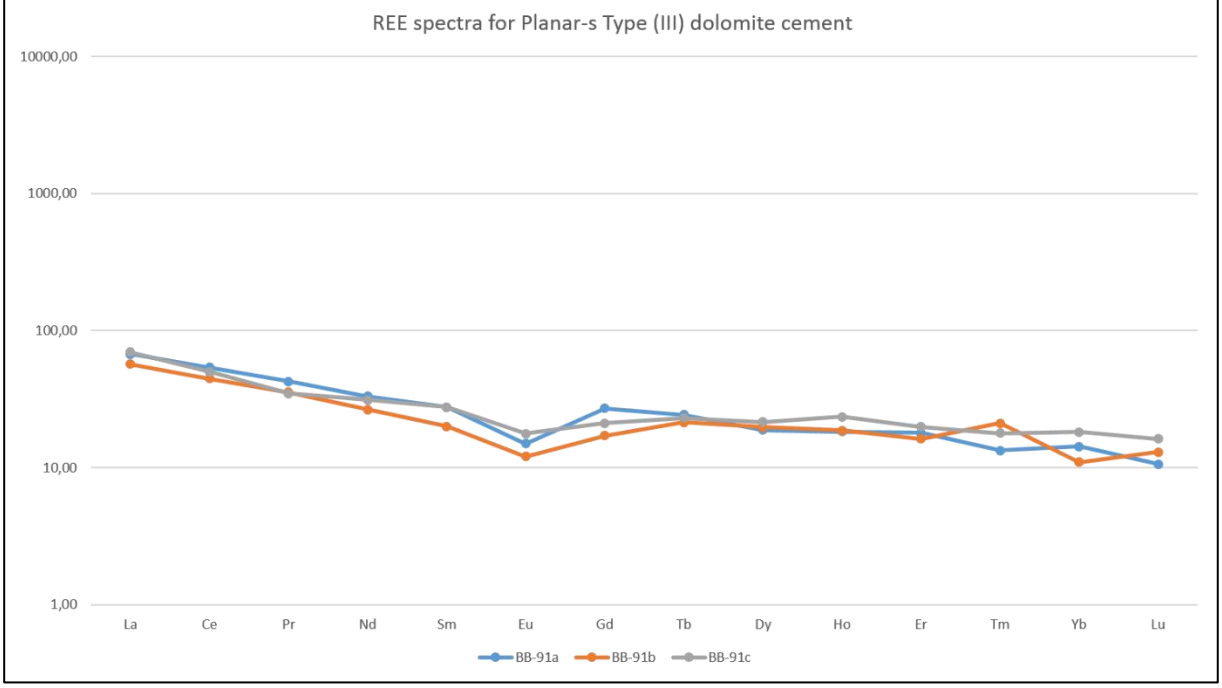

Figure 199: REE spectra for the subhedral (planar-s) fabric. The depletion in REE is more progressive. The REE values fluctuate at 70 times the chondrite, measured on sample BB-91 (A, B).

Fabric	Sample	La	Ce	Pr	Nd	Sm	Eu	Gd	Tb	Dy	Ho	Er	Tm	Yb	Lu
Type (IV)	BB-88	69,62	50,08	34,81	31,29	27,70	17,76	21,11	22,99	21,54	23,44	19,81	17,81	18,14	16,26
	BB-88	19,20	9,93	6,36	5,47	4,93	9,41	10,70	6,09	5,28	3,85	3,38	1,86	4,91	2,97

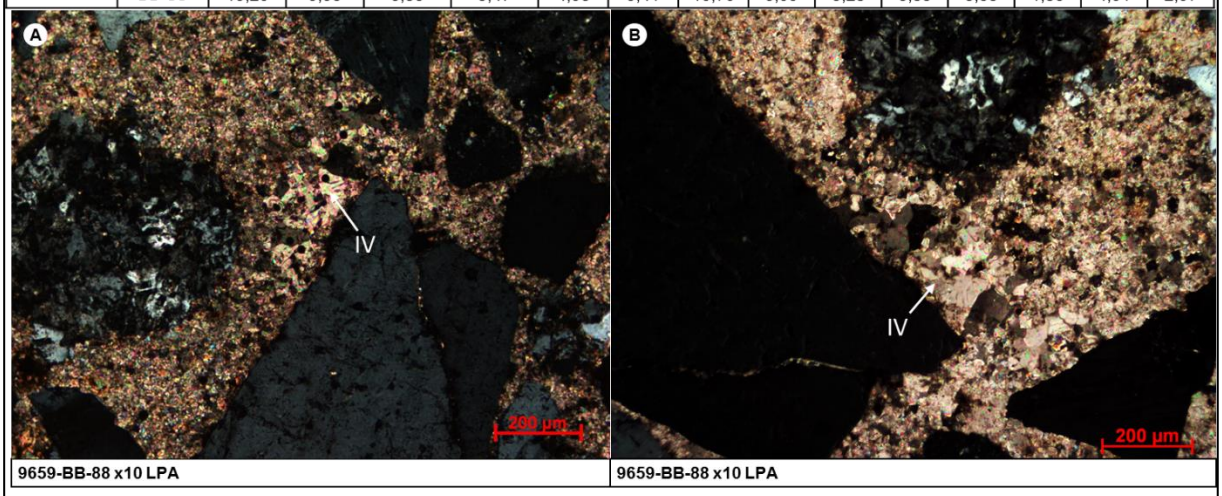

9659-BB-88 x10 LPA | 9659-BB-88 x10 LPA

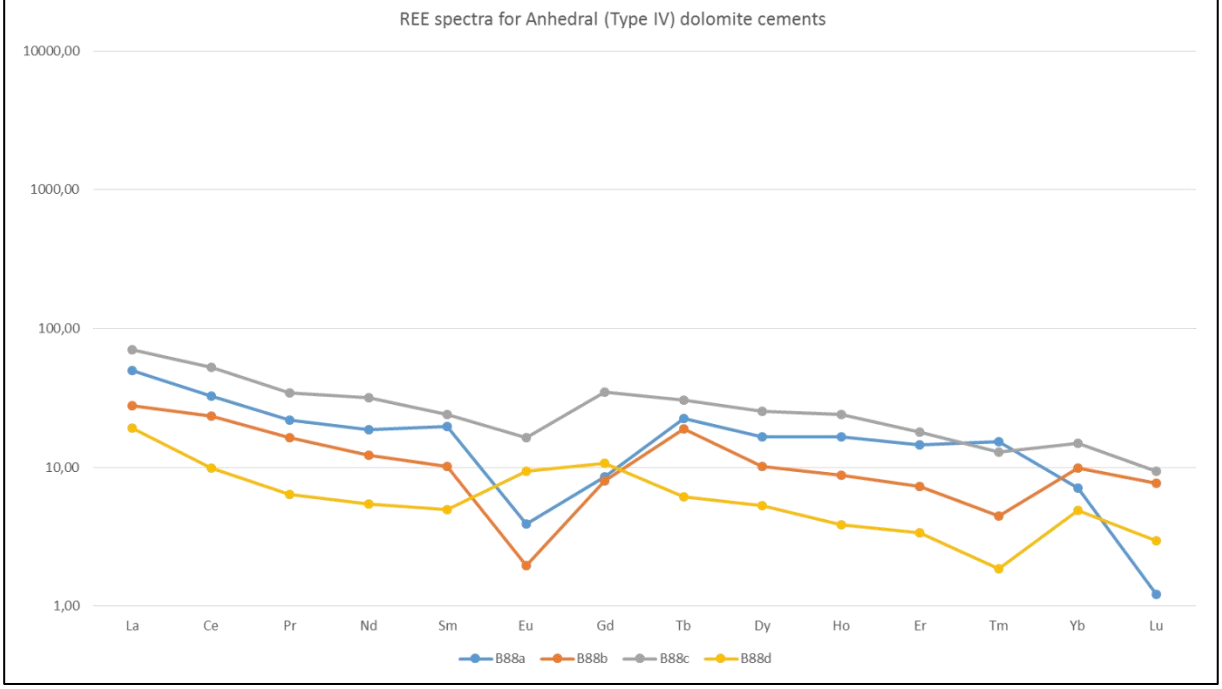

Figure 200: REE spectra for the non-planar (anhedral) dolomite cements for sample BB-88 (A, B).

Fabric	Sample	La	Ce	Pr	Nd	Sm	Eu	Gd	Tb	Dy	Ho	Er	Tm	Yb	Lu
Type (IV)	BB-88-Fe	153,16	130,51	84,05	72,65	54,73	31,26	74,87	90,58	93,09	91,58	89,38	81,38	76,40	74,39
	BB-88-Fe	174,26	145,84	101,83	90,59	66,89	51,15	69,85	85,87	97,56	100,18	98,75	82,19	92,55	89,84

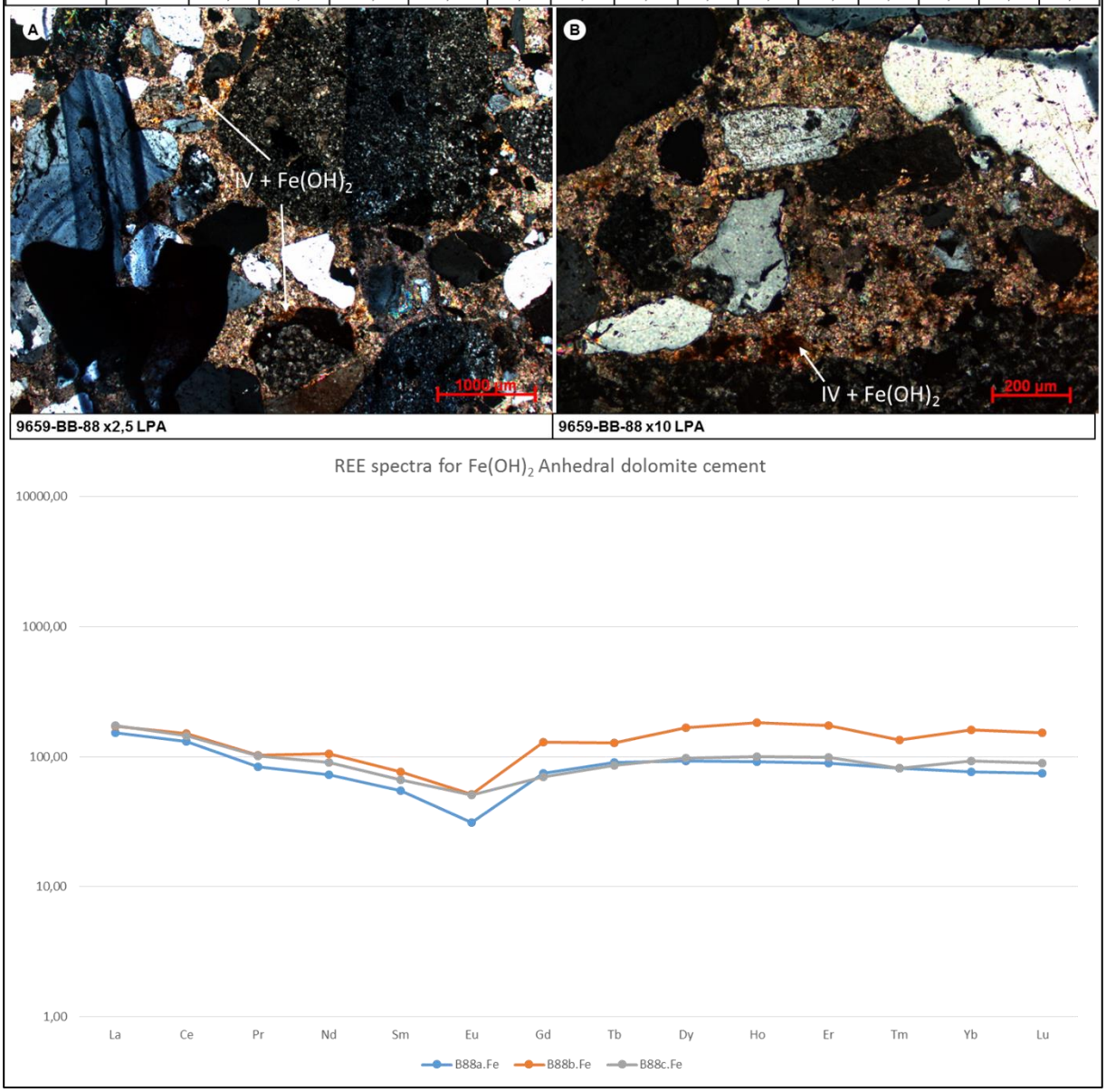

Figure 201: REE spectra of non-planar (anhedral) dolomite associated to Fe hydroxides for sample BB-88 (A, B).

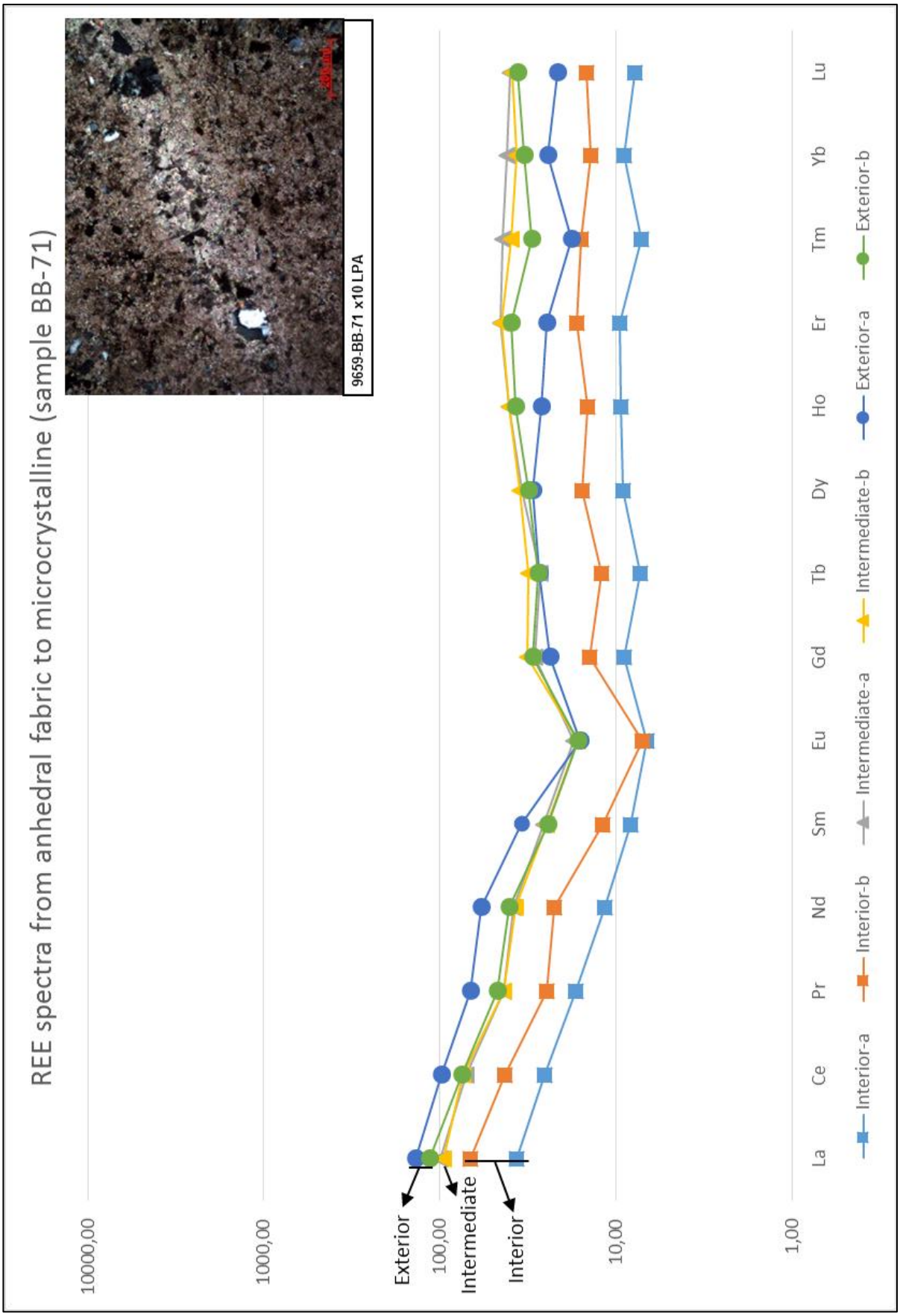

Figure 202: Comparison between the REE spectra for the microcrystalline fabric and a recrystallized phase of up to ø20µm for sample BB-71.

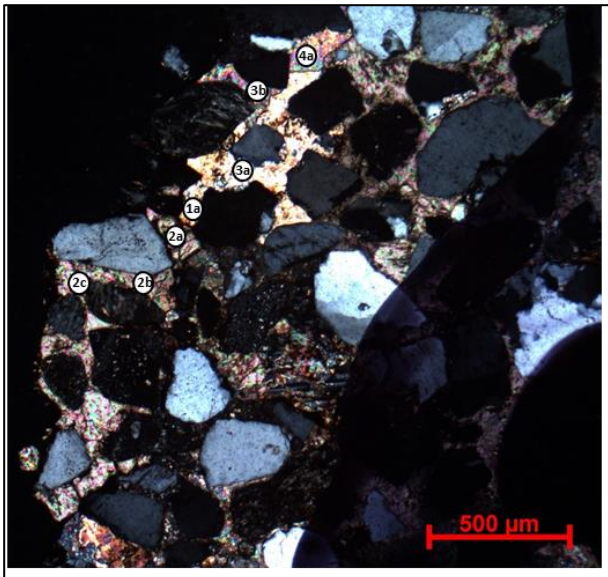

REEs	K2BS-1a	K2BS-2a	K2BS1-2b	K2BS1-2c	K2BS1-3a	K2BS1-3b	K2BS1-4a
La	164.56	207.17	97.05	180.17	117.30	154.85	327.00
Ce	89.72	123.98	10.93	32.46	15.99	37.85	140.62
Pr	67.89	93.53	63.58	68.97	63.90	70.37	156.25
Nd	74.40	76.59	49.02	61.93	50.55	55.14	119.26
Sm	20.95	27.70	39.86	26.35	32.43	34.46	54.05
Eu	37.30	26.64	15.28	23.27	34.10	16.16	49.02
Gd	14.07	36.68	13.57	65.83	33.67	22.11	37.69
Tb	3.60	27.98	16.62	30.47	18.56	21.88	42.11
Dy	28.86	33.33	13.41	33.74	24.39	17.36	38.62
Ho	16.48	36.63	5.31	32.78	24.73	16.85	37.91
Er	11.88	31.31	14.81	31.88	28.75	18.13	30.63
Tm	36.44	40.08	4.05	22.27	12.55	29.96	31.58
Yb	16.77	32.92	6.21	31.06	37.27	18.01	30.43
Lu	17.48	21.95	9.35	21.54	18.29	32.93	39.84

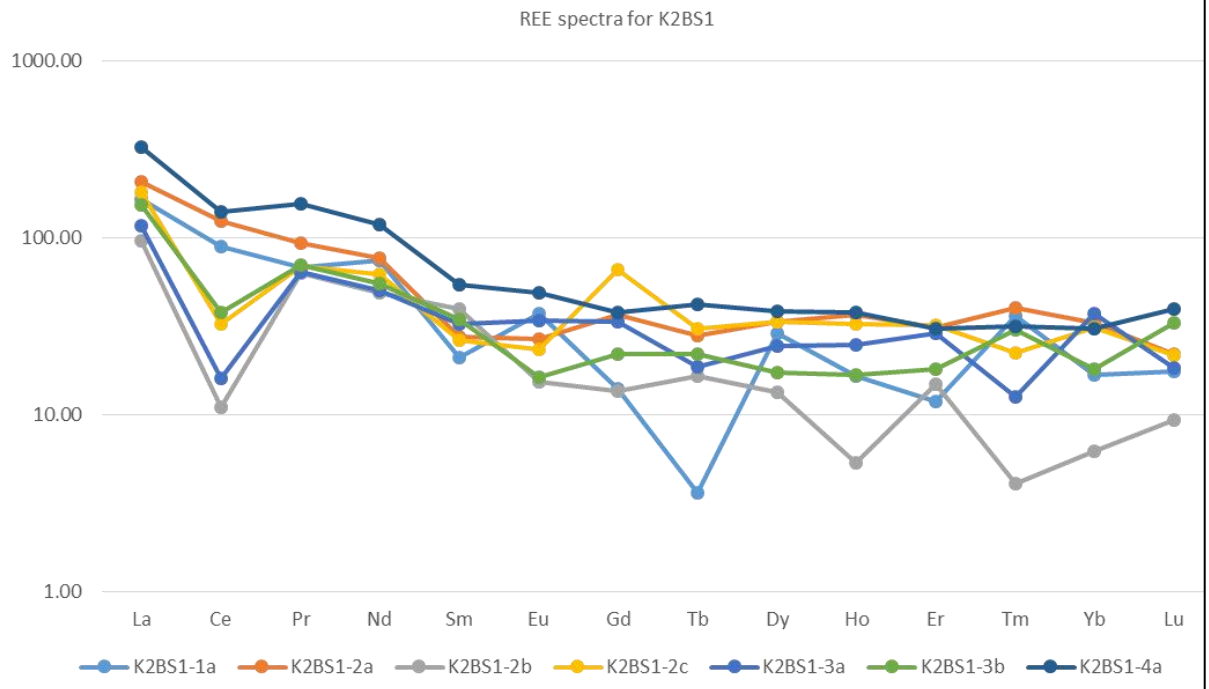

Spot/ppm	Na	Mg	Ca	Ti	Mn	Fe	Cu	Zn	Rb	Sr	Y	Ba	Th	U
K2BS1-1a	3800	5700	245000	680	6600	430000	620	98	37	560	25.0	170.0	6.1	264.0
K2BS1-2a	51	966	339000	22	2400	2530	6	19	-	88	44.3	7.7	4.5	5.0
K2BS1-2b	40	430	315000	-	200	800	-	-	-	96	19.9	8.5	0.4	-
K2BS1-2c	210	346	311000	-	1100	750	-	-	-	90	43.6	-	2.9	1.2
K2BS1-3a	-	256	309000	-	1490	640	-	-	-	96	31.2	-	4.0	-
K2BS1-3b	-	408	307000	-	346	180	-	-	-	58	37.0	-	3.2	-
K2BS1-4a	-	739	306000	-	802	350	-	-	-	155	55.6	-	5.0	-

Figure 203: The REE and trace element contents for the sample K2Bs-1 (sparry calcite with negative Ce anomaly).

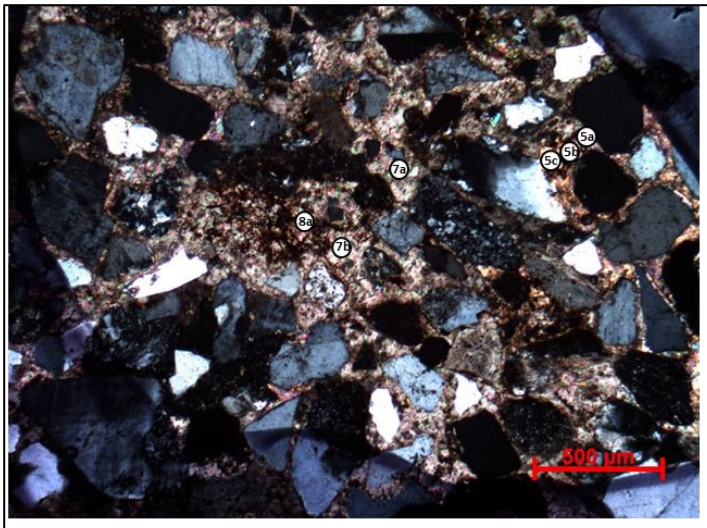

REEs	K2BS1-5a	K2BS1-5b	K2BS1-5c	K2BS1-7a	K2BS1-7b	K2BS1-8a
La	245.99	79.32	70.46	119.41	75.53	174.68
Ce	213.70	34.42	0.36	0.95	8.48	61.83
Pr	136.85	42.89	43.00	55.17	49.57	79.53
Nd	94.53	34.79	32.39	47.48	45.08	67.83
Sm	55.41	22.97	11.49	28.38	23.65	40.41
Eu	19.36	13.32	22.20	18.47	20.60	26.64
Gd	38.19	15.08	9.05	22.61	25.13	33.62
Tb	47.09	11.63	15.24	13.57	24.10	29.86
Dy	30.49	13.82	11.79	15.45	14.63	31.14
Ho	35.90	13.92	7.69	12.45	10.99	30.95
Er	31.25	14.13	9.13	8.75	12.56	31.44
Tm	23.08	8.10	6.48	7.29	4.57	27.89
Yb	20.50	16.77	10.12	10.56	7.02	29.69
Lu	25.61	13.41	6.10	7.32	8.94	25.89

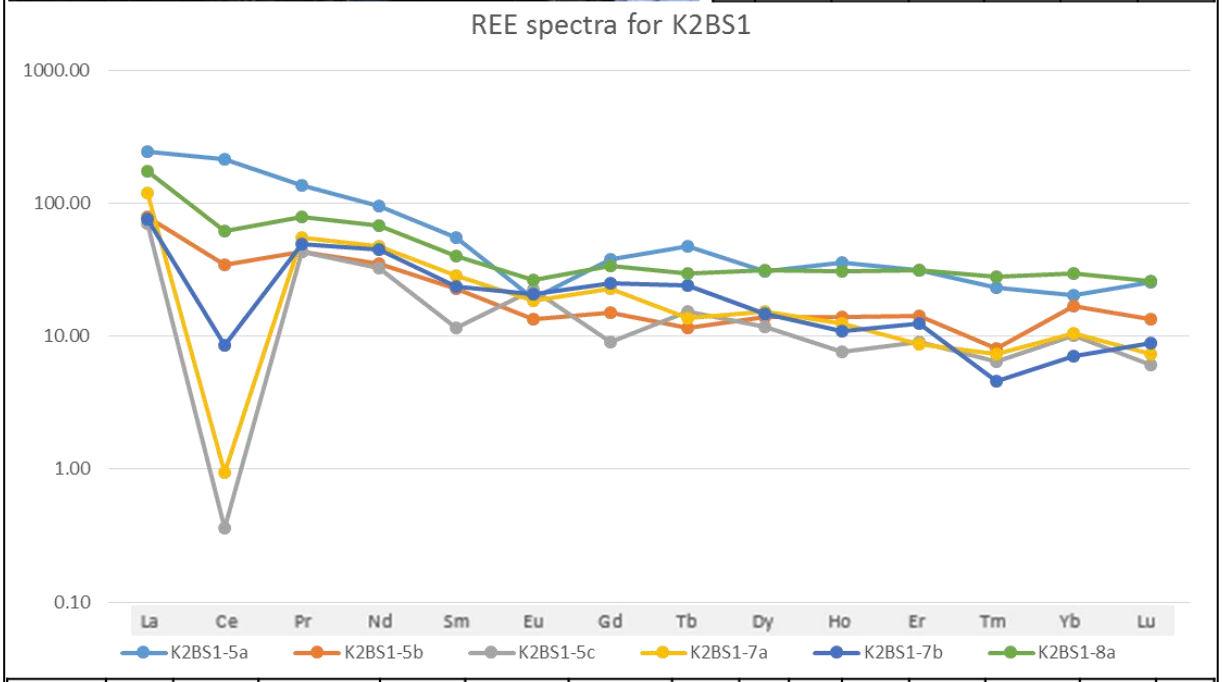

Spot/ppm	Na	Mg	Ca	Ti	Mn	Fe	Cu	Zn	Rb	Sr	Y	Ba	Th	U
K2BS1-5a	620	2470	324000	1870	17500	80000	129	55	-	179	61.6	146.0	8.0	5.2
K2BS1-5b	95	509	304000	24	1450	1890	-	-	-	121	22.7	5.9	1.2	1.1
K2BS1-5c	-	385	306000	-	-	355	-	-	-	115	19.8	-	-	-
K2BS1-7a	-	361	309000	-	-	270	-	-	-	112	19.3	-	-	-
K2BS1-7b	-	375	319000	-	1390	325	-	-	-	97	21.9	-	-	0.1
K2BS1-8a	74	1380	324600	485	5990	45800	65	66	-	164	49.2	11.9	40.3	4.2

Figure 204: The REE and trace element contents for the sample K2Bs-1 (sparry calcite with negative Ce anomaly).

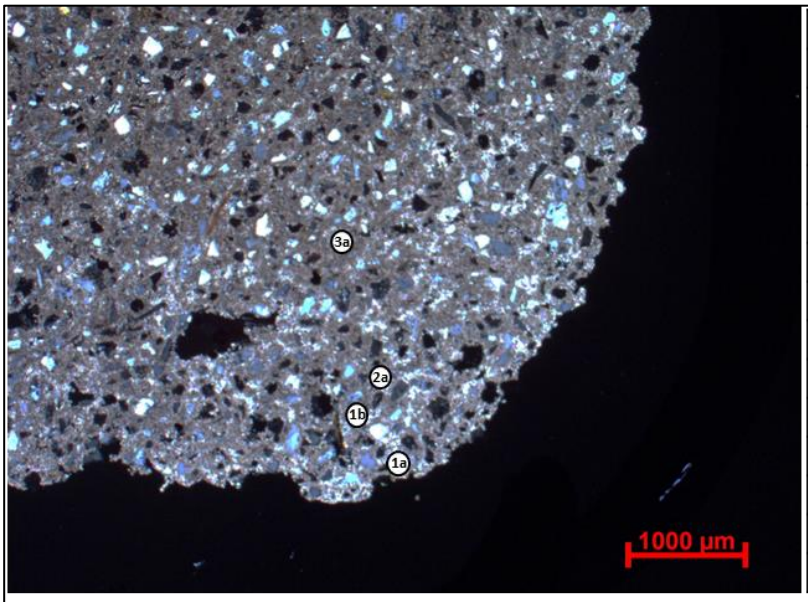

REEs	K2BS2-1a	K2BS2-1b	K2BS2-2a	K2BS2-3a
La	367.09	535.86	805.91	717.30
Ce	226.75	383.36	481.24	564.44
Pr	129.31	248.92	377.16	401.94
Nd	109.41	221.01	315.10	295.40
Sm	59.46	126.35	195.95	191.22
Eu	39.08	87.03	108.35	127.89
Gd	68.34	91.96	150.75	157.29
Tb	44.32	59.56	116.34	105.54
Dy	30.89	63.41	106.91	103.66
Ho	25.46	59.16	106.23	86.08
Er	40.00	51.25	111.25	73.75
Tm	23.89	42.91	106.48	57.89
Yb	19.25	37.89	82.61	55.90
Lu	31.71	41.46	77.24	48.37

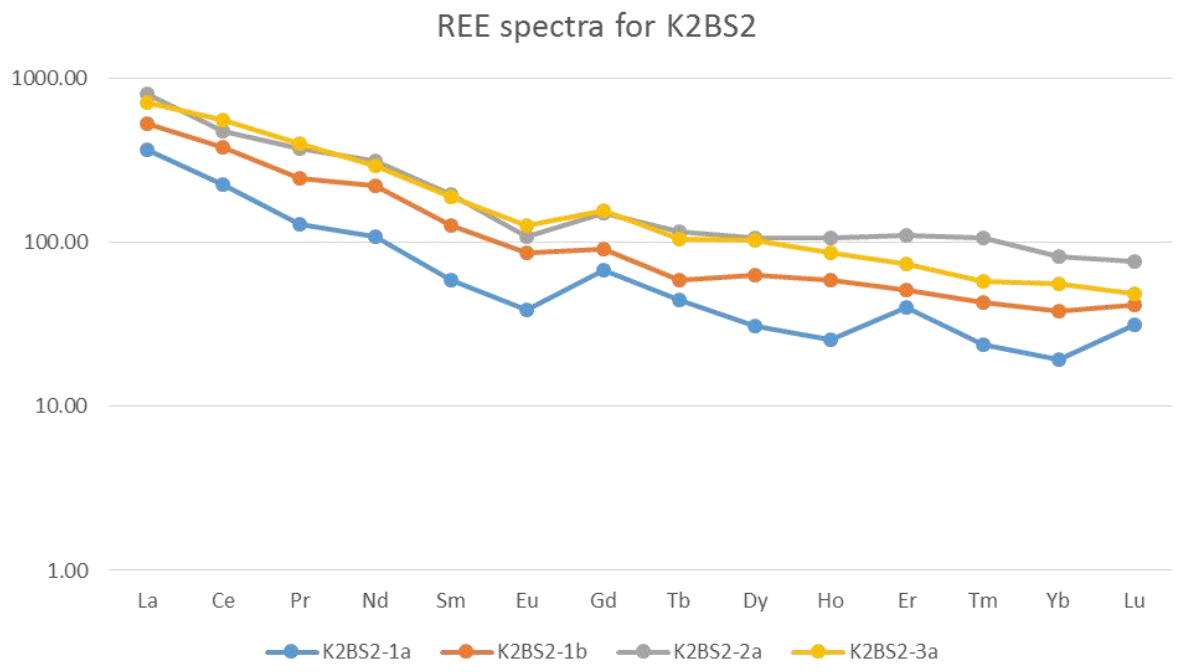

Spot/ppm	Na	Mg	Ca	Ti	Mn	Fe	Cu	Zn	Rb	Sr	Y	Ba	Th	U
K2BS2-1a	3210	9000	544000	2880	13800	11400	42	76	37	570	76.0	110.0	13.5	16.8
K2BS2-1b	950	7900	620000	1150	17000	10800	26	54	41	542	102.0	155.0	33.1	44.0
K2BS2-2a	1790	11000	550000	73000	14800	18600	46	122	71	800	165.0	280.0	20.2	23.7
K2BS2-3a	1485	4940	607000	650	11200	4550	10	32	18	675	173.0	94.0	37.5	45.3

Figure 205: The REE and trace element contents for the sample K2Bs-2 (micritic calcite).

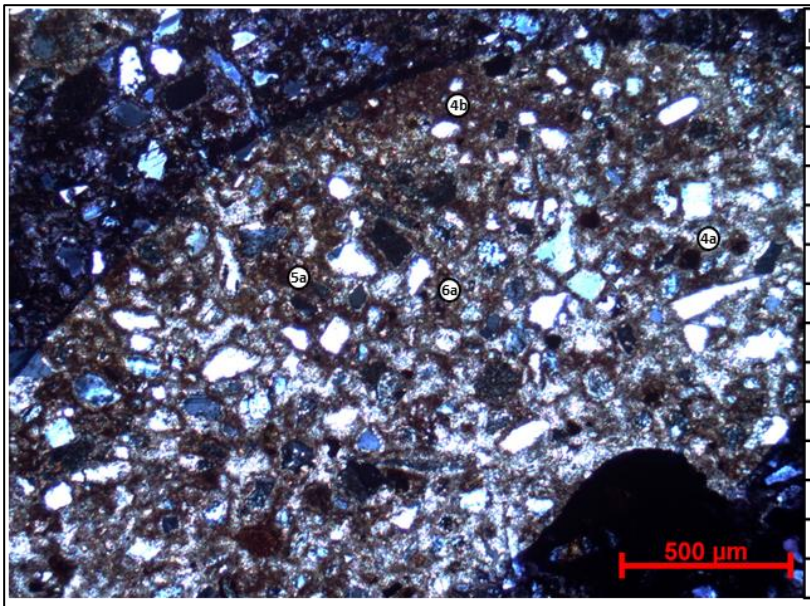

REEs	K2BS2-4a	K2BS2-4b	K2BS2-5a	K2BS2-6a
La	187.76	379.75	424.47	687.34
Ce	80.42	207.18	251.22	450.24
Pr	67.13	181.03	197.20	366.38
Nd	55.36	146.39	162.14	309.63
Sm	28.51	79.05	88.51	181.08
Eu	16.34	47.60	50.44	111.90
Gd	25.13	55.78	77.89	135.18
Tb	14.68	47.37	45.43	96.95
Dy	15.49	46.34	48.78	90.65
Ho	17.77	40.29	41.03	81.32
Er	15.44	34.75	36.88	74.44
Tm	17.41	29.15	32.39	60.73
Yb	14.41	28.76	31.06	46.89
Lu	14.55	27.20	26.02	45.93

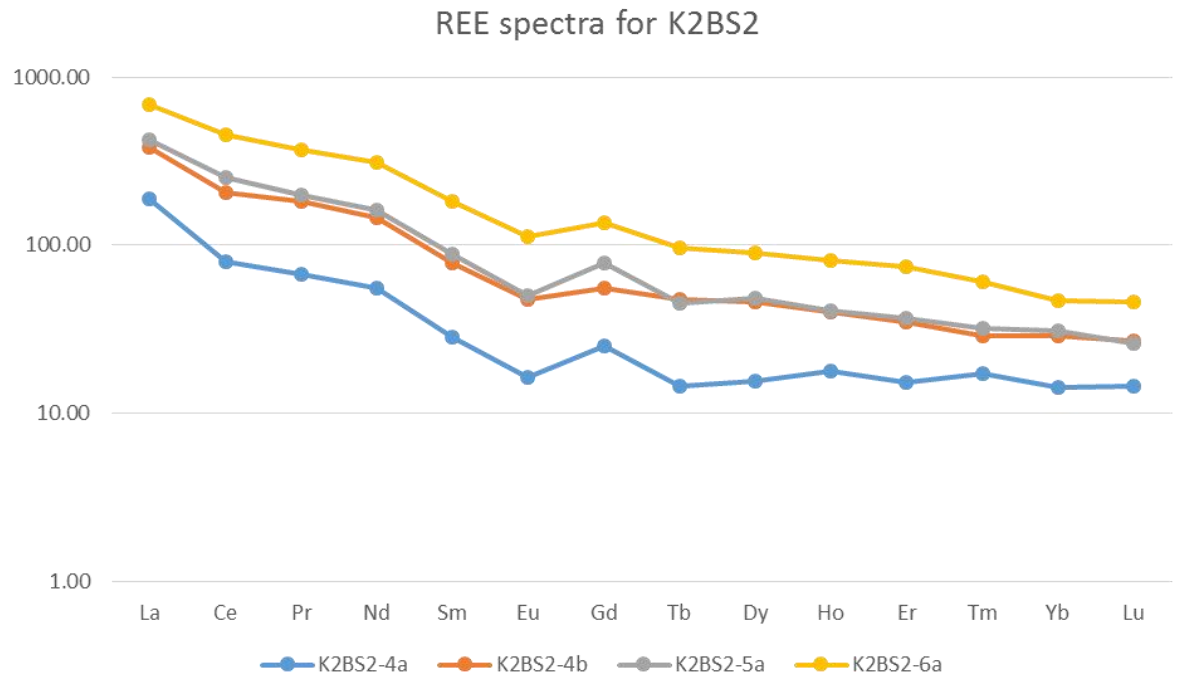

Spot/ppm	Na	Mg	Ca	Ti	Mn	Fe	Cu	Zn	Rb	Sr	Y	Ba	Th	U
K2BS2-4a	112	2830	509000	44	12010	1600	2	3	3	329	36.0	28.3	0.9	12.6
K2BS2-4b	570	3980	545000	496	11380	13600	13	18	12	393	81.5	59.5	2.7	56.0
K2BS2-5a	3100	13000	524000	2980	10800	65300	49	151	123	579	85.7	332.0	6.1	61.6
K2BS2-6a	3740	10180	547000	1702	10410	47600	42	87	56	682	172.0	252.0	8.0	140.5

Figure 206: The REE and trace element contents for sample the K2Bs-2 (micritic calcite).

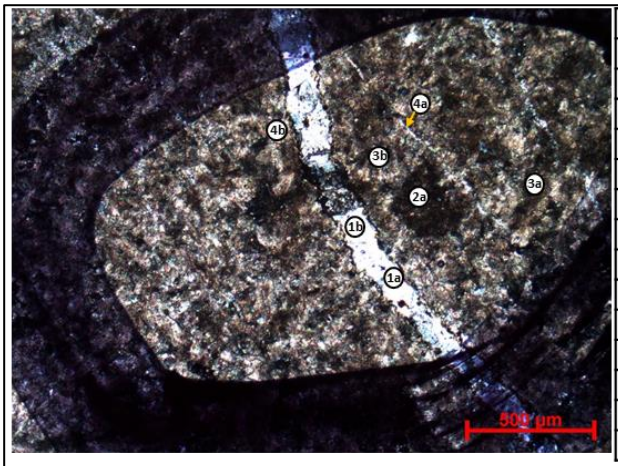

REEs	K2BS3A-1a	K2BS3A-1b	K2BS3A-2a	K2BS3A-3a	K2BS3A-3b	K2BS3A-4a	K2BS3A-4b
La	555.70	535.86	474.26	394.09	388.61	394.09	357.38
Ce	415.66	410.44	336.05	286.30	244.21	245.68	227.90
Pr	250.11	277.80	231.68	202.59	171.66	168.10	195.04
Nd	185.56	215.10	200.44	155.36	134.35	95.84	115.97
Sm	82.43	100.68	102.03	87.84	70.27	75.00	76.35
Eu	50.80	64.83	54.35	49.20	37.30	16.16	39.08
Gd	55.28	67.84	55.28	56.83	41.71	35.68	55.78
Tb	52.08	53.46	43.77	39.89	36.84	41.83	47.37
Dy	47.97	50.81	42.28	38.62	31.87	17.89	25.61
Ho	49.27	54.03	34.25	37.00	35.16	23.08	28.02
Er	49.88	54.81	32.38	31.56	26.63	50.63	19.38
Tm	41.70	46.15	34.01	25.91	21.46	21.86	31.17
Yb	45.53	52.17	33.54	28.39	32.61	39.13	13.04
Lu	36.99	45.12	30.89	34.15	38.21	35.77	37.40

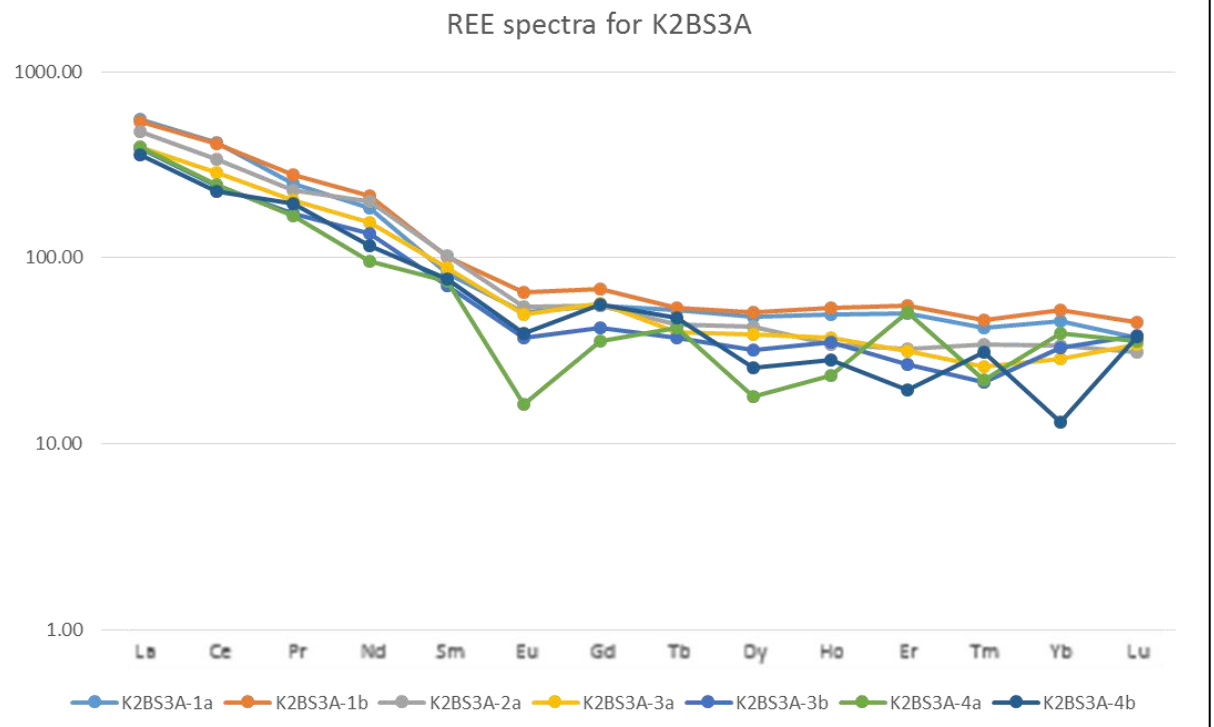

Spot/ppm	Na	Mg	Ca	Ti	Mn	Fe	Cu	Zn	Rb	Sr	Y	Ba	Th	U
K2BS3A-1a	224	2006	785000	-	5400	778	-	-	-	331	87.2	2.4	1.3	1.5
K2BS3A-1b	171	1766	787000	-	23630	860	-	2	-	361	102.7	10.1	0.4	0.7
K2BS3A-2a	2080	8990	866000	889	8060	8970	12	47	30	782	62.6	65.5	11.6	5.8
K2BS3A-3a	2510	14210	757000	2380	5480	22340	22	101	93	688	56.9	217.0	9.2	8.4
K2BS3A-3b	1180	9660	733000	1118	6460	11450	10	46	49	652	50.8	117.4	6.0	6.1
K2BS3A-4a	2020	4200	767000	229	19100	1660	-	-	12	433	69.2	15.0	1.1	10.1
K2BS3A-4b	3770	10860	754000	1510	6730	13000	20	-	58	718	56.7	83.0	7.9	4.8

Figure 207: The REE and trace element contents for the sample K2Bs-3A (calcite).

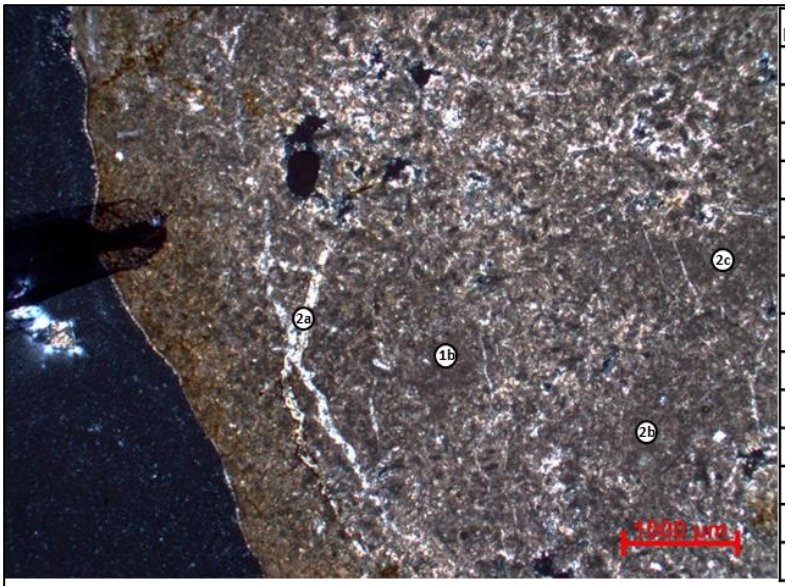

REEs	K2BS3B-1a	K2BS3B-2a	K2BS3B-2b	K2BS3B-2c
La	321.52	435.44	344.30	359.49
Ce	192.33	461.66	224.14	231.97
Pr	144.50	298.28	167.67	173.60
Nd	113.35	259.96	135.89	139.61
Sm	51.89	162.84	73.45	73.92
Eu	29.13	114.92	43.16	44.40
Gd	35.78	103.52	47.79	50.45
Tb	29.09	79.22	36.29	38.50
Dy	27.56	66.42	35.41	33.41
Ho	22.31	55.31	28.94	33.52
Er	24.69	46.25	31.06	28.88
Tm	20.77	35.38	24.62	25.47
Yb	24.16	32.11	26.96	26.96
Lu	26.22	26.91	28.50	26.79

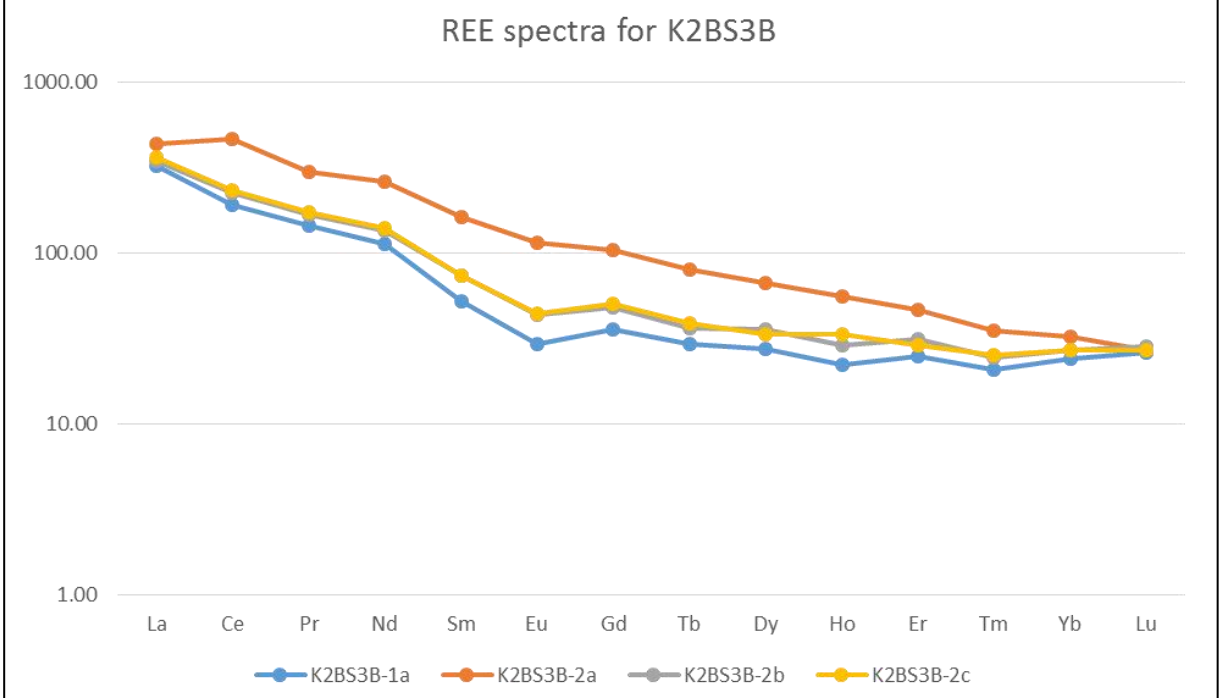

Spot/ppm	Na	Mg	Ca	Ti	Mn	Fe	Cu	Zn	Rb	Sr	Y	Ba	Th	U
K2BS3B-1a	1545	11660	799000	1374	7720	16310	19	54	54	741	45.2	130.3	6.6	5.7
K2BS3B-2a	33	660	787000	16	49600	983	1	5	1	253	89.5	39.5	0.3	0.5
K2BS3B-2b	1401	7840	781000	882	9190	9780	15	45	34	741	56.6	83.7	4.8	8.4
K2BS3B-2c	1785	7570	796000	961	9450	9050	22	42	30	767	58.0	86.9	4.8	8.3

Figure 208: The REE and trace element contents for the sample K2Bs-3B (marking that the late infilling calcite show a positive Ce anomaly and is depleted in Na and Mg, indicating a low salinity water source i.e. meteoric water influence during outcrop exposure).

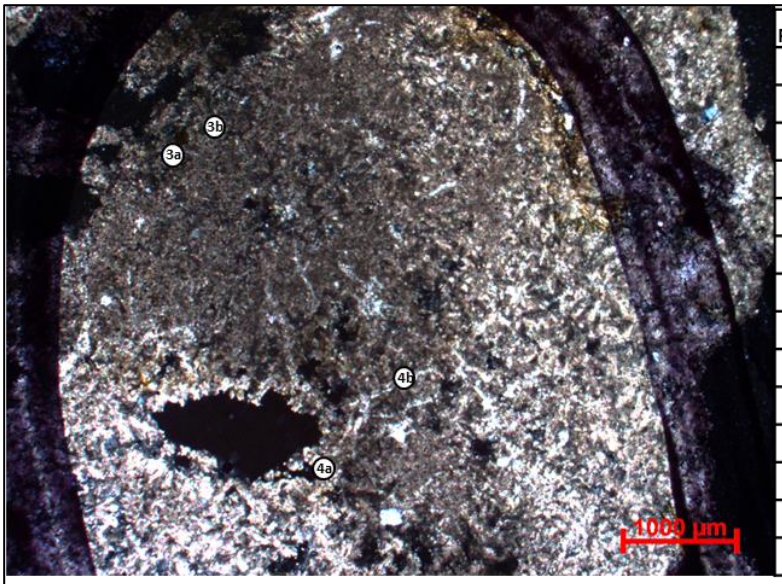

REEs	K2BS3B-3a	K2BS3B-3b	K2BS3B-4a	K2BS3B-4b
La	497.47	458.65	649.79	365.82
Ce	443.39	425.77	518.76	373.90
Pr	261.85	230.60	373.92	250.32
Nd	224.29	204.38	310.72	218.60
Sm	125.68	118.24	177.03	138.51
Eu	80.11	66.96	108.35	89.70
Gd	89.45	76.38	122.11	80.90
Tb	59.00	60.94	81.44	68.42
Dy	54.96	47.15	73.58	57.32
Ho	47.25	41.76	62.64	46.70
Er	44.50	37.19	56.88	38.44
Tm	36.52	27.94	38.06	28.62
Yb	39.25	32.73	40.99	20.99
Lu	34.92	33.33	35.37	17.07

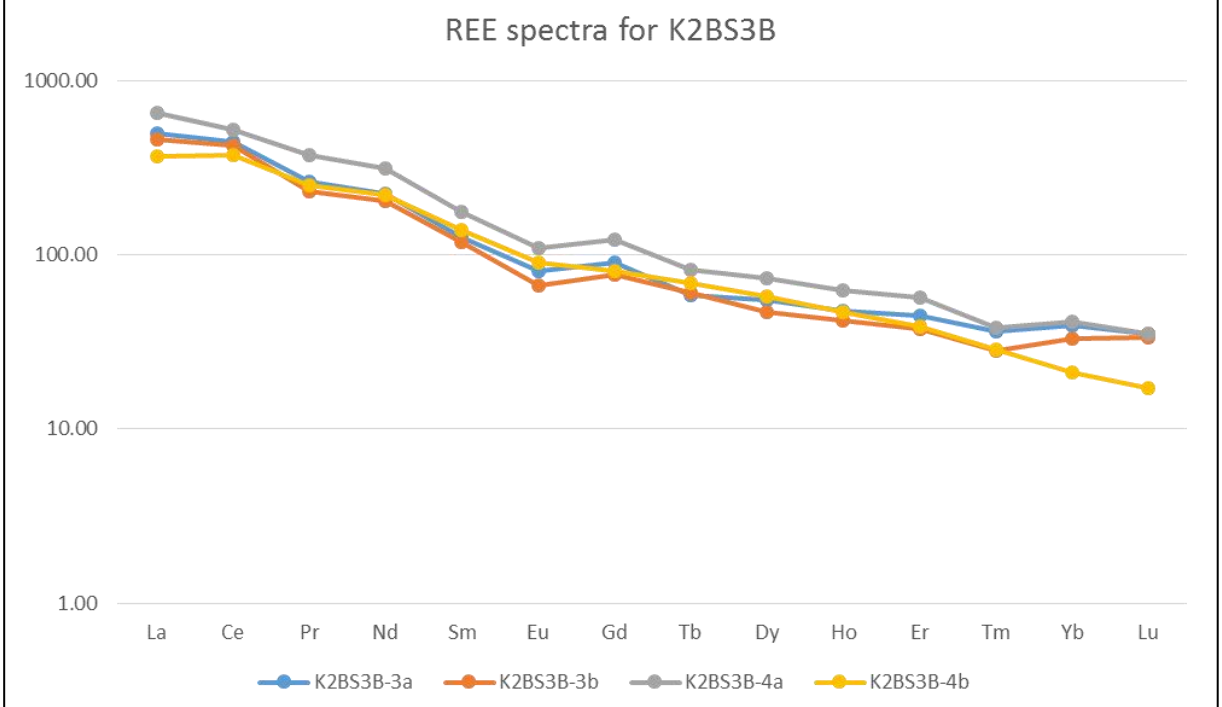

Spot/ppm	Na	Mg	Ca	Ti	Mn	Fe	Cu	Zn	Rb	Sr	Y	Ba	Th	U
K2BS3B-3a	1116	13180	792000	1382	11040	32080	30	72	65	751	92.3	170.1	12.1	8.8
K2BS3B-3b	1092	10150	825000	1560	16700	29900	31	61	58	698	79.7	203.0	8.1	8.3
K2BS3B-4a	1970	16800	838000	2560	7600	71700	72	106	90	937	126.0	214.0	13.1	13.1
K2BS3B-4b	-	1085	726000	119	40720	1810	2	7	3	272	69.5	53.4	0.4	0.8

Figure 209: The REE and trace element contents for the sample K2Bs-3B (different calcite generations with similar REE profiles).

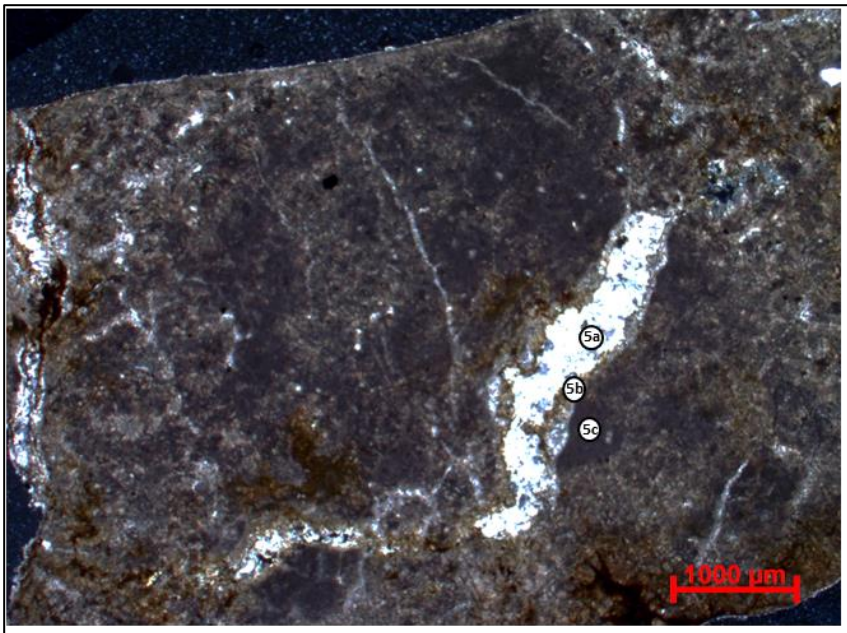

REEs	K2BS3B-5a	K2BS3B-5b	K2BS3B-5c
La	564.14	488.19	616.88
Ce	513.87	410.11	454.98
Pr	371.23	226.72	341.59
Nd	310.50	177.68	282.28
Sm	164.86	86.49	166.22
Eu	126.47	55.24	106.93
Gd	128.64	60.30	110.05
Tb	101.11	46.26	78.95
Dy	86.99	42.68	69.11
Ho	77.84	39.19	64.10
Er	75.50	39.56	53.00
Tm	53.44	34.21	45.06
Yb	52.80	38.51	45.59
Lu	46.95	34.15	45.93

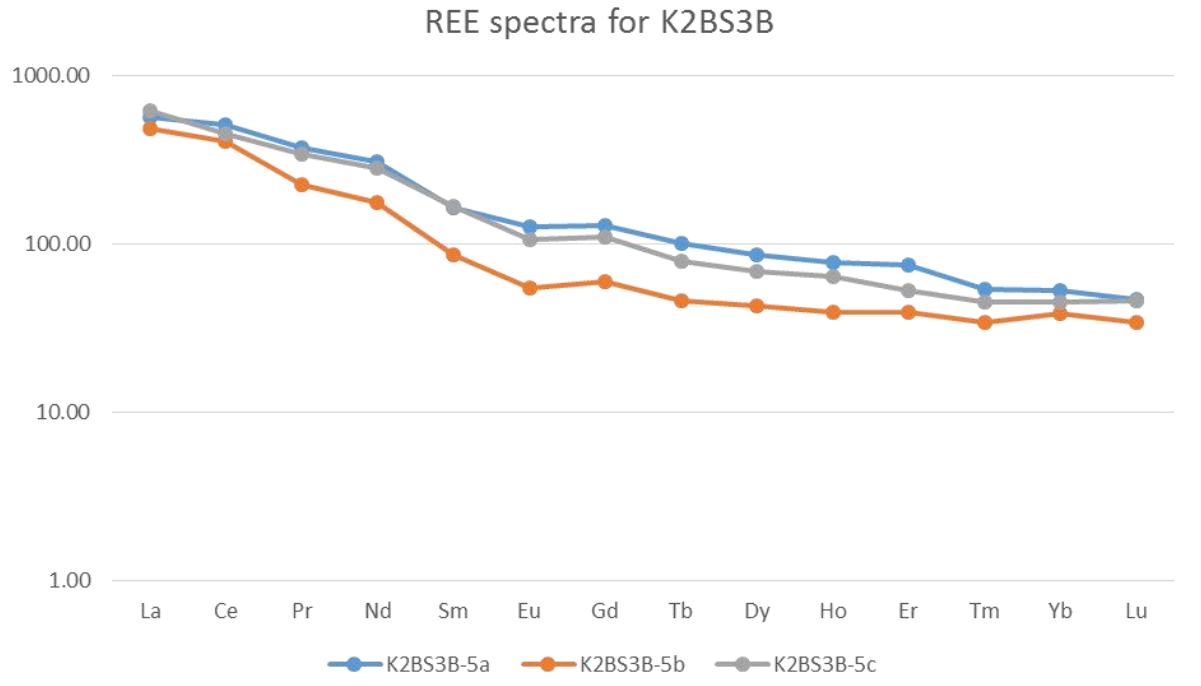

Spot/ppm	Na	Mg	Ca	Ti	Mn	Fe	Cu	Zn	Rb	Sr	Y	Ba	Th	U
K2BS3B-5a	-	1225	795000	-	40130	861	-	2	-	227	146.3	19.6	0.1	0.6
K2BS3B-5b	1140	4600	831000	872	26100	22010	19	31	29	427	70.0	109.2	5.2	6.2
K2BS3B-5c	5570	16640	791000	3600	7810	44300	63	152	133	943	119.4	362.0	15.5	8.6

Figure 210: The REE and trace element contents for the sample K2Bs-3B (two different calcite generations with similar REE profiles but different trace element content). The secondary calcite (white variety) has probably formed during the superficial exposure when the rock came in contact with meteoric water

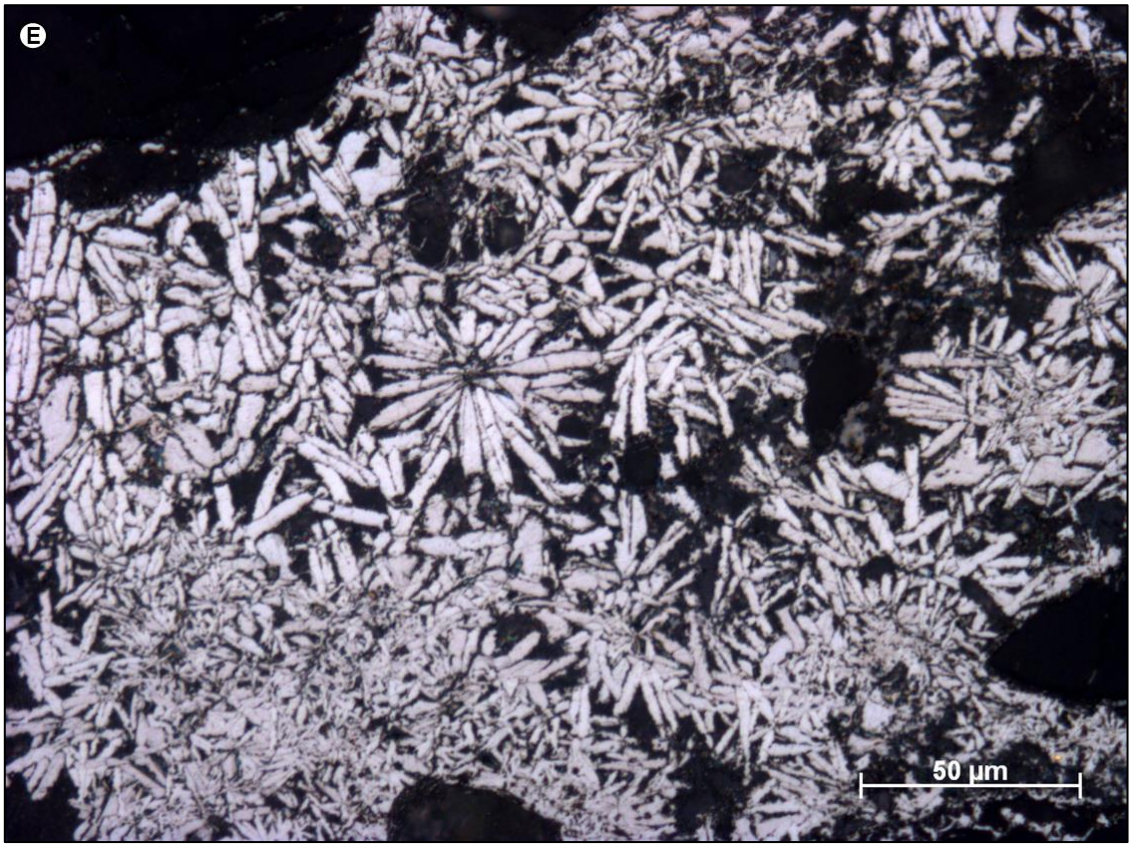

Figure 211: High resolution image of marcasite.

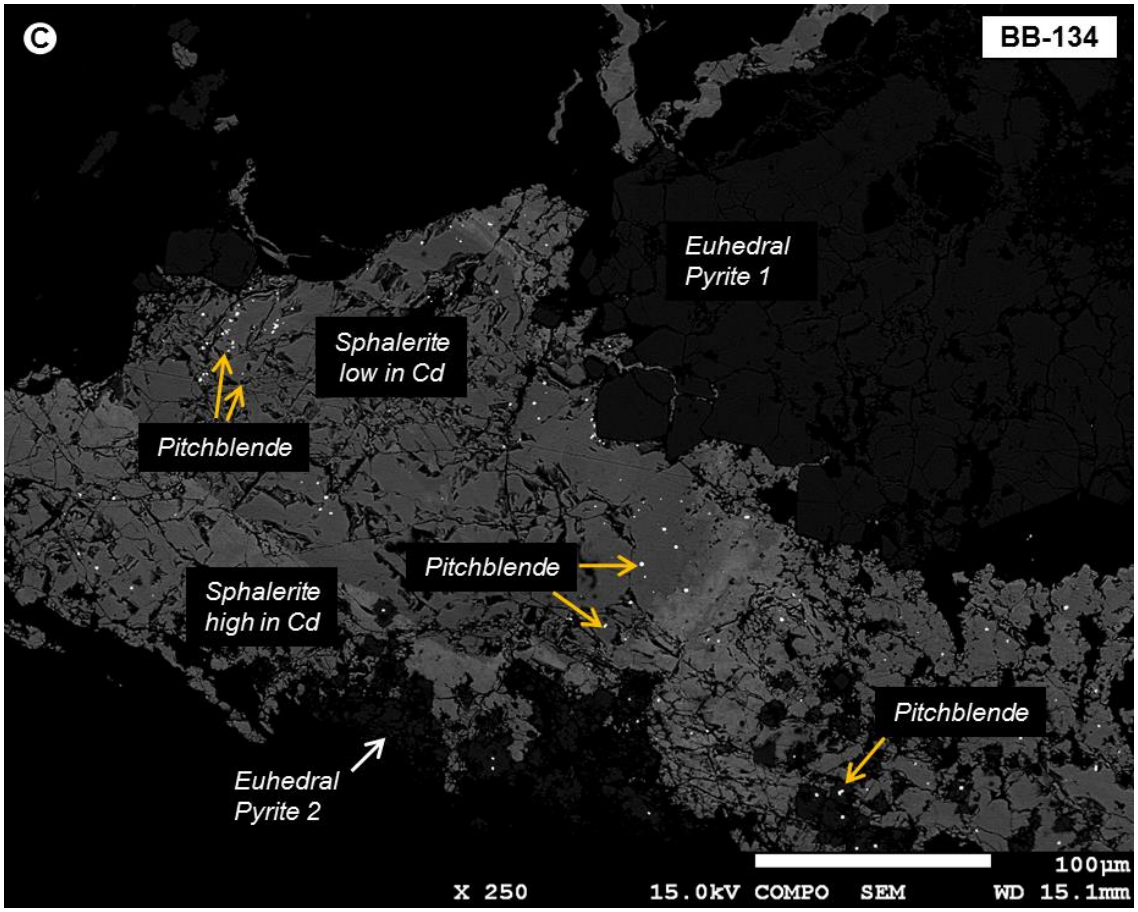

Figure 212: Examples of sphalerite - euhedral pyrite - pitchblende relationships. All pictures under BSE.

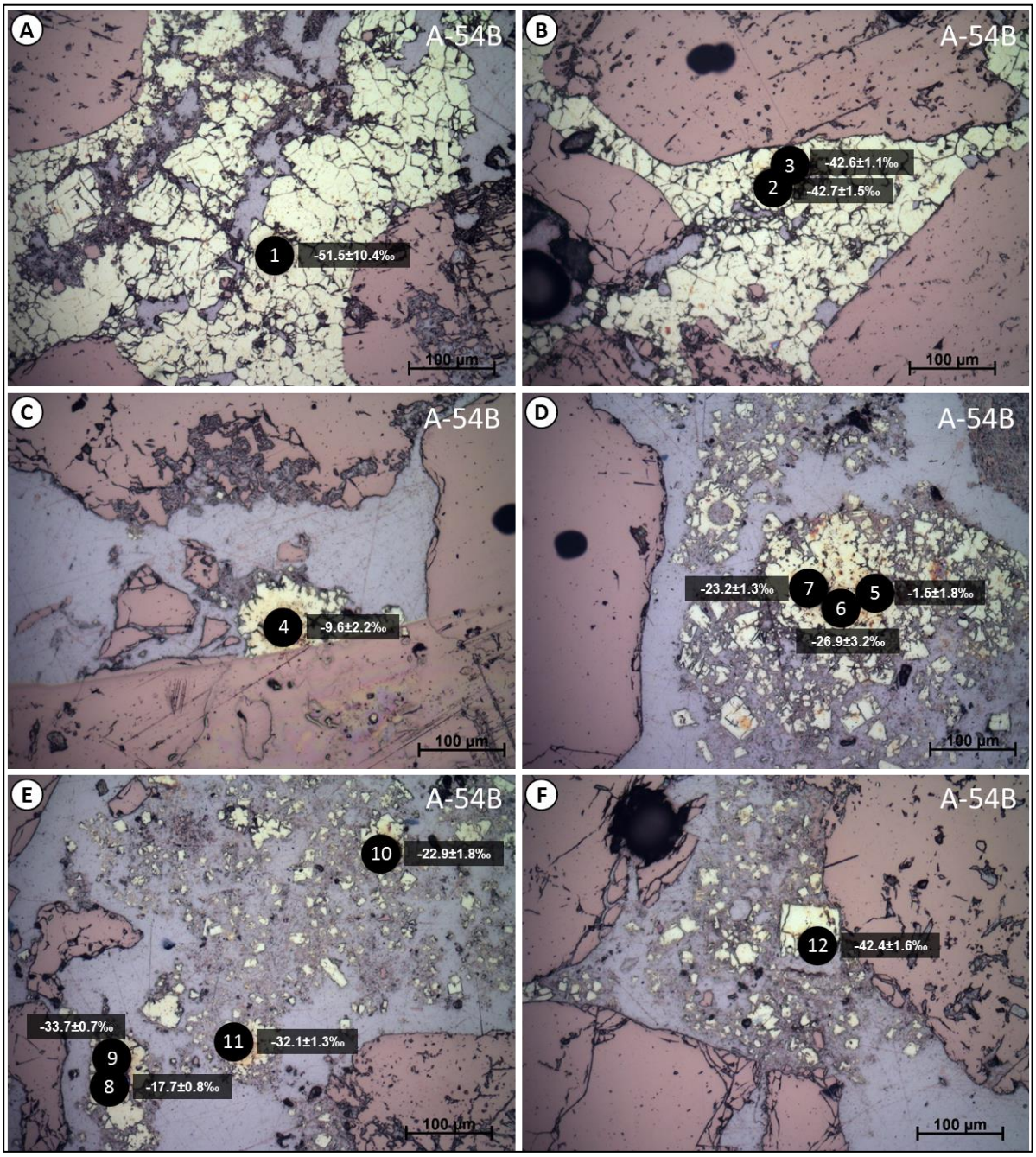

Figure 213: Optical microscopy under reflected light mode indicating the spots measured by SIMS on pyrite for $\delta^{34}S$ for sample 9659A-54B. Isolated framboids and pyrite cement were measured.

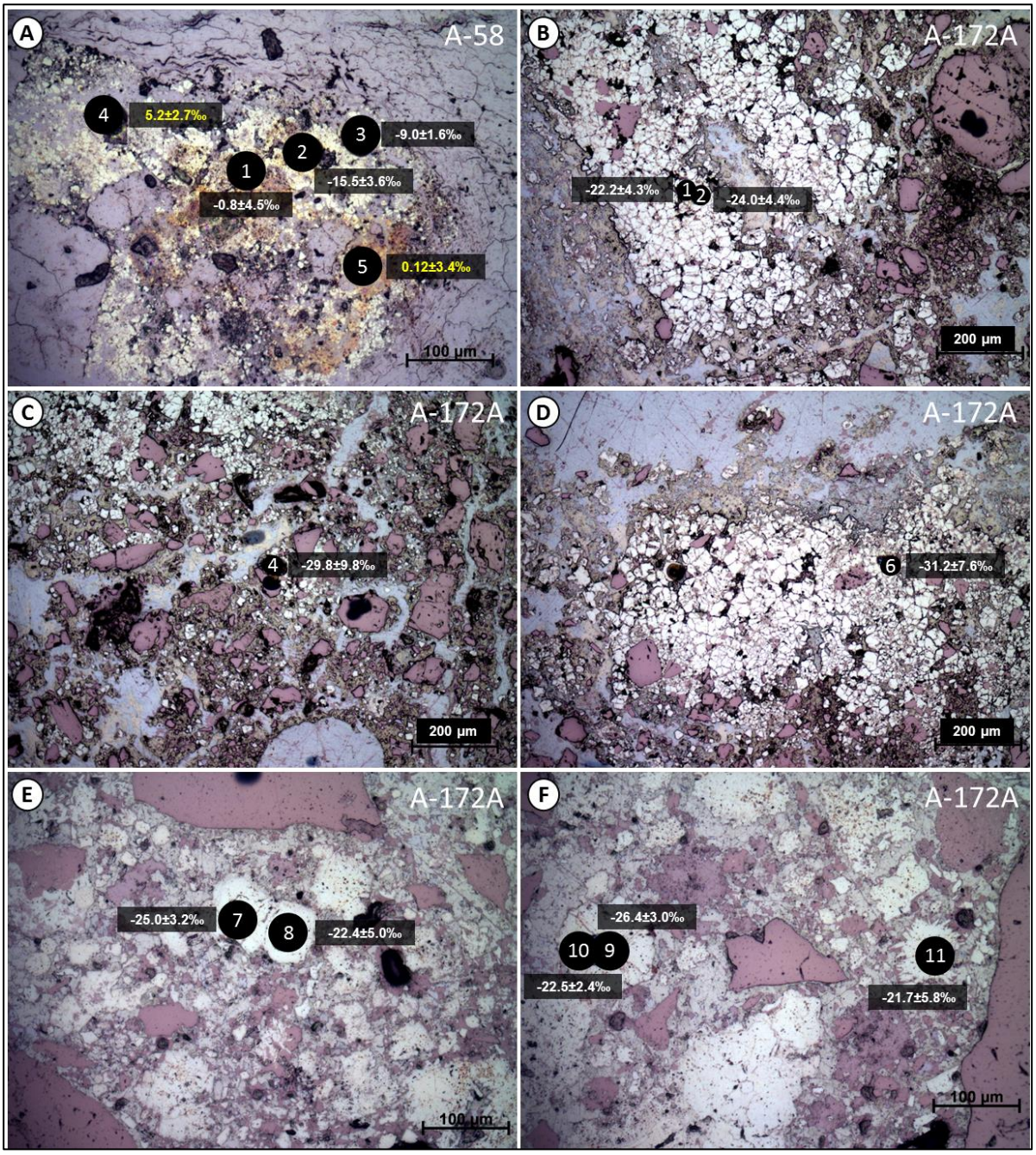

Figure 214: Optical microscopy under reflected light mode indicating the spots measured by SIMS on pyrite for $\delta^{34}S$ for samples 9659A-58 and 9659A-172A. Pyrite cementing sand grains were measured for A-58. Marcasite, framboids embedded within euhedral pyrite as well as framboids and euhedral pyrite with uranium inclusions were measured for A-172A.

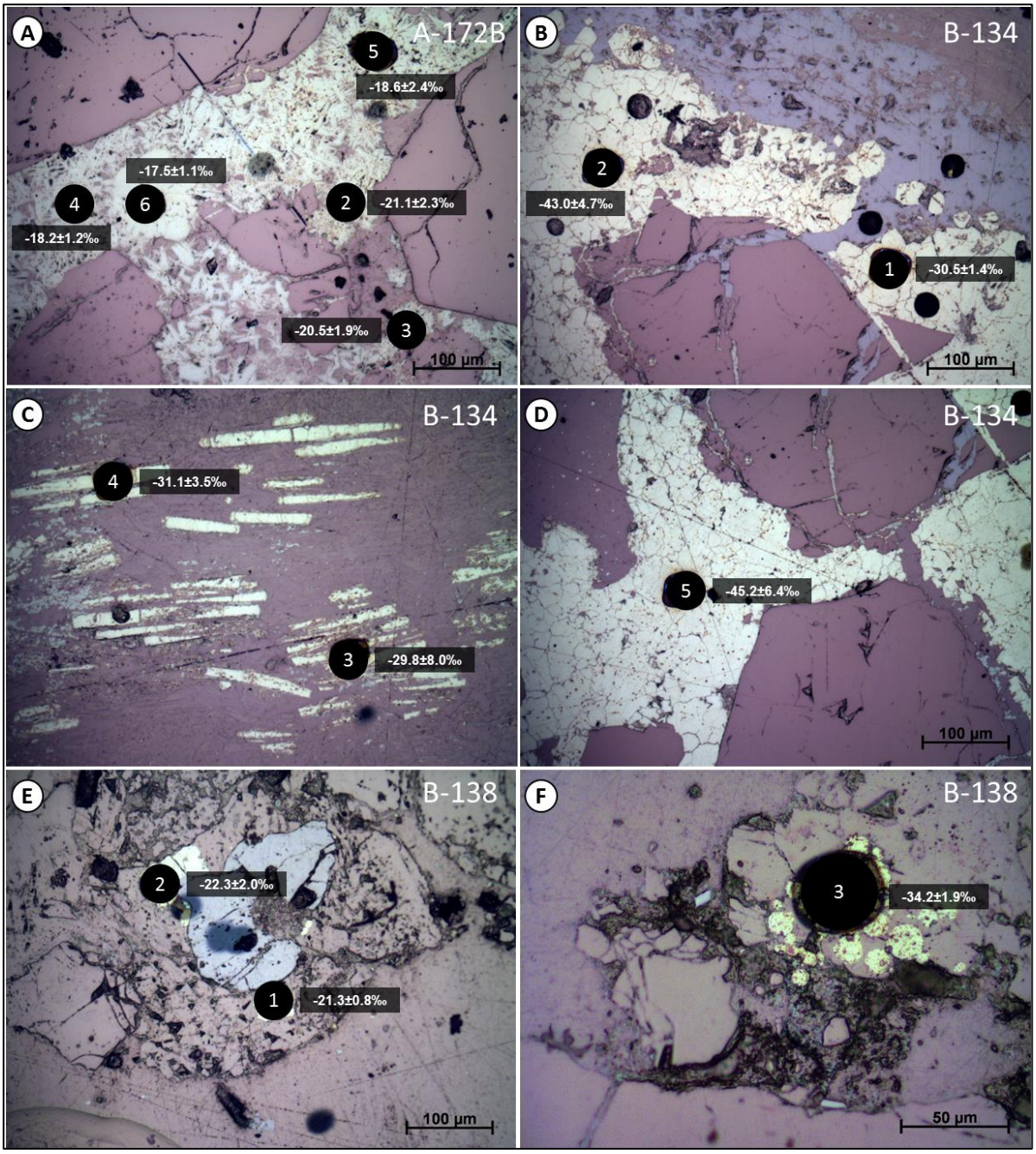

Figure 215: Optical microscopy under reflected light mode indicating the spots measured by SIMS on pyrite for $\delta^{34}S$ for samples 9659A-172B, 9659B-134 and 9659B-138. Marcasite was measured for A-172B. Pyrite inside organic matter and pyrite associated to sphalerite was measured for B-134. Finally, euhedral pyrite around ilmenite grains and framboidal pyrite encompassed by anhedral (Type IV) dolomite was measured for B-138.

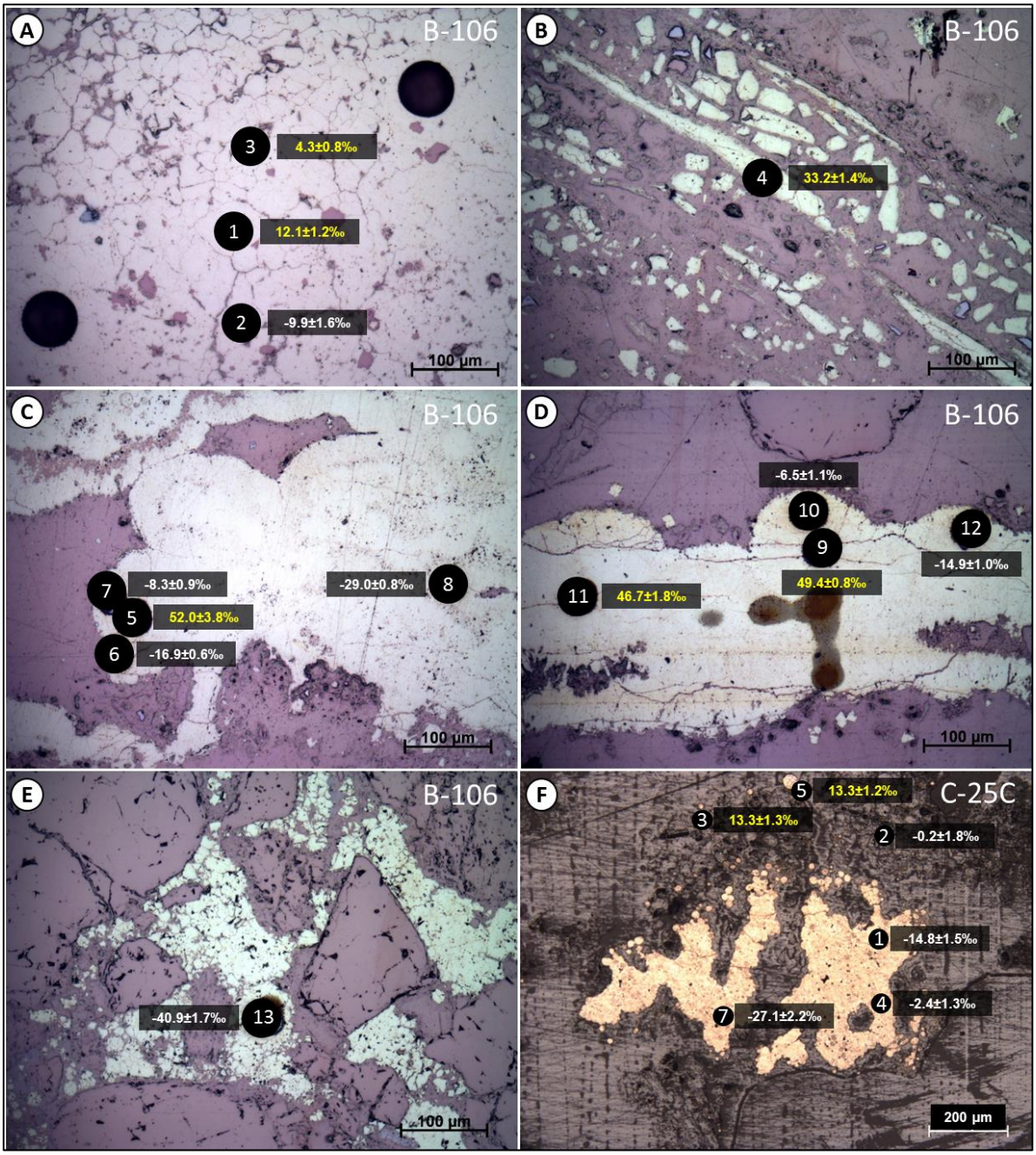

Figure 216: Optical microscopy under reflected light mode indicating the spots measured by SIMS on pyrite for $\delta^{34}S$ for samples 9659B-106 and 9659CC-25C. Framboids and euhedral pyrite associated to organic matter were measured.

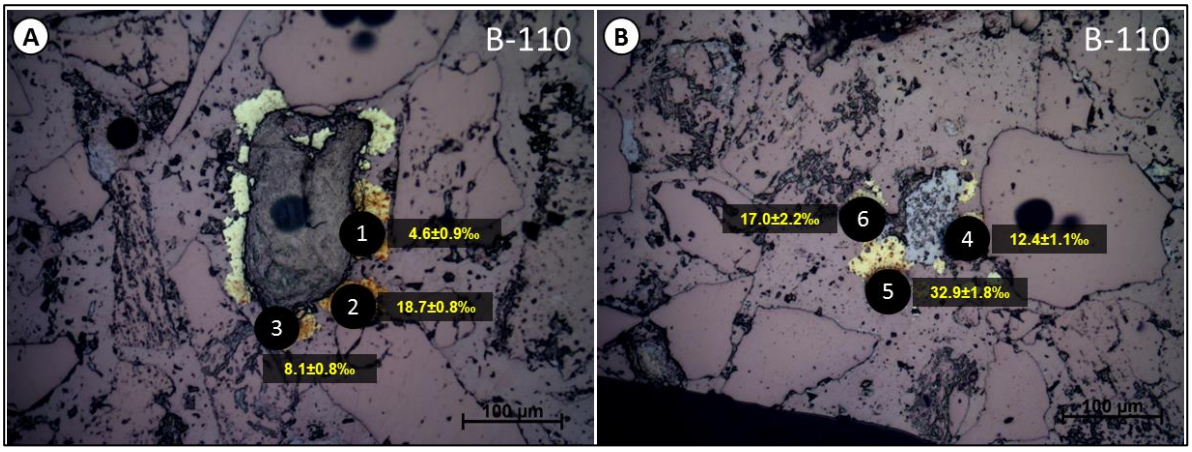

Figure 217: Optical microscopy under reflected light mode indicating the spots measured by SIMS on pyrite for $\delta^{34}S$ for sample 9659B-110. Euhedral pyrite around silicates, framboids and euhedral pyrite around ilmenite grains were measured.

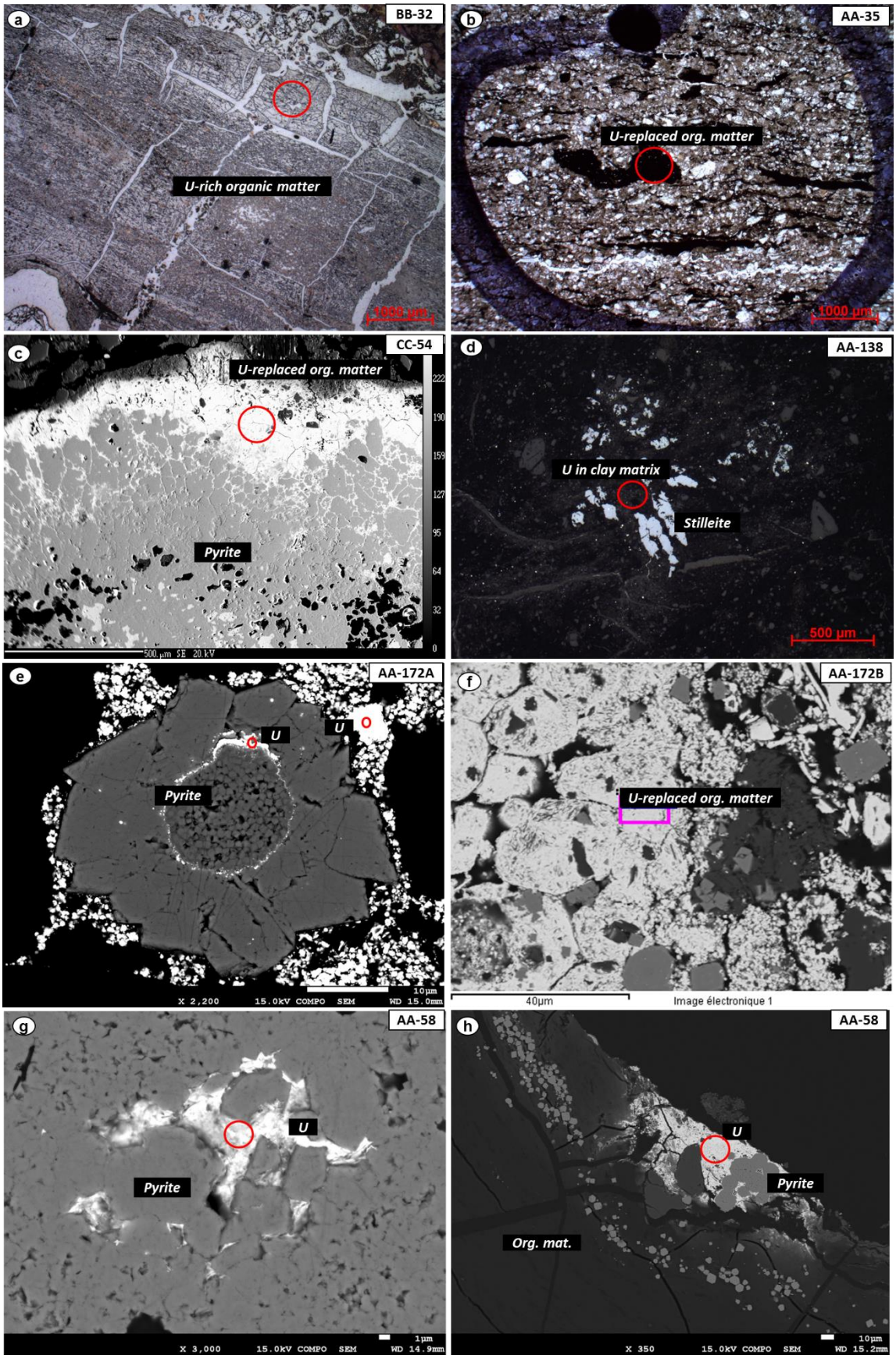

Figure 218: Examples of the uranium phases considered for the construction of the U ternary diagram.

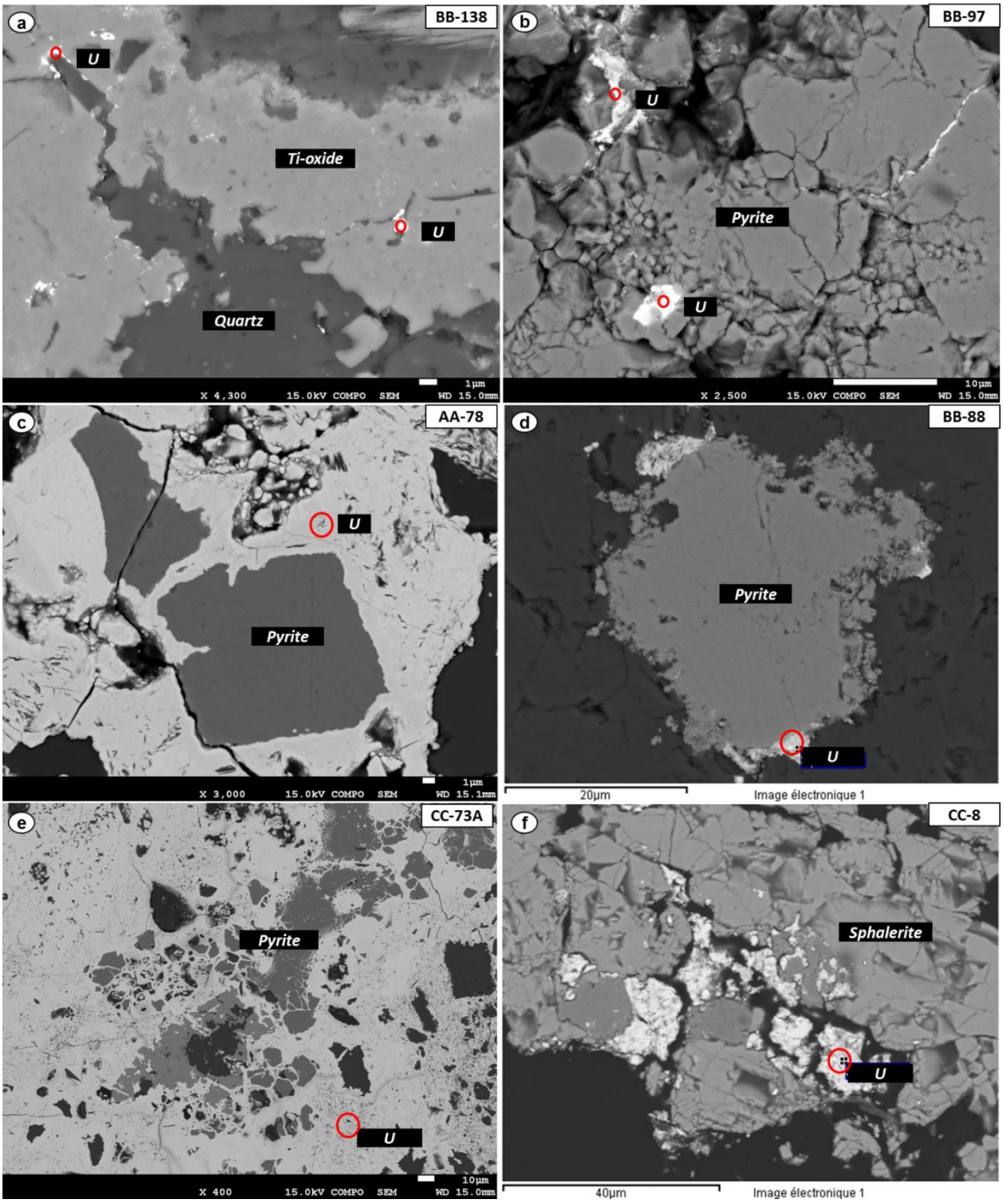

Figure 219: Examples of the uranium phases considered for the construction of the U ternary diagram.

APPENDIX II (TABLES – NUMERICAL DATA)

Table 14: Summary of the studied samples from the 9659 collection, with sampling depths, radioactivity measurements and a short description. Samples with SSPγ > 200 c/s are considered rich in uranium concentration. Sandstone: matrix supported sandstone; Sand: unconsolidated sand, O.M: organic matter content; Uranium: uranium phase not associated to organic matter; Claystone: very fine grained rock; Carbonate: carbonate cemented sandstone. With (*) the samples from which thin sections are currently available.

N/N	N° PhD **9659-**	DDH number (well N°)	depth from (m)	depth to (m)	SPPγ (c/s)	Description
1	AA-7	ZOOV_0699_6	123,27	123,36	-	O.M
2	AA-20	ZOOV_1050_6	122,65	122,90	-	O.M
3	AA-23	ZOOV_1050_9	132,55	132,75	-	O.M
4	AA-24*	ZOOV_1050_10	134,05	134,35	220	Sandstone
5	AA-28*	ZOOV_1050_14	143,41	143,95	93	Sandstone
6	AA-32	ZOOV_0710_3	114,95	115,45	-	O.M
7	AA-34*	ZOOV_0710_5	117,85	118,10	223	O.M
8	AA-35*	ZOOV_0710_6	119,40	119,60	**914**	Uranium
9	AA-36	ZOOV_0710_7	120,05	120,15	132	Carbonate
10	AA-37	ZOOV_0710_8	123,08	123,27	**-**	O.M
11	AA-39	ZOOV_0710_10	131,49	131,74	**-**	O.M
12	AA-41*	ZOOV_0710_12	134,16	134,25	**643**	O.M
13	AA-51	ZOOV_0709_4	114,92	115,22	**-**	O.M
14	AA-54*	ZOOV_0709_7	119,14	119,32	**1500**	O.M
15	AA-57*	ZOOV_0709_10	125,60	125,88	220	O.M
16	AA-58*	ZOOV_0709_11	126,35	126,55	**926**	O.M
17	AA-62	ZOOV_0709_15	136,99	137,19	90	O.M
18	AA-68*	ZOOV_0703_2	136,45	136,74	274	O.M
19	AA-72	ZOOV_0696_1	120,84	120,94	89	O.M
20	AA-76	ZOOV_0696_5	138,41	138,51	137	O.M
21	AA-78*	ZOOV_0696_7	150,38	150,48	b.d.l	Claystone
22	AA-82	ZOOV_0694_2	129,50	129,70	-	O.M
23	AA-84	ZOOV_0694_4	139,20	139,39	-	O.M
24	AA-105	ZOOV_0689_3	141,80	141,90	-	O.M
25	AA-114*	ZOOV_0414_4	157,80	158,10	320	O.M
26	AA-116	ZOOV_0693_1	144,75	145,05	**339**	O.M
27	AA-119	ZOOV_0693_3b	149,26	149,51	**85**	O.M
28	AA-133	ZOOV_0690_7	157,65	157,85	**-**	O.M
29	AA-137	ZOOV_0690_11	164,15	164,20	**-**	O.M
30	AA-138*	ZOOV_0690_12	174,65	174,84	**1022**	Uranium
31	AA-140	ZOOV_0686_2	145,45	145,60	-	O.M
32	AA-142*	ZOOV_0686_4	158,05	158,15	241	O.M
33	AA-147*	ZOOV_0682_1	141,50	141,60	99	Carbonate
34	AA-148	ZOOV_0682_2	144,70	145,00	**-**	O.M & Carb
35	AA-151	ZOOV_0682_5	156,55	156,85	83	O.M

36	AA-154*	ZOOV_0682_7b	160,06	160,16	**2113**	O.M
37	AA-156	ZOOV_0676_1	144,28	144,48	135	O.M & Carb
38	AA-157*	ZOOV_0676_2	149,61	149,66	85	Carbonate
39	AA-159*	ZOOV_0676_4	172,13	172,23	**757**	Sandstone
40	AA-171*	ZOOV_0670_2	168,29	168,34	97	Carbonate
41	AA-172*	ZOOV_0670_3	171,79	171,99	**5379**	Uranium
42	AA-177*	ZOOV_0989_5	173,75	174,16	48	Carbonate
43	BB-9*	ZOOV_0332_3	137,65	137,95	**585**	O.M
44	BB-10	ZOOV_0332_4	138,10	138,25	1542	O.M
45	BB-20	ZOOV_0147_4	139,69	139,94	131	O.M
46	BB-23	ZOOV_0147_7	149,59	149,69	-	O.M
47	BB-25*	ZOOV_0147_9	155,92	155,97	70	Carbonate
48	BB-32*	ZOOV_0364_6	138,77	138,87	184	O.M
49	BB-37	ZOOV_0364_11	149,05	149,10	74	Carbonate
50	BB-43	ZOOV_0119_5	141,85	142,00	97	O.M
51	BB-50	ZOOV_0149_1	133,25	133,55	-	O.M
52	BB-51*	ZOOV_0149_2	133,75	134,00	128	Sandstone
53	BB-53*	ZOOV_0149_4a	139,06	139,40	88	O.M
54	BB-55	ZOOV_0352_1	141,37	141,67	-	O.M
55	BB-66	ZOOV_0259_4a	155,60	155,65	56	Carbonate
56	BB-67*	ZOOV_0259_4b	156,25	156,30	56	Carbonate
57	BB-71*	ZOOV_0259_8	165,65	165,75	212	Carbonate
58	BB-72	ZOOV_0259_9	168,18	168,48	67	Carbonate
59	BB-77	ZOOV_0351_4	152,39	152,64	-	O.M
60	BB-78	ZOOV_0351_5	154,71	154,76	173	Carbonate
61	BB-88*	ZOOV_0180_10	182,10	182,14	73	Carbonate
62	BB-91*	ZOOV_0180_13	186,56	186,75	61	Carbonate
63	BB-94	ZOOV_0360_1	160,57	160,74	-	O.M
64	BB-97*	ZOOV_0360_4	174,72	174,77	105	Carbonate
65	BB-101	ZOOV_0360_8	183,92	183,97	88	Carbonate
66	BB-103	ZOOV_0360_10	185,58	185,63	114	Carbonate
67	BB-106*	ZOOV_0213_2	162,05	162,35	169	O.M
68	BB-110*	ZOOV_0213_1	175,34	175,39	75	Carbonate
69	BB-115	ZOOV_0593_1	160,00	160,25	82	O.M
70	BB-118*	ZOOV_0593_1	168,24	168,51	120	O.M
71	BB-120	ZOOV_0593_6	171,99	172,29	78	O.M
72	BB-121*	ZOOV_0593_7	175,26	175,31	71	Carbonate
73	BB-122A	ZOOV_0593_8	176,65	176,81	-	O.M
74	BB-122B	ZOOV_0593_8	176,65	176,81	88	Carbonate
75	BB-123	ZOOV_0593_9	178,99	179,19	97	O.M
76	BB-124	ZOOV_0593_10	179,79	179,84	87	Carb+O.M
77	BB-125*	ZOOV_0593_11	181,00	180,05	69	Carb+O.M
78	BB-126*	ZOOV_0593_12	182,54	182,59	81	Carbonate
79	BB-128	ZOOV_0886_1	190,25	190,55	61	Sand

80	BB-129*	ZOOV_0886_2	192,46	192,61	153	Carbonate
81	BB-130	ZOOV_0886_3	195,62	195,79	529	O.M
82	BB-131*	ZOOV_0886_4	196,04	196,30	139	Sand
83	BB-133*	ZOOV_0886_6	200,80	200,85	58	Carbonate
84	BB-134*	ZOOV_0886_7	209,40	209,70	**541**	O.M
85	BB-135*	ZOOV_0886_8	210,45	210,70	36	Carbonate
86	BB-137*	ZOOV_0886_10	212,68	212,73	73	Carbonate
87	BB-138*	ZOOV_0886_11a	215,85	215,15	153	O.M
88	BB-139	ZOOV_0886_11b	216,20	216,50	83	O.M
89	BB-143*	ZOOV_0895_4	202,00	202,95	77	Carbonate
90	BB-148*	ZOOV_0895_9	217,70	217,75	114	Carbonate
91	CC-5	ZOOV_1081_2_2	125,13	125,18	193	O.M
92	CC-6*	ZOOV_1081_2_3	131,63	131,73	173	Carbonate
93	CC-7	ZOOV_1081_2_4	131,63	131,73	**2049**	O.M
94	CC-8*	ZOOV_1080_1	179,00	179,05	**5361**	Uranium
95	CC-23	ZOOV_1077_2	155,85	156,25	**-**	O.M
96	CC-24	ZOOV_0774_1	136,70	136,90	**-**	O.M
97	CC-25*	ZOOV_0774_2	137,55	137,85	**6177**	O.M
98	CC-37	ZOOV_0075_6	194,87	194,97	**-**	Carbonate
99	CC-49	ZOOV_1100_9	156,00	156,20	**407**	O.M
100	CC-54*	ZOOV_1100_6	168,25	168,55	**7028**	Uranium
101	CC-57*	ZOOV_1100_9	177,35	177,55	123	Carbonate
102	CC-72	ZOOV_1062_4	177,45	177,55	-	Uranium
103	CC-73*	ZOOV_1062_5	182,89	183,17	70	Carbonate

Table 15: Summary of the studied samples from the 9606 collection, legend in accordance to Table 1. All samples were available only as thin sections, plus Gravel: gravels with grain size between 2-4 mm, Pebble: gravels with grain size between 4-20 mm, N/A: not available.

N/N	N° PhD **9606-**	DDH number (well N°)	depth from (m)	depth to (m)	SPPγ (c/s)	Description
1	2	ZOOV_0309_1_002	115,41	115,51	62	Sand
2	4	ZOOV_0309_1_004	118,15	118,25	65	Sand
3	8	ZOOV_0309_1_008	122,59	122,69	72	Sand
4	9	ZOOV_0309_1_009	123,58	123,68	62	Sand
5	11	ZOOV_0309_1_011	129,33	129,43	53	Sand
6	14	ZOOV_0309_1_014	132,68	132,77	59	Sand
7	17	ZOOV_0309_1_017	135,99	136,08	68	Sand
8	20	ZOOV_0309_1_020	139,32	139,40	77	Sand
9	21	ZOOV_0309_1_021	141,17	141,27	98	Sand
10	22	ZOOV_0309_1_022	142,10	142,20	70	Sand
11	23	ZOOV_0309_1_023	143,43	143,53	89	Sand
12	24	ZOOV_0309_1_024	144,72	144,82	97	Sand
13	25	ZOOV_0309_1_025	146,55	146,64	92	Sand
14	26	ZOOV_0309_1_026	148,15	148,25	111	Sand

15	29	ZOOV_0309_1_029	152,23	152,33	129	Sand
16	31	ZOOV_0309_1_031	154,56	154,65	82	Sand
17	33	ZOOV_0309_1_033	156,57	156,67	77	Sand
18	36	ZOOV_0309_1_036	160,46	160,56	78	Sand
19	38	ZOOV_0309_1_038	162,53	162,63	73	Sand
20	40	ZOOV_0309_1_040	164,53	164,63	82	Sand
21	41	ZOOV_0309_1_041	165,77	165,86	74	Sand
22	43	ZOOV_0309_1_043	168,01	168,11	75	Sand+O.M
23	44	ZOOV_0361_1_009	162,40	162.50	77	Sand
24	46	ZOOV_0361_1_011	164,30	164,40	103	Sand
25	49	ZOOV_0361_1_014	167,66	167,76	93	Sand
26	51	ZOOV_0361_1_016	169,52	169,62	71	Sand
27	53	ZOOV_0361_1_018	171,19	171,28	62	Sand
28	54	ZOOV_0361_1_020	173,76	173,85	85	Sand
29	56	ZOOV_0361_1_022	175,25	175.35	71	Sand
30	58	ZOOV_0361_1_024	177,10	177,20	82	Sand+O.M
31	59	ZOOV_0361_1_025	178,72	178,82	69	Sand
32	60	ZOOV_0361_1_026	179,78	179,88	69	Sand
33	62	ZOOV_0361_1_028	182,05	182,15	71	Sand
34	64	ZOOV_0361_1_031	187,27	187,37	69	Sand
35	65	ZOOV_0361_1_032	189,88	189,98	74	Sand
36	67	ZOOV_0391_1_001	112,69	112,79	66	Sand
37	69	ZOOV_0391_1_003	114,59	114,69	51	Sand
38	71	ZOOV_0391_1_005	116,33	116,43	68	Claystone
39	72	ZOOV_0391_1_006	117,35	117,45	74	Claystone
40	74	ZOOV_0391_1_008	119,87	119,97	493	Claystone
41	75	ZOOV_0391_1_009	120,70	120,80	70	Sand
42	76	ZOOV_0391_1_010	121,83	121,93	87	Sand
43	78	ZOOV_0391_1_012	123,55	123,65	70	O.M
44	82	ZOOV_0391_1_013	124,65	124,75	68	Carbonate
45	83	ZOOV_0354_2_001	113,00	113,10	65	Sand
46	84	ZOOV_0354_2_002	114,00	114,10	85	Sand
47	85	ZOOV_0354_2_003	115,07	115.17	70	Sand
48	88	ZOOV_0354_2_006	118,25	118,35	80	Claystone
49	90A	ZOOV_0354_2_008	119,85	119,95	120	Claystone+O.M
50	90B	ZOOV_0354_2_008	119,85	119,95	120	Claystone
51	93	ZOOV_0354_2_011	122,89	122,99	110	Sand+O.M
52	100	ZOOV_0354_2_019	131,64	131,74	80	Sand
53	101	ZOOV_0354_2_020	132,82	132,92	**200**	Claystone
54	102	ZOOV_0354_2_021	133,65	133,75	120	Sand
55	104	ZOOV_0354_2_023	134,97	135,07	150	Sand
56	105	ZOOV_0354_2_024	135,85	135,93	125	Sand
57	106	ZOOV_0354_2_025	136,41	136,49	120	Sand

58	108	ZOOV_0354_2_027	139,29	139,39	200	Sand
59	109	ZOOV_0354_2_028	140,23	140,33	195	Sand
60	113	ZOOV_0354_2_032	148,11	148,21	140	Sand
61	114	ZOOV_0354_2_033	149,06	149,16	80	Sand
62	115	ZOOV_0354_2_034	150,52	150,62	80	Claystone
63	117	ZOOV_0354_2_036	153,09	153,19	80	Sand
64	118	ZOOV_0354_2_037	156,60	156,70	70	Sand
65	119	ZOOV_0354_2_038	157,40	157,50	80	Sand
66	120	ZOOV_0354_2_039	158,19	158,29	80	Gravel
67	123	ZOOV_0354_2_042	161,25	161,35	80	Sand
68	124	ZOOV_0354_2_043	162,45	162,55	70	Sand
69	128	ZOOV_0354_2_047	166,22	166,52	80	Sand
70	129	ZOOV_0354_2_048	167,22	167,32	75	Pebble
71	132	ZOOV_0354_2_051	170,20	170,30	80	Sand
72	133	ZOOV_0354_2_052	171,27	171,37	75	Sand
73	136	ZOOV_0354_2_055	174,41	174,51	70	Sand
74	138	ZOOV_0354_2_057	176,30	176,39	170	Claystone
75	140	ZOOV_0354_2_059	181,20	181,30	80	Sand
76	142	ZOOV_0354_2_061	183,25	183,35	80	Claystone
77	143	ZOOV_0354_2_062	184,05	184,15	130	Claystone
78	144	ZOOV_0354_2_063	185,35	185,45	130	Sand
79	145	ZOOV_0354_2_064	186,35	186,45	130	Sand
80	146	ZOOV_0354_2_065	187,42	187,52	140	Claystone
81	147	ZOOV_0354_2_066	188,30	188,40	85	Claystone
82	149	ZOOV_0354_2_069	193,70	193,80	75	Sand
83	151A	ZOOV_0228_1_006	N/A	N/A	**1235**	N/A
84	151B	ZOOV_0228_1_006	N/A	N/A	**1036**	N/A
85	151C	ZOOV_0228_1_006	N/A	N/A	**1935**	N/A
86	151D	ZOOV_0228_1_006	N/A	N/A	**693**	N/A
87	153A	ZOOV_0680_1_001	N/A	N/A	N/A	N/A
88	153B	ZOOV_0680_1_001	N/A	N/A	N/A	N/A
89	154	ZOOV_0680_1_002	N/A	N/A	N/A	N/A

Table 16: Summary of the studied samples from the K2Bs collection, representing calcites to calcite cemented sandstones. The legend is in accordance to Table 1, plus Calcite: Calcite carbonate. With (*) the samples from which thin the sections are currently available. N/A: not available.

N/N	N° PhD **K2Bs-**	DDH number (well N°)	depth from (m)	depth to (m)	SPPγ (c/s)	Description
1	1*	Outcrop	N/A	N/A	N/A	Carbonate
2	2*	Outcrop	N/A	N/A	N/A	Calcite
3	3*	Outcrop	N/A	N/A	N/A	Calcite
4	4	Outcrop	N/A	N/A	N/A	Carbonate
5	6	Outcrop	N/A	N/A	N/A	Calcite
6	7	Outcrop	N/A	N/A	N/A	Calcite

Table 17: Example of the file sheet prepared during the sampling in Zoovch Ovoo, with the depth intervals and short description. All samples were contained inside the wells that were drilled during the period 2011-2014 (so-called old drills). Noting that the depths are not corrected. The Geiger counter used for the radioactivity measurements was SSPγ nº228. The abbreviations bf stands for “brut-fond” (background noise) and the “mrcx” for “morceaux” (pieces).

N°	N°sondage/prof. (non.corr. in m)	Description sommaire SONDAGE (D. RALLAKIS sampling)	prélèvement (cm)	poids global (g)	Activ. SPP γ, (c/s)
1	ZOOV_0081_1/143,90	grès moyen à fin carbonate, gris	7	220	bf
2	ZOOV_0081_1/176,20	grès très grossier carbonate, verdâtre	10	480	bf
3	ZOOV_0081_1/230,90	sable moyen à grossier carbonate, vert pâle	7	210	bf
4	ZOOV_0081_1/230,70	sable très gros à gravier carbonate, vert pâle	7	330	bf
5	ZOOV_0081_1/230,30	sable très gros à gravier carbonate à galets, vert pâle	8	430	bf
6	ZOOV_0081_1/239,80	grès grossier à très gros carbonate, vert pâle	8	295	bf
7	ZOOV_1066_1/142,85	sable grossier à très gros carbonate, jaune-orange	mrcx	25	80
8	ZOOV_0738_1/123,20	sable grossier à lit charbon cm + produit jaune	9	190	1050
9	ZOOV_0738_1/139,11	argiles noires compactes, non minéralisé	8	200	70
10	ZOOV_0738_1/139,45	carbonate massif, gris-vert	mrcx	65	75
11	ZOOV_0738_1/140,30	argiles noires compactes, non minéralisé	9	255	70
12	ZOOV_0738_1/141,30	argiles noires compactes, non minéralisé	7	200	70
13	ZOOV_0738_1/143,00	argiles noires compactes, réduit avec quelques traces d'oxydation, non minéralisé	7	185	80
14	ZOOV_0738_1/143,70	argiles compactes, gris verdâtres sombres	6,5	200	70
15	ZOOV_0738_1/144,50	sable moyen, matière organique noire friable, réduit avec quelques traces d'oxydation, gris-rouge	10	155	120
16	ZOOV_0738_1/144,80	sable moyen, réduit avec quelques traces d'oxydation, gris-rouge	6	135	bf
17	ZOOV_0738_1/146,00	sable grossier à gravier, réduit, lentilles de matière organique, gris-rouge	10	120	120
18	ZOOV_0738_1/146,16	sable grossier à gravier, avec quelques traces d'oxydation, mal trié	9	165	130
19	ZOOV_0738_1/147,13	sable fin, avec quelques traces d'oxydation, bien trié, gris-verdâtre	10	170	200
20	ZOOV_0738_1/147,26	sable moyen, réduit avec quelques traces d'oxydation, matière organique noire friable, mal trié,	mrcx	85	400
21	ZOOV_0738_1/158,20	grès moyen, bien trié, rouge-jaunâtre	10	295	bf
22	ZOOV_0743/142,20	grès grossier à très gros avec matière organique noire friable, mal trié, gris-verdâtre	7	150	100
23	ZOOV_0743/142,80	grès grossier à très gros avec matière organique noire friable, mal trié, gris-verdâtre	7	180	70
24	ZOOV_1142/191,90	morceaux de charbon et d'argile	mrcx	5	85
25	ZOOV_1142/205,55	sable très grossier + argiles, fragments de charbon, mal trié	5	85	**80**
26	ZOOV_1142/209,90	grés moyen à fin + argiles, carbonate massif, lentilles de MO, gris-verdâtre	11	755	bf
27	ZOOV_1142/229,30	sable très grossier + argiles, mal trié, gris-verdâtre	5	140	bf
28	ZOOV_1142/236,65	sable fin, reduit, à lit charbon cm, gris-verdâtre	6	115	100
29	ZOOV_1142/237,15	sable fin, reduit, à lit charbon cm, gris-verdâtre	7	120	bf
30	ZOOV_1142/274,60	sable fin, reduit, à lit charbon + Py, gris-verdâtre	7	175	70
31	ZOOV_1142/276,35	carbonate massif + argiles silicifiées, rouge clair à rouge	7	355	70
32	ZOOV_1142/296,80	grés grossier carbonate, gris-verdâtre	5	390	bf
33	ZOOV_1142/297,75	grés grossier carbonate, gris-verdâtre	3	255	bf
34	ZOOV_1142/306,00	grés fin carbonate, matière organique noire friable, gris-verdâtre	15	865	bf
35	ZOOV_1142/306,65	sable fin, à lit de MO, gris-verdâtre	7	300	bf
36	ZOOV_1142/307,00	sable fin carbonate + matière organique noire friable, gris-verdâtre	8	645	bf
37	ZOOV_1142/310,10	sable grossier carbonate, gris-verdâtre	12	430	bf
38	ZOOV_1146/201,80	morceaux de charbon, non minéralisé	mrcx	65	bf
39	ZOOV_1146/224,40	sable moyen à grossier + argiles + charbon, reduit, mal trié, gris-verdâtre	mrcx	145	bf
40	ZOOV_1136/285,30	carbonate massif à lit de MO, gris-verdâtre	6	340	bf
41	ZOOV_1136/281,81	sable moyen à grossier + matière organique noire friable, reduit, bien trié, gris-verdâtre	6	300	bf
42	ZOOV_1136/286,90	sable moyen à fin, à lit charbon cm, reduit, bien trié, gris-verdâtre	8	210	bf
43	ZOOV_1136/288,35	argiles compactes, + matière organique noire friable, non minéralisé	mrcx	115	bf
44	ZOOV_1136/291,40	sable très fin + carbonate massif, à lit de MO, gris-verdâtre	12	550	bf
45	ZOOV_1136/292,30	argiles silteuses, laminé, noir, marron-noir	7	210	bf
46	ZOOV_1136/294,50	sable fin carbonate massif, gris-verdâtre	6	205	bf
47	ZOOV_1136/320,00	sable très fin + carbonate massif, à lit de MO, gris-verdâtre	10	540	bf
1	UKOV_0007/197,50	charbon	-	265	bf
2	UKOV_0007/214,85	charbon	-	283	bf

Table 18: Example of the file sheet prepared during the sampling in Zoovch Ovoo with cumulative numbering for each well, depth intervals, short lithological description, length, weight and radioactivity of the samples. All samples were contained inside the wells drilled during July 2017. Noting that the depths are not corrected. The Geiger counter used for the radioactivity measurements was SSPγ nº228. The abbreviations bf stands for “brut-fond” (background noise) and the “mrcx” for “morceaux” (pieces).

N°	N°sondage/prof. (non.corr. in m)	Description sommaire SONDAGE (D. RALLAKIS sampling)	prélèvement (cm)	poids global (g)	Activ. SPP γ, (c/s)
1	ZOOV_1154/162,25-162,30	sable très grossier à gravier, morceaux de charbon, reduit, mal trié, gris-verdâtre	mrcx	290	bf
2	ZOOV_1154/164,05-164,15	sable très fin + silt argileuse, carbonaté, gris-verdâtre à rouge de vin	9,5	305	bf
3	ZOOV_1154/164,35-164,45	sable très fin + silt argileuse, carbonaté, verdâtre à rouge	10	160	bf
4	ZOOV_1154/180,55-180,62	argiles noir compactes, reduit, bien trié	7	120	bf
5	ZOOV_1154/181,22-181,34	sable très fin + argiles noir, à lit de MO, reduit, gris-verdâtre	12	170	bf
6	ZOOV_1154/189,45-189,50	silt argileuse + sable très fin, hydroxydes de Fer jaunâtres,reduit, gris-verdâtre	mrxc	15	bf
7	ZOOV_1154/190,80-190,90	sable fin à moyen , carbonaté, avec bioturbation, verte-rougeâtre	10	150	bf
1	ZOOV_1155/130,65-130,71	sable grossier + argiles noirs compactes, laminé, gris-verdâtre	6	105	bf
2	ZOOV_1155/132,18-132,22	sable fin à moyen à granules, argiles noirs compactes, laminé, gris-verdâtre	4	85	bf
3	ZOOV_1155/132,30-132,37	sable très fin + argles noirs compactes, laminé, gris-verdâtre	7	125	bf
4	ZOOV_1155/167,51-167,64	silt argileuse, rides mal visibles, gris	13	220	89
5	ZOOV_1155/167,64-167,73	argiles, tracts noirs de manganese (?), gris	9	160	287
6	ZOOV_1155/167,73-167,92	argiles avec petites rides silteux, gris-verdâtre à rouge	19	365	122
1	ZOOV_1157/164,61-164,80	niveau d'argiles gris sombre à argiles noirs entre argiles silteuse gris-vert	19	485	78
1	ZOOV_1156/120,40-120,50	debris charbonneux anguleux jusqu'a 1cm, sable moyen grossier à grossier, gris-vert	10	165	76
2	ZOOV_1156/128,57-128,72	charbon au sommet d'un banc de sable grossier	15	360	74
3	ZOOV_1156/131,77-131,85	lit de charbon + pyrite	8	160	119
4	ZOOV_1156/132,90-133,00	sable grossier à très grossier, intraclastes d'argiles avec debris de charbon, vert-jaunâtre	10	150	90

Table 19: Example of the petrographic sheet completed for every thin section studied.

Localisation : ZOOVCH OVOO Profile 1 Etudié 9659					***Echantillon : AA-35***			***Lame : 9659 AA-35***	
Eléments détritiques	*Type*	Eléments lithiques	Quartz	Feldspath K	Plagioclases	Muscovite	Biotite/Chlorite	Argiles	MO	Accessoires
	Ab.	-	++	++	+	+	+	-	++	-
	Obs.		Grains monocristallins sub-angulaires de quartz (max ⌀ 0.1 mm)	Grains arrondis de Feldspath-K (max ⌀ <0.1 mm)	Grains arrondis de plagioclase (max ⌀ 0.1 mm)	Les grains de muscovite sont dispersés et orientés	Les grains de chlorite et de biotite sont dispersés et orientés		Fragments ligneux souvent conservés avec une structure cellulaire	
Ciments et matrices	*Type*	Quartz secondaire		Carbonates				Argiles		Fer
	Ab.	-		-				+		-
	Obs.							Forment la matrice		
Minéralisations	*Type*	Sulfures		Oxydes/hydroxydes				Minéraux d'U		Autres
	Ab.	+		+				-		-
	Obs.	La pyrite est systématiquement associée à la matière organique		Dispersée grains d'ilménite et d'anatase						
Observations	- Grès bien stratifié. Les éléments détritiques dominants sont des grains de quartz, de feldspath et les micas. - De la matière organique. Localement bien préservée ou affectée par pyritisation. - La matrice est composée par des argiles. - La porosité est d'environ 5%.									

Table 20: Examples of the mean values for the concentration of dolomite cements in Ca, Mg, Fe+Mn (at%), obtained from microprobe analyses.

at.%	BB-143	BB-138	BB-88	BB-67	AA-157	BB-121	BB-71	AA-147	AA-171
Ca	53,18	52,72	53,56	52,06	58,80	49,09	53,42	59,20	54,31
Mg	41,00	44,95	40,91	38,51	34,52	34,94	40,40	34,60	40,91
Fe+Mn	5,82	2,32	5,53	9,43	6,68	15,97	6,18	6,20	4,78

Table 21: Mean values of Ca, Y, U and Th and the sum of REE content chondrite-normalized, for 10 different dolomite, analyzed by LA-ICP-MS (in ppm). Note that the mean values for Y, U and Th are not representative of each dolomite species as one sample can contain up to three different fabrics and very often extreme differences exist between the different fabrics.

Sample	**Ca**	**Y**	**U**	**Th**	**ΣREE**
AA-147	230550	81,95	49,29	4,85	802,36
AA-157	232405	107,99	46,03	5,23	**1205,45**
AA-171	239300	127,94	38,82	5,39	**1699,32**
AA-177	244195	84,74	17,25	3,56	**1017,56**
BB-67	238900	35,22	1,00	1,97	322,50
BB-71	194908	59,01	**348,02**	**16,66**	570,92
BB-88	208877	126,92	60,18	2,02	865,88
BB-91	207900	40,48	3.27	1,21	323,89
BB-129	225621	61,02	37,34	0,84	468,19
BB-135	242542	94,04	60,69	3,91	**1049,99**

Table 22: Mean values for REE content of dolomite cements in 10 samples, analyzed by LA-ICP-MS, chondrite-normalized (in ppm).

Sample	**La**	**Ce**	**Pr**	**Nd**	**Sm**	**Eu**	**Gd**	**Tb**	**Dy**	**Ho**	**Er**	**Tm**	**Yb**	**Lu**
AA-147	135,42	103,49	78,91	68,05	51,57	36,66	48,61	45,33	44,55	44,63	42,77	36,30	35,96	30,11
AA-157	212,44	161,01	126,89	112,47	79,15	47,39	67,24	67,66	66,20	63,86	58,02	54,14	46,26	42,72
AA-171	309,71	260,44	185,06	160,25	111,65	59,14	100,68	93,04	88,85	83,22	72,41	62,11	59,56	53,20
AA-177	185,96	133,22	97,11	89,44	67,19	42,21	63,28	59,75	56,61	55,29	48,93	42,26	41,39	34,92
BB-67	49,73	38,73	29,38	25,89	17,31	11,44	18,48	19,14	19,39	20,30	20,50	18,00	17,71	16,50
BB-71	122,34	82,71	51,50	43,64	23,82	16,31	25,50	23,46	26,69	30,02	31,90	30,04	30,75	32,24
BB-88	82,20	69,01	46,61	44,53	39,62	27,07	58,19	67,70	78,16	82,36	77,76	67,50	65,68	59,49
BB-91	44,80	39,39	27,22	23,77	21,50	12,51	19,70	21,36	21,27	21,66	20,17	19,01	16,54	14,99
BB-129	101,98	67,73	39,27	33,65	22,36	11,55	19,08	22,52	23,19	27,46	27,87	23,89	24,59	23,05
BB-135	151,66	152,78	100,40	83,31	56,47	41,39	61,23	64,94	65,16	62,85	60,67	51,01	52,69	44,43

Table 23: Values for REE content of the four different dolomite fabrics, analyzed by LA-ICP-MS, chondrite-normalized (in ppm).

Fabric	Sample	**La**	**Ce**	**Pr**	**Nd**	**Sm**	**Eu**	**Gd**	**Tb**	**Dy**	**Ho**	**Er**	**Tm**	**Yb**	**Lu**
Type (I)	AA-147	173,4	126,1	96,1	81,2	60,8	37,8	53,3	48,2	43,1	41,0	42,8	33,4	35,3	26,0
	AA-171	1865,0	1579,1	1174,8	1048,1	721,6	328,6	579,9	482,0	417,1	338,8	288,1	236,0	209,9	202,4
Type (II)	AA-157	264,1	199,0	147,6	146,6	110,8	48,0	51,8	85,9	50,4	46,5	62,5	92,7	27,3	22,7
	AA-171	143,0	132,0	91,8	85,3	73,6	40,7	69,9	74,8	75,6	72,7	61,1	48,9	46,3	33,0
Type (III)	BB-91	69,6	50,1	34,8	31,3	27,7	17,8	21,1	23,0	21,5	23,4	19,8	17,8	18,1	16,3
Type (IV)	BB-88	49,8	32,5	21,8	18,6	19,6	3,9	8,5	22,4	16,7	16,9	14,5	15,4	7,1	1,2

Table 24: Isotopic compositions of the dolomite and calcite samples and their relative carbonate content ($CaCO_3 + CaMg(CO_3)_2$). The SMOW values of $\delta^{18}O$ have been calculated using a conversion formula.

Sample	Carb. %	$\delta^{18}O$ (PDB)	$\delta^{18}O$ (SMOW)	$\delta^{13}C$ (PDB)	Sample	Carb. %	$\delta^{18}O$ (PDB)	$\delta^{18}O$ (SMOW)	$\delta^{13}C$ (PDB)
AA-36	24.8	-11.34	19.17	-6.08	**BB-126**	38.9	-9.71	20.85	-6.15
AA-147	31.4	-10.16	20.39	-5.59	**BB-129**	31.1	-10.62	19.91	-6.42
AA-157	32.2	-10.43	20.11	-6.06	**BB-133**	29.6	-10.51	20.03	-6.87
AA-171	36.3	-9.79	20.77	-6.48	**BB-135**	2.8	-10.62	19.91	-6.23
AA-177	41.4	-10.88	19.64	-6.71	**BB-137**	30.7	-10.00	20.55	-6.71
BB-25	16.9	-10.14	20.41	-5.78	**BB-138**	22.1	-10.10	20.45	-6.65
BB-37	21.9	-10.06	20.49	-6.70	**BB-148**	22.8	-9.96	20.59	-6.68
BB-66	40.4	-10.87	19.65	-6.80	**CC-57**	39.7	-10.71	19.82	-7.71
BB-67	43.0	-11.79	18.71	-7.51	**K2BS-1a**	25.00	-13.85	16.58	-6.15
BB-78	39.5	-9.96	20.59	-7.16	**K2BS-1b**	31.00	-13.78	16.65	-6.01
BB-139	21.6	-10.14	20.41	-6.63	**K2BS-2a**	62	-11.42	19.09	-6.35
BB-88	28.7	-11.02	19.50	-6.95	**K2BS-2b**	50	-11.41	19.10	-6.33
BB-91	26.2	-10.40	20.14	-6.44	**K2BS-3a**	79	-12.22	18.26	-6.04
BB-97	43.2	-11.04	19.48	-7.08	**K2BS-3b**	73	-12.13	18.36	-6.04
BB-71	57.1	-9.93	20.62	-6.58	**K2BS-4a**	41	-12.91	17.55	-8.64
BB-110	42.0	-11.25	19.26	-7.13	**K2BS-4b**	38	-12.81	17.65	-8.58
BB-121	18.7	-11.32	19.19	-5.86	**K2BS-6**	58	-11.21	19.30	-5.74
BB-125	37.4	-9.48	21.09	-7.27	**K2BS-7**	70	-10.92	19.60	-5.79

Table 25: Isotopic compositions of the carbonates studied in Sanchez (2010, 2011). The SMOW values of $\delta^{18}O$ have been calculated using a conversion formula.

Sample	$\delta^{18}O$ (PDB)	$\delta^{18}O$ (SMOW)	$\delta^{13}C$ (PDB)
Bayanshiree-1	-9.33	21.24	-4.95
Bayanshiree-2	-10.49	20.05	-6.13
Bayanshiree-3	-10.90	19.62	-6.64
Bayanshiree-4	-11.34	19.17	-6.19
Sainshand-1	-5.62	25.07	-0.19
Sainshand-2	-5.45	25.24	-0.59
Sainshand-3	-10.21	20.33	-6.46
Sainshand-4	-9.68	20.88	-6.12
Sainshand-5	-5.15	25.55	-3.12
Sainshand-6	-6.12	24.55	-2.64
Sainshand-7	-11.94	18.55	-4.47
Du 30 ST	-7.78	22.84	-5.23
Du 39 ST	-8.70	21.89	-6.96
Du 53 ST	-13.27	17.18	-5.39
Du 52 ST	-14.73	15.68	-7.48
Du 57 ST	-14.21	16.21	-6.01
Du 63 ST	-13.42	17.03	-8.34
Du 73 ST	-8.72	21.87	-5.74
Du 74 ST	-8.33	22.27	-7.01
Du 74 ST	-8.76	21.83	-6.93
Du 75 ST	-9.25	21.32	-7.02
Du 77 ST	-9.51	21.06	-6.46

Table 26: Examples from the EPMA study performed on different pyrite types. Picture (a) is contrasted to show the Uranium replacement on the organic matter.

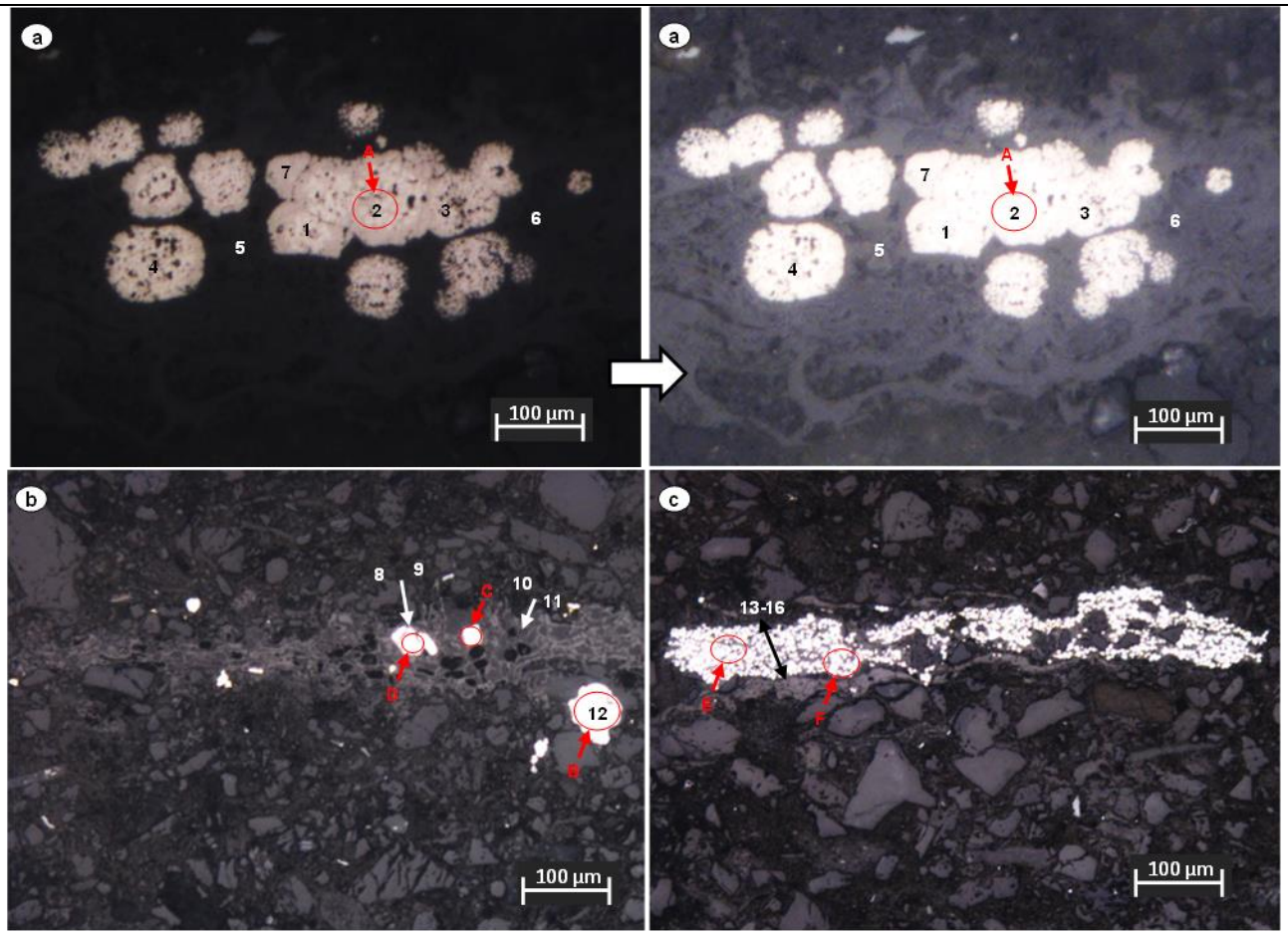

AA-35 EMPA
Analysis in wt% and detection limit in ppm

N/N	Fe	d.l	Co	d.l	Ni	d.l	Cu	d.l	Zn	d.l	As	d.l	Cd	d.l	S	d.l	Mo	d.l	U	d.l
1	42.89	1131	0.01	488	0	0	0	0	0	0	0.07	631	0.01	892	53.25	892	0	0	0.19	1252
2	42.59	1082	0.02	501	0.01	520	0	0	0	0	0.07	697	0	0	52.5	0	0.02	4314	0.21	1290
3	41.82	1114	0	484	0	0	0.07	625	0	0	0.1	665	0	0	52.1	0	0.07	4104	0.21	1269
4	42.31	1137	0.02	484	0	0	0	652	0	0	0.15	677	0	0	51.34	0	0.03	4631	0.23	1314
5	1.1	980	0.01	492	0	0	0	0	0	0	0	0	0.32	888	0.41	888	0.34	3689	54.35	1951
6	0.35	945	0	0	0	0	0	0	0	0	0	0	0.32	823	0.1	823	0.57	3319	49.83	1879
7	40.46	1055	0.07	458	0.07	513	0.18	630	0	1428	0.21	657	0	0	50.62	0	0	0	0.41	1252
8	43.7	1012	0.01	488	0	0	0	0	0	0	0.01	642	0	0	54.16	859	0.09	3796	0.09	1292
9	43.93	1105	0.03	475	0	0	0	0	0	0	0.04	668	0	0	53.97	783	0	0	0.16	1225
10	0.07	411	0	0	0	0	0.01	280	0.01	717	0	0	0	0	0.18	413	0.05	1495	0	-7
11	0.05	463	0	0	0	0	0	0	0	0	0	0	0	453	0.04	390	0	1428	0.01	674
12	43.59	1111	0.14	470	0.02	546	0.2	651	0	0	0.13	654	0.01	833	54.16	819	0.04	3723	0.17	1178
13	12.38	1005	0	494	0	0	0	0	0	0	0	0	0.23	921	14.51	655	0	0	37.16	1849
14	36.69	1024	0.01	508	0	0	0	0	0	0	0	0	0.06	956	43.4	686	0.18	3983	10.53	1495
15	40.41	1150	0	498	0.01	525	0	0	0	-1	0	-2	0.03	893	48.53	734	0	-1	5.75	1434
16	24.34	1073	0.01	489	0	0	0	0	0	1550	0	0	0.16	854	30.92	731	0	-1	18.73	1548

Table 27: The trace element content of pyrite cements in 10 samples, analysed by LA-ICP-MS. Colours are used to distinguish between the different pyrite habitus as well as their relationships with organic matter, uranium, carbonates and other sulfides i.e. marcasite and sphalerite.

Type/Association	'Source file'	V	Co	Ni	Cu	Zn	As	Se	Mo	Ag	Cd	Sb	Pb	Ni+Co	V+Ni	Mo+Cu	Zn+Cd	Pb+Ag
Framboids and overgrowth in U and O.M	A35-1.D	2.49	241.00	1910.00	2160.00	7.10	1850.00	0.00	329.00	25.30	1.10	17.10	765.00	2151.00	1912.49	2489.00	8.20	790.30
	A154C-1.D	56.90	389.00	3440.00	530.00	11.70	1290.00	0.00	37.50	2.89	9.90	45.70	1131.00	3829.00	3496.90	567.50	21.60	1133.89
	A154C-1.D	48.90	145.00	1520.00	232.00	23.20	1360.00	0.00	31.30	1.48	14.90	40.80	916.00	1665.00	1568.90	263.30	38.10	917.48
	C54C-1.D	0.90	1905.00	2728.00	1092.00	1.81	448.00	676.00	3.96	9.45	17.50	31.81	705.00	4633.00	2728.90	1095.96	19.31	714.45
	C54C-1.D	194.00	5680.00	8690.00	3210.00	6.50	922.00	2230.00	145.00	43.60	46.60	40.70	504.00	14370.00	8884.00	3355.00	53.10	547.60
Framboids isolated	A35-2.D	4.87	703.00	2320.00	1210.00	4.00	1335.00	2.00	1.28	10.10	0.80	4.87	692.00	3023.00	2324.87	1211.28	4.80	702.10
	A172B-7.D	2.92	22.30	0.00	6.10	8.00	4380.00	0.00	310.00	0.07	0.80	16.80	159.00	22.30	2.92	316.10	8.80	159.07
	A172B-7.D	0.36	6.10	0.00	0.36	10.30	4170.00	0.00	111.90	0.02	0.30	9.30	136.40	6.10	0.36	112.26	10.60	136.42
	A172B-8.D	10.90	358.00	920.00	7.30	34.00	2910.00	0.00	362.00	0.15	1.80	31.00	441.00	1278.00	930.90	369.30	35.80	441.15
	A172B-8.D	8.80	523.00	2220.00	7.30	16.90	4150.00	0.00	206.00	0.04	9.00	52.70	413.00	2743.00	2228.80	213.30	25.90	413.04
	A172B-8.D	0.04	27.30	348.00	1.00	8.90	5490.00	14.00	167.30	0.00	0.00	12.50	103.20	375.30	348.04	168.30	8.90	103.20
	A35-4.D	14.40	8.68	520.00	350.00	49.00	232.00	0.00	1270.00	5.50	0.00	4.90	176.00	528.68	534.40	1620.00	49.00	181.50
	A35-4.D	26.90	6.10	600.00	403.00	40.80	328.00	57.00	1630.00	7.16	1.30	7.35	225.00	606.10	626.90	2033.00	42.10	232.16
Euhedral isolated	A154C-2.D	29.80	20.90	170.00	19.20	12.90	3120.00	7.00	71.60	0.46	5.90	76.80	1085.00	190.90	199.80	90.80	18.80	1085.46
	A154C-2.D	40.70	290.00	2620.00	241.00	6.70	1050.00	16.00	18.70	0.87	8.40	40.20	1070.00	2910.00	2660.70	259.70	15.10	1070.87
	A154C-3.D	0.74	21.30	143.00	129.70	9.60	1750.00	1.10	304.00	2.54	1.00	8.74	62.30	164.30	143.74	433.70	10.60	64.84
	A154C-3.D	1.54	5.37	129.00	53.20	7.10	2011.00	0.00	288.00	0.64	0.00	5.32	40.90	134.37	130.54	341.20	7.10	41.54
	A154C-4.D	0.60	21.40	281.00	149.00	10.50	1554.00	0.00	300.00	2.70	0.65	7.26	94.90	302.40	281.60	449.00	11.15	97.60
	A154C-4.D	0.98	36.10	569.00	139.00	14.20	1861.00	0.00	321.00	2.29	1.20	10.39	117.00	605.10	569.98	460.00	15.40	119.29
Euhedral in OM	A35-2.D	21.80	2410.00	5090.00	18.00	4.50	567.00	3.00	8.50	0.16	0.00	9.31	1358.00	7500.00	5111.80	26.50	4.50	1358.16
	A35-3.D	0.29	98.10	399.00	34.10	2.80	230.00	4.00	0.21	0.06	2.70	3.57	301.00	497.10	399.29	34.31	5.50	301.06
Framboids with overgrowth Fully cemented OM	B106-1.D	3.19	2.49	45.30	0.96	3.34	1141.00	0.00	94.90	0.00	0.33	2.31	16.11	47.79	48.49	95.86	3.67	16.11
	B106-1.D	1.41	25.90	270.00	2.04	11.34	846.00	2.20	283.50	0.00	1.12	6.24	46.80	295.90	271.41	285.54	12.46	46.80
	B106-2.D	0.60	63.70	911.00	1.78	11.97	716.00	1.90	190.30	0.02	1.29	5.15	56.90	974.70	911.60	192.08	13.26	56.92
	B106-2.D	0.57	125.90	1181.00	5.78	12.92	1516.00	0.70	195.10	0.00	4.04	11.60	130.90	1306.90	1181.57	200.88	16.96	130.90
	B106-3.D	0.88	0.66	19.30	0.90	2.72	1120.00	0.00	100.60	0.01	0.62	2.49	24.30	19.96	20.18	101.50	3.34	24.31
	B106-3.D	1.73	4.76	97.90	1.16	4.35	2673.00	0.00	32.50	0.00	1.86	27.19	112.20	102.66	99.63	33.66	6.21	112.20
Framboids with overgrowth Partial cemented OM	B106-5.D	9.40	2.20	13.00	0.40	3.00	4780.00	3.50	16.60	0.00	8.10	55.00	231.00	15.20	22.40	17.00	11.10	231.00
	B106-6.D	22.90	1.20	204.00	18.90	10.20	5920.00	1.00	140.50	0.25	0.30	127.00	32.10	205.20	226.90	159.40	10.50	32.35
	B106-6.D	2.39	0.77	280.00	3.70	5.00	8210.00	27.00	130.00	0.12	0.00	36.80	19.20	280.77	282.39	133.70	5.00	19.32
Framboids inside Type IV	B138-2.D	8.30	1205.00	2460.00	462.00	5.40	7350.00	2.00	1349.00	6.26	52.80	43.40	1578.00	3665.00	2468.30	1811.00	58.20	1584.26
	B138-2.D	8.20	502.00	1150.00	267.00	12.10	6370.00	0.00	195.00	8.10	75.60	31.40	1045.00	1652.00	1158.20	462.00	87.70	1053.10
Euhedral inside Type IV	B138-1.D	3.30	1450.00	3260.00	22.60	4.80	2920.00	0.00	11.90	0.46	14.30	11.00	215.00	4710.00	3263.30	34.50	19.10	215.46
	B138-1.D	2.95	614.00	1690.00	14.90	3.90	4420.00	0.00	15.20	0.69	1.60	6.42	137.00	2304.00	1692.95	30.10	5.50	137.69
Euhedral in U	C54C-3.D	21.50	4480.00	8220.00	355.00	7.10	5730.00	537.00	90.50	8.66	80.20	76.00	350.00	12700.00	8241.50	445.50	87.30	358.66
	C54C-4.D	21.50	3030.00	4640.00	300.00	8.30	788.00	1445.00	11.60	10.00	34.30	18.80	200.40	7670.00	4661.50	311.60	42.60	210.40
	C54C-4.D	209.00	2430.00	7940.00	1.70	5.80	5030.00	58.00	67.20	0.46	48.40	66.10	141.80	10370.00	8149.00	68.90	54.20	142.26
	C54C-5.D	39.90	5330.00	11430.00	414.00	4.40	6060.00	589.00	247.00	9.20	86.30	99.40	385.00	16760.00	11469.90	661.00	90.70	394.20
Sphalerite	C8B-1.D	1110.00	1490.00	0.00	27200.00	-	8800.00	301000.00	2900.00	1850.00	-	5900.00	760.00	1490.00	1110.00	30100.00	-	2610.00
	C8B-1.D	240.00	4010.00	23000.00	137000.00	-	6000.00	272000.00	0.00	10100.00	-	26400.00	8300.00	27010.00	23240.00	137000.00	-	18400.00
Euhedral associated to Sphalerite	C8B-2.D	0.52	1108.00	4320.00	4.60	3.00	1143.00	0.00	5.20	0.46	0.20	46.40	61.90	5428.00	4320.52	9.80	3.20	62.36
	C8B-2.D	5.10	9730.00	27600.00	74.70	26.90	3040.00	890.00	36.20	10.00	5.10	116.00	407.00	37330.00	27605.10	110.90	32.00	417.00
Marcasite on Euhedral	A172B-3.D	4.40	43.90	560.00	4.60	8.40	13600.00	0.00	485.00	0.01	3.30	242.00	7.40	603.90	564.40	489.60	11.70	7.41
	A172B-3.D	2.84	143.00	1250.00	0.40	10.60	13480.00	3.00	554.00	0.08	4.80	222.00	110.00	1393.00	1252.84	554.40	15.40	110.08
Euhedral associated to marcasite	A172B-1D.D	6.70	1339.00	3950.00	7.40	14.70	836.00	0.00	9.70	0.01	98.90	52.20	1810.00	5289.00	3956.70	17.10	113.60	1810.01
	A172B-1D.D	3.23	3230.00	8200.00	123.90	56.70	2270.00	0.00	8.57	0.54	188.00	126.30	6600.00	11430.00	8203.23	132.47	244.70	6600.54
	A172B-2.D	5.17	3050.00	9100.00	18.50	31.80	1943.00	0.00	20.20	0.06	102.20	70.10	2950.00	12150.00	9105.17	38.70	134.00	2950.06
	A172B-2.D	2.38	2810.00	7180.00	66.70	52.30	2290.00	4.00	5.90	0.31	144.00	95.30	5330.00	9990.00	7182.38	72.60	196.30	5330.31
Euhedral and framboids inside U	A172B-5.D	134.00	1248.00	7730.00	67.50	20.40	7400.00	24.00	264.00	0.39	45.20	181.10	963.00	8978.00	7864.00	331.50	65.60	963.39
	A172B-5.D	10.60	1850.00	7710.00	24.90	11.50	1729.00	11.00	34.80	0.17	18.90	34.50	1192.00	9560.00	7720.60	59.70	30.40	1192.17
	A172B-6.D	13.80	543.00	2230.00	0.20	24.60	2690.00	0.00	19.20	0.01	5.90	35.50	1022.00	2773.00	2243.80	19.40	30.50	1022.01
	A172B-6.D	12.90	950.00	2970.00	4.80	13.70	2210.00	10.00	17.90	0.01	11.90	44.00	1174.00	3920.00	2982.90	22.70	25.60	1174.01

Table 28: Representative values for the concentration in trace element content of pyrite analyzed by the EMPA, measured in 13 samples. In one case (*) sphalerite cements and associated uranium phases (**).

at.%		Fe	Co	Ni	Cu	Zn	As	Cd	S	Mo	U
1	**AA-172B**	32.65	0.14	0.06	-	-	0.33	0.01	65.71	0.01	1.09
2	**AA-172B**	32.92	0.02	-	-	-	0.10	-	66.91	-	0.05
3	**CC-25A**	32.33	0.03	-	-	0.01	0.20	-	67.35	0.05	0.04
4	**CC-25A**	31.74	0.04	-	-	-	0.03	-	68.13	0.05	0.02
5	**CC-8B***	0.16	0.02	0.01	-	47.99	-	0.82	51.00	-	-
6	**CC-8B**	33.13	0.04	0.04	-	-	0.24	0.01	66.46	-	0.08
7	**CC-54C**	32.63	0.4	0.19	0.04	-	0.34	-	66.39	-	0.01
8	**CC-54C**	32.89	0.28	0.06	-	0.01	0.11	-	66.55	0.09	0.02
9	**CC-25B**	32.94	0.06	-	-	-	0.13	-	66.84	-	0.03
10	**CC-25B**	34.96	0.02	-	-	-	-	-	64.85	-	0.17
11	**CC-25C**	32.15	0.02	-	-	-	0.20	-	67.50	0.11	0.02
12	**CC-25C**	32.56	0.03	-	-	-	0.23	-	67.16	-	0.03
13	**BB-106**	32.15	0.02	-	-	-	0.20	-	67.50	0.11	0.02
14	**BB-106**	32.56	0.03	-	-	-	0.23	-	67.16	-	0.03
15	**BB-137**	32.07	0.06	0.01	0.04	-	0.02	-	67.8	-	0.01
16	**BB-137**	32.35	0.08	-	0.04	-	-	-	67.51	-	0.02
17	**BB-138**	31.31	0.01	-	-	-	0.37	-	68.28	-	0.02
18	**BB-138**	31.22	0.02	-	-	-	0.36	-	68.38	-	0.02
19	**BB-97**	31.26	0.28	0.07	0.01	-	-	-	68.34	0.02	0.02
20	**BB-97**	31.36	0.20	0.06	0.30	-	-	-	68.01	0.05	0.02
21	**BB-126**	31.32	-	-	-	-	0.02	-	68.59	0.06	0.01
22	**BB-126**	31.02	0.01	-	-	-	0.01	-	68.84	0.1	0.01
23	**AA-35****	41.7	0.01	0.01	0.01	0.01	0.01	1.53	54.61	-	2.11
24	**AA-35**	31.49	0.10	0.01	0.13	-	0.07	-	68.16	0.01	0.03
25	**AA-154C**	31.32	0.05	0.05	0.12	-	0.12	-	68.25	-	0.08
26	**AA-154C**	32.08	0.01	0.01	-	-	0.03	-	67.84	-	0.02
27	**AA-59**	31.78	0.01	0.01	-	-	0.18	-	68.00	0.01	0.01
28	**AA-59**	31.42	0.03	-	-	-	0.09	-	68.42	-	0.03

Table 29: Normalized on the basis of pyrite stoichiometry. Concentric marks overgrowth habitus of pyrite. Most of the minor elements are contained in concentrations below the detection limit.

at.%	Fe	S	Co	Ni	Cd	As	Cu	Zn	Mo	U	Comments
Py std	**0.96**	**2.04**	**-**	**-**	**-**	**-**	**-**	**-**	**-**	**-**	**Standard**
BB-106-1-1	0.96	2.03	-	-	-	-	-	-	-	-	cubic
BB-106-1-2	0.95	2.05	-	-	-	-	-	-	-	-	cubic
BB-106-1-3	0.95	2.04	-	-	-	-	-	-	-	-	cubic
BB-106-1-4	0.96	2.03	-	-	-	0.01	-	-	-	-	cubic
BB-106-1-5	0.95	2.05	-	-	-	-	-	-	-	-	cubic
BB-106-1-6	0.95	2.05	-	-	-	-	-	-	-	-	cubic
BB-106-2-1	0.96	2.03	-	-	-	-	-	-	-	-	cubic
BB-106-2-2	0.96	2.02	-	-	-	0.02	-	-	-	-	cubic
BB-106-2-3	0.97	2.01	-	-	-	0.01	-	-	-	-	cubic
BB-106-3-1	0.96	2.03	-	-	-	0.01	-	-	-	-	cubic
BB-106-3-2	0.97	2.03	-	-	-	-	-	-	-	-	cubic
BB-137-1	0.96	2.03	-	-	-	-	-	-	-	-	framboidal
BB-137-2	0.97	2.03	-	-	-	-	-	-	-	-	framboidal
BB-137-3	0.96	2.02	-	-	-	-	0.01	-	-	-	framboidal
BB-137-4	0.96	2.03	-	-	-	-	-	-	-	-	framboidal
BB-137-5	0.94	2.05	-	-	-	0.01	-	-	-	-	cubic
BB-137-6	0.93	2.05	-	-	-	0.02	-	-	-	-	cubic
BB-138-1-1	0.95	2.04	-	-	-	0.01	-	-	-	-	framboidal
BB-138-1-2	0.94	2.05	-	-	-	0.01	-	-	-	-	framboidal
BB-138-1-3	0.94	2.05	-	-	-	0.01	-	-	-	-	framboidal
BB-138-1-4	1.23	1.51	0.06	-	-	0.00	-	-	0.20	-	framboidal
BB-138-2-1	0.94	2.05	-	-	-	0.01	-	-	-	-	framboidal
BB-138-3-1	0.94	2.04	-	-	-	0.01	-	-	-	-	framboidal
BB-138-3-4	0.94	2.05	-	-	-	-	-	-	-	-	framboidal
BB-97-2-p1	0.94	2.05	0.01	-	-	-	-	-	-	-	
BB-97-2-p1	0.94	2.04	0.01	-	-	-	0.01	-	-	-	profile on
BB-97-2-p1	0.95	2.05	-	-	-	-	-	-	-	-	cubic
BB-97-2-p1	0.92	2.06	-	-	-	-	0.01	-	-	-	
BB-97-2-1	0.97	2.01	0.01	-	-	0.01	-	-	-	-	cubic
BB-97-2-2	0.95	2.04	-	-	-	-	-	-	-	-	cubic
BB-97-2-3	0.96	2.03	-	-	-	-	-	-	-	-	cubic
BB-97-2-4	0.95	2.03	-	-	-	0.01	-	-	-	-	cubic
BB-126-1	0.94	2.06	-	-	-	-	-	-	-	-	cubic
BB-126-2	0.93	2.07	-	-	-	-	-	-	-	-	cubic
BB-126-3	0.93	2.07	-	-	-	-	-	-	-	-	cubic
BB-126-4	0.97	2.02	-	-	-	-	-	-	-	-	cubic
BB-126-2-1	0.95	2.02	-	-	-	0.03	-	-	-	-	cubic
BB-126-2-2	0.95	2.05	-	-	-	-	-	-	-	-	cubic
BB-126-2-3	0.94	2.05	-	-	-	0.01	-	-	-	-	cubic
AA-35-2-5	0.94	2.04	-	-	-	-	-	-	-	-	framboidal
AA-35-1-1	0.95	2.05	-	-	-	-	-	-	-	-	framboidal
AA-35-1-2	0.95	2.04	-	-	-	-	-	-	-	-	framboidal
AA-35-1-3	0.94	2.05	-	-	-	-	-	-	-	-	framboidal
AA-35-1-4	0.96	2.03	-	-	-	-	-	-	-	-	framboidal
AA-35-1-7	0.94	2.05	-	-	-	-	-	-	-	-	concentric
AA-154C-1-1	0.96	2.04	-	-	-	-	-	-	-	-	cubic
AA-154C-1-2	0.96	2.03	-	-	-	-	-	-	-	-	cubic
AA-154C-2-1	0.95	2.04	-	-	-	0.01	-	-	-	-	cubic
AA-154C-2-2	0.94	2.05	-	-	-	-	-	-	-	-	cubic
AA-154C-2-3	0.94	2.05	-	-	-	-	-	-	-	-	cubic
AA-154C-2-4	0.96	2.04	-	-	-	-	-	-	-	-	cubic
AA-54-2-1	0.95	2.05	-	-	-	-	-	-	-	-	concentric
AA-54-2-2	0.95	2.04	-	-	-	0.01	-	-	-	-	framboidal
AA-54-1-1	0.94	2.05	-	-	-	0.01	-	-	-	-	framboidal
AA-54-1-2	0.95	2.05	-	-	-	-	-	-	-	-	concentric

AA-54-3-1	0.95	2.05	-	-	-	-	-	-	-	-	framboidal
at.%	**Fe**	**S**	**Co**	**Ni**	**Cd**	**As**	**Cu**	**Zn**	**Mo**	**U**	**Comments**
ZnS std	**-**	**1.51**	**-**	**-**	**-**	**-**	**-**	**1.48**	**-**	**-**	**Standard**
Py std	**1.00**	**2.00**	**-**	**-**	**-**	**-**	**-**	**-**	**-**	**-**	**Standard**
AA-172B-2-2	0.98	1.97	-	-	-	0.01	-	-	-	0.03	cubic
AA-172B-2-3	0.97	2.01	-	-	-	0.02	-	-	-	-	cubic
AA-172B-2-4	0.99	2.01	-	-	-	0.00	-	-	-	-	cubic
AA-172B-2-5	0.97	1.99	-	-	-	0.03	-	-	-	0.01	cubic
AA-172B-2-6	0.98	1.99	-	-	-	0.01	-	-	-	0.02	cubic
AA-172B-2-7	0.97	2.00	-	-	-	0.02	-	-	-	-	cubic
AA-172B-2-8	0.99	2.00	-	-	-	0.01	-	-	-	-	framboid
AA-172B-2-9	0.98	2.01	-	-	-	-	-	-	-	-	cubic
AA-172B-2-10	0.99	2.01	-	-	-	-	-	-	-	-	cubic
AA-172B-2-12	0.98	2.00	-	-	-	-	-	-	-	-	cubic
AA-172B-1-1	0.98	2.00	-	-	-	0.02	-	-	-	-	marcasite
AA-172B-1-2	0.98	1.99	-	-	-	0.03	-	-	-	-	marcasite
AA-172B-1-3	1.00	1.98	-	-	-	0.01	-	-	-	0.01	cubic
AA-172B-1-5	0.98	2.02	-	-	-	-	-	-	-	0.00	cubic
AA-172B-1-6	0.98	2.01	-	-	-	-	-	-	-	-	cubic
AA-172B-3-1	0.97	2.00	-	-	-	0.02	-	-	-	-	marcasite
AA-172B-3-4	0.99	2.00	-	-	-	0.02	-	-	-	-	cubic
AA-172B-3-5	0.98	2.01	-	-	-	0.01	-	-	-	-	cubic
CC-25A-1	0.97	2.02	-	-	-	0.01	-	-	-	-	cubic
CC-25A-2	0.98	2.01	-	-	-	0.01	-	-	-	-	cubic
CC-25A-3	0.95	2.04	-	-	-	-	-	-	-	-	cubic
CC-25A-4	0.97	2.02	-	-	-	0.01	-	-	-	-	cubic
59CC-8B-1	0.00	1.53	-	-	0.02	-	-	1.44	-	-	sphalerite
59CC-8B-2	0.01	1.53	-	-	0.01	-	-	1.46	-	-	sphalerite
59CC-8B-3	0.96	2.02	0.01	-	-	0.01	-	-	-	-	cubic
59CC-8B-4	0.99	1.99	-	-	-	0.01	-	-	-	-	cubic
59CC-54C-1	0.97	2.00	0.01	-	-	0.01	-	-	-	-	cubic
59CC-54C-3	0.99	2.01	-	-	-	-	-	-	-	-	cubic
59CC-54C-p1	0.12	0.05	-	-	0.04	-	-	-	0.01	2.78	
59CC-54C-p1	0.08	0.10	-	-	0.03	0.01	-	-	0.01	2.77	
59CC-54C-p1	0.82	1.73	-	-	0.01	0.03	-	-	-	0.40	
59CC-54C-p1	1.00	1.98	0.01	-	-	-	-	-	-	-	
59CC-54C-p1	0.88	1.83	0.01	-	-	0.02	-	-	-	0.25	
59CC-54C-p1	0.97	1.97	0.01	-	-	0.04	-	-	-	0.01	
59CC-54C-p1	0.88	1.69	0.01	-	0.01	0.01	-	-	-	0.39	
59CC-54C-p1	0.92	1.93	0.01	-	-	0.03	0.01	-	-	0.10	
59CC-54C-p1	0.98	1.99	0.01	0.01	-	0.01	-	-	-	-	
59CC-54C-p1	0.99	2.00	0.01	-	-	-	-	-	-	-	
59CC-54C-p1	0.96	2.00	0.02	0.01	-	0.01	-	-	-	-	
59CC-54C-p1	1.01	1.95	0.01	-	-	-	-	-	-	0.02	Profile on Py cluster (cubic)
59CC-54C-p1	0.96	2.01	0.01	0.01	-	0.01	-	-	-	-	
59CC-54C-p1	0.95	2.03	0.01	-	-	0.01	-	-	-	-	
59CC-54C-p1	0.99	2.00	0.01	-	-	-	-	-	-	-	
59CC-54C-p1	0.97	2.01	0.01	-	-	-	-	-	-	-	
59CC-54C-p1	0.97	2.01	0.01	-	-	0.01	-	-	-	-	
59CC-54C-p1	0.98	2.00	0.01	-	-	0.01	-	-	-	-	
59CC-54C-p1	1.03	1.93	0.01	-	-	0.01	-	-	-	0.02	
59CC-54C-p1	1.11	1.84	0.01	-	-	0.01	-	-	-	0.02	
59CC-54C-p1	1.09	1.87	-	-	-	0.01	-	-	-	0.02	
59CC-54C-p1	1.03	1.93	-	-	-	0.01	-	-	-	0.02	
59CC-54C-p1	0.97	2.01	0.01	-	-	0.02	-	-	-	0.00	
59CC-54C-p1	0.98	1.99	-	-	-	0.01	-	-	-	0.01	
59CC-54C-p1	0.96	2.02	-	-	-	0.01	-	-	-	-	
59CC-54C-p1	0.97	1.99	0.01	-	-	0.03	-	-	-	-	
59CC-25B-1	0.99	2.00	-	-	-	0.01	-	-	-	-	framboid
59CC-25B-2	0.98	2.02	-	-	-	-	-	-	-	-	framboid

59CC-25B-3	0.99	2.01	-	-	-	-	-	-	-	-	framboid
59CC-25B-4	0.99	2.00	-	-	-	0.01	-	-	-	-	framboid
59CC-25B-5	0.98	2.01	-	-	-	-	-	-	-	-	framboid
59CC-25B-6	1.01	1.99	-	-	-	-	-	-	-	-	framboid
59CC-25B-8	0.98	2.02	-	-	-	-	-	-	-	-	framboid
59CC-25B-9	0.99	2.01	-	-	-	-	-	-	-	-	concentric
59CC-25B-10	1.05	1.95	-	-	-	-	-	-	-	0.01	
59CC-25B-11	1.00	1.99	-	-	-	-	-	-	-	-	
59CC-25B-12	1.01	1.99	-	-	-	-	-	-	-	-	
59CC-25B-13	0.60	1.36	-	-	0.01	-	-	-	-	1.02	
59CC-25B-14	0.56	1.33	-	-	0.01	-	-	-	-	1.09	framboids in
59CC-25B-15	2.17	0.38	-	0.01	-	-	-	-	-	0.44	O.M
59CC-25B-16	0.37	1.31	-	-	0.01	-	-	-	-	1.30	
59CC-25B-17	0.36	1.30	-	-	0.01	-	-	-	-	1.33	
59CC-25B-18	0.40	1.28	-	-	0.01	-	-	-	-	1.31	
59CC-25B-19	0.46	1.20	-	0.01	0.02	-	-	-	-	1.32	
59CC-25C-p1	0.96	2.03	-	-	-	0.01	-	-	-	-	
59CC-25C-p1	0.98	2.01	-	-	-	0.01	-	-	-	-	
59CC-25C-p1	0.97	2.03	-	-	-	0.00	-	-	-	-	framboid
59CC-25C-p1	0.96	2.03	-	-	-	0.01	-	-	-	-	
59CC-25C-p1	0.97	2.02	-	-	-	0.01	-	-	-	-	
59CC-25C-p1	0.96	2.04	-	-	-	-	-	-	-	-	
59CC-25C-p2	0.97	2.03	-	-	-	-	-	-	-	-	marcasite
59CC-25C-p2	0.97	2.02	-	-	-	-	-	-	-	-	marcasite
59CC-25C-p2	0.98	2.02	-	-	-	-	-	-	-	-	marcasite
59CC-25C-p3	0.98	2.02	-	-	-	-	-	-	-	-	cubic
59CC-25C-p3	0.97	2.02	-	-	-	0.01	-	-	-	-	cubic
59CC-25C-p3	0.98	2.02	-	-	-	-	-	-	-	-	cubic
59CC-25C-1	1.02	1.98	-	-	-	-	-	-	-	-	framboid
59CC-25C-2-1	0.98	2.02	-	-	-	-	-	-	-	-	framboid
59CC-25C-2-2	0.99	2.00	-	-	-	-	-	-	-	-	framboid
59CC-25C-2-5	0.96	2.04	-	-	-	-	-	-	-	-	framboid
59CC-25C-2-6	0.98	2.02	-	-	-	0.01	-	-	-	-	framboid

Table 30: EMPA values in wt% corresponding to Profile A-B and C-D, projected on Figure 81, A and B. Detection Limit (D.L) in ppm.

A-B	**Wt%**	D.L ppm	**Wt%**	D.L ppm	**Wt%**	D.L ppm	**Wt%**	D.L ppm
Point	**U**	U	**Fe**	Fe	**S**	S	**Ti**	Ti
1	**74.62**	2921	**0.25**	2036	**0.07**	709	**0.05**	499
2	**74.37**	2939	**0.27**	1859	**0.16**	709	**0.00**	496
3	**68.10**	2863	**0.35**	1917	**0.11**	761	**0.04**	503
4	**70.86**	2828	**0.36**	1873	**0.98**	725	**0.07**	503
5	**69.69**	2861	**0.29**	2000	**1.68**	653	**0.07**	486
6	**72.97**	2917	**0.32**	1981	**0.08**	711	**0.09**	507
7	**72.96**	2900	**0.39**	1988	**0.07**	720	**0.06**	486
8	**72.12**	2826	**0.40**	2032	**0.07**	805	**0.09**	485
9	**75.11**	2860	**0.39**	1984	**0.18**	712	**0.11**	507
10	**18.62**	2146	**37.64**	2181	**33.30**	1097	**0.01**	431
11	**0.65**	1686	**48.55**	1966	**43.28**	1112	**0.00**	0
12	**29.64**	2282	**27.61**	2009	**22.69**	907	**0.03**	429
13	**67.40**	2822	**0.91**	2055	**0.39**	769	**0.04**	478
14	**74.14**	2858	**0.16**	2118	**0.16**	737	**0.02**	500
15	**77.13**	2964	**0.30**	2041	**0.04**	793	**0.01**	516
16	**74.27**	2893	**0.41**	1825	**0.07**	698	**0.03**	497
17	**77.30**	2944	**0.29**	2039	**0.09**	737	**0.01**	509
18	**74.94**	2955	**0.25**	2027	**0.08**	764	**0.02**	502
19	**70.24**	2867	**0.37**	2061	**0.03**	848	**0.09**	478
20	**74.65**	2797	**0.34**	1878	**0.00**	0	**0.11**	501

C-D	**Wt%**	D.L ppm	**Wt%**	D.L ppm	**Wt%**	D.L ppm	**Wt%**	D.L ppm
Point	**U**	U	**Fe**	Fe	**S**	S	**Ti**	Ti
1	**72.48**	2898	**0.9**	1996	**0.07**	691	**0.19**	499
2	**46.07**	2441	**0.57**	1621	**0.28**	564	**0**	392
3	**68.8**	2797	**0.42**	2100	**0.09**	645	**0.04**	466
4	**74.46**	3104	**0.9**	2015	**0.06**	613	**0.14**	507
5	**72.94**	3013	**1.08**	1826	**0.01**	704	**0.27**	508
6	**70.89**	2964	**0.84**	2061	**0.02**	755	**0.3**	493
7	**72.68**	2829	**1.11**	2039	**0.01**	782	**0.29**	509
8	**74.19**	2973	**0.72**	2104	**0.05**	785	**0.11**	501
9	**75.19**	2936	**0.99**	1930	**0.01**	747	**0.11**	509
10	**62.99**	2754	**0.87**	1954	**0.23**	761	**0.18**	450
11	**69.17**	2780	**1.23**	1850	**0.06**	693	**0.24**	484
12	**51.75**	2614	**0.6**	1787	**0.18**	599	**0.05**	405
13	**74.23**	2911	**1.17**	1949	**0**	-8	**0.21**	512
14	**75.56**	2935	**1.08**	2135	**0.05**	720	**0.19**	507
15	**38.13**	2176	**3.69**	1378	**0.34**	594	**0.04**	324
16	**76.39**	2956	**1.11**	2080	**0**	-3	**0.1**	516
17	**67.81**	2866	**1.08**	2098	**0.07**	637	**0.15**	476
18	**66.89**	2828	**0.93**	1659	**0.13**	510	**0.01**	458
19	**66.77**	2701	**0.9**	1948	**0.04**	737	**0.09**	468
20	**71.4**	2855	**1.14**	1880	**0.07**	767	**0.1**	489

Résumé

L'objectif de la thèse concerne l'analyse du système matières organiques (carbone)-uranium-sulfure qui contrôle la formation du gisement d'uranium de type de roll-front au Zoovch Ovoo (Mongolie). La formation cénomanienne du Sainshand est constituée de sédiments continentaux silicoclastiques déposés dans des milieux fluvio-lacustres. Le système global est en début de diagénèse et n'a pas été affecté par un enfouissement significatif, dont le maximum est estimé à <600 m. L'ensemble de l'étude indique que l'aquifère principal a été le siège probable d'activité microbienne subcontinue, qui est attestée par la formation à différents stades de l'histoire du bassin de pyrites dont les caractéristiques isotopiques attestent de processus complexes de fractionnement. La présence de matière organique en quantité significative et des pyrites peut expliquer l'efficacité du piège redox pour la réduction de l'uranium. Le modèle métallogénique présenté est celui d'un système mixte ou un processus de type roll-front qui est lié aux caractéristiques sédimentologiques de cette zone se superpose à un piège redox particulier assisté par les bactéries.

Mots clés: uranium, gisement, bactéries, roll-front, Zoovch Ovoo, Mongolie

Abstract

The objective of the PhD thesis concerns the analysis of the processes governing the carbon-uranium-sulfide system in the aquifers of the roll-front type Zoovch Ovoo uranium-deposit (Mongolia). The Cenomanian Sainshand Formation hosting the ore deposit contains reservoirs made of siliciclastic sediments deposited in fluvio-lacustrine settings. It appears that the uranium ore deposit at Zoovch Ovoo is primarily controlled by the distribution of the detrital organic matter in the sedimentary system as well as by the permeability network allowing the input of S, U and micro-organisms. The rather shallow aquifers probably underwent a nearly continuous bacterial activity which is responsible of many chemical features and processes controlling the U and sulfide precipitation. However, main uranium deposition events occur since the beginning of exhumation when enhanced fluid movement sustains roll-front activity. The latter displaces and combines the ingredients of the biochemical trap, allowing progressive enrichment in uranium through time.

Key words: uranium, deposit, bacteria, roll-front, Zoovch Ovoo, Mongolia